

AD-A267 972

93-18527

OSA Proceedings on  
**ULTRAFAST ELECTRONICS AND  
OPTOELECTRONICS**

**Volume 14**

**Edited by  
Jagdeep Shah and Umesh Mishra**

**Proceedings of the Topical Meeting  
January 25-27, 1993  
San Francisco, California**

*Cosponsored by*  
**Optical Society of America  
IEEE/Lasers and Electro-Optics Society**

*In cooperation with*  
**IEEE/Electron Devices**

*Supported by*  
**Air Force Office of Scientific Research  
National Science Foundation  
Office of Naval Research**

**Optical Society of America  
2010 Massachusetts Avenue, NW  
Washington, DC 20036-1023  
(202) 223-8130**

**OSA Proceedings on**  
**ULTRAFAST ELECTRONICS AND**  
**OPTOELECTRONICS**

**Volume 14**

**Edited by**  
**Jagdeep Shah and Umesh Mishra**

**Proceedings of the Topical Meeting**  
**January 25-27, 1993**  
**San Francisco, California**

*Cosponsored by*  
**Optical Society of America**  
**IEEE/Lasers and Electro-Optics Society**

*In cooperation with*  
**IEEE/Electron Devices**

*Supported by*  
**Air Force Office of Scientific Research**  
**National Science Foundation**  
**Office of Naval Research**

**Optical Society of America**  
**2010 Massachusetts Avenue, NW**  
**Washington, DC 20036-1023**  
**(202) 223-8130**

Articles in this publication may be cited in other publications. In order to facilitate access to the original publication source, the following form for the citation is suggested:

Name of Author(s), Title of Paper, OSA Proceedings on Ultrafast Electronics and Optoelectronics, Jagdeep Shah and Umesh Mishra, eds. (Optical Society of America, Washington, DC 1993), Vol. 14, pp. xx-xx.

ISBN Number            1-55752-275-8

LC Number            93-84929

Copyright ©1993, Optical Society of America

Individual readers of this proceedings and libraries acting for them are permitted to make fair use of the material in it as defined by Sections 107 and 108 of the U.S. Copyright Law, such as to copy an article for use in teaching or research, without payment of fee, provided that such copies are not sold. Copying for sale or copying for use that exceeds fair use as defined by the Copyright Law is subject to payment of copying fees. The code 1-55752-275-8/93/\$6.00 gives the per-article copying fee for each copy of the article made beyond the free copying permitted under Sections 107 and 108 of the U.S. Copyright Law. The fee should be paid through the Copyright Clearance Center, Inc., 21 Congress Street, Salem, MA 01970.

Permission is granted to quote excerpts from articles in this proceedings in scientific works with the customary acknowledgment of the source, including the author's name, name of the proceedings, page, year, and name of the Society. Reproduction of figures and tables is likewise permitted in other articles and books provided that the same information is printed with them and notification is given to the Optical Society of America. Republication or systematic or multiple reproduction of any material in this proceedings, including contents and abstracts, is permitted only under license from the Optical Society of America; in addition, the Optical Society may require that permission also be obtained from one of the authors. Electrocopying or electrostorage of any material in this proceedings is strictly prohibited. Address inquiries and notices to the Director of Publications, Optical Society of America, 2010 Massachusetts Avenue, NW, Washington, DC 20036. In the case of articles whose authors are employees of the United States Government or its contractors or grantees, the Optical Society of America recognizes the right of the United States Government to retain a nonexclusive, royalty-free license to use the author's copyrighted article for United States Government purposes.

The views and conclusions in this proceedings are those of the author(s) and should not be interpreted as necessarily representing endorsements, either expressed or implied, of the editors or the Optical Society of America.

Printed in the U.S.A.

**OSA Proceedings on**

**ULTRAFAST ELECTRONICS AND OPTOELECTRONICS**

**Volume 14**

Accession For	
NTIS CRA&I	<input checked="checked" type="checkbox"/>
DTIC TAB	<input type="checkbox"/>
Unannounced	<input type="checkbox"/>
Justification	
By	
Distribution /	
Availability Codes	
Dist	Avail and/or Special
A-1	

**DTIC QUALITY INSPECTED 3**



---

## **Technical Program Committee**

---

**Jagdeep Shah, Chair, AT&T Bell Laboratories**

**Umesh Mishra, Program Chair, University of California, Santa Barbara**

**F. Capasso, AT&T Bell Laboratories**

**H. C. Casey, Duke University**

**H. Fetterman, University of California, Los Angeles**

**M. Fischetti, IBM T. J. Watson Research Center**

**D. Grischkowski, IBM T. J. Watson Research Center**

**E. P. Ippen, Massachusetts Institute of Technology**

**M. C. Nuss, AT&T Bell Laboratories**

**M. Rodwell, University of California, Santa Barbara**

**H. Sakaki, University of Tokyo, Japan**

**P. Tasker, Fraunhofer Institute, Germany**

**C. Weisbuch, Thomson CSF, France**

**N. Yokoyama, Fujitsu Ltd., Japan**

---

## **Advisory Committee**

---

**D. M. Bloom, Stanford University**

**C. H. Lee, University of Maryland**

**F. Leonberger, United Technologies**

**G. A. Mourou, University of Michigan**

**T. C. L. G. Sollner, MIT Lincoln Laboratory**

## Contents

Preface . . . . .	xiii
-------------------	------

---

### Ultrafast Optoelectronic Devices

---

Overview of the Applications of High-Speed Optoelectronics . . . . .	1
<i>Tetsuhiko Ikegami and Ken'ichi Kubodera</i>	
Spectral-Hole Burning and Carrier Heating Nonlinearities in Active Waveguides (invited) . . . . .	6
<i>C. T. Hultgren, K. L. Hall, G. Lenz, D. J. Dougherty, and E. P. Ippen</i>	
Carrier Transport Effects in High Speed Quantum Well Lasers (invited) . . . . .	13
<i>Radhakrishnan Nagarajan</i>	
8.6-GHz Active, Passive, and Hybrid Mode-Locking of InGaAsP Extended-Cavity MQW Lasers with Monolithically Integrated Saturable Absorbers . . . . .	17
<i>P. B. Hansen, G. Raybon, U. Koren, B. I. Miller, M. G. Young, M. A. Newkirk, C. A. Burrus, and P. P. Iannone</i>	
Femtosecond Periodic Gain Vertical-Cavity Semiconductor Lasers . . . . .	21
<i>Wenbin Jiang, Mitsuaki Shimizu, Richard P. Mirin, Thomas E. Reynolds, and John E. Bowers</i>	
Picosecond Gain Dynamics in Vertical Cavity Surface Emitting Laser: Transient Carrier Heating and Gain Enhancement . . . . .	25
<i>Gary Wang, Radhakrishnan Nagarajan, Dan Tauber, and John E. Bowers</i>	

Transient Pulse-Response of InGaAs/InGaAsP Distributed Feedback Lasers for Multigigabit Transmission Systems . . . . .	29
<i>J. Kovac, C. Kaden, H. Schweizer, M. Klenk, R. Weinmann, and E. Zielinski</i>	
Ultrafast Heterobarrier Metal-Semiconductor-Metal Photodetectors . . . . .	33
<i>E. Stein Von Kamienski, H. G. Roskos, R. Kersting, J. Plettner, S. V. Averin, H. -J. Geelen, A. Kohl, B. Spangenberg, K. Leo, H. Kurz, and O. Hollricher</i>	
Ultrafast Photodection with an InAlAs/InGaAs Heterojunction Bipolar Transistor . . . . .	37
<i>T. F. Carruthers, M. Y. Frankel, and C. S. Kyono</i>	
Picosecond InAlGaAs Photovoltaic Detector with a Graded Superlattice Structure . . . . .	41
<i>J. M. Liu , L. P. Chen, C. T. Liu, C. A. Burrus, and A. Y. Cho</i>	
110 GHz Double Heterostructure GaInAs/InP p-i-n Photodiode . . . . .	45
<i>Yih-Guei Wey, Kirk S. Giboney, John E. Bowers, Mark J. W. Rodwell, Pierre Silvestre, Prabhu Thiagarajan, and Gary Y. Robinson</i>	
Ultrafast Carrier Transfer in GaAs MSM-Diodes . . . . .	49
<i>R. Kersting, K. Leo, J. Plettner, S. Averin, and H. Kurz</i>	
Ultrafast Metal-Semiconductor-Metal Photodetectors with Nanometer Scale Finger Spacing and Width . . . . .	53
<i>Mark Y. Liu , Stephen Y. Chou, Sotiris Alexandrou, and Thomas Y. Hsiang</i>	

---

### High Speed Electronic Devices

---

A 50 ps Cycle-Time Microprocessor: The Technological Challenges (invited) . . . . .	56
<i>Robert W. Keyes and Mark B. Ketchen</i>	
Ultra-Deep Submicron Si MOSFETs with $f_T$ Exceeding 100 GHz (invited) . . . . .	60
<i>R. H. Yan, K. F. Lee, Y. O. Kim, D. Y. Jeon, D. M. Tennant, and E. H. Westerwick</i>	

Resonant Tunneling Transistors (invited) . . . . .	65
<i>A. C. Seabaugh, E. A. Beam, Y. -C. Kao, J. H. Luscombe, and J. N. Randall</i>	
Theory of Ultra High Frequency Performance Heterojunction Bipolar Transistors (invited) . . . . .	71
<i>A. A. Grinberg and S. Luryi</i>	
Physics of Electron Transport in Ultra High Speed InP/GaInAs Heterojunction Bipolar Transistors (invited) . . . . .	77
<i>Dan Ritter, R. A. Hamm, A. Feyngenson, P. R. Smith, and J. Bude</i>	
InP High Electron Mobility Transistors: Status and Promise (invited) . . . . .	82
<i>Loi D. Nguyen</i>	
High Speed Heterojunction JFETs Grown by Non-Hydride MOCVD . . . . .	85
<i>M. M. Hashemi, J. B. Shealy, S. P. DenBaars, and U. K. Mishra</i>	
Resonant-Tunneling Transmission-Line Relaxation Oscillator . . . . .	91
<i>F. R. Brown</i>	
Fabrication of Microwave Compatible, Monolithic, High-Speed In <sub>0.53</sub> Ga <sub>0.47</sub> As/AlAs and InAs/AlSb Resonant Tunneling Diodes . . . . .	95
<i>E. Özbay, D. M. Bloom, D. H. Chow, and J. N. Schulman</i>	

---

### Terahertz Transients

---

THz Beam Emission by Carrier Transport or by Optical Rectification (invited) . . . . .	99
<i>X. -C. Zhang, Y. Jin, T. D. Hewitt, X. F. Ma, L. Kingsley, and M. Weiner</i>	
Optical Generation of Terahertz Pulses in Quantum Wells . . . . .	105
<i>Paul C. M. Planken, Martin C. Nuss, Igal Brener, Keith W. Goossen, Marie S. C. Luo, Shun Lien Chuang, and Loren Pfeiffer</i>	
Generation and Application of High-Power, 500 fs Electromagnetic Pulses . . . . .	108
<i>D. R. Dykaar, D. You, R. R. Jones, and P. H. Bucksbaum</i>	

All-Electronic Generation of Sub-Picosecond Shock-Waves and Their Application to a Terahertz Spectroscopy System . . . . .	.112
<i>Jeffrey S. Bostak, Daniel W. Van Der Weide, Ikuro Aoki, Bertram A. Auld, and David M. Bloom</i>	
Sub-Picosecond, Terahertz Radiation from High-Intensity Laser Plasmas . . . . .	.116
<i>H. Hamster, A. Sullivan, S. Gordon, R. W. Falcone, and W. White</i>	
Intense THz Beam from Organic Electro-Optic Materials . . . . .	.119
<i>X. -C. Zhang, T. -M. Lu, and C. P. Yakymyshyn</i>	
New Performance Limits of an Ultrafast THz Photoconductive Receiver . . . . .	.123
<i>N. Katzenellenbogen, Hoi Chan, and D. Grischkowsky</i>	

---

### Physics of Semiconductors

---

Application of Ultrafast Optoelectronics to the Characterization of Photonic Crystals (invited) . . . . .	.126
<i>G. Arjavalingam, W. M. Robertson, and S. Y. Lin</i>	
Ultrafast Optoelectronic Field Changes in GaAs . . . . .	.129
<i>T. Dekorsy, H. Heesel, S. Hunsche, T. Pfeifer, H. Mikkelsen, W. Kütt, K. Leo, and H. Kurz</i>	
Velocity Overshoot Dynamics in GaAs up to 200 kV/cm Observed Using Terahertz Radiation . . . . .	.134
<i>J. Son, W. Sha, J. Kim, T. B. Norris, J. F. Whitaker, and G. Mourou</i>	
Phase Relaxation Processes of Excitons in Island-Inserted Quantum Well Structures—Suppression of Relaxation and Giant Quantum Beats . . . . .	.138
<i>T. Matsusue, T. Saiki, M. Kuwata-Gonokami, H. Akiyama, and H. Sakaki</i>	
Observation of Bloch Oscillations in a Semiconductor Superlattice . . . . .	.142
<i>Peter Haring Bolivar, Patrick Leisching, Karl Leo, Jagdeep Shah, and Klaus Köhler</i>	

Femtosecond Optical Response of Low Temperature Grown In <sub>0.53</sub> Ga <sub>0.47</sub> As . . . . .	147
<i>B. C. Tousley, S. M. Mehta, A. I. Lobad, P. J. Rodney, P. M. Fauchet, and P. Cooke</i>	

Carrier Scattering and Excitonic Effects on Electron-Hole-Pair Diffusion Measured with Optical Fiber Probing Technique . . . . .	151
<i>Hidefumi Akiyama, Toshio Matsusue, and Hiroyuki Sakaki</i>	

---

### Novel Sources and Techniques

---

Passively Mode-Locked Diode-Pumped Solid-State Lasers for Optoelectronics Applications . . . . .	155
<i>U. Keller, T. H. Chiu, J. F. Ferguson, and K. J. Weingarten</i>	

NLTL-Based System for mm-Wave and Sub-mm-Wave Free-Space Electromagnetic Measurements . . . . .	158
<i>Y. Konishi, M. Case, R. Yu, M. J. W. Rodwell, and M. Kamegawa</i>	

Ultrafast Scanning Microscopy . . . . .	162
<i>S. Weiss, D. Botkin, and D. S. Chemla</i>	

Picosecond Electrical Sampling Using a Scanning Force Microscope . . . . .	166
<i>A. S. Hou, F. Ho, and D. M. Bloom</i>	

Applications of Time-Lens Optical Systems . . . . .	169
<i>M. T. Kauffman, A. A. Godil, W. C. Banyai, and D. M. Bloom</i>	

Femtosecond Field Emission Camera: A Device for Continuously Observing the Motion of Single Adsorbed Atoms and Molecules . . . . .	172
<i>Gary M. McClelland, Harry Heinzlmann, and Fumiya Watanabe</i>	

---

### (Sub)Millimeter Wave Devices

---

High Frequency Solid State Sources Using Ultrafast Techniques . . . . .	175
<i>D. V. Plant, D. C. Scott, M. Martin, F. K. Oshita, and H. R. Fetterman</i>	

On-Wafer Optoelectronic Techniques for Millimeter-Wave Generation, Control, and Circuit Characterization . . . . .	.179
<i>Sheng-Lung L. Huang, Chi H. Lee, and Hing-Loi A. Hung</i>	

Optoelectronic Phase Locking of Microwave Signals up to 4GHz Using a Laser-Diode-Based Electro-Optic Harmonic Mixer . . . . .	.183
<i>Ci-Ling Pan, Kai-Yuan Tang, and Hsiao-Hua Wu</i>	

---

### Photoconductive and Electro-Optic Sampling

---

Picosecond Detector, Optical Temporal Analyzer, and Free-Standing Circuit Probe (invited) . . . . .	.186
<i>J. Nees, S. Williamson, J. Kim, and S. Gupta</i>	

Electro-Optic Sampling at 150 fs . . . . .	.189
<i>U. D. Keil and D. R. Dykaar</i>	

Low-Temperature MBE Growth of III-V Materials on Si Substrates . . . . .	.193
<i>Michael Y. Frankel, Thomas F. Carruthers, and Bijan Tadayon</i>	

Photoconductive Sampling Circuits Using Low-Temperature GaAs Interdigitated Switches . . . . .	.197
<i>J. Allam, K. Ogawa, J. White, N. de B. Baynes, J. R. A. Cleaver, I. Ohbu, T. Tanoue, and T. Mishima</i>	

---

### Transmission Lines

---

High-Bandwidth Transmission Lines Using Low-Temperature-Grown-GaAs-on Quartz . . . . .	.201
<i>H. Cheng and J. F. Whitaker</i>	

High Speed Limits of Coplanar Transmission Lines . . . . .	.205
<i>U. D. Keil, D. R. Dykaar, A. F. J. Levi, R. F. Kopf, L. N. Pfeiffer, K. W. Goossen, S. B. Darack, and K. W. West</i>	

Subpicosecond Electrical Pulse Generation in GaAs by Nonuniform Illumination of Series and Parallel Transmission-Line Gaps . . . . .	.209
<i>Sotiris Alexandrou, Chia-Chi Wang, Roman Sobolewski, and Thomas Y. Hsiang</i>	

---

### Ultrafast Probes of Materials/Devices/Circuits

---

Subpicosecond GaAs Wafer Probe System . . . . .	.213
<i>M. S. Shakouri, A. Black, B. A. Auld, and D. M. Bloom</i>	
Highly Reproducible Optoelectronic Wafer Probes with Fiber Input . . . . .	.216
<i>M. D. Feuer, S. C. Shunk, M. C. Nuss, P. R. Smith, H. H. Law, and C. A. Burrus</i>	
Electro-Optic Sampling of High Speed Nonlinear Devices . . . . .	.220
<i>Kok Wai Chang and Wayne V. Sorin</i>	
120-GHz-Bandwidth Characterization of Microwave Passive Devices Using External Silicon-On-Sapphire Photoconductive Sampling Probe . . . . .	.224
<i>J. Kim, J. Son, S. Wakana, J. Nees, S. Williamson, J. Whitaker, and G. Mourou</i>	

---

### Superconductors

---

Optical Control of High Speed Circuit Using Picosecond High Temperature Superconductor Opening Switches . . . . .	.228
<i>Yuan-Qun Liu, Yi-Sern Lai, Wei-lou Cao, Chi H. Lee, S. N. Mao, X. X. Xi, T. Venkatesan, Zhi-Yuan Shen, Philip Pang, Dennis J. Kountz, and William L. Holstein</i>	
Response of a Nb/Al <sub>2</sub> O <sub>3</sub> /Nb Tunnel Junction to Picosecond Electrical Pulses . . . . .	.231
<i>C. Karadi, S. Verghese, C. A. Mears, J. Orenstein, P. L. Richards, and A. T. Barfknecht</i>	
Ultrafast Optical and Optoelectronic Response of Y-Ba-Cu-O . . . . .	.234
<i>T. Gong, L. X. Zheng, Y. Kostoulas, W. Xiong, W. Kula, K. B. Ucer, Roman Sobolewski, and P. M. Fauchet</i>	



Terahertz Spectroscopy of Superconducting Thin Film $\text{Ba}_{0.6}\text{K}_{0.4}\text{BiO}_3$ . . . . .	.238
<i>Yongqian Liu, John F. Whitaker, and Christine E. Platt</i>	
Ultrafast Quasiparticles Dynamics in High-Temperature Superconductors . . . . .	.242
<i>W. Albrecht, Th. Kruse, K. Leo, and H. Kurz</i>	
Author Index . . . . .	.246

## Preface

This volume is comprised of papers that were presented at the Fifth Topical Meeting on Ultrafast Electronics and Optoelectronics (formerly Picosecond Electronics and Optoelectronics), held in San Francisco, January 23-25, 1993. The purpose of this topical meeting, since its inception in 1985, has been to foster greater interaction between researchers in the electronics and optoelectronics communities who share a common interest in the physics and technology of ultrafast electronics and optoelectronics devices, their multigigahertz applications, and ultrafast measurement techniques. The number of abstracts submitted to this meeting was considerably larger than for the previous meetings, indicating the appeal of this interdisciplinary approach and the growing importance of this field. This preface serves as a summary and a guide to these Proceedings.

Ultrafast Optoelectronic Devices is concerned with high speed electronic devices and presents a discussion of the state-of-the-art devices such as resonant tunneling transistors, bipolar transistors and high electron-mobility transistors, and >100 GHz Si MOSFETs.

High Speed Electronic Devices discusses state-of-the-art optoelectronic devices such as lasers and detectors. Gain dynamics and carrier transport in semiconductor lasers, mode-locking of lasers, integrated laser-modulators, vertical cavity lasers, metal-semiconductor-metal photodetectors, HBT photodetectors, and photovoltaic photodetectors are some of the topics discussed in this section.

Terahertz Transients is concerned with the physics and technology of generation and detection of terahertz transients from semiconductors, and applications of terahertz transients generated by high power femtosecond lasers.

Physics of Semiconductors covers physics of semiconductors. This part includes a discussion of photonic bandgap, high field transport, Bloch oscillations, and coherent effects in semiconductor nanostructures.

Novel Sources and Techniques covers a discussion of novel sources, such as mode-locked diode-pumped solid-state lasers, as well as novel techniques such as high spatial and temporal resolution probes using scanning force microscopes, and time-reversal using a temporal imaging system.

(Sub)Millimeter Wave Devices covers generation, and control of millimeter- and submillimeter-wave radiation from solid state sources using picosecond lasers, and applications of such sources for circuit characterization.

Photoconductive and Electro-Optic Sampling covers recent advances in the field of photoconductive and electro-optic sampling techniques and materials; Transmission Lines covers recent advances in generation and propagation of sub-picosecond pulses using transmission lines; and

Ultrafast Probes of Materials/Devices/Circuits covers recent advances in ultrafast probes of materials, devices, and circuits.

The final section, Superconductors, covers the interaction of ultrashort pulses with superconductors, and its application in the optical control of an electrical circuit.

We gratefully acknowledge the grants from the Air Force Office of Scientific Research (AFOSR), the Office of Naval Research (ONR), and the National Science Foundation (NSF), which provided the funding for the meeting. We also take this opportunity to thank the members of the Advisory Committee and the Technical Program Committee for their substantial contributions to the success of the meeting. Finally, we would like to thank Monica Malouf and Ellen Murphy of the Optical Society of America for a thoroughly professional management of the meeting.

Jagdeep Shah  
*AT&T Bell Laboratories*

Umesh Mishra  
*University of California, Santa Barbara*

---

# **Ultrafast Optoelectronic Devices**

---

## Overview of the Applications of High-Speed Optoelectronics

Tetsuhiko Ikegami

*NTT R&D Headquarters, 1-1-7 Uchisaiwaicho, Chiyoda-ku, Tokyo 100, Japan*

Ken'ichi Kubodera

*NTT Interdisciplinary Research Laboratories, 3-9-11 Midoricho, Musashino-shi, Tokyo 180, Japan*

### ABSTRACT

Picosecond optical devices such as monolithic and hybrid OEICs, LiNbO<sub>3</sub> modulators and switches, and all-optical picosecond switches are reviewed for future high-bit-rate optical transmission and signal processing.

### 1. Introduction

Applications of high-speed opto-electronics are important technologies not only for the sophistication of today's high-bit-rate long-haul optical communication systems, but also for the realization of future ultra-high-bit-rate optical signal processing systems [1-3]. Key devices are hybrid or monolithic OEICs, LiNbO<sub>3</sub> modulators and switches, mode-locked LDs, and all-optical picosecond switches such as bistable memory LDs, and ultra-fast nonlinear-optical switches.

### 2. Applications of High-Speed Opto-Electronics

#### A. Sophistication in Today's Communication Systems

Figure 1 shows a hybrid receiver OEIC, consisting of an InGaAs twin p-i-n photodiode and a GaAs distributed amplifier, using a

small solder bump connection technique which allows precise chip alignment and gives low wire inductance and stray capacitance [4]. A 3-dB bandwidth of more than 22 GHz and a noise current of 19.4 pA/Hz<sup>1/2</sup> were obtained by this module. A 10-Gb/s optical CPFSK heterodyne detection experiment has been conducted using this device [5].

Monolithically integrated OEIC devices have been also investigated extensively. Figure 2 shows the recently reported receiver OEIC consisting of a p-i-n photodiode and a high electron mobility transistor (HEMT), fabricated using Si-planar-doping and Be-ion implantation techniques [6]. The receiver showed a 3-dB-down bandwidth of a 8 GHz and was capable of operation with a 10-Gb/s NRZ signal. Since monolithic OEIC devices have advantages of reduced cost and reliable performance, they are especially suitable for optical interconnection, switching systems, and optical subscriber networks.

A practical transmitter for up to the 10-Gb/s optical signal could be a combination of a single-mode DFB LD and a LiNbO<sub>3</sub> modulator or switch. By employing a LiNbO<sub>3</sub> ridged waveguide and a shielded coplanar traveling-wave electrode, 40-GHz modula-

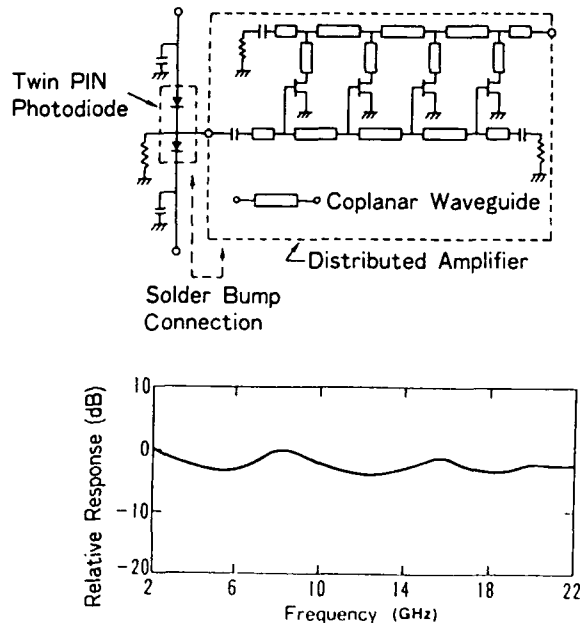


Figure 1. Hybrid photoreceiver OEIC with 23 GHz bandwidth [4.5].

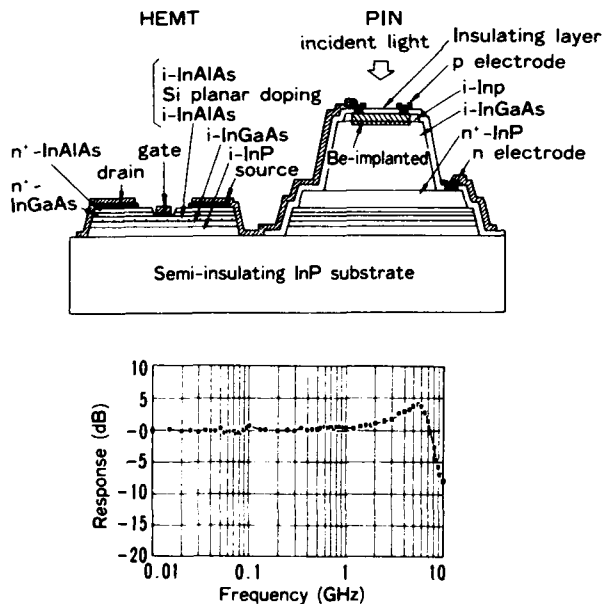


Figure 2. Monolithically integrated receiver OEIC consisting of p-i-n photodiode and HEMT [6].

tion with a low drive voltage of 3.6 V has been achieved at 1.55- $\mu\text{m}$  wavelength (Fig.3) [7]. Many successful high-bit-rate transmission experiments have been carried out using this optical modulator.

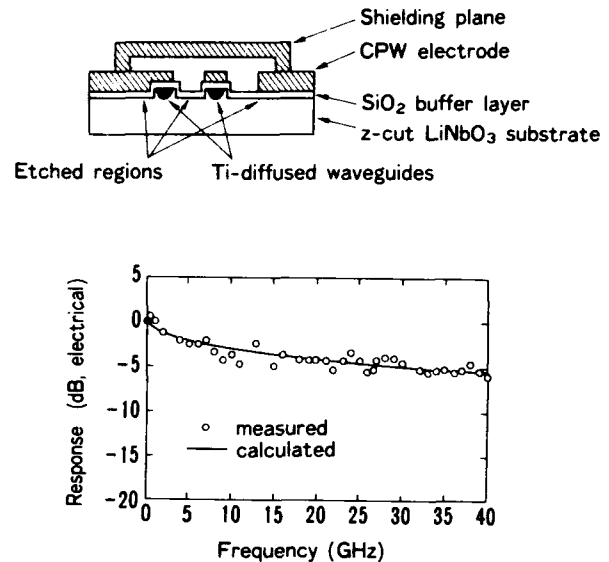


Figure 3.  $\text{LiNbO}_3$  optical modulator with 40 GHz bandwidth [7].

Figure 4 shows a monolithically integrated OOIC consisting of an InGaAs/InAlAs multiple quantumwell (MQW) modulator and an InGaAs/InGaAsP MQW DFB laser. The device size is very small (450  $\mu\text{m}$  in length) and is fabricated by the hybrid crystal growth of MOVPE and MBE [8]. A 3-dB bandwidth of 16 GHz and the drive voltage of 4.0 V have been demonstrated at 1.5- $\mu\text{m}$  wavelength. The output power from the MQW modulator was 6 mW.

## B. Innovation in Future Signal Processing Systems

A variety of new optical devices will be required to realize future optical processing systems such as T b/s transmission and ultrafast optical signal processing, making use of the superiority of the photonics such as broad band and parallel processing properties. Key devices expected at the present stage are high-repetition-rate LDs with picosecond or subpicosecond pulse widths, optical memory and logic devices, and ultrafast TDM switching devices.

A handy mode-locked LD with repetition rate up to 350 GHz has been developed recently using a monolithic colliding-pulse

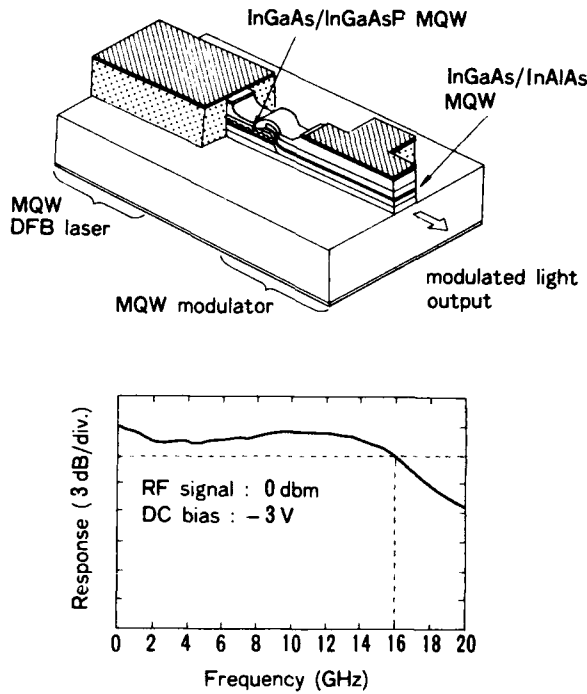


Figure 4. Monolithically integrated OOIC consisting of MQW modulator and DFB laser [8].

mode-locking technique [9]. The minimum pulse width was 640 fs, which is limited ultimately by the physical size of the saturable absorber waveguide.

An optical bistable LD has been reported using a side-light-injection type MQW bistable laser as optical memory and logic devices (Fig.5) [10]. Set-on and set-off operations have been demonstrated with a small control power of 40  $\mu\text{W}$  and switching speed of about 100 ps. The fabrication of the array structure of this device will be desired in the future for the development of optical parallel logic systems.

All-optical TDM gate switches utilizing nonlinear-optical materials (optical Kerr materials) are being studied to obtain much faster switching time than semiconductor devices [11,12]. Optical gating experiments such as signal demultiplexing and optical logic operations have been reported in a number of reports using silica glass fiber switches [13,14]. Figure 6 shows an experiment of a

three-terminal switch using a highly-nonlinear 48 cm-long  $\text{As}_2\text{S}_3$  glass fiber whose length is 1/1000 that of the conventional silica glass fiber [15]. The switching time was measured to be less than the detection resolution of 15 ps and the gate input power was of the order of 1W, which is comparable to the typical peak output power of Er fiber amplifiers.

Figure 7 shows the power versus speed map for various types of all-optical switching devices such as glass fiber switches, semiconductor-doped glass etalon devices [11], and organic switches [16], as compared with semiconductor LD devices and semiconductor O-E hybrid devices such as SEED [17]. It can be seen that glass and organic switches

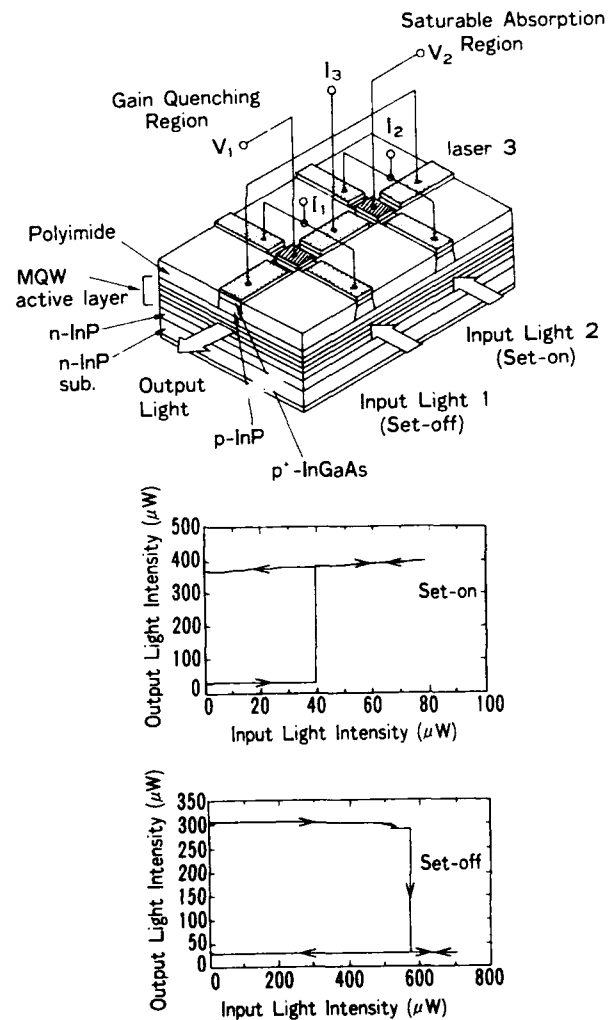


Figure 5. Side-light-injection type MQW bistable laser [10].

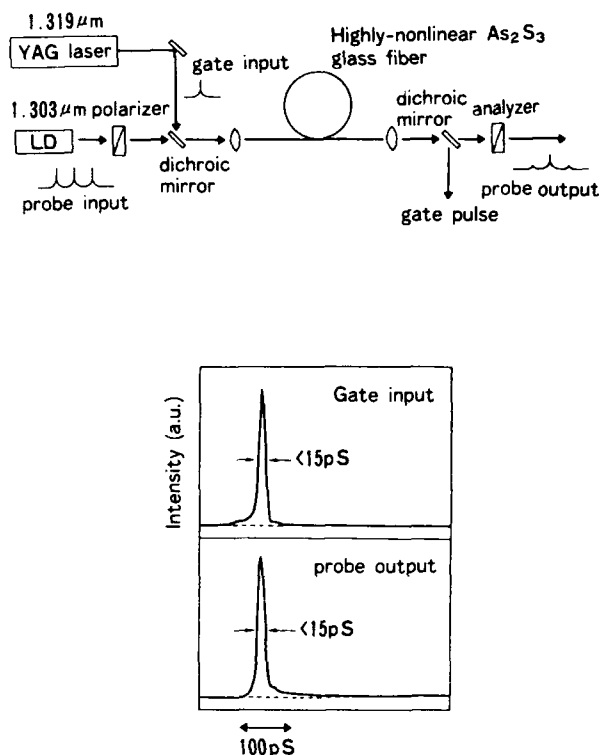


Figure 6. Experiment of three-terminal all-optical fiber switch using a highly-nonlinear chalcogenide glass [15].

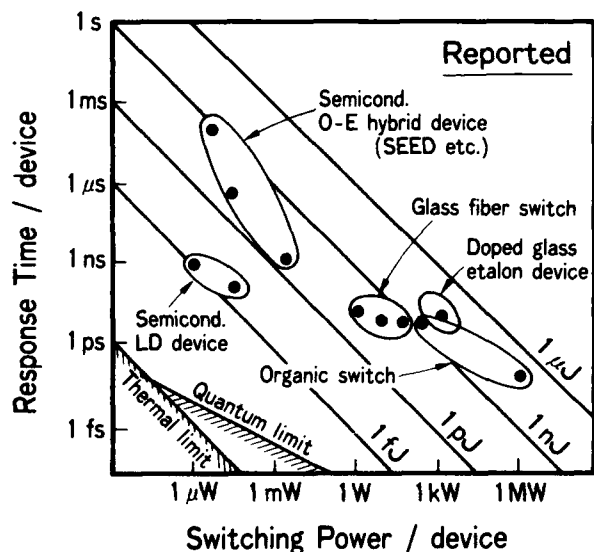


Figure 7. Power versus speed map for several kinds of all-optical switching devices.

will achieve fast switching times of less than 1 ps, while the switching time is restricted by the excited electron's lifetime for semi-

conductor devices. Studies on such nonlinear-optical switching devices are well under way, with importance being placed on material design and device optimizations.

### 3. Conclusion

High-speed optical devices such as receiver OEICs, picosecond modulators and switches, mode-locked LDs, and all-optical switches are key devices for future high-bit-rate optical systems. These devices should be investigated extensively keeping step with optical parallel processing devices and wavelength division switching devices, which are also conceptual devices for the architecture of next-generation systems.

### ACKNOWLEDGMENTS

The authors would like to thank the staff of NTT Opto-electronics Laboratories and NTT Interdisciplinary Research Laboratories for assistance with the publication of this paper.

### REFERENCES

1. P. W. Smith, "On the role of photonic switching in future communications systems," *IEEE Circuits and Devices Magazine* **May**, 9-14 (1987).
2. T. Ikegami and H. Kawaguchi, "Semiconductor devices in photonic switching," *IEEE J. Select. Area. Comm.* **6**, 1131-1140 (1988).
3. T. Ikegami and K. Kubodera, "Nonlinear optical devices for switching applications," in *Technical Digest of IEEE International Conference on Communications* (IEEE Communications Society, Atlanta, 1990), pp.1152-1156.
4. K. Katsura, T. Hayashi, F. Ohira, S. Hata, and K. Iwashita, "A novel flip-chip interconnection technique using solder bumps for high-speed photoreceivers," *IEEE J. Lightwave Tech.* **8**, 1323-1327 (1990).
5. N. Takachio, K. Iwashita, S. Hata, K. Onodera, K. Katsura, and H. Kikuchi, "A 10 Gb/s optical heterodyne detection experiment using a 23 GHz bandwidth balanced receiver," *IEEE*



- Trans. Microwave Theory Tech. **38**, 1900-1905 (1990).
6. Y. Akahori, Y. Akatsu, A. Kohzen, and J. Yoshida, "10-Gb/s high-speed monolithically integrated photoreceiver using InGaAs p-i-n PD and planar doped InAlAs/InGaAs HEMT's," IEEE Photonics Tech. Lett. **4**, 754-756 (1992).
  7. K. Noguchi, O. Mitomi, and M. Yanagibashi, "40 GHz Ti:LiNbO<sub>3</sub> optical modulator with driving voltage of 3.6 V," in *Technical Digest of 4th Optoelectronics Conference* (IEICE, Makuhari, Chiba, 1992), pp. PD4-5.
  8. K. Wakita, I. Kotaka, H. Asai, M. Okamoto, Y. Kondo, and M. Naganuma, "High-speed and low-drive-voltage monolithic multiple quantum-well modulator/DFB laser light source," IEEE Photonics Tech. Lett. **4**, 16-18 (1992).
  9. Y. K. Cher, M. C. Wu, T. Tanbun-Ek, R. A. Logan, and M. A. Chin, "Subpicosecond monolithic colliding-pulse mode-locked multiple quantum well lasers," Appl. Phys. Lett. **58**, 1253-1255 (1991).
  10. H. Uenohara, Y. Kawamura, H. Iwamura, K. Nonaka, H. Tsuda, and T. Kurokawa, "Side-light-injection MQW bistable laser using saturable absorption and gain quenching," Electron. Lett. **28**, 1973-1974 (1992).
  11. K. Kubodera, "Nonlinear optical devices for photonic switching," in *Photonic Switching II*, K. Tada and H. S. Hinton, eds. (Springer-Verlag, Berlin, 1990), pp. 23-29.
  12. K. Kubodera, "Picosecond switching devices and materials," in *Technical Digest of 4th Optoelectronics Conference* (IEICE, Makuhari, Chiba, 1992), pp. 110-111.
  13. B. P. Nelson, K. J. Blow, P. D. Constantine, N. J. Doran, J. K. Lucek, I. W. Marshall, and K. Smith, "All optical Gbit/s switching using nonlinear optical loop mirror," Electron. Lett. **27**, 704-705 (1991).
  14. M. Jinno and T. Matsumoto, "Ultrafast all-optical logic operations in a nonlinear Sagnac interferometer with two pump pulses," in *Technical Digest of Conference on Optical Fiber Communication* (OSA, 1991) p. 48.
  15. M. Asobe, T. Kanamori, and K. Kubodera, "Ultrafast all-optical switching using highly nonlinear chalcogenide glass fiber," IEEE Photonics Tech. Lett. **4**, 362-365 (1992).
  16. P. D. Townsend, J. L. Jackel, G. L. Baker, J. A. Shelburne, and S. Etemad, "Observation of nonlinear optical transmission and switching phenomena in polydiacetylene-based directional couplers," Appl. Phys. Lett. **55**, 1829-1831 (1989).
  17. A. L. Lentine, F. B. McCormick, R. A. Novotny, L. M. F. Chirovsky, L. A. D'asaro, R. F. Kopf, J. M. Kuo, and G. D. Boyd, "A 2 kbit array of symmetric self-electrooptic effect devices," IEEE Photonics Tech. Lett. **2**, 51-53 (1990).

## Spectral-Hole Burning and Carrier Heating Nonlinearities in Active Waveguides

C. T. Hultgren, K. L. Hall, G. Lenz, D. J. Dougherty, and  
E. P. Ippen

*Department of Electrical Engineering and Computer Science and  
Research Laboratory of Electronics, Massachusetts Institute of Technology,  
Cambridge, Massachusetts 02139*

### Abstract

Studies of active waveguides with short optical pulses provide information about fundamental carrier dynamics and nonlinear processes relevant to high speed modulation and optical communication. We investigate these dynamics in AlGaAs amplifiers around 0.8  $\mu\text{m}$  and InGaAsP amplifiers around 1.5  $\mu\text{m}$  using optical pulses approximately 100 fs in duration. Novel measurement techniques are employed to elucidate contributions to both gain and refractive index nonlinearities. By identifying a delay in the onset of carrier heating, we are able to observe an ultrafast dynamic we attribute to spectral-hole burning.

### Introduction

Semiconductor diode lasers offer potential for high-speed optical amplification and all-optical switching. The realization of such devices, however, will require knowledge of their ultrafast gain and refractive index dynamics. These dynamics have been studied previously in the frequency domain via nondegenerate four-wave mixing [1-5] and high-speed modulation response [6-8] experiments. Gain saturation [9] and spectral distortions [10] of short pulses traveling through active waveguides have also been investigated. With two pulse pump-probe experiments we have studied the temporal dynamics of active waveguides directly, on a femtosecond timescale [11-14]. In this paper, we present the results of our most recent studies of gain and refractive index nonlinearities in both AlGaAs and InGaAsP active waveguides. In each material system, we identify ultrafast effects due to two-photon absorption, carrier heating, spectral-hole burning, and an instantaneous refractive index nonlinearity.

### Background

Pump-probe experiments are valuable because they provide direct, time domain measurements of ultrafast nonlinearities in active waveguides. Generally, in these experiments, a beam of short pulses (typically  $\sim 100$  fs) is split into two, a strong pump beam and a weak probe beam. After traveling separate, but approximately equal paths, the two beams are recombined collinearly and are coupled to the active region of a diode laser. After propagating through the diode, the probe beam is selected for detection. A variable stepping stage in the pump path is used to set the delay between pump and probe pulses, and the change in probe transmission or phase is measured as a function of pump-probe delay.

Fig. 1 shows the measured change in probe transmission as a function of pump-probe delay for a bulk InGaAsP diode laser amplifier biased in the gain, transparency and absorption regimes [12,15]. The regimes of operation are distinguished by the long-lived change in probe transmission due to stimulated emission (gain) or absorption (absorption) of the pump. At the transparency point, there are no net stimulated transitions and no step change in probe transmission. Any transient effect due to spectral-hole burning would be expected to have a very fast time constant and an amplitude that scaled with the size and sign of the step. However, the nonlinear dynamics we observe all appear to have the same sign in the three regimes of operation. For instance, all three regimes show a gain compression that recovers with a 700 fs time constant. This compression is due to a heating of the carrier distribution (carrier heating) via free carrier absorption and stimulated transitions. There is an instantaneous gain compression in all three regimes that is associated with two-

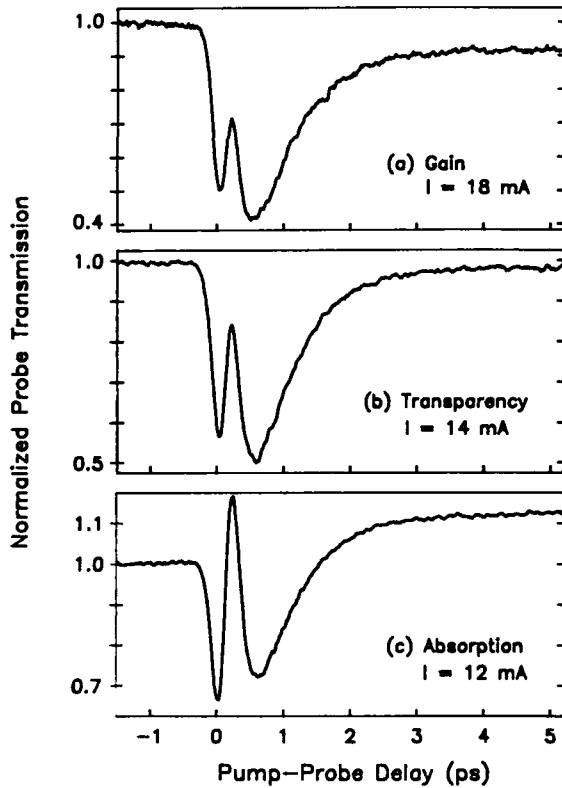


Figure 1. Probe transmission as a function of pump-probe delay for a diode biased in the gain, transparency and absorption regimes. The diodes are bulk V-groove lasers. The pump and probe pulses are both TE polarized.

photon absorption (TPA). Finally, in all three regimes, there is an intermediate transient increase in probe transmission, recovering with a time constant of  $\sim 200$  fs. We can model the results by describing the diode's response function as

$$h(t) = u(t) [a_0 + a_1 e^{-t/\tau_1} - a_2 e^{-t/\tau_2}] - a_3 \delta(t), \quad (1)$$

where  $\tau_1 = 200$  fs,  $\tau_2 = 700$  fs,  $u(t)$  is the unit step function, and  $\delta(t)$  models the instantaneous gain compression associated with TPA. The pump-induced gain change,  $\Delta g(t)$ , can be written as

$$\Delta g(t) = \int_{-\infty}^{\infty} S(t') h(t - t') dt', \quad (2)$$

where  $S(t')$  is the pump (or probe) pulse intensity. The corresponding change in probe transmission can be written as

$$\begin{aligned} \Delta T_{\text{probe}}(\tau) &= \int_{-\infty}^{\infty} S(t) \Delta g(\tau - t) dt \\ &= \int_{-\infty}^{\infty} G^2(\tau') h(\tau - \tau') d\tau', \end{aligned} \quad (3)$$

where  $G^2(\tau)$  is the experimentally determined pump-probe pulse autocorrelation function. We find that all the data in Fig. 1 can be fit by assuming  $\tau_1 = 200$  fs,  $\tau_2 = 700$  fs and by changing the amplitudes of the  $a_i$ 's, but not the sign. We have also measured gain and refractive index changes in bulk AlGaAs diodes at  $0.8 \mu\text{m}$  [11,14,16] and gain changes in bulk, multiple quantum well (MQW) [17] and strained-layer (SL) MQW diodes [18] at  $1.5 \mu\text{m}$ . All of our results can be analyzed by the procedure we have just described.

The pump-probe results performed to date have not provided a clear understanding of the physical mechanism responsible for the intermediate transient increase in probe transmission, described by  $a_1 e^{-t/\tau_1}$ . In this paper we will describe recent pump-probe results that have been obtained in below-band refractive index measurements on AlGaAs active waveguides and in gain measurements on InGaAsP SLMQW active waveguides. These new results suggest that there is a measurable delay in the turn-on of carrier heating. They also present the first clear time domain evidence of spectral-hole burning in diode laser amplifiers.

### AlGaAs Measurements

We have performed above- and below-band pump-probe studies of gain and refractive index nonlinearities in bulk AlGaAs active waveguides. These experiments employ a modelocked Ti:sapphire laser that generates optical pulses 100 femtoseconds in duration. The waveguides studied are commercial diode lasers (Hitachi HLP1400) that have been AR-coated on the rear facet. Our gain measurements are qualitatively similar to the InGaAsP pump-probe gain data shown in Fig. 1.

In addition to the gain measurements, we performed a series of above- and below-band refractive index measurements using a time-division interferometer (TDI) [16,19]. In these measurements, the pump and probe are orthogonally polarized and a polarizer after the diode is used to select the probe beam for detection. A third pulse, called the reference, is interfered with the probe pulse after the diode. The measured probe phase shift is proportional to the pump-induced refractive index change in the diode laser. Typical above-band refractive index dynamics are shown in Fig. 2. The diode laser bias current was set at 30 mA, and the pump-probe wavelength was tuned to access the gain, transparency, and absorption regimes. The long-lived step change in refractive index is caused by pump-stimulated carrier density changes. Since there is no net stimulated carrier density change at the transparency wavelength, no long-lived refractive index change occurs. All three regimes of operation exhibit a pos-

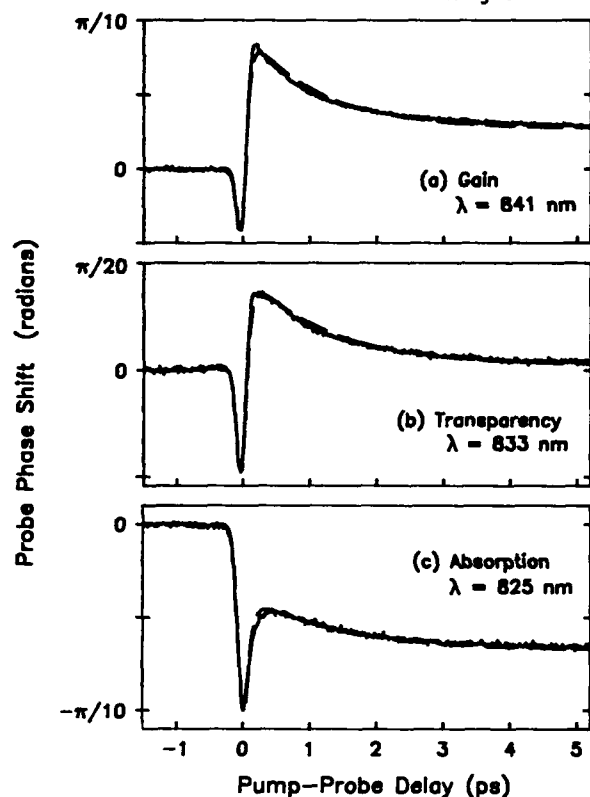


Figure 2. Measured probe phase shift as a function of above-band pump-probe delay in the gain, transparency and absorption regimes. The pump-probe wavelength is tuned to reach the different regimes.

itive refractive index transient which recovers with a  $\sim 1.3$  ps time constant. This dynamic is caused by carrier heating through free-carrier absorption or stimulated transitions. As the carriers cool back to their equilibrium temperatures, the refractive index recovers to an equilibrium value. In addition, we see an instantaneous (insofar as can be resolved by our 100 fs pulses) negative refractive index transient. We attribute this dynamic to a virtual process such as the optical Stark effect.

To reveal more about the carrier heating dynamic, we performed below-band refractive index measurements. We tuned the pump-probe wavelength to 874 nm, below the band gap of the diode laser active region. The below-band pump causes no stimulated transitions or spectral-hole burning, and the intensity transmission of the below-band probe is not affected by carrier temperature changes. However, the refractive index at the probe wavelength is still affected, through the Kramers-Kronig relation, by gain changes that occur above-band. Thus, the phase of the probe can sense the above-band dynam-

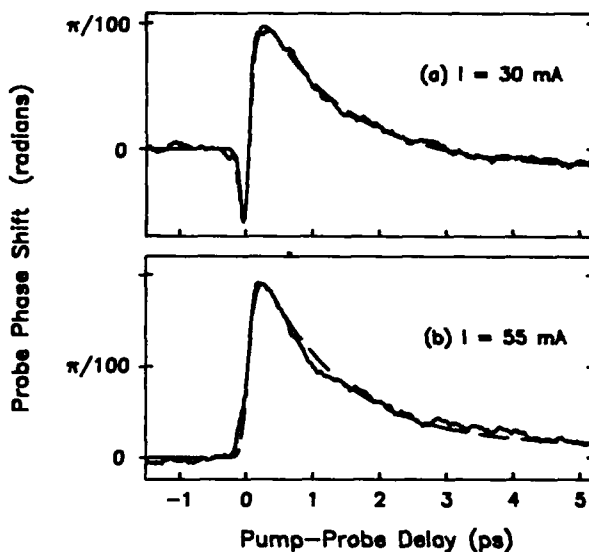


Figure 3. Measured probe phase shift as a function of below-band pump-probe delay. The pump-probe wavelength is 874 nm and the bias current is (a) 30 mA and (b) 55 mA.

ics. We performed pump-probe measurements at this below-band photon energy and obtained the results shown in Fig. 3. As in the above-band case, we see a positive refractive index change which has the  $\sim 1.3$  ps time constant indicative of the carrier heating dynamic. With a below-band pump, the only mechanism available for heating the carriers is free-carrier absorption. Thus, significant carrier heating can result from free-carrier absorption. Finally, the below-band measurement at 30 mA has the instantaneous negative refractive index dynamic that we saw for the above band measurements. By 55 mA this dynamic becomes negligibly small. We believe this is due to the absorption edge being pushed to higher energies, away from the probe wavelength, as the increasing carrier density fills states near the band edge [16].

We performed a fitting operation on these refractive index results and found that the data could be fit by a refractive index impulse response function of the form:

$$h(t) = u(t) [a_0 + a_2 e^{-t/\tau_2} (1 - e^{-t/\tau_{eff}})] - a_3 \delta(t), \quad (4)$$

where the  $a_2$  term governs the carrier heating dynamic ( $\tau_2 \simeq 1.3$  ps and  $\tau_{eff} = (\tau_1 \tau_2) / (\tau_2 - \tau_1) \simeq 0.12$  ps). Note that the response function has been written in this form so that later it can be compared to the response function we described originally (Eq. (1)). In Figs. 2 and 3, the dashed curves are the theoretical fits to the data obtained with the response

function of Eq. (4). The form of the carrier heating term suggests that there is a delay in the turn-on of the carrier heating dynamic. That is, carrier heating does not happen instantaneously, but rather it takes 100-200 fs for the distribution to thermalize. This could mean that it takes some finite amount of time for the highly excited free carriers that have absorbed pump photons to heat up the sea of free carriers at the bottom of the band.

This result suggests a new form for the response function for the gain dynamics:

$$h(t) = u(t) [a_0 - a_2 e^{-t/\tau_2} (1 - e^{-t/\tau_{eff}}) + (a_1 - a_2) e^{-t/\tau_1}] - a_3 \delta(t) \quad (5)$$

This equation is mathematically equivalent to Eq. (1), but now it includes the risetime in the carrier heating explicitly. In this form, the equation contains a residual term,  $(a_1 - a_2) e^{-t/\tau_1}$ , whose sign depends on the ratio  $a_1/a_2$ . When fitting our AlGaAs gain data, we find that this residual term is positive in the absorption regime, negative in the gain regime, and goes to zero near transparency. This is evidence for spectral-hole burning. No  $(a_1 - a_2)$  term is needed to fit the refractive index response, as one would expect from a symmetric spectral hole.

### InGaAsP Measurements

Strained-layer multiple quantum well diode lasers (SLMQW) [20] provide a unique opportunity for further pump-probe studies because the combination of the polarization selection rules [21] and the large intravalence band energy separation between light holes (lh) and heavy holes (hh) allow us to probe the hh-electron (e) transition when the pump is either below-band (TM polarized) or above-band (TE polarized). Fig. 4 shows a schematic of the energy lev-

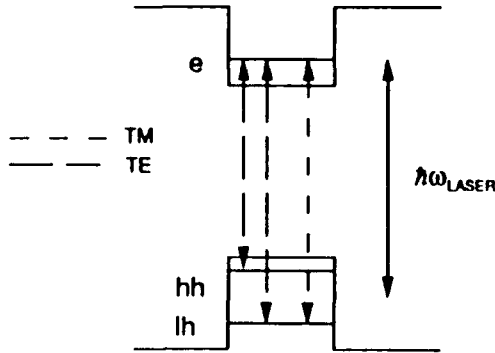


Figure 4. Schematic of the energy levels and allowed transitions in the strained quantum wells. Note that the pump-probe pulse energy is below-band for the lh-e transition.

els and the allowed transitions in the strained quantum wells. The measured emission wavelength for TE polarized light is  $1.53 \mu\text{m}$  and for TM polarized light is  $1.38 \mu\text{m}$  [20]. Note that the source laser used in our experiments is an Additive Pulse Mode-locked color center laser [22], tunable from  $1.48 \mu\text{m}$  to  $1.52 \mu\text{m}$ . Therefore, the laser is always below-band for the lh-e transition (TM polarized light). To study the polarization anisotropy of the nonlinear response, we use a novel heterodyne pump-probe technique in which the pump and probe pulses may be either co-polarized or cross-polarized [15]. In these experiments, acousto-optic modulators (AOM's) are used to shift the spectra of a probe pulse and a reference pulse. After the diode, the probe and reference beat at the AOM's difference frequency (in our case, 1 MHz), on a detector, and a radio receiver detects the beat.

Fig. 5 shows the measured change in probe transmission as a function of co-polarized pump-probe delay, for the diode biased in the gain, transparency

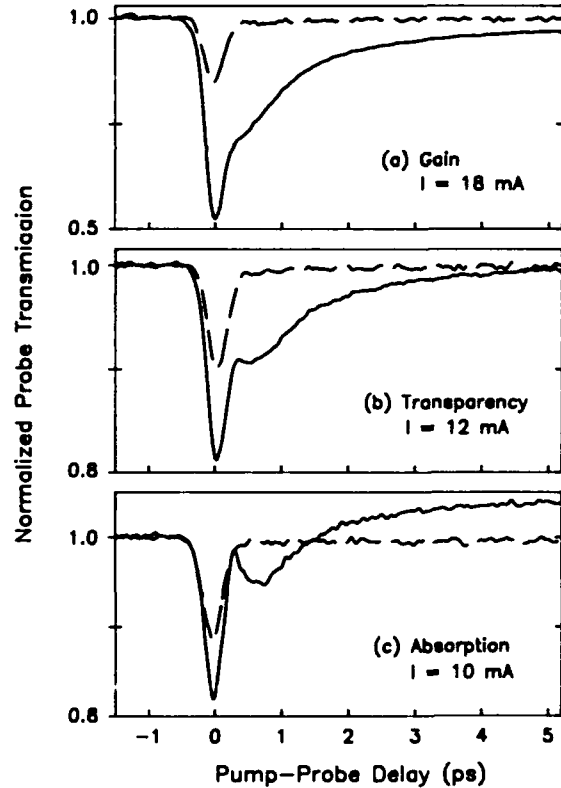


Figure 5. Probe transmission as a function of co-polarized pump-probe delay. The solid lines are for the TE-polarized pump-probe pulses and the dashed lines are for the TM polarized pulses. The bias current is tuned to reach the different regimes.

and absorption regimes. We reach these separate regimes by changing the current applied to the diode. The dashed lines are for TM polarized pump and probe. In this case, the pulses are below-band for the only transition they can access and only TPA is observed. The solid lines show the results for TE polarized pump and probe. We observe the step changes in gain associated with carrier density changes due to stimulated emission or absorption of the pump. In all three regimes there is an instantaneous decrease in transmission associated with TPA. Also, as was the case in the bulk amplifier, we observe gain compression due to carrier heating in all three regimes (recovering with a 1 ps time constant) as well as the intermediate transient increase in probe transmission (recovering with a time constant of  $\sim 200$  fs).

Fig. 6 shows the pump-probe results for the diode under bias conditions identical to those in Fig. 5, but here the probe is TE polarized and the pump is TM polarized. These results differ from the co-polarized results because the pump is essentially

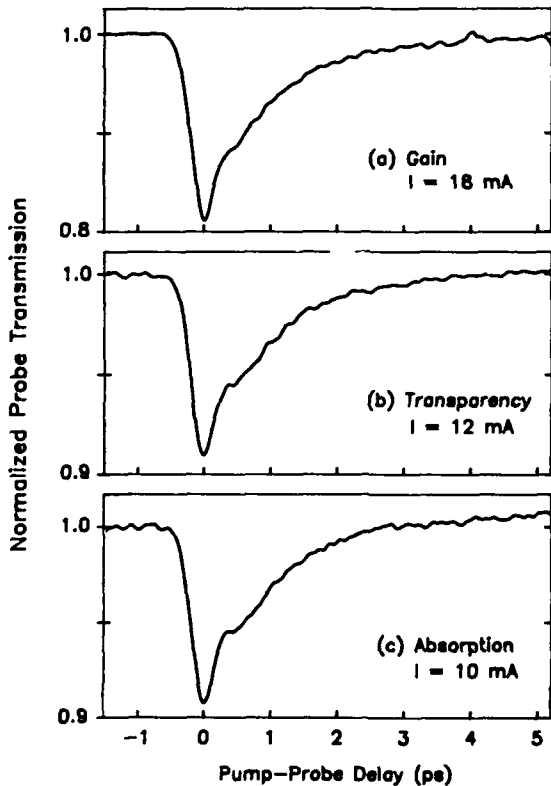


Figure 6. Probe transmission as a function of cross-polarized pump-probe delay. The probe pulses are TE polarized and the pump pulses are TM polarized. The bias conditions are identical to those in Fig. 5.

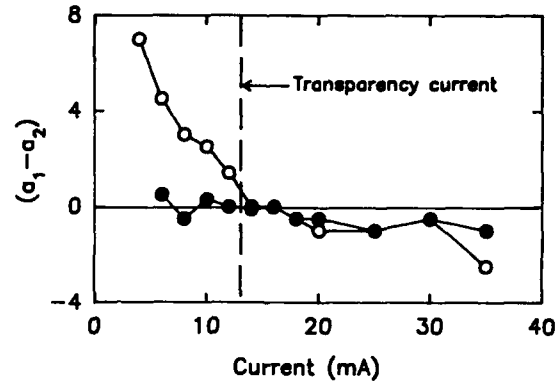


Figure 7. Magnitude of  $(a_1 - a_2)$ , the spectral-hole burning component of the system response function, as a function of bias current for co-polarized (open circles) and cross-polarized (solid circles) measurements.

below-band and cannot stimulate transitions. Therefore, there are no step changes in probe transmission due to density changes. For the same reason, there can be no spectral-hole burning and no heating of the carrier distribution due to stimulated transitions. Note however, that even in the absence of stimulated transitions, there is a significant gain compression due to carrier heating. These carriers are heated via free carrier absorption. Also note that the transient increase in gain, recovering with the  $\sim 200$  fs time constant is still present in this cross-polarized data. This result is consistent with the results of the below-band index measurements and suggests that there is a delay in the onset of carrier heating. Also, it suggests the data should be analyzed using the system response function described in Eq. (5).

We have performed the co-polarized and cross-polarized pump-probe experiments described above on the SLMQW diode lasers at a number of bias currents. Fig. 7 shows the magnitude of the residual term,  $(a_1 - a_2)$ , for the various bias currents and polarizations (open circle = co-polarized, and solid circles = cross-polarized). Both amplitudes  $a_1$  and  $a_2$  are normalized to  $a_3$ , the magnitude of the TPA term. Notice that in the cross-polarized data,  $(a_1 - a_2) \approx 0$  for all bias currents, as noted above. This result is consistent with a delay in the onset of carrier heating and no observed spectral-hole burning. For the co-polarized data, there is, in addition to the delayed carrier heating term, a transient bleaching in the absorption,  $(a_1 - a_2) > 0$ , that goes away at transparency. In the gain regime,  $(a_1 - a_2) < 0$ , consistent with spectral-hole burning. We point out that all our previous results on bulk V-groove diodes [12] and MQW diodes [17], when analyzed using a

system response function that includes a delay in the onset of carrier heating, also show a residual term whose time constant is  $\tau_1 = 100\text{--}200$  fs, and whose amplitude changes sign at the transparency point.

## Conclusion

Through a series of pump-probe measurements of various waveguide structures in the AlGaAs and InGaAsP material systems, we have found that the carrier heating nonlinearity present in both the gain and refractive index measurements has a delay in its onset. That is, it takes a finite amount of time for the carriers to be heated. By quantifying this delay in carrier heating, we have also been able to identify evidence of dynamic spectral-hole burning. Both the AlGaAs and InGaAsP material systems exhibit very similar behaviors in this regard. Aside from differences in the time constants of the processes, the ultrafast gain and refractive index behavior of the two materials are qualitatively the same.

We thank Chris Cook of M.I.T. Lincoln Laboratory for antireflection coating our diode lasers. Also, we thank Uzi Koren and Greg Raybon at AT&T Bell Labs for supplying the AR-coated SLMQW diodes. K. L. Hall gratefully acknowledges the support of a JSEP Fellowship. This work was supported in part by the AFOSR under Contract No. F49620-91-C-0091, by the Joint Services Electronics Program under Contract No. DAAL03-92-C-0001, by DARPA through the National Center for Integrated Photonics Technology, and by the NSF under Grant No. EET-8815834.

## References

1. L. F. Teimeijer, "Effects of nonlinear gain on four-wave mixing and asymmetric gain saturation in a semiconductor laser amplifier," *Appl. Phys. Lett.* **59**, 499 (1991).
2. S. R. Chinn, "Measurement of nonlinear gain suppression and four-wave mixing in quantum well lasers," *Appl. Phys. Lett.*, **59**, 1673, (1991).
3. R. Frankenberger and R. Schimpe, "Origin of nonlinear gain saturation in index-guided InGaAsP laser diodes," *Appl. Phys. Lett.* **60**, 2720 (1992).
4. K. Kikuchi, M. Kakui, C.-E. Zah, and T.-P. Lee, "Observation of highly nondegenerate four-wave mixing in  $1.5\text{ }\mu\text{m}$  traveling-wave semiconductor optical amplifiers and estimation of nonlinear gain coefficient," *IEEE J. Quantum Electron.* **28**, 151 (1992).
5. R. Nietzke, P. Panknin, W. Elsässer, and E. O. Göbel, "Four-wave mixing in GaAs/AlGaAs Semiconductor Lasers," *IEEE J. Quantum Electron.* **25**, 1399 (1989).
6. R. S. Tucker and I. P. Kaminow, "High-frequency characteristics of directly modulated InGaAsP ridge waveguide and buried heterostructure lasers," *J. Light-wave Technol.*, **LT-2**, 385, (1984).
7. R. Olshansky, P. Hill, V. Lanzisera, and W. Powazinik, "Frequency response of  $1.3\text{ }\mu\text{m}$  InGaAsP high-speed semiconductor lasers," *IEEE J. Quantum Electron.*, **23**, 1410, (1987).
8. C. B. Su, J. Eom, C. H. Lange, C. B. Kim, R. B. Lauer, W. C. Rideout, and J. S. LaCourse, "Characterization of the dynamics of semiconductor lasers using optical modulation," *IEEE J. Quantum Electron.*, **28**, 118, (1992).
9. Y. Lai, K. L. Hall, E. P. Ippen, and G. Eisenstein, "Short pulse gain saturation in InGaAsP diode laser amplifiers," *IEEE Photon. Technol. Lett.*, **2**, 711, (1990).
10. R. S. Grant and W. Sibbett, "Observations of ultrafast nonlinear refraction in an InGaAsP optical amplifier," *Appl. Phys. Lett.* **58**, 1119 (1991).
11. M. P. Kesler and E. P. Ippen, "Subpicosecond gain dynamics in GaAlAs laser diodes," *Appl. Phys. Lett.* **51**, 1765 (1987).
12. K. L. Hall, J. Mark, E. P. Ippen, and G. Eisenstein, "Femtosecond gain dynamics in InGaAsP optical amplifiers," *Appl. Phys. Lett.* **56**, 1740 (1990).
13. P. J. Delfyett, Y. Silberberg, and G. A. Alphonse, "Hot-carrier thermalization induced self-phase modulation in semiconductor traveling wave amplifiers," *Appl. Phys. Lett.* **59**, 10 (1991).
14. C. T. Hultgren and E. P. Ippen, "Ultrafast refractive index dynamics in AlGaAs diode laser amplifiers," *Appl. Phys. Lett.* **59**, 635 (1991).
15. K. L. Hall, G. Lenz, E. P. Ippen, and G. Raybon, "Heterodyne pump-probe technique for time-domain studies of optical nonlinearities in waveguides," *Opt. Lett.*, **17**, 874, (1992).
16. C. T. Hultgren, D. J. Dougherty, and E. P. Ippen, "Above- and below-band femtosecond nonlinearities in active AlGaAs waveguides," *Appl. Phys. Lett.*, **61**, 2767, (1992).
17. K. L. Hall, Y. Lai, E. P. Ippen, G. Eisenstein, and U. Koren, "Femtosecond gain dynamics and saturation behavior in InGaAsP multiple quantum well optical amplifiers," *Appl. Phys. Lett.*, **57**, 2888, (1990).
18. K. L. Hall, G. Lenz, E. P. Ippen, U. Koren, and G. Raybon, "Carrier heating and spectral-hole burning in strained-layer quantum-well laser amplifiers at  $1.5\text{ }\mu\text{m}$ ," *Appl. Phys. Lett.*, **61**, 2512, (1992).

19. M. J. LaGasse, K. K. Anderson, H. A. Haus, and J. G. Fujimoto, "Femtosecond all-optical switching in AlGaAs waveguides using a time division interferometer," *Appl. Phys. Lett.* **54**, 2068 (1989).
20. U. Koren, M. Oron, M. G. Young, B. I. Miller, J. L. De Miguel, G. Raybon, and M. Chien, "Low threshold highly efficient strained quantum well lasers at 1.5 micrometre wavelength," *Electron. Lett.*, **26**, 465, (1990).
21. G. Bastard, Wave Mechanics Applied to Semiconductor Heterostructures, (Halsted, New York, 1988).
22. J. Mark, L. Y. Liu, K. L. Hall, H. A. Haus, and E. P. Ippen, "Femtosecond pulse generation in a laser with a nonlinear external resonator," *Opt. Lett.*, **14**, 48, (1989).



# Carrier Transport Effects in High Speed Quantum Well Lasers

Radhakrishnan Nagarajan

Department of Electrical and Computer Engineering, University of California,  
Santa Barbara, California 93106

## Abstract

The high speed properties of quantum well lasers, like the amplitude modulation (AM) and frequency modulation (FM) response, and wavelength chirping are significantly affected by the carrier transport across the optical and current confining layers, and thermionic emission out of the quantum well active area.

## Introduction

Quantum well lasers have been theoretically and experimentally shown to have a larger intrinsic differential gain than bulk lasers, and this was predicted to lead to enhancements in the modulation bandwidths as well [1]. Experimentally, only recently have the modulation bandwidths in quantum well lasers been improved and surpassed those of bulk lasers [2-5]. Carrier transport effects were largely responsible for the poor dynamic performance of the early quantum well lasers.

In this paper, we will review the effects of carrier transport on the high speed properties of quantum well lasers. A large carrier transport time across the separate confinement heterostructure (SCH) of the laser causes a low frequency, parasitic-like rolloff that degrades the amplitude modulation response, and a small thermionic emission time out of the quantum well leads to poor carrier confinement and a corresponding decrease of the differential gain [2,6-13]. We derive analytical expressions for the AM modulation response, resonance frequency, damping rate and wavelength chirping to include the effects of carrier transport.

The carrier transport across the SCH region and the consequent carrier density variation there, also affects the linewidth enhancement parameter in the quantum

well lasers. This leads to enhanced frequency modulation response and increased wavelength chirping under intensity modulation in quantum well lasers with dominant carrier transport effects [12,14,15].

## Carrier Transport Model

Fig. 1 shows a SCH single quantum well (SQW). We will investigate carrier transport and capture in this structure, and the effect of these processes on the dynamic response of the laser. The carrier transport/dwell time in the SCH is given by  $\tau_r$  and has been derived assuming ambipolar carrier transport in the SCH, and the carrier escape time from the quantum well is given by  $\tau_e$  and has been derived using the thermionic emission theory [10].

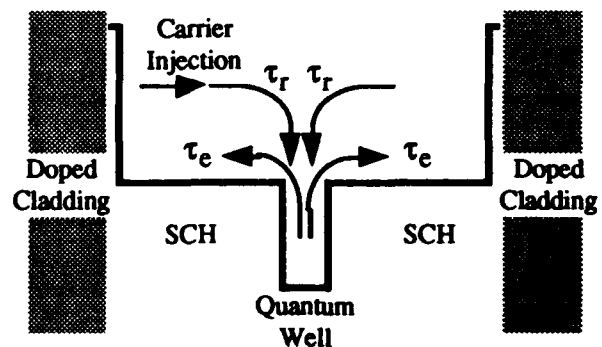


Figure 1. Schematic diagram of the carrier transport processes in a SCH SQW laser.

Including the transport processes in the rate equation analysis, the small signal amplitude modulation response can be written as given below, where a transport factor,  $\chi = 1 + \tau_r/\tau_e$ , has been introduced into the equations. The usual expressions for the damping

factor,  $\gamma$ , and the resonance frequency,  $\omega_r$ , are recoverable in the limit of  $\chi = 1$ , i.e. in the limit of short transport time across the SCH or very long thermionic emission time out of the quantum well.

$$M(\omega) = \left( \frac{1}{1 + j\omega\tau_r} \right) \frac{A}{\omega_r^2 - \omega^2 + j\omega\gamma}$$

$$\omega_r^2 = \frac{(v_g g_o / \chi) S_o}{\tau_p (1 + \epsilon S_o)} \left( 1 + \frac{\epsilon}{v_g g_o \tau_n} \right)$$

$$\gamma = \frac{(v_g g_o / \chi) S_o}{(1 + \epsilon S_o)} + \frac{\epsilon S_o / \tau_p}{(1 + \epsilon S_o)} + \frac{1}{\chi \tau_n}$$

The most significant effects of carrier transport are the low frequency rolloff in the modulation response due *only* to the transport time across the SCH, and the reduction of the effective differential gain to  $g_o/\chi$ . The low frequency rolloff significantly limits the -3 dB modulation bandwidth for large  $\tau_r$ , and is *indistinguishable* from parasitics. The differential gain reduction is only apparent in the *dynamic* sense, and it does not affect the *static* properties of the laser.

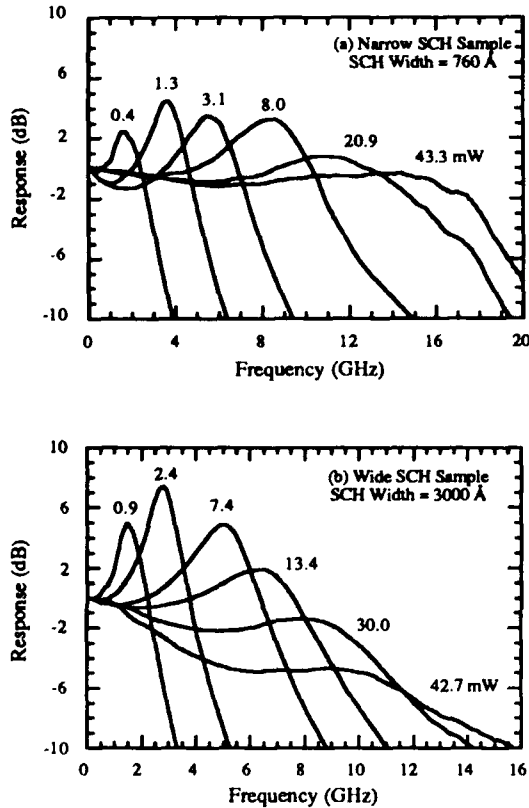


Figure 2. Experimental CW modulation response of (a) a narrow SCH and (b) a wide SCH SQW laser. The rolloff in the modulation response due to carrier transport are evident in the wide SCH sample.

Fig. 2. shows the results of varying the  $\tau_r$  by changing the SCH width. The samples both have 300  $\mu\text{m}$  long cavities and 2.5  $\mu\text{m}$  wide ridges. Although the devices are identical except for the SCH width, the modulation response of the sample with the wider SCH region is completely damped at about half the output power level, and the bandwidth of the narrow SCH sample is six times larger at higher power levels. The maximum CW modulation bandwidth for the narrow SCH sample is 18.1 GHz, which is the largest reported to date in SQW lasers.

The experimental data for the dependence of the high speed parameters on the thermionic emission time is obtained from two samples with different energy barriers in the SCH; one with  $\text{Al}_{0.15}\text{Ga}_{0.85}\text{As}$  SCH and the other with GaAs SCH. Fig. 3 shows the variation of the resonance frequency with the square root of power obtained from the modulation response data for the two cases considered here. The resonance frequency for the laser with  $\text{Al}_{0.15}\text{Ga}_{0.85}\text{As}$  SCH (higher barrier and hence a longer thermionic emission time) is almost twice that of the laser with GaAs SCH at equivalent power levels. The differential gain for the sample with the higher barrier is more than 2.5 times that of sample with a lower barrier. The gain compression coefficient,  $\epsilon$ , for both cases is about the same. Both devices have a 205  $\mu\text{m}$  long cavity and a 2  $\mu\text{m}$  wide ridge.

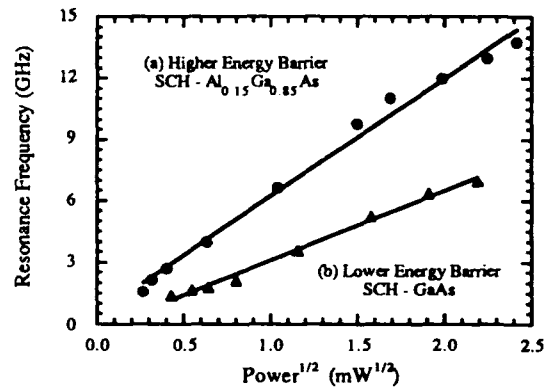


Figure 3. Effect on the resonance frequency of varying the carrier energy barrier in the SCH region.

The relative intensity noise (RIN) spectrum can be derived using the same formalism [16]. In the RIN, the additional low frequency rolloff present in the modulation response is absent. For large values of  $\tau_r$  the modulation bandwidth is severely reduced, although the *effective* differential gain, which is affected by  $\chi$  alone and not the low frequency rolloff, determined from the noise measurements will still be optimistic. This results in the over estimation of the modulation bandwidth inferred by the measurement of the resonance frequency from the RIN. It is generally

believed that the RIN measurement is a *parasitic free* means of determining the actual or potential modulation performance of a laser. In the presence of significant transport effects this is no longer true. These are illustrated in Fig. 4.

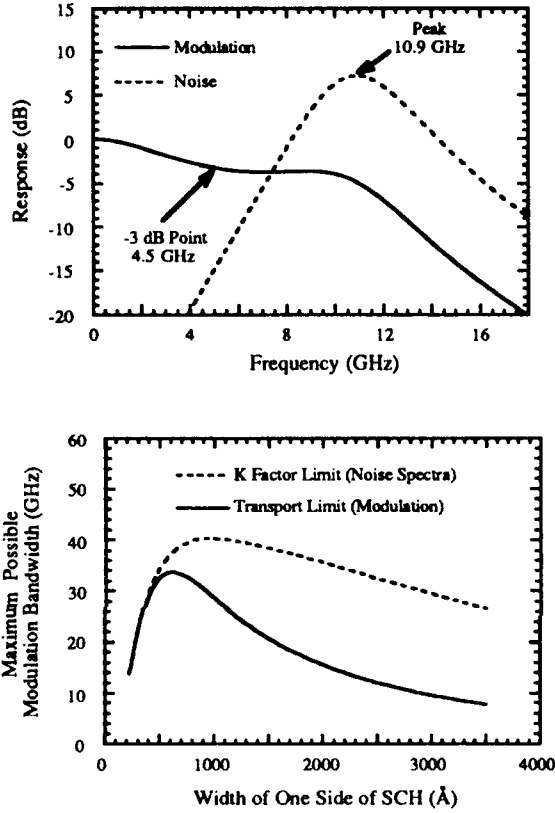


Figure 4 (a). Comparison of the noise spectrum and the modulation response for the same parameters. The noise spectrum indicates a much larger modulation bandwidth than is physically possible. (b) Comparison of maximum possible modulation bandwidth inferred from the modulation response and RIN measurements.

### Wavelength Chirping

Wavelength chirping or the broadening of the lasing mode under intensity modulation in a semiconductor lasers is directly proportional to the linewidth enhancement factor,  $\alpha$ . [17,18]. This wavelength or frequency variation under modulation is the result of index variations caused by changes in carrier density under dynamic conditions. Due to the dispersion in the optical fibers, wavelength chirping in high speed lasers causes the optical pulses to broaden during transmission leading to inter-symbol interference, and the resulting degradation of the signal response at the receiver. This imposes an upper limit to the data transmission rate in optical fiber communication systems.

In quantum well lasers the carrier density variation in the SCH regions also contribute to the total index change under modulation. This is particularly severe in lasers with enhanced carrier transport effects. Using the same carrier transport model, the expression for the effective structure dependent linewidth enhancement parameter,  $\alpha_{eff}$ , can be derived as [19],

$$\alpha_{eff} = \frac{4\pi}{\lambda g_o} \left( \frac{\partial n}{\partial N_{wo}} + \left( \frac{1}{\Gamma} - 1 \right) (\chi - 1) \frac{\tau_b}{(\tau_b + \tau_r)} \frac{\partial n}{\partial N_{bo}} \right)$$

where  $\partial n / \partial N_{wo}$  and  $\partial n / \partial N_{bo}$  are the variation of index with carrier density in the quantum well active region and the SCH region respectively,  $\lambda$  is the emission wavelength,  $\tau_b$  is the recombination lifetime in the SCH region.  $\chi$  is the transport factor that was previously introduced.

The first part of the expression for  $\alpha_{eff}$  is the contribution to the total wavelength chirp due to the intrinsic index variation in the active region, and the second part is the enhancement due to the carrier transport effects.

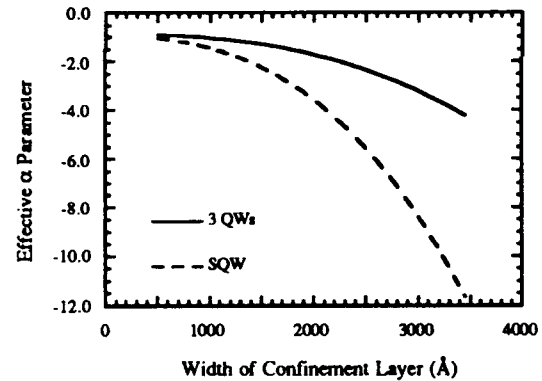


Figure 5. Variation of the effective  $\alpha$  parameter as a function of the SCH width for SQW and MQW laser structures.

Fig. 5 shows the variation of  $\alpha_{eff}$  with the width of the SCH. For a given carrier confinement energy in the SCH, laser structures with wide SCH regions have a larger amount of wavelength chirping. This translates into a higher FM efficiencies in lasers with wider SCH region. This trend has been experimentally observed recently [12,14,15]. Wavelength chirping is also a sensitive function of the optical confinement factor. The MQW lasers with larger optical confinement factors have lower amounts of wavelength chirping under current modulation. The increase in the amount of chirp with the SCH width is due primarily to the increase in the carrier transport time which is

proportional to the square of the SCH width, and the decrease in the optical confinement factor.

## Conclusions

In summary, the carrier transport has a significant effect on the high speed properties of quantum well lasers. Careful device design is required to take advantage of the enhancement in differential gain obtained by the use of quantum wells in the active area. A mere replacement of the active area in a bulk laser by quantum wells is not sufficient.

## Acknowledgments

This work was funded by DARPA, Rome Laboratories (Hanscom AFB) and Office of Naval Technology block program in Electro-Optics Technology.

## References

1. I. Suemune, "Theoretical Study of Differential Gain in Strained Quantum Well Structures," *IEEE J. Quantum Electron.* **27**, 1149 (1991).
2. R. Nagarajan, R. P. Mirin, T. E. Reynolds, and J. E. Bowers, "Effect of the Confinement Layer Composition on the Internal Quantum Efficiency and Modulation Response of Quantum Well Lasers," *IEEE Photon. Tech. Lett.* **4**, 832 (1992).
3. R. Nagarajan, T. Fukushima, J. E. Bowers, R. S. Geels, and L. A. Coldren, "High-Speed InGaAs/GaAs Strained Multiple Quantum Well Lasers with Low Damping," *Appl. Phys. Lett.* **58**, 2326 (1991).
4. L. F. Lester, S. S. O'Keefe, W. J. Schaff, and L. F. Eastman, "Multiquantum Well Strained-Layer Lasers with Improved Low Frequency Response and Very Low Damping," *Electron. Lett.* **28**, 383 (1992).
5. S. Weisser, J. D. Ralston, E. C. Larkins, I. Esquivias, P. J. Tasker, J. Fleissner, and J. Rosenzweig, "Efficient High-Speed Direct Modulation in *p*-Doped In<sub>0.35</sub>Ga<sub>0.65</sub>As/GaAs Multiquantum Well Lasers," *Electron. Lett.* **28**, 2141 (1992).
6. W. Rideout, W. F. Sharfin, E. S. Koteles, M. O. Vassell, and B. Elman, "Well-Barrier Hole Burning in Quantum Well Lasers," *IEEE Photon. Tech. Lett.* **3**, 784 (1991).
7. R. Nagarajan, T. Fukushima, S. W. Corzine, and J. E. Bowers, "Effects of Carrier Transport on High-Speed Quantum Well Lasers," *Appl. Phys. Lett.* **59**, 1835 (1991).
8. R. Nagarajan, T. Fukushima, M. Ishikawa, J. E. Bowers, R. S. Geels, and L. A. Coldren, "Transport Limits in High Speed Quantum Well Lasers: Experiment and Theory," *Photon. Tech. Lett.* **4**, 121 (1992).
9. T. C. Wu, S. C. Kan, D. Vassilovski, K. Y. Lau, C. E. Zah, B. Pathak, and T. P. Lee, "Gain Compression in Tensile-Strained 1.55  $\mu\text{m}$  Quantum Well Lasers Operating at First and Second Quantized Levels," *Appl. Phys. Lett.* **60**, 1794 (1992).
10. R. Nagarajan, M. Ishikawa, T. Fukushima, R. S. Geels and J. E. Bowers, "High Speed Quantum Well Lasers and Carrier Transport Effects," *IEEE J. Quantum Electron.* **28**, 1990 (1992).
11. N. Tessler, R. Nagar, and G. Eisentsein, "Structure Dependent Modulation Responses in Quantum-Well Lasers," *IEEE J. Quantum Electron.* **28**, 2242 (1992).
12. A. P. Wright, B. Garrett, G. H. B. Thompson, and J. E. A. Whiteaway, "Influence of Carrier Transport on Wavelength Chirp of InGaAs/InGaAsP MQW Lasers," *Electron. Lett.*, **28**, 1911, (1992).
13. B. Zhao, T. R. Chen, Y. Yamada, Y. H. Zhuang, N. Kuze, and A. Yariv, "Evidence for State Filling Effect on High Speed Modulation Dynamics of Quantum Well Lasers," *Appl. Phys. Lett.* **61**, 1907 (1992).
14. I. H. White, P. S. Griffin, K. A. Williams, G. H. B. Thompson, J. E. A. Whiteaway, and B. Garrett, "Spectral Dynamics of Long Wavelength Quantum Well Distributed Feedback Diode Lasers under Gain Switching," in Technical Digest of 13th IEEE International Semiconductor Laser Conference (1992), pp. 264.
15. H. Yamazaki, M. Yamaguchi, M. Kitamura, and I. Mito, "Analysis of FM Efficiency of InGaAs/InGaAsP SCH-MWQ LDs Taking Injection Carrier Transport into Account," in Technical Digest of 13th IEEE International Semiconductor Laser Conference (1992), pp. 174.
16. R. Nagarajan, M. Ishikawa, and J. E. Bowers, "Effects of Carrier Transport on Relative Intensity Noise and Critique of K Factor Prediction of Modulation Response," *Electron. Lett.* **28**, 846 (1992).
17. T. L. Koch, and J. E. Bowers "Nature of Wavelength Chirping in Directly Modulated Semiconductor Lasers," *Electron. Lett.* **20**, 1038 (1984).
18. C. H. Henry, "Theory of Linewidth of Semiconductor Lasers," *IEEE J. Quantum Electron.* **18**, 259 (1982).
19. R. Nagarajan, and J. E. Bowers, "Effects of Carrier Transport on Injection Efficiency and Wavelength Chirping in Quantum Well Lasers," *IEEE J. Quantum Electron.*, June 1993.

# 8.6-GHz Active, Passive, and Hybrid Mode-Locking of InGaAsP Extended-Cavity MQW Lasers with Monolithically Integrated Saturable Absorbers

P. B. Hansen, G. Raybon, U. Koren, B. I. Miller, M. G. Young, M. A. Newkirk, and C. A. Burrus

*AT&T Bell Laboratories, Crawford Hill Laboratory, Holmdel, New Jersey 07733*

P. P. Iannone

*Princeton University, Department of Electrical Engineering, Princeton, New Jersey 08544*

## Abstract

Active, passive, and hybrid mode-locking have been demonstrated in a monolithic extended-cavity semiconductor laser with an integrated saturable absorber. A 45- $\mu\text{m}$  long reverse-biased segment of multiple quantum wells acts as the saturable absorber. Active and hybrid mode-locking at a repetition rate of 8.6 GHz, resulted in 6.2-ps and 4.4-ps pulses. The extended-cavity laser also exhibits self-starting passive mode-locking at a repetition rate of 8.57 GHz with 5.5 ps pulses. Wavelength selectivity over a range of 15 nm with little change in the pulse width is facilitated by a broad spectrum.

## Introduction

Optical pulse sources with repetition rates in the 2 - 10 GHz range are of particular interest for applications in the next generation of lightwave systems. Maturing growth and processing techniques have allowed for fabrication of very long monolithic multi-section laser devices, which are suitable for mode-locking at such frequencies. Active mode-locking of 1.55- $\mu\text{m}$  lasers in which the cavity was extended monolithically by means of passive waveguide segments has previously been reported [1,2]. Recently, we obtained 9.0-ps pulses by active mode-locking of a 1-cm long extended-cavity laser at a repetition rate of 4.4 GHz [3]. However, the functionality of devices has been increased through integration of a large range of components such as saturable absorbers, Bragg reflectors, electro-absorption as well Mach-Zehnder modulators (See f.ex. Ref. 4 and references therein).

Passive and hybrid mode-locking of long-wavelength all-active semiconductor lasers have been reported yielding sub-picosecond pulse widths and repetition rates in the 40 GHz to 350 GHz range [5]. In the GaAlAs system, active, passive and hybrid mode-locking of all-active waveguide lasers have been demonstrated at repetition rates down to 5.5 GHz [6].

In this letter, we report an InGaAsP monolithic extended-cavity laser with an integrated passive waveguide and a saturable absorber. This laser device allows active, passive, as well as hybrid mode-locking at a repetition rate of 8.6 GHz. The mode-locking method is given by the applied biasing scheme. Pulses with durations of 4-5 ps are obtained by passive and hybrid mode-locking, whereas active mode-locking yields 6-9 ps pulses. A broad spectrum allows wavelength selectivity over a range of 15 nm with little change in the pulse profile by means of external filtering.

## Device

The monolithic extended-cavity laser which is shown schematically in Fig. 1 was fabricated using standard metal-organic vapor-phase epitaxy (MOVPE) growth and processing techniques [4]. A 1.3- $\mu\text{m}$  quaternary layer extends the entire length of the 5.0-mm long laser device and acts as a backbone waveguide for the optical wave. A stack of 6, 35- $\text{\AA}$  thick strain-compensated (1.2 % compressive) quantum wells separated by 90- $\text{\AA}$  thick barriers provides the gain as well as the saturable absorption in the active section. Two contacts are fabricated dividing the active section into a 600- $\mu\text{m}$  long gain section and, at the cleaved

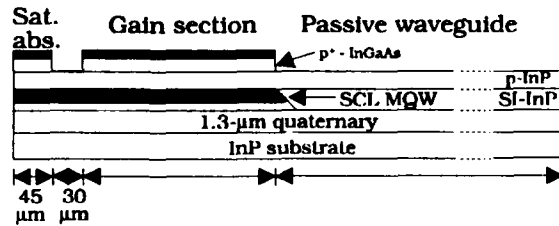


Figure 1. Schematic drawing of the monolithic extended-cavity laser with an integrated saturable absorber. SCL: Strain-compensated layers. MQW: Multiple quantum wells. SI: Semi-insulating.

facet, a 45- $\mu\text{m}$  long saturable absorber. The resistance between the gain and absorber contacts, which are separated by a 30- $\mu\text{m}$  wide etched groove through the  $p^+$ -InGaAs contacting layer, is 1.5  $k\Omega$ . The active segment is a buried heterostructure with semi-insulating (SI) InP regrown for current blocking. The laser cavity has been monolithically extended by incorporating a 4.3-mm long passive waveguide. A buried rib waveguide structure with the SI-InP acting as the cladding layer results in losses of 4-5 dB/cm which allows integration of a long passive waveguide while maintaining a threshold current of only 50 mA (40 mA and 10 mA applied to the gain and absorber sections, respectively).

### Mode-locking

A Hamamatsu Synchro-scan streak camera and a continuously scanning autocorrelator were used for recording the pulse profiles. The streak camera enables measurements of the pulse with a resolution of  $\sim 3$  ps for repetition rates that are a multiple of the 100-MHz trigger frequency. The autocorrelator provides a much improved resolution without restrictions to the repetition rate at the expense of sensitivity.

Active, passive as well as hybrid mode-locking of the monolithic extended-cavity laser were achieved at the fundamental cavity resonance frequency near 8.6 GHz. An 8.6-GHz RF signal superimposed on a DC current were applied to the gain section in order to actively mode-lock the laser. To prevent the 45- $\mu\text{m}$  long active section near the left facet in Fig. 1 to act as a saturable absorber, it was forward biased with a DC current of 10 mA. Figure 2a shows the measured pulse profile which exhibits a width of 6.2 ps. Changing the bias condition of the short active section so that it is reverse biased, hybrid mode-locking was demonstrated at a repetition rate of 8.6 GHz. A pulse width of 4.4-ps was measured for a voltage of -0.9 V as shown in Fig. 2b.

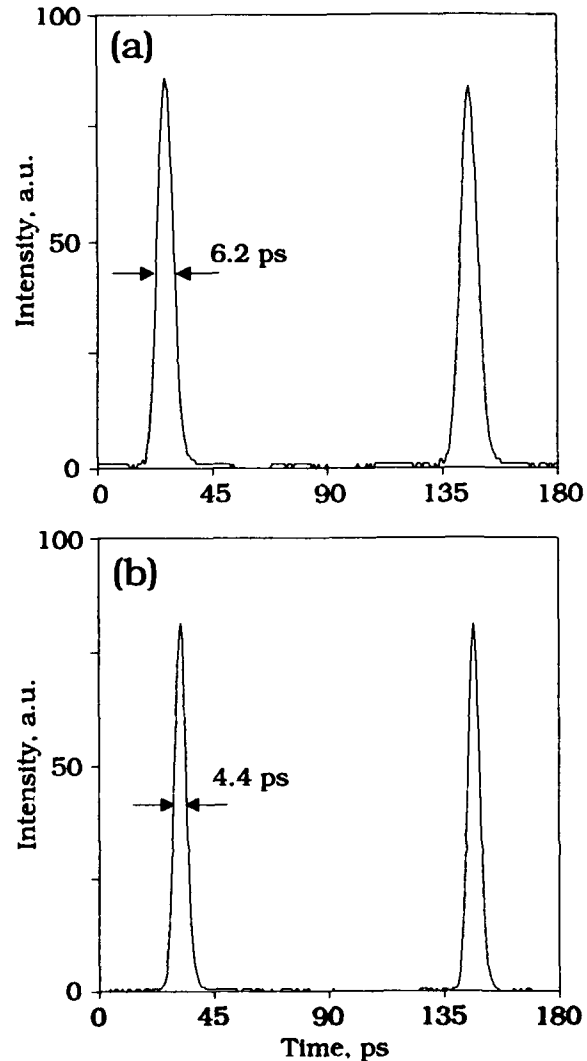


Figure 2. Measured pulse profiles generated by a) active mode-locking and b) hybrid mode-locking.

Self-starting passive mode-locking was observed with a frequency of 8.57 GHz when a constant current was applied to the gain section and the saturable absorber was reverse biased. Figure 3 shows the autocorrelation trace for a constant current of 200 mA and an absorber bias voltage of -0.9 V. Assuming a hyperbolic secant squared ( $\text{sech}^2$ ) pulse shape, the pulse width is estimated to be 5.5 ps. Secondary peaks, which are separated by 1 ps, are observed in the autocorrelation trace suggesting some structure in the pulse profile. The round trip time in the saturable absorber is  $\sim 1$  ps and the peaks are, therefore, indicative of residual reflections at the interface between the gain and the saturable absorber sections. A large difference in carrier densities and, therefore, in the effective refractive indices of the two sections is expected due to the drive conditions. This may lead to

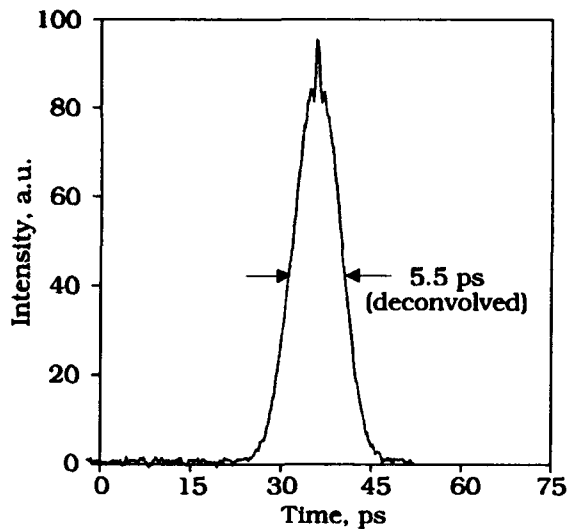


Figure 3. Autocorrelation trace of pulse train generated by passive mode-locking. The deconvolved pulse width is 5.5 ps assuming a  $\text{sech}^2$ -shaped pulse.

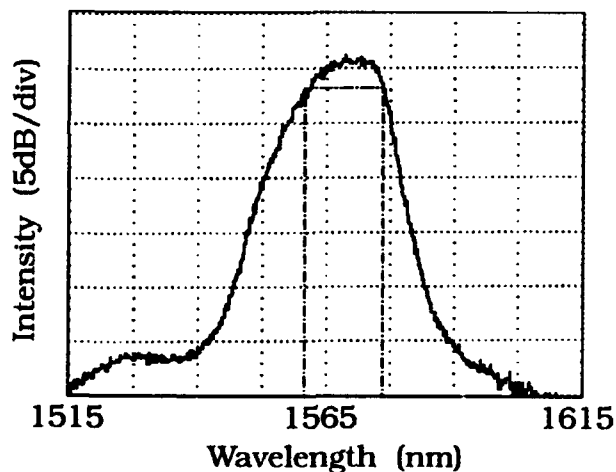


Figure 4. Optical spectrum corresponding to pulse train shown in Fig. 2b. The 3-dB width is 12 nm.

a residual reflection. This hypothesis is supported by the observed variation in peak strengths with absorber bias.

The width of the optical spectrum is mainly determined by the gain bandwidth of the quantum wells, because no intentional filtering has been incorporated into the laser cavity. The optical spectrum corresponding to the pulse train shown in Fig. 2b is shown Fig. 4. The 3-dB width is 12 nm indicating a time-bandwidth product of 7.0. A transform-limited output, which for a 12-nm wide spectrum corresponds to 200-fs pulses, would imply mode-locking of  $\sim 200$  modes at this repetition rate. Waveguide dispersion,

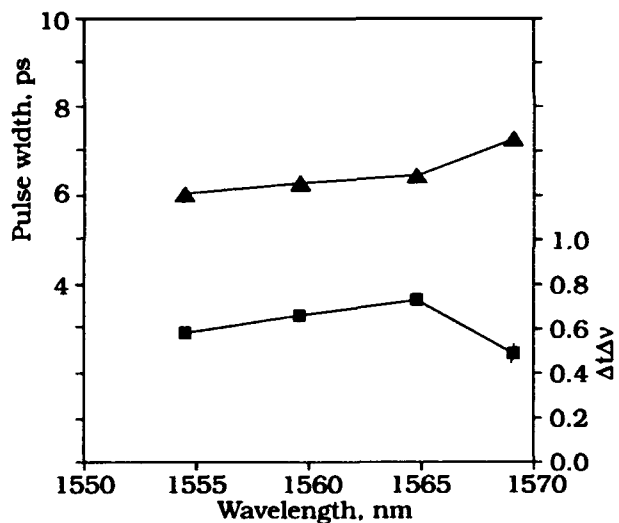


Figure 5. Pulse width and time-bandwidth product ( $\Delta t \Delta \nu$ ) versus wavelength selected by a tunable external 1-nm interference filter.

residual internal reflections, and a limited Q-factor of the laser cavity are likely to limit the bandwidth that can be effectively phase-locked and are, consequently, responsible for the pulses not being transform-limited.

#### Wavelength selectivity

Wavelength selectivity can be obtained by taking advantage of the excess bandwidth. An external interference filter, which could be tuned by adjusting the angle of incidence, was used to select a 1-nm band. Figure 5 shows the measured pulse width after filtering and the corresponding time bandwidth products against wavelength. The laser is operated as described above for hybrid mode-locking (See Figs. 2b and 4 for pulse profile and spectrum, respectively). The power of the pulse train after filtering is decreasing as the wavelength is tuned away from the peak wavelength of the emitted spectrum. Therefore, the tuning range was limited to 15 nm. The measured pulse widths range from 6.0 ps at a wavelength of 1554 nm to 7.2 ps at a wavelength of 1569 nm as shown in Figure 5. For all wavelengths in the 15 nm tuning range the time-bandwidth product after filtering was measured to be between 0.49 and 0.73 as indicated by the solid squares. Qualitatively similar results were obtained with a 2-nm interference filter both for active and hybrid mode-locking.

## Conclusion

In conclusion, active, passive as well as hybrid mode-locking of a monolithic extended-cavity laser with an integrated saturable absorber are demonstrated. The saturable absorber is obtained by reverse biasing a 45- $\mu\text{m}$  long section of MWQs. This section is forward biased during active mode-locking. All three mode-locking schemes are seen to provide short optical pulses at 8.6 GHz, which corresponds to the fundamental cavity resonance frequency of the 5.0-mm long device. Passive and hybrid mode-locking typically yields shorter pulse durations than active mode-locking. Hybrid mode-locking results in the shortest pulses, i.e. 4.4 ps, and, furthermore, offers the convenience of active mode-locking in terms of generating a pulse train phase-locked to the applied electrical drive signal. A 12-nm wide spectrum allowed wavelength selection by tuning an external 1-nm interference filter. Pulse durations between 6.0 ps and 7.2 ps were obtained over a tuning range of 15 nm. The corresponding time-bandwidth products ranged from 0.49 to 0.73.

## Acknowledgments

The authors would like to acknowledge N. Frigo and E. Ippen for a number of helpful discussions.

## References:

1. R. S. Tucker, U. Koren, G. Raybon, C. A. Burrus, B. I. Miller, T. L. Koch, and G. Eisenstein, "40 GHz active mode-locking in a 1.5 mm monolithic extended-cavity laser", *Elec. Lett.*, **25**, 621-622 (1989).
2. P. B. Hansen, G. Raybon, U. Koren, B. I. Miller, M. G. Young, M. -D. Chien, C. A. Burrus, and R. C. Alferness, "5.5-mm Long InGaAsP monolithic extended-cavity laser with an integrated Bragg reflector for active mode-locking", *Photon. Techn. Lett.*, **4**, 215-217 (1992).
3. G. Raybon, P. B. Hansen, U. Koren, B. I. Miller, M. G. Young, M. Newkirk, P. P. Iannone, C. A. Burrus, J. Centanni, and M. Zirngibl, "Active mode-locking at 4.4 GHz in a 1-cm long monolithic extended-cavity laser", *Technical Digest of LEOS'92 Annual Meeting* (Optical Society of America, Washington, DC, 1992), Paper DLT4.3.
4. T. L. Koch and U. Koren, "Semiconductor photonic integrated circuits", *IEEE J. Quantum Electron.*, **27**, 641-653 (1991).
5. Y. K. Chen, M. C. Wu, T. Tanbun-Ek, R. A. Logan, and M. A. Chin, "Subpicosecond monolithic colliding-pulse mode-locked multiple quantum well lasers", *Appl. Phys. Lett.*, **58**, 1253-1255 (1991).
6. D. J. Derickson, P. A. Morton, and J. E. Bowers, "Comparison of timing jitter in external and monolithic cavity mode-locked semiconductor laser", *Appl. Phys. Lett.*, **59**, 3372-3374 (1991).



# Femtosecond Periodic Gain Vertical-Cavity Semiconductor Lasers

Wenbin Jiang, Mitsuaki Shimizu, Richard P. Mirin, Thomas E. Reynolds, and John E. Bowers

Department of Electrical and Computer Engineering, University of California, Santa Barbara, California 93106

## Abstract

A periodic gain structure was used as the gain medium in an optically pumped mode-locked vertical-cavity surface-emitting semiconductor laser to decrease the effective carrier lifetime. A laser pulsewidth of under 190 fs was directly generated from the laser cavity.

Recent development in synchronously pumped vertical-cavity surface-emitting lasers (VCSELs) has revealed that VCSELs can be mode-locked to generate picosecond pulses with a peak power of 100 times larger than that from a mode-locked in-plane semiconductor laser [1-3]. For example, a mode-locked InGaAs/InP VCSEL generated 5 ps laser pulses with over 100 W peak power at 77 K [1, 2] and a mode-locked GaAs/AlGaAs VCSEL generated 14 ps laser pulses with over 10 W peak power at room temperature [3]. Research has since been focused on exploring the shortest possible pulses which can be directly generated from VCSELs. In this paper, we report our efforts in generating 190 fs laser pulses directly from the VCSELs.

An important factor which prevents subpicosecond pulse generation directly from the mode-locked VCSELs is the significant laser pulse chirping [4]. The time-bandwidth product of the pulses generated from this type of laser is usually 100 times larger than the Fourier transform limit [1-3]. Grating-pair chirp compensation schemes have been employed to compress the laser pulses externally, thus the laser pulses have been compressed to 320 fs for the GaAs/AlGaAs system [3] and 150 fs for the InGaAs/InP system [2]. Intracavity chirp compensation is usually an efficient way for subpicosecond pulse generation directly from a laser oscillator, but is not

very practical for large nonlinear chirp as in this type of laser [4]. An intracavity filter has thus been suggested to limit the extra bandwidth created by the pump induced cross-phase-modulation and the gain saturation induced self-phase-modulation. This is effective in controlling the time-bandwidth product of the laser pulses, while still maintaining the output laser pulsewidth unchanged or even shorter.

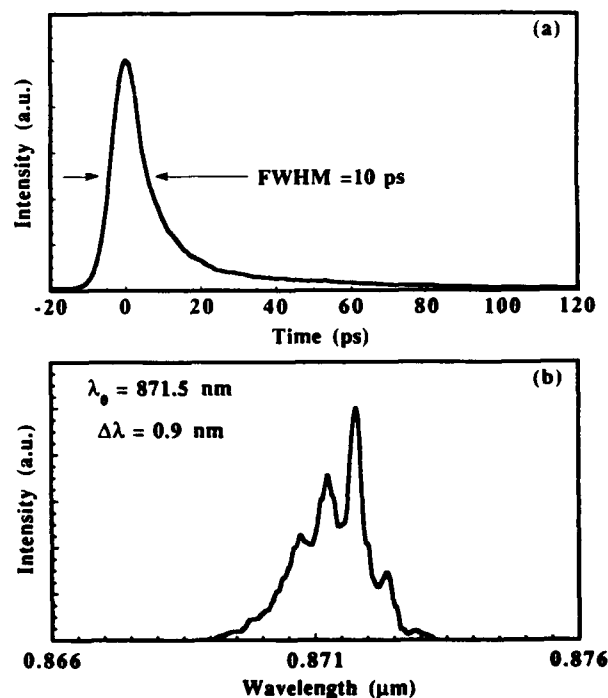


Figure 1 (a) The laser pulse from the VCSEL pumped by a mode-locked dye laser, measured with a streak camera, and (b) the correspondent laser pulse spectrum.

The experimental configuration is the same as that shown in Fig. 1 of Ref. 3 with a GaAs/AlGaAs multiple-quantum-well (MQW) active medium at room temperature. To control the chirping, we replaced the Brewster angle plate with a birefringent filter. The filter thickness was 0.5 mm. With the pump pulsewidth of 21 ps measured with Hamamatsu M1955 streak camera, we obtained the laser pulsewidth of 10 ps shown in Fig. 1(a) measured by the same streak camera. The specified resolution of the streak camera was 10 ps. The corresponding laser pulse spectrum is shown in Fig. 1(b). Although the filter was placed at Brewster angle, there was some modulation to the spectrum, caused by the residual Fabry-Perot effect of the filter. The time-bandwidth product of the pulses was 3.6, which is only one tenth of that reported earlier [3].

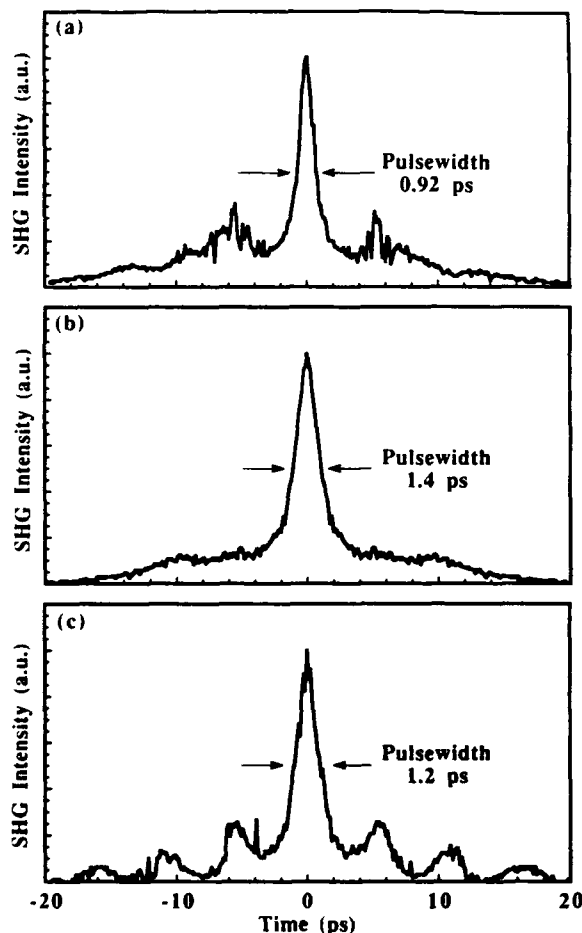


Figure 2. Autocorrelation traces of the laser pulses from the VCSEL pumped by a mode-locked Ti: sapphire laser with a birefringent filter of 0.5 mm thickness for three different laser cavity length detuning.

The laser pulse was asymmetrically shaped with a long tail, which implies the poor gain saturation. The intracavity laser pulse energy was, however, 4.1 nJ for a laser average output power of 10 mW at 80 MHz with an output coupler reflectivity of 97%, while the gain saturation energy of GaAs/AlGaAs MQWs active

medium was  $E_{\text{sat}} = 1.2$  nJ [4]. The gain should actually be deeply saturated.

To further understand this problem, a mode-locked Ti: Al<sub>2</sub>O<sub>3</sub> laser producing 100 - 200 fs pulses was used as the pump and the laser cavity was converted to 89 MHz to match the repetition rate of the Ti: Al<sub>2</sub>O<sub>3</sub> laser. To decrease the intracavity pulse energy for the same amount of output power, thereby minimizing the gain-saturation-induced SPM, the reflectivity of the output coupler was changed to 95%. With appropriate positioning of the birefringent filter, we obtained our shortest laser pulses directly from the laser oscillator, as shown by the autocorrelation trace in Fig. 2(a). Assuming a hyperbolic secant pulse shape, the laser pulsewidth was 0.92 ps. The average laser output power was 11 mW at the pump power of 200 mW. The side lobe at 5.5 ps away from the main peak in the autocorrelation trace was due to the residual Fabry-Perot effect of the filter. This effect could be suppressed at the price of broadened laser pulsewidth by detuning the laser cavity length, as shown in Fig. 2(b). The effect could also be strengthened again by the cavity detuning as shown in Fig. 2(c), where more subpulses were observed. Fig. 3 shows the spectrum of the 0.92 ps pulses. The time bandwidth product of the pulses was 0.85, indicating less chirping. The ripple in the spectrum confirmed the existence of the Fabry-Perot effect of the filter. The modulation mode spacing was 5 Å, so the time between the multiple pulses should be 5.2 ps, which was in good agreement with the autocorrelation measurement of 5.5 ps.

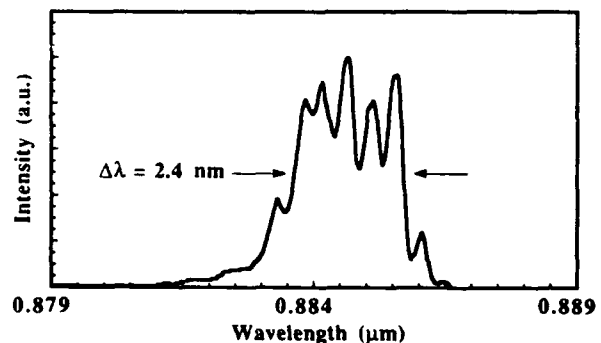


Figure 3. The pulse spectrum corresponding to Fig. 2(a).

To further suppress the pedestals and the subpulses, we replaced the 0.5 mm thick birefringent filter by a 1 mm thick birefringent filter. A thicker filter has a narrower bandpass. Figure 4(a) is the autocorrelation of the laser pulses from the laser cavity in this filter. The laser pulsewidth was 2.1 ps if a hyperbolic secant pulse shape was assumed. Although the laser pulsewidth was broadened, the pedestals were suppressed. If the birefringent filter thickness was further increased to 5 mm, the pulsewidth was broadened to 3.4 ps, as shown in Fig. 4(b), indicating that the bandpass of the filter was so narrow that it started to broaden the laser pulsewidth. Obviously, there was a compromise between minimum pulsewidth and minimum pedestals,

i.e. there was an optimum birefringent filter thickness to produce relatively pedestal-free pulse with the shortest possible pulsewidth.

The laser pulses in Figs. 2 and 4 were much longer than the pump pulses, which again indicated the poor tail shaping, or in other words, the poor gain saturation. The intracavity pulse energy in this case was actually 2.3 nJ, still larger than the gain saturation energy  $E_{\text{sat}}$ . To explain this contradiction, we assumed that there be an anti-gain-saturation mechanism in the laser. It is important to note that the gain medium in this laser was directly attached to one of the cavity mirrors. Spatial hole burning occurred during the laser operation because of a standing wave in the gain medium formed by the incident and the reflected beams. The carriers in the quantum wells outside of the high intensity regions would transport into these regions through thermionic emission, diffusion and tunneling, thus deterring the gain saturation. The carrier transport would not stop until carrier densities became equal everywhere. The duration needed to reach such an equilibrium was the dominant limitation in obtaining femtosecond pulses, if the pulse chirping was carefully excluded.

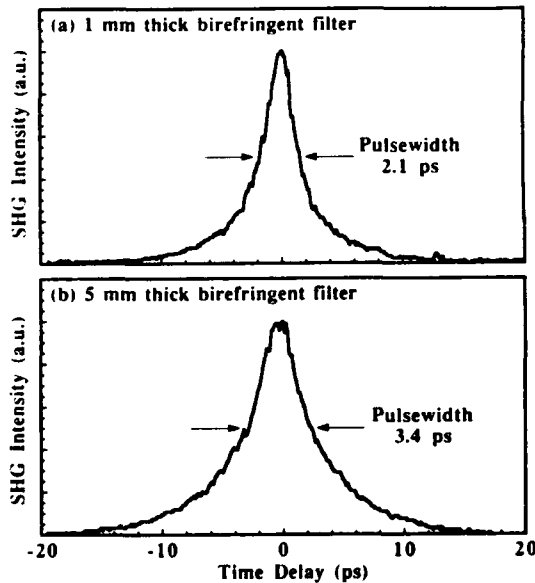


Figure 4 Autocorrelation traces of laser pulses from the VCSEL pumped by a mode-locked Ti: sapphire laser with a birefringent filter thickness of (a) 1 mm and (b) 5 mm.

To estimate the carrier transport time, the carrier diffusion time for the bulk active medium is a good reference. The diffusion equation to the problem is

$$\frac{\partial N(z,t)}{\partial t} = D \frac{\partial^2 N(z,t)}{\partial z^2} \quad (1)$$

where  $N(z, t)$  is the carrier density, and  $D$  is the diffusion coefficient. The solution to Eq. (1) is

$$N(z,t) = N_0 + N_1 e^{-t/\tau} \left| \sin \left( \frac{2\pi n}{\lambda_0} z \right) \right| \quad (2)$$

where  $N_0$  is initial carrier density at the peak of the standing wave in the gain medium (spatial hole), which equals to the carrier density at transparency to the laser central wavelength  $\lambda_0$ ,  $(N_0 + N_1)$  is the initial carrier density in the valley region of the standing wave in the gain medium (out side of spatial hole), and  $n$  is the refractive index of the gain medium. The carrier diffusion time,  $\tau$ , is given by

$$\tau = \frac{\lambda_0^2}{4\pi^2 n^2 D} \quad (3)$$

where  $\lambda_0 = 0.88 \mu\text{m}$  and  $n = 3.5$ . The ambipolar diffusion coefficient  $D = 5.0 \text{ cm}^2 \text{ s}^{-1}$ . From (3), we have  $\tau = 3.2 \text{ ps}$ .

The actual gain medium was a multiple quantum-well sample, so the carrier transport time must have been longer. If the thermionic emission and tunneling were included, however, the time was still on that order [5]. A gain window was thus opened for this picosecond pulse duration, within which the gain saturation was not complete even though the intracavity laser pulse energy was larger than the gain saturation energy. The laser pulses generated would either show long tail extending over this duration, or be accompanied by subpulses if extra resonances were possible through a Fabry-Perot effect.

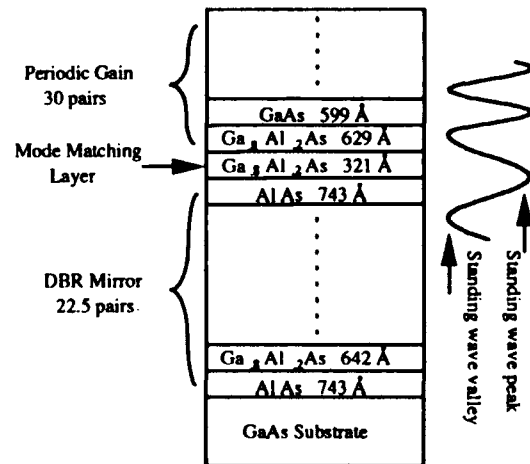


Figure 5 The DBR mirror and the periodic gain structure designed for the wavelength at 883 nm. The standing wave pattern next to the periodic gain structure shows that the valleys of the standing wave are located in the barriers and the peaks are located in the wells.

A solution to this problem is to place the gain only at the peaks in the optical standing wave pattern. This periodic gain structure has also the advantage of lowering the lasing threshold [6]. Fig. 5 schematically

shows the gain design. On the GaAs substrate were 22 pairs of AlAs/Ga<sub>0.8</sub>Al<sub>0.2</sub>As and an extra layer of AlAs, forming the distributed Bragg reflector (DBR) mirror. The AlAs thickness was 743 Å and the Ga<sub>0.8</sub>Al<sub>0.2</sub>As thickness was 642 Å. The gain region was a periodic structure with Ga<sub>0.8</sub>Al<sub>0.2</sub>As/GaAs of 30 pairs. The barrier Ga<sub>0.8</sub>Al<sub>0.2</sub>As was 629 Å thick and the well GaAs was 599 Å thick. Between the gain region and the DBR mirror was a 321 Å thick barrier Ga<sub>0.8</sub>Al<sub>0.2</sub>As used for the mode matching between the standing waves in the DBR mirror and in the gain region. This structure was designed for a wavelength of 883 nm. The standing wave pattern next to the periodic gain structure in the figure shows that the peaks of the standing wave were located in the wells of the structure, while the valleys of the standing wave were located in the barriers.

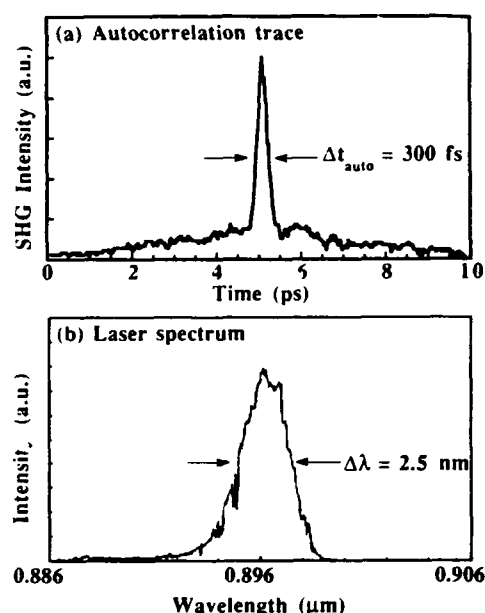


Figure 6 (a) The autocorrelation trace of the laser pulses from the periodic gain vertical-cavity surface-emitting laser. The FWHM of the autocorrelation trace is 300 fs. (b) The corresponding pulse spectrum with the spectral width of 2.5 nm centered at 896.2 nm.

An antireflection (AR) coating was done on the epitaxial side of the MBE grown wafer. This wafer was then mounted onto a heat sink in the laser cavity to replace the multiple-quantum-well (MQW) sample used earlier. The output coupler had a reflectivity of 97%. Birefringent filters were not necessary in the cavity since the periodic gain structure itself had a filter effect. The VCSEL was mode-locked by matching the laser cavity length again to that of the pump laser, the CW mode-locked Ti: sapphire laser operating at 89 MHz with the wavelength at 800 nm. At the pump power of 200 mW, the output power from the mode-locked VCSEL was 6 mW. The autocorrelation trace of the mode-locked pulses is shown in Fig. 6(a). The full

width at half maximum (FWHM) of the autocorrelation trace is 300 fs. The corresponding pulse spectrum is shown in Fig. 6(b). The spectral width is 2.5 nm. If a pulse shape of hyperbolic secant were assumed, the laser pulsewidth would be 190 fs and the time-bandwidth product  $\Delta\nu\Delta t$  become 0.18, which is smaller than the transform limited value of 0.32. If a pulse shape of single side exponential were assumed, the laser pulsewidth would be 150 fs and the time-bandwidth product  $\Delta\nu\Delta t$  become 0.14, which is slightly larger than the transform limited value of 0.11. The actual pulse shape, we believe, had a very rapid rising edge close to the Gaussian shape, but a slow falling tail following the exponential shape, which was similar to the behavior measured by the streak camera in Fig. 1(a). This could happen because of the residual carrier transport effect, which is partially supported by the large pedestals. Following this argument, the actual laser pulsewidth should be somewhere between 150 fs and 190 fs.

In conclusion, we designed a periodic gain structure as the gain medium for the mode-locked VCSELs. This structure successfully solved the problem of carrier transport from the valleys of the standing wave to the peaks (spatial hole), so that the laser pulsewidth directly generated from the VCSELs became much shorter than when a MQW structure was used as the gain. The periodic gain structure also acted as a spectral filter to curb the pulse chirping and increased the effective differential gain. The laser pulsewidth of under 190 fs was the shortest reported in any mode-locked semiconductor lasers.

This work was supported by DARPA and Rome Laboratories.

#### References:

1. W. B. Jiang, S. R. Friberg, H. Iwamura, and Y. Yamamoto, "High powers and subpicosecond pulses from an external-cavity surface-emitting InGaAs/InP multiple quantum well laser," *Appl. Phys. Lett.*, **58**, 807-809 (1991)
2. W. H. Xiang, S. R. Friberg, K. Watanabe, S. Machida, W. B. Jiang, H. Iwamura, and Y. Yamamoto, "Femtosecond external-cavity surface-emitting InGaAs/InP multiple-quantum-well laser," *Opt. Lett.*, **16**, 1394-1396 (1991)
3. W. B. Jiang, R. Mirin, and J. E. Bowers, "Mode-locked GaAs vertical cavity surface emitting lasers," *Appl. Phys. Lett.*, **60**, 677-679 (1992)
4. W. B. Jiang, D. J. Derickson, and J. E. Bowers, "Analysis of laser pulse chirping in mode-locked vertical cavity surface emitting lasers," *IEEE J. Quantum Electron.*, **29** (1993)
5. R. Nagarajan, M. Ishikawa, T. Fukushima, R. S. Geels, and J. E. Bowers, "High speed quantum-well lasers and carrier transport effects," *IEEE J. Quantum Electron.*, **28**, 1990-2008 (1992)
6. S. W. Corzine, R. S. Geels, J. W. Scott, R. H. Yan and L. A. Coldren, "Design of Fabry-Perot surface-emitting lasers with a periodic gain structure," *IEEE J. Quantum Electron.*, **25**, 1513-1524 (1989)

# Picosecond Gain Dynamics in Vertical Cavity Surface Emitting Laser: Transient Carrier Heating and Gain Enhancement

Gary Wang, Radhakrishnan Nagarajan, Dan Tauber, and John E. Bowers

Department of Electrical and Computer Engineering, University of California,  
Santa Barbara, California 93106

## Abstract

Enhancement of resonance frequency up to 87 GHz has been observed in a vertical cavity surface emitting laser. We derive an analytical expression for the intrinsic gain suppression factor based on carrier heating. The theory shows good agreement with the published experimental value of  $\epsilon = 1.5 \times 10^{-17} \text{ cm}^3$  for in-plane lasers. For the first time, we predict and experimentally observe a *negative* gain suppression factor for particular laser designs. A negative gain suppression factor can lead to the elimination of damping in semiconductor lasers. Using vertical cavity surface emitting lasers, we observe a negative gain suppression factor of  $-2.2 \times 10^{-17} \text{ cm}^3$ .

## Introduction

High speed modulation of vertical cavity surface emitting lasers (VCSELs) is essential for wide bandwidth, on-chip optical interconnects[1]. From a previous optical gain switching experiment, an intrinsically wide bandwidth for VCSELs has been predicted[2]. In recent demonstrations of an electrically pumped VCSEL, the bandwidth has been limited by RC parasitics due to the high series resistance of current injecting mirrors. However, to determine the intrinsic dynamic response beyond the RC limit, electrical gain switching experiments can be used. In this paper, we present the theory and experimental results of picosecond dynamics of electrically gain switched VCSELs. Most importantly, we predict and observe a negative gain suppression factor for lasers with a positive temperature derivative of gain. Furthermore, we propose that the damping limit can be greatly reduced with proper design.

## Theory

Previous studies on gain switching of in-plane lasers have shown the modulation bandwidth and resonance frequency of the laser are related [3]. The gain switched laser dynamics can be modeled using the coupled carrier-photon rate equations [3],

$$\begin{aligned} \frac{dN}{dt} &= \frac{\eta_i I}{qV} - v_g G(N, T_{\text{lattice}}, T_e) S - \frac{N}{\tau_n} \\ \frac{dS}{dt} &= \Gamma v_g G(N, T_{\text{lattice}}, T_e) S - \frac{S}{\tau_p} \end{aligned} \quad (1)$$

where  $N$  is the carrier density,  $S$  is the photon density,  $\eta_i$  is the internal quantum efficiency,  $\Gamma$  is the confinement factor,  $v_g$  is the group velocity,  $\tau_n$  and  $\tau_p$  are the carrier and photon lifetimes, respectively. The important result from the analysis of Eqs. (1) is that the resonance frequency of the laser is given by the inverse of the geometrical mean between the stimulated emission lifetime and the intracavity photon lifetime[3]. Due to the ultra short cavity length, a shorter photon lifetime can be achieved more easily for VCSELs than for in-plane lasers, even though the mirror reflectivities of VCSELs are significantly higher[2]; therefore, we can expect an enhancement of the resonance frequency and the intrinsic modulation bandwidth for VCSELs. In addition, the temporal variation of gain described by Eq. (1) depends significantly on the dynamics of the longitudinal mode. For structures such as distributed feedback (DFB) lasers or VCSELs, the lasing mode is restrained by the cavity design, whereas for in-plane laser, the lasing mode always occurs at the gain peak. Furthermore, the gain dynamics at the lasing mode can be significantly different if the transient variation of temperatures are considered.

The assumption that the carrier temperature is equal to the lattice temperature in Eq. (1) is valid only if we assume that the heat capacity of the electron gas inside the active region is infinite. However, this is not physical. Under electrical modulation, the energy of carriers pumped into the cavity will vary in time, which in turn causes a variation in the carrier temperature and lattice temperature. As the temperature of hot carriers fall, the lattice temperature will rise. This motivates us to investigate the temperature dependence of gain and derive the rate equations for the carrier temperature.

The temperature dependence of the gain coefficient  $g_T$  is negative for in-plane lasers, where the lasing mode always occurs at the gain peak. However, the lasing mode of VCSELs is restrained by the cavity design. If the lasing wavelength is placed at the longer wavelength side of the gain profile, then as the lattice temperature increases, the bandgap of the active region will shrink. The resulting effect is that the gain peak can shift into resonance with the lasing wavelength, therefore resulting in a positive  $g_T$ . Both Scott *et al.* [4] and Dudley *et al.* [5] have observed a decrease in lasing threshold as temperature increases for VCSEL structures.

To include the temperature dependence of gain in the rate equation analysis, we assume the carriers are injected with an excess energy  $\Delta_e$  above the conduction band edge. As the hot carriers are cooled from the injected level to the lasing level, heat is transferred from the carriers to the lattice via the emission of phonons. The rate at which the carrier temperature varies depends directly on the energy relaxation rate and heat capacity of electron gas  $C_{el}$ . Following previous works of Bimberg and Mycielski [6] on carrier heating due to spontaneous emission, we extend the formalism of the temperature rate equation for stimulated emission in a degenerate electron gas system. A similar equation has also been derived by Willatzen *et al.* [7]. By expanding the rate of energy change in terms of carrier density and carrier temperature, one can show that the rate of carrier temperature and lattice temperature change can be written as,

$$\frac{dT_e}{dt} = -\frac{T_e - T_{lat}}{\tau_x} + \left[ \frac{\eta_i I}{qV} \Delta_e - \frac{dN}{dt} \Delta_f \right] \frac{1}{C_{el}} \quad (2)$$

$$\frac{dT_{lat}}{dt} = \frac{C_{el}}{C_{lat}} \frac{T_e - T_{lat}}{\tau_x} - \frac{T_{lat} - T_{sink}}{\tau_{diff}}$$

where  $T_e$  is the carrier temperature and  $T_{lat}$  is the lattice temperature.  $\tau_x$  and  $\tau_{diff}$  are the energy relaxation time and thermal diffusion time in the lattice, respectively.  $\eta_i$  is the internal quantum efficiency,  $V$  is the volume of the active region, and  $\Delta_f = \partial U / \partial N$  is the Fermi energy of the electron gas. When deriving Eq. (2), we have assumed the energy relaxation for the holes is much faster than for the electrons, as is experimentally observed [8]. Excluding any form of

gain suppression in our rate equations, we linearized Eqs. (1) and (2) and obtained the standard modulation response,

$$M(\omega) = \frac{s}{i} = \frac{\eta_i \Gamma}{qV} \frac{\omega_r^2}{\omega_r^2 - \omega^2 + j\omega\gamma}$$

$$\omega_r^2 = \left( \frac{1}{\tau_s \tau_p} \right) \frac{1}{1 + \epsilon S} \quad (3)$$

$$\gamma = \left( \frac{1}{\tau_s} + \frac{1}{\tau_n} + \frac{\epsilon S}{\tau_p} \right) \frac{1}{1 + \epsilon S}$$

where  $\omega_r$  is the resonance frequency,  $\gamma$  is the damping frequency,  $\epsilon$  is the derived gain suppression factor, and  $g_T$  is the effective temperature derivative of the gain with respect to both carrier temperature ( $g_{Te} = dG/dT_e$ ) and lattice temperature ( $g_{Tl} = dG/dT_{lat}$ ). The analytical form of  $\epsilon$  and  $g_T$  are given by,

$$\epsilon = \left[ 1 - \frac{g_T}{g_o} \left( \frac{\Delta_f}{C_{el}} \right) \right] \tau_x g_o v_g \quad (4)$$

$$g_T = \left( (g_{Te} + g_{Tl}) \frac{C_{el}}{C_{lattice}} \frac{\tau_{diff}}{\tau_x} + g_{Te} \right)$$

where  $g_o$  is the differential gain. This result is valid for both in-plane lasers and VCSELs. Figure 1 shows the calculated  $\epsilon$  for quantum wells and bulk in-plane lasers with a negative temperature dependence of gain. The fact that  $\epsilon$  is higher in MQW in-plane lasers agrees well with experimental observations [9].

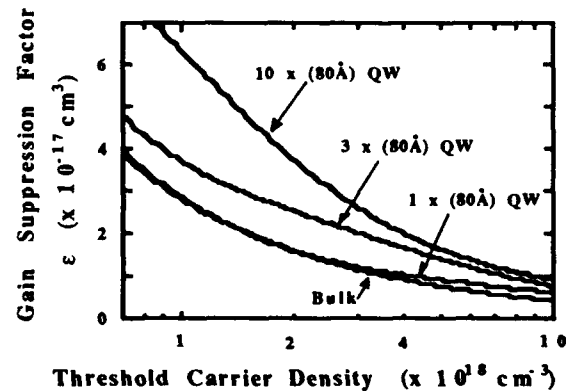


Figure 1. Theoretical prediction of gain saturation factor  $\epsilon$  vs. threshold carrier density for various in-plane laser structures. Parameters used:  $T = 300^\circ\text{K}$ ,  $g_o = 3 \times 10^{-16} \text{ cm}^2$ ,  $g_T = -30 \text{ cm}^{-1}\text{K}^{-1}$ ,  $\tau_x = 0.2 \text{ ps}$ , and  $v_g = 0.75 \times 10^{10} \text{ cm/s}$ .

All of the terms in the expansion for  $\epsilon$  are positive except for  $g_T$ . From Eq. (4), we can see that a positive  $g_T$  will have a significant effect on our result. A positive  $g_T$  yields a negative  $\epsilon$ , which will enhance, rather than suppress, the resonance frequency of the lasers. While the resonance frequency is enhanced for devices with a positive  $g_T$ , the damping rate is reduced due to a negative gain suppression factor. For increasing values of  $g_T$ , the damping can be eliminated and eventually becomes negative (Figure 2). Lasers operating with a negative damping rate will be unstable, but this can lead to possible new applications. The critical value of  $g_T$  which will lead to a zero damping is given by,

$$g_{T,o} = \frac{g_o C_{el}}{\Delta_f} \left( 1 + \frac{\tau_p}{\tau_x} \left( 1 + \frac{1}{\tau_n v_g g_o S_o} \right) \right) \quad (5)$$

The effect of  $g_T$  on the modulation response is shown in Figure 3. For  $g_T = +6 \text{ cm}^{-1}\text{K}^{-1}$ , the modulation response exhibits zero damping. Unstable responses are shown in the dashed lines.

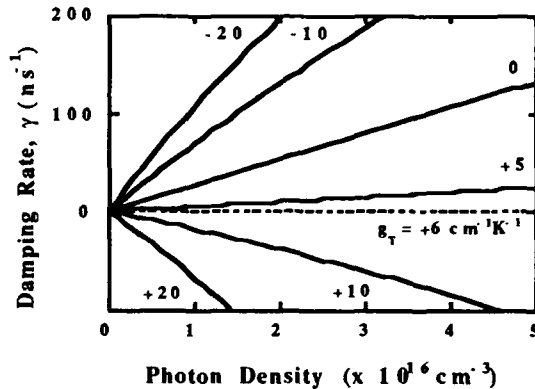


Figure 2. Damping rate vs. photon density for various values of  $g_T$ . For  $g_T = +6 \text{ cm}^{-1}\text{K}^{-1}$ , the damping frequency is zero. A positive  $g_T$  will lead to a negative damping rate, and the lasers will be unstable in that regime.

## Experiment

To verify our theory of gain enhancement, we investigated the modulation characteristics of VCSELs. From calculation of gain at the lasing wavelength, the devices have an estimated  $g_T$  of  $+10 \text{ cm}^{-1}\text{K}^{-1}$ . The VCSELs we studied [10] consist of an active region of three  $80 \text{ \AA}$   $\text{In}_{0.2}\text{Ga}_{0.8}\text{As}/\text{GaAs}$  strained quantum wells [3]. The top mirror has 16 periods of  $\text{AlAs}/\text{GaAs}$  distributed Bragg reflector (DBR), and the bottom mirror has 18.5 periods. The energy relaxation time of

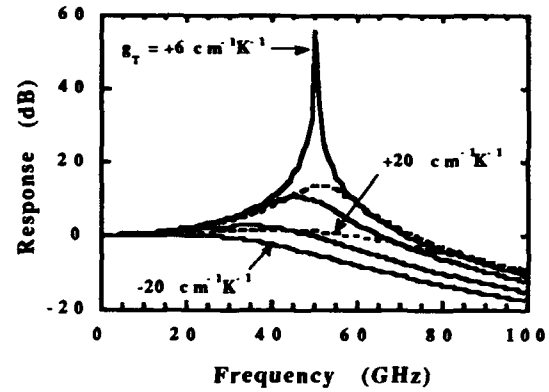


Figure 3. Calculated modulation response for various values of  $g_T$  at high photon density  $S_o = 4 \times 10^{16} \text{ cm}^{-3}$ . Responses in the stable regime are plotted in solid lines, and the unstable responses are plotted in the dashed lines. Damping is eliminated for  $g_T = +6 \text{ cm}^{-1}\text{K}^{-1}$ . The effect of damping due to spontaneous emission is neglected here.

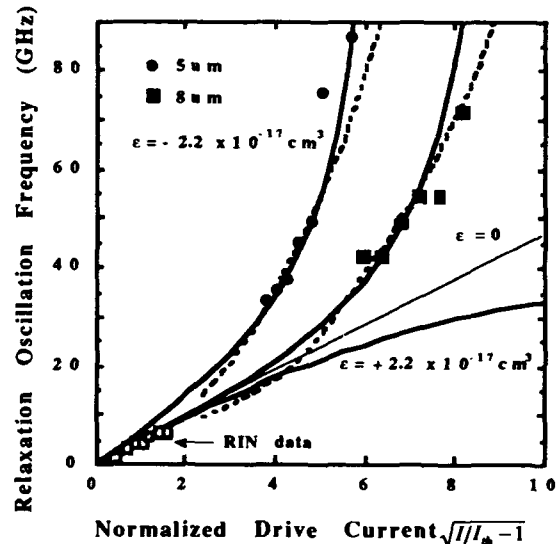


Figure 4. Relaxation oscillation frequency measured from electrical gain switching experiment, for vertical cavity surface emitting lasers with a positive temperature derivative of gain ( $g_T = +10 \text{ cm}^{-1}\text{K}^{-1}$ ). Circular and square dots are for  $5 \mu\text{m}$  and  $8 \mu\text{m}$  square devices, respectively. Solid lines are analytic small signal calculation, and dashed lines are numerical large signal simulation of gain switching experiment. The estimated  $\epsilon$  is  $-2.2 \times 10^{-17} \text{ cm}^3$ .

the carriers is estimated to be  $0.5 \text{ ps}$ . From Eq. (4), we predict an enhancement of resonance frequency which is characterized by a gain suppression factor of  $-2.1 \times 10^{-17} \text{ cm}^3$ . Since the high frequency response of VCSELs is still strongly limited by parasitic effects, it

would be difficult to accurately determine the relaxation oscillation frequency and damping frequency from modulation measurements. Instead, we measure the resonance frequency from CW relative intensity noise (RIN) measurements (Figure 4). However, as the laser is driven far above threshold, CW heating in the active layer severely limits the usefulness of this technique. To avoid this problems, we also measured the pulsed dynamic characteristics of the device with a streak camera. A step recovery diode is used to generate 12V 100 ps pulses at an 80 MHz repetition rate. A Hamamatsu M1955 streak camera in the synchro-scan mode is used to monitor the gain switched output. The period of the large signal relaxation oscillations is measured and the inverse of this period is plotted in Figure 4, along with the CW RIN data. This figure shows data for two VCSELs of different sizes. Maximum relaxation oscillation frequencies of 87 and 71 GHz are observed from 5  $\mu\text{m}$  and 8  $\mu\text{m}$  devices, respectively.

The figure also shows calculations based on positive and negative  $\epsilon$ . It can be seen that the data matches quite well with an  $\epsilon$  of  $-2.2 \times 10^{-17} \text{ cm}^3$ , in agreement with the estimated value. Note that these experimental results cannot be understood using conventional expressions for differential gain and damping frequency. The final calculation shown in Figure 4 is a large signal calculation of the inverse of the relaxation oscillation time based on a numerical integration of the rate equations including carrier heating. The inverse of the relaxation oscillation ringing time is approximately the same as the on-state small signal resonance frequency, as we assumed in the previous paragraph. We have verified this relation also for the case of very high driving signals (50 times threshold) and very high relaxation oscillation frequencies (90 GHz). It can be seen theoretically that the small signal and the large signal results are quite similar.

### Conclusions

In conclusion, we have analyzed the high frequency dynamics of semiconductor lasers including carrier heating. The calculated value of  $\epsilon$  agrees with published results for in-plane lasers. The theory is able to explain the variation of  $\epsilon$  between bulk and MQW lasers. Furthermore, we have predicted that with proper cavity design, one could observe an enhancement in the resonance frequency and elimination of damping in VCSELs or DFB lasers. An enhancement in the resonance frequency was observed in high speed VCSELs.

### Acknowledgments

The authors would like to thank D. Bimberg, E. Ippen, K. Hall, B. Gomatam, D. Babic, J. Karin, and R. Helkey for many informative discussions, and R. S. Geels, J. Scott, B. Young and L. A. Coldren for providing the VCSELs for the gain switching experiments. This work

is supported by the NSF Science and Technology Center of Quantized Electronic Structures, Grant #DMR 91-20007.

### References

1. M. W. Maeda, C. Chang-Hasnain, A. Vonlehmen, H. Izadpanah, C. Lin, M. Z. Iqbal, L. Florez, J. Harbison, "Multigigabits/s operation of 16-wavelength vertical-cavity surface emitting laser array," *Photonic Tech. Lett.* 3 863 (1991)
2. J. R. Karin, L. G. Melcer, R. Nagarajan, J. E. Bowers, S. W. Corzine, P. A. Morton, R. S. Geels, L. A. Coldren, "Generation of picosecond pulses with a gain-switched GaAs surface emitting laser," *Appl. Phys. Lett.* 57 963 (1990)
3. J. E. Bowers, "High speed semiconductor laser design and performance," *Solid State Electron.*, 30, 1-11 (1987)
4. J. W. Scott, B. Young, S. W. Corzine, L. A. Coldren, "Modeling temperature effects and spatial hole burning to optimize vertical cavity surface emitting laser performance," To be published in *IEEE J. Quantum Electron.*
5. J. J. Dudley, M. Ishikawa, D. I. Babic, B. I. Miller, R. Mirin, W. B. Jiang, J. E. Bowers, E. L. Hu., "144 °C operation of 1.3  $\mu\text{m}$  InGaAsP vertical cavity lasers on GaAs substrates," To be published in *Appl. Phys. Lett.*
6. D. Bimberg, J. Mycielski, "The recombination-induced temperature change of non-equilibrium charged carriers," *J. Phys. C: Solid State Phys.* 19 pp. 2363-2373, (1986)
7. M. Willatzen, A. Uskov, J. Mork, H. Olesen, B. Tromborg, A. P. Jauho, "Nonlinear gain suppression in semiconductor lasers due to carrier heating," *IEEE Photonics Technology Lett.*, vol. 3 606-609 (1991)
8. J. Shah, "Hot carriers in quasi-2D polar semiconductors," *IEEE J. Quantum Electron.*, QE-22, 1728-1743 (1986).
9. K. Uomi, T. Tsuchiya, M. Aoki, N. Chinone, "Oscillation wavelength and laser structure dependence of nonlinear damping effect in semiconductor lasers," *Appl. Phys. Lett.* 58 675-677 (1991)
10. R. S. Geels, S. W. Corzine, L. A. Coldren, "InGaAs vertical-cavity surface emitting lasers," *IEEE J. Quantum Electron.*, QE-27, 1359-1367 (1991)



# Transient Pulse-Response of InGaAs/InGaAsP Distributed Feedback Lasers for Multigigabit Transmission Systems

J. Kovac, C. Kaden, and H. Schweizer

4. Physikalisches Institut, Universität Stuttgart, Pfaffenwaldring 57,  
7000 Stuttgart-80, Germany

M. Klenk, R. Weinmann, E. Zielinski

Alcatel-SEL, Research Center, Lorenzstr. 10, 7000 Stuttgart-40, Germany

## Abstract

Optical excitation with picosecond pulses is used to investigate high frequency modulation properties of distributed feedback (DFB) lasers. Typical time constants like the rise and fall time and the full width at half maximum of the laser response were investigated. We show that intrinsic carrier dynamics mainly determine the transient behavior of the lasing pulse. A theoretical analysis of a 3 level system considering carrier dynamics yields coupled rate equations, which are appropriate for a description of the experiments. Furthermore spectral characteristics of DFB lasers in the picosecond time scale is analyzed with respect to multi- and single mode operation.

## Introduction

InGaAs/InGaAsP semiconductor lasers are key devices for optical-communication systems. Single mode devices like DFB lasers are necessary to meet the requirements for high data-rate systems based on optical fiber transmission links.

A powerful method to investigate fast processes in semiconductor lasers is the technique of light frequency up-conversion [1]. A careful adjustment of the excitation pulses in time and frequency domain results in a temporal and spectral resolution simultaneously, which allows to quantify the temporal behavior like the rise time and the fall time of the laser emission and which enables a direct observation of the carrier dynamics by transient spectra.

In this contribution we will discuss the pulse response of multiple quantum well MQW ( $L_z = 8$  nm) InGaAs/InGaAsP DFB lasers optimized for carrier- and light-confinement. The resonators are 500  $\mu\text{m}$  long and consist of DFB gratings of different periods ( $\Lambda = 220$  nm - 250 nm).

The light is coupled out by a slab waveguide. The optical modulation of the DFB was carried out by a pulse-compressed cw mode-locked Nd-YAG laser with a full width at half maximum (FWHM) of 9 ps. The up-converted signal was detected by an optical multichannel analyzer.

For a theoretical description of laser dynamics coupled rate equations were used. Intrinsic carrier dynamics are included by considering a 3 level system.

## Experimental results

The response of the device on a pulsed optical excitation is demonstrated in Fig. 1. The transient spectra indicate the main characteristics of the lasing process: the intensity of the laser mode increases and vanishes within 80 ps.

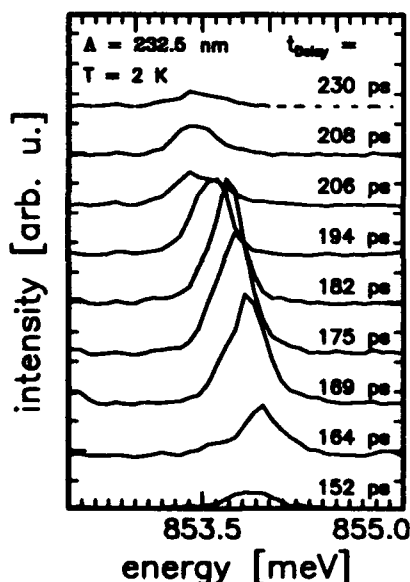


Figure 1. Transient spectra of a DFB mode at 77 K with a grating period of 232.5 nm

During this time, the lasing mode is chirping.

A detailed analysis of the lasing process can be carried out on the base of Fig. 2. The integrated intensity of the DFB mode (left axis) is depicted versus time. At first the spontaneous emission, respectively the amplified spontaneous emission of the device is detected. After a delay-on time of about 150 ps lasing starts. The rise time of the single mode is 7 ps, the fall time is 18 ps. At later times the emission passes into the spontaneous, respectively the amplified spontaneous emission.

One single pulse with a FWHM of 29 ps is observed, no relaxation oscillations appear. This can be explained by a build-up of the carrier density and a subsequent recombination via stimulated emission.

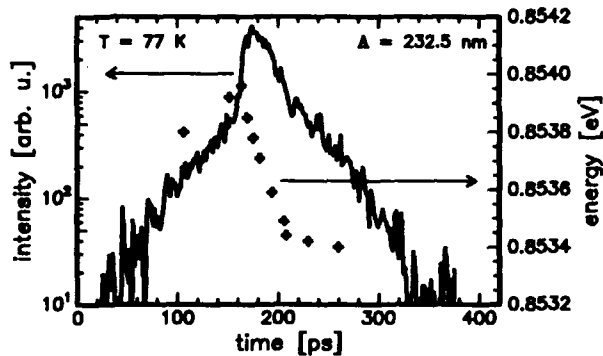


Figure 2.

Solid line: intensity of the DFB mode versus time

Crosses: energy shift of the DFB mode versus time

In the case of optical excitation electron-hole pairs are mainly generated in the energy levels of the InGaAsP-barriers. The intrinsic processes of relaxation, diffusion and capture of carriers from the barriers into the quantum wells populate the energy level responsible for lasing [2][3]. Recombination of electron-hole pairs leads to spontaneous, respectively amplified spontaneous emission. When threshold density is exceeded, lasing starts. The intensity of the DFB mode shows a steep rise. The interplay between the population of the lasing level and the reduction of the carrier density via stimulated emission determines the duration of the lasing process. When the carrier density is reduced below threshold density, lasing ends and spontaneous, respectively amplified spontaneous emission reduce the carrier density further.

The intrinsic carrier transport and relaxation effects in conjunction with spontaneous and stimulated emission lead to the mostly undesirable chirping of the lasing mode. In Fig. 2 the energy position of the DFB mode (right axis) during and slightly before and after lasing is plotted versus time. Before laser emission

starts there is a blue-shift. When threshold is reached an abrupt chirping of about 0.6 meV down to lower energies is observed. This can be understood by the dependence of the effective refractive index on the carrier density. First the carrier population in the quantum wells increases. When threshold is reached the subsequent reduction of the carrier density reduces the refractive index causing a red-shift. The change  $\delta n$  of the refractive index due to free carrier density  $N$  can be described by [4],

$$\delta n = - N q^2 / (2 m_{n/p} \omega^2 \epsilon_0 n)$$

where  $q$  is the electron charge,  $m_{n/p}$  the effective mass of the electron and hole respectively,  $\omega$  the lasing angular frequency,  $\epsilon_0$  the permittivity of free space and  $n$  the refractive index in the absence of free carriers.

This equation yields an estimation for the carrier density in the active region, which is reduced by the stimulated emission. The shift of 0.6 meV corresponds to a drop of the carrier density during the lasing process, which is in the range of the threshold density ( $\sim 10^{18} \text{ cm}^{-3}$ ).

The discussion above clearly demonstrates that the temporal behavior of the laser emission characterized by the delay-on time, the rise and fall time, the FWHM and the chirp of the mode corresponds to intrinsic carrier dynamics. Relaxation and diffusion of carriers are temperature dependent, so measurements at 2 K and 77 K were performed to show the influence of intrinsic processes on the time behavior of the lasing mode. The results are demonstrated in Fig. 3, where the intensity of the lasing mode is depicted versus time.

At 2 K the distinction between spontaneous, respectively amplified spontaneous emission and the lasing emission is less well defined compared to the threshold points at 77 K. The rise time of about 18 ps and the lasing period with a FWHM of 83 ps appear longer than at 77 K. At 2 K a prolonged diffusion and relaxation time lead to a delayed and prolonged capture of carriers into the lasing level in comparison to 77 K [5].

These results are confirmed by a comparison of different laser resonators with grating periods between 227.5 nm and 235 nm. The Bragg wavelengths of these resonators cover the gain region of the semiconductor material. The laser emission at 2 K starts and ends less abrupt and lasts longer compared to 77 K. The FWHMs at 2 K are between 40 ps and 80 ps and at 77 K between 17 ps and 50 ps. Hereby the FWHMs increase with increasing grating period. For a given grating period the FWHM at 2 K is about a factor of 1.5 to 2.5 longer than at 77 K. From these data we conclude, that different time constants of the intrinsic relaxation and transport effects at 2 K and at 77 K determine mainly the time behavior of the lasing pulse.

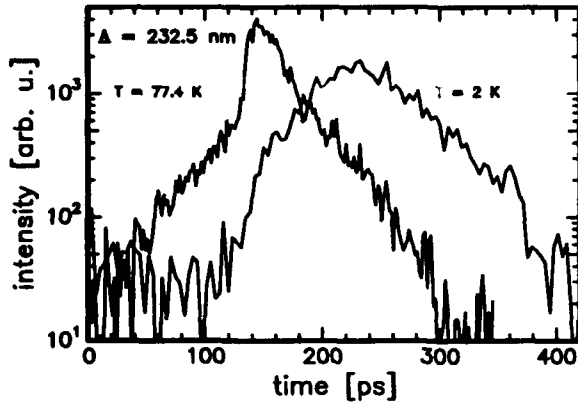


Figure 3.  
Intensity of the DFB mode at different temperatures

### Theoretical description

For the theoretical description of the experiments a 3 level system is used. We assume optical Lorentzian-shaped pulses  $g(t)$  (FWHM = 9 ps) generating a number of electron-hole pairs  $n_{exc}$  in an excited energy level. From this level diffusion, relaxation and capture of carriers into the lasing level of the QW are described by an overall relaxation constant  $\tau_{rel}$ :

$$\frac{\partial n_{exc}}{\partial t} = g(t) - \frac{n_{exc}}{\tau_{rel}}$$

The generation of electron-hole pairs was carried out by an excitation stripe along the resonator with a cylindrical lens. So a homogeneous carrier density along the resonator can be built up. This is the first condition, which allow us the use of spatially averaged rate equations [6] for the theoretical description of the time behavior of one lasing mode. The second condition requires, that time constants for the occupation of the lasing level are longer than the round-trip time of the light-wave in the resonator ( $\sim 10$  ps). Considering only the FWHM of the excitation pulse (9 ps), the limit of validity is reached. When the intrinsic processes at low temperature are taken into account, than the effective occupation time of the lasing level becomes longer and the following rates can be used:

$$\frac{\partial N}{\partial t} = \frac{n_{exc}}{V \cdot \tau_{rel}} - \frac{N}{\tau_{sp}} - \alpha \cdot (N - N_{tr}) \cdot S$$

$$\frac{\partial S}{\partial t} = \Gamma \cdot \alpha \cdot (N - N_{tr}) \cdot S - \frac{S}{\tau_p} + \Gamma \cdot \beta \cdot \frac{N}{\tau_{sp}}$$

The rates which determine the change of the carrier density  $N$  in the lasing level are i) the

population rate from the excited energy level, ii) the rate given by the spontaneous recombination lifetime  $\tau_{sp}$  and iii) the stimulated emission rate with the optical gain coefficient  $\alpha$ , the transparency density  $N_{tr}$  and the photon density  $S$ . The spontaneous recombination lifetime  $\tau_{sp}$  depends on the carrier density, which is taken into account by a sum of the non-radiative, the radiative and the Auger recombination. Non-linearities of the optical gain coefficient are considered by the gain compression factor  $\epsilon$ .

The rates for the photon density are given by i) the stimulated term with the confinement factor  $\Gamma$ , ii) the photon lifetime  $\tau_p$ , which describes the photon losses and iii) the fraction  $\beta$  of the spontaneous contribution emitted into the lasing mode.

Fig. 4 shows the temporal behavior of the photon density for different values of the relaxation constant  $\tau_{rel}$ . The excitation condition corresponds to the experimental preparation of the system and leads to one single response pulse in the time domain. With a relaxation constant of 10 ps a FWHM of 34 ps is obtained. This FWHM value approaches the measured one at 77 K. When the relaxation constant becomes longer the rise time and the FWHMs increase. For a relaxation constant of 300 ps a FWHM of 80 ps is obtained, which corresponds to the measured data at 2 K. For all excitation intensities, longer relaxation constants lead to longer rise times and FWHMs of the response pulses.

From comparison of the theoretical results with the experimentally found temperature dependent laser dynamics we conclude that DFB laser dynamics is mostly determined by carrier dynamics.

A new effect has been observed, which may influence bit error rates seriously at extremely high modulation speed. As mentioned above, the DFB grating is joined to an output-coupler, which leads to Fabry-Perot (FP) modes, if gain is high enough. At a temperature of 2 K we ob-

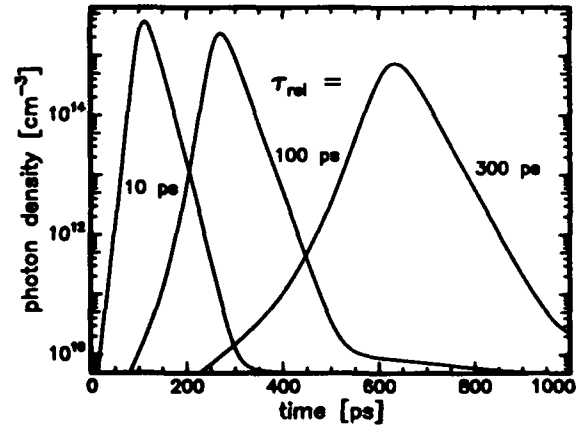


Figure 4.  
Calculated temporal behavior of the photon density for different relaxation constants

served a coupling of the DFB mode and the FP modes which appear at the gain maximum. First the FP modes rise. Still during the increase of the amplified spontaneous emission around the DFB mode the intensity of the FP modes decreases. When the DFB mode reaches threshold the FP modes are quenched.

From these data we conclude, that the threshold gain of the FP is reached very early about 160 ps before a stable DFB mode builds up. A built up time of roughly 16 round-trips is necessary to stabilize the DFB mode. The instantaneous appearance of the FP-modes after the excitation pulse suggests a fast relaxation process. In the sub-picosecond time domain a non-equilibrium distribution of electron and holes is changed into a Quasi-Fermi distribution efficiently via carrier-carrier scattering [7]. Therefore the carriers become redistributed over a wide energy range. At 2 K the gain conditions allow multimode emission for a short time of 1 to 3 round-trips. A following relaxation via optical and acoustic phonons leads to a built up of the DFB mode, which is preferred by the grating

## Conclusion

In summary we have studied the transient behavior of a InGaAs/InGaAsP MQW DFB laser after an optical excitation with picosecond-pulses.

The pulse response on a 9 ps excitation pulse is a single pulse, which is determined by relaxation and diffusion processes of carriers into the QWs: the FWHMs at 77 K are between 17 ps and 50 ps and at 2 K between 40 ps and 80 ps.

The analysis of a 3 level system results in coupled rate equations for the carrier and photon density. The solutions describe the temporal behavior of the experiment: Longer relaxation constants for the intrinsic transport and relaxation processes yield longer FWHMs for the pulse-response in agreement with the temperature dependent experimental findings.

At 2 K multimode (FP) and DFB emission show mode competition effects. Instantaneously after the pump pulse a low threshold for FP modes leads to short time duration (1-3 round-trips). DFB laser emission stabilizes after several round-trips.

## Acknowledgments

The authors thank M.H.Pilkuhn, G.Bacher, G.Mayer and E.Lach for stimulating and valuable discussions and expert experimental assistance.

## References

- [1] J.Shah, "Ultrafast Luminescence Spectroscopy Using Sum Frequency Generation", *IEEE Journal of Quantum Electronics*, Vol.24, No.2, pp. 276-288, (1988)
- [2] A.Weller, P.Thomas, J.Feldmann, G.Peter, E.O.Göbel, "Model Calculations of Diffusion Limited Trapping Dynamics in Quantum Well Laser structures", *Applied Physics A* 48, pp. 509-515 (1989)
- [3] W.Rideout, W.F.Sharfin, E.S.Koteles, M.O.Vassell, B.Elman, "Well-Barrier Hole Burning in Quantum Well Lasers", *IEEE Photonic Technology Letters*, Vol.3, No.9, pp. 784-786, (1991)
- [4] F.R.Nash, "Mode guidance parallel to the junction plane of double-heterostructure GaAs lasers", *J.Appl.Phys.*, Vol.44, No.10, pp. 4696-4707, (1973)
- [5] B.Deveaud, F.Clerot, A.Regreny, K.Fujiiwara, K.Mitsunaga, J.Ohta, "Capture of photoexcited carriers by a laser structure", *Appl.Phys.Lett.* 55 (25), pp. 2646-2648, (1989)
- [6] K.Y.Lau, A.Yariv, "High-Frequency Current Modulation of Semiconductor Injection Lasers" in *Semiconductor and Semiconductor*, Vol.22, Part B
- [7] T.Elsaesser, Jagdeep Shah, Lucio Rota, Paolo Lugli, "Initial Thermalization of Photoexcited Carriers in GaAs Studied by Femtosecond Luminescence Spectroscopy", *Phys.Rev.Letters*, Vol.66, No.13, pp. 1757-1760 (1991)

# Ultrafast Heterobarrier Metal-Semiconductor-Metal Photodetectors

E. Stein Von Kamienski, H. G. Roskos, R. Kersting, J. Plettner, S. V. Averin\*,  
H. -J. Geelen, A. Kohl, B. Spangenberg, K. Leo, and H. Kurz

*Institut für Halbleitertechnik, RWTH Aachen, Sommerfeldstrasse 24, W-5100 Aachen, Germany*

O. Hollricher

*Institut für Schicht-und Ionentechnik, Forschungszentrum Jülich, W-5170 Jülich, Germany*

## Abstract

We describe a heterostructure metal-semiconductor-metal photodetector with subpicosecond response time. In this diode, the intrinsic speed is enhanced by ultrafast real-space transfer of the photogenerated charge carriers from the light-absorbing layer to a reservoir layer underneath.

## Introduction

Planar interdigitated metal-semiconductor-metal (MSM) diode structures are useful as efficient high-speed photodetectors. Their intrinsic speed is limited by either the spacing of the metal fingers or the time during which the carriers retain a high mobility. This time may be limited by either the carrier lifetime or the capture time for trapping of the carriers. One way to increase the speed of the diode is to reduce the finger spacing [1]. Another way is the use of novel semiconductor materials such as low-temperature-grown (LT-)GaAs with a high density of trapping sites [2]. The speed of the diode is in this case improved at the expense of a reduced carrier collection efficiency.

We demonstrate that ultrafast real-space charge transfer in a semiconductor heterostructure is another mechanism to quickly turn off the current in the MSM diode after excitation by a short optical pulse. The light is absorbed in a thin layer of a high-bandgap material at the surface of the diode. The photogenerated carriers are either collected at the electrical contacts or are transferred from the top layer to a reservoir layer of a low bandgap material underneath. It is known that carriers can be transferred on a time scale of a few picoseconds from a high-bandgap to a low-bandgap material over distances on the order of 100 nm [3]. The carriers trapped

in the low-bandgap material recombine on a time scale much longer than the transfer time and do not contribute significantly to the photocurrent if the electrical bias of the MSM diode is moderate to keep the carriers confined.

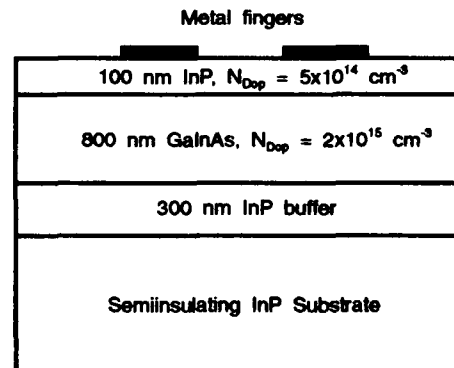


FIG. 1. Cross-section through the layer sequence of the heterostructure MSM diode

We test our approach towards subpicosecond MSM photodiodes with an InP/Ga<sub>0.47</sub>In<sub>0.53</sub>As heterobarrier diode operated in the visible spectral range. The bandgap of Ga<sub>0.47</sub>In<sub>0.53</sub>As is 0.73 eV, that of InP 1.35 eV. The conduction and valence band offsets are sufficient to confine carriers in the Ga<sub>0.47</sub>In<sub>0.53</sub>As layer. The InP cap layer has to be as thin as possible to allow rapid carrier transfer, but thick enough to ensure that a large part of the light is absorbed in this layer. We have chosen a thickness of 100 nm for the InP layer. It absorbs 32 % of the incident light at a laser wavelength of 750 nm (photon energy: 1.65 eV).

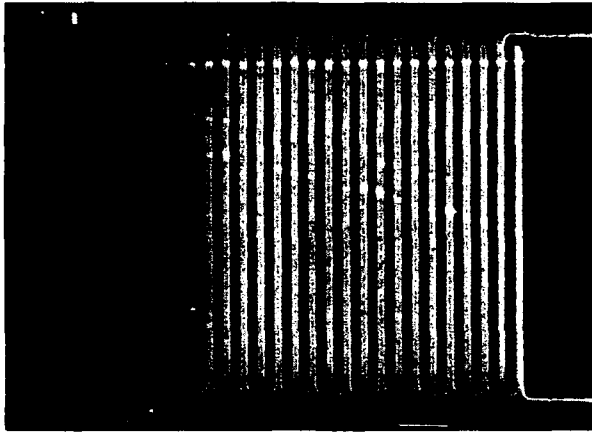


FIG. 2. SEM micrograph showing a top view of the MSM finger structure. Active diode area:  $20 \times 20 \mu\text{m}^2$ , finger width:  $0.5 \mu\text{m}$ , finger separation:  $0.5 \mu\text{m}$ .

#### Device Parameters

Figure 1 shows the layer sequence of our diode. The basic heterostructure consists of a  $800 \text{ nm}$  thick  $\text{Ga}_{0.47}\text{In}_{0.53}\text{As}$  layer with the  $100 \text{ nm}$  thick  $\text{InP}$  layer on top of it. Both layers are nominally undoped. They are grown by low-pressure metal-organic-vapor-phase-epitaxy (LP-MOVPE) on a semiinsulating  $\text{InP}$  substrate. A  $100 \text{ nm}$  thick  $\text{Ti/Pt/Au}$  film is deposited on top of the wafer. A  $20 \times 20 \mu\text{m}^2$  area of the metal film is patterned by electron beam lithography and subsequent Ar sputtering into an interdigitated finger structure with  $0.5 \mu\text{m}$  wide fingers that are  $0.5 \mu\text{m}$  apart from each other. We use the same patterning step to define a several mm long coplanar waveguide with  $20 \mu\text{m}$  wide lines and a line separation of  $20 \mu\text{m}$ . One end of the waveguide contacts the active interdigital area, the other end widens into contact pads for wire bonding. Figure 2 shows a top view of the interdigital area of the diode. Its capacitance is estimated to be  $25 \text{ fF}$ .

#### Electrooptic Characterization

For high-speed characterization, we excite the diode by  $100 \text{ fs}$  pulses from a Kerr-lens-modelocked Ti:Sapphire laser operating at  $750 \text{ nm}$ . We trace the electrical response of the device by electrooptic sampling in a  $\text{LiTaO}_3$  crystal positioned on the coplanar transmission line as closely to the interdigital area as possible. Figure 3 shows the detected electrical signal at a bias voltage of  $1.0 \text{ V}$  for energies of the incident optical pulses ranging from  $3 \text{ pJ}$  to  $26 \text{ pJ}$  (corresponding carrier density in the

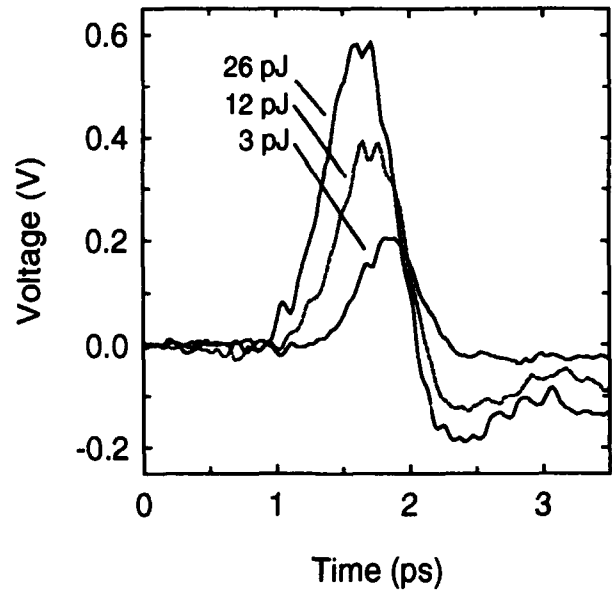


FIG. 3. Electrooptically measured response of the MSM diode (bias  $1.0 \text{ V}$ ) to excitation by a  $100 \text{ fs}$  optical pulse with pulse energy ranging from  $3 \text{ pJ}$  to  $26 \text{ pJ}$  (corresponding density of photogenerated carriers in the  $\text{InP}$  layer:  $2 - 15 \times 10^{17} \text{ cm}^{-3}$ ).

$\text{InP}$  layer:  $2 - 15 \times 10^{17} \text{ cm}^{-3}$ ). The response of the diode is extremely fast. We measure a full width at half maximum of the detected electrical pulses of  $0.6 \text{ ps}$ . This width is nearly independent of the energy of the optical pulses. The observed voltage swing ranges from  $0.2 \text{ V}$  to  $0.6 \text{ V}$  and does not depend linearly on the pulse energy. At low energy, the shape of the electrical pulse is unipolar. At high energy, the electrical waveform develops a bipolar characteristic. The trailing negative lobe of the bipolar signal is likely to have its origin in the dynamics of the intrinsic diode field resulting from spatial variations of the Schottky barrier height. The negative lobe may also be influenced by charge carriers that are unintentionally excited outside of the finger structure.

The importance of vertical carrier transfer for the high speed of the device is proven by a control experiment with a diode without a light-absorbing  $\text{InP}$  top layer. During the sputtering step in the patterning process, the  $\text{InP}$  between the fingers is selectively removed. Light absorption now occurs in the  $\text{Ga}_{0.47}\text{In}_{0.53}\text{As}$  layer only. Figure 4 shows the normalized detected electrical signal of the control measurement (top part of Fig. 4) in comparison with data for a diode with an  $\text{InP}$  layer between the fingers (bottom part of Fig. 4). The bias in both cases is  $1.0 \text{ V}$ , the data are taken at similar incident pulse energies around  $25 \text{ pJ}$ .

From Fig. 4, it is obvious that the heterobarrier structure in the light-absorbing region considerably enhances

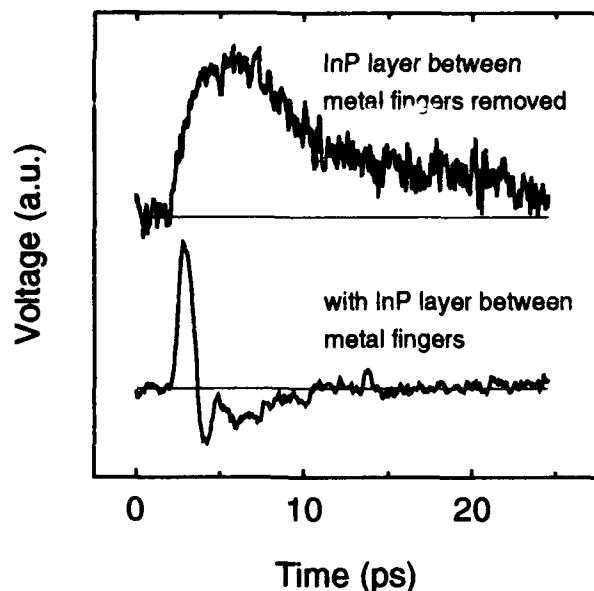


FIG. 4. Electrooptically measured response of MSM diodes after excitation by a 100 fs optical pulse, upper curve: without carrier transfer from InP to  $\text{Ga}_{0.47}\text{In}_{0.53}\text{As}$  (InP between the fingers removed, light is absorbed only in the  $\text{Ga}_{0.47}\text{In}_{0.53}\text{As}$  layer), lower curve: with carrier transfer from the InP cap layer to the  $\text{Ga}_{0.47}\text{In}_{0.53}\text{As}$  layer, the intrinsic speed of the diode. We attribute this increase in speed to the ultrafast transfer of carriers from the InP to the  $\text{Ga}_{0.47}\text{In}_{0.53}\text{As}$  layer.

### Photoluminescence Characterization

To investigate the charge transfer in a more direct way we trace the temporal evolution of the InP bandedge luminescence in an upconversion measurement. We use a diode with an active area of  $100 \times 100 \mu\text{m}^2$ , the finger width and spacing are 3  $\mu\text{m}$ , respectively [4]. The diode is not integrated into a transmission line. The setup for the upconversion measurement is described in Ref. 5. The MSM diode is excited by 100 fs optical pulses from a Ti:Sapphire laser operating at 710 nm (photon energy: 1.75 eV). The luminescence emitted through the finger structure is focused onto a  $\text{LiIO}_3$  crystal and mixed with a second time-delayed laser pulse. The sum frequency signal is spectrally analyzed in a monochromator.

Figure 5 shows the intensity of the luminescence at a wavelength of 906 nm (photon energy: 1.37 eV) as a function of time. The energy of the exciting laser pulse is 400 pJ. After excitation of the diode, the luminescence intensity decays with a time constant of 2 ps to a low residual level.

With the detection set to a photon energy of 1.37 eV, i.e. close to the bandedge of InP, the luminescence intensity is proportional to the carrier density in the InP

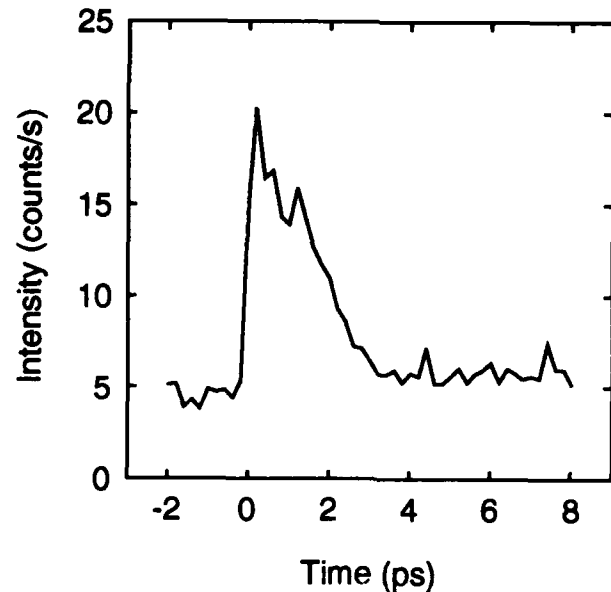


FIG. 5. Upconversion measurement of the InP bandedge luminescence of an MSM diode (biased with 0.2 V) excited by 100 fs optical pulses with a pulse energy of 400 pJ.

top layer. The rapid luminescence decay indicates a fast decrease of the carrier density in the  $\text{InP}$  layer. The observed time constant of 2 ps is too short for the carriers to be collected at the metal contacts [4]. Also trapping at defects or recombination can be excluded as processes able to reduce the carrier density so quickly. The fast luminescence decay is strong evidence for an efficient real-space transfer of the carriers from the InP to the  $\text{Ga}_{0.47}\text{In}_{0.53}\text{As}$  layer.

### Discussion

Real-space transfer of the charge carriers leads to a bandwidth of the MSM diodes comparable to that of LT-GaAs MSM-photodetectors [1,2]. The penalty for the high speed is a reduced carrier collection efficiency. We calculate from our data that only a few percent of all photogenerated carriers are collected in the contacts. The majority of the carriers recombines in the  $\text{Ga}_{0.47}\text{In}_{0.53}\text{As}$  layer on a time scale long compared to that of interest here. Reduction of the finger separation would clearly increase the carrier collection efficiency.

Although the time-integrated photocurrent is low, the switched voltage is high. At a bias of 1.0 V and an optical pulse energy of 12 pJ (26 pJ), we measure a voltage swing of 40 % (60 %) of the applied bias voltage. At such a high switching efficiency, ultrafast field screening effects and especially displacement current contributions are expected to be important. Screening effects, however, do not explain the different time response of the

MSM diodes with and without InP layer between the metal fingers (see Fig. 4). We expect effective field screening also when charge carriers are photogenerated exclusively in the  $\text{Ga}_{0.47}\text{In}_{0.53}\text{As}$  layer. Screening effects certainly influence the shape of the electric pulses generated in both diode types and will have to be included in future model calculations.

### Conclusion

In summary, we have demonstrated that heterostructure InP/ $\text{Ga}_{0.47}\text{In}_{0.53}\text{As}$  MSM-diodes are extremely fast photodetectors for photon energies above the bandgap of InP. Our experiments show that the observed subpicosecond response of the diodes results from an extremely fast carrier trapping process in the form of a transfer of carriers from the InP layer into the  $\text{Ga}_{0.47}\text{In}_{0.53}\text{As}$  layer. The switched voltage is very high. The carrier collection efficiency is modest but can be improved by a reduction of the finger separation. For applications in the visible and near-infrared spectral range ( $\lambda < 900$  nm), if speed is more important than quantum efficiency, this device may be an interesting alternative to other ultrafast photodetectors.

\* Permanent address: Institute of Radioengineering and Electronics, Square Academician Vvedensky 1, 141120 Frjazino, Moscow, CIS. The stay at Aachen has been

made possible by financial support from the Deutsche Forschungsgemeinschaft.

### References

1. S. Y. Chou, Y. Liu, W. Khalil, T. Y. Hsiang, and S. Alexandrou, *Appl. Phys. Lett.* **61** (1992) 819.
2. Y. Chen, S. Williamson, T. Brock, F. W. Smith, and A. R. Calawa, *Appl. Phys. Lett.* **59** (1991) 1984.
3. R. Kersting, X. Q. Zhou, K. Wolter, D. Grützmacher, and H. Kurz, *Superlatt. Microstruc.* **7** (1990) 345; and R. Kersting, R. Schwedler, K. Leo, and H. Kurz, in *Proc. 4th Int. Conf. on InP and Related Materials*, Newport, RI (1992) 565.
4. The increase of the active area of the diode used for the upconversion experiment brings the advantage of a higher luminescence intensity without increase of the density of the photogenerated carriers. The larger spacing of the fingers raises the transit time for electrons to reach the metal contacts to more than 15 ps.
5. R. Kersting, K. Leo, J. Plettner, S. Averin, and H. Kurz, in these Proceedings; see also R. Kersting, J. Plettner, K. Leo, S. Averin, and H. Kurz, *Appl. Phys. Lett.*, scheduled for publication in Febr. 1993.



## Ultrafast Photodection with an InAlAs/InGaAs Heterojunction Bipolar Transistor

T. F. Carruthers, M. Y. Frankel, and C. S. Kyono

Naval Research Laboratory, Washington, DC 20375-5338

### Abstract

Unmodified InAlAs/InGaAs heterojunction bipolar transistors were illuminated with visible-wavelength femtosecond pulses; electrical responses were measured electro-optically. 2.4-ps emitter photocurrent transients, corresponding to a bandwidth in excess of 200 GHz, were observed. Slow photocurrent components due to holes trapped in the base could be eliminated with appropriate base biasing. An equivalent-circuit model successfully accounts for the observed photocurrents.

### Introduction

In a previous study we demonstrated that ultrafast optical studies of heterojunction bipolar transistors (HBTs) can provide information about carrier dynamics within the device [1]. The photocurrent transient of an HBT is composed of a fast component, due to the transit of electrons out of the base and into the emitter, and of much slower components due to the presence of photogenerated holes in the base. The duration of the fast component is much briefer than the microwave bandwidth of the device would suggest [1,2]; that of the slow component is determined by the lifetime of the excess positive charge in the base. The slow photocurrent component is itself composed of more than one component, and these components can be made to cancel at an appropriate base bias, leaving only the fast photocurrent response.

For this study the emitter photocurrent transients of InAlAs/InGaAs HBTs were measured with subpicosecond time resolution; impulse photoresponses as fast as 2.4 ps were measured. We believe these to be the fastest responses observed in an active device. Internal quantum efficiencies of these unmodified microwave HBTs were estimated to be as high as 0.4 at 620 nm. The relative simplicity of their fabrication and ease of integration with other active components may make HBT-based devices attractive candidates as high-speed

photodetectors. The same types of responses as are reported here have been observed in every HBT we have studied, including AlGaAs/GaAs, InP/InGaAs, graded-base band gap, and self-aligned electrode devices.

### Experiment

The abrupt-junction, single heterostructure devices were grown by molecular beam epitaxy on a semi-insulating (100) InP substrate. The 290-nm-thick  $\text{Ga}_{0.47}\text{In}_{0.53}\text{As}$  collector was  $n$ -doped at  $2 \times 10^{16} \text{ cm}^{-3}$ ; above it lay a 100- or 150-nm-thick  $\text{Ga}_{0.47}\text{In}_{0.53}\text{As}$  base,  $p$ -doped at  $1 \times 10^{19} \text{ cm}^{-3}$ , with a 30-nm undoped buffer layer separating it from the 140-nm  $\text{Al}_{0.48}\text{In}_{0.52}\text{As}$  emitter,  $n$ -doped at  $5 \times 10^{17} \text{ cm}^{-3}$ . Above the emitter were  $n^+$  100-nm  $\text{Al}_{0.48}\text{In}_{0.52}\text{As}$  and 140-nm  $\text{Ga}_{0.47}\text{In}_{0.53}\text{As}$  emitter cap layers. Beneath the collector was a 480-nm  $n^+$ - $\text{Ga}_{0.47}\text{In}_{0.53}\text{As}$  subcollector. Standard photolithography and wet chemical etching were used to define the HBT mesas; the metal contact areas were defined by polyimide. Nominal base-emitter and base-collector areas for the non-self-aligned structures are  $3 \times 9 \mu\text{m}^2$  and  $14 \times 14 \mu\text{m}^2$ , respectively, and the emitter electrode area is  $1 \times 6 \mu\text{m}^2$ . The average dc current gains were approximately 62 and 38 for the 100- and 150-nm-thick base devices, respectively; unity-current-gain frequencies were 23 and 35 GHz, respectively.

Wafers containing the HBTs to be studied were mounted on a wafer probe station. Optical pulses with durations of  $\sim 150$  fs at a wavelength of 620 nm were generated by a colliding-pulse mode-locked laser. The pulses were focused from above onto the active region of an HBT just to one side of the emitter electrode, and photocurrent transients were simultaneously monitored with a 50-GHz sampling oscilloscope and with a  $\text{LiTaO}_3$  electro-optic probe with subpicosecond time resolution [3] positioned between the device's contact pads. Microwave probes, cables and bias tees comprising the test circuit all had bandwidths of 60 GHz.

## Results

Figures 1(a) and 1(b) present sampling oscilloscope traces of the emitter and base responses of a 100-nm base HBT to 220-fJ pulses; Fig. 2 shows the collector phototransient for a nominally identical device measured in a common-emitter circuit. The responses are shown in all figures at the same series of base biases  $V_{BE}$ .

In all of the traces the photoresponse is composed of a fast component followed by a slow tail. All of the data in Fig. 1 and 2 are fit with a function having the same time parameters: the fast component cannot be resolved by the sampling oscilloscope and is fit with a Gaussian having a full width at half-maximum (fwhm) of 13 ps, and the tail is fit with two exponentials having decay times of 12 and 130 ps. The amplitudes of the three components are fit to the data, and the fits are presented as lines in Figs. 1 and 2. The shapes of the base and collector photocurrents vary only slightly with base bias, and the slow component of the photoresponse persists at all values of  $V_{BE}$ .

The emitter photocurrent, however, exhibits a striking dependence upon  $V_{BE}$ . The slow part of the photoresponse appears as an undershoot at small base biases; as  $V_{BE}$  is increased, the slow response changes from an undershoot to an overshoot whose amplitude increases with increasing  $V_{BE}$ . A bias—in this case about 0.6 V—can be found at which the slow component nearly disappears.

Emitter photocurrent traces, again measured with the sampling oscilloscope, are shown for an HBT with a 150-nm base in Fig. 3. The fast responses appear to be much the same, although with lower amplitudes. As before, the tail of the response changes from an undershoot to an overshoot as  $V_{BE}$  increases; for this device the slow components are nulled out at  $V_{BE} \approx 0.75$  V. The slow component of the tail, however, is much faster than that of the 100-nm base device; the best fit of the exponential decay time constant to all traces is 47 ps. As for the 100-nm devices, the base and collector photocurrents do not vary much with  $V_{BE}$  and can be fit with the same exponential time constants that fit the emitter photocurrents.

The responsivities of the fast emitter photocurrent components of the 100- and 150-nm-base HBTs are 0.039 and 0.016 A/W, respectively. Most of the incident light is absorbed in the  $\text{Ga}_{0.47}\text{In}_{0.53}\text{As}$  emitter cap layer; if the light is assumed not to be partially blocked by the edge of the emitter electrode nor to be absorbed by the polyimide films, the internal quantum efficiency of the 100-nm HBT is at least 0.4.

The fast response of the 100-nm base device of Fig. 1 is resolved by electro-optic measurements of the emitter photocurrent, which are presented in Fig. 4. The tails appear as undershoots and overshoots at base biases below and above 0.7 V, respectively. At  $V_{BE} = 0.7$  V only the fast component of the photocurrent remains, and the response possesses a fwhm of 5.5 ps. (This bias is slightly different from that in Fig. 1, since the fast exponential in the latter case is not

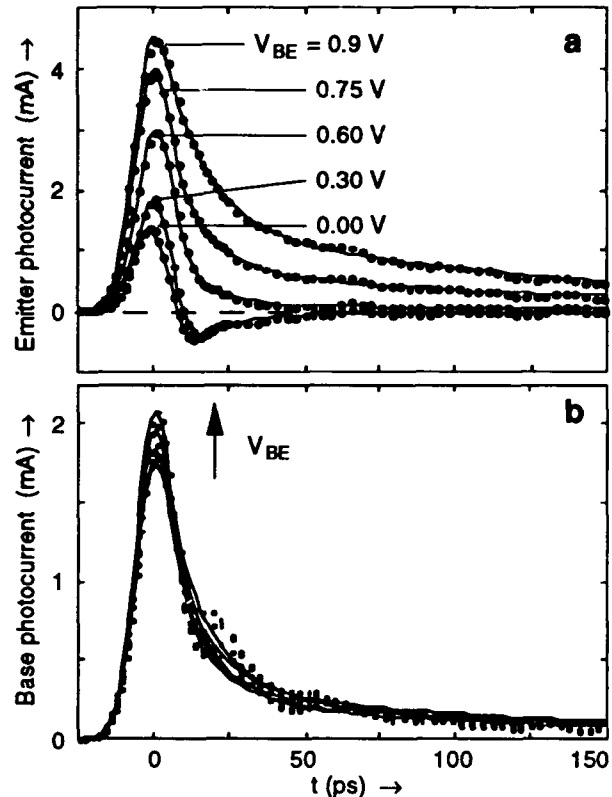


Figure 1. (a) Emitter and (b) base photocurrent transients, measured simultaneously with a sampling oscilloscope, of a 100-nm base HBTs at a series of base biases  $V_{BE}$  in response to 220-fJ optical pulses. Data are shown as points and fits, discussed in the text, are shown as lines.

resolved by the sampling oscilloscope and causes an apparent offset of the fast response.)

The fast response of the 100-nm base device of Fig. 1 is resolved by electro-optic measurements of the emitter photocurrent, which are presented in Fig. 4. The tails appear as undershoots and overshoots at base biases below and above 0.7 V, respectively. At  $V_{BE} = 0.7$  V only the fast component of the photocurrent remains,

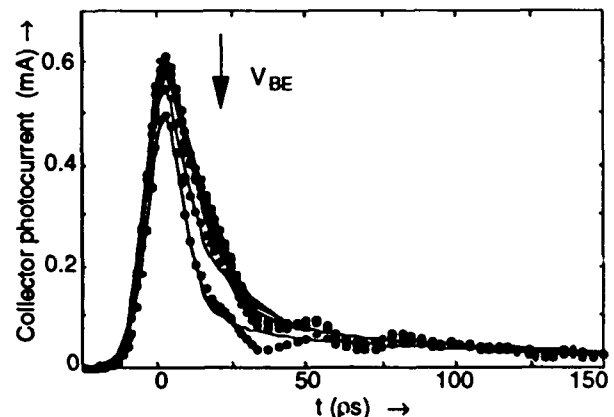


Figure 2. Sampling oscilloscope traces of collector photocurrent transients of a device nominally identical to that of Fig. 1 and at the same series of base biases. The same time parameters were used in the fits as those in Fig. 1.

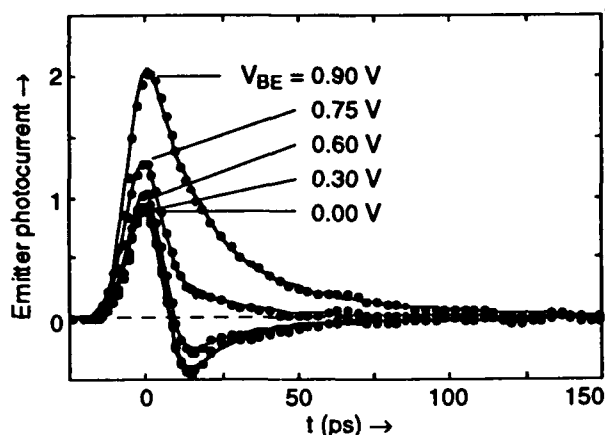


Figure 3. Sampling oscilloscope traces of emitter photocurrent transients of a 150-nm-base HBT in response to 220-fJ optical pulses at a series of base biases  $V_{BE}$ . Data are shown as points and the fits as lines.

and the response possesses a fwhm of 5.5 ps. (This bias is slightly different from that in Fig. 1, since the fast exponential in the latter case is not resolved by the sampling oscilloscope and causes an apparent offset.)

On additional 100-nm-base devices, the normally exposed part of the base surface extrinsic to the active device was covered with  $\sim 45$  nm of emitter material. This procedure reduced the extrinsic recombination current but increased the base resistance, due to the difficulty of making an ohmic contact to the base. These devices exhibit responses qualitatively similar to those of Fig. 4, although the time scales of the slow components are much longer. The responsivity is about half that of the device of Fig. 1. Figure 5 shows the electro-optically measured emitter photocurrent of such a device at a base bias of 0.54 V, where the slow components disappear. The device exhibits an extremely fast phototransient fwhm of  $2.38 \pm 0.06$  ps, corresponding to a photodetection bandwidth in excess of 200 GHz. We believe that this is the fastest optoelectronic response reported for an active semiconductor device.

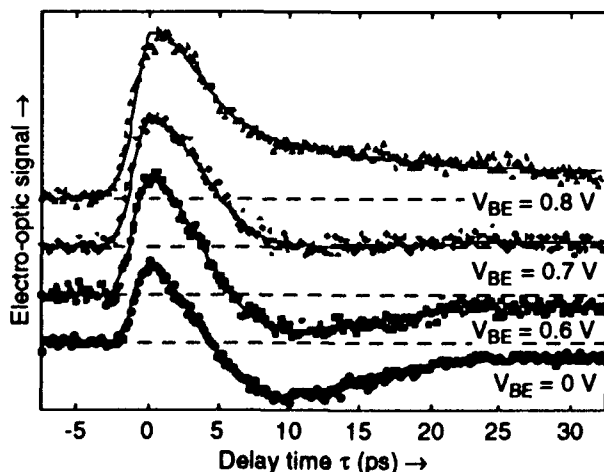


Figure 4. Electro-optic sampling traces of the emitter photoresponse of the HBT of Fig. 1 at a series of base biases. The fwhm of the fast component is 5.5 ps.

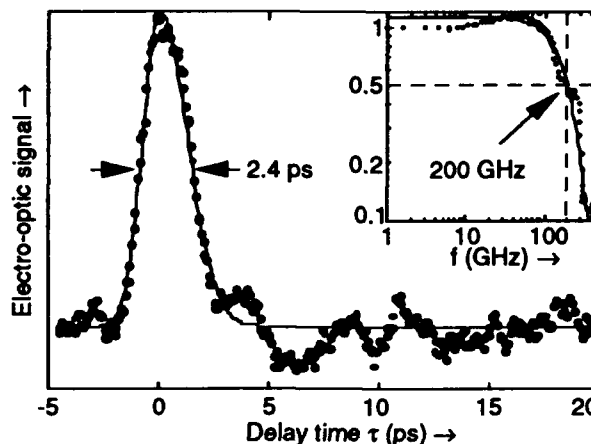


Figure 5. An electro-optic scan of an HBT with a 100-nm covered extrinsic base.  $V_{CE} = 3.0$  V;  $V_{BE} = 0.54$  V. Inset: A Fourier transform of the time-response data, showing a 200-GHz photodetection bandwidth.

### Discussion

Carrier injection and extraction in HBTs can be understood using a modified Ebers-Moll model. A simplified common-collector circuit, applicable to the cutoff and active regions of operation, is shown in Fig. 6. The model elements represent specific transistor processes. The diode  $I_f$  describes electron injection at the base-emitter junction. The current source  $I_f$ , equal to the current through the diode  $I_f$ , describes ideal electron collection by the collector. The diode  $I_r$  describes various base recombination mechanisms.  $R_b$  and  $R_{ce}$  describe the junction access and terminal contact resistances.

Additional carrier injection mechanisms have to be accounted for under illumination. Carriers generated in the emitter and subcollector regions have a negligible effect on the photocurrent. Holes photogenerated in the base are trapped by the junction potential barriers. Electrons generated in the base rapidly diffuse to the junctions and are injected into the emitter and collector. Injection into the emitter is assumed to be negligible, except at low or negative base biases; injection into the collector appears as a current source  $I_{phc}$  between the intrinsic collector and base. For modeling small-signal transient operation we add the emitter junction depletion ( $C_{je}$ ) and diffusion ( $C_{de}$ ) capacitances and a base-collector junction depletion ( $C_{jc}$ ) capacitance. The rf probes present 50- $\Omega$  terminations as  $R_{te}$  and  $R_{tb}$ .

The optical impulse response due to the injected charge  $Q_{phc}$  consists of two exponentially-decaying components with radically different time constants. The fundamental physical processes become apparent when the time constants are simplified as

$$\tau_{fast} \approx (R_{te} + R_{ce}) / (1/C_{jc} + 1/C_{te}), \quad (1a)$$

$$\tau_{slow} \approx (C_{jc} + C_{te}) / (1/R_t + 1/R_{tb}), \quad (1b)$$

where  $C_{te} = C_{de} + C_{je}$  and  $R_{tb} = R_b + R_{tb}$ . The fact that  $\tau_{slow}$  is several times faster for the 150-nm-base HBT than for the 100-nm device is primarily due to a

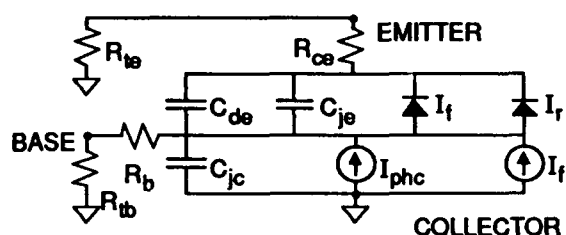


Figure 6. HBT equivalent circuit including photocarrier generation currents.

much lower  $R_b$  for the former device. Values for  $\tau_{slow}$  calculated from Eq. (1b) and measured device parameters are about one-third lower than those observed.  $\tau_{fast}$  is approximately the same for these two devices and agrees approximately with that calculated from Eq. (1a). It is not apparent to us why the response of the covered-extrinsic-base device of Fig. 5 is so much faster than that of the others.

The fast time-constant component is dominated by electron injection from the emitter contact and transport to the collector. The slow component is determined by hole storage in the base, with holes eliminated via flow out the base contact ( $R_{tb}$  term) and recombination in the base ( $R_r$  term). It has been responsible for the high optical gains and slow operating speeds of conventional photo-HBTs [4,5]. The fast component is of primary interest in this study, since it may be several orders of magnitude faster than the slow. Both of these time constants are nearly bias-independent at moderate bias levels.

The biasing of an HBT can be adjusted to optimize its performance as a high-bandwidth photodetector. The amplitudes of the fast and slow emitter photo-response components can be reduced to

$$fast : I_e(0) \approx \frac{Q_{phc} \tau_{fast}}{(R_{te} + R_{ce}) R_e C_{jc} C_{te}} \left( \frac{R_e C_{te}}{\tau_{fast}} - 1 \right), \quad (2a)$$

$$slow : I_e(0) \approx \frac{Q_{phc} \tau_{fast}}{(R_{te} + R_{ce}) R_e C_{jc} C_{te}} \left( 1 - \frac{R_e C_{te}}{\tau_{slow}} \right), \quad (2b)$$

where  $R_e = (R_r R_f) / (R_r + R_f)$ , and  $R_r$  and  $R_f$  are junction diode dynamic resistances.

The fast component is always positive, since  $C_{te} R_e \gg \tau_{fast}$ ; it increases somewhat with increasing bias. The slow component is negative and nearly constant at low biases. However, as  $C_{te} R_e$  falls below  $\tau_{slow}$  in magnitude, the emitter photocurrent slow component undergoes an abrupt polarity change. This effect can be observed in Figs. 1a, 3, and 4, and it allows a large photoresponse bandwidth increase by nulling out the slow photocurrent components with proper biasing.

The slow emitter photocurrent has components due to three physical mechanisms—the decaying photoinduced positive base potential produces a widening depletion region, forcing electrons to flow out of the emitter and producing a negative photocurrent; the decaying photoinduced potential also results in back-

injection of excess base electrons into the emitter, giving a negative photocurrent; the photoinduced potential is still positive, producing electron injection from the emitter and a positive photocurrent. At low biases the photoinduced electron injection from the emitter to base is negligible and the result is a nearly constant flow of excess electrons out of the emitter, producing a negative photocurrent. At high biases forward electron injection from the emitter to the base becomes dominant, and the emitter photocurrent becomes positive. This process is independent of the incident light intensity provided that small-signal conditions prevail.

## Conclusions

We have shown that HBTs can be used as high-speed and potentially efficient photodetectors and that they might be more easily integrated into monolithic circuits than other types of detectors. The efficiency of such a photodetector can be increased at the expense of speed by increasing the base thickness; but if the emitter and collector band gaps were reduced so that photocarriers were created there as well, the efficiency might be increased with very little sacrifice in bandwidth. A modified Ebers-Moll equivalent-circuit model satisfactorily explains the time scales and magnitudes of the observed photocurrents.

## Acknowledgements

The authors would like to thank S. C. Binari, W. Kruppa, and K. Ikossi-Anastasiou for the design, fabrication, and microwave measurements of the HBTs, H. Hier of Allied Signal Corporation for the growth of the semiconductor wafers, and K. J. Williams for rewarding discussions. Partial funding support from the Office of the Chief of Naval Research and from the Office of Naval Technology is gratefully acknowledged.

## References

1. T. F. Carruthers, I. N. Duling III, O. Aina, M. Mattingly, and M. Serio, "Responses of InP/Ga<sub>0.47</sub>In<sub>0.53</sub>As Heterojunction Bipolar Transistors to 1530 and 620 nm Ultrafast Optical Pulses," *Appl. Phys. Lett.* **59**, 327 (1991).
2. M. Matloubian, H. Petherman, M. Kim, A. Oki, J. Camou, S. Moss, and D. Smiti, "Picosecond Optoelectronic Measurement of S Parameters and Optical Response of an AlGaAs/GaAs HBT," *IEEE Trans. Microwave Theory Tech.* **38**, 683 (1990).
3. M. Y. Frankel, J. F. Waiaker, G. A. Mourou, and J. A. Valdmanis, "Experimental Characterization of External Electrooptic Probes," *IEEE Microwave and Guided Wave Lett.* **1**, 60 (1991).
4. Zh. I. Alferov, F. A. Akhmedov, V. I. Korol'kov, and V. G. Nikitin, "Phototransistor Utilizing a GaAs-AlAs Heterojunction," *Sov. Phys. Semicond.* **7**, 780 (1973).
5. S. Chandrasekhar, M. K. Hoppe, A. G. Dentai, C. H. Joyner, and G. J. Quin, "Demonstration of Enhanced Performance of an nP/InGaAs Heterojunction Phototransistor with a Base Terminal," *IEEE Electron Device Lett.* **12**, 550 (1991).

# Picosecond InAlGaAs Photovoltaic Detector with a Graded Superlattice Structure

J. M. Liu and L. P. Chen

*Department of Electrical Engineering, University of California,  
Los Angeles, California 90024*

C. T. Liu

*AT&T Bell Laboratories, Allentown, Pennsylvania 18103*

C. A. Burrus

*AT&T Bell Laboratories, Crawford Hill Laboratory,  
Holmdel, New Jersey 07733-0400*

A. Y. Cho

*AT&T Bell Laboratories, Murray Hill, New Jersey 07974*

## Abstract

We report a novel graded-superlattice photovoltaic detector with a steady-state response of picosecond speed. No dc bias voltage is required for its operation. The intrinsic response speed does not depend on the device size. An impulse response of 43-ps full width at half-maximum is observed for a typical device of 108  $\mu\text{m}$  in diameter. The measured response speed varies from 29 to 58 ps for devices of various sizes ranging from 51 to 502  $\mu\text{m}$ .

Existing high-speed photodetectors are generally photoconductive devices which require a dc bias and a load resistor. The speed of these devices depends strongly on the bias voltage and the load resistance. In contrast, photovoltaic devices are not subject to these constraints. However, photovoltages generated in semiconductor structures usually decay slowly and are not used for high-speed applications. Although a photoexcited polarization with a 200-ps decay time was previously observed in a sawtooth superlattice structure [1], it was only a transient phenomenon without a steady-state response. For practical applications, it is desirable that a high-speed detector can sustain a steady-state signal under continuous light illumination while having a picosecond response speed.

We describe in this paper an InAlGaAs photovoltaic detector which shows both steady-state response and picosecond speed. The function of this picosecond photovoltaic detector is based on the recently demonstrated steady-state photovoltaic effect in asymmetrical graded superlattices, in which a de-

vice response time of 2 ns was observed [2]. Its equivalent circuit is distinctly different from that of a conventional photoconductive detector, such as a *p-i-n* or avalanche photodiode. Neither a dc bias voltage nor a resistive load is required for its operation. As a result, it can be used to directly drive a capacitive load, such as a field effect transistor [3]. Its intrinsic response speed is independent of the size of the device. The measured full width at half-maximum (FWHM) of the impulse response varies from 29 to 58 ps for devices of various sizes ranging from 51 to 502  $\mu\text{m}$ .

As reported in [2], it is necessary to grow the structure at a low temperature, e.g. 500 °C, for a low minority-carrier lifetime and a low majority-carrier mobility to successfully observe a steady-state photovoltage. Figure 1 shows the energy band diagram of the graded InAlGaAs structure used for the picosecond device, which is different from the structure used in [2]. The structure is doped in *p*-type with a doping concentration of  $5 \times 10^{17} / \text{cm}^3$  in the graded layers and with all the other layers heavily doped. The active region consists of ten periods of 100-nm graded  $\text{In}_{0.53}(\text{Al}_x\text{Ga}_{1-x})_{0.47}\text{As}$  layers with *x* ramped from 0 to 0.4 and 3-nm  $\text{In}_{0.52}\text{Al}_{0.48}\text{As}$  barrier layers between neighboring graded layers. This structure was designed to match the 1.165 eV photon energy of the laser light used in our experiment.

The devices were mounted on high-speed Wiltron K connectors [4]. The active area of a device was defined by an etched mesa under the top metallization and the device was back-illuminated through a hole in the substrate metallization [4]. Ten devices with mesa diameters ranging from 51 to 502  $\mu\text{m}$  were prepared with the same procedure. The devices show

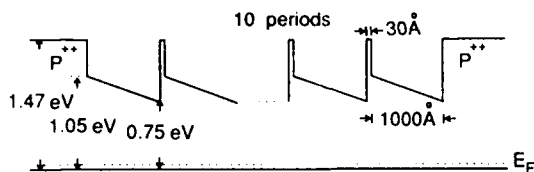
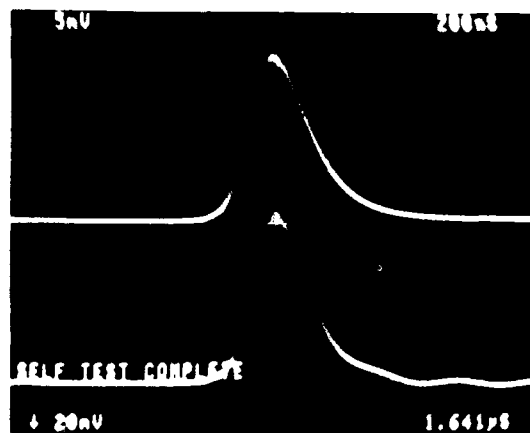


**Figure 1.** Energy-band diagram of the graded superlattice structure.

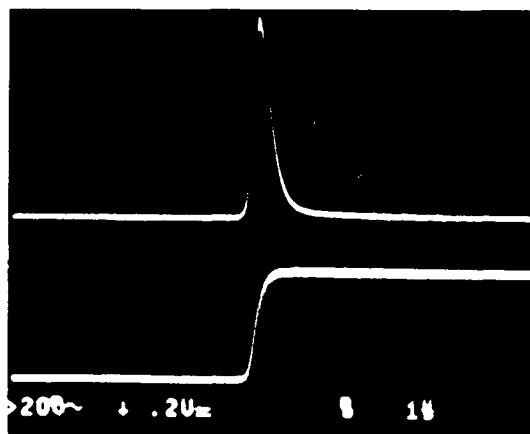
linear or nearly linear  $I$ - $V$  characteristics which are symmetric with respect to the zero voltage point for the range of voltage interested in our experiment. In the following, we describe the performance of a typical device which has a mesa diameter of  $108\text{ }\mu\text{m}$ .

We first verified that the device has a steady-state photovoltage by illuminating it with Q-switched Nd:YAG laser pulses of duration ranging from 200 ns to  $2\text{ }\mu\text{s}$  at  $1.064\text{ }\mu\text{m}$  wavelength. In the experiment, the voltage signal generated by the laser light was sent directly into an oscilloscope for monitoring. No bias was needed and the signal displayed on an oscilloscope is independent of the input impedance of the oscilloscope. These characteristics are distinctly different from those of a photoconductive detector. Figure 2 shows the steady-state signal of our photovoltaic detector (upper trace) in comparison to that of a picosecond  $p$ - $i$ - $n$  InGaAs/InP photodiode (lower trace), both illuminated with a 250-ns laser pulse. The traces shown in Fig. 2(a) were taken with a Tektronix 11302 oscilloscope of  $50\text{ }\Omega$  input impedance. They are almost identical and both display the true shape of the laser pulse. In contrast, Fig. 2(b) shows the traces of signals taken with a Tektronix 2246 oscilloscope of  $1\text{ M}\Omega$  input impedance. As can be clearly seen, the signal from our detector still displays the pulse shape but not that from the  $p$ - $i$ - $n$  photodiode. This indicates that the signal from our detector is truly a photovoltage [2]. This  $108\text{-}\mu\text{m}$  device has a responsivity of  $\sim 0.3\text{ V/W}$  in the linear region and saturates at  $\sim 0.3\text{ V}$  at high laser intensities.

The response speed of this device was studied with 1.6-ps pulses at  $1.053\text{ }\mu\text{m}$  wavelength obtained through fiber-grating compression of a cw actively mode-locked Nd:YLF laser which has a pulse repetition rate of 76 MHz. It was monitored with a Tektronix 7851 sampling oscilloscope through an S4 sampling head which has a 25-ps response speed and a  $50\text{-}\Omega$  input impedance. Figure 3 shows the impulse response of the  $108\text{ }\mu\text{m}$  device observed on the oscilloscope. This trace has a scope-limited 10-90% rise time of 25 ps, a fall time of 50 ps, and a FWHM of



(a)



(b)

**Figure 2.** Oscilloscope traces of the steady-state signals of a  $108\text{ }\mu\text{m}$  photovoltaic detector (upper trace) and a picosecond  $p$ - $i$ - $n$  InGaAs/InP detector (lower trace) in response to a 250-ns laser pulse. The oscilloscope used an input impedance of (a)  $50\text{-}\Omega$  and (b)  $1\text{ M}\Omega$ .

50 ps. Accounting for the 25-ps oscilloscope response speed, we deduced a FWHM detector response of 43 ps and a detector rise time of less than 10 ps with the sum-of-squares technique. This represents a typical impulse response and is not the fastest observed in our experiments. For devices of various sizes ranging from 51 to  $502\text{ }\mu\text{m}$  in diameter, the measured detector FWHM varies from 29 to 58 ps and shows

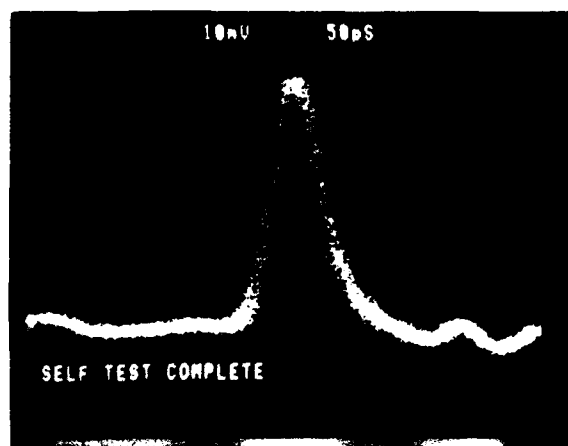


**Figure 3.** Impulse response of a 108  $\mu\text{m}$  device excited by a 1.6-ps laser pulse.

little correlation with the device size [5]. This is another unique characteristic of our device which is not expected of a photodiode.

The major difference between our device and conventional photodiodes is that there is no  $p$ - $n$  junction in our device. The generation of the photovoltage depends on the separation of the photoexcited electrons and holes by the built-in field in the graded band structure [6, 2]. This photovoltage decays by dielectric relaxation. Internal to the device, both electrons and holes flow in the same direction. This is not the case for conventional photovoltaic devices which depend on the generation of photovoltages through  $p$ - $n$  junctions.

The equivalent circuit of our device is shown in Fig. 4, where  $C_i$  is the intrinsic capacitance of the graded active layers,  $R_i$  is the internal resistance of these layers,  $R_s$  is the contact resistance,  $L_p$  is the parasitic inductance,  $C_p$  is the parasitic capacitance, and  $R_L$  is the load resistance. Because the entire structure of our device is heavily doped in  $p$ -type,  $R_i$  is on the order of 1  $\Omega$ , which is typically much smaller than  $R_s$  and  $R_L$ . The product of  $R_i$  and  $C_i$  is the dielectric relaxation time  $\tau_M$  [6]. The intrinsic speed of our device is determined only by  $\tau_M$ , which is independent of the size and structure of the device and is estimated to be  $\sim 2$  ps for our device. The discrepancy between this ultimate theoretical speed and the small variation of the measured speed among devices of different sizes are believed to be caused by the parasitic effects. In contrast,  $R_i$  in a conventional photodiode, which is typically operated under a reverse bias, is larger than  $R_s$  and  $R_L$  and is independent of  $C_i$ . As a result, the intrinsic speed of a conven-

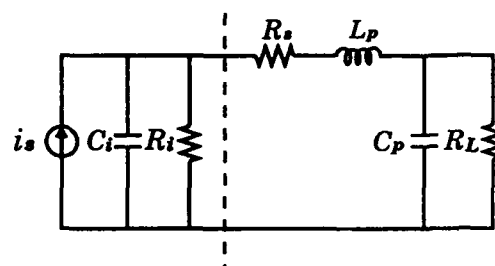


**Figure 4.** Equivalent circuit of the photovoltaic detector. The dashed line separates the intrinsic circuit of the graded superlattice layers to the left from that of the parasitics and the load resistance to the right.

tional photodiode depends on its size and structure while its output signal is strongly influenced by the parasitics and the load resistance. By comparison, the output signal of our device does not depend on  $R_L$  as long as  $R_s \ll R_L$  and its dependence on the parasitics is very different from that of a conventional photodiode because of the fundamental differences in the equivalent circuits.

In conclusion, a novel graded-superlattice InAl-GaAs photovoltaic detector with a steady-state response of picosecond speed is demonstrated. The intrinsic response speed does not depend on the device size. Its equivalent circuit is distinctly different from that of a conventional photodiode. Neither a dc bias voltage nor a resistive load is required for its operation.

## References

- [1] F. Capasso, S. Luryi, W.T. Tsang, C.G. Bethea, and B.F. Levine, "New transient electrical polarization phenomenon in sawtooth superlattices," *Phys. Rev. Lett.* **51**, 2318-2321 (1983).
- [2] C.T. Liu, J.M. Liu, P.A. Garbinski, S. Luryi, D.L. Sivco, and A.Y. Cho, "Steady-state photovoltaic effect in asymmetrical graded superlattices," *Phys. Rev. Lett.* **67**, 2231-2234 (1991).
- [3] C.T. Liu, J.M. Liu, and A.Y. Cho, "Realization of a photovoltaic transistor based on a steady-state internal polarization effect in asymmetric semiconductor superlattices," *Appl. Phys. Lett.* **59**, 2787-2789 (1991).
- [4] C.A. Burrus, J.E. Bower, and R.S. Tucker, "Improved very-high-speed packaged InGaAs pin

punch-through photodiode," *Electron. Lett.* **21**, 262-263 (1985).

- [5] J.M. Liu, L.P. Chen, C.T. Liu, C.A. Burrus, and A.Y. Cho, "Picosecond response of steady-state photovoltaic effect in an asymmetrical graded semiconductor superlattice structure," submitted

to *Appl. Phys. Lett.*

- [6] C.T. Liu and S. Luryi, "Photovoltaic transistor based on a steady-state internal polarization effect in asymmetric semiconductor superlattices," *Appl. Phys. Lett.* **59**, 393-395 (1991).



# 100 GHz Double Heterostructure GaInAs/InP p-i-n Photodiode

Yih-Guei Wey, Kirk S. Giboney, John E. Bowers, and  
Mark J. W. Rodwell

*Department of Electrical and Computer Engineering, University of California,  
Santa Barbara, California 93106*

Pierre Silvestre, Prabhu Thiagarajan, and Gary Y. Robinson  
*Department of Electrical Engineering, Colorado State University,  
Fort Collins, Colorado 80523*

## Abstract

We report double heterostructure GaInAs/InP p-i-n photodiodes with pulsedwidths as short as 3.0 ps, bandwidths exceeding 100 GHz, and external quantum efficiency of 50%.

## Introduction

High-speed, high efficiency photodetectors sensitive at 1.3 and 1.55  $\mu\text{m}$  are vital components for the development of large-capacity digital and analog optical fiber communications systems and instrumentation. Such photodetectors are generally subject to performance limitations such as carrier transit time, RC time constant, diffusion current, and carrier trapping. Until now, high-speed long wavelength photodiodes have had 3-dB bandwidths of no more than 70 GHz due to these limitations [1, 2]. Our photodiode design utilizes a GaInAs/InP p-i-n double heterostructure with graded bandgap layers to reduce the heterojunction barrier height and minimize carrier trapping at the hetero-interfaces. An additional graded layer at the p-GaInAs/pInP contact interface reduces the contact resistance significantly over that of previously reported devices [2, 3]. Leakage current and reverse breakdown voltage are also improved by replacing  $\text{SiN}_x$  passivation with a self-aligned polyimide passivation.

A pump-probe electro-optic sampling system based on a Ti:Sapphire laser allows direct measurement of the ultrafast photodiode with subpicosecond resolution at 972 nm. Measured pulsedwidths as short as 3.0 ps full-width at half-maximum (FWHM), and 3-dB

bandwidths as large as 110 GHz are observed for a  $2\text{ }\mu\text{m} \times 2\text{ }\mu\text{m}$  device at low bias voltages.

## Materials & Fabrication

The heterostructure shown in Figure 1 was grown by gas-source molecular beam epitaxy at 500°C nominally lattice matched to a (100) semi-insulating InP substrate. Molecular beams of  $\text{As}_2$  and  $\text{P}_2$  were produced by thermal decomposition of  $\text{AsH}_3$  and  $\text{PH}_3$ , and Be and Si were used as dopants. One Ga effusion cell and two In cells, one for InGaAs at 0.4  $\mu\text{m/hr}$  and one for InGaAsP ( $\lambda_g = 1.15\text{ }\mu\text{m}$ ) at 1.2  $\mu\text{m/hr}$  and InP at 1.0  $\mu\text{m/hr}$ , were used. This procedure ensured constant alloy composition, precise layer thickness, and abrupt heterointerfaces during growth of the graded bandgap regions [4].

The device cross-section is shown in Figure 2. Fabrication is described as follows. Ti(50 nm)/Pt(75 nm)/Au(150 nm)/Ni(100 nm) is lifted off on the wafer with a tri-level mask technique. The PMMA(1  $\mu\text{m}$ )/Si(50 nm)/AZ4110(1  $\mu\text{m}$ ) tri-level mask is first prepared by patterning the AZ4110 resist on top of Si and soft-baked PMMA. The silicon layer is etched by chlorine reactive ion etch (RIE) and the PMMA (e-beam resist) is etched by oxygen RIE. The undercut of PMMA is formed by oxygen plasma in a plasma enhanced etching machine. The nickel layer serves as etch mask for  $\text{Cl}_2$  RIE mesa etch through the intrinsic layer. The n-InP layer is defined by 1HCl:1H<sub>2</sub>O wet etching with AZ4110 patterned plasma-enhanced-chemical-vapor-deposition (PECVD)

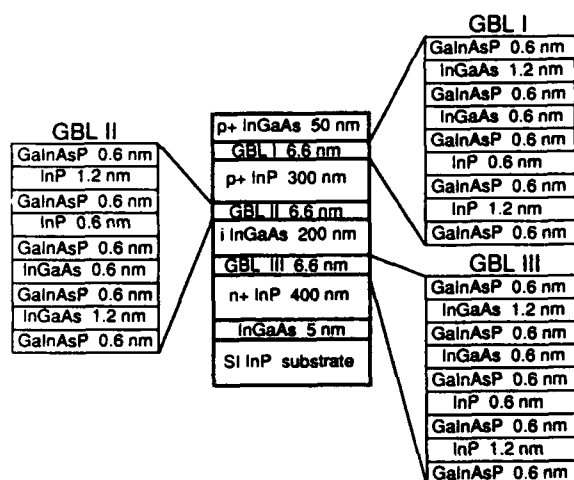


Figure 1. Photodiode epitaxial structure.

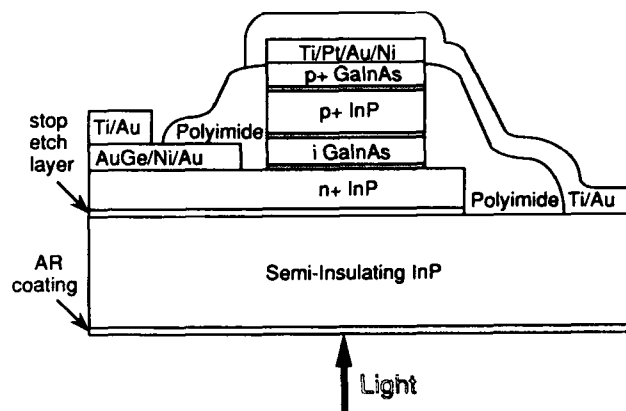


Figure 2. Photodiode cross-section.

SiO<sub>2</sub> mask. 1H<sub>3</sub>PO<sub>4</sub>:1H<sub>2</sub>O<sub>2</sub>:38H<sub>2</sub>O is used to etch the GaInAs stop etch layer followed by a light HCl etch. The mask is removed after the wet etching. The tri-level mask is again used in the n-metal liftoff. The n-metal consists of AuGe(50 nm)/Ni(7.5nm)/Au(100nm). The ohmic annealing is done in the rapid thermal annealer at 420°C for 30 sec. in nitrogen ambient. Dupont PI 2723 polyimide is used as the sidewall passivation layer. The mesa sidewall is etched with 1H<sub>2</sub>SO<sub>4</sub>:1H<sub>2</sub>O<sub>2</sub>:100H<sub>2</sub>O for the passivating etch, then rinsed with water. The polyimide is spun on at 5 krpm, softbaked at 70°C for 15 min., exposed, developed, and rinsed. The curing temperature is at 120°C/180°C/300°C for 20 min. in each stage with temperature ramp no more than 10 °C/min. The finishing cure is at 370°C in graphite strip heater in N<sub>2</sub> ambient. The mesa top is still covered with polyimide

until the cured polyimide is etched along with AZ4330 planarizing layer by oxygen RIE. The final metallization Ti(25nm)/Au(400nm) forms the coplanar waveguide (CPW) for device testing. The backside of the substrate is Br: Methonal chemi-mechanically polished to 100 μm thick and coated with a SiN<sub>x</sub> anti-reflection (AR) film optimized for 1.3 μm wavelength. An SEM photograph of the finished device is shown in Figure 3. The CPW has low parasitic capacitance and is suitable for a 100 μm pitch microwave probe.

## Measurements & Results

Time domain responses of the photodiodes are measured by pump-probe electro-optic sampling, using the InP substrate as the electro-optic modulator [5]. A passively mode-locked Ti:Sapphire laser delivering pulses with 200 fs autocorrelation FWHM and 972 nm center wavelength is used as the measurement source, and the pump and probe beams are focussed through the backside of the wafer. The devices are contacted by microwave probe through their CPW, and DC bias is delivered through an external bias tee except in the case of the 7 μm x 7 μm devices, which have integrated bias tees with separate DC probe connections. A 50 GHz sampling oscilloscope monitors the device output and provides a 50 ohm AC termination.

An electro-optic measured response of a 2 μm x 2 μm device under 3 V reverse bias is shown in Figure 4 and is seen to have a FWHM of 3.3 ps. The measured response is very close to the impulse response since the measurement resolution is roughly an order of magnitude better than the observed pulse FWHM. The electrical frequency response plotted in the inset of Figure 4 is found from the magnitude of the Fourier transform of the time response, and it shows a 3-dB bandwidth of 110 GHz. Responses as short as 3.0 ps FWHM were observed at 2 V reverse bias, but slow tails limited the corresponding bandwidths to 103 GHz.

The 3-dB electrical bandwidths of various size photodiodes biased at 3 V on the same wafer are plotted along with model predictions as a function of area in Figure 5. Note that the 4 and 9 μm<sup>2</sup> device bandwidths are nearly equal since they are essentially transit-time limited, while RC limitations gradually dominate the bandwidths as device size increases.

The external quantum efficiency as measured on 30 μm x 30 μm devices is 50% at 0.97 μm

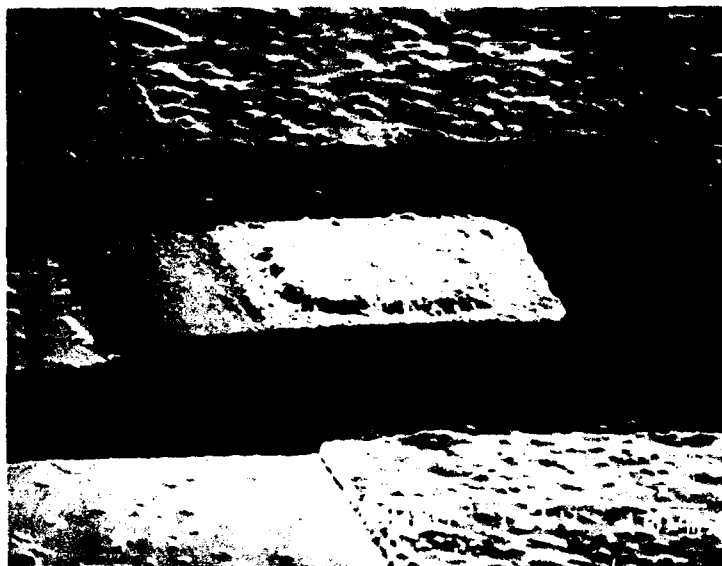


Figure 3. SEM photograph of finished  $5\ \mu\text{m} \times 5\ \mu\text{m}$  photodiode.

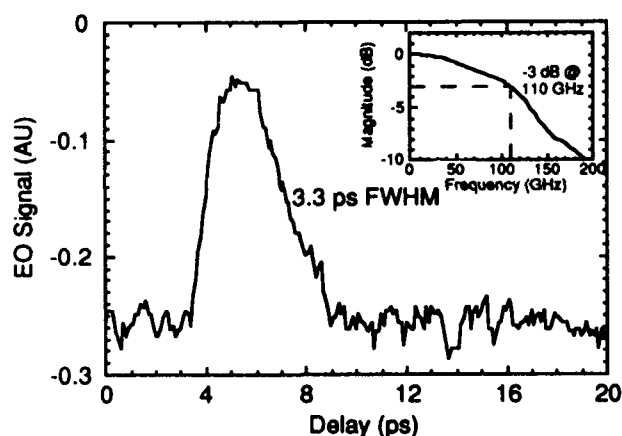


Figure 4. Measured time response and corresponding electrical frequency response of a  $2\ \mu\text{m} \times 2\ \mu\text{m}$  photodiode under 3 V reverse bias.

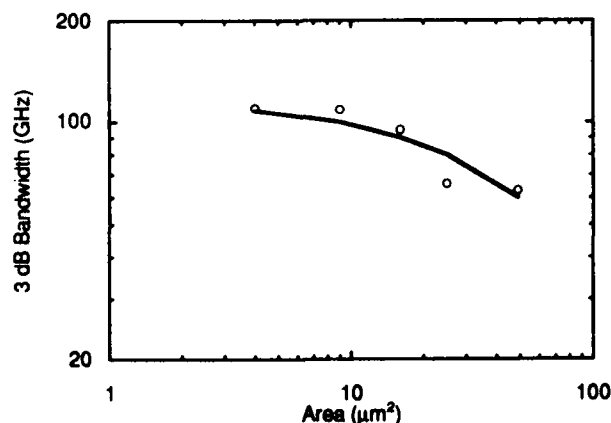


Figure 5. 3-dB electrical bandwidth vs. photodiode area from measurements (circles) and model (line).

wavelength. The efficiency is enhanced by reflection from the p-contact metal, however since this surface is somewhat rough, the smaller devices may be slightly less efficient. There is significant reflection at the substrate-air interface at  $0.97\ \mu\text{m}$  because the AR coating was designed for  $1.3\ \mu\text{m}$ . The external quantum efficiency should be around 32% at  $1.3\ \mu\text{m}$  and about 19% at  $1.55\ \mu\text{m}$ . It is expected that the bandwidth will not decrease at longer wavelengths since illumination from the n-side assures hole-dominated transport. Thus, the bandwidth-efficiency product for the transit-time limited devices should be in the 20 to 35 GHz range at fiber communications wavelengths.

## Conclusions

We have fabricated and measured photodetectors with bandwidths greater than 100 GHz that will be useful at fiber communications wavelengths. This demonstrates that graded bandgap layers at each hetero-interface can eliminate carrier trapping effects, yielding low series resistance for high-speed devices.

## Acknowledgments

The authors thank Tom Reynolds for depositing AR coatings. This work is sponsored by the Office of Naval Technology Block Program on Electro-Optics Technology.

Yih-Guei Wey is now with A T & T Bell Laboratories, Holmdel, NJ 07733.

## References

1. J. E. Bowers and C. A. Burrus, Jr., "Ultrawide-Band Long-Wavelength p-i-n Photodetectors," *J. Lightwave Technol.*, vol. 5, no. 10, pp. 1339-1350, Oct., 1987.
2. Y. G. Wey, D. L. Crawford, K. Giboney, J. E. Bowers, M. J. Rodwell, P. Silvestre, M. J. Hafich, and G. Y. Robinson, "Ultrafast Graded Double-Heterostructure GaInAs/InP Photodiode," *Appl. Phys. Lett.*, vol. 58, no. 19, pp. 2156-2158, May 13, 1991.
3. J. G. Wasserbauer, J. E. Bowers, M. J. Hafich, P. Silvestre, L. M. Woods, and G. Y. Robinson, "Specific Contact Resistivity Of InGaAs/InP p-Isotype Heterojunctions," *Electron. Lett.*, vol. 28, no. 17, pp. 1568-1570, Aug. 13, 1992.
4. P. Silvestre, M. J. Hafich, T. Vogt, A. Nanda, G. Y. Robinson, J. J. Dudley, J. E. Bowers, K. M. Jones, and M. M. Al-Jassim, "Gas-Source Molecular-Beam Epitaxial Growth of InGaAsP for 1.3- $\mu\text{m}$  Distributed Bragg Reflectors," *J. Vac. Sci. Technol. B*, vol. 10, no. 2, pp. 956-958, Mar.-Apr., 1992.
5. K. J. Weingarten, M. J. W. Rodwell, D. M. Bloom, "Picosecond Optical Sampling of GaAs Integrated Circuits," *IEEE J. Quantum Electron.*, vol. 24, no. 2, pp. 198-220, Feb., 1988.

## Ultrafast Carrier Transfer in GaAs MSM-Diodes

R. Kersting, K. Leo, J. Plettner, S. Averin\*, and H. Kurz

*Institut für Halbleitertechnik, RWTH Aachen, Sommerfeldstr. 24, W-5100 Aachen, Germany*

\*S. Averin is now at Institute of Radioengineering and Electronics, Moscow, Russia

The high-speed performance of MSM-diodes has been studied by various techniques probing the electrical response of the devices [1–4]. The *internal carrier transport* in MSM-devices has not been studied yet. In this paper, we report on time resolved studies of the internal carrier transport in MSM-diodes. The experiments are performed with femtosecond luminescence upconversion with a time resolution of 200 fs. We show that the luminescence emitted from the photogenerated carriers within the MSM-diodes is strongly reduced within the first picoseconds. This effect is discussed in terms of spatial carrier separation, intervalley transfer and field screening. Field induced intervalley scattering is identified as the dominant mechanism and observed in the time domain for the first time [5].

The MSM-photodiode structures are fabricated on epitaxial n<sup>+</sup>-type ( $N_D = 2 \times 10^{15} \text{ cm}^{-3}$ ) GaAs by electron beam lithography using Al as a Schottky contact metal. The samples have an active area of  $100 \times 100 \text{ } \mu\text{m}$  with  $3 \text{ } \mu\text{m}$  finger width and spacing. During our luminescence-upconversion measurements, the MSM-diodes are connected directly to the bias source. Our setup (Fig. 1) differs only in minor details from the scheme described in Ref. [6]. Carriers are generated within the diodes by excitation with 100 fs laser pulses of a Kerr-lens-modelocked Ti-Sapphire laser at 710 nm. The luminescence emitted between the fingers of the diode is focused dispersion-free by a mirror optic onto a nonlinear optical crystal (Lithium Iodate). Sum frequency light is generated if luminescence and reference pulse temporally overlap in the nonlinear crystal. This signal is dispersed by a monochromator and detected by a single photon counting system. The temporal evolution of the luminescence is mapped by delaying the reference pulse with respect to

the pulse exciting the sample. Group velocity dispersion between luminescence and reference pulse within the 1 mm thick crystal of Lithium Iodate limits the time resolution to less than 200 fs. All data presented here are measured at room temperature.

The luminescence emitted after optical excitation between the fingers of the MSM diodes is proportional to the photogenerated densities of holes in the valence band and of the electrons in the  $\Gamma$  band only.

$$I_{lum}(t) = f_e(t) \times f_h(t) \quad (1)$$

A change of the time-resolved luminescence signal when bias is applied to the diode therefore reflects a change of carrier densities. This can be induced by spatial separation of electrons and holes in the electrical field. On the other hand, a field induced transfer of electrons in k-space from the  $\Gamma$ - to the side valleys reduces the luminescence intensity. These electrons do not contribute to the luminescence signal because optical transitions are not possible between electrons in the side valleys and the photogenerated holes.

The GaAs band edge luminescence at 1.45 eV (0 kV/cm) is plotted in Fig. 2 as a function of time. The luminescence rises with a time constant of about 1 ps. This ultrafast rise results from the direct relaxation of electrons in the  $\Gamma$  valley after excitation with 1.74 eV photons. Intervalley scattering of the photogenerated carriers is suppressed because the electrons are generated in the  $\Gamma$  valley below the X- and L- valley threshold [7]. The luminescence decays with a time constant of about 30 ps. This results from carrier recombination, trapping, and dilution of the carrier plasma by expansion of the plasma from the surface into the bulk of the sample. A reduction of the luminescence intensity is clearly visible if bias is applied to the diode. For short delay

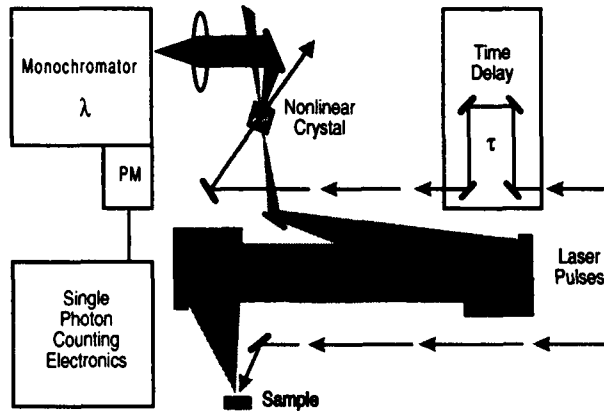


Figure 1: Experimental setup.

times, the suppression of the luminescence is significant. For longer times the measured curves converge. The comparison of Fig. 2 (a) and (b) shows that this reduction increases with decreasing excitation density.

In Fig. 3, the intensity ratio of the band edge luminescence for 0 kV/cm and 27 kV/cm field (2 ps after excitation) is plotted as a function of excitation density. For higher excitation densities (about  $5 \times 10^{17} \text{ cm}^{-3}$ ), the signal intensities become comparable, indicating that the field is completely screened. At low excitation densities (about  $2 \times 10^{16} \text{ cm}^{-3}$ ), the luminescence is suppressed if a 27 kV/cm field is applied. This strong field-induced reduction of the luminescence intensity in the low density case could result from three different phenomena: i) spatial separation of electrons and holes by drift transport through the external applied field. ii) electron injection from the  $\Gamma$  valley into the side valleys. iii) heating of the carrier distribution in the electrical field. The luminescence spectra (inset Fig. 3) show hot carrier distributions with similar temperatures for all applied fields and rule out the last explanation.

A simple estimate of the field-induced transport velocities shows that the fast reduction of the luminescence intensity cannot be explained by charge separation in real space: To separate electrons and holes over the  $3 \mu\text{m}$  finger spacing within 2 ps would require a drift velocity for electrons and holes more than one order of magnitude larger than the saturation drift velocity in GaAs of about  $10^7 \text{ cm/s}$  [8]. Velocity overshoot of the electrons also cannot cause such a fast separation [9]. We explain the decrease of the luminescence intensity at low excitation densities and high bias by field-induced transfer of  $\Gamma$  electrons to the indirect valleys. This explanation is supported by a careful inspection of the dynamics in the first few ps as shown in Fig. 4. For 0 kV/cm field,

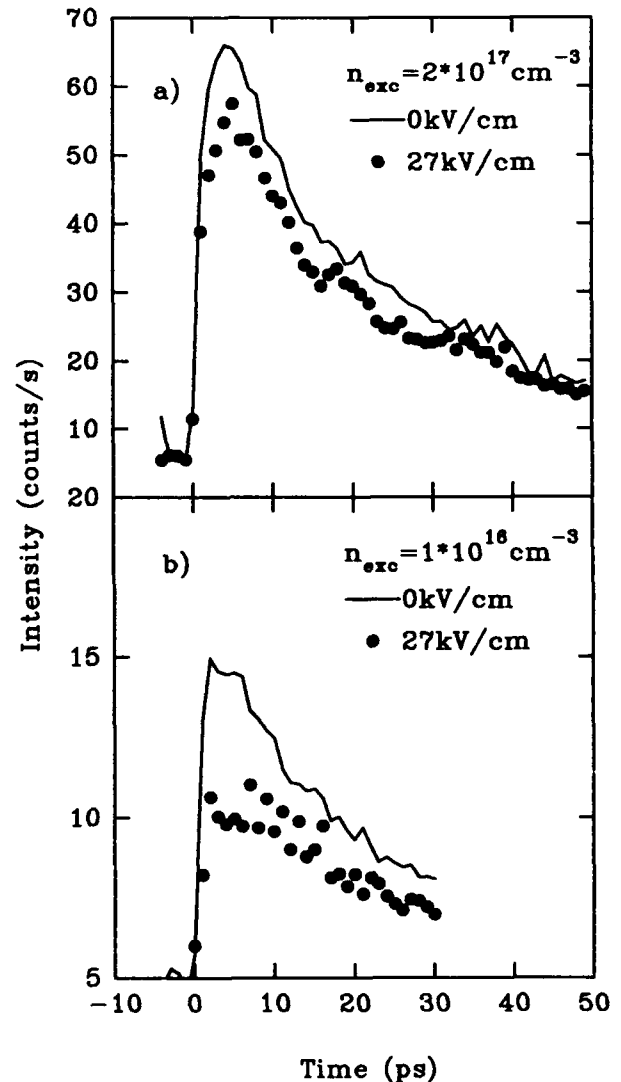


Figure 2: Time resolved GaAs band edge luminescence at different fields and excitation densities.

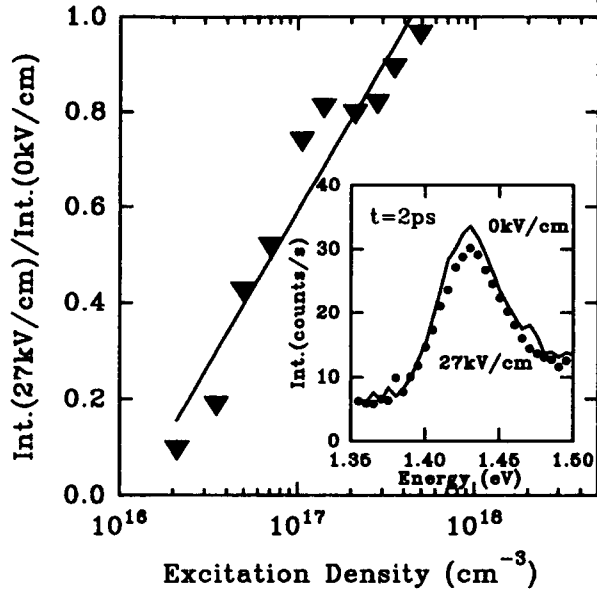


Figure 3: Dependence of the luminescence ratio at 27kV/cm and 0kV/cm on the excitation density obtained at a time delay of 2 ps. Inset: Time resolved luminescence spectra at 2 ps delay.

the luminescence intensity reaches a maximum 3 ps after excitation; at 27 kV/cm field the luminescence intensity is reduced, but increases until 6 ps and converges at longer times to the 0 V curve (s. Fig. 1). This is also obvious from the difference curve also plotted in Fig. 4 (symbols). In the case of 27 kV/cm field, a fraction of electrons is injected into the side valleys leading to the reduced luminescence. The applied field is screened within the first ps, which suppresses further intervalley transfer of electrons. After the field is screened, the electrons return from the side valleys leading to a further increase of the luminescence. The curves for zero and 27 kV/cm field converge when all carriers have returned from the indirect valleys. A simple model calculation of the electron density assuming exponential time dependence of relaxation and intervalley transfer yields good agreement with the difference curve of the experimental data (Fig. 4). The evaluated time constants are 950 fs for the transfer from the  $\Gamma$  - to the satellite valleys and 4.6 ps for the return. This time constant of the return agrees with the time measured for carriers transferred to the indirect valleys after generation by 2 eV photons [7].

At very high fields of about 130 kV/cm (see Fig. 5) the internal field is no longer screened by the photogenerated carriers. Thus the electrons do not return completely after the field is screened. A dy-

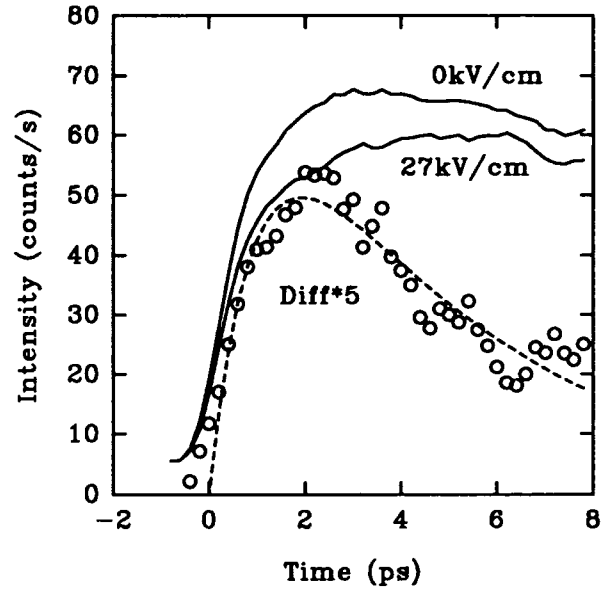


Figure 4: Temporal evolution of the band edge luminescence at an excitation density of  $2 \times 10^{17} \text{ cm}^{-3}$  for 0 kV/cm and 27 kV/cm fields. Also plotted is the magnified difference between both traces (symbols) and the model calculation of the difference (dashed line).

namic equilibrium establishes between injection into the side valley and reinjection into the  $\Gamma$  valley. Thus the measured curves (0 kV/cm and 130 kV/cm) do not converge for longer times. The difference curve also plotted in Fig. 5 shows a similar decay time constant as the absolute curves.

Our interpretation is in good agreement with theoretical estimates: The Monte Carlo calculations of Wysin et al. [9] have shown that in the case of our measurement conditions (1.74 eV laser pulses, 27 kV/cm) about 70% of the electrons are transferred within 600 fs into the L-valley. We have also performed some simple estimates how charge separation in real-space influences the decrease of luminescence in the case of applied field. Electrons accelerated from the  $\Gamma$ -point by the electrical field have to gain about 0.33 eV until a transfer into the L-valley is possible by phonon scattering. The spatial distance electrons move until intervalley transfer occurs after a time  $\Delta t$  can be estimated as

$$s = \int_0^{\Delta t} v(t) dt, \quad (2)$$

when carrier-carrier-scattering and phonon emission

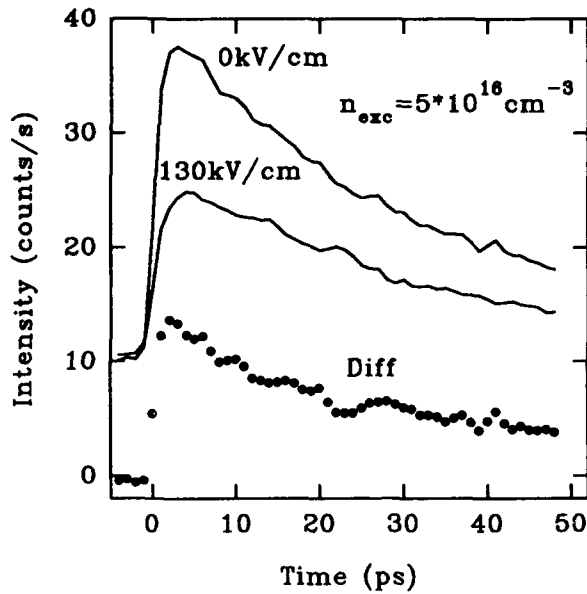


Figure 5: Temporal evolution of the GaAs band edge luminescence at high fields. Also plotted is the difference curve (symbols).

is omitted. Assuming parabolic bands, one obtains:

$$s = \frac{\Delta E_{FL}}{e|\vec{E}|} \quad (3)$$

For a field of 27 kV/cm and a threshold of  $\Delta E_{FL} = 330$  meV an electron moves about 120 nm. Thus, electrons move only a small part of the finger width (3  $\mu\text{m}$ ), and the carrier separation plays a minor role in the luminescence dynamics. One possibility to avoid the intervalley transfer would be to reduce the finger spacing down to about 120 nm. Recent results have shown that ultrafast devices with finger widths smaller than 100 nm can be fabricated [10, 11].

In conclusion, we have investigated the ultrafast carrier transport in GaAs MSM diodes using time-resolved luminescence spectroscopy with 200 fs time resolution. The experimental data show the *internal carrier* transfer within the diodes. The luminescence traces reveal the influence of bias and excitation density on the carrier dynamics. Field-induced intervalley transfer is found to be a dominant transfer mechanism.

We would like to thank T. Dekorsy, H. Roskos and R. Scholz for fruitful discussions. This work has been supported by the Volkswagen-Stiftung, by

the Alfried-Krupp-Stiftung, and the Deutsche Forschungsgemeinschaft. The stay of one of the authors (S.A.) at Aachen has also been supported by the Deutsche Forschungsgemeinschaft.

## References

- [1] B. J. van Zeghbroeck, W. Patrick, J.M. Halbout and P. Vettiger. *IEEE Electron Dev. Lett.* **9**, 527 (1988).
- [2] J. E. Bowers and C. A. Burrus. *IEEE J. Lightwave Technol.* **5**, 139 (1987).
- [3] C. Moglestue, J. Rosenzweig, J. Kuhl, M. Klingenstein, M. Lambsdorff, A. Axmann, Jo. Schneider and A. Hülsmann. *Appl. Phys. Lett.* **70**, 2435-2448 (1991).
- [4] M. Klingenstein, J. Kuhl, J. Rosenzweig, C. Moglestue and A. Axmann. *Appl. Phys. Lett.* **58**, 2503-2505 (1991).
- [5] R. Kersting, J. Plettner, K. Leo, S. Averin and H. Kurz. *Appl. Phys. Lett.* In Press.
- [6] J. Shah. *IEEE J. Quantum Electron.* **24**, 276 (1988).
- [7] J. Shah, B. Deveaud, T. C. Damen, W. T. Tsang, A. C. Gossard and P. Lugli. *Phys. Rev. Lett.* **59**, 2222 (1987).
- [8] E. Constant. *Non-Steady-State Carrier Transport in Semiconductors in Perspective with Submicrometer Devices*. In *Hot Electron Transfer in Semiconductors*, edited by L. Reggiani, p. 227. Springer Verlag Berlin, 1985.
- [9] G. M. Wysin, D. L. Smith and A. Redondo. *Phys. Rev. B* **38**, 12514 (1988).
- [10] Y. Liu, P. B. Fischer and S. Y. Chou. *Picosecond Metal-Semiconductor-Metal Photodetectors with sub-100-nm Finger Spacing and Finger width in GaAs*. In *OSA Proceedings on Picosecond Electronics and Optoelectronics*, edited by T. C. L. G. Sollner and J. Shah, p. 97. Optical Society of America, 1991.
- [11] S. Y. Chou and M. Y. Liu. *IEEE J. Quantum Electron.* **28**, 2358 (1992).



## Ultrafast Metal-Semiconductor-Metal Photodetectors with Nanometer Scale Finger Spacing and Width

Mark Y. Liu and Stephen Y. Chou

*Department of Electrical Engineering, University of Minnesota, Minneapolis, Minnesota 55455*

Sotiris Alexandrou and Thomas Y. Hsiang

*Laboratory for Laser Energetics, University of Rochester, Rochester, New York 14623*

### Abstract

We report the fabrication and measurement of ultrafast nanoscale metal-semiconductor-metal photodetectors. The finger spacing and width as small as 25 nm are fabricated using electron beam lithography. Electro-optic sampling was performed at various wavelengths to measure the detectors' response time. The fastest detectors have response times and 3-dB bandwidths of 0.87 ps and 510 GHz on low-temperature GaAs, 1.5 ps and 300 GHz on bulk GaAs, and 3.7 ps and 110 GHz on bulk Si. To our knowledge, they are the fastest photodetectors of their kind. Scaling rules are also proposed.

Much progress has been reported recently on ultrafast metal-semiconductor-metal photodetectors (MSMPD's). MSMPD's on many semiconductor materials, such as GaAs [1-3], Si [4,5], InGaAs [6,7], have demonstrated picosecond response time. Proper scaling of the detector finger spacing and finger width is essential to achieve high speed and high sensitivity [8]. In this paper, we report our work on ultrafast MSMPD's with nanometer scale finger structures. High-speed characterization was performed using an electrooptic sampling system consisting of a wavelength tunable femtosecond Ti:Al<sub>2</sub>O<sub>3</sub> laser. Measurements show that the detectors are the fastest of their kind. Impulse response of Si MSMPD's strongly depends on the laser wavelength, which indicates that the carriers generated deep inside the semiconductor bulk play an important role in detector operation.

Our MSMPD's are fabricated on three different semiconductor materials: LT-GaAs, bulk GaAs, and bulk Si. For electrooptic sampling measurement,

coplanar striplines were fabricated on the substrates and integrated with the detectors. Both shunt and in-line connection of detectors and transmission lines were used in the measurements. Nanometer scale fingers were fabricated using electron beam lithography and a lift-off technique. Finger spacing and width as small as 25 nm have been achieved (Fig. 1).

To understand the operation of the nanoscale MSMPD's, we used a one-dimensional Monte-Carlo method to simulate the intrinsic carrier transit time between the metal fingers, and calculated device capacitance [8]. Based on the theoretical and experimental data, we propose the scaling rules for high-speed and high-sensitivity MSMPD's. (1) Reduce finger spacing to decrease carrier transit time, therefore increase speed for transit-time-limited MSMPD's and increase sensitivity for recombination-time-limited MSMPD's. (2) Reduce finger width and detector area to decrease the detector capacitance. (3) Reduce light absorption depth to eliminate carriers generated deep inside the semiconductor bulk. (4) Use shorter and thicker metal fingers to reduce the finger resistance.

Electrooptic sampling measurements were performed to measure the impulse responses of the MSMPD's. A colliding-pulse modelocked dye laser with 100 fs pulsewidth and 620 nm wavelength was used for measuring the GaAs detectors [9]. As shown in Fig. 2, the MSMPD on LT-GaAs with 300 nm finger spacing and width has a response time of 0.87 ps and 3-dB bandwidth of 510 GHz, which are limited by the carrier recombination time. However, as the finger spacing and width decrease, the device capacitance increases since the device active area keeps unchanged [8], and the response time is limited by the RC time constant (Table 1).

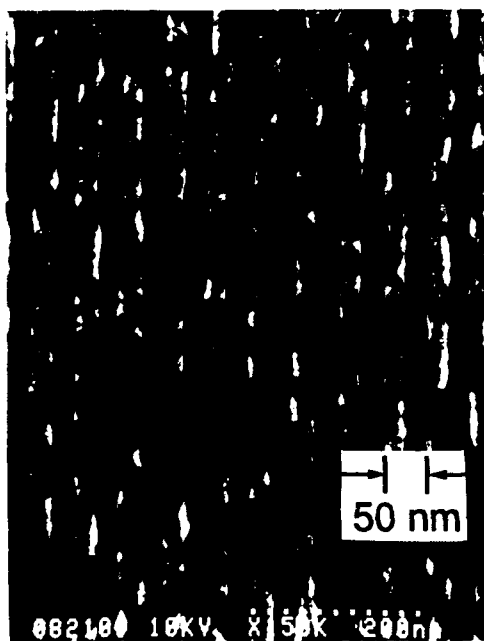


Fig. 1. Scanning electron micrograph of a MSMPD with 25 nm finger spacing and finger width. The metals are Ti and Au.

Both femtosecond dye laser and Ti:Al<sub>2</sub>O<sub>3</sub> laser were used to measure Si MSMPD's [10]. The wavelength of Ti:Al<sub>2</sub>O<sub>3</sub> laser is tunable at 700-1000 nm range and can be frequency-doubled to 350-500 nm range. Fig. 3 shows the impulse responses of a Si MSMPD illuminated with optical pulses at 465 nm and 725 nm. The detector has a longer tail at 725 nm due to the greater absorption depth of Si at this wavelength. Measurement at other laser wavelengths were also performed. Table 2 summarizes the results for Si MSMPDs. For finger spacing and width ranging from 100 nm and 300 nm, the response times measured at 620 nm are same, because the light absorption depth of Si at 620 nm is about 3  $\mu$ m and

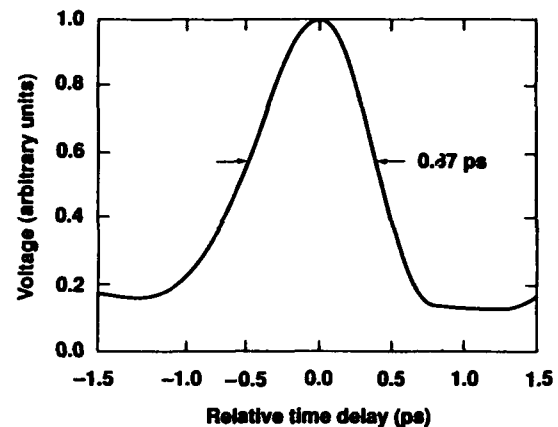


Fig. 2. Impulse response of a LT-GaAs MSMPD with 300 nm finger spacing and width.

therefore the tail comes from the transit time of the carriers generated deep inside the semiconductor. At 400 nm, however, the absorption depth reduces to only about 0.1  $\mu$ m, therefore, the response time of the detectors is determined by the transit time of carriers across the fingers. The fastest Si MSMPD has a response time of 3.7 ps, 3-dB bandwidth of 110 GHz, and finger spacing and width of 200 nm. This is, to our knowledge, the fastest photodetector on crystalline Si.

In summary, we have fabricated MSMPD's on LT-GaAs, bulk GaAs, and bulk Si with finger spacing and width as small as 25 nm. Electrooptic sampling measurements were performed to measure the detector impulse responses at various wavelengths. The fastest MSMPD's had finger spacing and width, FWHM response time, and 3-dB bandwidth, respectively, of 300 nm, 0.87 ps, and 510 GHz for LT-GaAs; 100 nm, 1.5 ps, and 300 GHz for bulk GaAs; and 200 nm, 3.7 ps, and 110 GHz for bulk Si. To our knowledge, they are the fastest photodetectors of their kind.

Table 1. Theoretical and experimental data of LT-GaAs and bulk GaAs MSMPDs.

Semiconductor	LT-GaAs			Bulk GaAs
Finger spacing/width (nm)	300/300	200/200	100/100	100/100
Intrinsic transit time (ps)	1.1	0.8	0.4	0.4
RC ( $\ln 2$ ) constant (ps)	0.52	1.04	1.56	1.56
Measured response (ps)	0.87	1.0	1.6	1.5
Measured bandwidth (GHz)	510	440	280	300

Table 2. Theoretical and experimental data of Si MSM PDs

Laser wavelength (nm)	620			400	
Absorption length	~ 3 $\mu$ m			~ 100 nm	
Finger spacing/width (nm)	300/300	200/200	100/100	300/300	200/200
Intrinsic transit time (ps) (from 1-D simulation)	5.6	3.5	2.7	5.6	3.5
Measured response (ps)	11	11	11	5.5	3.7
Measured bandwidth (GHz)	41	41	41	75	110

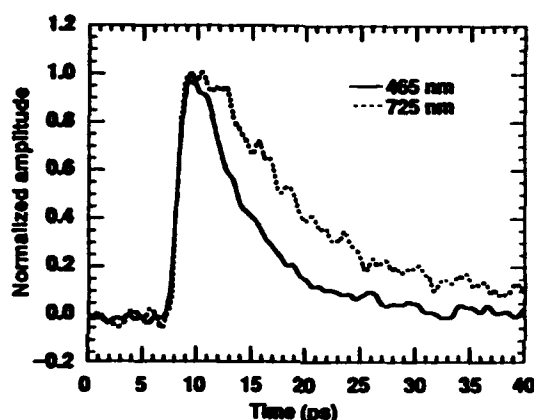


Fig. 3. Impulse response of a Si MSMPD with 200 nm finger spacing and width. The laser wavelengths are 465 nm (solid line) and 725 nm (dotted line).

## Acknowledgments

The work at the University of Minnesota was supported in part by NSF grant ECS-9120527, ARO grant DAAL03-90-058, and Packard Foundation through a Packard Fellowship. The work at the University of Rochester was supported in part by NSF grant ECS-9203490, the DOE Office of Inertial Confinement Fusion under Cooperative Agreement No. DE-FC03-92SF19460, the University of Rochester, and the New York State Energy Research and Development Authority.

## References

1. B. J. van Zeghbroeck, W. Patrick, J. M. Halbout, and P. Vettiger, "105-GHz bandwidth metal-semiconductor-metal photodiode," *IEEE Electron. Device Lett.* **2**, 527-529, (1988).
2. C. Mogilestue, J. Rosenzweig, J. Kuhl, M. Klingenstein, M. Lambsdorff, A. Axmann, J. Schneider, and A. Hulsman, "Picosecond pulse response characteristics of GaAs metal-semiconductor-metal (MSM) photodetectors," *J. Appl. Phys.* **70**, 2435-2448, (1991).
3. Y. Chen, S. Williamson, T. Brock, F. W. Smith, and A. R. Calawa, "375-GHz photodiode on low-temperature GaAs," *Appl. Phys. Lett.* **59**, 1984-1986, (1991).
4. S. Y. Chou, Y. Liu, and T. F. Carruthers, "32 GHz metal-semiconductor-metal photodetectors on crystalline silicon," *Appl. Phys. Lett.* **61**, 1760-1762 (1992).
5. T. Y. Hsiang, S. Alexandrou, R. Sobolewski, S. Y. Chou, and Y. Liu, "Sub-picosecond characterization of nanometer-scale metal-semiconductor-metal photodiodes", in *Technical Digest of Conference of Lasers and Electro-Optics* (Optical Society of America, Washington, DC, 1992), paper JFD-5.
6. J. B. D. Soole and H. Schumacher, "InGaAs metal-semiconductor-metal photodetectors for long wavelength optical communications," *IEEE J. Quantum Electron.* **27**, 737-752 (1991).
7. E. H. Böttcher, D. Kuhl, F. Hieronymi, E. Dröge, T. Wolf, and D. Bimberg, "Ultrafast semiinsulating InP:Fe-InGaAs:Fe-InP:Fe MSM photodetectors: modeling and performance," *IEEE J. Quantum Electron.* **28**, 2343-2357 (1992).
8. S. Y. Chou and M. Y. Liu, "Nanoscale tera-hertz metal-semiconductor-metal photodetectors," *IEEE J. Quantum Electron.* **28**, 2358-2368 (1992).
9. S. Y. Chou, Y. Liu, W. Khalil, T. Y. Hsiang, and S. Alexandrou, "Ultrafast nanoscale metal-semiconductor-metal photodetectors on bulk and low-temperature-grown GaAs," *Appl. Phys. Lett.* **61**, 819-821 (1992).
10. S. Alexandrou, C. C. Wang, T. Y. Hsiang, M. Y. Liu, and S. Y. Chou, "A 75-GHz silicon metal-semiconductor-metal Schottky photodiode," *Appl. Phys. Lett.*, submitted.

---

## **High Speed Electronic Devices**

---

## A 50 ps Cycle-Time Microprocessor: The Technological Challenges

Robert W. Keyes and Mark B. Ketchen

*IBM Research Division, Thomas J. Watson Research Center, PO Box 218,  
Yorktown Heights, New York 10598*

Straightforward extrapolation of the rapid evolution of Si technology suggests that sub-ns cycle-time microprocessors will be reported within the next five to seven years. The primary technological trend that makes this evolution possible is miniaturization; there is an intimate connection between circuit speeds and miniaturization, and high levels of integration. Miniaturization is a key to circuit speed because small size leads to high speed through the reduction of distances and capacitances. Miniaturization means making everything smaller; connections, capacitances, insulation, and anything else on a chip must feel the impact of miniaturization.

Another major trend that has influenced microprocessors is increasing chip sizes. These trends together have led to a very rapid increase in

the number of devices on a chip. The larger numbers of devices have made the steady enhancement of the function on a single chip possible. The important manifestations of the increased functionality have been a steady increase in the word length used in the processors, from 4 to 8 to 16 to 32 to 64 bits, the inclusion of special-purpose functional units, and the placement of increasing amounts of memory on a processor chip, allowing rapid access to instructions and data.

Miniaturization in microprocessors is evidenced by the increase in the density of transistors on chips, plotted against year in Figure 1. Figure 2 shows what has happened to the clock period of microprocessors during the same time. The data before 1985 are taken from reviews, the data after

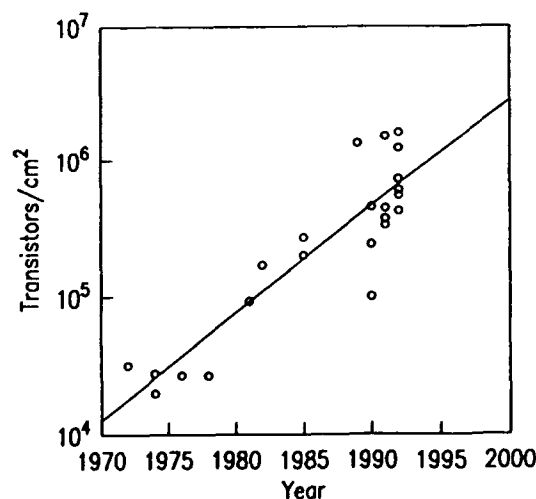


**Figure 1.** Transistor density as a function of year for representative microprocessors.

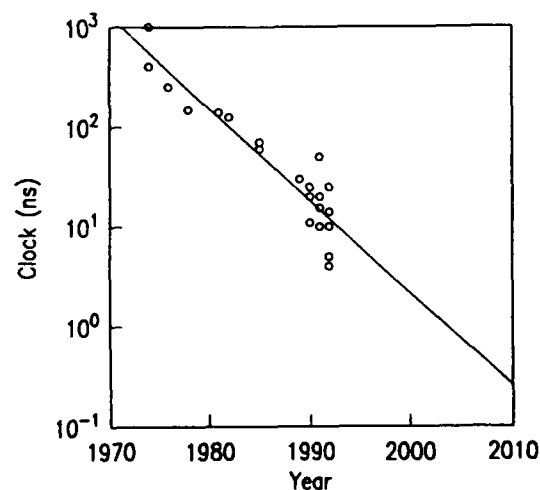


**Figure 2.** Microprocessor cycle time as a function of year.

that date are from the digests of the ISSCC conferences.

The long history of progress has been made possible by a continuing series of technological innovations. For example lithographic exposures have been migrated to ever-shorter wavelengths. Optical systems have been adapted to the new wavelengths and to increasing field sizes. Control of all aspects of processing has been improved. The temperatures of processes have been lowered to decrease the distances that atoms can migrate. The elimination of defects has been extended to smaller sizes. History lends confidence to the ability of fabrication technology to continue to make increasingly miniaturized devices.

The devices universally used in today's microprocessors are field-effect transistors, FETs. The miniaturization of FETs is often guided by "scaling" rules. According to one widely accepted scaling of semiconductor devices, dimensions, capacitances, voltages, and currents are all reduced by the same factor, say  $f$ , as miniaturization progresses. Scaling voltage in proportion to dimension maintains constant electric fields [1]. The time to charge capacitances

$$t = \text{capacitance} \times \text{voltage} / \text{current}$$

then also varies by the same factor  $f$ . The most obvious line of thought about a 50 ps cycle time is straightforward application of this kind of scaling. At present 5 ns cycle time microprocessors are known [2]. As the time scale is proportional to dimensions, reduction of all dimensions by a factor 100 would meet the objective of a 50 ps cycle time in the context of this scaling.

We first look at the scaling of a representative fast contemporary microprocessor chip by a factor of ten. The first column of numbers in the following table presents some properties of a present-day chip [2]. The second column lists the values of the same parameters when dimensions are reduced by a factor ten in the way prescribed by constant-field scaling.

Chip size (cm)	1.5	0.15
Technology	CMOS	CMOS
Gate length ( $\mu\text{m}$ )	0.5	0.05
Wire pitch ( $\mu\text{m}$ )	2.5	0.25
Transconductance (mS/mm)	150	1500
Cycle (ns)	5	0.5

The scaled numbers will be hard to realize. Constant-field implies that the voltage levels are re-

duced in proportion to dimension. The current 3.3 V and 5 V supplies become 0.3 to 0.5 V. It will not be possible to maintain the scaling of the transconductance, because an oxide gate insulator thickness of only 10 Å is implied by simple scaling from the present 100 Å. Tunneling is believed to limit the oxide thickness to something above 40 Å. The degradation of the transconductance by the thick oxide might be compensated by an unpredictable amount by the phenomenon of "velocity overshoot" [3].

Increased ohmic resistances would also be encountered. The resistance per unit length of interconnections would increase by a factor 100, which would presumably lead to resistances 10 times greater when wire lengths are decreased by a factor 10. The increase in wire resistance could be partly compensated by the use of additional layers of wire on the chip. Series resistance in the devices would further degrade the useful transconductance [3]. The impact of the larger wire resistance could be further lessened by cooling to 77 K, which would also improve the transconductance somewhat. However, scaling by another factor ten seems completely out of the question. Wires would be only about 100 Å thick and resistances would be increased by 100 times. Voltage would be reduced to 0.05 V, barely above the room temperature thermal voltage. Scaled oxide insulator thickness's would be 1 Å. The scale of dimensions becomes far beyond the most optimistic projections of technology. Exploration of other approaches is indicated.

Furthermore, however, microprocessor chips have not evolved in this way. 5 V microprocessors were introduced in 1975, and 5 V power supplies are still common, 17 years later. The consequence of

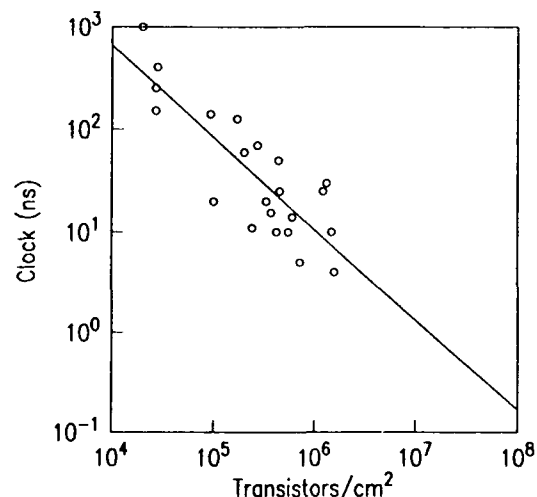


Figure 3. Microprocessor cycle time as a function of transistor density.

this failure to decrease voltage in proportion to dimension has been larger currents and smaller capacitance charging times than predicted by constant field scaling. Thus, although lithographic dimensions have decreased by about an order of magnitude during the time in question, the decrease in microprocessor clock times has been closer to two orders of magnitude.

The information in Figures 1 and 2 is plotted in a different way in Figure 3. Here the transistor density is the abscissa and the clock time is the ordinate. The square root of the reciprocal of the transistor density is a measure of the length scale. It is seen that the clock time is nearly inversely proportional to the density, meaning that it is proportional to the square of the length scale. This is the kind of result that is obtained from constant voltage scaling of devices. Of course, it would be overly simplistic to assert that the evolution of microprocessors has been a matter of straightforward constant voltage scaling.

The point is that devices cannot continue to evolve in the same way. The effects of constant supply voltage with decreasing dimensions have been contained by clever device designs and the introduction of complementary circuitry, CMOS. The presence of high electric fields, together with increasing densities of power dissipation, are forcing a movement to lower voltages; 3.3 V power supplies are being introduced and the need for even lower voltages is well-recognized. However, a number of limitations plague the evolution of conventional MOS field-effect transistors to still smaller size and lower voltages, a new regime of device physics is being encountered [5]. The simple constant-field scaling that has often served large devices does not suffice. It is difficult to invert a silicon surface with voltages approaching (energy gap/electron charge). Tunneling and reliability concerns prevent oxide gate insulators from being thinned in proportion to other dimensions.

A new device concept that would remove these foreseeable limitations would be most welcome. In fact, many proposals for alternatives have been advanced in the three and a half decades since the introduction of the transistor. None have found a place in the logic circuitry of information processing systems, even though some were the focus of substantial development efforts. The reasons are not difficult to discern. Three terminal devices are needed to allow isolation between input and output and have been lacking in some proposals. High gain is required to allow the large noise margins that are essential to the operation of circuits in compact systems of a great many devices and to make large

fan-out possible. The gain mechanism of the transistor, the control of mobile charges by charges of the opposite sign through Coulomb attraction, has so far proved unique. It was also the basis for the vacuum triode, and so has been the sole basis of electronic amplification for eighty years. No other phenomenon that can make comparably large gains available to electronics is known. The future lies with innovation in transistors.

Turning from devices to other aspects of microprocessor technology, increasing resistance is a long-recognized limitation to miniaturization. Simple scaling of all dimensions by a factor  $f$  means that the length of a conductor is decreased by  $f$  but its cross-section is decreased by  $f^2$ ; the resistance is increased by  $1/f$ . This kind of scaling poses a problem for the continued miniaturization of microprocessors. The problem has been managed so far by not scaling the wire dimensions in proportion to the other components, but instead increasing the number of layers in which wiring may be placed. This allows the wire density, that is, the length of wire in a unit area, to be increased without thinning the wires. How far can this route be followed? It is hard to know. Increases in the number of wire layers on chips has come slowly; most microprocessors have only three layers of wire. On the other hand, the feasibility of many layers is shown by multi-chip modules that have several tens of wiring layers. Also, as mentioned above, the little exploited cooling of chips to 77 K, where the resistivity of wires can be only 1/5 of the value at 300 K, is another approach to controlling interconnection resistance.

A limitation on the actual use of fast devices in microprocessors is found in the distribution of the clock signal that synchronizes operation of circuitry throughout the chip. As the circuit delays decrease and the size of chips remains constant or increases, the demands on the precision with which a clock signal can be distributed around the chip increases. All sources of variability in the delay of the clock must be more tightly controlled to contain it to a given fraction of the circuit delay. An improved method of clocking may be found in optical clocking; the distribution of pulses from a mode-locked diode laser to a multiplicity of destinations in a plane has been demonstrated.

Still another problem that must be solved is the removal of heat at increasing densities from chips. The reduction of capacitances is, in addition to aiding circuit speed, a route to low power; charge stored in a capacitance is drawn from a power supply and energy (charge  $\times$  voltage) is eventually dissipated as heat. However, as capacitance scales only

linearly with dimension and the number of components per unit area increases quadratically as size is decreased, the density at which electrical energy is converted to heat increases. The density of heat production is further increased by the faster operation possible with smaller components.

Fortunately, several approaches can be combined to control dissipation. The use of dynamic circuitry, which uses energy only when a switching occurs, has been introduced over the last decade. Controlling power is an additional motivation for the reduction of voltages, as mentioned in connection with devices. The use of "sleep modes," turning off parts of a chip that are not in active use until they are needed, is becoming common. Nevertheless, cooling of high performance microprocessor chips will continue to demand attention.

Comparison with current microprocessor technologies and extrapolation suggests that a 50 nm technology would satisfy the interconnection requirements for a chip that contained  $2 \times 10^8$  transistors per  $\text{cm}^2$  with a cycle time of 50 ps. Interconnections would be 150 nm metal lines and spaces in four layers. A typical wire, 15 transistor pitches or 10  $\mu\text{m}$  long, would have a resistance of 10 ohms and a capacitance of 1 fF. The wire RC product is only 10 fs, compared to the approximately 1 or 2 ps risetime required of the circuit and the 0.1 ps propagation time on the wire. A 1 mA current in a wire would mean a current density of  $5 \times 10^6$  A/ $\text{cm}^2$ , high, but probably not beyond the range to be expected of new alloys and structures in the next decade. The demands on lithography are roughly comparable to those anticipated for 1 gigabit memory chips.

Advances in device properties that cannot now be foreseen will be needed. Containment of heat production will allow a power supply voltage no larger than 1 V. Even allowing for an improved dielectric, each logic gate would have a capacitive load of 1 fF. Obtaining 1 ps pulse rise times will apparently require devices with a transconductance of 0.002 to 0.004 S in an area no greater than 0.5  $\mu\text{m}^2$ , corresponding to at least 5 S/mm in a field-effect transistor. The characteristics of a 30 nm gate length silicon MOSFET recently proposed and analyzed approach those of the required device within a factor of two [5].

Heat removal technology will also be strained. The wire density allows a capacitance density of 25 nF/ $\text{cm}^2$  to be estimated. With a 50 ns cycle the capacitance may be charged perhaps every 200 ps, and with voltage of 1 V, 100 W/ $\text{cm}^2$  will be dissipated. With considerable effort, the removal of heat at such density has been demonstrated [6].

Instead of attempting to discuss other difficult system issues, a recently proposed rough guide to system performance may be used to estimate the kind of chip that might be built from our speculative technology [7]. The estimate of cycle time suggested by Hsi and Tucker may be stated in the form

$$T_c = \alpha t_L + \beta A^{1/2} / t_D.$$

Here  $t_L$  is the logic delay time,  $t_D$  is the delay per unit length on the wiring, and  $A$  is the system area. By fitting the parameters  $\alpha$  and  $\beta$  to the performance of large systems and making a bold leap to microprocessors with  $t_L = 2$  ps and  $t_D = 70$  ps/cm we find that a 50 ps cycle time is attained with a chip of area 0.02  $\text{cm}^2$ . While this is a small chip in the perspective of contemporary microprocessors it contains four million transistors in the assumed technology.

Thus innovation in many areas of technology, wiring, lithography, circuit and device concepts, power management and cooling, and clocking will be needed to sustain the momentum of the advancing microprocessor art. There are also many opportunities, in the form of heterojunctions and variable band gaps, new dielectrics, and new processing methods to be exploited. The 50 ps cycle time processor appears to be not far beyond the reach of technologies that are in view at this time.

## REFERENCES

1. R. H. Dennard, et al, IEEE J. Sol.-State Ckts. 9, 256-68 (1974).
2. IEEE International Solid-State Circuits Conference Digest, Session 6, 104-115 (1992).
3. G. A. Sai-Halasz, et al, IEEE Electron Device Lett. EDL-9, 464 (1988); G. G. Shahidi, D. A. Antonidas, and H. I. Smith IEEE Electron Device Lett. EDL-9, 94 (1988).
4. M. Nagata, IEEE J. Sol.-St. Circuits 27, 465-72 (1992).
5. D. J. Frank, S. E. Laux, and M. V. Fischetti, IEDM 92, paper 21.1, 553-556 (1992).
6. D. B. Tuckerman and R. F. W. Pease, IEEE Electron Device Letters EDL-2, 126-129 (1981).
7. C. G. Hsi and S. G. Tucker, 1990 IEEE International Conference on Computer Design, 49-55 (1990).



# Ultra-Deep Submicron Si MOSFETs with $f_T$ Exceeding 100 GHz

R. H. Yan, K. F. Lee, Y. O. Kim, D. Y. Jeon, D. M. Tennant, and  
E. H. Westerwick

AT&T Bell Laboratories, 101 Crawfords Corner Road,  
Holmdel, New Jersey 07733

## Abstract

We have implemented Si MOSFETs with polysilicon gate lengths of  $\sim 0.1 \mu\text{m}$ . These devices measured a record 116 and 51 GHz intrinsic  $f_T$ , unity-current-gain cutoff frequency at room temperature, for N and PMOS, respectively. They also show good turn-off characteristics, meeting very large scale integration (VLSI) requirement.

## Introduction

Miniaturization improves the speed of devices and the packing density of integrated circuits. For Si MOSFETs, scaling the channel length into the ultra-deep submicron regime leads to better performance, for example, higher cutoff frequencies  $f_T$ , due to reduced carrier transit time across shorter device active regions [1-5], as shown in Figure 1. Previously, we have demonstrated 89-GHz  $f_T$  Si MOSFETs, measured at room temperature with gate lengths of  $\sim 0.15 \mu\text{m}$  [1]. With very different device structures, Si bipolar transistors have achieved 64-GHz  $f_T$  with polysilicon emitters [4] and 75 GHz with  $\text{Si}_{1-x}\text{Ge}_x$  bases [5]. In this paper, we report that  $f_T$ 's of 116 and 51 GHz at room temperature have been realized with  $\sim 0.1 \mu\text{m}$  gate length N and PMOS devices, respectively. We will also discuss the device design issues and processing challenges for these ultra-deep submicron devices.

## Device Design

Although scaling Si MOSFET gate length tends to lead to better device performance due to reduced carrier transit time, device miniaturization is more than just gate length shrinkage. For instance, one

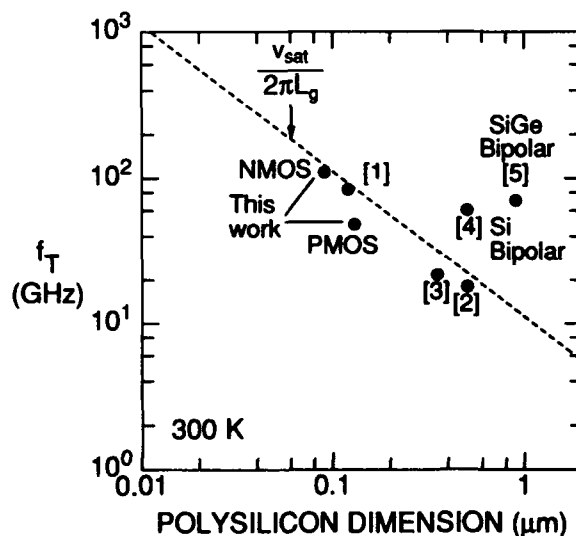


Figure 1. Cutoff frequency,  $f_T$  versus gate length for NMOS field effect transistors [1-3] or emitter width for Si-based bipolar transistors [4,5]. The dashed line estimates  $f_T \approx v_{sat}/2\pi L_g$  for NMOS devices, where  $L_g$  is the gate length and  $v_{sat}$  is the electron saturation velocity ( $\sim 7 \times 10^6$  cm/sec at room temperature).

of the most important criteria for deep submicron MOS device design for VLSI applications is good subthreshold leakage current control. With  $10^6$ – $10^9$  devices on a single chip, each individual device should have standby current in the nA to pA range to have a reasonable chip standby power consumption.

Although high substrate doping can help with suppressing source-to-drain leakages, the resulting high threshold voltage, large junction capacitance, and degraded surface channel mobility discourage such approach. Such design constraints are shown schematically in Figure 2(a). Our solution is to use the concept of *vertical doping engineering* [6] to circumvent such obstacles. Placing a heavily doped region as a ground-plane underneath the channel but above the junction, as in Figure 2(b), the field lines from the drain are screened from the source, and the device subthreshold leakages are therefore controlled. Not only that the junction parasitic capacitances are reduced and that the inversion layer mobilities could be maintained high due to reduced surface fields [1], the doping levels in the channel are also reduced so the high threshold voltage problems are alleviated [6].

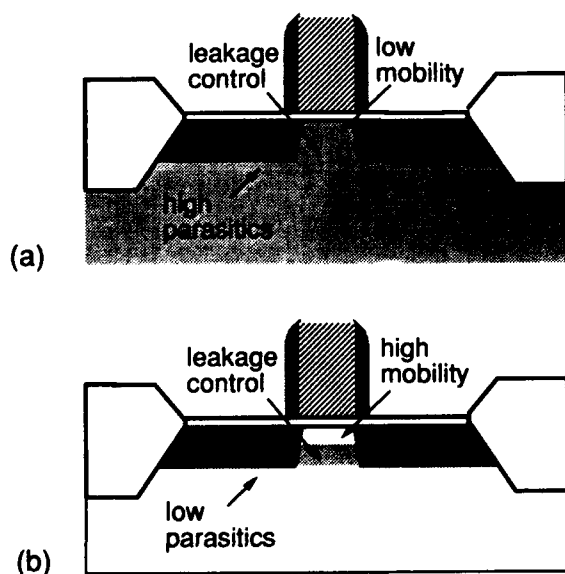
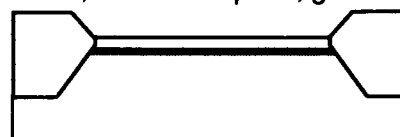


Figure 2. (a) Conventional device structure, and (b) Vertical Doping Engineering structure. Structure (b) alleviates the problems of high threshold voltages, large junction capacitances, and degraded surface mobilities in structure (a).

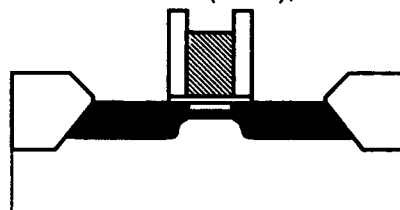
(a) isolation, channel implant, gate oxidation



(b) gate definition, junction formation



(c) junction formation (cont.), salicide



(d) contact window, metalization

Figure 3. Simplified device fabrication procedure. The whole process is quite conventional, and this is advantageous from processing control point of view.

## Processing Technology

Miniaturization of the device size calls for advancements of all processing fronts in both lateral and vertical directions. For lateral scaling, in addition to lithography requirement, other parasitics elements should also be controlled. However, the fabrication procedure should resemble conventional processing as much as possible so that previous manufacturing experience could be utilized to ensure fabrication quality.

Figure 3 illustrate a simplified process flow of our devices. After isolation, the channel is implanted and the 40 Å thick gate oxide is grown at 800 °C for 18 min. in dry  $O_2$ . The inset of Figure 6 shows the lattice image of the gate oxide. Figure 4 shows the channel profile for NMOS devices. The good agreement between the measured profile and the simulated profile is important for device design and optimization.

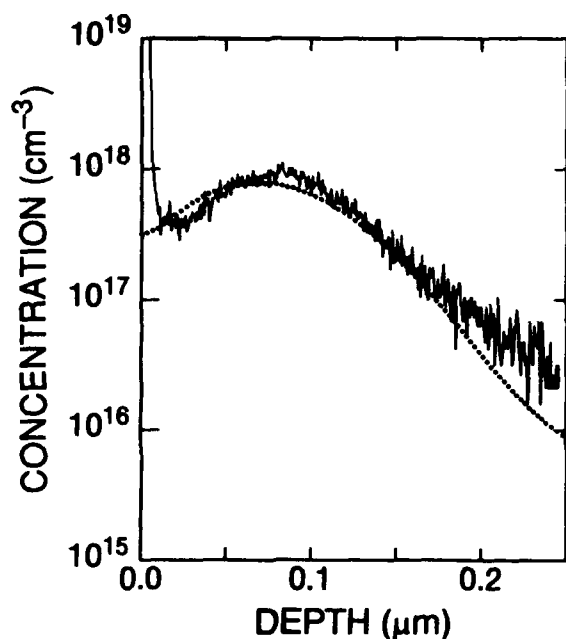


Figure 4. Channel doping profile for NMOS. The solid line is for SIMS analysis data, the dotted line for processing simulation results.

The gate stack is then deposited and patterned with e-beam lithography and dry etching. The gate etching process should have good selectivity on the polysilicon over the thin layer of gate oxide so that the source/drain (S/D) areas can be protected during the etching. To meet this need, reactive ion etching (RIE) with pure  $Cl_2$  chemistry was used [7].

Shallow S/D junctions are then formed using 10 keV  $As_2^+$  ion implantation with rapid thermal annealing (RTA) at 1030 °C for 10 sec. The final  $n^+-p$  junction depth is  $\sim 400$  Å [8]. A self-aligned sidewall spacer was then defined with a two-step etching using  $CF_4$  RIE and  $CHF_3$  RIE after deposition of a 2000 Å TEOS film [7].

To reduce parasitic resistance on gate and S/D, self-aligned  $TiSi_2$  silicide (salicide) was initially used. Figure 6 shows the high resolution TEM micrograph of a fabricated device cross section. The silicide in this device is  $TiSi_2$ . Although the gate resistance for the salicide on  $n^+$ -polysilicon is under control, the severe linewidth dependence of the sheet resistance on  $p^+$ -polysilicon gate, as indicated in Figure 5, makes PMOS gates highly

resistive. Replacing  $TiSi_2$  with  $PtSi$ , the linewidth dependence was improved dramatically, maintaining 4-5  $\Omega/\square$  from 0.5  $\mu m$  down to 0.1  $\mu m$  wide polysilicon lines [9]. Controlling silicide resistance on narrow gates is critical for achieving high speed performance.

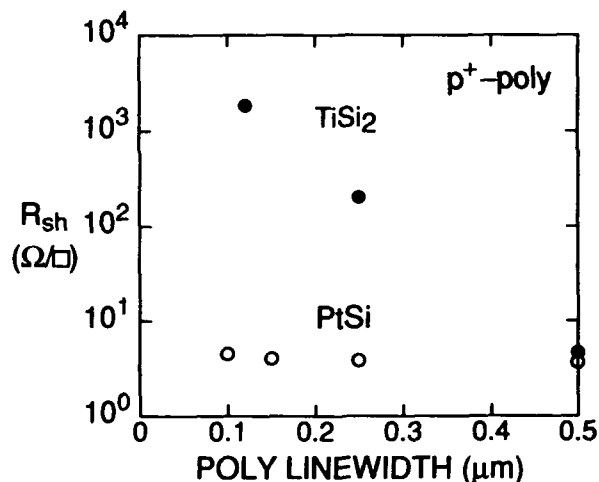


Figure 5. Linewidth dependence of silicide sheet resistance on  $p^+$ -polysilicon for PMOS devices. The closed dots are for  $TiSi_2$ , the open circles for  $PtSi$ .

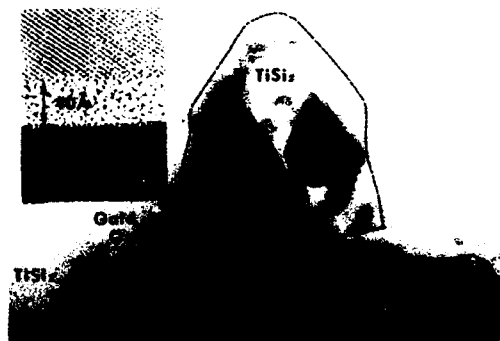


Figure 6. High resolution TEM micrograph of device cross section. The lattice image of the gate oxide is shown in the inset. Self-aligned  $TiSi_2$  silicides are used for gate, source, and drain.

### Device Characteristics

Figure 7(a) and (b) shows room temperature linear current-voltage characteristics for N and PMOS, respectively. The transconductances are 570 and 290  $\mu\text{S}/\mu\text{m}$ . The gate lengths for these devices are approximately 0.13  $\mu\text{m}$ . The room temperature subthreshold slopes for these devices are 84 and 87 mV/dec, suitable for VLSI applications [9,10].

Intrinsic small-signal current gains as a function of frequency are obtained by Y-parameter subtraction technique from microwave measurements [1]. The test structure is designed in a way that the device input capacitance of 0.1  $\mu\text{m}$  device

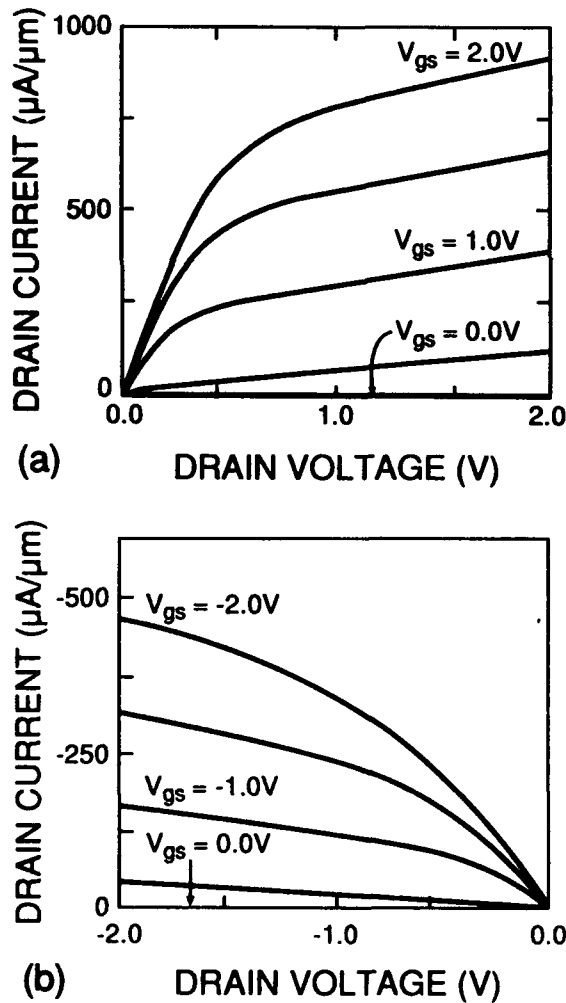


Figure 7. Current-voltage characteristics at room temperature for (a) NMOS, and (b) PMOS devices. The gate lengths for the two devices are  $\sim 0.13 \mu\text{m}$ .

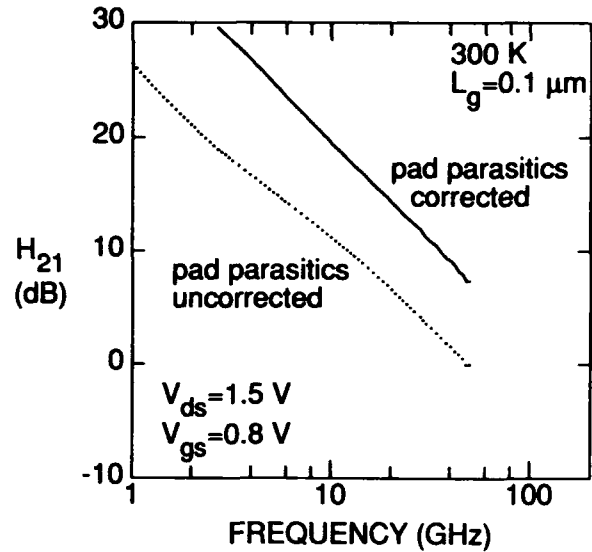


Figure 8. Small signal current gain  $H_{21}$  versus frequency, measured up to 50 GHz at room temperature. The solid (dashed) line is with (without) pad parasitics extraction. The extrapolated cutoff frequency with a -20 dB/dec slope is 116 GHz with pad parasitics extracted.

is approximately the same as the input pad capacitance. As shown in Figure 8, the subtracted intrinsic current gain values are about 3 dB higher than the uncorrected ones. This particular 0.1- $\mu\text{m}$  NMOS device has measured a room temperature unity-current-gain cutoff frequency ( $f_T$ ) of 116 GHz, with drain biased at 1.5 V and gate at 0.8 V.

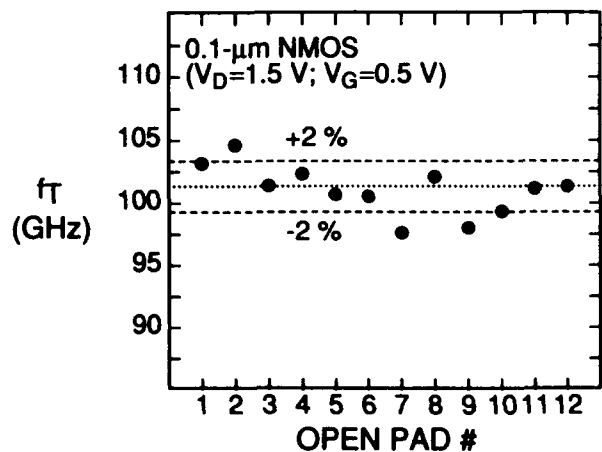


Figure 9. Variation of  $f_T$  extracted with different open pad structures across the wafer,  $\pm 2\%$  ( $\sigma$ ) for the 0.1- $\mu\text{m}$  devices.

The error margins associated with this Y-parameter subtraction technique is established to be  $\pm 2\%$  for 0.1- $\mu\text{m}$  devices by comparing the extracted  $f_T$  values over a 2.4 cmx2.4 cm e-beam written area. These  $f_T$  values are shown in Figure 9. As summarized in Figure 1, the 0.13- $\mu\text{m}$  PMOS has measured an  $f_T$  of 51 GHz [9].

### Acknowledgments

The authors would like to acknowledge the contributions of G. M. Chin, M. D. Morris, R. W. Johnson, K. Early, M. R. Pinto, C. S. Rafferty, M. D. Feuer, and L. Manchanda, and the support of A. Ourmazd, A. M. Voshchenkov, R. G. Swartz, J. Bokor, and R. E. Howard.

### References

- [1] R. H. Yan, et al., "89-GHz  $f_T$  Room-Temperature Silicon MOSFET's", *IEEE Electron Device Lett.*, **13**, pp. 256-258, May. 1992.
- [2] C. Raynaud, et al., "High-Frequency Performance of Submicrometer Channel-Length Silicon MOSFETs", *IEEE Electron Device Lett.*, **12**, pp. 667-669, Dec. 1991.
- [3] A. E. Schmitz, et al., "A Deep Submicron Microwave/Digital CMOS/SOS Technology", *IEEE Electron Device Lett.*, **12**, pp. 16-17, Jan. 1991.
- [4] M. Nanba, et al., "A 64GHz Si Bipolar Transistor Using In-Situ Phosphorus Doped Polysilicon Emitter Technology" *IEDM Tech. Dig.*, 1991, pp. 443-446.
- [5] G. L. Patton, et al., "75-GHz  $f_T$  SiGe-Base Heterojunction Bipolar Transistors", *IEEE Electron Device Lett.*, **11**, pp. 171-173, Apr. 1990.
- [6] R. H. Yan, et al., "Scaling the Si MOSFET into the 0.1- $\mu\text{m}$  Regime Using Vertical Doping Engineering", *Appl. Phys. Lett.*, **59**, pp.3315-3317, Dec. 1991.
- [7] D. Y. Jeon, et al., "Gate Technology for 89 GHz Vertical Doping Engineered Si MOSFET", *J. Vac. Sci. Technol.*, **10**, pp.2922-2926, Nov/Dec 1992.
- [8] B. G. Park, et al., "Ultrashallow Junctions for ULSI Using  $\text{As}_2^+$  Implantation and Rapid Thermal Anneal", *IEEE Electron Device Lett.*, **13**, pp. 507-509, Oct. 1992.
- [9] K. F. Lee, et al., "0.1  $\mu\text{m}$  P-Channel MOSFETs with 51 GHz  $f_T$ ", *IEDM Tech. Dig.*, 1992, pp. 1012-1014.
- [10] R. H. Yan, et al., "High Performance 0.1- $\mu\text{m}$  Room Temperature Si MOSFETs", *1992 Sym. VLSI Tech. Tech. Dig.*, pp.86-87.

# Resonant Tunneling Transistors

A. C. Seabaugh, E. A. Beam, Y. -C. Kao, J. H. Luscombe, and J. N. Randall

Central Research Laboratories, Texas Instruments Incorporated,  
PO Box 655936, MS 134, Dallas, Texas 75265

## Abstract

Resonant tunneling transistors can perform more logic per transistor than conventional transistors. By exploiting their unique characteristic, circuit functional density and speed can be increased without changing the lithographic design rule. In addition, resonant tunneling transistors, in which the control electrode directly modulates the carrier transport, scale to smaller dimensions than conventional transistors. In this paper, the measured negative differential resistance and transconductance characteristics of several resonant tunneling transistors are described.

## Introduction

With the maturation of molecular beam epitaxy (particularly InP-based), resonant tunneling devices now operate at room temperature with millimeter-wave switching speeds [1]. Shown in the schematic diagram of Figs. 1 and 2 are four basic resonant tunneling transistor (RTT) geometries which include both potential-effect and field-effect charge control mechanisms [2].

In contrast to conventional semiconductor devices, reducing the size of resonant tunneling devices should improve the switching characteristics. The natural

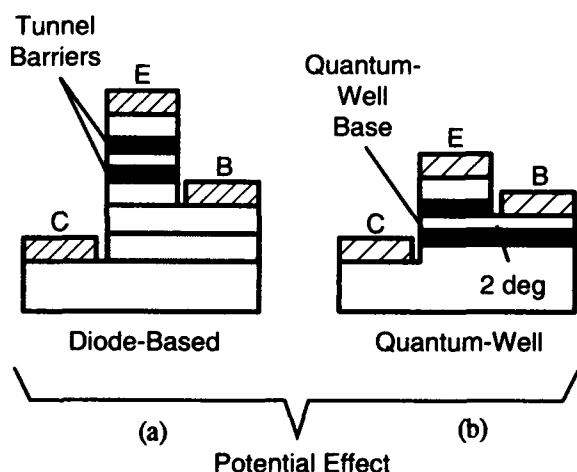


Figure 1. Schematic diagrams of two vertical resonant tunneling transistors: (a) a resonant tunneling diode is incorporated into the emitter (E) epitaxy of a bipolar or hot electron transistor, and (b) direct electrical contact is made to the quantum well base (B) which is a two-dimensional electron gas (2deg) formed between base/emitter and base/collector barriers. The collector contact is labeled C.

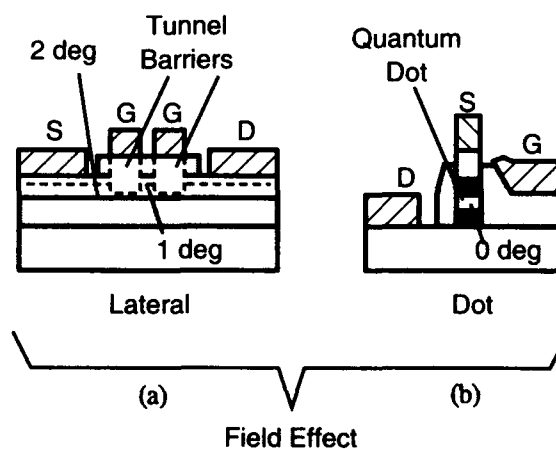


Figure 2. Schematic diagrams of (a) a field-effect lateral resonant tunneling transistor in which the potential profile for electrons in a two-dimensional electron gas (2deg) is modulated by depletion barriers or epitaxially-formed tunnel barriers and (b) a gated quantum dot transistor in which the central transport region is quantized in all spatial dimensions. Source, drain, and gates are labeled S, D, and G, respectively.

06785

consequence of scaling most RTTs is to decrease the electron gas dimension and increase the separation between electronic states. When carriers are confined in two mutually-perpendicular directions, the density of states becomes sharply peaked and equilibrium electrons occupy the lowest energy subband. For this case, the injected electron distribution is nearly monoenergetic resulting in narrow resonant switching thresholds.

As an introduction to RTTs, the I-V characteristics of each of the configurations shown in Figs. 1 and 2 will be discussed. For a more thorough review, the reader is referred to references [1,3].

### Resonant Tunneling Bipolar Transistor

As an example of the diode-based transistor, a schematic energy band diagram for a resonant tunneling bipolar transistor (RTBT) is shown in Fig. 3. The device consists of a double barrier RTD in the emitter of an InP/In<sub>0.53</sub>Ga<sub>0.47</sub>As double heterostructure bipolar

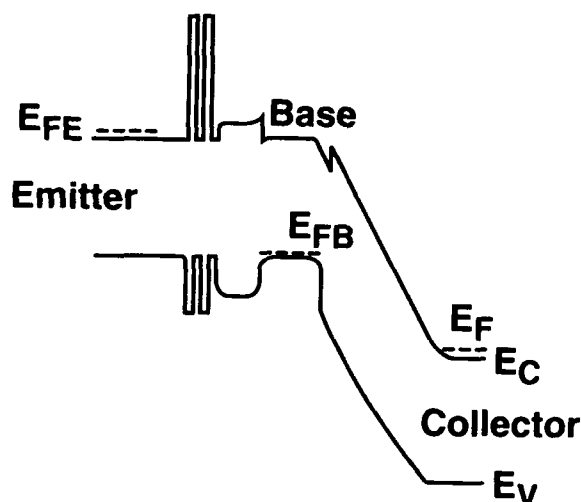


Figure 3. Schematic energy band diagram for the resonant tunneling bipolar transistor.

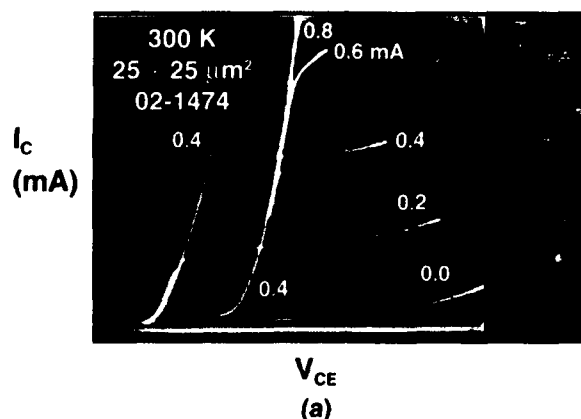


Figure 4. Resonant tunneling bipolar transistor (a) common emitter characteristics and

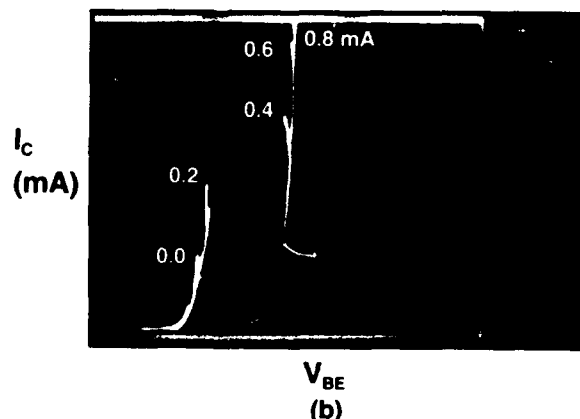
transistor. The layer diagram for the RTBT is shown in Table 1.

The room temperature common-emitter transistor characteristics for the RTBT are shown in Fig. 4(a) and (b) for an RTBT suitable for logic circuit integration. Peak-to-valley current ratio of approximately 20 is obtained with peak current density of 9 kA/cm<sup>2</sup>, current gain exceeding 100, and base/collector break-down voltage exceeding 5 V.

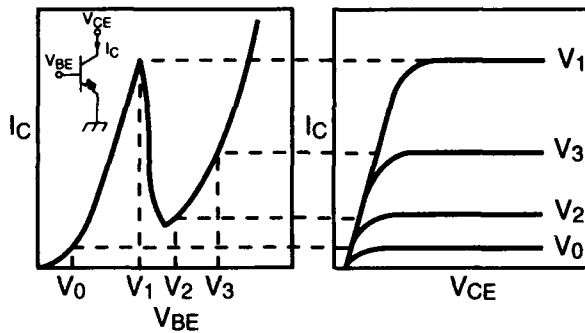
In logic circuits the RTBT is voltage biased rather than current biased. Under voltage bias RTTs exhibit a characteristic negative transconductance. As shown in Fig. 5, a monotonic increase in the base/emitter voltage causes the collector current to serpentine between on and off states.

Layer thickness nm	Doping density $\times 10^{18}$ (cm <sup>-3</sup> )	Semiconductor
150	5	n++ In <sub>0.53</sub> Ga <sub>0.47</sub> As
50	1	n+ In <sub>0.53</sub> Ga <sub>0.47</sub> As
2	-	In <sub>0.53</sub> Ga <sub>0.47</sub> As
2	-	AlAs
1	-	In <sub>0.53</sub> Ga <sub>0.47</sub> As
2	-	InAs
1	-	In <sub>0.53</sub> Ga <sub>0.47</sub> As
2	-	AlAs
2	-	In <sub>0.53</sub> Ga <sub>0.47</sub> As
40	1	n- In <sub>0.53</sub> Ga <sub>0.47</sub> As
10	5	n++ In <sub>0.53</sub> Ga <sub>0.47</sub> As
5	3	n+ InP
45	5	n++ In <sub>0.53</sub> Ga <sub>0.47</sub> As
10	3	n+ InP
40	0.5	n InP
10	1	n+ In <sub>0.53</sub> Ga <sub>0.47</sub> As
80	30	p++ In <sub>0.53</sub> Ga <sub>0.47</sub> As
20	-	In <sub>0.53</sub> Ga <sub>0.47</sub> As
500	0.02	n- InP
600	5	n++ In <sub>0.53</sub> Ga <sub>0.47</sub> As
substrate	Fe-doped	InP

Table 1. Bipolar resonant tunneling transistor layer diagram for the transistor shown in Fig. 4 and grown by metalorganic molecular beam epitaxy (Wafer 02-1474).



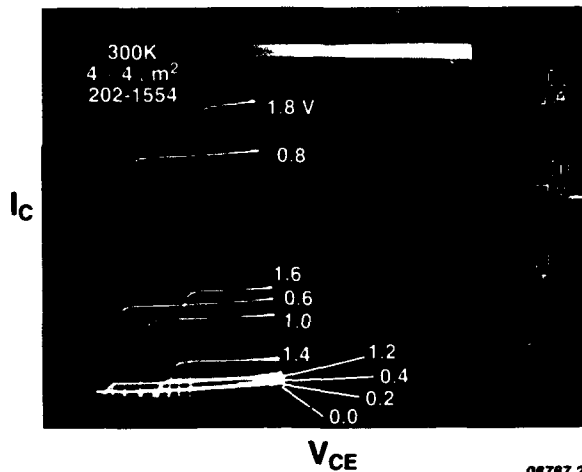
(b) simultaneous measurement of base/emitter voltage characteristics.



08784

Figure 5. Schematic diagram of a resonant tunneling transistor characteristic exhibiting negative transconductance under base/emitter voltage bias.

A representative room temperature I-V characteristic for the RTBT under base/emitter voltage bias is shown in Fig. 6. The negative transconductance in this device is higher than 125 mS per millimeter of emitter periphery.

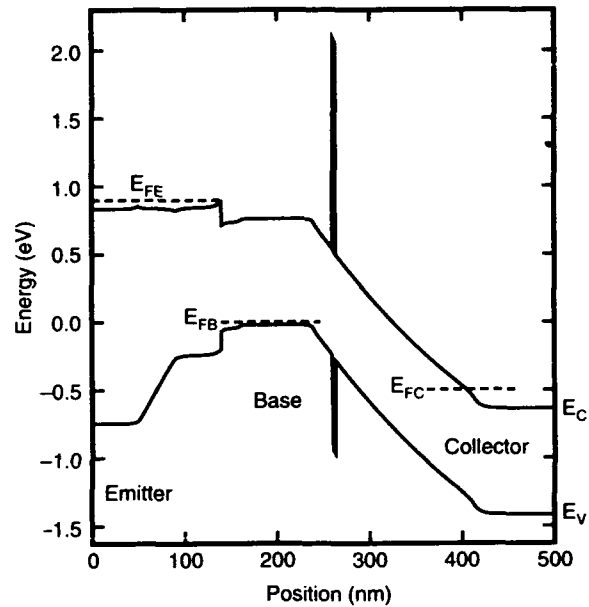


08787.2

Figure 6. Resonant tunneling bipolar transistor under base/emitter biases from 0 to 1.8 V. This transistor differs from Table 1 only by the width of the InGaAs layer between the p++ InGaAs base and the InP collector. In this transistor, the InGaAs layer is 40 nm.

### Bipolar Quantum-Well Resonant Tunneling Transistor

The computed energy band diagram for a bipolar quantum-well resonant tunneling transistor (BiQuaRTT) is shown in Fig. 7. The quantum well base is defined by an InGaAlAs/InGaAs heterojunction emitter and an AlAs tunnel barrier in the base/collector junction [4]. As the base/collector voltage is varied the transmission of electrons across the triangular potential well at the base/collector junction is dramatically modulated resulting in a multi-peak current-resonance characteristic.



06746

Figure 7. Computed energy band diagram for the bipolar quantum-well resonant tunneling transistor.

The current resonances in the BiQuaRTT correspond to alignment of the minority electron distribution in the base with quantized base transmission resonances. These alignments give rise to a modulation of the transmission probability for electrons traveling from base to collector. By changing the thickness of the triangular potential well preceding the AlAs tunnel barrier, the number of transmission resonances can be readily changed as shown in Fig. 8. The number of current peaks in each transistor increases with the width of the triangular potential well.

### Lateral Field-Effect Resonant Tunneling Transistor

In the lateral RTT shown in Fig. 2(a), the potential between source and drain is modulated by the introduction of lateral tunnel barriers. The barriers are produced by narrow metal gates above the 2deg which form a double-barrier lateral potential profile. While the metal gate embodiments of this transistor are restricted to cyogenic operation [5-7], other lateral heterojunction embodiments [8] show prospects for room temperature operation [9].

To illustrate the dependence of transmission coefficient on gate bias for the field-effect lateral RTT, consider the band profile of a triple quantum well heterostructure utilizing InP/InGaAs heterostructures, Fig. 9(a). For bias voltages less than approximately  $2(E_F - E_0)/q$ , parallel electron transmission across the quadruple barrier structure is high as shown by the gray lines in the computed transmission coefficient plot of



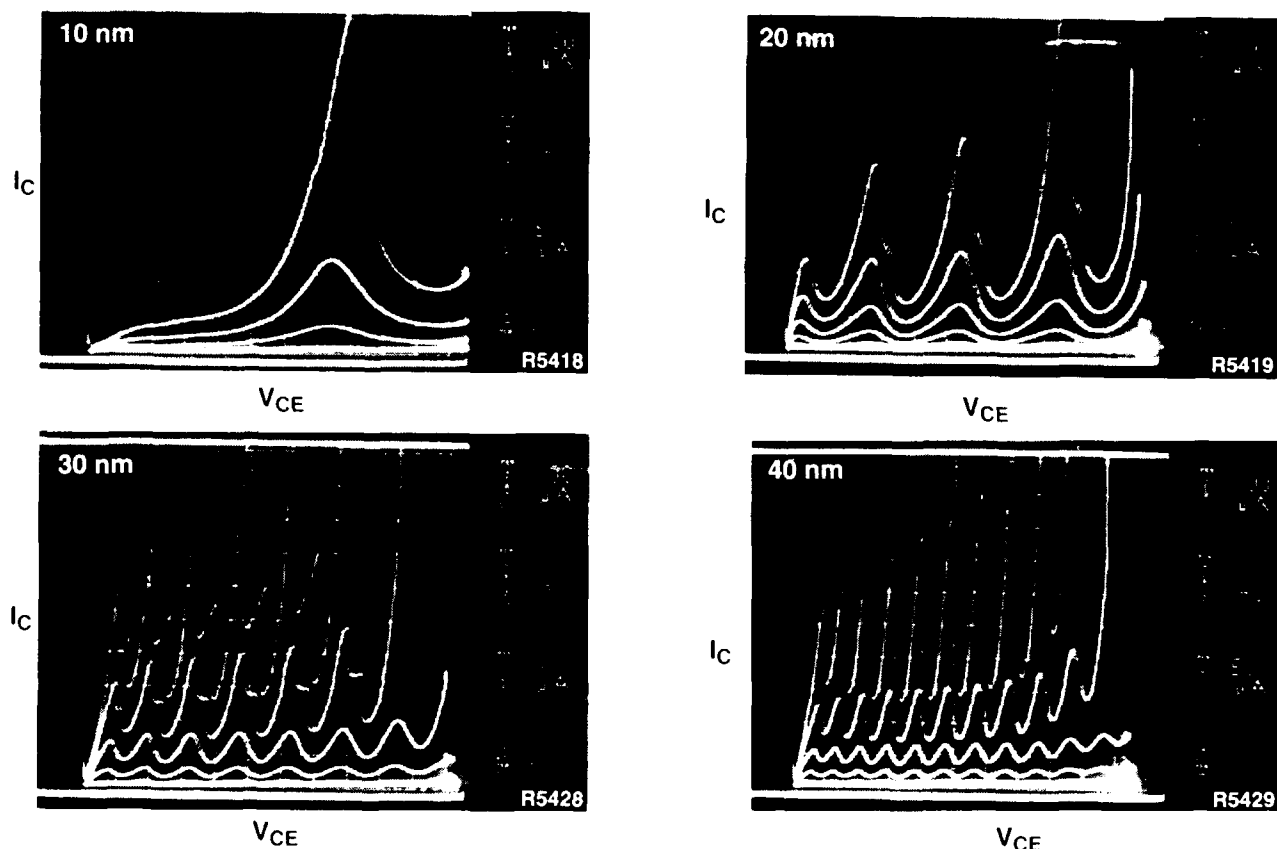


Figure 8. Common emitter transistor characteristics (77 K) for four bipolar quantum well resonant tunneling transistors differing by the width of the triangular potential well in the

base/collector junction (indicated in the upper left-hand corners). All transistors have identical geometries with emitter areas of  $80 \mu\text{m}^2$  and were grown by molecular beam epitaxy.

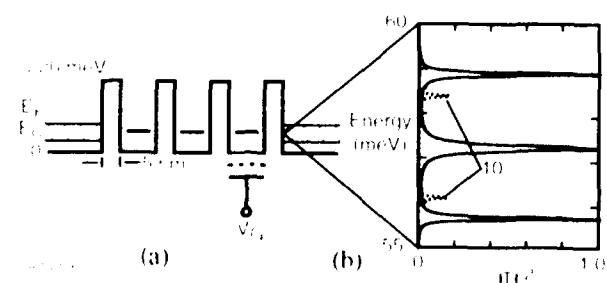


Figure 9. Field effect lateral resonant tunneling transistor: (a) schematic band diagram for an InP/InGaAs heterostructure and its computed one-dimensional transmission coefficient, for two different cases. First as shown by the solid line in (a) and the gray line in (b) and second with the third well lowered by 40 meV as shown by the dotted lines in both (a) and (b).

of Fig. 9(b). If the band profile is altered, by the presence of a nearby gate potential, the transmission coefficient for the structure is reduced. In the calculation, of Fig. 9, this gate bias is approximated by

the lowering of the conduction band minimum of the third well by 40 meV (dotted line in Fig. 9(a)); the resultant computed decrease in the transmission coefficient is shown in Fig. 9(b). As with the RTBT a multiple transconductance characteristic results.

#### Vertical Field-Effect Resonant Tunneling Transistor (toward quantum dot transistors [10-12])

A vertical field-effect RTT has recently been proposed and demonstrated by Longenbach, et al. [13] and allows the investigation of transfer characteristics which should be obtainable near the quantum dot regime. We have utilized the approach of Longenbach, but with the inclusion of a triple barrier, coupled-quantum-well resonant tunneling diode (3bRTD) to add logic functionality [12]. Shown in Fig. 10(a) is a schematic view of the RTT, consisting of the combination of an InP/In<sub>0.53</sub>Ga<sub>0.47</sub>As 2deg heterostructure above a 3bRTD formed of AlAs/In<sub>0.53</sub>Ga<sub>0.47</sub>As heterojunctions, all grown on an InP substrate. Ohmic contacts are formed to the source (S) and drain (D) of the device with the

source metallization alloyed to form an ohmic connection to the 2deg. Dual gate electrodes ( $G_1$  and  $G_2$ ) are placed on either side of the source contact.

The 3bRTD forms the channel of a vertical field effect transistor (FET). The gate potential controls the electron density in the 2deg which then controls the conducting cross section of the 3bRTD. Shown in Fig. 10(b) is the schematic current-voltage (I-V) characteristic of such an RTT. With both gates biased at 0 V with respect to the source, a dual peak I-V characteristic is obtained. Application of a fixed negative bias (depletion mode) sufficient to deplete the 2deg (defined as -1 V in Fig. 9(b)) decreases the current cross section of the device by an amount approximately equal to the area under the gate. Thus, in the dual gate configuration of Fig. 1(a), application of [0,-1] and [-1,0] biases to gates [ $G_1, G_2$ ] respectively result in the same I-V characteristic. If the 2degs under both  $G_1$  and  $G_2$  gate electrodes are depleted, [-1,-1], the current

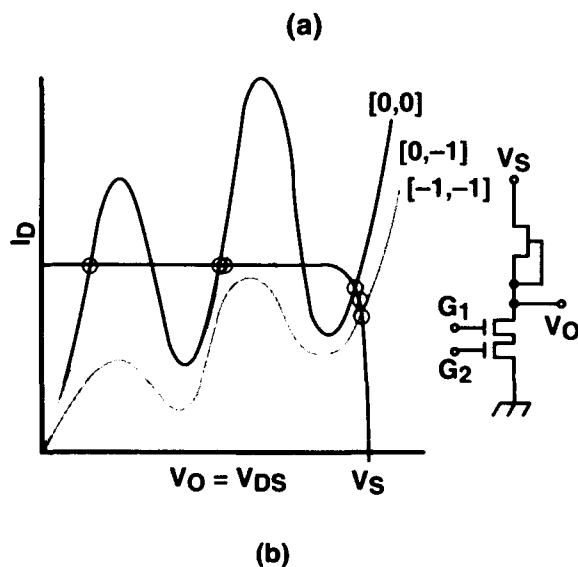
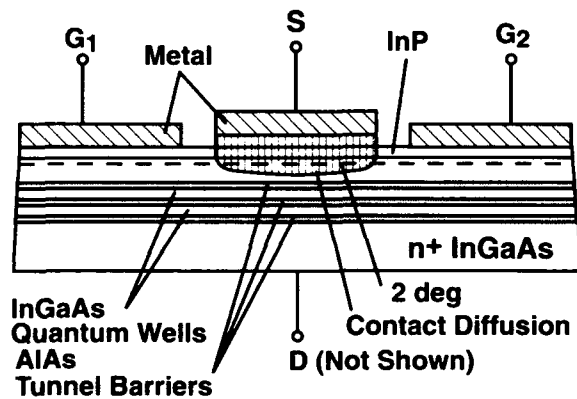
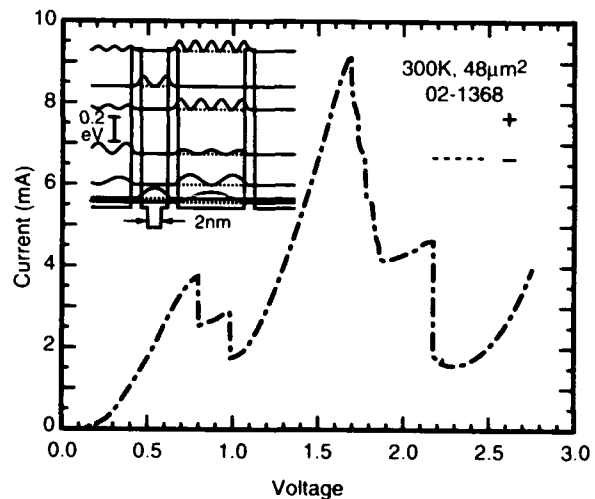


Figure 10. Vertical field-effect resonant tunneling transistor (a) schematic diagram and (b) idealized current-voltage characteristics.

cross section of the device is restricted to approximately the area under the source electrode. To obtain the greatest current modulation requires the use of a source contact on the order of one micron in length such that the lateral depletion under the gates is sufficient to entirely deplete the area under the source.

Also shown in Fig. 10(b) is a circuit diagram of a ternary memory cell using the depletion mode logic levels previously described. On power-up the circuit output voltage,  $V_O$ , is low, indicated by the intersections of the [0,0] 3bRTD characteristic with the FET load line at the circled point preceding the first resonance peak. An intermediate logic level is obtained with [0,-1] or [-1,0] biases and the high output voltage state occurs for [-1,-1] biases. Thus,  $V_O$  displays one of three different output levels corresponding to the highest previous sum of the two binary gate inputs.

The triple-barrier RTD structure, shown in the inset of Fig. 11 has now been successfully demonstrated using an AlAs/InGaAs/InAs/InGaAs/AlAs/InGaAs/AlAs heterostructure of thicknesses of 1.5/1/2/1/1.5/10/1.5 nm, respectively. Including contact layers the layer structure was grown in the sequence: 600 nm InGaAs ( $5 \times 10^{18} \text{ cm}^{-3}$ ), 50 nm InGaAs ( $2 \times 10^{17} \text{ cm}^{-3}$ ), 2 nm InGaAs spacer, the coupled-quantum-well heterostructure, 2 nm InGaAs spacer, 50 nm InGaAs ( $2 \times 10^{17} \text{ cm}^{-3}$ ), and 300 nm InGaAs ( $5 \times 10^{18} \text{ cm}^{-3}$ ). Essentially no dc hysteresis is observed for this 3bRTD. The heterostructure design for low second valley current and transistor results will be reported elsewhere [14].



08787

Figure 11. Room temperature current-voltage characteristics for a triple barrier resonant tunneling diode. Inset: computed energy band diagram, transmission resonances, and wave functions. The dotted/dashed lines correspond to a positive/negative voltage ramp, respectively.

## Discussion

An essential element of a practical logic technology is the need to control device switching voltages precisely as has been discussed recently in the popular press [15]. The switching voltage of a resonant tunneling diode is determined to first order by the absolute width of the quantum well layer. When the width is controlled precisely, by use of an atomic layer epitaxial technique [9], the resonant peak voltage is *uniform across the entire wafer*, allowing tight device matching. By epitaxial control of the double barrier dimensions, circuit switching thresholds are determined to a precision comparable to that obtained by use of the bandgap in conventional bipolar transistor circuits. Since the transmission probability for resonant tunneling electrons is largely insensitive to temperature, the resonant peak current is less sensitive to temperature than are the saturated currents in conventional semiconductor devices.

## Conclusions

The transistor characteristics of several potential-effect and field-effect resonant tunneling transistors have been outlined. These transistors offer the prospect for a room temperature device technology with higher functional efficiency and greater scalability than conventional devices.

## Acknowledgements

We would like to acknowledge the technical assistance, useful discussions, and contributions of R. Aldert, G. Baker, L. Cooper, D. Chasse, G. Frazier, C. Mikkelson, B. Newell, E. Pijan, P. Stickney, A. Taddiken, and R. Thomason and the support of the Air Force Wright Laboratory, Defense Advanced Research Projects Agency, and the Office of Naval Research.

## References

1. A. C. Seabaugh and M. A. Reed, "Resonant Tunneling Transistors", in Heterostructures and Quantum Devices (a volume of VLSI Electronics), N. G. Einspruch and W. R. Frensley, eds. (Academic Press, Orlando, FL, to be published 1993).
2. S. Luryi, "Hot Electron Transistors" in High Speed Semiconductor Devices, S. M. Sze, ed. (John Wiley & Sons, New York, 1990), pp. 399-461.
3. F. Capasso, S. Sen, and F. Beltram, "Quantum Effect Devices" in High Speed Semiconductor Devices, S. M. Sze, ed. (John Wiley & Sons, New York, 1990), pp. 465-520.
4. A. C. Seabaugh, Y.-C. Kao, W. R. Frensley, J. N. Randall, and M. A. Reed, "Resonant transmission in the base/collector junction of a bipolar quantum-well resonant tunneling transistor", *Appl. Phys. Lett.* **59**, 3413-3415 (1991).
5. K. E. Ismail, P. F. Bagwell, T. P. Orlando, D. A. Antoniadis, and H. I. Smith, "Quantum phenomena in field-controlled semiconductor nanostructures", *Proc. IEEE* **79**, 1106-1116 (1991).
6. S. Y. Chou, D. R. Allee, R. F. Pease, and J. S. Harris, "Lateral resonant tunneling transistors employing field-induced quantum wells and barriers", *Proc. IEEE* **79**, 1131-1139 (1991).
7. A. C. Seabaugh, J. N. Randall, Y.-C. Kao, J. H. Luscombe, and A. M. Bouchard, "In<sub>0.52</sub>Al<sub>0.48</sub>As/In<sub>0.53</sub>Ga<sub>0.47</sub>As lateral resonant tunneling transistor", *Electronics Lett.* **27**, 1832-1834 (1991).
8. S. Luryi and F. Capasso, "Resonant tunneling of two-dimensional electrons through a quantum wire: a negative transconductance device", *Appl. Phys. Lett.* **47**, 1347-1348 (1985), erratum *Appl. Phys. Lett.* **48**, 1693 (1986).
9. A. C. Seabaugh, J. H. Luscombe, J. N. Randall, P. C. Colter, A. Dip, G. M. Eldallal, and S. M. Bedair, "Atomic layer epitaxy of quantum-well devices, *J. Thin Solid Films*, to be published (1993).
10. W. B. Kinard, M. H. Weichold, and W. P. Kirk, "Fabrication of a gated gallium arsenide heterostructure resonant tunneling diode", *J. Vac. Sci. Technol. B* **8**, 393-396 (1990).
11. M. W. Dellow, P. H. Beton, M. Henini, P. C. Main, and L. Eaves, "Gated resonant tunneling diodes", *Electronics Lett.* **27**, 134-136 (1991).
12. P. Guéret, N. Blanc, R. Germann, and H. Rothuizen, "Confinement and single-electron tunneling in Schottky-gated, laterally squeezed double-barrier quantum-well heterostructures", *Phys. Rev.* **68**, 1896-1899 (1992).
13. K. F. Longenbach, Y. Wang and W. I. Wang, "Two-dimensional electron gas modulated resonant tunneling transistor", *Appl. Phys. Lett.* **59**, 967-969 (1991).
14. C. H. Mikkelson, A. C. Seabaugh, E. A. Beam, J. H. Luscombe, and G. A. Frazier, "Coupled quantum-well field-effect resonant tunneling transistor for multi-valued logic/memory applications", submitted to *IEEE Trans. Electron Devices* (1993).
15. For example, R. W. Keyes, "The future of solid-state electronics", *Physics Today*, August, 1992, pp. 42-48.

# Theory of Ultra High Frequency Performance Heterojunction Bipolar Transistors

A. A. Grinberg and S. Luryi

AT&T Bell Laboratories, Murray Hill, New Jersey 07974

## Abstract

We consider the high-frequency operation of an abrupt-heterojunction transistor with ballistic transport in the base. The fundamental frequency cutoff in such devices is shown to be limited by the *dispersion* in the minority-carrier times of flight across the base, rather than the average time of flight itself.

## Introduction

Electrical characteristics of a high-speed bipolar junction transistor are in large part determined by the transport of minority carriers across the base. The concept of diffusion across a base of width  $W_B$  is valid only if the particles undergo multiple collisions in the region, i.e., when  $W_B \gg l_{sc}$ , where  $l_{sc}$  is the scattering length. In the opposite limit,  $W_B \leq l_{sc}$ , the transport is largely ballistic.

Recently, we presented [1] an exact solution of the Boltzmann equation for the minority carrier transport in a narrow base. A key ingredient of our approach is formulation of the boundary conditions for the distribution function  $f(\mathbf{r}, \mathbf{k}, t)$ . It is clear that functions  $f(0, \mathbf{k})$  and  $f(W_B, \mathbf{k})$  cannot be preset, because they themselves depend on the solution in the base. In a Boltzmann description, the boundary conditions must specify the distribution of *inbound* particles moving toward the base at both junctions.

$$f(0, \mathbf{k}) \equiv f_0^{(+)}(\mathbf{k}) \quad \text{for } \mathbf{k} \cdot \hat{\mathbf{z}} > 0; \quad (1a)$$

$$f(W_B, \mathbf{k}) \equiv f_W^{(-)}(\mathbf{k}) \quad \text{for } \mathbf{k} \cdot \hat{\mathbf{z}} < 0. \quad (1b)$$

Neither of these functions determines the carrier concentration, the drift velocity, or the current at the respective boundary, but combined they constitute a

complete set of boundary conditions for the transport equation. The actual shape of functions (1) depends on transport outside the base.

In heterojunction bipolar transistors (HBT) the minority carriers can be injected into the base "over a cliff" of energy  $\Delta$ , Fig. 1:

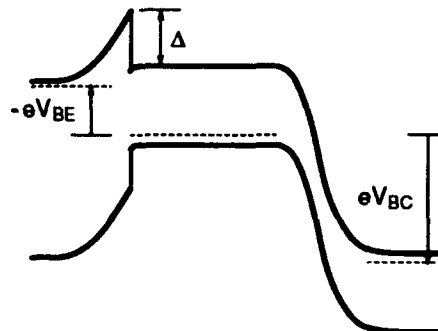


Figure 1. Schematic band diagram of an abrupt-junction heterostructure bipolar transistor (a-HBT). Minority carriers are injected into the base "over a cliff" of energy  $\Delta$ .

We assume a "thermionic" condition at the base-emitter interface and a "perfect sink" condition at the base-collector interface:

$$f_0^{(+)}(\mathbf{k}, u) = e^{-\frac{E_{\mathbf{k}} - \Delta}{kT}} \Theta(uk/k_0 - 1); \quad (2a)$$

$$f_W^{(-)}(\mathbf{k}, u) = 0, \quad (2b)$$

where  $u$  is the cosine of the angle between  $\mathbf{k}$  and the  $z$  axis,  $E_{\mathbf{k}} \equiv \hbar^2 k^2 / 2m$ ,  $\hbar k_0 \equiv \sqrt{\Delta / 2m}$ , and  $\Theta(x)$  is the step function.

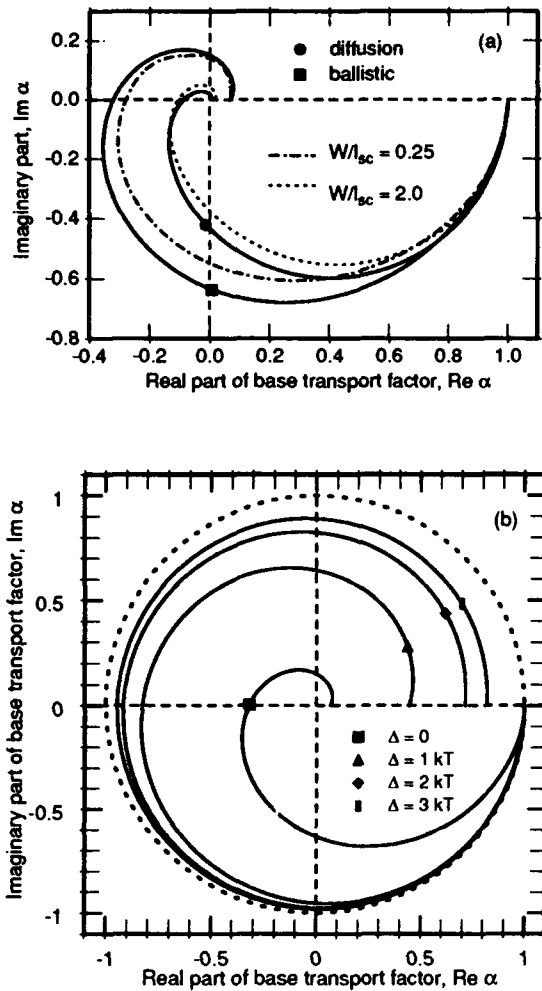


Figure 2. Phase trajectories for the base transport factor.

(a) Homoijunction bipolar transistors.  $\alpha_B(\omega)$  is traced in the complex plane for different scattering lengths and base thicknesses. Solid curves represent the universal spirals obtained in the diffusion ( $l_{sc} \ll W_B$ ) and the ballistic ( $W_B \ll l_{sc}$ ) limits.

(b) Heterojunction bipolar transistors with ballistic base transport.  $\alpha_B(\omega)$  is plotted for four different injection energies  $\Delta$ . The curve for  $\Delta = 0$  (e.g., graded-gap HBT) is equivalent to the ballistic case in Fig. 2a. For convenience, on the same graph we present the  $\alpha_B$  corresponding to an artificial initial distribution describing a perfectly collimated monochromatic beam (dotted line).

For a short-base transistor  $W_B \leq l_{sc}$ , the form of inbound distribution (1a) has a strong influence on the device current gain at high frequencies. In a ballistic transistor, the high-frequency gain roll-off occurs due to the scatter in the velocities and the incident angles of in-bound particles [2], and the signal decay is analogous to the Landau damping of density waves in

collisionless plasmas. Members of the carrier ensemble, injected into the base at a given time with different normal components of the velocity, arrive at the base-collector junction at different times, thus washing out a modulation introduced at the injection plane.

For a homoijunction transistor, the Landau damping is nearly as efficient in degrading the gain as is scattering in the base. Figure 2a shows the base transport factor  $\alpha_B(\omega)$ , calculated for different ratios of the scattering length to the base thickness and plotted as a trajectory in the complex plane. Increasing the frequency corresponds to moving clockwise with increasing phase  $\phi_B \equiv \arg(\alpha_B)$  and spiraling in toward the origin  $|\alpha_B| \rightarrow 0$ . If we neglect recombination in the base (reasonable at high frequencies), then the spirals, corresponding to either the purely diffusive or the purely ballistic limits (solid lines in Fig. 1) are *universal* in the sense that they are independent of the base width, the diffusion coefficient, the temperature, etc. At high enough  $\omega$ , the magnitude of gain  $|\alpha_B|$  decreases exponentially.

In contrast, for a ballistic HBT with an *abrupt* emitter-base heterojunction, the high-frequency current gain has a strong temperature dependence, Fig. 2b. The main effect of temperature is to increase dispersion of the incident distribution. In the purely ballistic regime, the magnitude of  $\alpha_B$  decreases with the frequency only to the extent that the distribution of transit times  $\tau_B$  across the base has a finite *width* – due to the temperature broadening of the incident velocity distribution. In the limit  $\Delta \gg kT$ , it is that width  $\Delta\tau$  rather than  $\tau_B$  itself that sets the fundamental limit on the frequency performance of HBT.

A ballistic transistor with a sufficiently collimated mono-energetic injected beam of minority carriers, such that

$$\Delta\tau \ll \tau_B, \quad (3)$$

will be referred to as the coherent transistor [3] or CT. A good approximation to such a beam can be obtained from the passage across an abrupt heterointerface at low temperatures. For carriers traveling across the base with a normal velocity  $v_B$ , a periodic modulation of the injection at the emitter interface with a frequency  $f$  sets up an electron density wave of wavelength  $\lambda = v_B/f$ . When (3) is fulfilled, the amplitude of this wave does not appreciably decay over the entire base width  $W_B$ . As discussed below, the coherent transistor has both the common-emitter current gain  $\beta$  and the power gain exceeding unity at frequencies far above the usual cutoff frequencies, limited by the time-of-flight delays.

## Equivalent Microwave Circuit of Abrupt-Junction HBT

Figure 3 shows the microwave circuit of a HBT with abrupt emitter-base heterojunction. It includes the intrinsic parameters  $R_E$  and  $C_E$  (the differential resistance and capacitance of the emitter-base junction, respectively),  $C_C$  and  $g_A$  (the collector junction capacitance and the Early conductance),  $\alpha_B$  and  $\xi_C$  (the base and collector transport factors, see below), and  $R_B$  (the intrinsic base resistance), as well as the extrinsic collector capacitance  $C_{Cx}$  and the parasitic resistances,  $R_{Bx}$ ,  $R_{Cx}$ , and  $R_{Ex}$ .

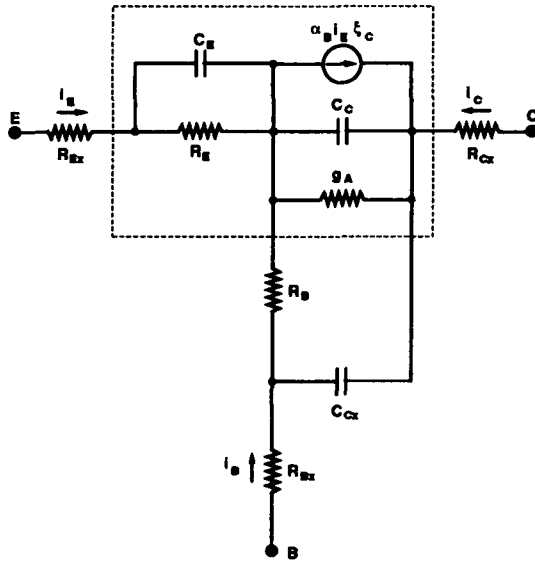


Figure 3. Equivalent circuit of a HBT with abrupt emitter-base junction. Dashed line indicates the portion described by the matrix (4).

Let us write down explicitly the common-base admittance matrix  $Y^{bi}$ , describing the two-port block corresponding to the portion of the circuit indicated by the dashed line (this block represents the intrinsic transistor without  $R_B$ ). Neglecting the Early effect, expressed by the conductance  $g_A$ , we have

$$Y^{bi} = \begin{bmatrix} g_E + i\omega C_E & 0 \\ -g_E \alpha_B \xi_C & i\omega C_C \end{bmatrix}. \quad (4)$$

where  $g_E \equiv 1/R_E$  is the differential emitter conductance.

The equivalent circuit in Fig. 3 is valid for any abrupt-junction HBT. The ballistic and the diffusion varieties differ only by the Early effect, which modulates the output conductance in a diffusive HBT, while being entirely absent in the ballistic case. For  $g_A = 0$ , the intrinsic admittance matrix (4) is formally identical in both limits. Of course, the base transport

factors  $\alpha_B$  involved are different.

## Current Gain

**Base transport factors.** In the diffusion limit, neglecting recombination, the transport factor  $\alpha_B$  is described by the well-known formula,

$$\alpha_B = \frac{1}{\cosh[(2i\phi_B)^{1/2}]} \quad (5)$$

$$\approx \begin{cases} (1 + i\phi_B)^{-1} & \text{for } \phi_B \ll 1 \\ 2e^{-\phi_B} e^{-i\phi_B} & \text{for } \phi_B \geq 1 \end{cases}$$

where  $\phi_B = \omega \tau_D$  and  $\tau_D = W_B/2D$  is the base transit time by diffusion. Accordingly, the current gain  $\beta = |\alpha_B/(1 - \alpha_B)|$  at low frequencies rolls-off at 10 dB/dec, but above  $f_T = 1/2\pi \tau_D$  it becomes exponentially small.

In the ballistic limit, the expression for  $\alpha_B$  reduces to a quadrature. The current gain  $\alpha_B(\omega)$  depends in this case only on the initial distribution of the electron velocities in the direction toward collector [2]. The latter can be replaced by a normalized distribution  $\rho(\tau)$  of the time of flights across the base and  $\alpha_B(\omega)$  can be written in the form

$$\alpha_B = \int \rho(\tau) e^{-i\omega\tau} d\tau. \quad (6)$$

In other words,  $\alpha_B$  represents the characteristic function of a random variable  $\tau$ . The thermal distribution (2a) corresponds to

$$\rho(\tau) = e^{-\frac{\Delta}{kT} - \frac{mW_B^2}{2kT\tau^2}}. \quad (7)$$

The frequency dependence of  $\beta$ , calculated from Eqs. (6) and (7), is shown in Fig. 4.

It is instructive to derive an approximate analytical expression for the gain in the limit

$$kT \ll \Delta. \quad (8)$$

In this limit, to lowest order in  $kT/\Delta$ , the mean and the variance of the distribution (6) are given by

$$\bar{\tau} \approx \tau_B (1 - kT/2\Delta + \dots); \quad (9a)$$

$$\Delta\tau^2 \approx \langle (\tau - \bar{\tau})^2 \rangle \approx \tau_B^2 (kT/2\Delta)^2, \quad (9b)$$

where  $\tau_B \equiv \sqrt{mW_B^2/2\Delta}$ . It follows from Eqs. (9) that for a thermal distribution  $\Delta\tau/\bar{\tau} \approx kT/2\Delta$ , and hence the inequality in Eq. (8) is equivalent to that in Eq. (3) which defines the coherent regime. In the limit (8) we find the following asymptotic expression for  $\alpha_B$ :

$$\alpha_B = \frac{e^{-i\omega\tau_B}}{1 - i\omega\tau_B/2\tilde{\Delta}}, \quad (10)$$

where  $\tilde{\Delta} \equiv \Delta/kT$ . The approximate dependence

$\beta^2(\omega)$ , calculated from Eq. (10) is plotted in Fig. 4 by the dotted line. We see that Eq. (10) gives an excellent approximation to the exact result for  $\bar{\Delta} = 5$ . It can be used, therefore, to calculate the peak gain values. The maxima  $\beta_v$  occur at those values of  $\omega = \omega_v$  where

$$\text{Im}(\alpha) = 0 ; \quad \text{Re}(\alpha) > 0 , \quad (11)$$

which gives for  $\omega\Delta\tau \leq 1$  and  $v = 1, 2, \dots$

$$\omega_v \tau \approx 2\pi v , \quad (12a)$$

$$\beta(\omega_v) \approx \frac{2}{\omega_v^2 \Delta \tau^2} . \quad (12b)$$

We see that the peaks decrease with the frequency as  $\omega^{-2}$ , i.e., at the rate of 20 dB/dec.

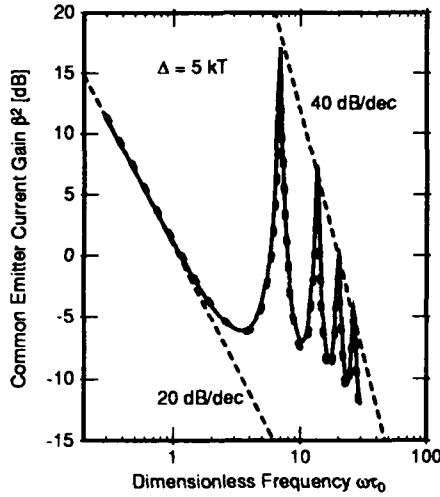


**Figure 4.** Base transport limited current gain of a coherent transistor. Solid line shows  $\beta^2(\omega)$ , calculated from Eq. (6), dotted line from Eq. (10). The dashed lines indicate the gain roll-off in the conventional frequency range ( $f < f_T$ ) and the extended range ( $f > f_T$ ).

The nature of the current-gain peaks in an extended frequency range is best understood by considering the case of a "perfectly" coherent transistor, in which all injected electrons travel toward the collector with the same velocity  $v_B = (2\Delta/m)^{1/2}$ . In this case, a periodic modulation of the injection at the emitter interface sets up in the base an electron density wave of the form:

$$n(z, t) = n_0 e^{i\omega(t - z/v_B)} , \quad (13)$$

where  $n_0$  is the amplitude of the concentration modulation. At any point in the base, the electron current density  $J(z, t)$  equals  $-en v_B$  and hence  $\alpha_B = \exp(-i\omega\tau_B)$ , which is the limit of Eq. 10 as  $\Delta\tau \rightarrow 0$ . The magnitude of the common-emitter current gain becomes

$$\beta = |2 \sin(\omega\tau_B/2)|^{-1} . \quad (14)$$

The usual procedure for the determination of  $f_T$  in a microwave transistor is to extrapolate the data measured at relatively low frequencies to unity gain at 10 dB/decade. Since for  $\omega\tau_B \leq 1$ , the gain (14) rolls off at 10 dB/decade, the extrapolation procedure will produce the usual value  $f_T = 1/(2\pi\tau_B)$ . However, Eq. (14) predicts additional resonances at extended frequencies (12a). Their physical origin is as follows. Neglecting recombination, the only reason for the base current to flow is to maintain neutrality of the base layer. The resonant frequencies (12a) correspond to an integer number  $v$  of periods  $\lambda = v_B/f$  of the density wave (13) in the base. To the extent that the wave is not decaying in amplitude in a perfect CT, the total minority-carrier charge in resonance does not fluctuate at all. The output current modulation is thus accomplished with no rf current input, hence the "infinite" gain. In an imperfectly coherent transistor, the density wave is Landau damped to some extent and the base current has a finite value at all frequencies, cf. Fig. 4. Note that in a diffusion transistor, the total injected charge in the base oscillates at any frequency.

*Inclusion of the collector delay.* The stark contrast between the coherent ballistic and the diffusive modes of base transit by minority carriers, can also be seen from Fig. 5, where we include a transit angle  $\theta \equiv \omega\tau_C$  across the base-collector junction. The inclusion of a collector delay is accomplished by simply multiplying  $\alpha_B$  with a collector transport factor  $\xi_C$ . Assuming a saturated drift velocity  $v_s$  in the base-collector junction, this factor is of the form

$$\xi_C = \frac{1 - e^{-i\theta}}{i\theta} = \frac{\sin(\theta') e^{-i\theta'}}{\theta'} , \quad (15)$$

where  $\theta' = \omega\tau'_C$  and  $\tau_C = 2\tau'_C = W_C/v_s$  with  $W_C$  being the width of the base-collector space-charge layer. The dotted line in Fig. 5 shows the common-emitter current gain, limited only by the collector transit  $\tau_C = 1$  ps. This curve corresponds to setting  $\tau_D = \tau_B = 0$ , which gives  $\alpha_B = 1$  for either diffusive or ballistic base transport. The dashed line corresponds to a diffusive transport with  $\tau_D = 2$  ps (while keeping the same  $\tau_C = 1$  ps). The cutoff has shifted to lower frequencies, as expected. The solid line represents a CT with  $\tau_C = 1$  ps,  $\tau_B = 2$  ps. We see the dramatic reemergence of a large gain in the frequency range, where not only the diffusive transistor, but even the transistor with no base delay at all, are completely damped. This effect is due to the addition of a coherent delay, which boosts the overall phase of  $\alpha = \alpha_B \xi_C$ , bringing about the condition (11) that maximizes  $\beta$ , while  $|\alpha|$  is still large ( $\approx 0.7$ ).

It is instructive to consider why the phaseshift, obtained in a coherent base transport, is advantageous compared to that arising in the saturated-velocity transport across the base-collector space-charge region. Mathematically, the disadvantage of gaining the phase in collector transit results from the factor  $\sin(\theta')/\theta'$  in Eq. (15), which diminishes the magnitude of  $\xi_c$  at high frequencies. Physically, the difference is rooted in the nature of screening of a dynamic charge moving inside or outside a conductor. Minority carriers moving inside the base induce a base current only to the extent that their total charge varies in time. In contrast, carriers moving in the depleted layer induce currents of equal magnitude in both the base and the collector electrodes.

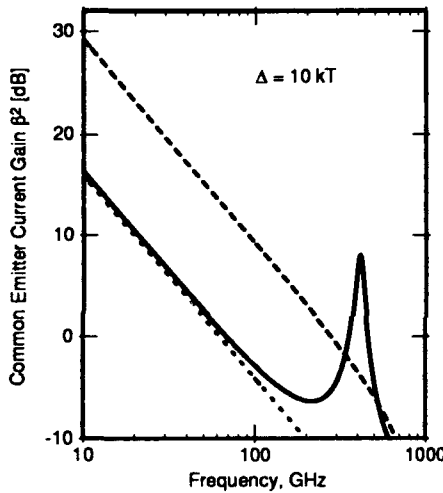


Figure 5. The intrinsic current gain, including the collector delay  $\tau_c = 1$  ps. Dashed lines correspond to zero base delay, dotted lines to a diffusive delay  $\tau_b = 2$  ps, and solid lines to a CT with  $\Delta = 10$  kT and  $\tau_b = 2$  ps.

## Power Gain

It is easy to evaluate all the two-port parameters of the circuit in Fig. 3 in an explicit form [3]. We shall not present here these cumbersome expressions but confine ourselves to the consideration of simplest cases and plots of the results.

In the intrinsic limit,  $R_{ex} = R_{bx} = R_{cx} = 0 = C_{cx}$ , and assuming  $\varphi_E \approx \omega R_E C_E \ll 1$ , the unilateral gain  $U$  is of the form

$$U = \frac{|\alpha_B \xi_c|}{4 \omega^2 C_C^2 R_B r_{22}}, \quad (16)$$

where  $r_{22} \equiv \Re(z_{22}) = R_\varphi + R_E$  is the real part of common-emitter output impedance,

$$R_\varphi = \frac{\cos(\varphi) - \cos(\varphi + \theta)}{\omega C_C \theta} |\alpha_B|, \quad (17)$$

and  $\varphi = \varphi_E + \varphi_B$ . The frequency dependences of  $|U|$ ,  $r_{22}$  and  $|h_{21}^e|^2$  in the intrinsic limit of a CT are plotted in Fig. 6. Note that while in the low-frequency region one has  $U > 0$ , the sign of  $U$  changes on passing the peaks of  $|U|$ . In the range where  $U < 0$ , the transistor is active even if  $|U| < 1$ , since one can bring about the regime with  $U > 1$  by adding an external resistance.

The idea of using phase shifts in a bipolar transistor to extend the active operation to higher frequencies originates with Wright [4] and has since been discussed by a number of authors (see references, cited in [3]). A cornerstone of that discussion has been the negative  $r_{22}$  which can be achieved due to the phase delay  $\theta$  in minority-carrier drift across the collector space-charge region. This concept is quite analogous to the dynamic negative impedance in transit-time diodes [5]. Even a small absolute value of negative resistance, achievable in a diffusive transistor, leads to an active behavior, according to Eq. (16). Unfortunately, however, this idea is severely limited by parasitic effects [6].

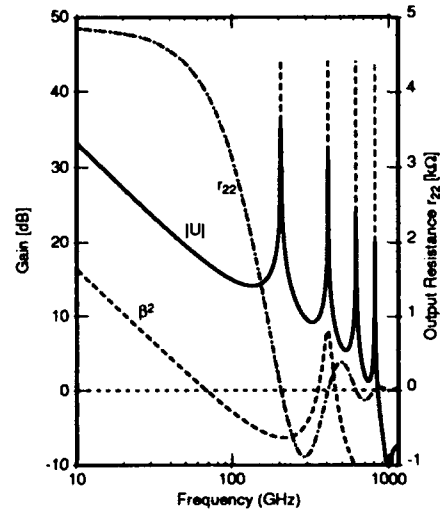


Figure 6. Frequency dependences of the unilateral gain  $|U|$ , the output resistance  $r_{22} \equiv \Re(z_{22})$ , and the common-emitter current gain  $\beta \equiv |h_{21}^e|$  in the intrinsic limit of a coherent transistor. Assumed parameters:  $\Delta = 10$ ,  $\tau_c = 1$  ps,  $\tau_b = 2$  ps,  $C_c = 0.5$  fF,  $R_E = 5 \Omega$ ,  $R_B = 25 \Omega$ .

To illustrate these effects, consider a model in which we retain the parasitic resistances but eliminate the extrinsic capacitance,  $C_{cx} = 0$ . In this case, the unilateral gain can be reduced to the following form:



$$U = \frac{|\alpha_B \xi_C|}{4 \omega^2 C_C^2 (R_B + R_{Bx})} \frac{1}{R_x^{\text{eff}} + r_{22}}, \quad (18)$$

where  $R_x^{\text{eff}} \equiv R_{Cx} (R_E + R_{Ex}) / (R_B + R_{Bx})$  and

$$r_{22} = R_\phi + R_E + R_{Ex} + R_{Cx}. \quad (19)$$

The gist of the matter is that with diffusive transport in the base there is no way of avoiding a penalty in the magnitude of the term  $R_\phi$  responsible for negative output resistance, Eq. (17). In the intrinsic case, this term has only a mild competition from  $\omega C_C R_E$  and the negative dynamic  $r_{22}$  can easily be achieved, so long as  $R_E$  is sufficiently low. With the parasitic elements added, we need to minimize the resistance  $(R_x^{\text{eff}} + r_{22})$ , which requires  $R_\phi$  be large and negative. If  $\phi \ll 1$  and  $\phi + \theta = 2\pi$ , then  $R_\phi$  equals  $-|\alpha_B| \phi^2 / 4\pi \omega C_C$ , which is small even for  $|\alpha_B| \approx 1$ . On the other hand, if the condition  $\phi + \theta = 2\pi$  is accomplished with approximately equal contributions from both  $\phi_B \approx \theta \approx \pi$ , then, for the diffusive transport mechanism,  $R_\phi$  becomes small because of  $\alpha_B \sim \exp(-\phi_B)$ . With realistic values of the parasitics, this term is inadequate for making  $U$  negative.

With the coherent transport in the base, we have the opportunity to enhance the overall phase by increasing the delay  $\phi_B$ , keeping the collector delay  $\theta \leq 1$ . In this case,  $R_\phi \approx -\sin(\phi + \theta') / \omega C_C$  and  $r_{22}$  can be made negative, provided

$$\omega C_C (R_E + R_{Ex} + R_{Cx} + R_x^{\text{eff}}) < 1. \quad (20)$$

Note that the longer the base, the lower is the frequency at which the phase relation in (17) is optimal. Therefore, inequality (20) can be fulfilled, provided the base width  $W_B$  is sufficiently long, while the base transport can still be regarded as ballistic. The latter condition is limited by the momentum relaxation of low-energy minority carriers in the base. If the ballistic scattering length is sufficiently long, then the speed of a coherent transistor is limited by the parasitics, as is evident from (20).

With the value of parasitic elements estimated from the standard low-temperature heterostructure parameters we have found [3] that the coherent transistor retains its active behavior in an extended frequency range. The unilateral gain  $|U|$  and the current gain  $|h_{21}^s|^2$  of an exemplary circuit are plotted in Fig. 7. As in the intrinsic case, the unilateral gain is negative between the two peaks, indicating that  $r_{22} < 0$  in that region. Interestingly, the current gain has been largely damped away by the parasitics, although a trace of the peak is clearly seen near  $\omega \tau_B = 2\pi$ . We see that the conventional  $f_T$  of this device would be about

100 GHz, but the transistor is active up to frequencies which are a factor of  $2\pi$  higher.

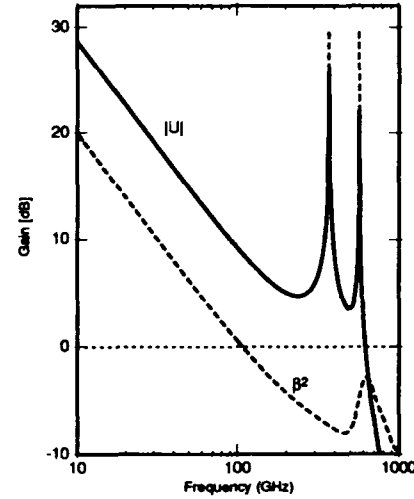


Figure 7. The unilateral gain  $|U|$  and the current gain  $\beta \equiv |h_{21}^s|$  of an abrupt-junction ballistic transistor, loaded with parasitic elements as in Fig. 3. Assumed parameters:  $\Delta = 14.4 \text{ meV}$ ,  $T = 4.2 \text{ K}$ ,  $\tau_c = 1 \text{ ps}$ ,  $\tau_b = 1 \text{ ps}$ ,  $C_E = 10 \text{ fF}/\mu\text{m}$ ,  $C_C = 0.5 \text{ fF}/\mu\text{m}$ ,  $C_{Cx} = 1 \text{ fF}/\mu\text{m}$ ,  $R_E = 5 \Omega \cdot \mu\text{m}$ ,  $R_B = 25 \Omega \cdot \mu\text{m}$ ,  $R_{Bx} = 25 \Omega \cdot \mu\text{m}$ ,  $R_{Ex} = 20 \Omega \cdot \mu\text{m}$ ,  $R_{Cx} = 20 \Omega \cdot \mu\text{m}$ .

To summarize, the active transistor behavior at extended frequencies  $f > f_T$  results physically from the phaseshift between the collector current and voltage, acquired during the minority-carrier transit across the base. In a coherent transistor this phaseshift is not accompanied by a degradation in the magnitude of  $\alpha_B$ ; this enables the device to retain its active nature when loaded with parasitics.

## References

1. A. A. Grinberg and S. Luryi, "Diffusion in a short base", *Solid St. Electron.* **35**, 1299 (1992).
2. A. A. Grinberg and S. Luryi, "Ballistic versus diffusive base transport in the high-frequency characteristics of bipolar transistors," *Appl. Phys. Lett.* **60**, 2770 (1992).
3. A. A. Grinberg and S. Luryi, "Coherent Transistor", submitted to *IEEE Trans. Electron Devices*.
4. G. T. Wright, "Transistor transit-time oscillator", *Electron. Lett.* **3**, 234 (1967); "Small-signal theory of the transistor transit-time oscillator (translator)", *Solid-St. Electron.* **22**, 399 (1979).
5. S. M. Sze, *Physics of Semiconductor Devices*, New York: Wiley-Interscience (1981) Chap. 10.
6. S. Tiwari, "Frequency dependence of the unilateral gain in bipolar transistors", *IEEE Electron Device Lett.* **EDL-10**, 574 (1989).

# Physics of Electron Transport in Ultra High Speed InP/GaInAs Heterojunction Bipolar Transistors

Dan Ritter

*Department of Electrical Engineering, Technion, Haifa, Israel and AT&T Bell Laboratories, Murray Hill, New Jersey 07974*

R. A. Hamm, A. Feygenson, P. R. Smith, and J. Bude

*AT&T Bell Laboratories, Murray Hill, New Jersey 07974*

## Abstract

New physical phenomena InP/Ga<sub>0.47</sub>In<sub>0.53</sub>As Heterojunction Bipolar Transistors are presented. Ballistic versus diffusive base transport is discussed, as well as impact ionization and transport across an energy barrier in the collector.

## Introduction

Heterojunction Bipolar Transistors (HBTs) of InP/Ga<sub>0.47</sub>In<sub>0.53</sub>As are ultra fast electronic devices which exhibit subpicosecond response times [1]. These devices are of special interest because they can be integrated monolithically with InP/GaInAsP optoelectronic devices operating at wavelengths of 1.5  $\mu\text{m}$  and 1.3  $\mu\text{m}$  [2].

The base transit time is the dominant delay component in Si bipolar transistors [3]. In InP/GaInAs HBTs by contrast, the base transit time is very short, and the dominant delay components are parasitic RC time constants. To better understand the physics of base transport, the base transit time was measured in devices with base thicknesses in the 50 nm to 400 nm range. From the results the scattering mean free path of thermalized electrons in the base was extracted.

Conventional InP/GaInAs HBTs suffer from low breakdown voltage. It is shown that the reason for this behavior is an anomalous electric field dependence of the impact ionization coefficient in Ga<sub>0.47</sub>In<sub>0.53</sub>As [4]. An anomalous temperature dependence of the impact ionization constant was observed as well. The experimental results were reproduced using a full band Monte Carlo simulation which helps understand the origin of these effects.

The breakdown voltage was significantly improved in a structure called a Composite Collector HBT (CCHBT), in which most of the collector is made of InP rather than GaInAs [5]. However, in the CCHBT there is an energy barrier in the collector, which must be overcome by the electrons. Low temperature measurements show that electron transport across the barrier is achieved by hot electron thermionic emission [6].

## Base transport

The base of an HBT can be very narrow, without degrading neither the current gain, nor the base resistance [7]. The narrow base makes it possible to achieve a subpicosecond base transit time. In addition, in InP/GaInAs HBTs the electrons have a low effective mass, resulting in a high diffusion constant of electrons in the base. Moreover, in abrupt junction HBTs the electrons are injected from an energy ramp, and transit a fraction of the base with velocities higher than the thermal velocity. This is commonly referred to as the ballistic effect.

To determine the relative importance of the above mentioned effects the frequency response of HBTs with base thicknesses in the range of 50 nm to 400 nm was measured, and analyzed. The base doping level was  $5 \times 10^{19} \text{cm}^{-3}$ .

The unity gain bandwidth of the devices,  $f_T$ , is given in Table 1. The value in parenthesis for the 50 nm base was achieved in HBTs that were produced using an improved photolithography mask set than used for all the other devices, and the high value of  $f_T$  is due to a reduction of the parasitic RC time constants.

The base transit time,  $\tau_B$ , was estimated using the expression

$$\frac{1}{2\pi f_T} = \tau_E + \tau_C + \tau_B \quad (1)$$

where  $\tau_E$  is the emitter delay time and  $\tau_C$  the collector delay time. Assuming that  $\tau_E + \tau_C$  are similar in all the devices (except for the one with  $f_T = 144$  GHz) it can be seen from table 1 that the maximum error in the value of  $\tau_B$  is 2 psec. It is shown below that the error bar can be reduced to 0.2 psec.

$W_B$ (nm)	50	100	200	300	400
$f_T$ (GHz)	78 (144)	67	35	24	16.5
$1/2\pi f_T$ (psec)	2.0 (1.1)	2.4	4.5	6.6	9.6
$\tau_B$ (psec)	0.3	0.7	2.8	4.9	7.9

Table 1. Unity gain bandwidth and base transit time of InP/GaInAs HBTs with different base thicknesses. See text for the evaluation of  $\tau_B$ .

To model the base transport a simple Monte Carlo simulation was carried out using only two parameters: the momentum (and energy) relaxation mean free path of the energetic electrons injected from the emitter (also called the ballistic mean free path), and the momentum relaxation mean free path of the thermalized electrons. The injected electrons were assumed to lose both their forward momentum and their excess energy after the first collision. The velocity of the injected electrons was taken as  $10^8$  cm/sec. This velocity corresponds to an excess energy equal to the bandgap discontinuity between InP and  $\text{Ga}_{0.47}\text{In}_{0.53}\text{As}$  of 250 meV, taking the non-parabolicity of the conduction band into account. The thermal velocity distribution was calculated for a temperature 300 K using an electron effective mass of 0.04.

The results of the simulation are given in Fig.1 together with the experimental data. The momentum relaxation mean free path of the thermalized electrons was determined to be 60 nm by fitting the calculated base transit times to the data points at the base thicknesses of 400 nm and 300 nm. The value of the ballistic mean free path,  $L_b$ , does not affect the base transit time for the large base thicknesses. Because of the uncertainty in the value of  $\tau_B$  in narrow bases the ballistic mean free path cannot be determined from the data, and is left as a parameter. The curve for  $L_b = 0$  is identical to the result obtained by solving the Boltzmann equation in a short base [8].

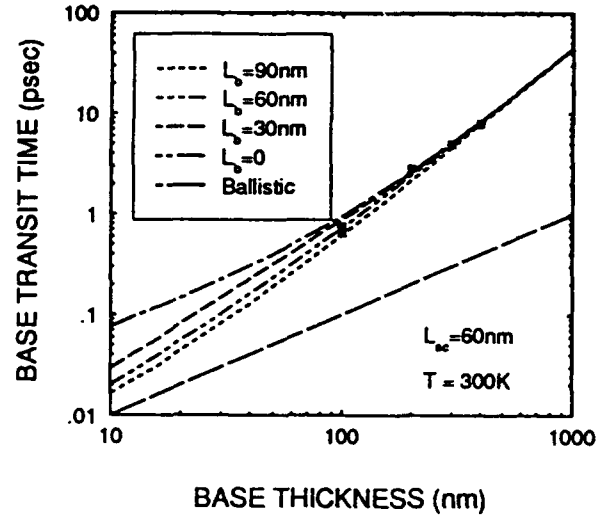


Figure 1. Base transit time versus base thickness. Monte Carlo simulation and experimental results.

The diffusion constant  $D$ , and the momentum relaxation mean free path,  $L_{sc}$ , are related by the expression

$$D = \frac{1}{3} L_{sc} V_t \quad (2)$$

where  $V_t$  is the average thermal velocity. For GaInAs at 300 K  $V_t = 5.3 \times 10^7$  cm/sec. Using Eq.2 a diffusion constant of  $105 \text{ cm}^2/\text{sec}$  is obtained. Similar results were obtained in time of flight measurements [9], and a recent theoretical calculation using the dielectric function approach also agrees with this value [10]. It must be pointed out, however, that this diffusion constant, which corresponds to a mobility of about  $4,200 \text{ cm}^2/\text{V-sec}$ , is surprisingly high for electrons in a heavily doped p-type material, and is close to the value of the mobility in undoped  $\text{Ga}_{0.47}\text{In}_{0.53}\text{As}$ .

Practical devices have a base thickness of the order of 50 nm. The base transit time in such devices, obtained by the simulation, is plotted in Fig.2 as a function of the ballistic mean free path of the injected electrons. The curve demonstrates that ballistic injection reduces the base transit time, however, for reasonable values of the ballistic mean free path the base transit time is much longer than the ballistic transit time. This was pointed out before in Ref.8.

From Fig.2 a more accurate evaluation of the base transit time can be obtained. Since a reasonable range for the ballistic mean free path is 10-100 nm, the base transit time is in the range of 0.2-0.4 psec. From Table 1 and Eq.1 one thus obtains that  $\tau_E + \tau_C = 1.6-1.8$  psec in the device with the 50 nm thick base. Assuming that  $\tau_E + \tau_C$  are identical in all the devices  $\tau_B$ , as given in Table 1, was obtained.

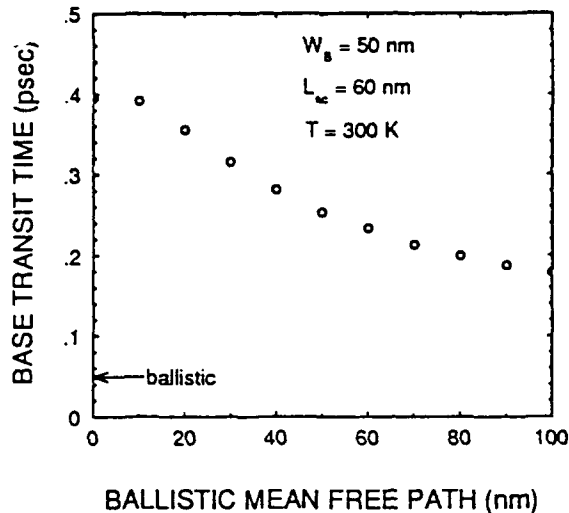


Figure 2. Base transit time versus ballistic mean free path of the injected electrons.

#### Impact ionization in GaInAs

It is well known that in most semiconductors the impact ionization coefficient decreases with temperature due to enhanced electron scattering at higher temperatures [11-12]. Therefore, in Si and GaAs bipolar transistors the breakdown voltage always decreases with temperature. The output characteristics of a typical InP/GaInAs HBT in the common emitter configuration are shown in Fig.3 at room temperature and at 423K. It can be seen that the breakdown voltage is low, and increases with temperature.

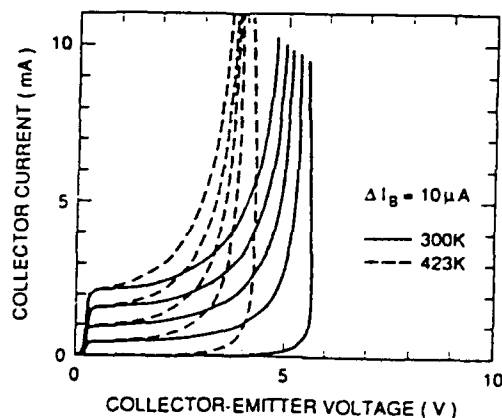


Figure 3. - Common emitter characteristics of an InP/GaInAs HBT at two temperatures.

To better understand the breakdown behavior of the devices the collector multiplication factor,  $M_n$ , was

measured as a function of the base collector voltage at different temperatures [4]. The results are shown in Fig.4, where it can be seen that at the range of voltages where breakdown takes place the multiplication factor indeed increases with temperature.

From Fig.4 the field dependence of the electron ionization coefficient,  $\alpha$ , is obtained, as shown in Fig.5 [4]. Note that  $\alpha$  exhibits an anomalous electric field dependence. In most semiconductors  $\log(\alpha)$  is a linear function of the inverse electric field. In  $\text{Ga}_{0.47}\text{In}_{0.53}\text{As}$  the electric field dependence is much weaker. This causes the low breakdown and the "non-saturated" nature of the curves shown in Fig.3.

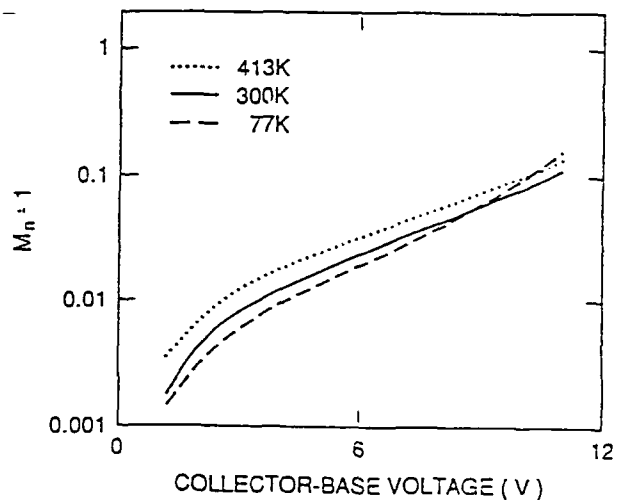


Figure 4. - Collector multiplication vs. base collector voltage at different temperatures.

The impact ionization coefficient of GaInAs was calculated by using a full band Monte Carlo simulation [13]. The results are given in Fig.6, and agree remarkably well with the experimental results.

Some insight into the physics of the anomalous behavior of impact ionization in GaInAs can be obtained from Fig.7 where the probability for impact ionization is plotted vs. electron energy for different electric fields. Clearly, the widely assumed energy threshold for impact ionization does not exist at low electric fields. Instead, a two peak threshold can be observed. The anomalous temperature and electric field dependence is associated with the low energy peak. More details on the results of the simulation will be given elsewhere [14].

#### The composite collector HBT

A significant improvement of the breakdown behavior of the InP/GaInAs HBTs can be achieved using struc-

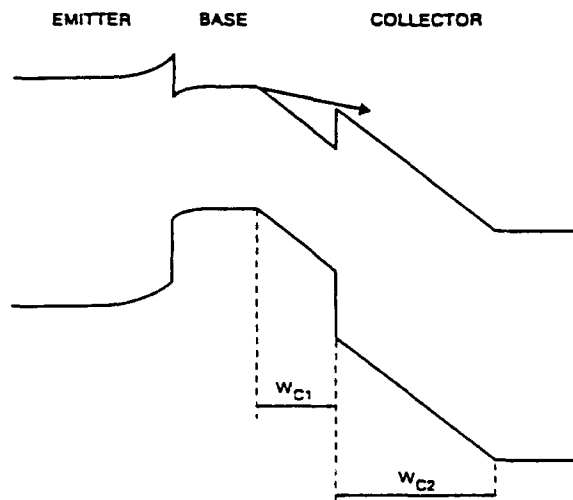


Figure 8. Schematic bandstructure of a composite collector heterojunction bipolar transistor. The arrow indicates electron flow across the barrier.

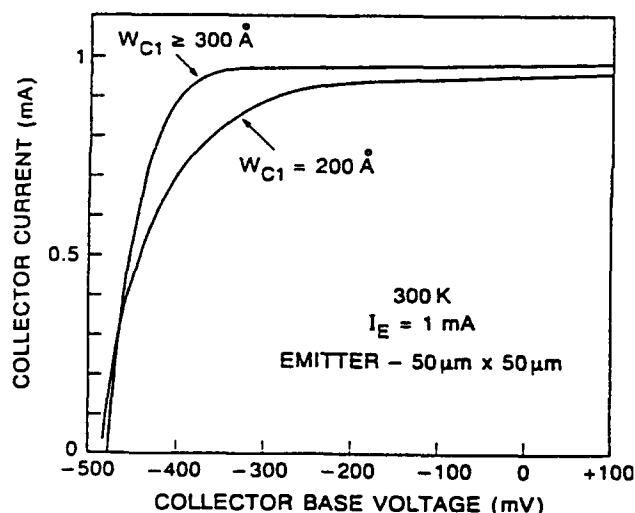


Figure 9. Common base characteristics of CCHBTs at 300 K, at a low current density.

drop across the base-collector junction is independent of the collector current and the full switching behavior was observed.

The bistable hot electron transport across an energy barrier was fully described before [15], and is only briefly repeated here. At voltages lower than the switching point, electrons accumulate at the potential minimum, and the current is mainly due to tunneling through the barrier. The accumulated electrons screen the applied electric field, and as a result the electrons do not heat up in the low bandgap section of the collector. As the voltage across the collector is increased, tunneling through the barrier increases, and the accumulated

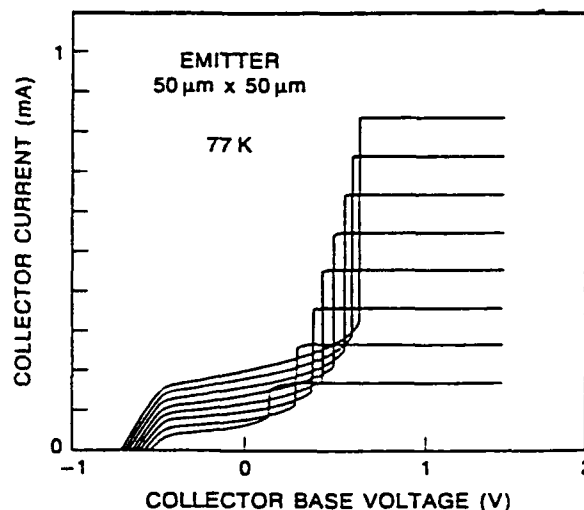


Figure 10. Common base characteristics of a CCHBT with  $W_{C1} = 40$  nm at 77 K. Emitter current is 1 mA per step.

electron concentration decreases. The electric field in the low bandgap section thus increases, and the electrons in the low bandgap section of the collector are heated by the electric field. This increases the thermionic emission rate over the barrier, and the electric field in the low bandgap section is further increased. The above mechanism is a positive feedback process, which is responsible for the switching event.

At 300 K the thermionic emission rate of electrons at equilibrium with the lattice is sufficiently large to avoid electron accumulation at low current densities. However, at high current densities electron accumulation does take place, and gives rise to step-like characteristics as can be seen in Fig. 11. The step-like turn on characteristics at high current densities are undesirable, but can be suppressed by n-type doping of the barrier vicinity.

Fig. 12 depicts the characteristics of a CCHBT in which 5 nm thick layers on both sides of the collector energy barrier were n-type doped to a level of  $5 \times 10^{18} \text{ cm}^{-3}$ . The switching voltage is shifted towards lower values, and the device turn on voltage is much lower. The effect of the doped layers on the switching voltage can be explained in the following manner. The doped layer at the barrier is fully depleted at the turn on voltage of the devices. The positive charge of the ionized impurities in the low bandgap side of the barrier tends to neutralize the negative space charge of the electrons that accumulate at the barrier, and therefore the screening effect of the accumulated electrons is reduced. Moreover, the ionized impurities on the large bandgap side of the barrier reduce the triangular barrier width so that the tunneling rate increases. As a result, even at high current densities low electric fields are

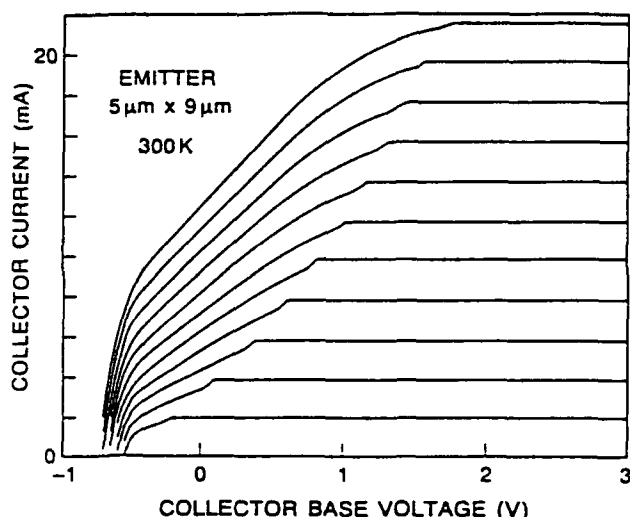


Figure 11. Common base characteristics of a CCHBT with  $W_{C1} = 40$  nm at 300 K, at a high current density. Emitter current is 2 mA per step.

sufficient for the switching event to occur.

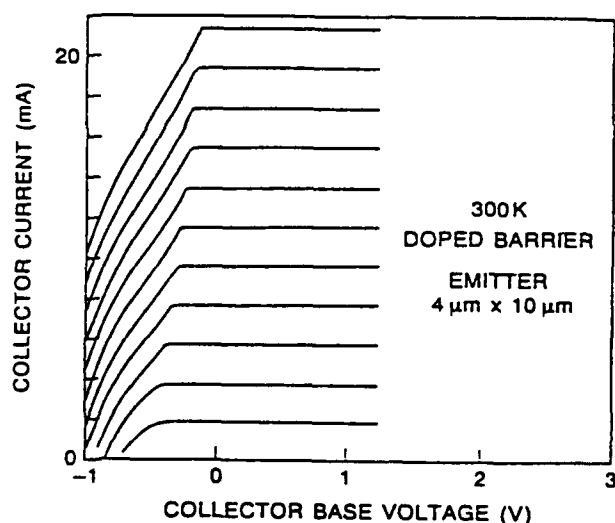


Figure 12. Common base characteristics a CCHBT with  $W_{C1} = 40$  nm at 300 K, at a high current density. The heterointerface vicinity is doped as described in the text. Emitter current is 2 mA per step.

## References

1. Y.K. Chen, R.N. Nottenburg, M.B. Panish, R.A. Hamm, and D.A. Humphrey, "Subpicosecond InP/GaInAs heterostructure bipolar transistors", *IEEE Electron Device Lett.*, EDL-10, 267-269 (1989).
2. S. Chandrasekhar, L.M. Lunardi, A.H. Ganuck, D. Ritter, R.A. Hamm, M.B. Panish, and G.J. Qua, "A 10 Gbit/sec OEIC photoreceiver using InP/GaInAs heterojunction bipolar transistor", *Electron. Lett.*, 28, 466-468 (1992).
3. Tzu-Yin Chiu, Mark T.Y. Liu, Kwing F. Lee "Determination of base and emitter delay time in advanced self aligned bipolar technology", proceedings of the 1991 IEEE Bipolar/BCMOS Circuits and Technology Meeting, p.158.
4. D. Ritter, R.A. Hamm, A. Feyngenson, and M.B. Panish "Anomalous electric field and temperature dependence of collector multiplication in InP/GaInAs heterojunction bipolar transistor", *Appl. Phys. Lett.* 60, 3150-3152 (1992).
5. A. Feyngenson, D. Ritter, R.A. Hamm, P.R. Smith, R.K. Montgomery, R.D. Yadvish, H. Temkin, and M.B. Panish, "InGaAs/InP composite collector heterostructure bipolar transistors", *Electron. Lett.*, 28, 607-609 (1992).
6. D. Ritter, R.A. Hamm, A. Feyngenson, H. Temkin, M.B. Panish, and S. Chandrasekhar, "Bistable hot electron transport in InP/GaInAs composite collector heterojunction bipolar transistors", *Appl. Phys. Lett.* 61, 70-72 (1992).
7. H. Kroemer, "Heterostructure bipolar transistors and integrated circuits", *Proc. IEEE*, 70,13 (1982).
8. A. Grinberg and S. Luryi, "Diffusion in a short base", *Solid State Electron.*, 35, 1299-1304 (1992).
9. M.S. Lundstrom, P.E. Dodd, M.L. Lovejoy, E.S. Harmon, M.R. Melloch, B.M. Keyes, R.A. Hamm, and D. Ritter, "Electron transport in thin base InP/GaInAs HBTs "proceedings of the 50th Device Research Conference, 1992.
10. T. Kaneto, K.W. Kim, and M.A. Littlejohn, "A comparison of minority electron transport in InGaAs and GaAs", *Appl. Phys. Lett.*, in press.
11. Federico Capasso, "Physics of avalanche photodiodes" in "Semiconductors and Semimetals" vol. 22D, 1-170, Ed. W.T. Tsang, (Academic Press, Orlando 1985).
12. G.E. Stillman and C.M. Wolfe, "Avalanche photodiodes" in "Semiconductors and Semimetals" vol.12, 291-257, Ed. R.K. Willardson and A.C. Beer, (Academic Press, New York 1977).
13. J. Bude and K. Hess, "Thresholds of impact ionization in semiconductors" *J. Appl. Phys.* 72, 3354-3561 (1992).
14. J. Bude, K. Hess, D. Ritter, R.A. Hamm, and A. Feyngenson, unpublished.
15. D. Arnold, K. Hess, and G.J. Iafrate, "Electron transport in heterostructure hot-electron diodes", *Appl. Phys. Lett.* 53, 373-375 (1988).

# InP High Electron Mobility Transistors: Status and Promise

Loi D. Nguyen

*Hughes Research Laboratories, 3011 Malibu Canyon Road, Malibu, California 90265*

## I. INTRODUCTION

The InP HEMT technology, once an exotic technology in a few research laboratories, has begun to gain acceptance in the microwave and millimeterwave community. Comparing to GaAs transistors, InP HEMTs exhibit significantly lower noise figures, higher gain, and higher cutoff frequencies [1], [2]. As a result, they are now the most promising candidate for ultralow-noise, ultrahigh-frequency, and ultrabroad-band amplifiers.

In order to improve the performance of InP HEMTs further, significant efforts have been devoted to improve the electron transport properties [3], [4], reduce the parasitic resistances and gatelength [5], [6], and develop a scaling model for sub-100 nanometer (nm) gatelength HEMTs [7]. Together, these efforts have led to a successful fabrication of a 50-nm gatelength InP HEMT with a state-of-the-art (extrinsic) transconductance ( $g_m$ ) of 1740 mS/mm and a state-of-the-art (extrinsic) current-gain cutoff frequency ( $f_T$ ) of 340 GHz [8] -- the latter figure-of-merit corresponds to a total delay of only 0.47 ps and represents a 70% improvement over typical  $f_T$  values of comparable 0.1- $\mu$ m gatelength devices.

The 50-nm gatelength InP HEMT is currently the most promising device to extend the operating frequency of 3-terminal semiconductor devices to the entire millimeterwave spectrum, as well as to provide a low-cost alternative to ultralow-noise masers and SIS mixers at cryogenic temperatures.

The main body of this paper is divided into 3 sections: Section II reviews the present status of InP HEMTs; Section III describes recent advances in 50-nm gatelength InP HEMT technology; and, lastly, Section IV discusses the potential of 50-nm gatelength InP HEMTs for ultrahigh-frequency and ultralow-noise receivers.

## II. PRESENT STATUS OF InP HEMTs

The InP HEMT presently exhibits the lowest noise figures among all 3-terminal semiconductor devices. For example, using 0.10 to 0.15- $\mu$ m gatelength technology, workers at Hughes and GE have independently reported a noise figure below 1.0 dB at 60 GHz for InP HEMTs, which is approximately 0.5 dB lower than the best reported results for GaAs HEMTs [1], [2].

The InP HEMT is also the first 3-terminal semiconductor device which has demonstrated useful gain above 100 GHz. Recently, workers at TRW reported a successful demonstration of a 7.3 dB amplifier at 140 GHz using a 0.1  $\mu$ m gatelength InP HEMT [9]. Assuming a simple 6 dB roll off, this result indicates a power-gain cutoff frequency ( $f_{max}$ ) of 325 GHz.

In the last few years, the InP HEMT has also gained more acceptance in the microwave and millimeterwave community. At Hughes, for example, we are now manufacturing 0.1  $\mu$ m gatelength InP HEMTs for low-noise applications covering the frequency range from 10 to 94 GHz. Our present Pilot Line has been in operation for approximately two years and is producing devices with a typical noise figure between 1.2 and 1.4 dB at 60 GHz.

As the InP HEMT technology becomes more mature, it begins to be viewed as a critical technology for high performance Monolithic Microwave/Millimeterwave Integrated Circuits (MMICs). Some recent examples are the demonstration of a 5 to 100 GHz MMIC distributed amplifier with 5 dB gain [10], a 75 to 100 GHz MMIC cascode amplifier with 8.0 dB gain [11], and a 12 GHz MMIC low-noise amplifier with 0.8 dB noise figure [12], all realized with InP HEMT technology.

### III. 50 nm GATELENGTH InP HEMTs

The most promising approach to improve the performance of InP HEMTs further is to reduce their gate length. We at Hughes have successfully developed a first-order scaling model for HEMTs and a material and device fabrication capability to explore the potential of 50 nm gate length devices.

We have successfully designed and fabricated a 50 nm gate length pseudomorphic InP HEMT -- a HEMT with an 80% (In mole fraction) GaInAs channel -- with a state-of-the-art (extrinsic)  $g_m$  of 1740 mS/mm and a state-of-the-art (extrinsic)  $f_T$  of 340 GHz [8]. Figure 1 shows the dependence of  $f_T$  with gate length for InP HEMTs fabricated at our laboratories. The average electron velocity is approximately  $2.6 \times 10^7$  cm/s for the lattice-matched devices (53% indium mole fraction) and  $3.1 \times 10^7$  cm/s for the pseudomorphic devices (80% indium mole fraction).

### IV. POTENTIAL APPLICATIONS

The 50 nm gate length InP HEMT is currently the most promising candidate to extend the operating frequency of 3-terminal semiconductor devices to the upper end of the millimeterwave spectrum. In addition, it has potential to be a low-cost alternative to ultralow-noise masers and SIS mixers at cryogenic temperatures.

In order to realize these potentials, one must optimize 50 nm gate length InP HEMTs specifically for high  $f_{max}$ . This task has not yet been accomplished. Our current 50-nm gate length InP HEMTs suffer a high output conductance of 260 mS/mm -- 5 times higher than that of a typical 0.1- $\mu$ m gate length device -- and, as a result, their  $f_{max}$  is limited to approximately 250 GHz. We believe that further optimization of the layer structure, source-drain spacing, and gate cross section will improve their  $f_{max}$  to over 500 GHz.

The projected 500 GHz  $f_{max}$  should extend the operating frequency of InP HEMTs to at least 220 GHz and enable the realization of ultrahigh-resolution millimeterwave radars. The high  $f_{max}$  should also improve the noise figure at low frequencies. At cryogenic temperatures, a 50-nm InP HEMT with 500 GHz  $f_{max}$  should perform as well as a maser and provide a low-cost alternative or ultralow-noise sensing and telecommunication applications.

### SUMMARY

Significant progress has been made in InP HEMT technology in the last few years, resulting in lower noise figures, higher gain, and wider bandwidth for radars and telecommunication systems. By the mid-1990s, this author believes that InP HEMTs and MMICs will (1) gain wide acceptance in the microwave

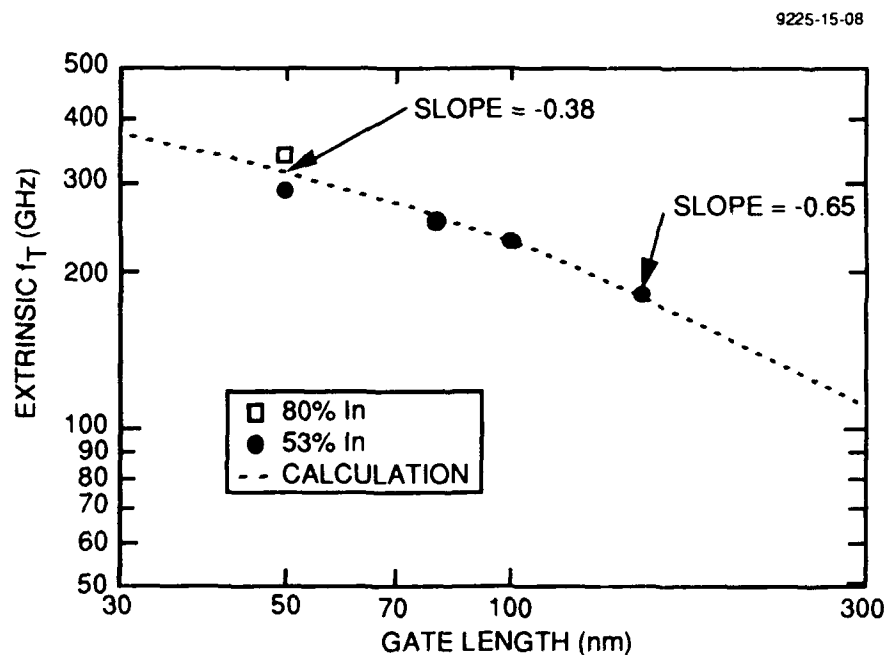


Fig. 1. Dependence of  $f_T$  on gate length for InP HEMTs



and millimeterwave community, (2) enable the realization of ultrahigh-resolution millimeterwave radars, and (3) provide a low-cost alternative to masers at cryogenic temperatures.

## REFERENCES

1. Mishra et al., IEDM Tech. Dig., Dec. 1988.
2. Duh et al., IEEE Microwave and Guided Wave Lett., vol. 1, no. 5, 1991.
3. Hong et al., J. Appl. Phys., vol. 64, no. 4, Aug. 15, 1988.
4. Chin et al., J. Vac. Sci. Technol., vol. B8, no. 2, Mar./Apr. 1990.
5. Mishra et al., IEDM Tech. Dig., Dec. 1989.
6. Nguyen et al., IEDM Tech. Dig., Dec. 1990.
7. Nguyen et al., IEEE Proceedings of the IEEE, vol. 80, no. 4, Apr. 1992.
8. Nguyen et al., IEEE Trans. Electron Devices, vol. 39, no. 9, Sep. 1992.
9. Tan et al., IEDM Tech. Dig., Dec. 1991.
10. Majidi-Ahy et al., Microwave Millimeter-Wave Monolithic Circuits Sym., 1990.
11. Majidi-Ahy et al., GaAs IC Sym., 1990.
12. Rosenbaum et al., IEEE MTT-S Dig., 1991.

## High Speed Heterojunction JFETs Grown by Non-Hydride MOCVD

M. M. Hashemi, J. B. Shealy, S. P. DenBaars, and U. K. Mishra

*Electrical and Computer Engineering Department and Materials Department,  
University of California, Santa Barbara, California 93106*

### **Abstract**

Indium Phosphide channel JFET's with InGaAs lattice matched gate have been fabricated using liquid, non-hydride column V precursors. The incorporation of low bandgap InGaAs gate layer not only suppresses hole injection under forward bias but also makes fabrication of HJFETs very reproducible and easy. Self-aligned devices made by selective etching of the gate resulted in devices with current gain cut-off frequency as high as 22 GHz with transconductance over 200 mS/mm for gate length of about 0.65  $\mu\text{m}$ .

### **Introduction**

There has been much interest in the integration of optical devices along with electronic devices to develop opto-electronic integrated circuits (OEIC's) which are projected to have advantages of higher speed, smaller size, and higher reliability compared with discrete devices. The InP system is the only candidate for long-wavelength optical

communication systems despite the lack of a mature InP device technology, especially in electronic devices. Indium Phosphide with high peak electron drift velocity, and large intervalley separation ( $\Gamma-L \approx 0.63$  eV,  $\Gamma-X \approx 0.73$  eV) is a desirable material for high speed devices. In spite of excellent material properties, fabrication of high speed, high performance FETs with InP channel has been a challenge in the past. Immature processing technology along with low Schottky barrier height ( $\phi_B < 0.5$  eV for n-InP) and the high interface density of states between insulators and InP makes fabrication of MESFET impractical and MISFETs an unstable technology. Therefore, the JFET is a reasonable compromise for a electronic device in InP system.

Heterojunction gate FETs were first implemented in GaAs channel device using p-AlGaAs material as the gate by Umebachi et.al. [1]. More complete characterization of a n-GaAs/P-AlGaAs HFET was reported by Morkoc et.al [2] with power gain cut-off

frequency ( $f_{\max}$ ) around 7-8 GHz. Recently the same idea was applied to InGaAs channel HJFET using p-InP [3] or p-GaAs [4] as the gate material. In all the previously reported HFETs the gate material has been selected to be of larger bandgap material primarily to enhance the built-in potential necessary to improve the noise margin of the digital circuits.. However, hole injection from gate to the channel under forward bias condition, which substantially limits the switching and high frequency characteristics of JFETs, has not been addressed in previously reported HJFETs. Recently [5,6], we have reported a novel  $p^+$ -InGaAs/n-Inp heterojunction combination as the gate and channel layer, respectively to increase the high frequency performance of the HJFETs. This combination is the first reported HJFET using InP as the channel. The  $p^+$ -InGaAs gate layer offers several advantages over the p-InP layer used in the conventional homojunction JFETs: i) large valence band discontinuity for hole injection suppression ( $\Delta E_v \approx 0.37$  eV), lower gate resistance (both bulk and contact resistances), and ii) ease of self-aligned fabrication using selective etching of the gate layer.

### **Device Fabrication**

The HJFET structure was grown by non-hydride MOCVD at atmospheric pressure and at a substrate temperature of 560 °C using tertiarybutylphosphine (TBP), and tertiarybutylarsine (TBA) as the alternative source for phosphine and arsine, respectively. TBP and TBA are relatively

new less toxic liquid alkyl column V sources replacing the extremely toxic and hazardous hydrides (phosphine, arsine) [7,8]. Epitaxial growth starts with a 5000 Å thick semi-insulating InP:Fe buffer layer. Next, a 2500 Å thick n-channel layer doped at  $2-3 \times 10^{17} \text{ cm}^{-3}$  with electron mobility of  $\approx 3000 \text{ cm}^2/\text{V.s}$  is grown followed by a 125 Å thick undoped lattice matched  $\text{In}_x\text{Ga}_{1-x}\text{As}$  ( $x=0.53$ ) spacer to account for diffusion of zinc during subsequent growth of the  $p^+$  layer. Finally, a 2500 Å thick lattice matched p-type  $\text{In}_x\text{Ga}_{1-x}\text{As}$  ( $x=0.53$ ) layer doped in excess of  $10^{19} \text{ cm}^{-3}$  was grown. Epitaxial cross section and energy band diagram is shown in figure 1.

Device processing starts with gate metallization (Ta/Au 200Å/2800Å) and lift-off to define a 1 µm long gate. The gate metal was used as the mask for etching the InGaAs  $p^+$ -layer. This was achieved using a selective wet chemical etch with controllable undercut resulting in a "T-shaped" gate structure. The gate length of the devices measured in this study were about 0.6 µm. Next the source-drain contacts (AuGe/Ni/Au 1500Å/150Å/2000Å) are formed by lift-off either in a self-aligned or non self-aligned fashion. Finally, the devices were isolated and annealed. During the isolation step the gate pad is isolated from the source region by forming an air bridge under the feed metal connecting gate pad to gate metal. This eliminates parasitic gate capacitance and gate leakage important for high frequency operation of HJFETs. Figure 2 shows the SEM micrograph and corresponding cross

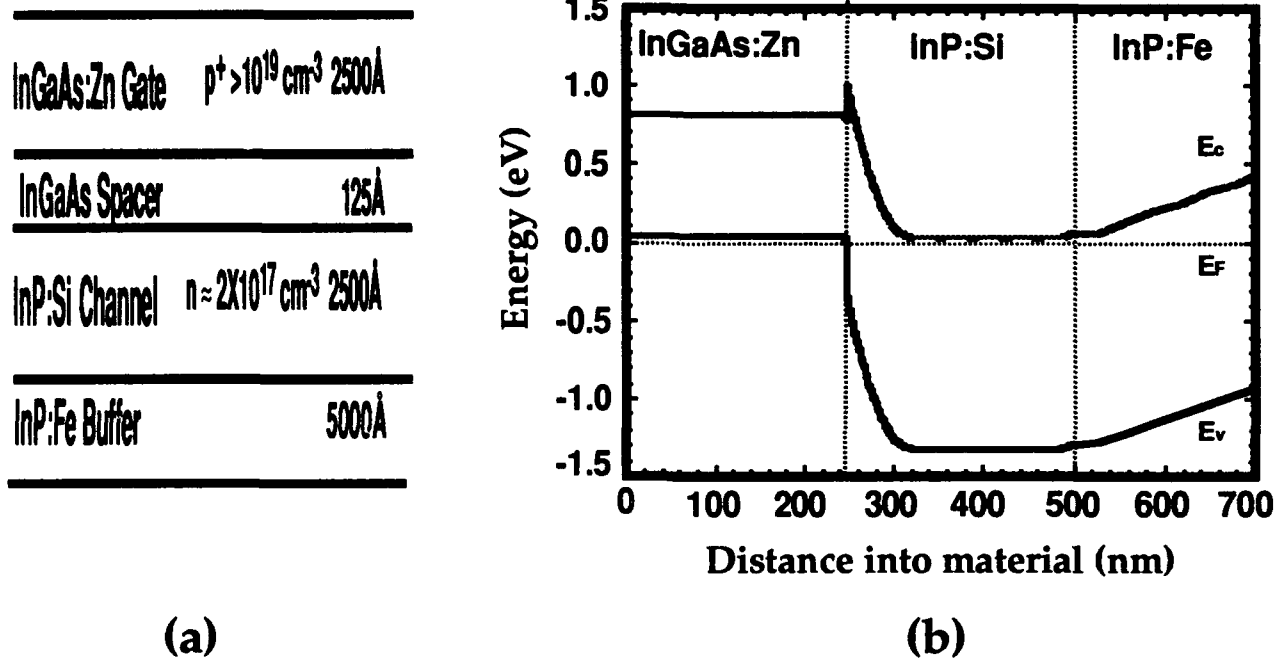


Figure 1. Schematic diagram of epitaxial layer structure, and calculated energy band diagram.

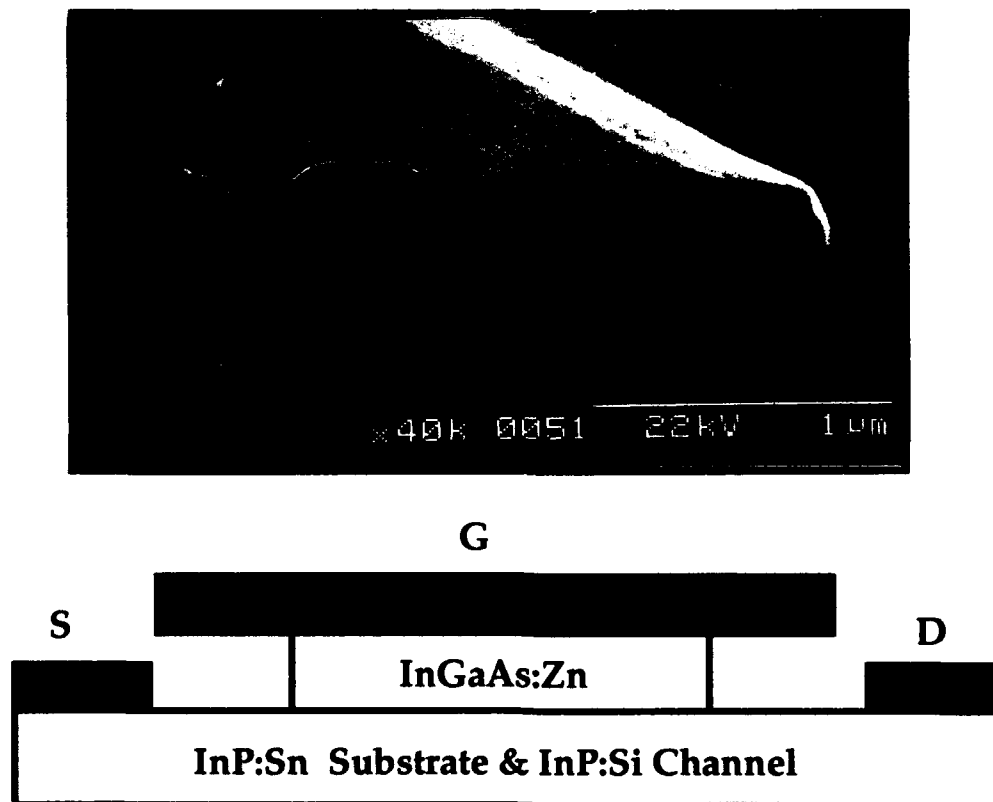


Figure 2. SEM micrograph and schematic representation of self-aligned HJFET

section of a completed self-aligned Device.

### **Results**

The I-V characteristic of a typical  $130\text{ }\mu\text{m} \times 0.6\text{ }\mu\text{m}$  HJFET is shown in Fig 3. The HJFET had a saturation current of 400 mA/mm at  $V_{gs}=+1.5\text{ V}$ , a pinch-off voltage of  $-3.2\text{ V}$  and an output conductance of 1.0 mS/mm. The transconductance,  $g_m$ , remains relatively steady at a value of 130 mS/mm for a gate bias as high as  $+1.5\text{ V}$ . Both breakdown voltages exceeded 20 V for a drain to source spacing of  $4\text{ }\mu\text{m}$ .

The S-parameters of the device were measured as at  $V_{ds} = 5\text{ V}$  a function of gate-source voltage and the current gain cut-off frequency ( $f_T$ ) and power gain cut-off frequency ( $f_{max}$ ) are presented in figure 4. The maximum  $f_T$  and  $f_{max}$  were 14.3 GHz and 37.5 GHz, respectively which are among the highest reported values for InP JFETs. High value of  $f_T$  and  $f_{max}$  have been obtained over a wide range of gate bias ( $f_T > 10\text{ GHz}$ ,  $f_{max} > 28\text{ GHz}$  for  $-1.5\text{ V} < V_{gs} < +1.0$ ). We achieved  $f_T$  as high as 21 GHz with extrinsic transconductance of 230 mS/mm for a self-aligned devices. By using self-aligned scheme we were able to obtain such a high transconductance and  $f_T$  at the expense of low breakdown and power gain cut-off frequency ( $f_{max}$ ) of 9 V and 9 GHz, respectively. These degradation are possibly due to high electric field, and higher parasitic gate-drain capacitance (including the electrode's capacitance as well as the lower domain capacitance in InP based devices).

In optimizing HJFET structures, spacer layer thickness plays an important role in

device performance, since one has to insure that the metallurgical junction coincides with the electrical junction. If the spacer layer is too thin the Zinc atoms will diffuse into the channel during the growth of  $p^+$ -GaInAs layer affecting the electrical characteristics of the junction. On the other hand, if the spacer layer is too thick the modulation efficiency of the channel would degrade. For comparison we fabricated and measured three samples with different thicknesses. Sample A, sample B, sample C with spacer layer thickness of  $50\text{ }\text{\AA}$ ,  $125\text{ }\text{\AA}$ ,  $250\text{ }\text{\AA}$ , respectively. The results of both D.C. and R.F. results are summarized in table 1. It is clear that current density drops as the spacer layer thickness reduces due to compensation of the Si dopant in the channel by Zinc atoms. However breakdown voltage increases with decreasing spacer layer which is possibly due to accommodation of peak electric in the larger bandgap material. Finally the R.F. performance shows profound dependence on the spacer layer with  $f_T$  and  $f_{max}$  ranging from 8-18 GHz, and 8-28 GHz respectively, with higher values corresponding to thicker spacer layer.

### **Conclusion**

A new type JFET structure was proposed and demonstrated. This heterostructure JFET (HJFET) uses  $p^+$  GaInAs as the gate, and n InP as the channel. Current gain cut-off frequencies ( $f_T$ ) as high as 21 GHz was obtained using a self-aligned structure. These results makes HJFET an attractive candidate for high frequency logic and optoelectronic circuit.

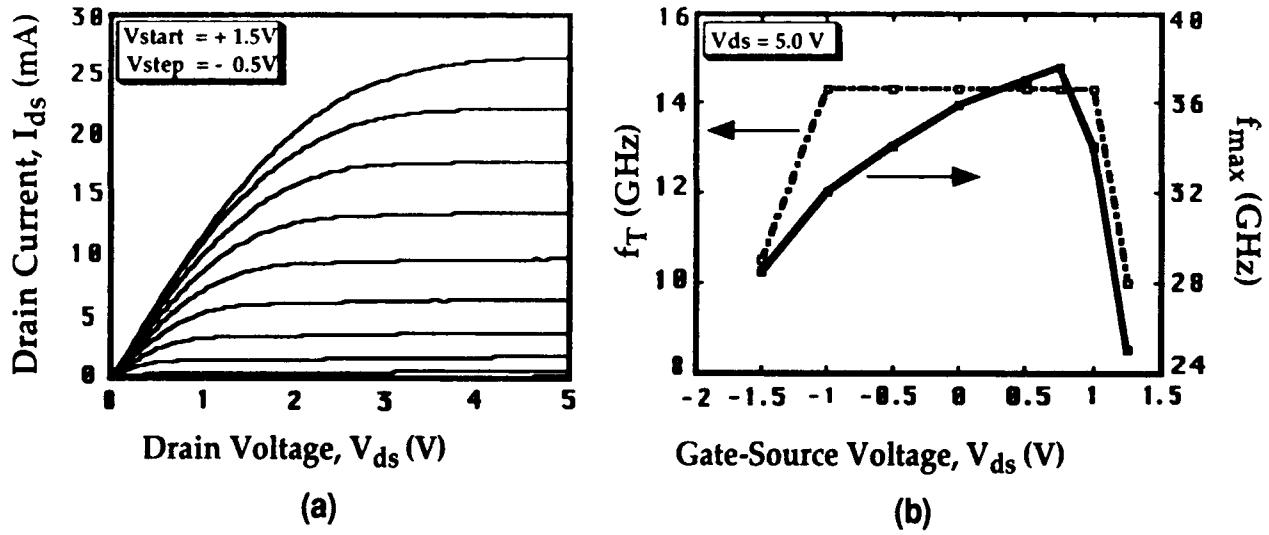


Figure 3. DC and RF performance of HJFET  $130\ \mu\text{m} \times 0.6\ \mu\text{m}$ , (a) drain current characteristics, (b) bias dependence of  $f_T$  and  $f_{max}$ .

Table 1. DC and RF performance comparison of HJFETs with different spacer layer thickness

	Sample A	Sample B	Sample C
Spacer Thickness	50 Å	125 Å	250 Å
Current Density	217 mA/mm	300 mA/mm	472 mA/mm
Breakdown Voltage	35 V	23 V	6 V
Transconductance	97 mS/mm	111 mS/mm	70 mS/mm
$f_T$	8 GHz	10 GHz	18 GHz
$f_{max}$	8 GHz	25 GHz	28 GHz

**References**

- [1] S. Umebachi, K. Asahi, M. Inoue, and G. Kano, IEEE Trans. Elec. Dev. ED-22, 613, 1975.
- [2] H. Morkoc, S.G. Bandy, R. Sankaran, G.A. Antypas, and R.L. Bell, IEEE Trans. Elec. Dev. ED-25, 619, 1978.
- [3] D. Wake, A.W. Nelson, S.Cole, S. Wong, I.D. Henning, and E.G. Scott, IEEE Elec. Dev. Lett. EDL-6, 626, 1985.
- [4] C.L. Lin, H.H. Wieder, R. Zuleeg, IEEE Elec. Dev. Lett. EDL-11, 30, 1990.
- [5] M.M. Hashemi, J.B. Shealy, S.P. DenBaars, and U.K. Mishra, IEDM Tech. Dig., 311, 1993.
- [6] M.M. Hashemi, J.B. Shealy, S.P. DenBaars, and U.K. Mishra, To be published in IEEE Elec. Dev. Lett., Feb., 1993.
- [7] C.A. Larsen, N.I. Buchan, S.H. Li, and G.B. Stringfellow, J. Cryst. Growth, Vol.93, 15, 1988.
- [8] C.H. Chen, C.A. Larsen, G.B. Stringfellow, D.W. Brown, and A.J. Robertson, J. Cryst. Growth, Vol.77, 11, 1986.

# Resonant-Tunneling Transmission-Line Relaxation Oscillator

E. R. Brown

*Lincoln Laboratory, Massachusetts Institute of Technology,  
Lexington, Massachusetts 02173-9108*

## Abstract

A new type of resonant-tunneling oscillator is analyzed that does not require dc bias stability in the negative-differential-resistance region. The oscillator consists of a resonant-tunneling diode coupled to a transmission line in such a way that repetitive switching of the diode occurs across the negative-resistance region. The output waveform consists of a sequence of pulses having a repetition rate determined by the electrical delay of the transmission line and a pulse width determined by the switching time of the diode. When the electrical delay is comparable to the switching time, the output is quasi-sinusoidal. Numerical simulations with a prototype resonant-tunneling diode yield a maximum repetition rate of 192 GHz and a pulse width of 2 ps.

## Introduction

The resonant-tunneling diode (RTD) has been one of the most successful quantum-transport devices. The trademark characteristic of the RTD, the negative-differential-resistance (NDR) region, has been observed at room temperature in many different material systems and over a very wide range of current density. The NDR region has been used as the basis for high-frequency oscillations and high-speed switching. For example, double-barrier RTDs made from the InAs/AlSb system have oscillated up to 712 GHz [1], and similar diodes made from the GaAs/AlAs system have switched from the peak point to the valley region in a time near 2 ps [2]. Much of the interest in RTDs stems from the fact that these results are among the highest oscillation frequencies and the lowest switching times reported to date for electronic devices.

In spite of these successes, the double-barrier RTD has one fundamental shortcoming for the oscillator application. The steep slope in the NDR region

makes it very difficult to achieve dc bias stability in this region. Consequently, only small-area diodes having a suitably high differential resistance can be used. In the case of oscillators, the small area leads to a low output power relative to other two-terminal negative-resistance devices, such as Gunn and IMPATT diodes. To overcome this shortcoming, one must design either an RTD oscillator that does not require dc stability in the NDR region or a new type of RTD that provides a wider NDR region for greater ease of dc biasing in large-area diodes. The present oscillator approach makes it possible to bias the RTD in a positive-differential-resistance (PDR) region so that dc bias stability can be easily achieved.

## Relaxation Oscillator

The new RTD oscillator is based on the repetitive switching through the NDR region between dc-stable points lying below the peak point and above the valley point. To establish this type of oscillation, we imagine that the RTD is connected to one end of a short-circuited transmission line, as shown in Fig. 1. The transmission line has a characteristic impedance  $Z_0$  and an electrical time delay  $t_d$ . The RTD is biased through a bias resistor  $R_L$  with a supply voltage  $V_B$ . The quiescent operation point is initially just below the peak or just above the valley, and the RTD is induced to switch toward the valley or peak, respectively, by a slowly applied voltage ramp  $\Delta V$ . Once the first switch occurs, a pulse travels down the line, is reflected from the short with inverted polarity, and arrives back at the RTD after a time  $2t_d$ . If  $2t_d$  is sufficiently greater than the RTD switching time  $t_s$ , then the return pulse will induce the RTD to switch back to the initial operating point. The subsequent return pulse then induces a switch similar to the first one, and the process repeats at a rate of  $(4t_d)^{-1}$ . The overall process is classified as a relaxation oscillation because the RTD dwells in either of its PDR regions between switching events.



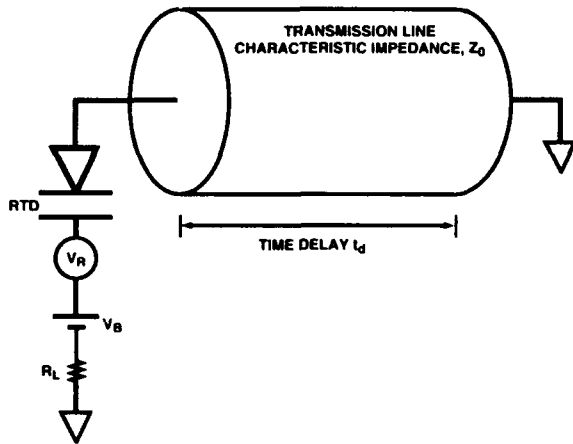


Fig. 1. Schematic diagram of the resonant-tunneling transmission-line relaxation oscillator.

### Device Models

To demonstrate the operational characteristics of the oscillator, we have simulated it numerically using the program SPICE3E. The transmission line is represented by the standard SPICE3 model, which is lossless and dispersionless. The RTD is represented by the parallel combination of a nonlinear voltage-controlled current generator and a nonlinear capacitance. The voltage dependence of the current generator is designed to be an accurate physical representation of the RTD, taking advantage of the transcendental functions available in SPICE3E. The current-voltage (I-V) characteristic of the RTD is assumed to have the form

$$I = c_1 V \left[ \tan^{-1}(c_2 V + c_3) - \tan^{-1}(c_2 V + c_4) \right] + c_5 V^m + c_6 V^n,$$

where the constants  $c_1$  through  $c_4$  are determined by the turn-on voltage, peak voltage, peak current, and peak differential conductance of the RTD, and the constants  $c_5$  and  $c_6$  are determined after obtaining  $c_1$  through  $c_4$  by fitting to the valley current and one arbitrary point beyond the valley. The exponents  $m$  and  $n$  ( $n > m$ ) are chosen to obtain a satisfactory fit to the overall I-V curve beyond the valley point. The two  $\tan^{-1}$  terms occur in the stationary-state tunneling theory of the RTD, with a Lorentzian form used for the transmission probability and a degenerate electron population assumed on the cathode side of the resonant-tunneling structure. The two polynomial terms account for the excess current, which is the primary current component beyond the valley point. The capacitance of the RTD is represented by the SPICE model for a back-biased junction diode,  $C = C_0 [1 + V/V_J]^{-1/2}$ , where  $C_0$  is the zero-bias capacitance and  $V_J$  is the built-in potential. The diode reverse saturation current is made negligibly small.

Shown in Fig. 2 is the I-V curve simulated here. It applies to a  $4\text{-}\mu\text{m}^2$  RTD having a peak current density of  $1.8 \times 10^5 \text{ A cm}^{-2}$  and a specific capacitance at the peak of  $1.4 \text{ fF } \mu\text{m}^{-2}$ . The model I-V curve

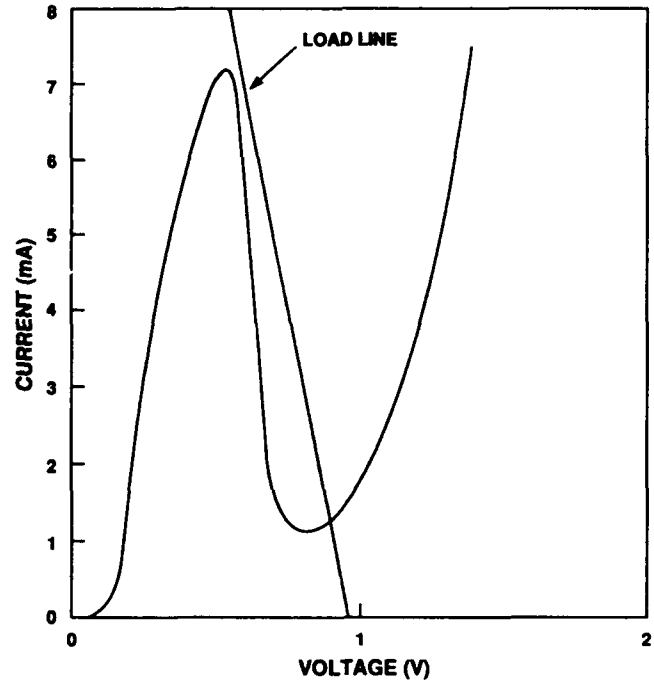


Fig. 2. Current-voltage characteristic of RTD modeled as relaxation oscillator. The straight line shows the dc load line presented to the RTD after the application of the start-up ramp.

has the parameters  $c_1 = 0.0052$ ,  $c_2 = 24.5$ ,  $c_3 = 5.0$ ,  $c_4 = 15.0$ ,  $c_5 = 0.0000809$ ,  $c_6 = 0.0014$ ,  $m = 1$ , and  $n = 5$ . The resulting peak-to-valley current ratio PVCR is 6.3, which is equal to the highest room-temperature PVCR obtained with GaAs/AlGaAs RTDs (i.e., GaAs quantum wells and AlGaAs barriers) but is sub-standard for  $\text{In}_{0.53}\text{Ga}_{0.47}\text{As}/\text{AlAs}$  RTDs. The capacitance parameters are  $C_0 = 14.0 \text{ fF}$  and  $V_J = 0.1 \text{ V}$ , which yields  $C = 5.5 \text{ fF}$  at the peak voltage.

### Numerical Results

The voltage difference across the RTD is shown in Fig. 3 for four different transmission-line delays under the conditions  $Z_0 = 50 \Omega$ ,  $R_L = 50 \Omega$ , and  $V_B = 0.75 \text{ V}$ . The amplitude and duration of the start-up ramp are  $0.2 \text{ V}$  and  $10 \text{ ps}$ , respectively. In Fig. 3(a), we see that  $t_d = 0.9 \text{ ps}$  yields a single switching event followed by ringing around the valley point of the RTD. The smallest  $t_d$  for which the switching is persistent is approximately  $1.0 \text{ ps}$ . In this case the waveform is quasi-sinusoidal, as shown in Fig. 3(b). Oscillatory behavior is also observed with the longer times of  $3 \text{ ps}$  in Fig. 3(c) and  $10 \text{ ps}$  in Fig. 3(d). However, it is apparent from the latter waveforms that with increasing delay time the RTD voltage resembles a square wave. The minimum and maximum voltage levels of the square wave represent the dwell of the RTD voltage below and above the peak and valley points, respectively.

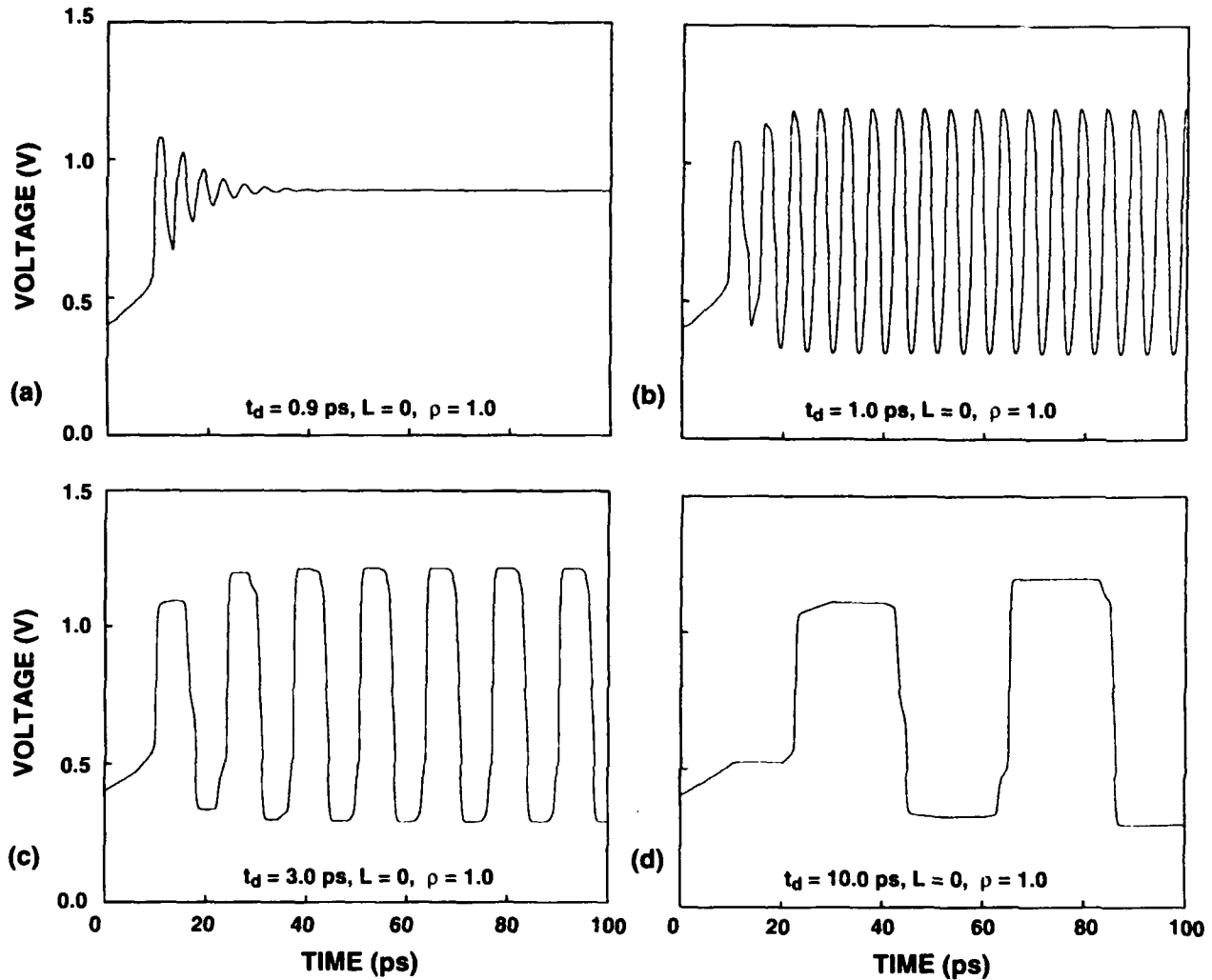


Fig. 3. Relaxation oscillator waveforms of voltage difference across the RTD for various transmission-line delays: (a)  $t_d = 0.9$  ps, (b)  $t_d = 1.0$  ps, (c)  $t_d = 3$  ps, (d)  $t_d = 10$  ps.

The output voltage waveforms across  $R_L$  are shown in Fig. 4 for the same electrical delays. For  $t_d = 1.0$  ps in Fig. 4(b), we find a quasi-sinusoidal waveform at a frequency of 192 GHz and a power of 0.5 mW. However, it is apparent from Figs. 4(c) and 4(d) that the oscillator output waveform becomes highly non-sinusoidal with increasing delay time. The waveform consists of a sequence of pulses having a full width at half-maximum of 1.9 ps and repetition time of approximately  $4t_d$ . During the repetition period two pulses occur having opposite polarities. These pulses represent the two switching events required to complete one cycle around the dynamic load line of the RTD. For both polarities, the pulse width is somewhat greater than the 10-90% switching time  $t_R$  of the RTD between the peak and valley points. An analytic expression for  $t_R$  is given by  $4.4\Delta V/C/\Delta I$ , where  $\Delta V$  is the difference between the valley and peak voltages,  $C$  is the capacitance at the peak point, and  $\Delta I$  is the difference between the peak and valley currents [3]. For the present RTD

we have  $\Delta V = 0.28$ ,  $\Delta I = 6.0$  mA, and  $C = 5.5$  fF, so that  $t_R = 1.1$  ps. The difference between  $t_R$  and the relaxation oscillator pulse width is caused by the fact that the oscillator switches over a wider voltage range, between the peak and a point approximately 0.4 V beyond the valley.

#### Non-Ideal Transmission Line

Two important practical issues concerning this oscillator are the degree to which the power reflection from the short-circuited end of the transmission line can deviate from unity and the sensitivity of the oscillator to the form of the start-up ramp. To address the first issue the short circuit was replaced with a load resistor whose resistance  $R_T$  was increased up to the point where oscillations were just maintained. This defines a minimal power reflection  $\rho = [(R_T - Z_0)/(R_T + Z_0)]^2$ . For the 1.0, 3.0, and 10.0 ps delays, the minimal power reflections were 97, 69, and 59%, respectively. To address the second issue,

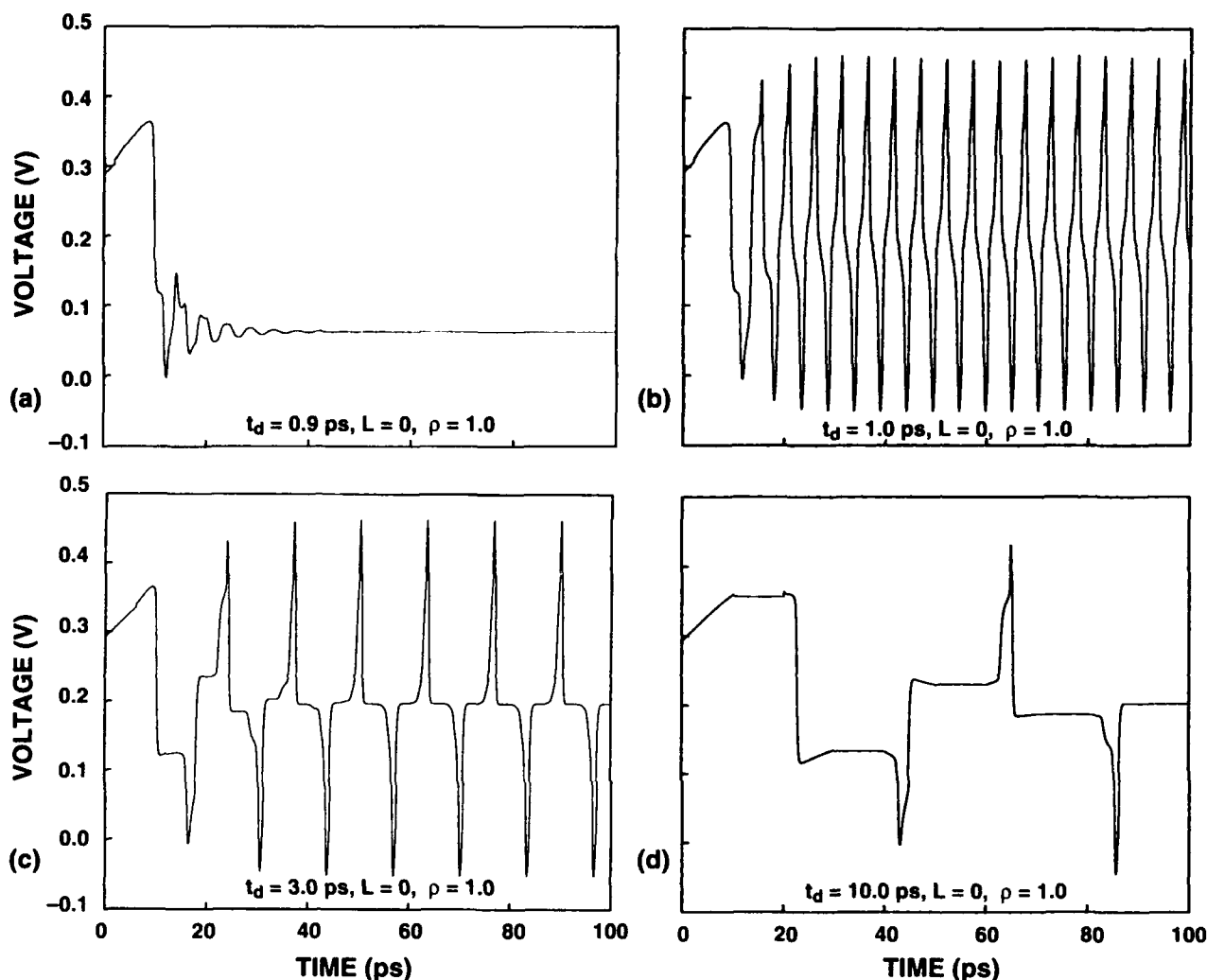


Fig. 4. Relaxation oscillator waveforms of voltage across the load resistor for various transmission-line delays: (a)  $t_d = 0.9$  ps, (b)  $t_d = 1.0$  ps, (c)  $t_d = 3$  ps, (d)  $t_d = 10$  ps.

the start-up ramp duration was increased from 10 ps to 1 ns in several steps. In all cases the steady-state waveforms were practically identical, proving that the only role of the start-up ramp is to trigger the first switching event. No energy is required from the ramp to sustain the oscillations.

### Conclusion

In conclusion, a new oscillator is proposed that entails the repetitive switching of an RTD connected to a short-circuited transmission line. When the electrical delay of the line is much greater than the RTD switching time, the oscillator generates a pulse train having a repetition rate equal to  $(4t_d)^{-1}$  and a pulse width equal to  $t_s$ . When the electrical delay is comparable to the switching time, the oscillator output is quasi-sinusoidal. Consequently, the relaxation oscillator is a compact electrical design that can function either as a picosecond pulse generator or as a high-frequency cw source.

### Acknowledgements

The author thanks J. P. Mattia for assistance with the numerical simulations, R. A. Murphy for useful comments on the manuscript, and C. L. Dennis, M. W. Geis and M. J. W. Rodwell for technical discussion. This work was sponsored by the Air Force Office of Scientific Research.

### References

1. E. R. Brown, J. R. Söderström, C. D. Parker, L. J. Mahoney, K. M. Molvar, and T. C. McGill, *Appl. Phys. Lett.*, **58**, 2291 (1991).
2. J. F. Whitaker, G. A. Mourou, T. C. L. G. Sollner, and W. D. Goodhue, *Appl. Phys. Lett.*, **53**, 385 (1988).
3. E. R. Brown, C. D. Parker, T. C. L. G. Sollner, A. R. Calawa, M. J. Manfra, C. L. Chen, S. W. Pang, and K. M. Molvar, *Proc. SPIE*, **1288**, 122 (1990).

# **Fabrication of Microwave Compatible, Monolithic, High-Speed In<sub>0.53</sub>Ga<sub>0.47</sub>As/AlAs and InAs/AlSb Resonant Tunneling Diodes**

**E. Özbay and D. M. Bloom**

*Edward L. Ginzton Laboratory, Stanford University, Stanford, California 94305-4085*

**D. H. Chow and J. N. Schulman**

*Hughes Research Laboratories, 3011 Malibu Canyon Road, Malibu, California 90265*

## **Abstract**

We report the fabrication of monolithic, microwave integrated circuit compatible, high-speed In<sub>0.53</sub>Ga<sub>0.47</sub>As/AlAs and AlSb/InAs RTD's. Switching transition times of 1.7 psec are measured using electro-optic sampling techniques.

## **Introduction**

It is widely believed that InAs and In<sub>0.53</sub>Ga<sub>0.47</sub>As based resonant tunneling diodes (RTD's) can be significantly faster than GaAs-based RTD's due to their substantially higher peak current densities [1,4]. In this paper, we report the design and fabrication of microwave integrated circuit compatible In<sub>0.53</sub>Ga<sub>0.47</sub>As/AlAs and InAs/AlSb RTD's.

Peak current density is a crucial figure of merit for high speed RTD switching applications [2]. Extremely high peak current densities (up to  $4.5 \times 10^5$  A/cm<sup>2</sup>) have already been demonstrated in InGaAs/AlAs/InAs RTD's [1,3,4]. Similarly, InAs/AlSb RTD's have peak current densities as high as  $5 \times 10^5$  A/cm<sup>2</sup> and have been used in hybrid microwave oscillators with operating frequencies up to 712 GHz [1,5]. Based on published current-voltage characteristics, the expected switching transition times of these high-peak current density RTD's can be estimated to be around 1 psec [2,6]. However,

all of these high peak current density RTD's have been fabricated using simple device processing technologies, which are not suitable for measuring the expected high-speed switching transitions.

The anticipated In<sub>0.53</sub>Ga<sub>0.47</sub>As/AlAs and InAs/AlSb RTD switching times represent a significant improvement over the best previously observed times of 6 psec in GaAs/AlAs RTD's [7]. Although Whitaker et al. reported 2.0 psec measurements using GaAs/AlAs based RTD's [8], those measurements remain controversial. As described by Brown et al. [6], those switching experiments were done under an overdrive condition, in which measured switching times do not represent the true switching times of the devices. In fact, the expected minimum switching times of these GaAs based devices (with peak current densities of  $4 \times 10^4$  A/cm<sup>2</sup>), is around 12 psec [2].

## **Experiment**

We have developed a monolithic, microwave compatible fabrication process for InAs and In<sub>0.53</sub>Ga<sub>0.47</sub>As based high-speed RTD's to be used for high-speed applications. Proton isolation techniques are not effective for semiconductors like InGaAs and InAs, which have relatively small energy gaps. Therefore, a mesa-type processing technique must be used to achieve isolation. The design for the

microwave-compatible RTD structure is shown in Fig. 1. The procedure used to fabricate the structure is as follows. Gold is evaporated to be used as the top ohmic metal and also as a mask to protect the mesa area. The quantum well and the upper conducting layers are etched

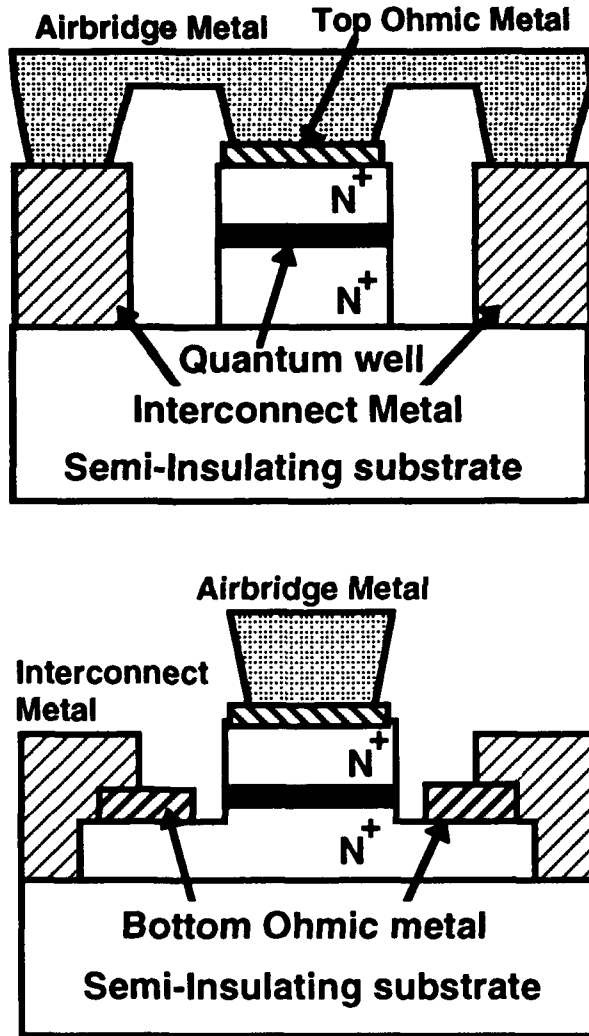


Figure 1. Cross sections of the microwave integrated circuit compatible RTD structures.

away until the bottom conductive layer is reached, and a layer of Au is deposited to be used as the bottom ohmic metal. Then, using an isolation mask, we etch away all of the epilayers except the active areas. This is followed by an evaporation of Ti/Au interconnect metal, which forms coplanar waveguide (CPW) transmission lines on top of the semi-insulating InP substrate. A 2.5 micron thick Au layer is used as an airbridge to

connect the center of the CPW to the top ohmic metal of the RTD.

This fabrication process has first been used to investigate  $\text{In}_{0.53}\text{Ga}_{0.47}\text{As}/\text{AlAs}$  based RTD's. Devices were grown on 2-inch semi-insulating InP substrates. Growth started with a  $0.5\ \mu\text{m}$ , n-type InGaAs contact layer, with  $n=1.5 \times 10^{19}\ \text{cm}^{-3}$ . This layer was followed by a  $500\ \text{\AA}$  thick, lightly doped ( $n=10^{17}\ \text{cm}^{-3}$ )  $\text{In}_{0.53}\text{Ga}_{0.47}\text{As}/$  layer. The double barrier region consisted of a  $41\ \text{\AA}$   $\text{In}_{0.53}\text{Ga}_{0.47}\text{As}$  quantum well sandwiched between two identical  $16\ \text{\AA}$  (6 monolayers) AlAs barriers and two  $15\ \text{\AA}$  (5 monolayers) undoped  $\text{In}_{0.53}\text{Ga}_{0.47}\text{As}$  layers. The structure was completed by two  $0.1\ \mu\text{m}$ , n-type  $\text{In}_{0.53}\text{Ga}_{0.47}\text{As}$  contact layers doped to  $10^{18}\ \text{cm}^{-3}$ , and  $1.5 \times 10^{19}\ \text{cm}^{-3}$ . The details of the growth and a more complete analysis of this material system can be found in another reference[4].

Figure 2 shows the typical I-V characteristics of a device we have obtained from the above epitaxial design and the fabrication process. The device has a peak current density of  $3.3 \times 10^5\ \text{A}/\text{cm}^2$  with a peak to valley ratio of 7.

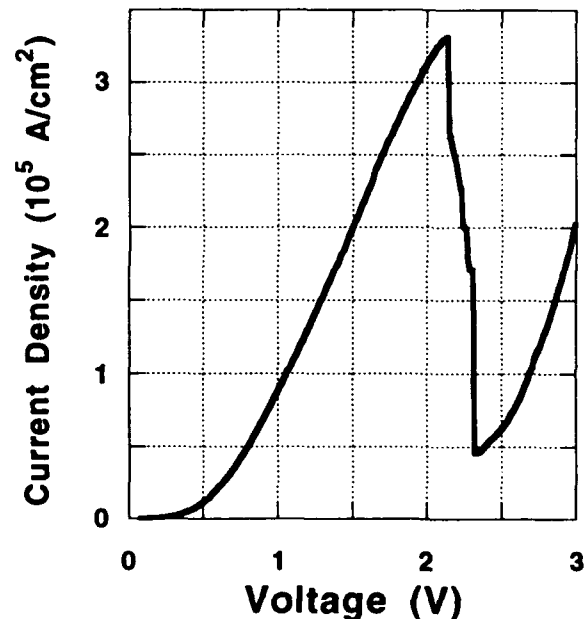


Figure 2. Current-voltage characteristic of an  $\text{In}_{0.53}\text{Ga}_{0.47}\text{As}/\text{AlAs}$  resonant tunneling diode.

This fabrication process has also been used to investigate InAs/AlSb RTD's. This time devices were grown on 2-inch diameter semi-insulating GaAs substrates. Growth started with a 0.2  $\mu\text{m}$ , undoped InAs buffer layer, followed by a 0.8  $\mu\text{m}$  thick InAs with  $n=2.0 \times 10^{18} \text{ cm}^{-3}$ . This layer was followed by a 500  $\text{\AA}$  thick, lightly doped ( $n=10^{17} \text{ cm}^{-3}$ ) InAs layer. The double barrier region consisted of a 75  $\text{\AA}$  InAs quantum well sandwiched between two identical 18 $\text{\AA}$  (6 monolayers) AlSb barriers. An undoped 100 $\text{\AA}$  InAs layer was grown after the double barrier region. The structure was completed by a 0.2  $\mu\text{m}$ , n-type InAs contact layer doped to  $2.0 \times 10^{18} \text{ cm}^{-3}$ .

Figure 3 shows the I-V characteristics of a device we obtained from the preceding epitaxial design and fabrication process. The device has a peak current density of  $3.3 \times 10^5 \text{ A/cm}^2$  with a peak-to-valley ratio of 3.3.

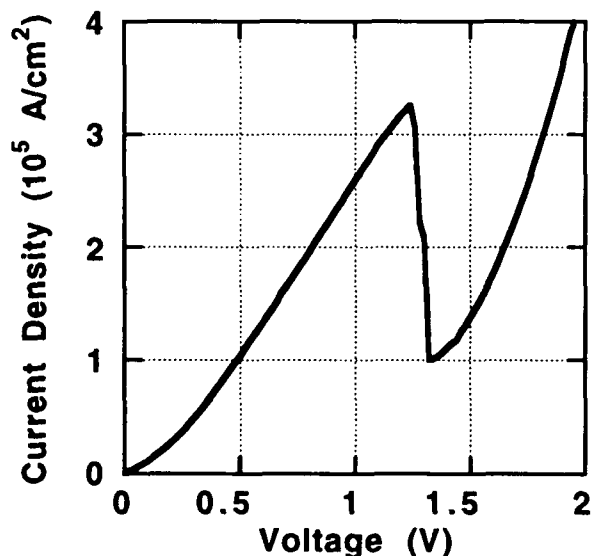


Figure 3. Current-voltage characteristic of an InGaAs/AlAs resonant tunneling diode.

The expected switching time of this InAs/AlSb RTD can be calculated by using the analysis explained in Ref. 2, which concludes that the minimum obtainable rise time in an RTD is approximately  $5R_N C$ , where  $R_N$  is the average negative resistance, i.e., the voltage difference between peak and valley points divided by the available current, and  $C$  is the device capacitance. From this analysis, the

device has an estimated RC switching time of 1 psec. The switching time of this InAs/AlSb RTD is still limited by the RC time constant, as the full width at half maximum of the electron transmission coefficient for the device is 2.92 meV, giving an intrinsic response time of 200 fsec.

In order to measure the switching times of these InAs/AlSb RTD's, we have used voltage step forming structures which consist of a 50  $\Omega$  coplanar transmission line with an RTD shunted to ground from the center conductor of the coplanar transmission line [7]. Switching was demonstrated by applying a DC bias and a sine wave to the transmission line. As the RTD switches, a step waveform begins to propagate along the transmission line. The resulting waveform can be measured by electro-optically sampling the voltage at a point just past the device. The length of the transmission line was chosen to be long enough to allow measurement of the pulse risetime before any reflections return from the output pad. This allows us to see the actual switching of the device, independent of bond pad capacitance. Electronic probing techniques by contrast, will be limited by the bond pad capacitance rather than by the device characteristics.

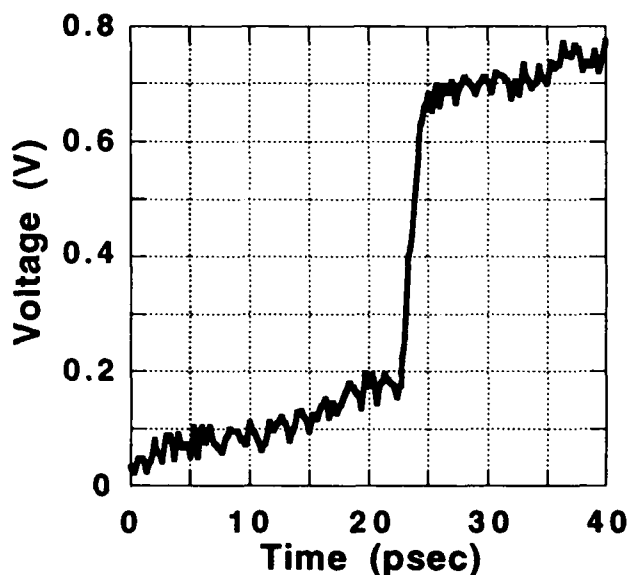


Figure 4. 1.7 psec switching transition time is measured using electro-optic sampling techniques.

Figure 4 shows a typical switching waveform of an InAs/AlSb RTD measured by electro-optic sampling techniques. 10-90% switching transition times as low as 1.7 psec were measured with voltage swings of 400-600 mV. When the response of the electro-optic sampling system is deconvolved from this measurement, the typical switching transition time is found to be around 1.2 psec which is very close to estimated switching times. This is a factor of 5 improvement over previous high speed measurements using GaAs based RTD's. To the best of our knowledge, this measurement is the fastest documented switching time for any semiconductor device. The measurement of these high speed transitions shows the feasibility of the fabrication process for high speed RTD integrated circuit applications.

## Conclusion

In summary, we have designed and fabricated  $\text{In}_{0.53}\text{Ga}_{0.47}\text{As}/\text{AlAs}$  and InAs/AlSb based, microwave integrated circuit compatible resonant tunneling diodes. The resulting devices had peak current densities of  $3.3 \times 10^5 \text{ A/cm}^2$ . Switching transition times of 1.7 psec were measured using electro-optic sampling techniques.

## Acknowledgments

The authors are grateful to J. Sheridan, M. Kauffman and I. Aoki for the invaluable help on the high frequency measurements, to L. Warren and H. Dunlap for technical assistance. This work was supported by DARPA managed by NOSC under subcontract from the Mayo Foundation on Contract No. N66001-89-C-0104 and by the SDIO/IST managed by ONR under Contract No. N00014-89-K-0067.

## References

1. D.H. Chow, J.N. Schulman, E. Özbay, and D.M. Bloom, "High Speed InAs/AlSb and InGaAs/AlAs Resonant Tunneling Diodes," Proceedings of the Materials Research Society Conference, Boston, 1992.
2. S. K. Diamond, E. Özbay, M. J. W. Rodwell, Y. C. Pao, J. S. Harris and D.M. Bloom, "Resonant tunneling diodes for switching applications," *Appl. Phys. Lett.*, **64**, pp. 153-155 (1989).
3. D.H. Chow, J.N. Schulman, E. Özbay, and D.M. Bloom, "Investigation of  $\text{In}_{0.53}\text{Ga}_{0.47}\text{As}/\text{AlAs}$  Resonant Tunneling Diodes for High Speed Switching," *Appl. Phys. Lett.*, **61**, pp. 1685-1687 (1992).
4. T.P.E. Broekaert, and C.G. Fonstad, " $\text{In}_{0.53}\text{Ga}_{0.47}\text{As}/\text{AlAs}$  resonant tunneling diodes with peak current densities in excess of  $450 \text{ kA/cm}^2$ ," *J. Appl. Phys.* **68**, pp. 4310-4312 (1990).
5. E.R. Brown, J.R. Söderstrom, C.D. Parker, L.J. Mahoney, M.K. Molvar, and T.C. McGill, "Oscillations up to 712 GHz in InAs/AlSb resonant-tunneling diodes," *Appl. Phys. Lett.*, **58**, pp. 2291-2293 (1991).
6. E.R. Brown, C.D. Parker, A.R. Calawa, M.J. Manfra, T.C.L.G. Sollner, C.L. Chen, S.W. Pang, and K.M. Molvar, "High-speed resonant tunneling diodes made from the  $\text{In}_{0.53}\text{Ga}_{0.47}\text{As}/\text{AlAs}$  material system," *Proc. SPIE* **1288**, p.122 (1990).
7. E. Özbay, S. K. Diamond, and D.M. Bloom, "Pulse forming and triggering using resonant tunneling diode structures", *Electronics Letters*, **26**, pp. 1046-1048 (1990).
8. J.F. Whitaker, G.A. Mourou, T.C.L.G. Sollner, and W.D. Goodhue, "Picosecond switching time measurement of a resonant tunneling diode," *Appl. Phys. Lett.* **53**, pp.385-387 (1988).

---

## **Terahertz Transients**

---



# THz Beam Emission by Carrier Transport or by Optical Rectification

X. -C. Zhang, Y. Jin, T. D. Hewitt, and X. F. Ma

*Physics Department, Rensselaer Polytechnic Institute, Troy, New York 12180-3590*

L. Kingsley and M. Weiner

*US Army LABCOR, Pulse Power Center, Electronic Technology and Devices Laboratory,  
Fort Monmouth, New Jersey 07703*

## Abstract

We provide recent experimental evidences of THz radiation from semiconductor generated by photocarrier transport and by terahertz optical rectification.

## Introduction

In recent years, different photonic and optoelectronic techniques have been used to generate THz bandwidth free space radiation [1-5]. Developing new radiation sources will have a substantial impact on high-speed, broadband characterization of dielectric materials [6-10]. To explore the radiation mechanism of THz beam is crucial for a physical understanding of the origin of the radiation, as well as for realizing an intense THz source application [11-13].

With illumination by femtosecond laser pulses, a GaAs sample emits pulsed submillimeter-wave radiation. To distinguish between the contribution from carrier transport and from subpicosecond optical rectification is crucial for a physical understanding of the origin of the radiation, as well as for realizing an intense THz source application. In this talk, we will review the current progress of optically induced THz radiation from semiconductors.

We report recent results which demonstrate the contribution from both the subpicosecond optical rectification (SOR) and the photocarrier transport effect. When the

subpicosecond optical rectification was separated from background radiation due to carrier transport and the semiconductor was excited at resonance, we observed an enhancement of the submillimeter-wave nonlinear susceptibility. We also discuss the magnetic effect on THz radiation by applying the Lorentz force on the transient carriers.

## Experiment

The experimental setup shown in Fig. 1 is a time-resolved optoelectronic coherent sampling arrangement.

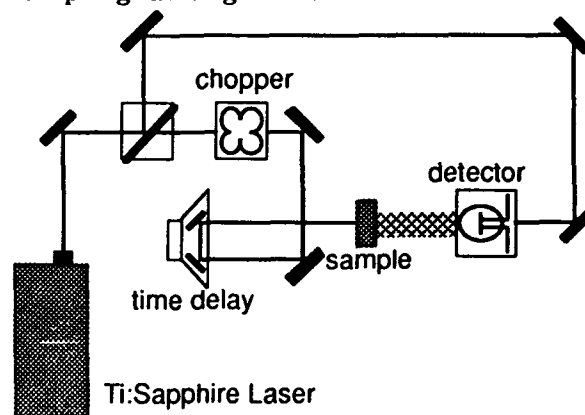


Figure 1

Normal optical incidence on the GaAs surface is used to distinguish the forward subpicosecond optical rectification signal from the carrier transport effect. Under normal incidence the THz signal from the accelerated carriers driven by the surface

depletion field can not be measured in the forward direction because no radiation is emitted along the current flow direction. However, subpicosecond optical rectification can radiate in the forward direction under normal incident illumination.

Fig. 2 shows the THz radiation (in the forward direction) from a  $\langle 111 \rangle$  GaAs bulk sample for three incident angles ( $\phi=0$  and  $\phi=\pm 50$  degrees). The photon energy is 1.52 eV. The center trace ( $\phi=0$ ) is due to subpicosecond optical rectification only, while the upper and lower traces ( $\phi=\pm 50$ ) combine radiation from both the SOR and carrier transport effects. The timing shifts of the waveforms taken at oblique angles are due to an increase in the THz beam path from tilting the sample.

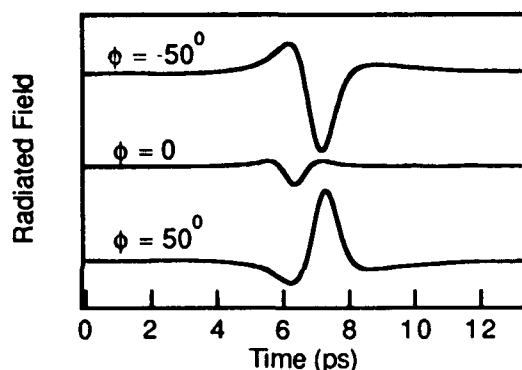


Figure 2

Besides the use of normal incident illumination of the bulk GaAs to confirm the subpicosecond optical rectification, we also examined the THz radiation from superlattice structures. Here we measured the THz radiation from a GaAs/In<sub>0.1</sub>Ga<sub>0.9</sub>As  $\langle 111 \rangle$  oriented superlattice with photon energies below and above the barrier potential.

Fig. 3 shows the THz signal versus optical incident angle (polar angle) from  $\langle 111 \rangle$  oriented GaAs bulk and superlattice samples. When the photon energy (1.39 eV) is less than the barrier potential of GaAs, the radiation signal increases slowly with increasing polar angle (about 4 times). In this case the carriers are injected directly into the wells and, since quantum confinement will limit the photocurrent, the radiation is mainly from optical rectification. When the photon energy (1.53 eV) is above the barrier potential, the THz signal increases quickly with increasing polar angle (over 20 times). The "free" photocarriers (above the barrier) can

accelerate in the static field to radiate a THz signal.

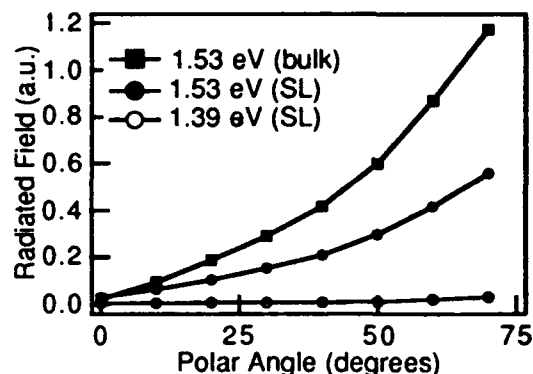


Figure 3

We have measured the temporal waveforms at two energies. At the same oblique angle, a higher energy (1.53 eV) excitation leads to temporal broadening of the THz signal, while a much cleaner and shorter THz waveform is measured when a lower energy (1.39 eV) excitation is used. When the superlattice is replaced by a GaAs sample (superlattice substrate), the THz signal is nearly doubled at a photon energy of 1.53 eV, but the same dependence on polar angle is observed. The rectified signal, even at resonance, is smaller than the contribution from the photocurrent (off-normal incident angle).

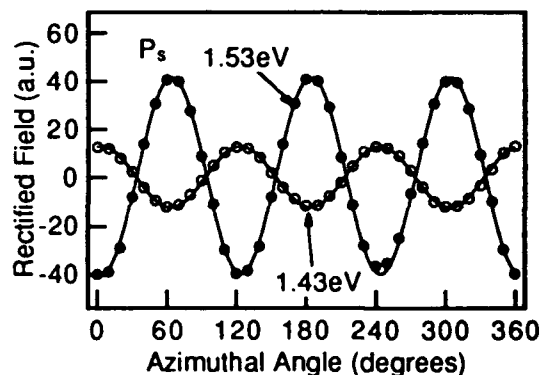


Figure 4a

We have measured the dependence of the SOR signal on crystallographic orientation. In this measurement, a  $\langle 111 \rangle$  oriented GaAs sample was rotated around its surface normal. Fig. 4a and 4b show the SOR signal vs crystal azimuthal angle at two optical energies (1.43 eV and 1.53 eV) and two optical polarization,

$P_p$  and  $P_s$  respectively. The open and solid dots are the experimental data. The SOR signal has opposite polarity at these two energies. A three-fold rotation symmetry is observed at both photon energies.

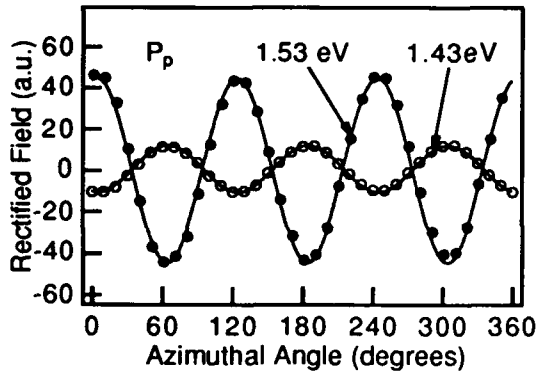


Figure 4b

Since the submillimeter-wave radiation is proportional to the second time derivative of the low frequency polarization, we can calculate the angular dependence of the nonlinear polarization (low frequency) to obtain information about rectification. The optical rectification field, from a  $\langle 111 \rangle$  oriented GaAs under a normal incident angle, can be calculated from the nonlinear polarization  $P_p$  and  $P_s$  corresponding to different polarization geometries of the incident beam (light polarization is parallel and perpendicular to the dipole detector axis respectively). The nonlinear polarization  $P_p$  and  $P_s$  (SI) are given by:

$$\begin{aligned} P_p(0, \omega, -\omega) &= -P_s(0; \omega, -\omega) \\ &= \frac{4}{\sqrt{6}} d_{14}(0; \omega, -\omega) \cos(3\theta) E E^* \quad (1) \end{aligned}$$

Where the azimuthal angle  $\theta$  is measured with respect to the  $[1, 1, -2]$  direction, and  $d_{14}$  is a nonlinear optical susceptibility tensor element having a frequency response from 100 GHz to several terahertz (mainly characterized by the optical pulse duration). The curves in Fig. 4, which are normalized to the experimental data, are plots of the reversed electric fields calculated from the nonlinear polarizations in equation (1). The curves fit the experimental data at 1.43 eV well. However, to fit the experimental data at 1.53 eV, the sign of the susceptibility needs to be changed. After the sign of  $d_{14}$  is reversed, the plots at 1.53 eV fit the data well.

We observed resonance enhancement and sign reversal of the nonlinear susceptibility (DC-THz) near the bandgap of zincblende crystals by using a terahertz optical rectification technique. The SOR signal changes dramatically when the laser energy is tuned near the GaAs bandgap. When the photon energy is tuned around 1.35 eV (70 meV lower than the bandgap), the rectified signal is nearly unchanged for small energy tuning. When the laser is tuned to the bandgap, the amplitude of the SOR signal increases. It reaches a peak when the laser energy is just above the bandgap. Further tuning of the laser energy to the higher energy side results in a polarity change of the radiation signal.

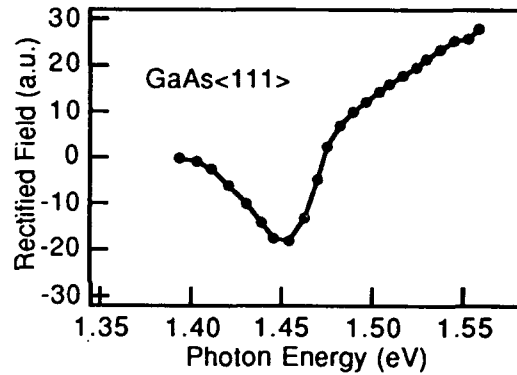


Figure 5

Fig. 5 is a plot of the SOR signal from a  $\langle 111 \rangle$  GaAs sample vs optical excitation energy (normal incident angle). The resonance enhancement near the bandgap is pronounced. We measured about a 106 times increase of the rectified field when the laser energy was tuned from 1.40 eV to 1.46 eV.

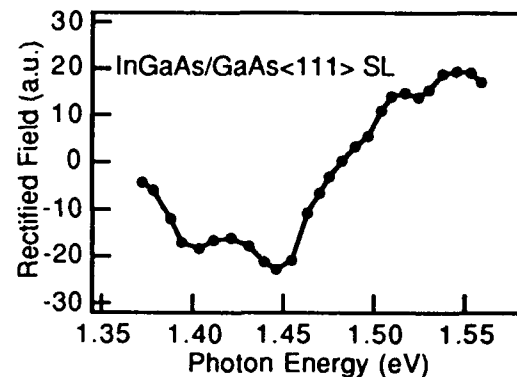


Figure 6

We also measured the SOR signal from a  $\langle 111 \rangle$  InGaAs/GaAs superlattice sample vs optical excitation energy at normal incidence, as shown in Fig. 6.

Besides the resonance due to GaAs (barriers), an additional resonance, which is due to the bound states in the InGaAs quantum wells, is observed at 1.40 eV. The origin of a small feature at 1.53 eV is not clear yet. During the laser energy tuning, the temporal duration of the rectified field remained essentially unchanged. We also observed similar resonant behavior from  $\langle 111 \rangle$  oriented CdTe samples. Both the resonance enhancement and sign reversal near the bandgap of CdTe ( $E_g$  is about 1.50 eV) are observed, as shown in Fig. 7. The strong radiation signal around 1.4 eV may be due to the impurity states in CdTe. Photoluminescence shows intense impurity luminescence emission.

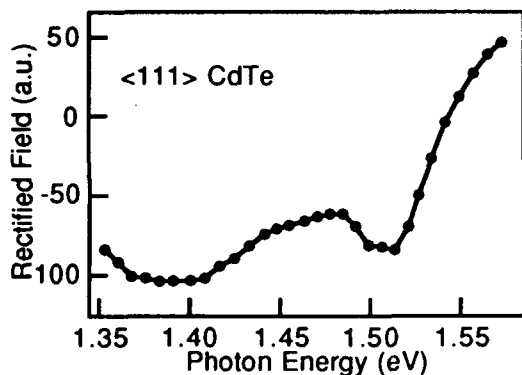


Figure 7

We also calculated the nonlinear polarization from a perfect  $\langle 100 \rangle$  oriented GaAs. The calculation showed no SOR signal in the forward direction under normal incidence, regardless of the azimuthal rotation of the crystal. This calculated result has been verified in our experiment. Since  $\langle 100 \rangle$  oriented GaAs can not emit a forward THz beam, we fabricated a pair of parallel planar electrodes on a  $\langle 100 \rangle$  GaAs to apply an external bias. The result of the forward radiation from a biased  $\langle 100 \rangle$  GaAs sample (pure transient photocurrent) is plotted in Fig. 8. This is a comparison of the forward radiation driven by the transient photocurrent in the biased external field and that generated by ultrafast optical rectification. Clearly, no sign reversal is measured from the biased  $\langle 100 \rangle$  GaAs. We have tested a large number of

$\langle 111 \rangle$  GaAs samples, a small variation in flip-over energy is observed.

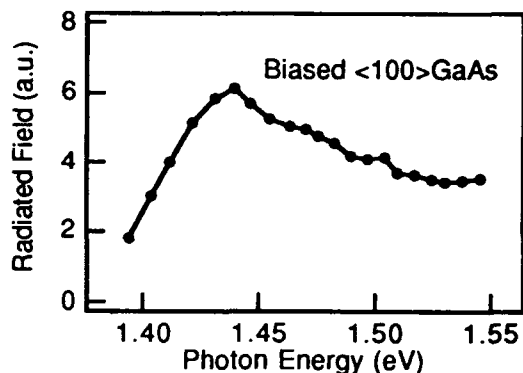


Figure 8

In a configuration of normal incidence, the forward THz radiation from bulk zincblende crystals is purely due to optical rectification [5]. However this is not the case if an external magnetic field is applied orthonogally to the carriers flow direction [6]. The static electric field drives the photoinduced electrons and holes in opposite directions (Coulomb interaction), and the magnetic field deflects both carriers (Lorentz interaction). In semiconductors with different effective mass of the electron and hole, even though both carriers are bent to same side of the sample by the magnetic force, their different mobility results a macroscopic electric field  $E_H$ . Fig. 9 schematically illustrates the experimental setup and sample configuration (top view).

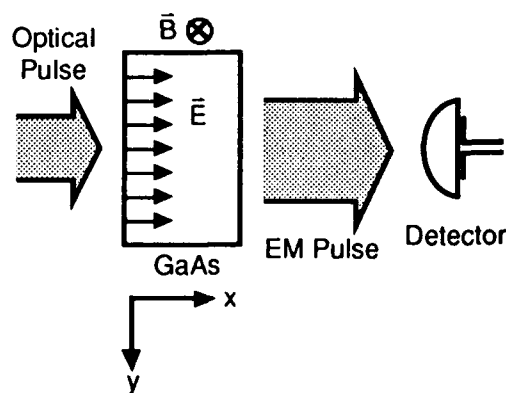


Figure 9

When an  $\langle 100 \rangle$  GaAs diode is illuminated with femtosecond optical pulses at normal incidence, there is no forward THz radiation. However if an external magnetic field is applied to the semiconductor wafer with its field perpendicular to the static electric field of the GaAs emitter, THz radiation develops in

the forward direction due to the Lorentz force on the moving charges (optically induced carriers). The polarization of the THz beam is perpendicular to the direction of magnetic field.

Two magnets are set in parallel, to create a nearly uniform magnetic field in the gap between the magnets. A <100> GaAs wafer is inserted into the gap. Fig. 10(a) shows the measured THz beam waveforms under the magnetic field. The three curves are the temporal waveforms of the radiation at magnetic field  $B=0$  (center),  $B=0.32$  Tesla (top) and  $B=0.32$  Tesla with opposite direction of the magnetic field (bottom). Under normal incidence and zero magnetic field, there is no radiation measured in the forward direction (middle curve) as expected. However when an external magnetic field is applied to the sample, forward radiation is generated (top and bottom curves). The direction of the magnetic field determines the polarization of the radiation, this is because opposite magnetic fields will bend the carriers in opposite directions, as shown by the polarity changes in the top and bottom curves in Fig. 10.

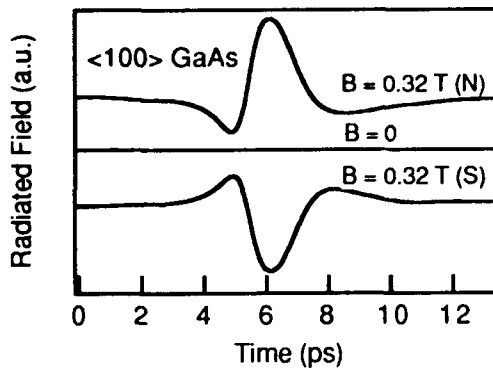


Figure 10(a)

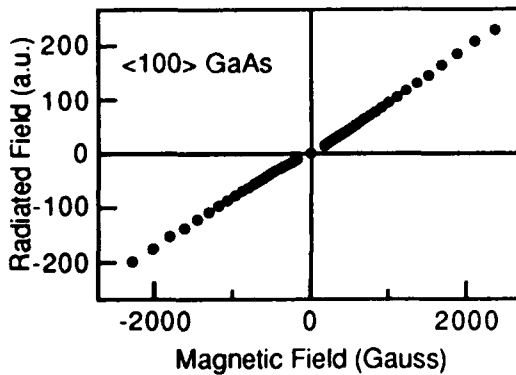


Figure 10(b)

We can estimate the dependence of THz radiation on the strength of the magnetic field. It is well known that the projection trace of a moving charge will bend under a magnetic field if the magnetic field direction is not parallel to the initial charge velocity direction. Since the driving forces on the carriers are the Coulomb force and the Lorentz force, the equation of the acceleration of an electron in a semiconductor is:

$$\bar{a} = \frac{d\bar{v}}{dt} = -\frac{e}{m_e^*} (\bar{E} + \bar{v} \times \bar{B}) \quad (2)$$

where  $m_e^*$  is the effective mass of the electron. Because of the heavier mass of the hole, we have ignored hole motion. If we assume a uniform electric field in x-direction, and a uniform magnetic field in the z-direction, the solution for the y component of the carrier acceleration, with the proper initial conditions, has the simple form:

$$a_y = -\frac{eE_x}{m_e^*} \sin\left(\frac{eB_z}{m_e^*} t\right) \quad (3)$$

This classical treatment of a moving charge does not take into consideration the saturated velocity in semiconductors. For a magnetic field strength of 0.1 Tesla, the cyclotron frequency  $eB_z/m_e^*$  of an electron in GaAs is about 0.25 THz. For a very short measurement time (for example, less than 2 ps), we can take the lowest order term in the Taylor expansion, and rewrite the equation (3) as:

$$a_y = -\left(\frac{e}{m_e^*}\right)^2 E_x B_z t \quad (4)$$

Since the measured, radiated electric field is proportional to the charge acceleration y-component at far field (dipole detector is polarized in y direction), the forward radiation should be described by the charge acceleration  $a_y$ . Equations (3) and (4) clearly show that the polarity of the forward radiation depends on the direction of  $E_x$  and  $B_z$  (we ignore the contribution from holes due to their larger effective mass). Fig. 10(b) is a plot of the amplitude of the radiation field (peak value) versus the strength of the magnetic field. The magnitude of the radiated electric field component in the forward direction is found to be linearly proportional to the strength of a moderate magnetic field ( $B < 0.1$  Tesla) as predicted by equation (10), and substantially

deviates from linearity for stronger magnetic fields.

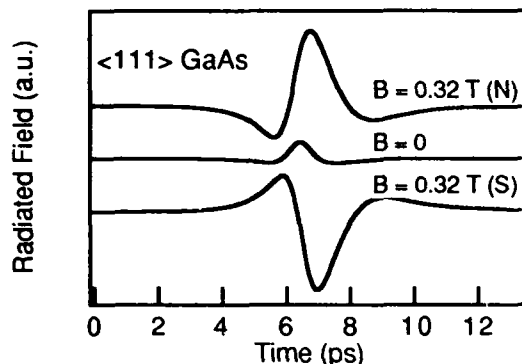


Figure 11

Fig. 11 is a plot of THz radiation from a  $\langle 111 \rangle$  GaAs under external magnetic fields. This figure is similar to Fig. 2 which plots THz radiation vs polar angle. The center traces in Fig. 2 and Fig. 11 are due to purely optical rectification, the top and bottom traces are due to the contribution from optical rectification and from transient photocarriers. The temporal broadening of the radiation waveforms ( $B \neq 0$ ) in Fig. 11 are due to the finite photocarrier lifetime.

### Summary

In summary, THz radiation can be generated by transient photocarriers and by subpicosecond optical rectification. Typically, the radiation by transient photocarriers has a longer pulse duration due to the finite photocarrier lifetime. The radiation by subpicosecond optical rectification can be measured in the forward direction from  $\langle 111 \rangle$  oriented zincblende crystals. A magnetic field can control the direction and polarization of a THz beam generated from a semiconductor.

### Acknowledgment

This work was supported in part by the National Science Foundation under grant ECS-9211566 and by the U.S. Army Research

Office Scientific Services Program under contract DAAL03-91-C-0034. We would like to acknowledge D. Grischkowsky and H. Chan (IBM) for their support of this work. We also thank Coherent, Newport-Klinger, and Thorlabs Inc. for equipment donations. We also thank technical assistant from J. Liu.

### References

1. G. Mourou, C.V. Stancampiano and D. Blumenthal, *Appl. Phys. Lett.*, **38**, 470 (1981)
2. D.H. Auston, K.P. Cheung and P.R. Smith, *Appl. Phys. Lett.*, **45**, 284 (1984); P.R. Smith, D.H. Auston, and M.C. Nuss, *IEEE J. Quantum. Elect.* **24**, 255 (1988)
3. Ch. Fattinger and D. Grischkowsky, *Appl. Phys. Lett.*, **53**, 1480 (1988); *Appl. Phys. Lett.*, **54**, 490 (1988)
4. D.H. Auston, and M.C. Nuss, *IEEE J. Quantum. Electron.* **24**, 184 (1988)
5. A.P. DeFonzo, M. Jarwala and C.R. Lutz, *Appl. Phys. Lett.*, **50**, 1155 (1987); *Appl. Phys. Lett.*, **51**, 212 (1987)
6. X.-C. Zhang, B.B. Hu, J.T. Darrow and D.H. Auston, *Appl. Phys. Lett.* **56**, 1011 (1990)
7. D. Grischkowsky, Soren Keiding, Martin van Exter, and Ch. Fattinger, *J. Opt. Soc. Am. B*, **7**, 2006 (1990)
8. M.C. Nuss, D.H. Auston, and F. Capasso, *Phys. Rev. Lett.*, **58** 2355 (1987)
9. B.I. Greene, J.F. Federici, D.R. Dykaar, A.F.J. Levi, and L.N. Pfeiffer, *Opt. Lett.* **16**, 48 (1991)
10. X.-C. Zhang and D.H. Auston, *J. Appl. Phys.* **71**, 326 (1992)
11. S.L. Chueng, S. Schmitt-Rink, B.I. Greene, P.N. Faeta, and A.F.J. Levi, *Phys. Rev. Lett.* **68**, 102 (1992)
12. H.G. Roskos, M.C. Nuss, J. Shah, K. Leo, D.A.B. Miller, A.M. Fox, S. Schmitt-Rink, and K. Kohler, *Phys. Rev. Lett.*, **68**, 2216 (1992)
13. X.-C. Zhang, Y. Jin, K. Yang, and L. J. Schowalter, *Phys. Rev. Lett.* **69**, 2303 (1992)

# Optical Generation of Terahertz Pulses in Quantum Wells

Paul C. M. Planken, Martin C. Nuss, Igal Brener, and Keith W. Goossen  
*AT&T Bell Laboratories, Crawford Corner Road, Holmdel, New Jersey 07733-3030*

Marie S. C. Luo and Shun Lien Chuang  
*Department of Electrical and Computer Engineering, University of Illinois at Urbana-Champaign,  
Urbana, Illinois 61801-2992*

Loren Pfeiffer  
*AT&T Bell Laboratories, Murray Hill, New Jersey 07974*

## Abstract

We report on the generation of terahertz pulses from the optical excitation of excitons in GaAs/Al<sub>0.3</sub>Ga<sub>0.7</sub>As quantum wells. In general there are two contributions to the THz signals for nonzero field. The first arises from the creation of excitons in states in which they are already polarized. This leads to a time-dependent polarization that grows with the integrated pulse energy and radiates a short electrical transient. The second one arises from the coherent excitation of *both* light hole and heavy hole excitons. The time evolution of the coherent superposition of these two exciton states gives rise to charge oscillations that radiate a terahertz signal consisting of several oscillations of the electric field. By applying a field to the sample we can tune the oscillation frequency from 1.4 to 2.6 THz.

## THz pulses from the creation of polarized e-h pairs

It has been known for some time that terahertz electrical transients can be generated from the surface of many semiconductors, such as Si, GaAs and InP, when the surface is illuminated with a femtosecond laser pulse.[1,2] The effect was originally explained by the acceleration of the photoexcited carriers within the surface depletion field of the semiconductor. The resulting time varying current  $J(t)$  radiates an electromagnetic transient  $E \propto \partial J / \partial t$  that consists of a single cycle of the electric field and contains frequency components up to a few terahertz. Consistent with this explanation in terms of current transport are the observed dependence of the amplitude and polarity of

the radiated field on the strength and polarity of the built-in field[1,2], and also the observed amplitude increase with increasing carrier mobility as inferred from temperature dependent measurements. Recently, a further mechanism in those experiments was proposed in terms of optical rectification and the field-induced second-order nonlinear susceptibility  $\chi^{(2)}$ , that is equally well capable of explaining many of the above observations made in the generation of THz pulses from semiconductor surfaces.[3] The latter explanation does not involve current transport but instead is based on the photoexcitation of electrons and holes in the depletion field into states in which they are already polarized. This creates apolarization  $P$  that grows with the integrated pulse energy, and hence radiates an electrical transient according to  $E \propto \partial^2 P / \partial t^2$ . In quantum wells, current transport at low temperatures is strongly inhibited in the direction perpendicular to the layers, allowing us to prove that the creation of polarized electron-hole pairs can be a source of THz radiation.[4] In Fig.1 we

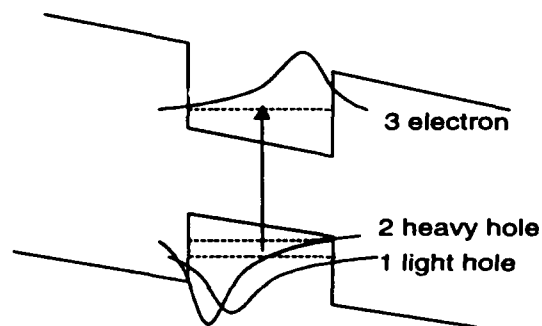


Fig. 1. Wavefunction envelopes of the electron, lh and hh in a quantum well biased with an electric field.

schematically draw the electron and hole envelope wavefunctions in a biased quantum well. The wavefunctions of the electron and hole(s) are spatially displaced, resulting in a dipole moment  $\mu$  after optical excitation. Our sample consists of 82 periods of 145 Å thick GaAs wells, separated by 102 Å  $\text{Al}_{0.3}\text{Ga}_{0.7}\text{As}$  barriers on a Si doped substrate. A field perpendicular to the quantum wells can be applied through a semi-transparent chromium Schottky contact on top. In the experiment, a 80 fs pulse from a modelocked Ti:sapphire laser resonantly excites the exciton transitions in the sample. The detected THz waveforms as a function of field in the sample are plotted in Fig. 2.

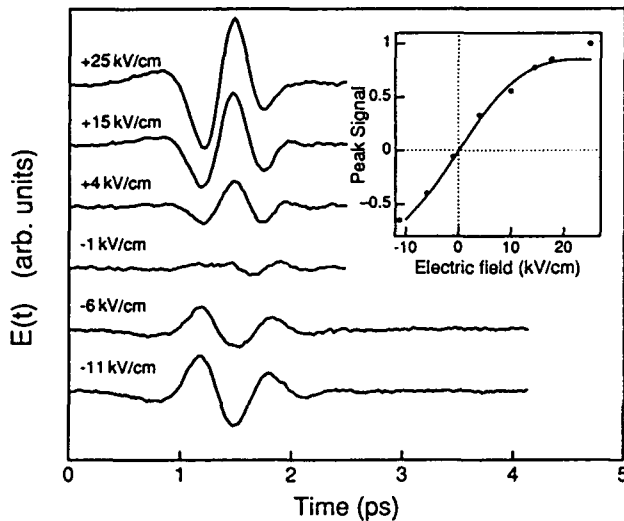


Fig. 2. Measured THz waveforms from the quantum wells at 77 K for several field strengths. The inset shows the peak amplitude of the waveforms (in arb. units) as a function of field strength in the quantum wells.

We can see that for decreasing positive field strengths the signal decreases until it becomes almost zero when the built-in field is nearly canceled. This suggests that contributions to the THz signal that are not field-induced are small.

For negative field strengths, the amplitude increases again but this time the polarity of the signal is reversed. Because transport current is strongly inhibited by the  $\text{AlGaAs}$  barriers at 77 K, we can reach flatband and even apply moderately large forward bias (negative) fields. We can eliminate transient transport currents as the source of THz radiation in our data by the following arguments: There are two contributions to the transport current in a quantum well: thermionic emission and tunneling through the barriers. Carrier sweep out times from quantum wells have been measured in a  $\text{GaAs}/\text{Al}_{0.2}\text{Ga}_{0.8}\text{As}$  quantum well structure with 65 Å barriers.[5] They deduced a tunneling time of a few hundred picoseconds for carrier tunneling at field

strengths comparable to ours. This implies that transport current by carrier tunneling in our sample (which has thicker and higher barriers) will be at least 100 times lower than in bulk GaAs. They also showed that below 100 K, thermionic emission from quantum wells, with a barrier height comparable to ours, is negligible compared to the tunneling current. At a sample temperature of 77 K we can therefore safely assume that current transport by thermionic emission is not a significant source of THz radiation in our experiment.

The above arguments confirm that transport current in our quantum wells is at least 100 times lower than in bulk GaAs. However, the THz signal amplitude at 15 kV/cm is down by only a factor of two compared to the measured signal amplitude generated in bulk GaAs at the same temperature. We therefore conclude that the generation of THz pulses from quantum wells is caused by the creation of polarized electron-hole pairs only. The dependence of the generated peak amplitude of the THz radiation on the applied electric field is shown in the inset of Fig. 3. Initially, the amplitude rises linearly with field, but shows saturation for higher fields. There are two reasons for this: First, the barriers prevent the dipole moment from growing linearly with electric field. Second, the oscillator strength of the transition decreases as the electron and hole wavefunctions are pulled apart.

### Oscillatory THz radiation from the coherent excitation of LH and HH excitons

In the previous section the broad exciton linewidths in the sample prevented us from seeing effects of the simultaneous excitation of the lh and hh excitons. This is probably caused by the large number of wells (82) in that sample. The well to well thickness variations give rise to inhomogeneous broadening of the exciton transitions. For a smaller number of wells the inhomogeneous broadening will therefore be reduced and we may expect to see effects from the coherent excitation of both lh and hh excitons.[6] The new sample is a metal-i-n Schottky diode with a multiple quantum well (MQW) in the intrinsic region. The MQW consists of only 15 periods of 175 Å GaAs wells, separated by 150 Å  $\text{Al}_{0.3}\text{Ga}_{0.7}\text{As}$  barriers with a 50 Å semi-transparent chromium contact on top. We can control the electric field in the sample by applying a voltage between the Schottky contact and the doped substrate. The lh-hh splitting as a function of electric field is taken from the measurement of photocurrent spectra at 4 K. Both the lh and the hh envelope states of the quantum well in an electric field are sketched in Figure 1.

Detected THz waveforms as a function of electric field in the sample are shown in Fig. 3. Immediately apparent



in Fig. 3 is the oscillatory tail of the signal when the laser overlaps both the lh and hh excitons at 1.527 eV. The oscillatory part of the signal, that follows an initial single cycle discussed in the previous section, has a frequency that increases with electric field. The frequency of the oscillations changes from 1.4 THz at flatband to almost 2.6 THz at the highest electric field.

This can be seen more clearly when we calculate the Fourier transforms of just these oscillations as shown in the inset of Fig. 3. To our knowledge this system constitutes the first tunable terahertz emitter. The measured frequencies agree very well with the lh-hh splitting as measured in photocurrent spectra and dephase within a few picoseconds. The oscillatory tail is

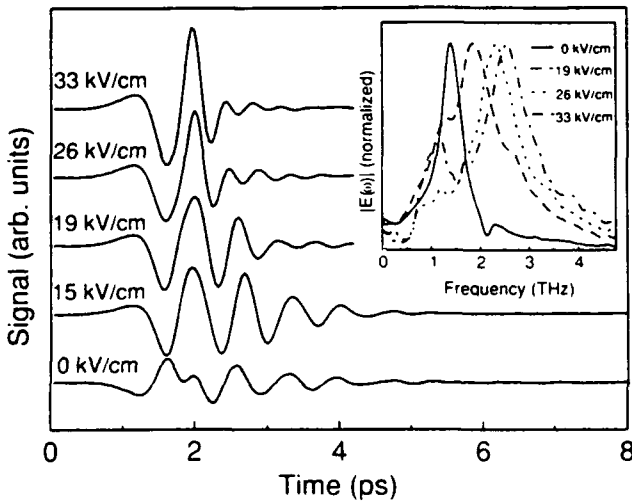


Fig. 3 Measured THz waveforms at 10 K for several electric fields in the MQW. The laser is tuned to the lh and hh excitons. The inset shows the Fourier transforms of only the oscillatory part of the signal.

only present when we excite both the lh and hh excitons. Interestingly, the oscillations are still strongly present at flatband when there is no electric field in the sample. The origin of the terahertz radiation is that in an electric field, a coherent superposition of the hh and lh excitons leads to charge oscillations in the well at the lh-hh splitting frequency.

This can be seen from the following: For simplicity we concentrate on the induced far-IR polarization in the  $z$ -direction. This polarization can be written in the three-band model (Fig. 4) using a density-matrix formulation as

$$P(t) = \frac{e\ell}{V} \sum_k [(z_{11} - z_{33})\rho_{11} + (z_{22} - z_{33})\rho_{22} + 2\text{Re}(z_{12}\rho_{12})]$$

where the self-dipole moments are defined as  $z_{11} = \langle lh|z|lh \rangle$ ,  $z_{22} = \langle hh|z|hh \rangle$ , and  $z_{33} = \langle e|z|e \rangle$ , and

the intersubband transition dipole moment as  $z_{12} = \langle lh|z|hh \rangle$ .  $\rho_{11}$  is the generated lh density,  $\rho_{22}$  the generated hh density and  $\rho_{12}$  the coherence between the hh and lh states. In equation (1),  $(z_{11} - z_{33})$  and  $(z_{22} - z_{33})$  are the net displacements between the lh and the electron, and between the hh and the electron, respectively. The last term in equation (1),  $z_{12}\rho_{12}(t)$ , is proportional to  $e^{i(\omega_2 - \omega_1)t}$ , with  $\hbar(\omega_2 - \omega_1)$  the hh-lh energy splitting, and is responsible for the charge oscillations. The radiated electric field is  $E(t) \propto \partial^2 P / \partial t^2$ , and contains both the initial transient due to the creation of polarized electron-hole pairs[3] and the oscillatory tail  $\propto \cos(\omega_1 - \omega_2)t$  caused by the charge oscillations. We can therefore expect to see terahertz radiation as long as there is a nonvanishing transition dipole moment  $z_{12}$ .

### Acknowledgments

We would like to acknowledge the assistance of G. E. Doran and B. Tell in the fabrication of the photoconducting antenna used in the experiments and thank D. A. B. Miller, J. Shah, and D. S. Kim for valuable discussions. The work at the University of Illinois was supported by the Office of Naval Research under grant (N00014-90-J-1821) and the supercomputer time was supported by the National Center for Supercomputing Applications at the University of Illinois.

### References

1. X.-C. Zhang, B. B. Hu, J. T. Darrow, and D. H. Auston, *Appl. Phys. Lett.* **56**, 1011 (1990).
2. X.-C. Zhang, J. T. Darrow, B. B. Hu, D. H. Auston, M. T. Schmidt, P. Tham, and E. S. Yang, *Appl. Phys. Lett.* **56**, 2228 (1990).
3. S. L. Chuang, S. Schmitt-Rink, B. I. Greene, P. N. Saeta, and A. F. J. Levi, *Phys. Rev. Lett.* **68**, 102 (1992).
4. P. C. M. Planken, M. C. Nuss, W. H. Knox, D. A. B. Miller, and K. W. Goossen, *Appl. Phys. Lett.* **61**, 2009 (1992).
5. A. M. Fox, D. A. B. Miller, G. Livescu, J. E. Cunningham, and W. Y. Jan, *IEEE J. Quantum Electr.*, **QE-27**, 2281 (1991).
6. P. C. M. Planken, M. C. Nuss, I. Brener, K. W. Goossen, M. S. C. Luo, S. L. Chuang, and L. Pfeiffer, *Phys. Rev. Lett.* **69**, 3800 (1992).

# Generation and Application of High-Power, 500 fs Electromagnetic Pulses

D. R. Dykaar

*AT&T Bell Laboratories, Murray Hill, New Jersey 07974-2070*

D. You, R. R. Jones, and P. H. Bucksbaum

*Physics Department, University of Michigan, Ann Arbor, Michigan 48109-1120*

## Abstract

We have generated sub-single-cycle pulses of electromagnetic radiation with pulse energies of up to  $0.8 \mu\text{J}$  and pulse lengths shorter than 500 fsec.

The transmitter is a GaAs wafer illuminated at normal incidence by 120 fsec, 770 nm pulses from a Ti:Sapphire chirped-pulse amplifier system, while a pulsed electric field is applied across the surface. The generated pulses are used to study FIR radiation from an  $\langle 111 \rangle$  InP wafer in an external bias field. The results can be explained by radiation from nonlinear polarizations.

Picosecond and sub-picosecond far-infrared (FIR) electromagnetic pulses have been generated using a number of optical switching techniques.[1-4] Most interesting for high power applications is the planar photoconductor which produces coherent FIR radiation in the directions of optical specular reflection and transmission when illuminated with ultrashort laser pulses.[4] Both GaAs and InP wafers have been used for this purpose.

## Introduction

The FIR energy reported to date have been quite low (50 nJ or less),[5] so that the pulses have only been used to study linear absorption spectroscopy.[6] In this paper, we report scaling these pulses to high energy ( $0.8 \mu\text{J}$ ) while maintaining both high bandwidth and short pulse duration (450 fsec). The megawatt peak power can be used in nonlinear optics and

multiphoton spectroscopy.[7] We demonstrate focused peak fields in excess of  $150 \text{ kV/cm}$ . We demonstrate saturation of the FIR energy with laser fluence. The maximum radiation is produced with a laser fluence of only  $40 \mu\text{J/cm}^2$ .

A significant amount of effort has been devoted to the theoretical study of the FIR radiation. Two models are currently being used to explain this phenomenon. In the first model[4], the FIR radiation is produced by transient photocarriers generated by the laser pulses and accelerated either by an external bias field or the internal depletion field. In the second model [8], field induced optical rectification is proposed to account for the dependence of the FIR radiation on the crystallographic orientation. Both models have successfully explained some previous experimental results for unbiased semiconductor wafers [8]. However, FIR radiation from biased wafers has not been fully investigated.

We use the FIR pulses from the GaAs as bias field for the InP wafer. The observed FIR radiation from InP can be explained as radiation from nonlinear polarizations induced by the laser field and bias field.

## Generation of High Power FIR pulses

GaAs  $\langle 100 \rangle$  wafers are used to generate high power FIR pulses. A Ti:sapphire chirped-pulse amplifier,[9] is used to produce 120 fsec pulses at 770 nm, with a repetition rate of 10 Hz. Its output is split into two parts. The first part is used to illuminate the GaAs wafer. The second part is used to pump a  $\langle 111 \rangle$  InP wafer.

Aluminum electrodes 1 cm apart are connected to the GaAs wafer with silver paint to provide a bias field in the surface plane. To reduce arcing the electrodes are attached to opposite faces. The bias field is applied in a slow (50  $\mu$ sec) pulse provided by an automotive spark coil synchronized with the laser. The laser beam is expanded to illuminate the wafer as well as the electrodes to obtain efficient FIR generation. Radiation is observed in both transmitted and reflected directions with comparable amplitudes, but usually only the transmitted radiation is used.

The FIR pulse energy is measured with a helium cooled bolometer (Infrared Laboratories) or a room temperature pyroelectric detector (Molelectron Detector, Inc., model P1-42cc). The pyroelectric detector is 300 times less sensitive than the bolometer, but has a substantially higher saturation fluence.

The FIR spectrum of our pulses is measured using an interferometer.[10] Typical interferograms measured with the bolometer (Fig. 1) are 600 fsec wide, independent of the laser intensity, laser polarization and bias field. For a  $\langle 100 \rangle$  crystal (GaAs) the second order polarization is perpendicular to the crystal surface, and therefore doesn't contribute to forward radiation so the various relational dependences are not observed. The Fourier transform of the interferogram yields a spectral width of 1 THz (see inset in Fig. 1).

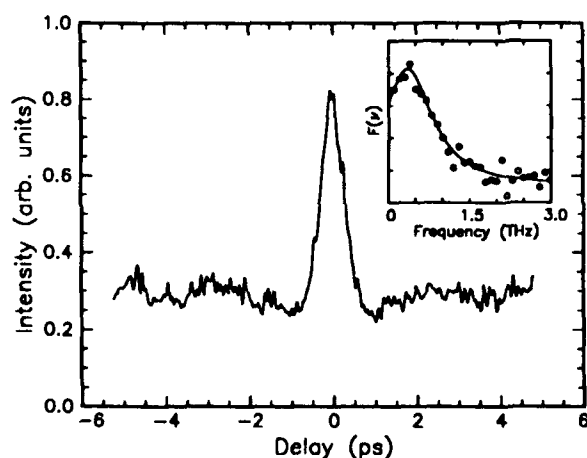


Figure 1. Interferogram obtained by collecting the total FIR energy transmitted through the analyzing polarizer as a function of delay in one leg of the interferometer. Inset: Spectrum  $F(v)$  of the FIR pulses obtained from the interferogram.

We have examined the FIR pulse energy for different intensities and polarizations of the illuminating laser beam. We find no dependence on laser polarization, but there is a nonmonotonic

dependence of the FIR energy on laser fluence. As shown in Fig. 2, at low bias fields ( $E < 4$  kV/cm) the maximum FIR pulse energy occurs for the largest laser fluence, and there is no clear evidence of saturation, even at the highest laser fluence of 2 mJ/cm<sup>2</sup>. This is consistent with previously observed results.[4]

At high bias fields, however, the maximum energy occurs at a laser fluence of 40  $\mu$ J/cm<sup>2</sup>. The mechanism for this saturation is not understood.

The maximum FIR pulse energy is obtained from a 3.5x3.5 cm<sup>2</sup> GaAs wafer biased with an external field of 10.7 kV/cm. A 425 mV signal is observed from the pyroelectric detector, whose responsivity is 490 mV/ $\mu$ J. This corresponds to 0.8  $\mu$ J of FIR energy.

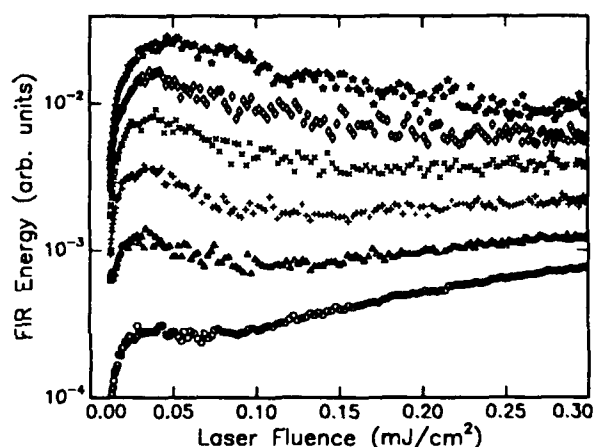


Figure 2. Generated FIR energy as a function of pump laser fluence for selected bias fields.  $\circ$ : 1.5 kV/cm;  $\Delta$ : 3.0 kV/cm;  $+$ : 4.5 kV/cm;  $\times$ : 6 kV/cm;  $\diamond$ : 7.5 kV/cm;  $\star$ : 9 kV/cm. Note that for large bias fields there is a pronounced maximum in the FIR generation at a relatively low laser fluence.

### Application of High Power FIR Pulses

The FIR pulses from the GaAs wafer are focused by a 10 cm paraboloidal mirror into a 4 mm spot and projected on the front surface of the InP wafer as a transient bias field. The FIR radiation from the InP wafer is measured in the transmitted direction. A spatial filter is placed behind the InP to eliminate the transmitted FIR produced by the GaAs. A 25 cm spherical mirror is used to focus the FIR signals from the InP into the bolometer. The dependence of the FIR energy on the crystallographic orientation is studied in this configuration.

The FIR pulses from the InP are also characterized with the interferometer. For an

unbiased InP the measured pulse length is as short as 130 fsec, which is close to the duration of the laser pulse. This is identified as optical rectification.[11] When a bias field is applied the measured pulse width is 280 fsec. This suggests the a different mechanism which we believe is the radiation from transient current. Because the radiation from the transient photocarriers has a much longer time scale and does not depend on the crystallographic orientation, its effect may be approximated by adding a constant to the radiated energy.

FIR energy is recorded, when the bias field is applied, as the laser field is slowly rotated in the semiconductor surface. The data show a 2-fold variation as a function of the angle between the crystal axis and the bias field. This can be explained as due to the superposition of second order and third order nonlinear polarizations  $\overline{P}^{(2)}$  and  $\overline{P}^{(3)}$ . Since the radiated FIR field is proportional to  $\overline{P} = \overline{P}^{(2)} + \overline{P}^{(3)}$ , the FIR energy can be expressed as,

$$E \sim A + \frac{1}{9} [\chi^{(2)}]^2 E(\omega) E^*(\omega) + 36 [\chi^{(3)}]^2 E^2(0) E(\omega) E^*(\omega) + \frac{24}{\sqrt{6}} \chi^{(2)} \chi^{(3)} E(0) E(\omega) E^*(\omega) \cos(2\theta + \alpha)$$

where  $\chi^{(2)}$  and  $\chi^{(3)}$  are the second and third order nonlinear susceptibilities respectively,  $E(\omega) E^*(\omega)$  is the laser field,  $\theta$  is the angle between the laser field and  $(1\ 1\ 2)$ , and  $\alpha$  is the angle between  $(1\ 1\ 2)$  and the bias field,  $E(0)$ . The term,  $A$ , is included to account for the radiation from transient current. We have scanned the polarization of the laser field for fixed  $\alpha$  (Fig.3). There is good agreement between the data and our calculation.

In addition the data of Fig. 3 shows a higher (6-fold) symmetry which may be due to a higher order optical nonlinearity. The carrier contribution,  $A$ , is the only term that does not explicitly depend on the optical field, so it should be possible to *temporally* distinguish between the coherent (short time) and carrier (longer time) contributions.

## Conclusion

In conclusion, we have generated high energy FIR pulses of 0.8  $\mu$ J and 450 fsec pulse width. Its application to InP has verified radiation from

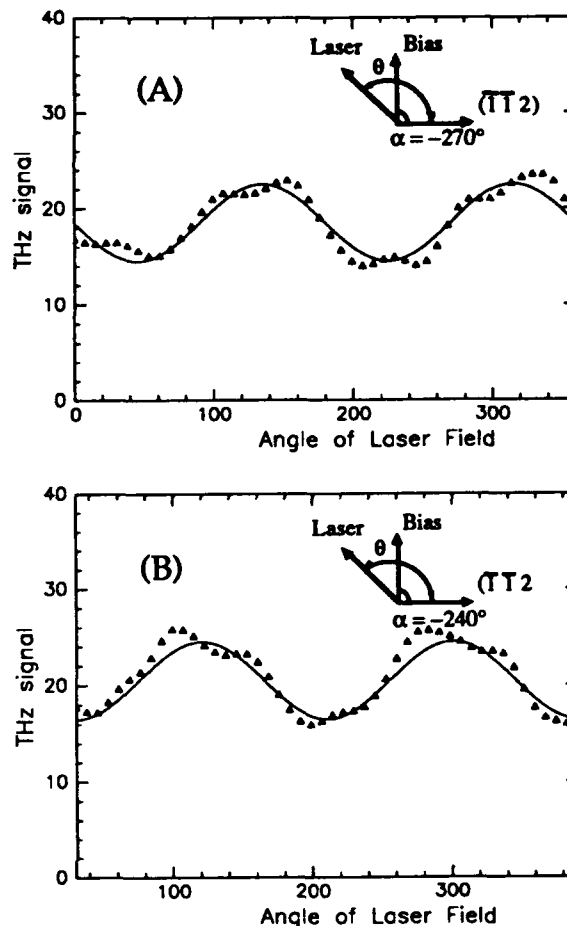


Figure 3. FIR energy as a function of the direction of laser field for (A)  $\alpha = -270$  and (B)  $\alpha = -240$ .

nonlinear polarization induced by both the incident optical field and transient bias field.

## Acknowledgment

This research is supported by the National Science Foundation.

## REFERENCES

1. G. Mourou, C. V. Stancampiano, A. Antonetti, and A. Orszag, *Appl. Phys. Lett.* **39**, 295 (1981).
2. D. H. Auston, K. P. Cheung, and P. R. Smith, *Appl. Phys. Lett.* **45**, 284 (1984).
3. Ch. Fattinger, and D. Grischkowsky, *Appl. Phys. Lett.* **53**, 1480 (1988).

4. Justin T. Darrow, Xi-Cheng Zhang, David J. Auston, *IEEE J. Quantum Electron.* **28**, 1607 (1992).
5. B. I. Greene, P. N. Saeta, D. R. Dykaar, S. Schmidt-Rink, and S. L. Chuang, *IEEE J. Quantum Electron.* **28**, 2302 (1992).
6. D. Grischkowsky, Soren Keiding, Martin van Exter, and Ch. Fattinger, *J. Opt. Soc. Am.B* **7**, 2006 (1992).
7. R. R. Jones, D. You, and P. H. Bucksbaum, Submitted to *Phys. Rev. Lett.* (1992).
8. S. L. Chuang, S. Schmitt-Rink, B. I. Greene, and A. F. J. Levi, *Phys. Rev. Lett.* **68**, 102 (1991).
9. J. Squier, F. Salin, G. Mourou, and D. Harter, *Opt. Lett.* **16**, 324 (1991).
10. B. I. Greene, J. F. Federici, D. R. Dykaar, R. R. Jones, and P. H. Bucksbaum, *Appl. Phys. Lett.* **59**, 893 (1991).
11. X. -C. Zhang, Y. Jin, K. Yang, and L. J. Schowalter, *Phys. Rev. Lett.* **69**, 2303 (1992).

# All-Electronic Generation of Sub-Picosecond Shock-Waves and Their Application to a Terahertz Spectroscopy System

Jeffrey S. Bostak, Daniel W. Van Der Weide, Ikuro Aoki, Bertram A. Auld, and David M. Bloom

*Edward L. Ginzton Laboratory, Stanford University, Stanford, California 94305*

## Abstract

We have developed electronic circuits that generate and detect subpicosecond shock-waves. We have used these circuits with integrated antennas in a system capable of free space spectroscopy with greater than 10 dB signal to noise from 5 GHz to 1 THz. This system was used to characterize a sub-millimeter wave filter from 6.4 GHz to 1 THz. In particular, 250-375 GHz measurements are demonstrated with 2 dB accuracy over a 20 dB dynamic range.

## Introduction

In the study and application of picosecond electromagnetic pulse propagation, generation and detection of these pulses is usually done with ultrashort optical pulses driving photoconductive switches which are used both as transient generators and samplers.<sup>1,2</sup> These systems have been applied to problems in THz spectroscopy. Fourier analysis of the detected pulses, with and without a test sample in the beam path, yields the magnitude and phase of the transmission of the sample as a function of frequency.

In contrast to this hybrid optical/electronic approach, we have developed an all-electronic system using monolithic nonlinear transmission lines (NLTLs) as ultrafast voltage step generators for both generating picosecond pulses and driving monolithically integrated diode samplers for detection of these pulses. Advantages of this approach lie in its relative simplicity and robustness. Recently, similar all-electronic systems have been applied to THz spectroscopy, but have been limited to frequencies below 250 GHz<sup>3</sup>. We have used our system to perform spectroscopic measurements from 250 to 375 GHz with 2 dB accuracy over a 20 dB

dynamic range. We have also demonstrated measurements up to 1 THz with 10 dB signal to noise ratio.

## Nonlinear Transmission Lines

Nonlinear transmission lines are synthetic structures of series inductors (approximated by sections of high-impedance transmission line) with varactor diodes periodically placed as shunt elements. On this structure a voltage shock-wave develops from a sinusoidal input because the propagation velocity varies with the nonlinear capacitance-voltage relationship of the diodes,  $v_p = 1/\sqrt{LC_{tot}(V)}$ ,

where  $L$  is the inductance and  $C_{tot}(V)$  the sum of the varactor and parasitic capacitance of the line, all per unit length. Limitations of the NLTL arise from its periodic cutoff

frequency,  $\omega_{per} = 2/\sqrt{LC_{tot}(V)}$ , waveguide dispersion, interconnect metallization losses, and diode resistive losses.

## Measurement of Subpicosecond Fall-Time

To make the measurement shown in Fig. 1, we packaged a monolithic NLTL/sampler chip<sup>4</sup> and shorted the test port of the sampler with a gold bond ribbon to get a known broadband termination. While the short distorts the back edge of the pulse, it does not affect the initial falling edge. At room temperature, we measured a ~1 V, 1.8 ps fall time with a +25 dBm, 6.56 GHz input. Test port and strobe inputs to the sampler were offset by 0.5 Hz by splitting the output of a signal source and running the strobe arm through a rotating phase shifter to allow the sampled waveform to be traced out in equivalent time and viewed on an oscilloscope. We then

lowered the packaged assembly into a dewar flask of liquid nitrogen. Steady improvement in both amplitude and fall time was noted until the packaged circuit was completely immersed, resulting in a minimum fall time of 880 fs with a 3.5 V amplitude. The liquid nitrogen does not significantly load the circuits because its relative permittivity is low,  $\epsilon_r = 1.4$ . A root-sum-squares deconvolution of the measured fall time with the sampler aperture time (assuming that the two times are equal) gives 620 fs. This means that the -3 dB bandwidth of the sampling bridge is  $\sim 560$  GHz. It also indicates that the periodic cutoff frequency  $\omega_c = 2/\sqrt{LC_{tot}}(V)$  ( $\geq 2\pi \times 500$  GHz for circuits described here) is now a significant limitation to circuit performance.

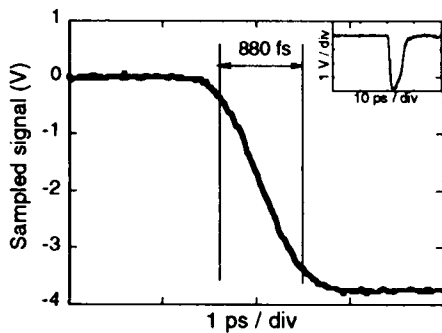


Figure 1. An 880 fs measured fall time shock-wave generated on a nonlinear transmission line and measured by an on-chip sampler at  $T=77$  K. The inset is a quarter period of the waveform.

### Applications to a Free Space Transmission System

We have applied the ultrafast pulse generating capability of the NLTL to drive antennas and a sampler in a coherent, all-electronic free-space signal generation system of Fig. 2, which is described in more detail elsewhere.<sup>5,6,7</sup> In addition to the increased spectral content of the driving NLTL's due to cryogenic operation, we made other improvements to our earlier published work on this system. We used integrated magnetic dipole (slot) antennas measuring  $5 \mu\text{m}$  wide and  $190 \mu\text{m}$  long, resonant at  $\sim 330$  GHz due to length foreshortening. We also used high resistivity ( $10 \text{ k}\Omega \text{ cm}$ ) silicon hyper-hemispheres<sup>8</sup> to collect and focus the quasi-optical beam. Finally, we chopped the signal with a PIN diode modulator to avoid spurious electrical reflections from a mechanical chopper. With this improved system we produced the freely propagating THz pulse shown in Fig. 3. This waveform has ringing associated with the resonance of the antennas and its shape was well-predicted by scale modeling.

By blocking the beam, we could determine the useful spectral range of the system. The Fourier transform of the time-domain signal detected under both conditions is shown in Fig. 4 and indicates measurable radiation beyond 3 THz. The distance between the system generator and detector is 48 cm.

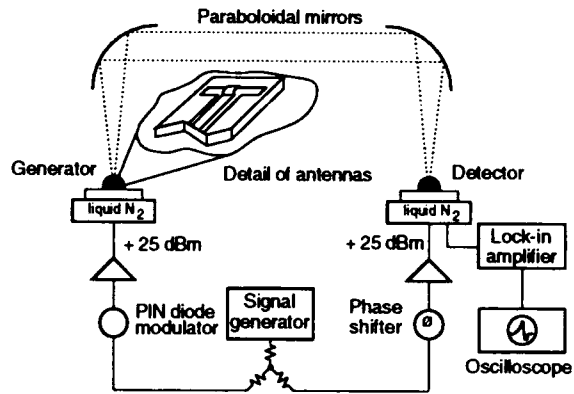


Figure 2. Diagram of THz signal generation/detection system. Inset shows detail of the magnetic dipole (slot) antennas.

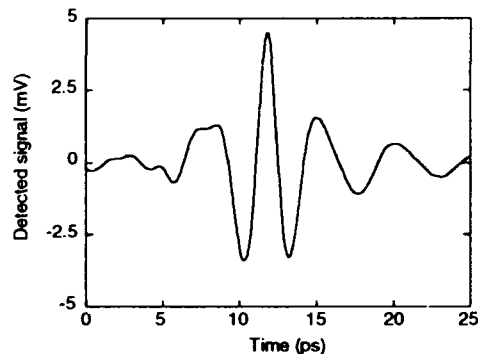


Figure 3. Detail of time-domain response of THz signal generation system.

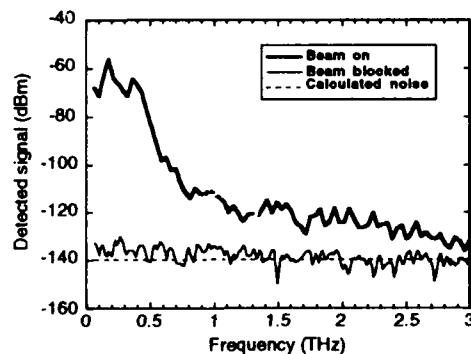


Figure 4. Frequency-domain response of THz signal generation system, both with and without beam blocked. The spectrum is not continuous: individual frequency points are connected by a line as a guide to the eye.

## Free Space Spectroscopy

### Description

To improve the system, the single signal generator and mechanical phase shifter were replaced with two microwave synthesizers which were phase locked and offset in frequency by 5 Hz. This step eliminated any harmonic distortion due to the mechanical phase shifter and allowed operation at a higher intermediate frequency<sup>9</sup>, moving the measurement further away from low frequency phase noise. Also, the PIN diode modulator and lock-in amplifier were eliminated. Although lock-in detection does offer very low noise amplification (cf. Figure 4 and Figure 6), it can degrade the slew rate of fast signals with high dynamic range<sup>10</sup>. The oscilloscope was replaced with a Stanford Research Systems SR760 FFT Spectrum Analyzer, which directly computes Fourier spectra of signals with 90 dB dynamic range. Finally, room temperature operation was selected because of the ease of making repeatable measurements. The improved system is shown in Figure 5.

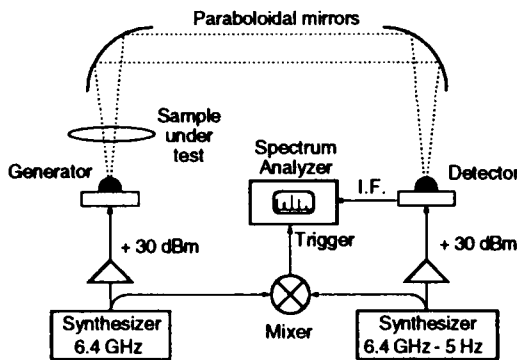


Figure 5 Diagram of THz free space spectroscopy system.

To perform a free space spectroscopic measurement, a sub-millimeter wave filter under test can be placed in the THz beam. By taking the ratio of the detected signal spectrum with and without the filter in place, the transmission of the filter as a function of frequency can be obtained. Because the system detects voltage, not power, both the magnitude and phase of the transmission can theoretically be obtained. So far, however, we have only used the system to obtain transmission magnitude.

In this experiment, the filter under test was a multiple bandpass filter. Because the filter was small, it was placed close to the transmitter, where the beam diameter is smallest. The manufacturer<sup>11</sup> had used a backward-wave oscillator spectrometer to characterize the magnitude of the filter transmission

magnitude from 235 to 390 GHz. The filter's passbands were measured by the manufacturer to be centered around 279 and 348 GHz. It was our goal first to characterize the filter in the 235 to 390 GHz region as the manufacturer had done, and second, to characterize the filter at still higher frequencies up to the terahertz regime.

### Results

A comparison of the manufacturer's measurement to ours is shown in Figure 6. Compared with the data provided by the manufacturer, our data is accurate within 2 dB over a 20 dB dynamic range from -7 to -27 dB transmittance. Below -27 dB transmittance, our system was not capable of accurately reproducing the manufacturer's data. We can attribute limitation to a lower dynamic range in our system. One way to improve the dynamic range would be to use broadband antennas. The magnetic dipole antennas currently used are resonant antennas and have a radiation resistance that is a strong function of frequency. A second way to improve the dynamic range of the system would be to reduce the effects of phase noise on the measurement results. This could be accomplished by using synthesizers with less phase noise. Alternatively, the intermediate frequency could be increased so that the downconverted harmonics are spaced further apart in frequency and are less susceptible to the phase noise of adjacent harmonics.

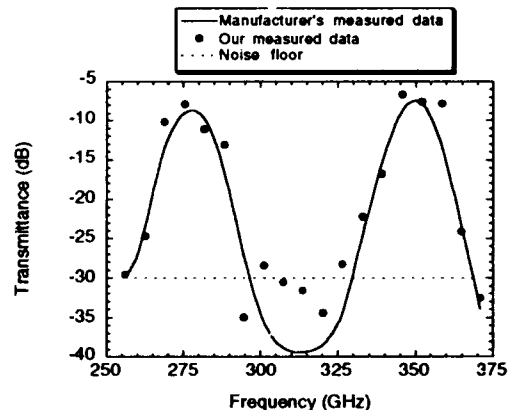


Figure 6. Manufacturer data and measured data for sub-mm wave filter.

Figure 7 shows data from a measurement that spans the frequency range from 6.4 GHz to 1 THz. Here we plot separately the foreground (detected signal with no filter in place), the radiation with the filter in place, and the background (detected signal with beam blocked). The light trace, which represents the foreground radiation, shows the same sort of monotonically decreasing frequency spectrum that was shown in Figure 4. The dark trace, which represents the filter measurement, shows clearly



visible transmission peaks out to 1 THz. This periodic repetition of the signal peaks verifies that the filter is indeed an etalon, and not a simple bandpass filter. If signal-to-noise ratio is calculated as the ratio of foreground signal to background signal, the signal-to-noise is seen to be at least 20 dB over the entire frequency range from 6.4 GHz to 1 THz. A more conservative estimate, which accounts for the effects of phase noise between the two synthesizers, however, is the ratio of detected passband to stopband in the "filter" signal. Still, using this definition, the signal-to-noise is at least 10 dB over the entire frequency range.

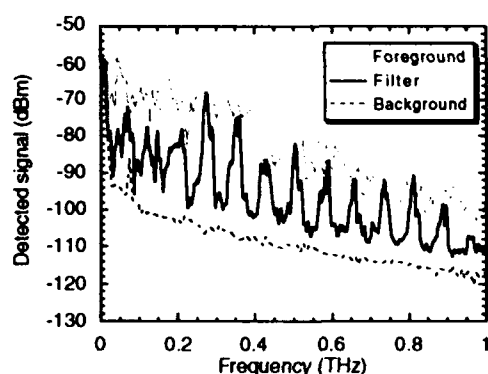


Figure 7 Extended frequency range measured data for sub-mm wave filter.

## Conclusion

We have developed an all-electronic system capable of free space spectroscopy with greater than 20 dB signal to noise from 5 to 375 GHz and greater than 10 dB signal to noise over the full range from 5 GHz to 1 THz. An improved antenna design and microwave source should further improve signal to noise, making this system a compact, useful network analysis tool.

## Acknowledgment

This work is supported by the Joint Services Electronics Program under Contract No. N00014-92-J-1050. J. S. Bostak acknowledges a Joint Services Electronics Program fellowship. The authors wish to thank J. Martin and P. Prather for circuit assembly.

They also acknowledge discussions with M. Rodwell, E. Özbay, and M. Kauffman. Thanks are due to Watkins-Johnson Co. for loans of equipment.

1. P. R. Smith, D. H. Auston, and M. C. Nuss, "Subpicosecond photoconducting dipole antennas," *IEEE J. Quant. Elect.*, **24**, 255-260 (1988).
2. C. Fattinger and D. Grischkowsky, "Terahertz beams," *Appl. Phys. Lett.*, **54**, 490-492 (1989).
3. Y. Konishi, M. Kamegawa, M. Case, R. Yu, M. J. W. Rodwell, and R. A. York, "Picosecond electrical spectroscopy using monolithic GaAs circuits," *Appl. Phys. Lett.*, **61**, 2829-2831 (1992).
4. R.A. Marsland, C.J. Madden, D.W. Van Der Weide, M. S. Shakouri, D.M. Bloom, "Monolithic integrated circuits for mm-wave instrumentation," *IEEE GaAs IC Symp. Tech. Dig.*, **19**, 19-22, (1990).
5. D.W. Van Der Weide, J.S. Bostak, B.A. Auld, and D.M. Bloom, "All-electronic free-space picosecond pulse generation and detection," *Electron. Lett.*, **27**, 1412-1413, (1991).
6. Y. Konishi, M. Kamegawa, M. Case, R. Yu, and M. J. W. Rodwell, "Coherent, broadband millimeter-wave spectroscopy using monolithic GaAs circuits," in *Optical Millimeter-Wave Interactions: Measurements, Generation, Transmission and Control* (IEEE/LEOS, Newport Beach, CA, 1991).
7. D.W. Van Der Weide, J.S. Bostak, B.A. Auld, D.M. Bloom, "All-electronic generation of 880 fs, 3.5 V shockwaves and their application to a 3 THz free-space signal generation system," *Appl. Phys. Lett.*, **62**, 22-24, (1993).
8. N. Katzenellenbogen, et al. "Efficient generation of 380 fs pulses of THz radiation by ultrafast laser pulse excitation of a biased metal-semiconductor interface," *Appl. Phys. Lett.*, **58**, 222-4 (1991).
9. M. J. W. Rodwell, University of California, Santa Barbara, Santa Barbara, CA (personal communication).
10. D. Kruse, Stanford Research Systems, Inc. Sunnyvale, CA (personal communication).
11. Center for Submillimeter Radiophysics, Saint Petersburg, Russia, in cooperation with the Max-Planck-Institut für Festkörperforschung, Stuttgart, West Germany.

## Sub-Picosecond, Terahertz Radiation from High-Intensity Laser Plasmas

H. Hamster, A. Sullivan, S. Gordon, and R. W. Falcone

*Physics Department, University of California, Berkeley, California 94720*

W. White

*Lawrence Livermore National Laboratory, Livermore, California 94550*

### **Abstract**

Laser pulses with terawatt intensities and 100 femtosecond duration are focused onto gas and solid targets. Strong emission of coherent Terahertz radiation is observed.

Ponderomotive forces generated in the focus of an intense laser pulse in a plasma are sufficient to create a very large density difference between ionic and electronic charges. An ultrashort laser pulse can be used to excite the laser plasma and is expected to produce a powerful electromagnetic transient.<sup>1</sup> Here we report the observation of this effect.

We have focused 120 fs laser pulses<sup>2</sup> with intensities  $> 10^{18}$  W/cm<sup>2</sup> on gases and solids. A liquid helium cooled bolometer is used in conjunction with a Fourier transform spectrometer to characterize the emitted far infrared radiation (FIR). We observe a strong resonant

enhancement of the radiation if the plasma frequency is close to the inverse pulse length of the laser. At these plasma densities, the emission extends over several cycles of a plasma oscillation. The Terahertz pulse is polarized and has a frequency equal to the plasma frequency. The emission frequency can simply be tuned by changing the pressure in the target chamber and hence changing the plasma frequency. For non-resonant excitation of the plasma at high densities ( $\geq 10^{18}$  cm<sup>-3</sup>) we observe the emission of an approximately half-cycle electromagnetic wave form with a width of 0.4 ps and a frequency centered around 1.5 THz (Fig. 1).

We have performed an optical gating experiment using an GaAs wafer as a transient mirror illuminated by a femtosecond optical pulse. This confirms that the radiation is emitted in less than 0.8 ps.

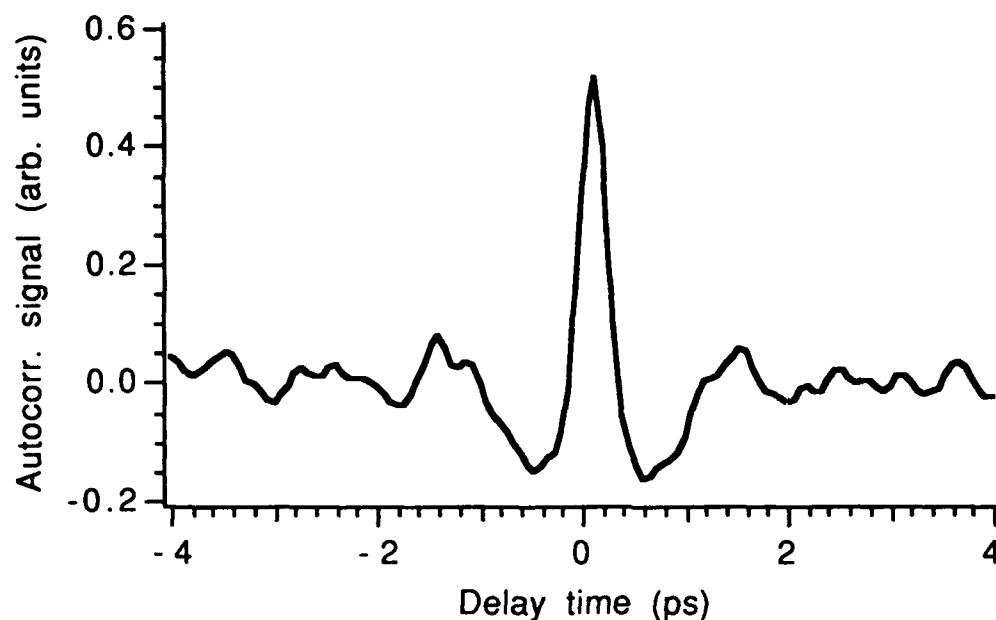


Figure 1: Autocorrelation of the emitted THz signal under non-resonant excitation. The plasma density is  $2 \times 10^{19} \text{ cm}^{-3}$ .

The strongest FIR signal is observed from a solid density plasma. We observe up to 500 nJ on a pyroelectric detector. For the laser solid interaction, we report a strong correlation between the intensity of the FIR signal, a hard x-ray signal and the emission of MeV electrons. This may allow novel experiments with ultrafast time resolution, cross-correlating beams that simultaneously span the electromagnetic spectrum from meV to MeV energies.

We have developed a linearized hydrodynamic model which accounts for the motion of a cold plasma driven by the strong ponderomotive forces present in the laser

focus. We predict and observe the main emission to be in a direction  $\approx 45$  degrees from the direction of pulse propagation (Fig. 2). For plasma densities below  $10^{18} \text{ cm}^{-3}$  the model is in excellent agreement with the observations, while a more sophisticated model appears to be necessary for high densities.

The emission of a strong FIR radiation indicates the existence of wake fields in excess of  $10^8 \text{ V/cm}$ . The existence of such fields has been predicted previously.<sup>3</sup> This effect promises to be a new source for high power, ultra short pulse far infrared radiation.

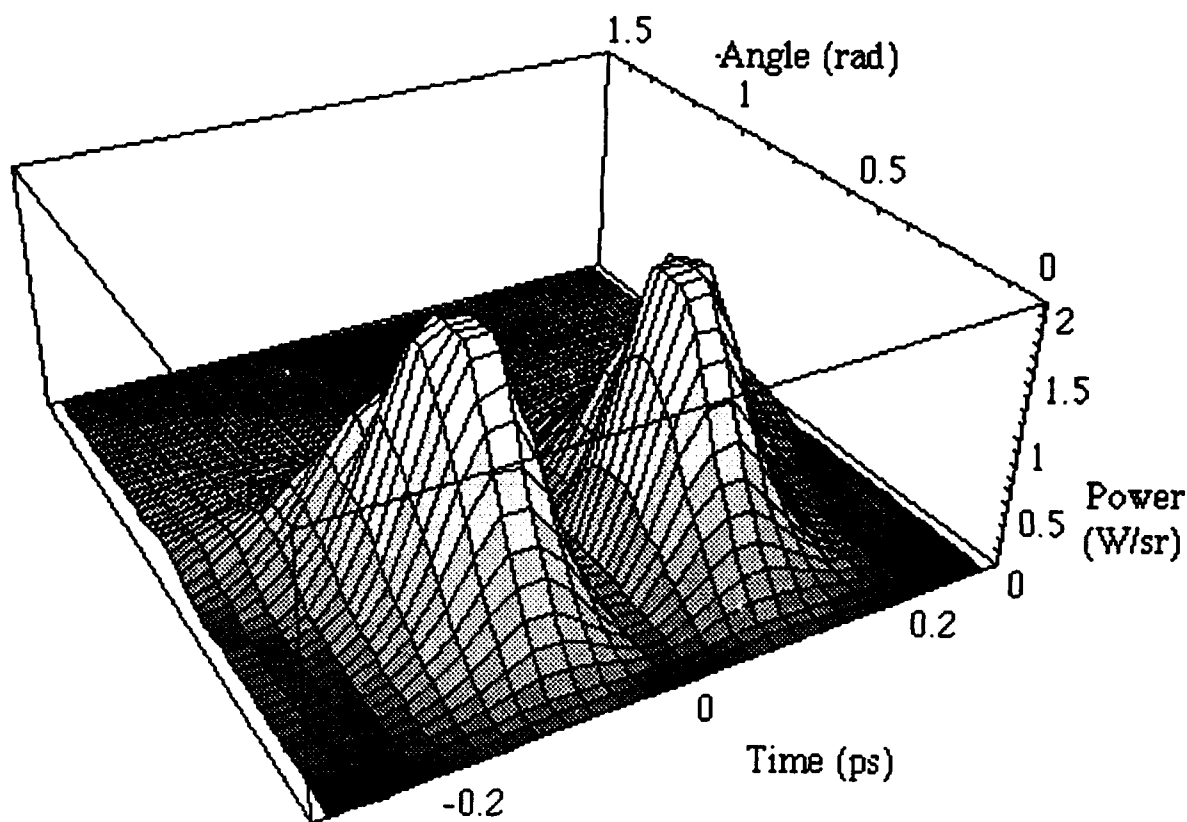


Figure 2: Calculated radiation pattern.

The vertical axis denotes intensity, the bottom axis is time (ps) and the right hand axis is the view angle in degrees from the beam propagation direction. The data is calculated for a plasma density of  $2 \times 10^{19} \text{ cm}^{-3}$ . The pulse length is 0.15 ps, the pulse energy is 20 mJ and the beam diameter 4  $\mu\text{m}$ .

#### REFERENCES

1. H. Hamster, R.W. Falcone, in *Ultrafast Phenomena VII*, C.B. Harris, E.P. Ippen, G. A. Mourou, A. H. Zewail, eds. (Springer-Verlag, Berlin, 1990) pp. 122-124.
2. A. Sullivan, H. Hamster, H.C. Kapteyn, S. Gordon, W. White, H. Nathel, R.J. Blair, R.W. Falcone, *Opt. Lett.* **16**, 1406 (1991).
3. P. Sprangle, E. Esarey, A. Ting, *Phys. Rev. Lett.* **64**, 2011 (1990); S. Wilks, W. Kruer, M. Tabak, A. Langdon : *Phys. Rev. Lett.* **69**, 1383 (1992).

# Intense THz Beam from Organic Electro-Optic Materials

X. -C. Zhang and T. -M. Lu

*Physics Department, Rensselaer Polytechnic Institute, Troy, New York 12180-3590*

C. P. Yakymyshyn

*General Electric Research and Development Center, 1 River Road, Schenectady, New York 12301*

## Abstract

We report THz optical rectification from organic electro-optic crystals. The magnitude of the rectified field from an organic salt is one and two orders larger than that from GaAs and LiTaO<sub>3</sub>, respectively.

## Introduction

In recent years different photonic and optoelectronic techniques have been used to generate THz bandwidth free space radiation [1-5]. Optical rectification is one technique used for generating subpicosecond submillimeter-wave radiation [6]. Developing new radiation sources will have a substantial impact on high-speed, broadband characterization of dielectric materials. We extend previous work on generating free space pulsed THz radiation, and report the observations of efficient optical rectification and sub-millimeter wave generation by an organic electro-optic crystal.

## Experiment

The organic crystal we used is Dimethyl Amino 4-N-Methylstilbazolium Tosylate (DAST), which is a member of the Stilbazolium salt family [7].

Under appropriate conditions, DAST crystallizes in the acentric monoclinic Cc space group, point group m (standard

orientation). In this crystalline form the chromophores align in a herringbone motif with a 20° half-angle from the crystallographic a axis, resulting in a well-aligned polar molecular packing. Powder second harmonic generation efficiency 1000 times that of an Urea reference standard at a fundamental wavelength of 1.9  $\mu$ m was reported. Electro-optic measurements at 820 nm resulted in a Pockels coefficient of  $r_{11} > 400$  pm/V [7,8] and Maker fringe measurements at 1.905  $\mu$ m provided  $d_{11} = 600 \pm 100$  pm/V. Crystals of DAST were grown by slow evaporation of saturated methanol solutions. Crystal plates as large as 6 x 8 x 1.5 mm with shiny facets and dark red color in transmitted light were grown from solution over several weeks. Typical DAST samples used were 4 x 5 mm with thicknesses varying from 0.2 to 1.7 mm.

The experimental setup is a coherent laser beam and THz beam pump-probe arrangement and has been described elsewhere [6]. A cw Ar laser pumped, mode-locked Ti:sapphire laser (Coherent MIRA) was used as the source of optical pulses. A 50  $\mu$ m photoconducting antenna was used as the detector.

Fig. 1 shows the temporal waveform of the radiated field from a 0.4 mm thick DAST sample. The largest radiated signal detected by a 50 micron photoconducting antenna (time-averaged) was 9.8 mV, corresponding to an electric field of nearly 2 V/cm. A persistent

oscillation with a period of 1.04 ps following the main peak of the waveform was repeatable in all of the DAST samples, but disappeared when the DAST sample was replaced by a semiconducting (GaAs) or insulating ( $\text{LiTaO}_3$ ) sample. The origin of this oscillation is not clear at present, but is possibly due to intrinsic molecular vibrational contributions to the subpicosecond submillimeter-waves.

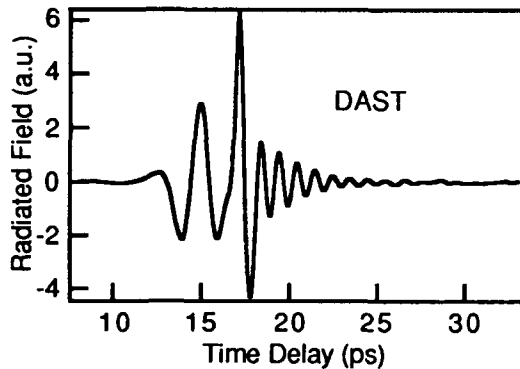


Fig. 1: THz radiation from an organic crystal DAST.

We verified the linear dependence of the radiated field amplitude on optical intensity expected from optical rectification by attenuating the incident optical power with a set of calibrated neutral density filters.

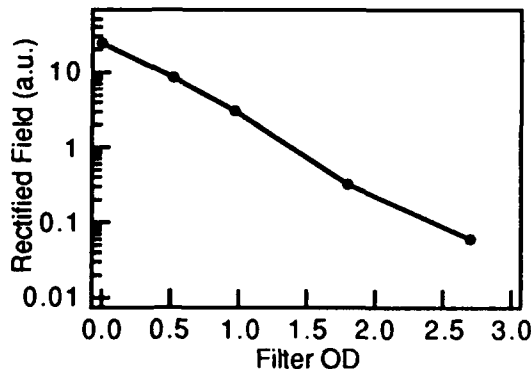


Fig. 2: Amplitude of the radiated field vs optical power. Neutral density filter is used to attenuate optical intensity.

Fig. 2 shows the peak amplitude of the radiated field versus the incident optical power density, with OD = 0 corresponding to  $1.26 \text{ MW/cm}^2$ . A linear relationship was found up to the damage threshold of several  $\text{MW/cm}^2$ .

We also measured the amplitude of the radiated field at three different incident

photon energies, as shown in Fig. 3. The input power was kept below 110 mW and the optical absorption over the photon energy range of 1.38 eV to 1.57 eV was found to be nearly constant. In addition, with 820 nm optical illumination on DAST samples, we observed a second harmonic signal at 410 nm at the input crystal face (the crystal is highly absorbing at 410 nm), presumably due to scattering at the rough crystal surface.

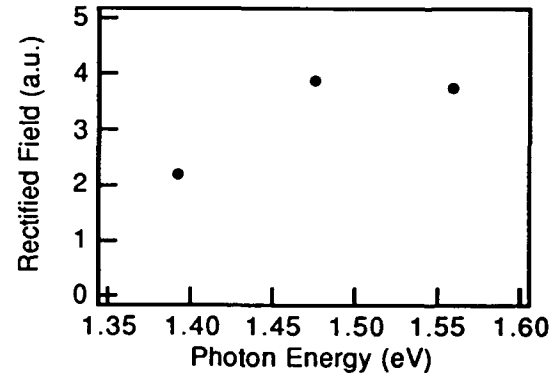


Fig. 3: Amplitude of the radiation vs photon energy.

For the optical polarizations parallel and perpendicular to the dipole detector axis the nonlinear polarization from the organic crystal DAST (m, standard orientation) are:

$$P_p = [(3d_{11} + d_{21} + 2d_{26})\sin(\theta) + (d_{11} - d_{21} - 2d_{26})\sin(3\theta)]EE^* \quad (1)$$

and

$$P_s = [(d_{11} + 3d_{21} - 2d_{26})\sin(\theta) + (-d_{11} + d_{21} + 2d_{26})\sin(3\theta)]EE^* \quad (2)$$

where  $\theta$  is the azimuth rotation angle referenced to the crystal b axis. Figure 4(a) and (b) plot the radiation waveforms vs the azimuthal angle with a 10 degrees increment from an a-cut DAST crystal with two optical polarizations. Persistent oscillation from the a-cut crystal is not as pronounced as that from a c-cut crystal.

Figure 5 and Figure 6 are the plots of peak values of the radiation vs the rotation angle from a c-cut DAST crystal. The solid and open dots are the experimental data. The curves (calculated from equations (1) and (2)) through the experimental data points are determined by a best-fit using the three

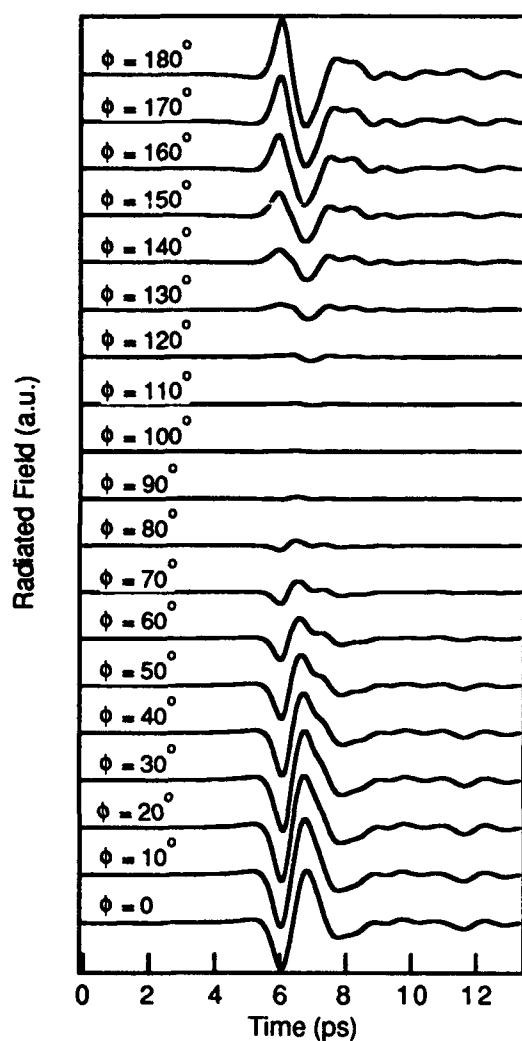


Fig. 4(a): Radiation waveforms vs  $\theta$  (azimuthal angle) from an a-cut DAST crystal. Light polarization is parallel to the detector.

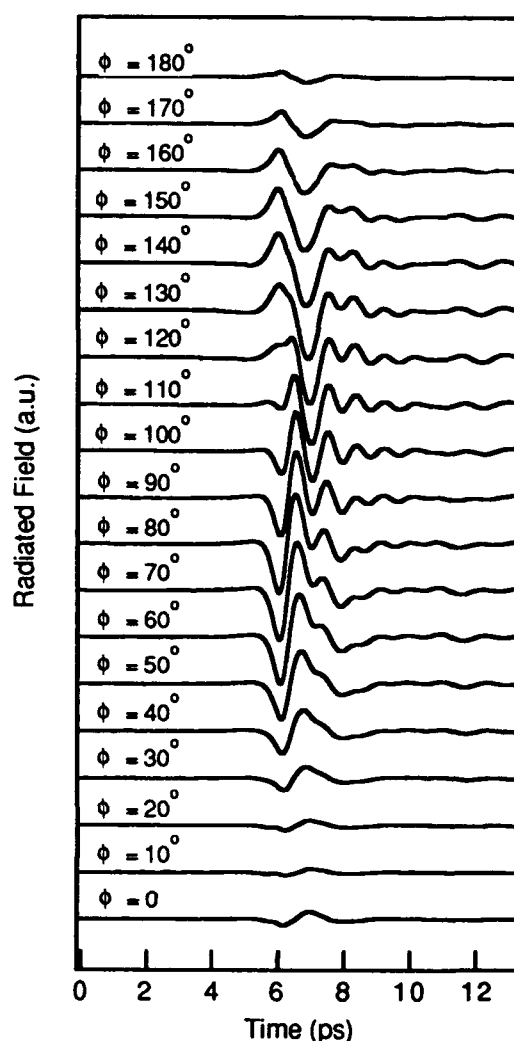


Fig. 4(b): Same as Fig. 4(a). The light polarization is perpendicular to the detector.

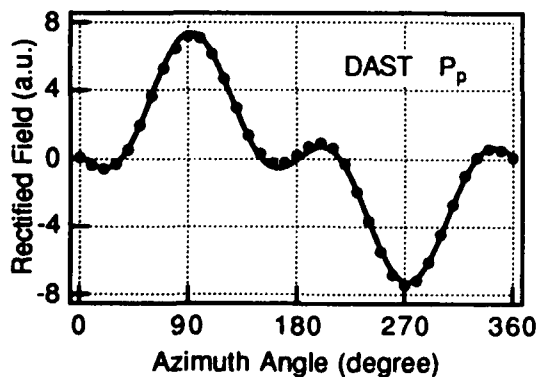


Fig. 5: Peak value of optical rectification signal vs a c-cut DAST crystal azimuth angle. The optical polarization is parallel to the dipole detector axis.

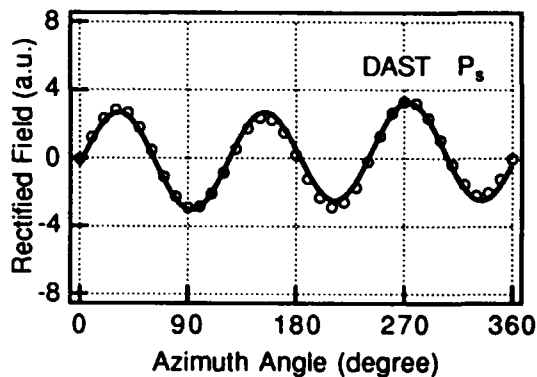


Fig. 6: Peak value of optical rectification signal vs a c-cut DAST crystal azimuth angle. The optical polarization is perpendicular to the dipole detector axis.

parameters  $d_{11}$ ,  $d_{12}$  and  $d_{26}$ , resulting in  $d_{12} = -0.4 d_{11}$  and  $d_{26} = d_{12}/295$ . Provided the absolute value of any single coefficient is known the remaining coefficients can be computed.

### Conclusion

In conclusion, we report optical rectification and subsequent generation of subpicosecond submillimeter-wave radiation from a nonlinear organic crystalline salt. With optical excitation at a wavelength of 820 nm and a 150 fsec pulse duration, the magnitude of the rectified field from the organic salt Dimethyl Amino 4-N-Methylstilbazolium Tosylate (DAST) is 185 times larger than that from a  $\text{LiTaO}_3$  crystal, and 42 times greater than the rectified signal from our best unbiased GaAs and InP crystals [9-11]. This organic crystal presently provides the most intense Terahertz radiated field among all of the natural non-externally biased materials we know. Due to the large second-order nonlinear susceptibilities and ease of use in a practical experimental setup, these organic crystals are excellent candidates for generating THz radiation.

### Acknowledgment

This work was supported in part by the National Science Foundation under grant ECS-9211566, by the U.S. Army Research Office under contract DAAL03-90-G-0082, and by the DARPA under contract F49620-91-C-0075. We also thank technical assistant from X.F. Ma and Y. Jin.

### References

1. G. Mourou, C.V. Stancampiano and D. Blumenthal, *Appl. Phys. Lett.*, **38**, 470 (1981)
2. D.H. Auston, K.P. Cheung and P.R. Smith, *Appl. Phys. Lett.*, **45**, 284 (1984)
3. A.P. DeFonzo, M. Jarwala and C.R. Lutz, *Appl. Phys. Lett.*, **50**, 1155 (1987)
4. Ch. Fattinger and D. Grischkowsky, *Appl. Phys. Lett.*, **59**, 262 (1991)
5. X.-C. Zhang, B.B. Hu, J.T. Darrow and D.H. Auston, *Appl. Phys. Lett.* **56**, 1011 (1990); X.-C. Zhang and D.H. Auston, *J. Appl. Phys.* **71**, 326 (1992)
6. B.B. Hu, X.-C. Zhang, D.H. Auston and P.R. Smith, *Appl. Phys. Lett.* **56**, 506 (1990); L. Xu, X.-C. Zhang and D.H. Auston, *Appl. Phys. Lett.* **61**, 1784 (1992)
7. C.P. Yakymyshyn, S.R. Marder, K.R. Stewart, E.P. Boden, J.W. Perry, and W.P. Schaefer, preceeding of Organic Materials for Nonlinear Optics, Oxford, England, (1990)
8. C.P. Yakymyshyn, K.R. Stewart, E.P. Boden, P.D. Phelps, *Proceedings of Optical Society of America Annual Meeting*, Paper FD6, (1990)
9. X.-C. Zhang, X.F. Ma, Y. Jin, T.-M. Lu, E. P. Boden, P. D. Phelps, K. R. Stewart and C. P. Yakymyshyn, "THz Optical Rectification from Highly Nonlinear Organic Crystals," *Appl. Phys. Lett.* **61**, Dec. 28 (1992)
10. X.-C. Zhang, Y. Jin, and X.F. Ma, *Appl. Phys. Lett.* **61**, 1764 (1992)
11. X.-C. Zhang, Y. Jin, K. Yang and L.J. Schowalter, *Phys. Rev. Lett.* **69**, 2303 (1992)



## New Performance Limits of an Ultrafast THz Photoconductive Receiver

N. Katzenellenbogen, Hoi Chan and D. Grischkowsky

IBM Watson Research Center, P.O. Box 218, Yorktown Heights, NY 10598

Telephone (914)-945-2057

Common to all recently demonstrated optoelectronic sources of pulsed THz radiation has been the problem to properly characterize the source with receivers of limited bandwidths. To date the broadest bandwidth receiver has used ion-implanted, silicon-on-sapphire (SOS), photoconductive switches (1). Here, we report a new type photoconductive receiver with a measured response exceeding 6 THz. This receiver uses a new composite optoelectronic chip (shown in Fig. 1a) consisting of an active layer of ion-implanted polysilicon on top of a thick thermal oxide on a high-resistivity silicon substrate. By using as the transmitter an identical receiver in a high-performance optoelectronic THz beam system, we were able to characterize the receiver with exceptional precision. Excellent agreement with a Drude theory model for the photoconductive response was obtained.

The antenna structure shown in Fig. 1b is used for both the receiver and the transmitter, for which a bias voltage replaces the current amplifier. The structure is embedded in a coplanar transmission line consisting of two parallel 5- $\mu\text{m}$ -wide aluminum lines separated by 10  $\mu\text{m}$ . The operation is based on the creation of photocarriers in the electric field in the gap between the two arms of the antenna. A colliding-pulse mode-locked (CPM) dye laser provides the 5 mW focused beam of 623 nm, 80 fsec excitation pulses. As illustrated in Fig. 1c, the THz radiation from the source chip is collected and collimated by the silicon lens attached to the back-side of the chip. The resultant diffraction limited beam of pulses of THz radiation is

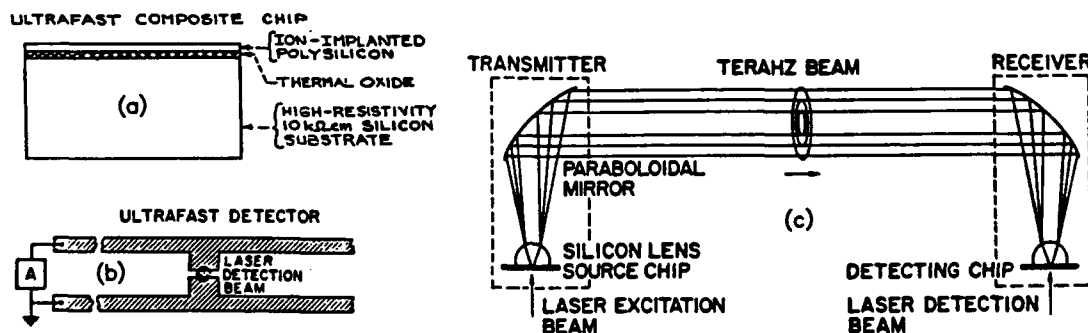


Fig.1 (a) Cross-section of the composite-chip. (b) Receiving and transmitting antenna structure. (c) THz collimating and focusing optics.

recollimated by a paraboloidal mirror. The THz beam incident upon the receiver is focused by a second matched paraboloidal mirror onto a second silicon lens, which in turn focuses it onto the receiving antenna.

Using this receiver, we now measure a source spectrum with a FWHM bandwidth almost twice as broad as the initial experimental characterization of a similar system using SOS chips (1). The improved performance is due to the following changes. Firstly, the positions of the paraboloidal mirrors were set to have a unity transfer function for the THz radiation. Secondly, exceptional care was taken to match the foci of the silicon lenses to the antenna positions. For the on-axis focusing a series of observations were made using lenses of the same curvature, but with thicknesses varying in steps of  $50\text{ }\mu\text{m}$ . In the plane of the chip the position of the focus was adjusted to  $\pm 20$  microns. Thirdly, as shown in Fig. 1a, a new composite-chip was used to eliminate the absorption of the incoming THz radiation by the sapphire substrate of the previously used SOS detection chip. The  $0.5\text{ }\mu\text{m}$ -thick active layer of LPCVD polysilicon of the composite chip was annealed at 1000 degrees C for 1 hour in a nitrogen atmosphere and was later implanted with 200 keV and 100 keV oxygen ions both at a dose of  $10^{13}/\text{cm}^2$ . The  $0.7\text{ }\mu\text{m}$ -thick thermal oxide layer was grown on a high resistivity silicon substrate.

The THz pulse measured with the ultrafast receiver is shown in Fig. 2a. The fall-time (90%-10%) from the peak of the pulse to the minimum is only 127 fsec, as shown in the expanded view of Fig. 2b. This exceptional time resolution demonstrates that a photoconductive receiver can be much faster than is generally realized, but is consistent with the earlier prediction (for SOS chips) of a 150 fsec time resolution (1). The numerical Fourier transform of this pulse peaks at approximately 0.5 THz and extends

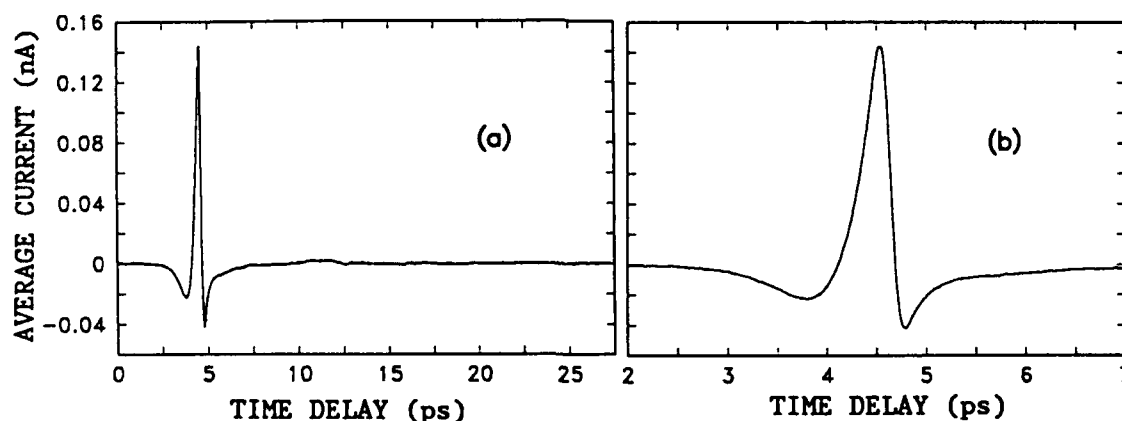


Fig.2 (a) THz pulse measured by the ultrafast receiver. (b) Measured THz pulse on an expanded time scale.

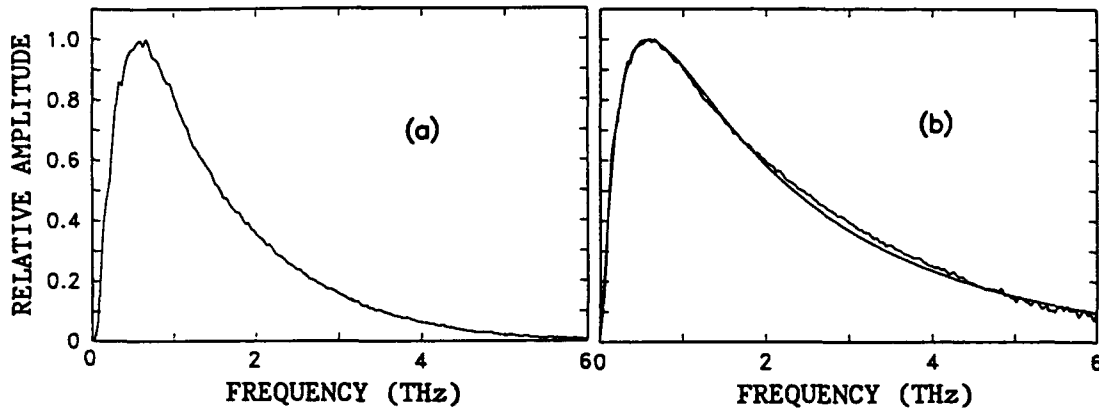


Fig.3 (a) The numerical Fourier transform of Fig. 2a, equal to the receiver power spectrum. (b) Comparison of the calculated receiver amplitude spectrum with the measured amplitude spectrum (square root of Fig. 3a).

to 6 THz, as shown in Fig. 3a. The measured spectrum is the product of the transmitter and receiver amplitude spectra. However, because here the transmitter and receiver are identical, the receiver amplitude spectrum shown in Fig. 3b is simply the square root of the measured spectrum of Fig. 3a.

Because of the extremely fast electrical response, the current in the ultrafast antenna follows the current  $J(t)$  in the semiconductor, where  $J(t)$  is determined by the convolution of the photoconductive response function and the 80 fsec (FWHM)  $\text{sech}^2$ -shaped laser driving pulse. Following the theoretical procedure of Ref.(1), the response function is derived from simple Drude theory with a scattering time of 120 fsec and a carrier lifetime of 600 fsec. The receiver response is obtained by considering a transmitter in the small antenna limit corresponding to the Hertzian dipole, for which the generated radiation field is proportional to the time-derivative of the  $J(t)$ . Evaluation of this time-derivative shows that the Hertzian dipole antenna generates a 150 fsec FWHM pulse of THz radiation. Conversely, by the reciprocity principle, 150 fsec is also the time resolution of the photoconductive receiver. The corresponding amplitude spectrum for the receiver is shown in Fig. 3b. The excellent agreement with experiment shows that, to a very good approximation, the semiconductor response follows Drude theory and that the resulting response time is limited by the ballistic acceleration of the photocarriers.

1. D. Grischkowsky and N. Katzenellenbogen, Proc. of the Psec. Elect. and Optoelect. Conf., Salt Lake City, Utah, March 13-15, 1991, T.C.L. Gerhard Sollner and Jagdeep Shah, Eds. (Opt. Soc. of Am., Washington D.C. 1991), Vol.9, pp. 9-14.

---

# **Physics of Semiconductors**

---

## Application of Ultrafast Optoelectronics to the Characterization of Photonic Crystals

G. Arjavalingam, W. M. Robertson\*, and S. Y. Lin

IBM Research Division, T. J. Watson Research Center, PO Box 218,  
Yorktown Heights, New York 10598

### Abstract

The application of coherent microwave transient spectroscopy to the characterization of photonic band structure will be discussed. The dispersion relation for electromagnetic wave propagation in two-dimensional dielectric arrays is measured. We will also report the observation of surface waves in these photonic crystals.

The analogy between electromagnetic-wave propagation in arrays of dielectrics and electron-wave propagation in crystals is now well known. For example, the scattering and interference of electromagnetic waves in uniform arrays of dielectrics gives rise to re-

gions of the spectrum in which transmission is inhibited (i.e. band gaps) [1,2]. By extension, the dispersion of allowed modes in these "photonic crystals" is expected to resemble electronic band structure in real crystals. In this talk, we describe the application of ultrafast optoelectronics to the characterization of photonic crystals. The dispersion relation for electromagnetic wave propagation in arrays of dielectric cylinders is measured using the coherent microwave transient spectroscopy (COMITS) technique [3,4]. Using prism coupling and COMITS in reflection, the existence of surface modes in suitably-terminated cylinder arrays is demonstrated, and the dispersion of this mode is measured.

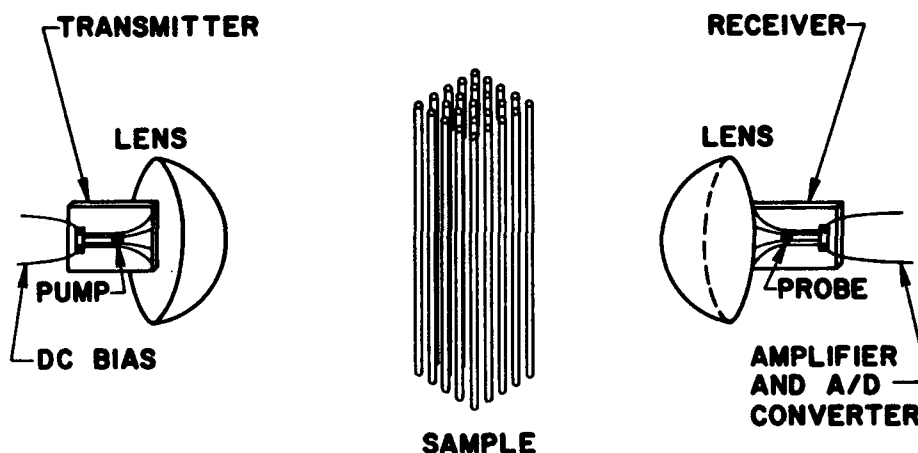


**Figure 1.** Schematic of the coherent microwave transient spectroscopy experimental set up. The photonic crystal is made of 100 mm long 0.74mm diameter alumina ceramic rods arranged in a triangular array with 2.137 mm lattice constant.

Briefly, optoelectronically-pulsed antennas are used for radiation and reception of ultrafast electromagnetic transients as shown in figure 1. [3]. The transients are the basis of a broadband microwave spectroscopy technique. To characterize a photonic crystal, two waveforms are measured: the first with the sample between the two antennas, and the second without (reference). The complex numerical Fourier transform of the former is divided by the Fourier transform of the latter. The amplitude spectra clearly show regions of the spectrum corresponding to band gaps [4]. Additionally, the phase spectrum is used to calculate the propagation constant at each frequency. For instance, figure 2 shows the measured dispersion relation for propagation along the  $\langle y \rangle$  direction of a triangular array with 2.13 mm lattice constant. Similar results are obtained for square arrays of rods, and also cylinders of air in solid dielectric, in various propagation directions [5].

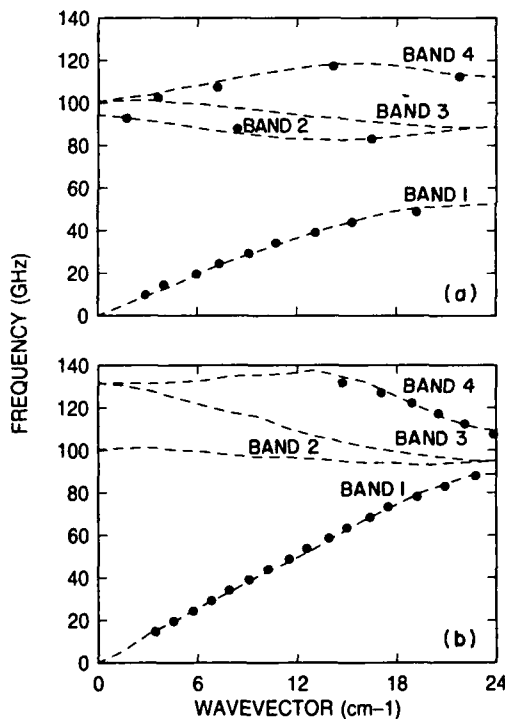


**Figure 2.** The electromagnetic dispersion along the  $\langle y \rangle$  direction with polarization (a) parallel and (b) perpendicular to the rod axis. The points are experimental values and the lines are theoretical predictions.

The existence of surface modes in photonic crystals was demonstrated with COMITS in a reflection configuration [6], together with a prism-coupling technique [7]. The experimental set up is shown schematically in figure 3. A fused silica prism is used to phase match the incident microwave radiation to the

surface mode [8]. The broadband nature of COMITS ensures coupling to this mode at some frequency in the available bandwidth. The prism angles were chosen so that, when the electromagnetic transient is incident normal to the input face, the angle of incidence on the reflecting face is just above critical for total internal reflection (TIR). The E-field is polarized parallel to the rods (s-polarized).

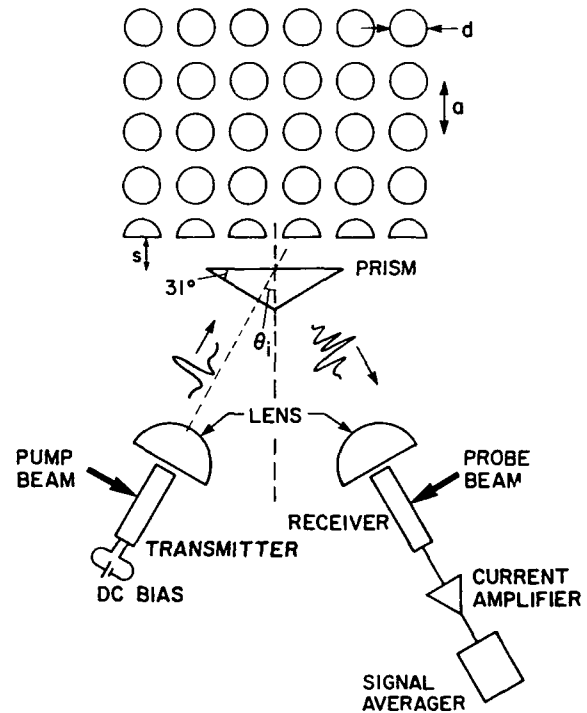


**Figure 3.** Experimental configuration for COMITS measurements in total-internal-reflection. The E-field is parallel to the rod axes.  $d = 0.74 \pm 0.03$  mm,  $a = 1.87$  mm.  $s$  is varied from 0 to 5 mm. The rods are drawn much larger than their size relative to the prism.

The photonic crystals for the surface-mode experiments consist of  $0.74 \text{ mm} \pm 0.03 \text{ mm}$  diameter 100 mm long alumina ceramic cylinders arranged in square array of 1.87 mm lattice constant. The photonic band structure of this sample, well known from other measurements [4], exhibits a band gap between 45 GHz and 70 GHz. Two samples were constructed, one with full-rod terminated surfaces, and the other with one surface terminated by hemi-cylinders. The hemi-cylinders were fabricated by grinding some of the rods. Time-domain waveforms were acquired first with no sample in the vicinity of the reflecting face of the prism, and then with the photonic crystal of one termination or the other at various distances from the reflecting face. The waveforms were then Fourier numerically transformed. Figure 4 shows the amplitude spectra with the two different terminations with the sample-to-prism dis-

tance  $S = 2.2$  mm. A clear dip corresponding to energy being coupled out to the surface mode is seen with the hemi-cylindrically terminated sample. We found that the coupling efficiency is a function of the separation  $S$ , with an optimum different from 0 mm. Using the prism angle and the frequency of the dip, the wave vector of the evanescent mode can be calculated. Indeed, the dispersion of the surface mode can be determined by repeating the experiment with different prism angles [9].

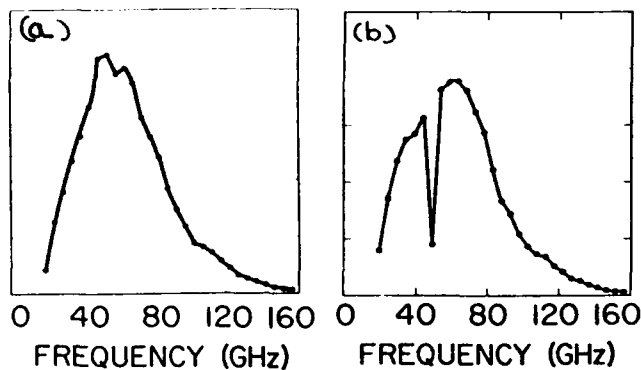


**Figure 4.** Amplitude spectra obtained by numerically Fourier transforming the time-domain data. (a) Cylindrical-rod terminated crystal. (b) Hemi-cylindrical rod terminated crystal. Both spectra correspond to  $S = 2.2$  mm.

### Acknowledgments

The authors thank R.D. Meade and colleagues of MIT for providing the theoretical calculations shown in figure 2.

\*Present Address: National Research Council Canada, Institute for Information Technology, M-50 Montreal Road, Ottawa, Ont., Canada K1A 0R6.

### REFERENCES

1. E. Yablonovitch, *Phys. Rev. Lett.*, **58**, 2059 (1987).
2. S. John, *Phys. Rev. Lett.*, **58**, 2486 (1987).
3. G. Arjavalingam, Y. Pastol, J.-M. Halbout, and G.V. Kopcsay, *IEEE Trans. Microwave Theory Tech.*, **38**, 615 (1990).
4. W.M. Robertson, G. Arjavalingam, R.D. Meade, K.D. Brommer, A.M. Rappe, and J.D. Joannopoulos, *Phys. Rev. Lett.*, **68**, 2023, (1992).
5. W.M. Robertson, G. Arjavalingam, R.D. Meade, K.D. Brommer, A.M. Rappe, and J.D. Joannopoulos, to be published in *Journal of Optical Society - B*, Feb. 1993.
6. W.M. Robertson, G. Arjavalingam, and G.V. Kopcsay, *Appl. Phys. Lett.*, **57**, 1958, (1990).
7. W.M. Robertson, and G. Arjavalingam, et al., to be published in *Optics Letters*.
8. A. Otto, *Z. Physik*, **181**, 232, (1965).
9. S.Y. Lin, W.M. Robertson, and G. Arjavalingam, unpublished.

## Ultrafast Optoelectronic Field Changes in GaAs

T. Dekorsy, H. Heesel, S. Hunsche, T. Pfeifer, H. Mikkelsen, W. Kütt, K. Leo, and H. Kurz

*Institut für Halbleitertechnik, RWTH Aachen, Sommerfeldstr. 24, D-5100 Aachen, Germany*

### Abstract

We investigate the field dynamics in GaAs after femtosecond injection of free charge carriers on a subpicosecond time scale with two different optical methods: Reflective Electro-Optic Sampling (REOS) and Differential Transmission Spectroscopy (DTS). The first method is applied to bare (100) orientated GaAs surfaces for the observation of ultrafast screening of built-in surface fields via free carrier transport. DTS is applied to an externally biased GaAs film. The field evolution is monitored via the Franz-Keldysh (FK) effect. We compare the experimental results with elaborate numerical calculations for the spatial carrier distributions, the linear electro-optic (EO) effect and the FK effect including excitonic contributions. The comparison gives a detailed information on the carrier density dependence of the screening dynamics and carrier drift velocities on a subpicosecond time scale. Screening effects due to an instantaneous polarization are not significant for the interpretation of the experimental results.

### Introduction

A detailed understanding of transient electric fields in the presence of optically generated carriers is essential for the development of any

optoelectronic device. We report on two optical methods, which provide a measurement of the electric field dynamics in bulk GaAs on a subpicosecond time scale.

The REOS technique directly measures the screening of the built-in surface field at (100) oriented GaAs surfaces due to ultrafast separation of the optically excited carriers via free carrier transport. Measurements are performed at different initial surface field conditions and different optical excited carrier densities. The comparison of the experimental results to numerical simulations based on a drift-diffusion model for non-equilibrium carrier distributions yields insight into the carrier drift velocities and screening dynamics on a subpicosecond time scale.

The second method is the observation of transmission changes of a white-light probe continuum due to the FK effect. We apply this technique to an externally biased GaAs film and model the observed differential transmission changes.

### Reflective Electro-Optic Sampling

REOS is highly sensitive to field induced changes in the refractive index due to the linear electro-optic effect [1]. We use a pump-probe set-up (CPM-laser,  $\tau_{FWHM}=50$  fs,  $\hbar\omega=2$  eV) for the time resolved detection of surface field changes. The data-acquisition is accomplished via a



fast averaging technique. The detected transient EO-reflectivity changes are proportional to electric field changes  $\Delta E_z(t)$  perpendicular to a (100) oriented GaAs surface:

$$\frac{\Delta R(t)}{R_0} = \frac{R_{[0\bar{1}1]} - R_{[01\bar{1}]}}{R_0} = n_0^3 r_{41} \Delta E_z(t), \quad (1)$$

where  $n_0$  is the isotropic refractive index and  $r_{41}$  is the EO-coefficient of GaAs. All isotropic carrier induced changes in the refractive index can be neglected in the REOS detection geometry. The sensitivity of  $10^{-7}$  in  $\Delta R$  allows the detection of electric field changes of 100 V/cm.

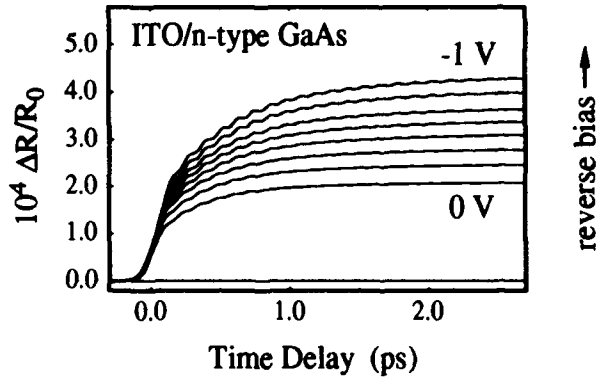


Figure 1: REOS signals at ITO/n-GaAs sample ( $N_D = 3 \times 10^{17} \text{ cm}^{-3}$ ) at different reversed bias voltages (0 V to -1 V) and an excitation density of  $5 \times 10^{17} \text{ cm}^{-3}$ .

To demonstrate the REOS sensitivity towards electric field changes, we perform experiments on transparent GaAs-Schottky junctions of Indium-Tin-Oxide (ITO). The static built-in field is varied by an externally applied voltage. The REOS signals at reverse bias voltages from 0 V to 1.0 V are presented in Fig. 1. In the first picosecond, the signal dynamics at a fixed voltage are determined by the transport of the photoexcited carriers and the associated decrease in the surface field. For longer times, the signals reach a quasi-equilibrium level. This equilibrium level rises with increasing reverse bias due to the increase in  $E_z$  changes and in the depletion width. The rise of the equilibrium level as a function of applied voltage is in accordance with field changes calculated from a Schottky model. The minute oscillations are coherently generated

LO-phonons, revealing an increasing oscillation amplitude with increased applied voltage [1].

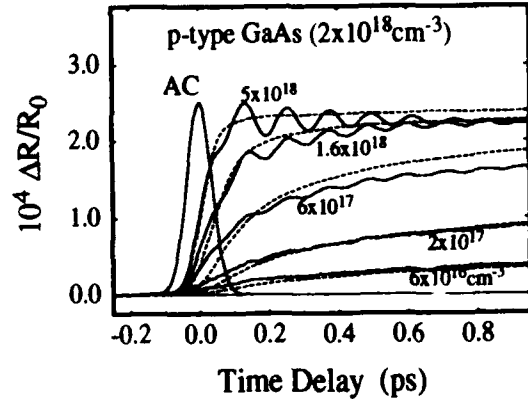


Figure 2: REOS signal for p-doped GaAs ( $N = 2 \times 10^{18} \text{ cm}^{-3}$ ) at different optical excitation densities ( $6 \times 10^{16}$  to  $5 \times 10^{18} \text{ cm}^{-3}$ ). The theoretical curves are based on transport calculations (dashed lines).

Figure 2 depicts the subpicosecond REOS signatures of a p-doped (100) GaAs ( $N = 2 \times 10^{18} \text{ cm}^{-3}$ ) at different excited carrier densities ( $6 \times 10^{16} \text{ cm}^{-3}$  to  $5 \times 10^{18} \text{ cm}^{-3}$ ). At high excitation densities the signals saturate, indicating a complete screening of the surface field, even within the duration of the pump pulse. At low excitation densities the signal rises slower since the number of carriers is too small to achieve a fast and complete screening on this time scale. The dashed curves are calculated via a drift-diffusion-model for the photoexcited electrons and holes [2]. The transient field distributions are evaluated via the Poisson equation and the EO-response is calculated via an optical transfer-matrix method. The most relevant simulation parameters are the electron and hole high-field drift velocities, which were adjusted to  $5 \times 10^6 \text{ cm/s}$  in accordance with MC-calculations [3]. The same parameters have been used for the whole set of excitation densities covering a range of 2 orders of magnitude. As a result of the fast L-valley scattering associated with the 2 eV excitation, even on a subpicosecond time scale no velocity overshoot is observed. Additionally, the calculations provide a determination of the initial surface field (350 kV/cm in this case). The observed screening dynamics is reproduced

quantitatively by the calculations based on classical carrier transport in this excitation and field range.

A qualitative description of the observed screening is given by the following more intuitive explanation. The initial surface field is screened by a polarization given by the spatial separation  $\Delta z$  of electrons and holes

$$P(\Delta t) = qN_{\text{exc}}(z, \Delta t)\Delta z(\Delta t). \quad (2)$$

For low excitation densities ( $< 5 \times 10^{17} \text{cm}^{-3}$ ) the screening dynamics is mainly determined via the carrier separation  $z(\Delta t) = v_d \Delta t$  on a picosecond time scale, where  $v_d$  is the carrier drift velocity. At high excitation densities ( $> 1 \times 10^{18} \text{cm}^{-3}$ ) the screening dynamics is determined via  $N_{\text{exc}}$ , while only a small separation  $\Delta z$  is required for a complete screening of the surface field. Thus the screening is accomplished on the time scale of the pump pulse.

The REOS experiments are very closely related to recent THz-emission experiments performed on free semiconductor surfaces [4]. Here, we directly observe the polarization changes at the surface. In the THz-radiation experiments, the second time derivative of this polarization is measured via the emission of associated electromagnetic waves. Regarding the REOS experiments at excitation densities about  $2 \times 10^{18} \text{cm}^{-3}$ , the screening is accomplished within the pump pulse duration. This should lead to the emission of THz-radiation with main frequency components of 10 - 20 THz, which presently can not be detected with standard photoconducting antennas with a frequency response limited to a few THz.

Our REOS experiments can be entirely understood in the carrier transport picture in the excitation regime investigated here. We do not need to include the effect of an optical rectification mechanism (ORM) at the samples surface, as recently proposed in a theory by Chuang *et al.* to be responsible for the generation of THz-radiation [5]. Additionally, the proposed pump pulse polarization dependence of the ORM is not observed in the REOS experiments [1]. One possible explanation for the discrepancy are the differences in the excitation

geometry between REOS and THz-experiments (REOS: nearly normal incidence ( $< 5^\circ$ ); THz-emission:  $40^\circ$  to  $70^\circ$ ). The balance between transport-induced screening and ORM may also depend on the excitation energy [6].

### Time-resolved Franz-Keldysh Modulation

Transient electrical field changes in an externally biased thin GaAs film are observed via changes in differential transmission spectra. Optical excitation is performed with a 50 fs pump pulse at 2 eV. Differential transmission spectra from a white light continuum (1.3 eV - 1.9 eV) are recorded with an optical multichannel analyzer with and without applied electric field ( $\Delta T/T_0 = (T_E - T_0)/T_0$ ). This modulation technique allows the observation of electroabsorption only, without contributions due to band filling etc. The spectra are numerically corrected for the chirp of the probe continuum, providing a time resolution of  $\approx 100$  fs. The sample consists of 220 nm intrinsic GaAs embedded between intrinsic and n-doped  $\text{Al}_{0.5}\text{Ga}_{0.5}\text{As}$  grown on (100) oriented n-GaAs substrate. The sample is prepared with electrical contacts (front: transparent Schottky contact; substrate: ohmic contact). Optical windows for transmission measurements are opened over an area of  $2 \text{ mm}^2$  by wet chemical etching.

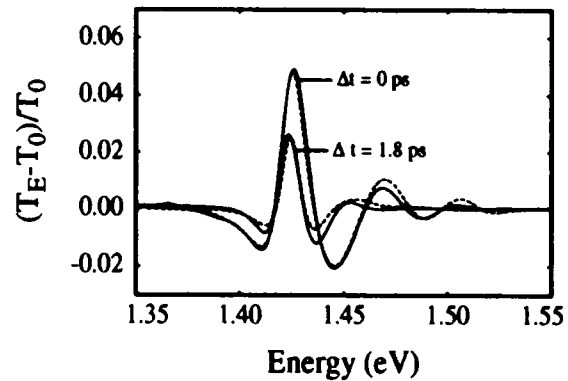


Figure 3: DT-Spectra of experimental (solid lines) and theoretical (dashed lines) FK modulation for an externally biased intrinsic GaAs film for time delays of 0 ps and 1.8 ps at an exci-

tation density of  $2 \times 10^{16} \text{cm}^{-3}$ . The modulation field amplitude is 34 kV/cm.

Figure 3 shows the comparison between experimental results and numerical calculations for an excitation density of  $2 \times 10^{16} \text{cm}^{-3}$  at different time delays. The amplitude of the field modulation is 34 kV/cm. The signal amplitude and the period of the FK oscillations are reduced for longer time delays due to the screening of the electric field. The model incorporates the drift-diffusion model as described above for the calculation of the time dependent field. The imaginary part of the dielectric function  $\epsilon_2(\omega)$  is calculated via a numerical solution of the time-independent Schrödinger equation including the Coulomb potential for the exciton in an electric field [7, 8]. The spatial variation of  $\epsilon_2(\omega)$  is used for the calculation of the DTS signal via an optical transfer-matrix method as shown in Fig. 3. The model reproduces the experimental curves satisfactorily for all time delays. The high field drift velocities are restricted to  $8 \times 10^6 \text{cm/s}$  and  $5 \times 10^6 \text{cm/s}$  for holes. The strong damping of the FK oscillations for higher energies and longer time delays is due to a strong field inhomogeneity in the GaAs film and can not be explained in terms of a strong collisional broadening. At this low excitation density, a decrease of the FK effect is observed up to 5 ps delay in agreement with the drift-diffusion model, which predicts a quasi-equilibrium for the spatial carrier distributions at this time delay.

## Conclusion

We have presented two different electro-optic methods for the observation of free carrier induced screening of electric fields at GaAs surfaces and in a GaAs modulator structure. The screening dynamics are well understood in a drift-diffusion model for the free carrier transport. For the direct comparison of experiments and theory, extensive numerical calculations based on an optical transfer-matrix method have to be performed. The comparison yields information about the involved carrier drift velocities, the built-in electric fields and in case of the DTS

measurements also on the exciton dynamics in transient electric fields. The effect of an instantaneous polarization on the time scale of the pump pulse has not to be taken into account in both experiments for the geometry and excitation conditions we have used.

## Acknowledgments

We thank B. Görig (Humboldt University, Berlin) for supplying the ITO-GaAs sample and A. Förster, H. Lüth (ISI, KFA Jülich), and K. Köhler for high-quality GaAs MBE samples. This work was supported by the "Deutsche Forschungsgemeinschaft", the "Alfried-Krupp-Stiftung", and the "Volkswagen Stiftung".

## References

1. T. Pfeifer, T. Dekorsy, W. Kütt, and H. Kurz, "Generation mechanism of coherent LO phonons in surface-space-charge fields of III-V-compounds," *Applied Physics A* **55**, 482-488 (1992).
2. T. Dekorsy, T. Pfeifer, W. Kütt, and H. Kurz, "Subpicosecond carrier transport in GaAs surface-space-charge fields," *Phys. Rev. B* **47**, in press.
3. G. M. Wysin, D. L. Smith, and A. Redondo, "Picosecond response of photoexcited GaAs in a uniform electric field by Monte Carlo dynamics," *Phys. Rev. B* **38**, 12514-12524 (1988).
4. X.-C. Zhang and D. H. Auston, "Optoelectronic measurement of semiconductor surfaces and interfaces with femtosecond optics," *J. Appl. Phys* **71**, 326-328 (1992).
5. S. L. Chuang, S. Schmitt-Rink, B. I. Green, P. E. Saeta, and A. J. Levi, "Optical rectification at semiconductor surfaces," *Phys. Rev. Lett.* **68**, 102-105 (1992).
6. X.-C. Zhang, Y. Jin, K. Yang, and L. J. Schowalter, "Resonant nonlinear susceptibility near the GaAs band gap," *Phys. Rev. Lett.* **69**, 2303-2306 (1992).
7. D. F. Blossey, "Wannier excitons in an electric field: I. Optical absorption by bound

- and continuum states," *Phys. Rev. B* **2**, 3976-3990 (1970).
8. H. Heesel, S. Hunsche, H. Mikkelsen, T. Dekorsy, K. Leo, and H. Kurz, "Dynamics of electric field screening in a bulk GaAs modulator," submitted to *Phys. Rev. B*.

# Velocity Overshoot Dynamics in GaAs up to 200 kV/cm Observed Using Terahertz Radiation

J. Son, W. Sha, J. Kim, T. B. Norris, J. F. Whitaker, and G. Mourou

Center for Ultrafast Optical Science, University of Michigan, 2200 Bonisteel Blvd.,  
Ann Arbor, Michigan 48109-2099

## Abstract

Transient velocity overshoot dynamics in GaAs have been studied at electric fields up to 200 kV/cm using a terahertz radiation technique.

## Introduction

Since the generation and detection of single-cycle THz pulses were first demonstrated [1], studies have mostly taken two directions. One is to use this technique for the characterization of materials such as dielectrics, semiconductors, and superconductors in the far-infrared

region [2]. The other is the efficient generation and control of THz signals for possible applications of directional sub-millimeter wave pulses [3].

However, it has recently been realized that the transient carrier dynamics of semiconductors can be investigated using the material of interest as a THz source [4]. The THz waveform, measured in the far field with a detector having subpicosecond gate duration, carries direct information on the acceleration of electrons under transient excitation. With this technique, we have experimentally studied the temporal characteristics and field dependence of velocity overshoot in GaAs up to an electric field of 200 kV/cm.

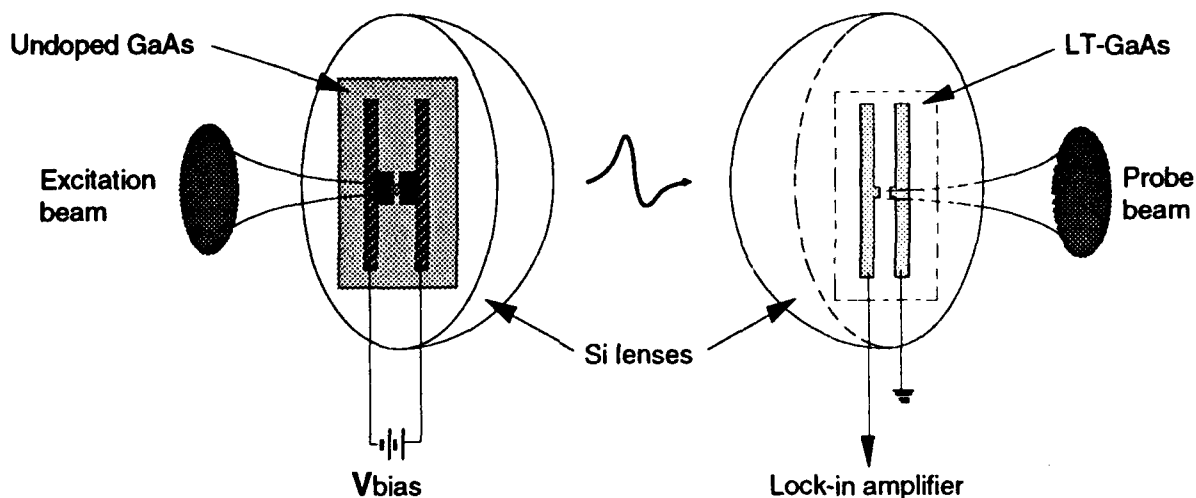


Figure 1. Experimental configuration of THz radiation system.

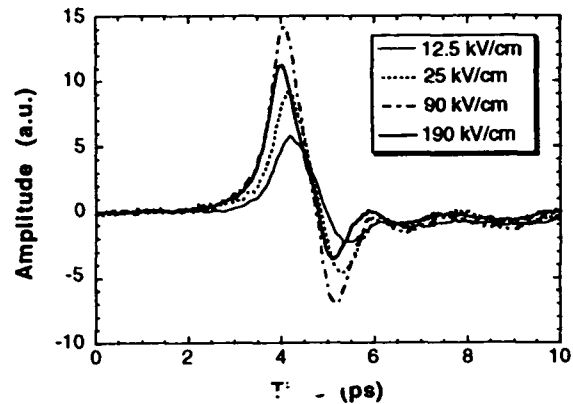
## Experiment

For the transmitter, a reverse-biased lateral p-i-n structure is used to provide a uniform electric field in an undoped GaAs region. The ohmic contacts are made by the deposition of p and n metals, which are Au/Zn/Ni/Au and Ni/Ge/Au/Ti/Au respectively, followed by annealing after each deposition. The separation between the p and n regions (that is, the i-region) is 4  $\mu\text{m}$ , and the electrode width is 50  $\mu\text{m}$ . Breakdown occurs at around a nominal electric field of 205 kV/cm (82 V/4  $\mu\text{m}$ ). The i-region is photoexcited with 80-fs optical pulses from a self-mode-locked Ti:sapphire laser, which is tuned at 860 nm to excite carriers at the room-temperature band edge. Also, the average power of the pump beam is kept below 0.5 mW to avoid generating such a large number of carriers that the applied field is screened. This lateral p-i-n is fabricated on a 500- $\mu\text{m}$ -thick GaAs layer, which is attached to a 12.7-mm-diameter hemispherical high-resistivity Si lens to collimate the radiation as illustrated in Fig. 1. The radiated signal is detected by a photoconductive receiver antenna fabricated on an epitaxial layer of GaAs grown at low temperature. This material has a demonstrated carrier response of much less than a picosecond [5], and the receiver can thus provide a gate duration of < 0.5 ps FWHM when illuminated by the ultrafast optical pulses. This detector is also mounted on a high-resistivity Si lens.

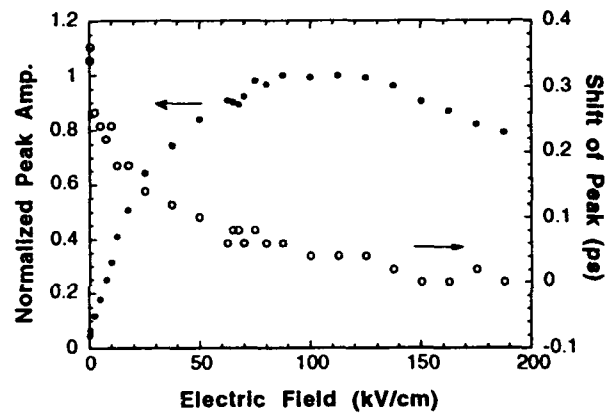
## Results

The far-field radiation from the p-i-n transmitter is proportional to the time derivative of the device photocurrent. Since the carrier life-time is much longer than a few tens of ps, the radiated waveform is a measure of the carrier acceleration.

We measured the THz radiation waveforms for a wide range of electric fields (E) up to 200 kV/cm. Some of the waveforms are shown in Fig. 2(a). The amplitude of the positive peak (shown in Fig. 2(b)) increases as E increases, reaching a maximum at a dc bias of 90 kV/cm, and then slightly decreases as E is further increased. The peak and roll-off (>90 kV/cm) of the THz pulse amplitude indicate that at very high E, the maximum



(a)

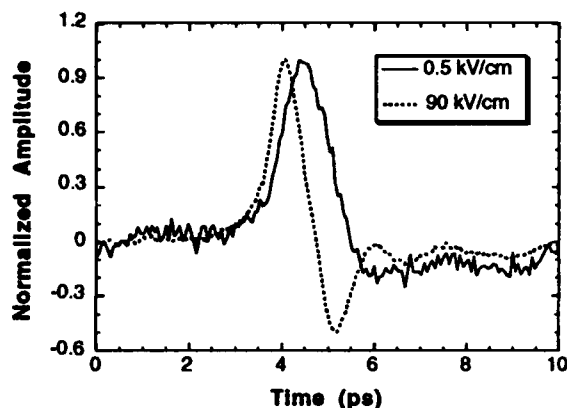


(b)

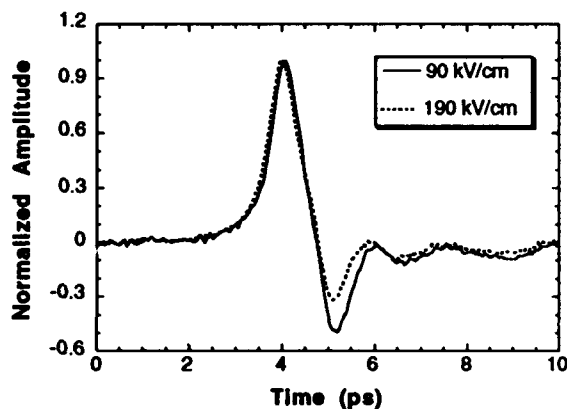
Figure 2. (a) Time-domain waveforms detected by photoconductive receiver and (b) the normalized amplitude and time shift of the positive peaks with respect to the electric field.

electron acceleration saturates. It should also be noted, as shown in Figs. 2(a) and (b), that the positive peak (i.e., the position of the maximum acceleration) arrives at earlier times as E increases, as expected (300 fs separation between peaks for biases of 0.5 and 190 kV/cm).

While the positive waveform represents the carrier acceleration, the negative one represents the deceleration. As seen in Fig. 3(a) and (b), the waveform at low field (0.5 kV/cm) is observed to be essentially unipolar, while at high field (90 kV/cm), it is bipolar. This indicates that the photocurrent displays an over-



(a)



(b)

Figure 3. Comparison of the waveforms with normalization. (a) While the waveform at 0.5 kV/cm is unipolar, that at 90 kV/cm is bipolar, which indicates velocity overshoot. (b) The smaller negative peak at 190 kV/cm shows that the overshoot (deceleration of the carriers) decreases at very high fields.

shoot at high fields. To prove that the electric field in the gap remains constant during the photocurrent overshoot, we performed an experiment in which two equal-intensity pump beams separated by 10 ps were incident on the gap, and we found that the amplitude of the waveform measured with the prepump present still maintained 95% of that without the prepump. Thus, we attribute the bipolar waveform at high fields to velocity overshoot due to the k-space transfer of electrons from the  $\Gamma$  to L or X valleys. A better quantity to describe the phenomenon, the degree of

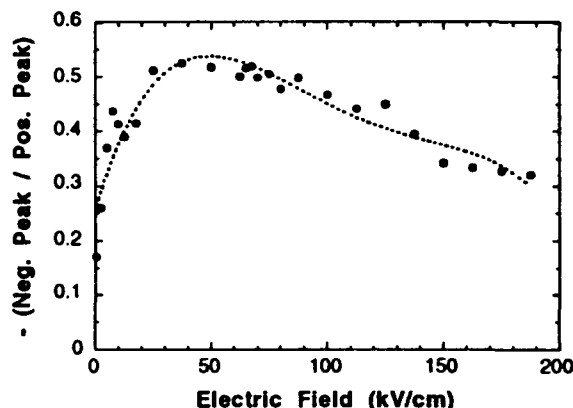


Figure 4. The degree of overshoot, which is defined as the ratio of the magnitudes of the negative and positive peaks.

overshoot, can be defined as the ratio of the magnitudes of the negative and positive peaks. Our results are plotted in Fig. 4; we found a maximum in this ratio of around 37 kV/cm. This is consistent with a Monte-Carlo simulation [6] showing the maximum degree of overshoot at 35 kV/cm with 1.5 eV photoexcitation (and a similar definition of degree of overshoot). Further interpretation of the saturation of the maximum acceleration and degree of overshoot would benefit from Monte-Carlo simulations which extended to very high fields and included realistic band structures. In addition, experiments with higher time resolution are also in progress to determine the cause of the roll-off of the degree of overshoot.

## Conclusion

We have observed the transient velocity overshoot dynamics of photoexcited carriers in GaAs at high fields up to 200 kV/cm by THz radiation. While a unipolar pulse is measured at low fields, a bipolar waveform is observed at high fields due to velocity overshoot. The degree of overshoot is maximum at 37 kV/cm for 1.45-eV photoexcitation. At higher fields (>100 kV/cm), the overshoot decreases, which might be explained by the carriers in satellite valleys maintaining high velocity at very high electric fields.

## Acknowledgments

This research is supported by AFOSR contract number AFOSR-90-0214 (University Research Initiative) and by the National Science Foundation through Center for Ultrafast Optical Science under STC PHY 8920108.

## References

1. D. H. Auston, K. P. Cheung, and P. R. Smith, "Picosecond photoconducting Hertzian dipoles," *Appl. Phys. Lett.* **45**, 284-286 (1984).
2. D. Grischkowsky, S. Keiding, M. van Exter, and Ch. Fattinger, "Far-infrared time-domain spectroscopy with terahertz beams of dielectrics and semiconductors," *J. Opt. Soc. Am. B* **7**, 2006-2015 (1990); J. M. Chwalek, J. F. Whitaker, and G. A. Mourou, "Submillimetre wave response of superconducting YBCO using coherent time-domain spectroscopy," *Electron. Lett.* **27**, 447-448 (1991).
3. D. H. Auston and X.-C. Zhang, in Proceedings of Picosecond Electronics and Optoelectronics Topical Meeting, G. Sollner and J. Shah, eds. (Optical Society of America, Washington, DC, 1991), pp. 2-8.
4. L. Xu, X.-C. Zhang, and D. H. Auston, "Terahertz radiation from large aperture Si p-i-n diodes," *Appl. Phys. Lett.* **59**, 3357-3359 (1991); W. Sha, J. Rhee, T. B. Norris, and W. J. Schaff, "Transient carrier and field dynamics in quantum-well parallel transport: From the ballistic to the quasi-equilibrium regime," *J. Quantum Electron.* **28**, 2445-2455 (1992); B. B. Hu, X.-C. Zhang, and D. H. Auston, "Observation of negative transient photoconductivity in GaAs," in Technical Digest of Quantum Electronics and Laser Science Conference (Optical Society of America, Washington, DC, 1991), postdeadline paper QPDP17.
5. S. Gupta, M. Y. Frankel, J. A. Valdmanis, J. F. Whitaker, G. A. Mourou, F. W. Smith, and A. R. Calawa, "Subpicosecond carrier lifetime in GaAs grown by molecular beam epitaxy at low temperatures," *Appl. Phys. Lett.* **59**, 3276-3278 (1991).
6. G. M. Wysin, D. L. Smith, and A. Redondo, "Picosecond response of photoexcited GaAs in a uniform electric field by Monte Carlo dynamics," *Phys. Rev. B* **38**, 12514-12524 (1988).



# Phase Relaxation Processes of Excitons in Island-Inserted Quantum Well Structures—Suppression of Relaxation and Giant Quantum Beats

T. Matsusue

*Institute of Industrial Science, University of Tokyo, 7-22-1 Roppongi,  
Minato-ku, Tokyo 106, Japan*

T. Saiki and M. Kuwata-Gonokami

*Department of Applied Physics, Faculty of Engineering, University of Tokyo,  
7-3-1 Hongo, Bunkyo-ku, Tokyo 113, Japan*

H. Akiyama

*Research Center for Advanced Science and Technology, University of Tokyo,  
4-6-1 Komaba, Meguro-ku, Tokyo 153, Japan*

H. Sakai

*Quantum Wave Project, ERATO, Research Development Corporation of Japan,  
4-3-24 Komaba, Meguro-ku, Tokyo 153, Japan*

## Abstract

Degenerate four wave mixing measurements are performed on exciton resonance in island inserted quantum wells, where AlAs islands are embedded in the center of the GaAs quantum wells. It is found that the island insertion causes strong suppression of phase relaxation of the excitons. Deep quantum beats are also observed and attributed to coherent lateral oscillations of excitons between adjacent regions with one monolayer well width difference.

## 1 Introduction

In addition to the steady interest in standard quantum wells (QWs), optical properties of novel quantum confined structures such as quantum wires and quantum dots have attracted increasing interests toward new phase of physics and future ultrafast devices. In order to tailor the electronic states of QWs, a technique to insert a thin potential layer into a QW has been proposed and attempted with molecular beam epitaxy (MBE) [1]-[3]. For example, the insertion of one monolayer (ML) of AlAs or InAs into a GaAs QW as an repulsive or attractive potential pushes its energy level up or down uniformly. If the amount inserted is a half ML, random islands of potential are created, which modify in-plane electronic states. If a vicinal substrate is used, periodic modulation of the potential can be realized. We have so far investigated these structures regarding growth processes, electric transport properties, and optical properties [1]-[4].

Degenerate four wave mixing (DFWM) is an efficient technique to understand microscopic behaviors of electronic states in condensed matter, and has been successfully performed to study dynamics of excitons and free carriers in QWs and bulk semiconductors [5, 6]. We now

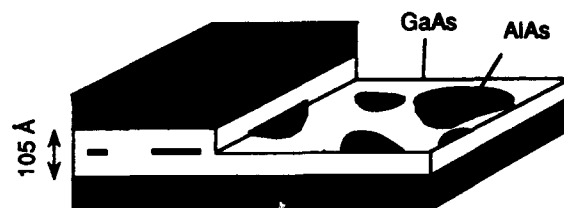


Figure 1: Schematic illustration of island-inserted quantum well (I<sup>2</sup>QW).

apply DFWM to study AlAs island inserted GaAs QW structures as shown in Fig. 1 to see how coherent motion of excitons in QWs is modified by the random islands inserted in the center of the wells.

## 2 Samples

Two samples were investigated; an island-inserted QW (I<sup>2</sup>QW) sample and a reference sample of normal QW (NQW) without island insertion. The samples were grown by MBE on (001) surfaces of semi-insulating GaAs substrates at 600°C. After deposition of a buffer layer of GaAs and an Al<sub>0.3</sub>Ga<sub>0.7</sub>As layer, 30 periods of I<sup>2</sup>QW or NQW structures were grown followed by a 200Å GaAs cap layer. The growth sequence of one period of I<sup>2</sup>QW was as follows (1ML=2.83Å); growth of 28ML AlAs, growth interruption for 10s, growth of 18ML GaAs, interruption for 60s, deposition of Al with an amount corresponding to 0.5ML of AlAs, interruption for 20s, growth of 18.5ML GaAs, and interruption for 60s. To enhance the migration of Al atom and to form large islands of AlAs, migration enhanced epitaxial technique was used

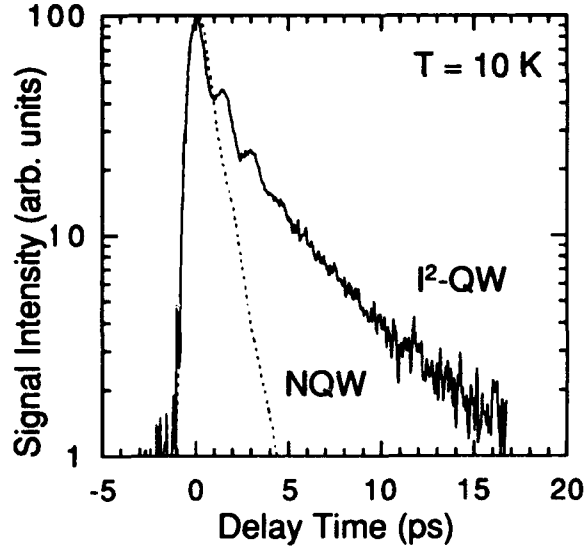


Figure 2: Self-diffraction intensity vs delay time for I<sup>2</sup>QW and NQW. The well width is 105Å.

at the 0.5ML AlAs island formation; flux of As, which was normally on, was cut during the Al deposition. The growth sequence of one period of NQW was similar except for no island insertion; growth of 28ML AlAs, growth interruption for 10s, growth of 37ML GaAs, and interruption for 60s. Previous study[3] on similarly prepared samples has indicated that the characteristic lateral sizes of interface and/or islands in these NQW and I<sup>2</sup>QW structures are 50-70Å at the bottom GaAs-on-AlAs interface of each QW, more than 1000Å at the top AlAs-on-GaAs interface, and 90-140Å for the AlAs islands inserted in I<sup>2</sup>QWs.

For transmission-type optical measurements, the samples were attached to Al<sub>2</sub>O<sub>3</sub> plates by epoxy glue, and their substrates were removed by wet etching.

The NQW sample shows photo-absorption at 1.559eV with 5meV FWHM (Full Width at Half Maximum) at 27K which includes structure of several small peaks with 2.0meV separation. These peaks are caused by well width fluctuations of one ML unit. The lateral size of roughness at the bottom GaAs-on-AlAs interfaces is far less than 100Å. This interface is referred to as pseudosmooth, since it is homogeneous if averaged over the area of exciton diameter. On the other hand, the roughness of top AlAs-on-GaAs interfaces are more than 1000Å in the lateral dimension, and larger than exciton diameter. Thus, they are perceived separately. The absorption spectrum of I<sup>2</sup>QW shows a single broader peak at 1.579eV with 8meV FWHM at 7K. This shows that the potential due to inserted AlAs islands are averaged by the exciton diameter. The absorption peak is inhomogeneously broadened, because the sizes of the islands and the exciton are comparable.

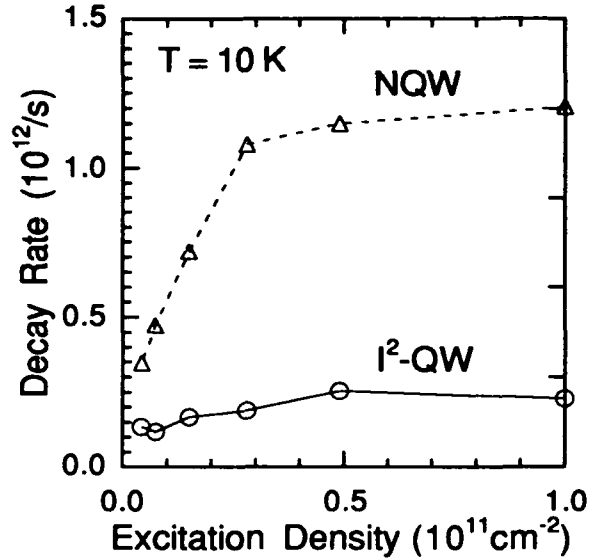


Figure 3: Decay rate of self-diffraction intensity vs excitation density for I<sup>2</sup>QW and NQW.

### 3 DFWM experiment

In DFWM measurements, simple two-pulse self-diffraction-type geometry in parallel polarization was used [5]. The first pulse creates polarization, or coherent excitons. The second pulse interfere with the polarization to generate the self-diffracted signal. Time integrated intensity of the self-diffracted light was measured changing the time delay of the second pulses. The light source was a commercial femto-second mode-locked Ti:sapphire laser. Pulses from the laser had pulse duration of 170fs, spectral width of 7.5meV, and repetition rate of 76MHz, and were focused on the samples with a spot diameter of 80μm. The photon energy was tuned to the heavy-hole exciton resonance. The samples were cooled down below 10K in a continuous-flow-type He cryostat.

Figure 2 shows the observed self-diffracted signal intensities as functions of the delay time for I<sup>2</sup>QW and NQW. Excitation density is estimated to be  $1 \times 10^{11} \text{ cm}^{-2}$ . Two features are clear for I<sup>2</sup>QW: slow dephasing and deep beats. Even when the excitation density is reduced to the order of  $10^9 \text{ cm}^{-2}$ , these features are unchanged for I<sup>2</sup>QW, whereas the decay of NQW signal becomes slow. This is shown in Fig. 3, which is the plots of decay rate against the excitation density for I<sup>2</sup>QW and NQW. Rapid increase of the decay rate in NQW for increasing excitation density is caused by carrier-carrier scattering. The very small change observed in I<sup>2</sup>QW implies that the carrier-carrier scattering is suppressed in I<sup>2</sup>QW. A possible explanation for this result is that the inserted random islands have made the excitons localized, and hence, reduced the interaction length of the excitons.

We assigned the origin of the beats to the one ML

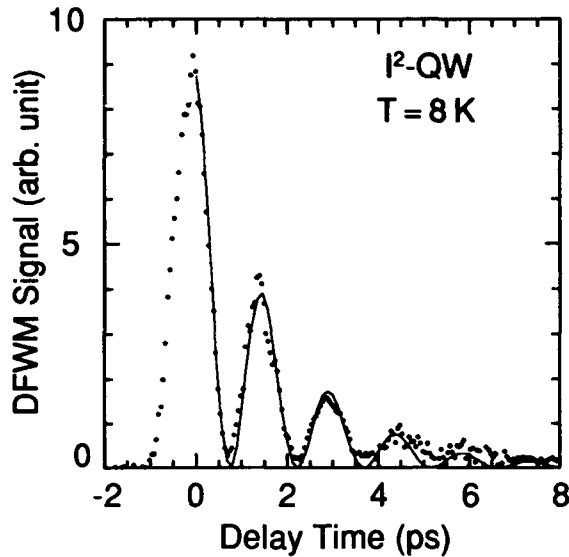


Figure 4: Detection-frequency-resolved self-diffraction intensity vs delay time at low energy region for I<sup>2</sup>QW. The solid line represents fitting on the basis of three band model in Ref.[5] with  $\Delta E = 2.85\text{meV}$  and  $T_2 = 3.67\text{ps}$ . The origin of the delay time as arbitrary.

well width fluctuation. The inverse of the beat periods multiplied by the Planck's constant gives energy difference of the two states responsible to the beats. The periods of observed beats are 1.83ps for NQW and 1.45ps for I<sup>2</sup>QW. These values correspond to the energy difference of 2.25meV and 2.85meV, respectively. The energy shift caused by the one ML well width difference is 2.0meV in NQW (measured), and is 2.8meV in I<sup>2</sup>QW (calculated). These values show very good agreements with the values obtained from the beat periods. The energy differences between the heavy-hole exciton and the light-hole exciton in NQW and I<sup>2</sup>QW were about 12meV, which is much larger than the energy differences corresponding to the beat periods.

To acquire more information, we tried measuring the self-diffracted signal of I<sup>2</sup>QW selecting the detection frequency. Adding a monochromator in front of the detector to ordinary DFWM setup, we measured the self-diffracted light intensity against delay time at various photon energy. The frequency resolution was as small as 0.9meV. Although the beat period does not change, the modulation depth of the beats gets deeper for lower detection photon energy. At low energy region, full modulation was observed, as shown in Fig. 4. We need to construct a theoretical framework for quantitative analyses of the detection-frequency-resolved DFWM. However, these results are enough to imply that the low energy localized states are important to produce deep beats.

The point here is that such deep beats can only be explained by "quantum beats", not by "classical beats" [5, 7]. The "quantum beat" is from coherent oscillation of

one exciton within coupled two states, whereas the "classical beat" is a beat of macroscopic polarization from independent two oscillators. In the latter case, a deep beat is impossible in DFWM. Moreover, any beat should not appear at all, when the system has strong inhomogeneous broadening. This is discussed quantitatively in Ref.[5], and the reason is as follows: It is true that the macroscopic linear polarization created by the first pulse may disappear at a node of the "classical beat", where each two kinds of dipoles are out-of-phase. However, the interaction with the second pulse causes rephasing of all the dipoles. What we observe is the intensity of the self-diffracted photon echo signal which is emitted at the twice the delay time of the second pulse. The two kinds of dipoles become all in-phase at the emission of the echo. Therefore, the beat in the DFWM signal for independent two states is impossible under the strong inhomogeneous broadening. It is only allowed as a result of incomplete rephasing under a finite inhomogeneous broadening, and never reaches a modulation depth of 100%.

From the beat depth, we can conclude that the observed beats are the "quantum beats", and that the responsible adjacent exciton states with well widths of one ML difference are not isolated, but coupled quantum mechanically in spite of the large size more than 1000Å. In other words, quantum interference of "laterally coupled wells" are observed, which consist of QWs of one ML well width difference having large sizes more than 1000Å.

We should now discuss the reason why no deep beat is observed for NQW, and also in high energy part of I<sup>2</sup>QW signal. Although the observed modulation depth is small in NQW, we consider the beat to be "quantum beat". This is because the lateral coupling between the wells with different well width is expected to occur in NQW as well as in I<sup>2</sup>QW. In NQW, however, excitons are more delocalized, so that more wells are laterally coupled than in I<sup>2</sup>QW. Then, additional inhomogeneity is introduced within the coupled region, such as well width difference of more than two ML, long range distribution of potential roughness, different coupling strengths at various boundaries between the wells with different well width. Thus, it is difficult to make deep beats in NQW. To solve these problems clearly, further study such as time resolved DFWM is necessary [7].

The second point of discussion is origin of the slow dephasing in I<sup>2</sup>QW; why the dephasing is slow while the island insertion broadens the absorption line, and reduces electron mobility[3] and electron-hole-pair diffusivity[4]. Potential roughness due to inserted islands causes inhomogeneously distributed energy levels. This can make absorption line broad, and transporting electrons scattered. However, the DFWM measurement depicts only the dephasing corresponding to the homogeneous broadening[6], which has nothing to do with the inhomogeneous broadening. Therefore, the island insertion makes the inhomogeneous broadening large, but does not shorten the decay of DFWM signal, or the dephasing.

Strictly speaking, potential roughness causes not only inhomogeneous broadening, but also localization. Probably, the localization and the shortened interaction length are the reason of the suppressed dephasing.

#### 4 Conclusion

Degenerate four wave mixing measurements are performed on exciton resonance in I<sup>2</sup>QW, or island inserted QWs, where AlAs islands are embedded in the center of the GaAs quantum wells. The island insertion causes strong suppression of phase relaxation of the excitons. This means that the interaction among excitons is weakened, most likely because of localization. Deep quantum beats are also observed. They are attributed to coherent lateral oscillations of excitons between adjacent regions with one monolayer well width difference.

#### Acknowledgments

The authors would like to thank Dr. K. Ema for supporting our experiment. They also thank T. Noda, J. Motohisa, and Professor K. Leo for helpful discussions. This work is supported by a Grant in Aid from the Ministry of Education, Science and Culture, and by the Research Development Corporation of Japan through the ERATO program for Quantum Wave Project.

#### References

- [1] T. Noda, M. Tanaka, and H. Sakaki, "Electron mobility and roughness scattering in potential inserted quantum wells (PI-QWs)", *J. of Crystal Growth*, **95**, 60-63 (1989).
- [2] Jean-Yves Marzin, and Jean-Michel Gérard, "Experimental probing of quantum-well eigenstates", *Phys. Rev. Lett.*, **62**, 2172-2175 (1989).
- [3] T. Noda, J. Motohisa, and H. Sakaki, "Atomic structure of monolayer AlAs islands on GaAs and its anisotropy revealed by mobility study in island-inserted quantum wells", *Surface Science*, **267**, 187-190 (1992), and references therein.
- [4] T. Matsusue, H. Akiyama, and H. Sakaki, "Diffusion of two-dimensional excitons in psuedo-random potentials embedded in quantum well structures", 6th Int. Conf. on Superlattices, Microstructures and Microdevices, Tu-P-43 (Xi'an, 1992), to be published in *Superlattices and Microstructures*, and reference therein.
- [5] K. Leo, E. O. Göbel, T. C. Damen, J. Shah, S. Schmitt-Rink, W. Schäfer, J. F. Müller, K. Köhler, and P. Ganser, "Subpicosecond four-wave mixing in GaAs/Al<sub>x</sub>Ga<sub>1-x</sub>As quantum wells", *Phys. Rev. B*, **44**, 5726-5737 (1991).
- [6] T. Yajima, and Y. Taira, "Spatial optical parametric coupling in picosecond light pulses and transverse relaxation effect in resonant media", *J. Phys. Soc. Japan* **47**, 1620-1626 (1979).
- [7] M. Koch, J. Feldmann, G. von Plessen, E. O. Göbel, P. Thomas, and K. Köhler, "Quantum beats versus polarization interference: An experimental distinction", *Phys. Rev. Lett.*, **69**, 3631-3634 (1992).

# Observation of Bloch Oscillations in a Semiconductor Superlattice

Peter Haring Bolivar, Patrick Leisching, and Karl Leo

*Institut für Halbleitertechnik, RWTH Aachen, Sommerfeldstrasse 24, W-5100 Aachen, Germany*

Jagdeep Shah

*AT&T Bell Laboratories, Crawford Corner Road, Holmdel, New Jersey 07733*

Klaus Köhler

*Fraunhofer-Institut für angewandte Festkörperphysik, Tullastrasse 72, W-7800 Freiburg, Germany*

## Abstract

We investigate the polarization decay in biased superlattices with transient degenerate four-wave mixing. The signals have a strong periodic modulation in the field regime where the cw optical spectra show the transitions of a Wannier-Stark ladder. The period of the oscillations is in excellent agreement with Bloch oscillation theory. The oscillation period can be tuned over a large range by varying the electric bias field in the superlattice.

## Introduction

The relaxation dynamics of coherent optical excitations in semiconductor heterostructures have recently gained much interest [1,2]. A number of studies have addressed the relaxation dynamics of the polarization itself, e.g. many-body effects in the decay of the polarization, using degenerate four-wave mixing (FWM) [3-5]. Several recent experiments have studied the dynamics of optically excited superpositions of transitions (wavepackets) in semiconductors. The freedom in the design of semiconductor heterostructures allows to adjust wavefunctions and transitions energies by a suitable sample design and by varying the electric field in situ. Of particular interest for both basic research and applications are experiments where the wavepackets show distinct *spatial dynamics*. The first example of such experiments was the observation of coherent charge oscillations in a coupled double quantum well heterostructure by transient four-wave mixing and pump-

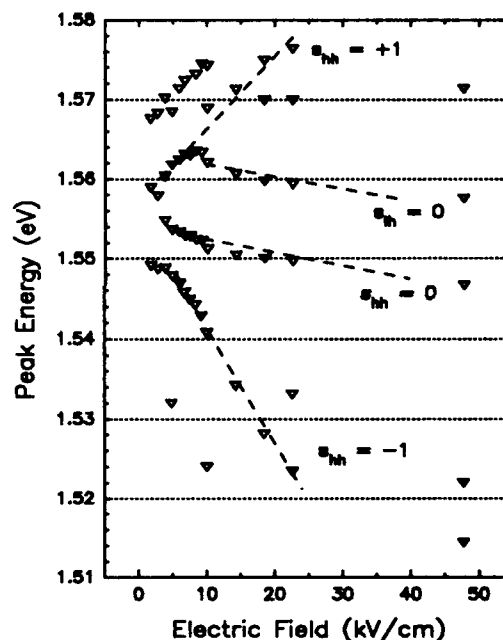


Figure 1: Wannier-Stark-ladder of the GaAs/AlGaAs superlattice. Plotted are the photocurrent peaks as a function of the electric field.

probe experiments [6]. Recently, it was shown that the oscillating electron wavepacket in the double quantum well structure emits coherent radiation in the THz regime [7], which demonstrates a novel principle for the generation of coherent radiation in the infrared.

Semiconductor superlattices have recently gained much attention as a model system for the investigation of the

electronic states in a periodic potential (Bloch states [8]). The dynamics of Bloch states in a homogeneous electric field has long been an intriguing problem in solid state physics. In an ideal case, when scattering can be completely neglected, the electrons will accelerate due to the electric field till they reach the upper edge of the band. There, they will be reflected and return to the initial state. These "Bloch oscillations" (BO) in the Brillouin zone have a period

$$\tau_B = \frac{h}{eFd}, \quad (1)$$

where  $d$  is the lattice constant. Bloch oscillations in the time domain are closely related to the Wannier-Stark [9] ladder (WSL) in the frequency domain [10]. The extended Bloch states become localized due to the field. The energy band is transformed into evenly spaced ladder states with energies

$$E_N = E_0 + n\Delta E, \quad n=0, \pm 1, \pm 2, \dots \quad (2)$$

where

$$\Delta E = eFd = h/\tau_B. \quad (3)$$

Neither BO and WSL have not been experimentally observed in bulk solids. A necessary condition for the observation of BO is that the scattering time is larger than the Bloch oscillation time. The electric field required for a sufficient localization of the Bloch functions in the bulk exceeds the breakdown fields by far.

Esaki and Tsu have pointed out that the situation is much more favorable in a semiconductor superlattice (SL) due to larger period, which leads to much narrower bands (minibands) and to a localization at much lower fields than in the bulk [11]. WSL, which are the frequency-space equivalent of BO in the mini-Brillouin zone, have indeed been observed in semiconductor superlattices with various optical techniques [12,13]. Recent time-resolved experiments in a semiconductor superlattice gave indications for BO [14]. The observation of Bloch oscillations in such a system is both proof of a theoretical concept and important for applications: It was predicted [11] that the electrons oscillating in a superlattice miniband emit coherent electromagnetic radiation. The frequency of the radiation could be tuned by changing the applied bias.

## Results and Discussion

We here report about the observation of Bloch oscillations [15] in a nominally undoped semiconductor superlattice containing 40 periods of 100Å thick GaAs and 17Å thick  $\text{Al}_{0.3}\text{Ga}_{0.7}\text{As}$  layers grown by molecular beam epitaxy (MBE) on n-doped GaAs substrate. All thicknesses are nominal. On top of the sample, a transparent Cr/Au Schottky is evaporated to enable the application of an electric bias field across the intrinsic SL. The sample is mounted on a sapphire disk and the substrate is removed by selective wet etching to allow experiments in transmission configuration. Results of a Kronig-Penney calculation give an electron miniband width of about 19meV and a heavy-hole miniband width of about 2meV for the nominal sample parameters. The optical characterization indicates that the nominal thicknesses are precise within 10%.

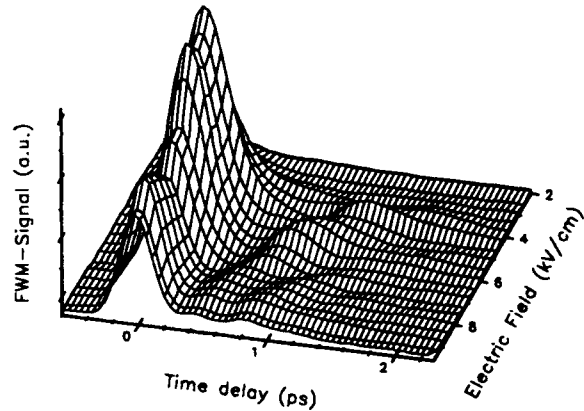
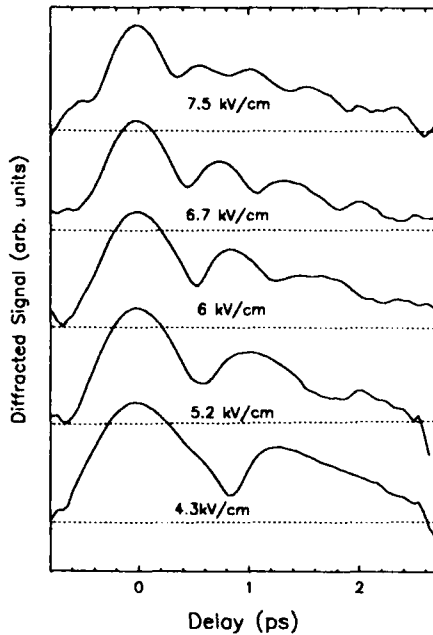


Figure 2: FWM signal as a function of time delay and electric field.

Figure 1 shows the peaks in the low-temperature photocurrent (PC) spectrum of the sample as a function of the bias voltage. For higher fields ( $\geq 5$  kV/cm), the spectra show a Wannier-Stark ladder with spectral shifts as expected for the sample parameters. Some of the transitions are labeled with the number of the transition (Eq. 2) and an index giving the heavy-hole (hh) or light-hole (lh) type of the transition. A close inspection of the PC data shows transition with indices up to  $n=3$ , proving that the wavefunctions are delocalized over more than six periods. The photocurrent data also show

some deviations from the simple WSL picture. The ladder transitions are not completely linear with field and show anticrossings, in good agreement with theoretical predictions which include Coulomb effects [16]. Additionally, anticrossings of transitions are



**Figure 3:** Four-wave mixing traces as a function of the delay time for various electric fields. Lattice temperature and excitation density are 8.5K and  $2 \times 10^9 \text{ cm}^{-2}$ /period, respectively.

visible, in particular in the low-field regime.

As laser source for the time-resolved experiments, we use a Kerr-lens mode-locked (KLM) Titanium-Sapphire laser emitting 100fs (FWHM) pulses. The set-up for the time-resolved optical experiments is a standard two-beam degenerate four-wave mixing set-up [17]. Detected is the time-integrated signal in direction  $k_3 = 2k_2 - k_1$ . The decay of this signal as a function of the delay time reflects the dephasing of the transition. The lattice temperature is about 10K in the experiments presented here. The carrier density is kept low to avoid dephasing due to carrier-carrier scattering ( $n_{\text{exc}} = 2 \times 10^9 \text{ cm}^{-2}$  per period). The low excitation density also keeps the field screening by the photo-excited carriers low [18].

Figure 2 shows transient FWM data as a function of delay time and electric field. The excitation energy is at 1.537eV, which is slightly below the center of the

superlattice transitions. The bandwidth of the laser (about 17meV) is large enough to cover several transitions of the WSL, at least for the lower fields. The excitation density is about  $2 \times 10^9 \text{ cm}^{-2}$  per period of the SL. In the low field regime (not shown), the data show a periodic modulation due to quantum beats between the excitons associated to the heavy-hole and the light-hole minibands. The period is not significantly dependent on the electric field. For somewhat larger fields, the signals show a periodic modulation with a period which decreases strongly with increasing field, which is the signature of Bloch oscillations. Figure 3 shows transient FWM data as a function of delay time for several electrical fields. More than four oscillations in the polarization decay are visible. The overall decay time of the signals, which can be related to the dephasing of the excitation [17], is about 1.5ps and not significantly dependent on the electric field.

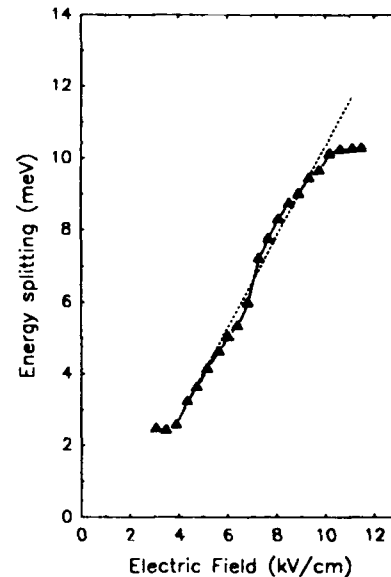


**Figure 4:** Energy splitting eFd as calculated from Eq 3 vs. electric field. The dashed line gives the expected slope for the SL period of 117Å.

Figure 4 displays the energies calculated from the period of the oscillations observed in the FWM signals using Eq. 3. The energy shows the expected linear dependence on the electric field. The proportionality constant is in good agreement with that expected from the parameters of the superlattice (dashed line), which confirms that the modulation of the FWM signals is caused by Bloch oscillations of the photoexcited electrons in the mini-

Brillouin zone of the superlattice. For the highest field, the electrons perform more than four oscillations with a period of about 450fs before the oscillation is damped due to relaxation processes. For lower fields, the number of oscillations decreases due to the increase of the oscillation period relative to the dephasing time. The period of the oscillations can be tuned over a rather large field range, in contrast to the previous results in coupled quantum wells. In the coupled well system, the modulation of the oscillations decreases strongly with increasing distance from the resonance. The localization in superlattices is much more gradual with increasing field, thus allowing a much larger tuning. Our results already show a tuning range of more than 400%. SL are thus a more promising system for the generation of tunable radiation than coupled quantum wells. Recently, we have further extended the tuning range and have observed up to eight oscillations before dephasing of the wavepacket.

A number of open questions about Bloch oscillations in superlattices could be addressed in further studies: (i) The influence of the excitonic and Coulomb coupling [16], as observed in the cw spectra, on the dynamics should be clarified (ii) The signal of Fig. 2 shows an oscillation of the absolute FWM signal when the electric field is tuned. Also, the FWM signal is nearly disappearing in the transition region between the miniband and WSL regime. These effects are not understood yet (iii) It would be interesting to investigate whether the oscillations can be observed at 77K and above. This is particularly interesting for a device application of the Bloch oscillator as THz source. The emission of THz radiation has recently indeed been observed [19] using the same experimental technique as for the double quantum well emission experiments [7].

## Conclusion

In conclusion, we have unambiguously observed Bloch oscillations in a semiconductor superlattice. The decay of the transient four-wave mixing signal has a periodic modulation which shows more than four oscillations of the electrons in the Brillouin zone before the coherence is lost. The period of the oscillation can be tuned over a large range and is in excellent agreement with Bloch oscillation theory.

## Acknowledgments

We are indebted to R. Schwedler and F. Brüggemann for performing the sample characterization, H. Bakker, G. Bastard, H. Kurz, H. Roskos, and C. Waschke for useful discussions, D. Laschet for sample preparation, and P. Ganser for help with the sample growth. Financial support from the Deutsche Forschungsgemeinschaft (contract Le 747/2) and the Alfried Krupp Stiftung is gratefully acknowledged.

## References

1. E.O. Göbel, *Festkörperprobleme (Advances in Solid State Physics)* **30**, Ed. U. Rössler (Vieweg, Braunschweig 1990), p. 269.
2. J. Kuhl, A. Honold, L. Schultheis, and C.W. Tu, *Festkörperprobleme (Advances in Solid State Physics)* **29**, Ed. U. Rössler (Vieweg, Braunschweig 1989), p. 157.
3. K. Leo, M. Wegener, J. Shah, D.S. Chemla, E.O. Göbel, T.C. Damen, S. Schmitt-Rink, and W. Schäfer, *Phys. Rev. Lett.* **65**, 1340 (1990).
4. D.S. Kim, J. Shah, T.C. Damen, W. Schäfer, F. Jahnke, S. Schmitt-Rink, and K. Köhler, *Phys. Rev. Lett.* **69**, 2725 (1992).
5. S. Weiss, M.-A. Mycek, J.-Y. Bigot, S. Schmitt-Rink, and D.S. Chemla, *Phys. Rev. Lett.* **69**, 2685 (1992).
6. K. Leo, J. Shah, E.O. Göbel, T.C. Damen, S. Schmitt-Rink, W. Schäfer, and K. Köhler, *Phys. Rev. Lett.* **66**, 201 (1991); K. Leo, J. Shah, T.C. Damen, A. Schulze, T. Meier, S. Schmitt-Rink, P. Thomas, E.O. Göbel, S.L. Chuang, M.S.C. Luo, W. Schäfer, K. Köhler, and P. Ganser, *IEEE J. Quantum Electronics* **QE 28**, 2498 (1992).
7. H.G. Roskos, M. C. Nuss, J. Shah, K. Leo, D.A.B. Miller, A. M. Fox, S. Schmitt-Rink, K. Köhler, *Phys. Rev. Lett.* **68**, 2216 (1992).
8. F. Bloch, *Z. Phys.* **52**, 555 (1928).
9. G.H. Wannier, *Rev. Mod. Phys.* **34**, 645 (1962).
10. G. Bastard and R. Ferreira, in *Spectroscopy of Semiconductor Microstructures*, NATO ASI Series (Plenum Press, New York 1989), p.333.
11. L. Esaki and R. Tsu, *IBM J. Res. Dev.* **14**, 61 (1970).
12. E.E. Mendez, F. Agulló-Rueda, and J.M. Hong, *Phys. Rev. Lett.* **60**, 2426 (1988).
13. P. Voisin, J. Bleuse, C. Bouche, S. Gaillard, C.



- Alibert, and A. Regreny, *Phys. Rev. Lett.* **61**, 1639 (1988).
14. J. Feldmann, K. Leo, J. Shah, D.A.B. Miller, J. E. Cunningham, S. Schmitt-Rink, T. Meier, G. von Plessen, A. Schulze, and P. Thomas, *Phys. Rev. B* **46**, 7252 (1992); K. Leo, J. Feldmann, J. Shah, S. Schmitt-Rink, J.E. Cunningham, D.A.B. Miller, *Proc. 8th International Quantum Electronics Conference, Vienna 1992*, p. 248.
15. K. Leo, P. Haring Bolivar, F. Brüggemann, R. Schwedler, and K. Köhler, *Solid State Commun.* **84**, 943 (1992).
16. M.M. Dignam and J.E. Sipe, *Phys. Rev. Lett.* **64**, 1797 (1990).
17. T. Yajima, and Y. Taira, *J. Opt. Soc. Jpn.* **47**, 1620 (1979).
18. The fields for the time-resolved data have been corrected for the screening effects. A detailed investigation of the field screening will be published elsewhere.
19. C. Waschke et al., submitted for publication.

# Femtosecond Optical Response of Low Temperature Grown In<sub>53</sub>Ga<sub>47</sub>As

B. C. Tousley

*U.S. Army Photonics Research Center and Department of Electrical Engineering and Computer Science,  
United States Military Academy, West Point, New York 10996*

S. M. Mehta, A. I. Lobad, P. J. Rodney, and P. M. Fauchet

*Laboratory for Laser Energetics, 250 East River Road, Rochester, New York 14623-1299*

P. Cooke

*Army Research Laboratory, Fort Monmouth, New Jersey 07703-5016*

## I. Introduction

Low Temperature III-V MBE (LTMBE) grown materials have generated significant interest recently, due to their ultrafast recombination time, their relatively high mobility (even after post growth anneal), and the high resistivity as a result of this anneal [1]. The device applications for these materials include subpicosecond photoconductive switching, use as a buffer layer for active layers of high speed electronic devices, and use as optical waveguides [2]. The optical response of LTMBE GaAs and In<sub>52</sub>Al<sub>48</sub>As has been examined and their usefulness as a photoconductive switch has been demonstrated [3,4,5]. The ternary III-V material In<sub>53</sub>Ga<sub>47</sub>As, lattice matched to InP, has been used extensively for optoelectronic devices operating at the direct bandgap of .75 eV. Here, we report the results of an ultrafast characterization of the optical response of LTMBE In<sub>53</sub>Ga<sub>47</sub>As as a function of growth temperature and excitation intensity, near the conduction band edge. We have used optical pump-probe femtosecond spectroscopy, utilizing an APM NaCl:OH Color Center Laser, which delivers nominally 200 fs pulses, tunable from 1.47-1.65  $\mu$ m, at a 76 MHz repetition rate, and with a usable output power of 100 mW. We have investigated the optical response of samples grown over a range of temperatures from 660° C down to 250° C, using a range of wavelengths and optical intensities. We have also attempted to demonstrate the feasibility of this material as a subpicosecond photoconductive switch by using electro-optic sampling.

## II. Experimental Conditions

### A. Sample Preparation and Characterization

The LTMBE In<sub>53</sub>Ga<sub>47</sub>As samples were grown at the U.S. Army Research Laboratory, and are listed in Table 1. The samples were grown over a variety of temperatures, and the growth rate was 1  $\mu$ m per hour on (001) oriented semi-insulating InP substrates. The temperature of the MBE chamber was carefully ramped down to the desired growth temperature under As rich conditions. The growth temperature, measured with a reactor thermocouple, is estimated to be 100° C higher than the actual growth temperature (due to offset). The Beam Equivalent Pressure (BEP) ratio was approximately 35, and we used RHEED and double crystal X-ray diffraction to gain a qualitative measurement of the crystallinity. All samples were grown nominally lattice matched to InP. Hall measurements were taken in order to determine the minority carrier concentration, the resistivity, and the mobility. One should note however that most samples were close to full depletion. Some of the samples were annealed in-situ following growth, at a temperature of 600° C, under an As overpressure, for 10 minutes. From previous studies, it is generally accepted that in LTMBE GaAs and In<sub>52</sub>Al<sub>48</sub>As, excess As incorporation increases as the growth temperature is lowered, and below 200° C the material grows polycrystalline as the number of defects rapidly increases [6,7]. The large density of states near

**Table 1. LTMBE In<sub>53</sub>Ga<sub>47</sub>As Samples**

Sample #	Growth Temperature (°C)	Crystallinity	Minority Carrier Density (/cm <sup>3</sup> )	Mobility (cm <sup>2</sup> /(V.s))
G909	660	SC	4.0 x 10 <sup>15</sup>	5400
G906	550	SC	1.5 x 10 <sup>16</sup>	4000
G915	300	SC/PC	1.5 x 10 <sup>17</sup>	2350
G908	250(A)	R	2.7 x 10 <sup>17</sup>	150
G910	250	R/PC	2.0 x 10 <sup>17</sup>	1100

*A = Annealed in-situ for 10 mins at 600° C under As overpressure;*

*SC = single crystal, PC = polycrystalline, R = relaxed*

the band-edge, due to traps/defects, modifies the absorption edge, which is shown in Figure 1; absorption plots of normal growth temperature and LTMBE (250° C)  $\text{In}_{.53}\text{Ga}_{.47}\text{As}$  samples, taken using a Perkin-Elmer spectrophotometer, indicate the large number of near band edge states in the low temperature grown material. In the LTMBE material the absorption edge is smeared because of the enhancement of band tailing.

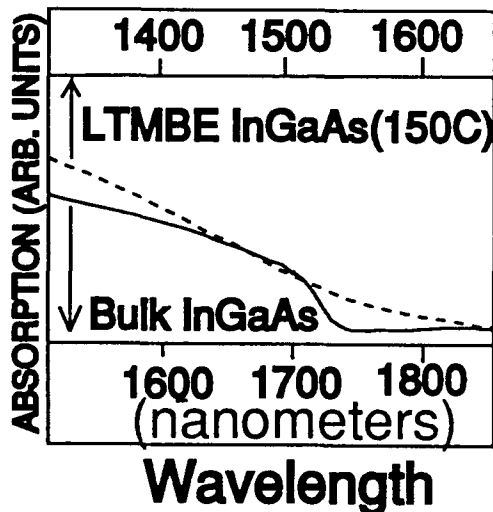


Figure 1. Absorption of  $\text{In}_{.53}\text{Ga}_{.47}\text{As}$  and LTMBE  $\text{In}_{.53}\text{Ga}_{.47}\text{As}$

### B. Experimental Apparatus

Our experimental apparatus is the typical pump-probe femtosecond time resolved transmission and reflection spectroscopy. The pump-probe source is an APM NaCl:OH(-) color center laser. A rapid scanning arm of a Michelson interferometer is the variable delay line for the pump signal, and we use differential detection and signal averaging to obtain our data. The probe beam is heavily attenuated compared to the pump beam, and the beams are orthogonally polarized to eliminate coherent artifacts. The pump beam is focussed using 10X objectives or lenses, which allows us to bleach the Bloch states. We were able to tune the laser (and hence our excitation energy) over a variety of wavelengths, although we concentrated our investigations near the bottom of the  $\Gamma$  valley. We obtained both transmitted and reflected signals, although qualitatively there was no difference in the temporal response.

### III. Experimental Results

We observe that in LTMBE  $\text{In}_{.53}\text{Ga}_{.47}\text{As}$  the recombination time drops as the growth temperature is reduced. Figure 2 is a composite plot of the differential transmission through samples W678, G906, G915, G908, and G910 where the decay times (recombination time) are respectively  $> 100$  ps,  $\sim 12$  ps, 4.3 ps, 2.8 ps, and 520 fs. Sample W678 is the bulk control sample grown at normal MBE growth temperatures. Here we define the decay time as the  $1/e$  point of the decay from the peak of the transmitted or

absorbed signal. This data was all taken at an excess energy of 50 meV above the conduction band edge. Qualitatively there was no difference in decay time over the range of wavelengths we excited the samples. The estimated excited carrier density is  $3 \times 10^{17}/\text{cm}^3$  which corresponds to a change of absorption of  $\sim 5 \times 10^2/\text{cm}$ . The measured absorption of G910 was  $7.8 \times 10^3/\text{cm}$  at  $1.54 \mu\text{m}$ . We note that for both G910 and G908 samples were grown at  $\sim 250^\circ\text{C}$ , but only G908 has been in-situ annealed at high temperature. Sample G910 displays induced absorption, while sample G908 is bleached. Note that the bulk control sample, W678, displays behavior indicative of the bleaching of optically coupled Bloch states by the injection of an initially nonthermal electron-hole plasma. Because there is no scattering to satellite valleys, we observe the thermalization and cooling of the plasma near the conduction band edge, including carrier cooling by LO phonon emission and the effects of band gap renormalization [9].

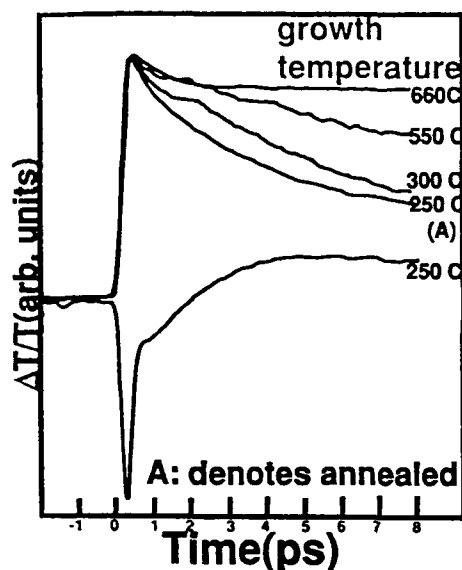


Figure 2. Experimental Differential Transmission of LTMBE  $\text{In}_{.53}\text{Ga}_{.47}\text{As}$

The differential transmission is plotted for the different samples.

### IV. Modeling

We have modeled the conditions of our experiment, using an approach similar to that of Nunnenkamp, *et al.*[10]. The results shown in Figure 3, are in good agreement with the data. Our simulations represent degenerate pump-probe spectroscopy, where we analyze single wavelength pump and probe. The injection of a nonequilibrium carrier distribution, bandfilling, and cooling by coupling to optic phonons is included in the examination of the temporal dependence of the differential transmission. We neglect the effects of the Coulomb enhancement factor. This is consistent with the absorption curve near the conduction band edge (Figure 1). The maximum change of differential transmission (due to

bleaching) is  $\sim 15\%$ , which corresponds to a change of absorption of  $\sim 5 \times 10^2/\text{cm}$ .

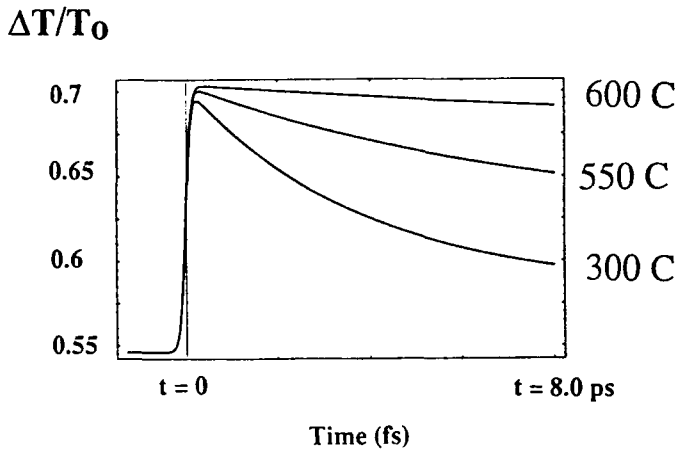


Figure 3. Modeling of Pump Probe of LT  $\text{In}_{0.53}\text{Ga}_{0.47}\text{As}$  Differential Transmission with various effective recombination times

### V. Discussion

From Shockley-Read-Hall theory the minority carrier lifetime is inversely dependent on the product of the defect density, the capture cross section, and the thermal velocity [3]. Utilizing reasonable data from LTMBE GaAs and  $\text{In}_{0.52}\text{Al}_{0.48}\text{As}$  results, one would expect that the recombination time should drop below 1 ps as the number of defects exceeds  $5 \times 10^{17} \text{ cm}^{-3}$  [3]. Due to the large number of traps it has been established that the recombination time reduction is due to nonradiative processes [8]. We observe a reduction in recombination time as a function of growth temperature in LTMBE InGaAs, consistent with that previously observed in LTMBE GaAs and  $\text{In}_{0.52}\text{Al}_{0.48}\text{As}$  [4]. Sample G908 ( $T_g = 250^\circ\text{C}$ ) displays induced absorption and after annealing (Sample G910) the ultrafast component reverses sign to display transient bleaching. Induced absorption in  $200^\circ\text{C}$  grown unannealed  $\text{In}_{0.52}\text{Al}_{0.48}\text{As}$  has been observed and when annealed the sample behavior also changes from induced absorption to induced bleaching [4]. The induced absorption has been previously explained as possibly due to the large density of near band edge states, created from the traps/defects, which results in larger free carrier absorption (FCA) [4]. The signal change from induced absorption to transient bleaching was attributed to the net reduction of trapped states as a result of As precipitate formation by annealing.

Our analysis suggests that FCA is not the reason for the induced absorption. At the minority carrier densities ( $2.7 \times 10^{17} \text{ cm}^{-3}$ ) and measured mobilities in sample G910, the FCA is less than  $10 \text{ cm}^{-1}$ , and thus is negligible compared to one photon absorption ( $\sim 10^3 \text{ cm}^{-1}$ ). Additionally, surface field effects can be discarded because the absorption depth is significantly longer than our sample thickness, and we have conducted differential transmission spectroscopy, as opposed to previously conducted LTMBE GaAs transient reflectivity measurements [3,4].

It is well established that in GaAs [1] the  $\text{As}_{\text{Ga}}$  antisite defect is associated with the "deep" electronic level EL2. In GaAs EL2 is located at a midgap location approximately .84 eV above the heavy hole valence band. When LTMBE GaAs is grown, the concentration of the antisite defect states dramatically rises to  $\sim 10^{19} \text{ cm}^{-3}$ , and depending upon the location of the Fermi energy and the lattice temperature these states are significantly populated. The deep state defect EL2 has been recently observed in  $\text{In}_x\text{Ga}_{1-x}\text{As}$  grown on GaAs [6], with  $x$  in the range  $.045 < x < .18$ . The energy level of these defects remains roughly at midgap, and scales appropriately as the In composition is increased. The defects are formed well away from the Ga substrate. Our analysis suggests that the LTMBE material acts like a three level system, as shown in Figure 4. LTMBE  $\text{In}_{0.53}\text{Ga}_{0.47}\text{As}$  forms

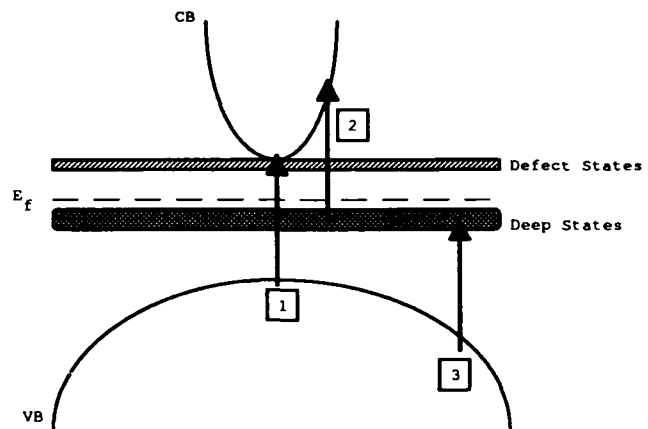


Figure 4. Simplified Band Diagram of LTMBE  $\text{In}_{0.53}\text{Ga}_{0.47}\text{As}$

defect states near the band edge which enhance the Urbach tail, and these are clearly observed in Figure 1. Deep states with extended wavefunctions in  $k$ -space are created, and these are associated with anti-site defects positioned roughly at midgap. These deep states are of the density of  $10^{18} - 10^{19} \text{ cm}^{-3}$ , which is significantly greater than the conduction band DOS at the  $\Gamma$  valley center. The Fermi energy at 300 K is near the deep state location which suggests that most of the states are occupied. It is also well known that (in GaAs) these deep states act as traps/recombination centers. On the other hand, only a small fraction of the near band edge defect states are filled at room temperature.

From Figure 4, there are three likely optical transitions for  $1.55 \mu\text{m}$  (.75 eV) radiation. Transition 1 is the usual conduction - valence band transition. Transition 2 is the transition from the *occupied* deep state to the conduction band. Transition 2 is strong because these deep donor states are delocalized in  $k$ -space. Transition 3 is a transition from the heavy hole valence band to an unoccupied defect state. The deep states are heavily populated at room temperature, and therefore Transition 3 will most likely occur only when a significant number of these states are vacant.

The differential transmission signal will reflect the sum of all three of these transitions. In the bulk  $600^\circ\text{C}$  MBE material only Transition 1 is observed. The femtosecond

optical response of Transition 1 has been described previously. As expected, we observe transient bleaching (see Figure 2,  $T_g = 600^\circ\text{C}$ ). In LTMBE materials, Transition 2 may be stronger because of the larger DOS. Therefore, Transition 2 sees a much larger absorption cross section than Transition 1. When the deep states have been *depopulated* (by a pump pulse exciting Transition 2), the absorption cross section for Transition 3 will also be much larger than that of Transition 1. Thus immediately after the pump pulse illuminates the sample, the sum of the three transitions results in *induced absorption*. After a few ps, when trapping by the recombination centers and cooling of the total distribution to the lattice temperature has occurred, Transition 2 and 3 are effectively shut off, and we observe band filling of the near band edge states.

## VI. Applications and Conclusion

We have also attempted to utilize LTMBE  $\text{In}_{.53}\text{Ga}_{.47}\text{As}$  as a subpicosecond photoconductive switch and test its response with an electro-optic sampling system. However, in contrast to LTMBE GaAs and  $\text{In}_{.52}\text{Al}_{.48}\text{As}$ , because the resistivity of LTMBE  $\text{In}_{.53}\text{Ga}_{.47}\text{As}$  is unchanged from that of normal growth *n* type material, even after post growth anneal, we were unsuccessful. This precludes its immediate use as a photoconductive switch. Assuming nondegeneracy and the Fermi level pinned at midgap, the Fermi-Dirac occupation function (near the conduction band edge, and ignoring the apparent doping of electrons in the defect states) is seven orders of magnitude larger in intrinsic  $\text{In}_{.53}\text{Ga}_{.47}\text{As}$  than in intrinsic GaAs at  $300^\circ\text{K}$ , resulting in lower resistivity. Inclusion of excess As merely makes the material even more conductive.

Even with the unchanged resistivity LTMBE  $\text{In}_{.53}\text{Ga}_{.47}\text{As}$  still may find use as an optical waveguide material. The total induced change of absorption (in sample # G910) at  $10^{17}$  injected carriers per  $\text{cm}^3$  results in a change of  $\Delta n_{\text{imag}}$  of  $\sim .15\%$ , and this corresponds to a change of absorption of  $\sim 4.5\%$  ( $\Delta\alpha = 135\text{ cm}^{-1}$ ). Given that this change of absorption occurs in a  $1\text{ }\mu\text{m}$  thick sample and has a subpicosecond recovery time, there exist possibilities for ultrafast nonlinear devices based on the LTMBE  $\text{In}_{.53}\text{Ga}_{.47}\text{As}$  material. We are currently attempting to circumvent the resistivity obstacle by growing the quaternary  $\text{In}_x(\text{GaAl})_{1-x}\text{As}/\text{InP}$  at low temperature, with and without strain. It is already known that increasing the aluminum content increases the resistivity [2], even in the low temperature grown material. This should result in improved photoconductive switch response.

In summary we have investigated and modeled the femtosecond optical response of LTMBE  $\text{In}_{.53}\text{Ga}_{.47}\text{As}$  as a function of wavelength, excitation intensity and thin film sample growth temperature. We have determined there is a growth temperature dependent recombination time in this material, similar to that in other LTMBE III-V semiconductor materials. Below  $250^\circ\text{C}$ , the material displays induced absorption, as a result of the creation of a large density of deep defect states. Although this material as currently grown would be incompatible for use as a

photoconductive switch, its ultrafast optical response may present optical nonlinearities which could be of use in planar or waveguide devices. We intend to explore this, as well as attempting to increase the sample resistivity by increasing the aluminum content or introducing strain.

We acknowledge support from ONR Grant No. N00014-91-J-1488 and ARO Grant No. DAAL03-91-G-0173.

## References

1. F.W. Smith, "Device Applications of Low-Temperature-Grown GaAs", *MRS Proceedings #241, LT GaAs and Related Materials*, pp3-12, (1991)
2. H. Kunzel, N. Grote, P. Albrecht, J. Boettcher, and C. Bornholdt, "Low-Temperature MBE-Grown  $\text{In}_{.52}\text{Al}_{.48}\text{As}/\text{InP}$  Optical Waveguides", *Elect. Lett.* 28, 844 (1992).
3. S. Gupta, P.K. Bhattacharya, J. Panulapati, and G. Mourou, "Subpicosecond photoresponse of carriers in low-temperature molecular beam epitaxial  $\text{In}_{.52}\text{Al}_{.48}\text{As}/\text{InP}$ ", *Appl. Phys. Lett.* 57, 1543 (1990).
4. S. Gupta, M.Y. Frankel, J. A. Valdmanis, J. F. Whittaker, G. A. Mourou, F. W. Smith, and A. R. Calawa, "Subpicosecond carrier lifetime in GaAs grown by molecular beam epitaxy at low temperatures", *Appl. Phys. Lett.* 59, 3276 (1991).
5. D.R. Kykaar, D.J. Eaglesham, U.D. Keil, B.I. Greene, P.N. Saeta, L. N. Pfeiffer, R. F. Kopf, S. B. Darack, and K.W. West, "Molecular Beam Epitaxy of Low Temperature Grown GaAs Photoconductors", *MRS Proceedings #241, LT GaAs and Related Materials*, p245, (1991).
6. A.C. Irvine, and D.W. Palmer, "First Observation of the EL2 Lattice Defect in Indium Gallium Arsenide Grown by Molecular-Beam Epitaxy", *Phys. Rev. Lett.* 68, 2168 (1992).
7. A. Claverie, K.M. Yu, W. Swider, Z. Liliental-Weber, M.O'Keefe, R. Kilaas, J. Panulapati, and P.K. Bhattacharya, "Structural characterization of low-temperature molecular beam epitaxial  $\text{In}_{.52}\text{Al}_{.48}\text{As}/\text{InP}$ ", *Appl. Phys. Lett.* 60, 989 (1992)
8. H.M. van Driel, X.Q. Zhou, W.W. Ruehle, J. Kuhl, and K. Ploog, "Photoluminescence from hot carriers in low-temperature-grown gallium arsenide", *Appl. Phys. Lett.* 60, 2246 (1992).
9. B.C. Tousley, S.M. Mehta, A.I. Lobad, P.J. Rodney, and P.M. Fauchet, to be presented at *Conference on Lasers and Electro-Optics* May 1993, Baltimore, Md
10. J. Nunnenkamp, J.H. Collet, J. Klebiczki, J. Kuhl, and K. Ploog, "Subpicosecond kinetics of band-edge absorption in  $\text{Al}_{.25}\text{Ga}_{.75}\text{As}$ ", *Phys. Rev. B*, Vol. 43, # 17, pp. 14047-14054, (1991).
11. K. Seeger, *Semiconductor Physics*, (Springer-Verlag, New York, 1991), pp346-360.

# Carrier Scattering and Excitonic Effects on Electron-Hole-Pair Diffusion Measured with Optical Fiber Probing Technique

Hidefumi Akiyama

*Research Center for Advanced Science and Technology,  
University of Tokyo, 4-6-1 Komaba, Meguro-ku, Tokyo 153, Japan*

Toshio Matsusue

*Institute of Industrial Science, University of Tokyo, 7-22-1 Roppongi,  
Minato-ku, Tokyo 106, Japan*

Hiroyuki Sakaki

*Quantum Wave Project, ERATO, Research Development Corporation of Japan,  
4-3-24 Komaba, Meguro-ku, Tokyo 153, Japan*

## Abstract

We have demonstrated lateral diffusion measurements of photo-excited electron-hole pairs at various excitation densities for non-doped and p-type modulation-doped GaAs/Al<sub>0.3</sub>Ga<sub>0.7</sub>As multiple quantum well structures at 77K, using a new all-optical time-of-flight technique with a single-mode optical fiber probe. Systematic measurements at various electron and hole densities showed that strong electron-hole scattering reduces the diffusivity, but that exciton formation weakens scattering and enhances the diffusivity.

## 1 Introduction

Electron-hole-pair transport is an important process in ultrafast optoelectronic devices because it affects significantly the high frequency response of the devices [1]-[2]. Moreover, the size of devices is more and more decreasing these days in order to realize small transit time and/or quantum effects [3], where the electron-hole-pair diffusion and surface recombination are serious problems. In some devices which have both waveguide structures and optically-active regions, the electron-hole-pair diffusion modifies largely the interaction between the electron-hole pairs in the optically-active regions and the light in the optical waveguides.

To study the electron-hole-pair lateral diffusion process in quantum well (QW) structures and also to model the coupling between QWs and optical waveguides, we developed a time-resolved optical probing system where a single-mode optical fiber was directly connected to GaAs/AlGaAs QW samples. In this paper, we present a complete description of this technique and the results of the lateral diffusion measurements of photo-excited electron-hole pairs in non-doped and p-type modulation-doped GaAs/Al<sub>0.3</sub>Ga<sub>0.7</sub>As multiple quantum well (MQW) structures at 77K.

To investigate lateral transport properties of electron-hole pairs or plasma [4]-[6] in non-doped samples as well as doped ones, the diffusivity, or the diffusion constant, is more convenient to measure than the drift mobility,

because they are insensitive to electric fields owing to the charge neutrality. The diffusivity of the photo-excited electron-hole pairs or plasma can be measured by transient grating technique [4] or time-of-flight technique [6] with various forms. Hillmer et. al. [6] realized the time-of-flight measurements with high spatial resolution by observing time-resolved photo-luminescence through a pin-hole in a lithographic mask, and studied the temperature dependence and the well width dependence of the electron-hole-pair diffusion in GaAs/Al<sub>0.5</sub>Ga<sub>0.5</sub>As QWs. This method combined with photon counting technique is suitable for measurements changing the excitation density widely.

Revising Hillmer's method by use of a single-mode optical fiber, we have developed the following new time-of-flight measurement system which is flexible, easy to handle, and convenient to analyze.

## 2 Experiment

The principle of our experiment is shown in figure 1. The sample with GaAs/AlGaAs MQW structures grown on GaAs substrate is directly attached to the end of an optical fiber which is polished and flattened with an optical fiber connector. Time-resolved photo-luminescence measurement is performed through the fiber. Since the electron-hole pairs which are apart from the excited area cannot be coupled to the light mode in the fiber, the electron-hole-pair lateral diffusion makes the decay of the detected luminescence fast, which is quantitatively described as follows: When the radial intensity profile of the excitation light in the fiber is approximated as a Gaussian one (Gaussian radius:  $w_{exc}$ ), the density distribution of the electron-hole pairs just after the short pulse excitation is proportional to  $\exp[-2(x^2 + y^2)/w_{exc}^2]$ . The electron-hole pairs then diffuse laterally with the diffusion constant  $D$  and recombine with the lifetime  $\tau$ , which is expressed by the following equation for the density  $c(x, y, t)$ .

$$\frac{\partial}{\partial t}c = D \left( \frac{\partial^2}{\partial x^2} + \frac{\partial^2}{\partial y^2} \right) c - \frac{c}{\tau}.$$

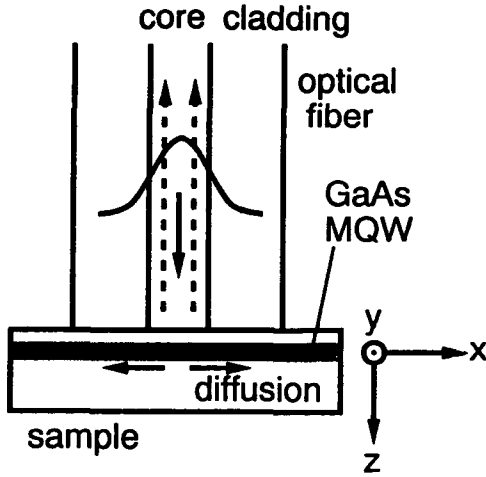


Figure 1: Principle of experiment.

This equation is solved analytically for the Gaussian initial condition. The solution is the Gaussian distribution with the Gaussian radius  $[w_{exc}^2 + 8tD]^{1/2}$  multiplied by the linear recombination term, that is;

$$c(x, y, t) = c_0(1 + 8tD/w_{exc}^2)^{-1} \times \exp[-2(x^2 + y^2)/(w_{exc}^2 + 8tD) - t/\tau]$$

The luminescence intensity observed through the fiber is proportional to the electron-hole-pair density at the central area within the Gaussian radius  $w_{obs}$ , where  $w_{obs}$  is the Gaussian radius of the intensity profile in the fiber for the light at the observation wavelength. Integrating  $c(x, y, t)$  for  $x$  and  $y$  with the weight function  $\exp[-2(x^2 + y^2)/w_{obs}^2]$ , we obtain the analytical expression of the luminescence intensity  $I(t)$  thus observed through the fiber.

$$I(t) = I_0[1 + 8tD/(w_{exc}^2 + w_{obs}^2)]^{-1} \exp[-t/\tau]. \quad (1)$$

For step-index single-mode optical fibers, the Gaussian radius  $w$  for the radial mode profile of the light (wavelength  $\lambda$ ) can be estimated from the formula:

$$w = (d/2)(0.65 + 1.619/V^{1.5} + 2.879/V^6),$$

$$V = 2\pi(NA)(d/2)/\lambda.$$

where  $NA$  and  $d$  are the numerical aperture and the core diameter of the fiber, respectively, and  $V$  is called the V-number or the normalized frequency parameter. By comparing the measured time-resolved luminescence intensity through the fiber and the above expression of  $I(t)$ , we can obtain the values of  $D$  and  $\tau$ .

Note here that  $D$  and  $\tau$  are, in general, not constants as functions of the time because they are density-dependent. Thus, the determination of  $D$  and  $\tau$  by a fit with the function  $I(t)$  given by eq.(1) is sometimes unsuccessful. To know the values of the parameters under the corresponding excitation density, we should direct our attention to the initial decay time  $\tau_{ini}$ , which is

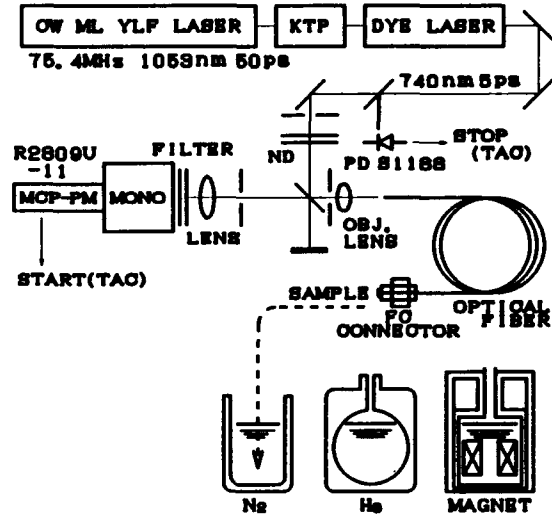


Figure 2: Experimental setup.

to be compared with the following equation derived from eq.(1).

$$1/\tau_{ini} = 8D/(w_{exc}^2 + w_{obs}^2) + 1/\tau.$$

The values of the two unknown parameters are determined from the measurements with more than two kinds of optical fibers with different core diameters; e.g. a thick one whose diameter is so large that  $\tau_{ini}$  represents  $\tau$ , and a thin one where the diameter is comparable to the diffusion length and  $\tau_{ini}$  is sensitive to the value of  $D$ . Another merit of this procedure is the easiness of the analysis free from complex nonlinear fitting by a supercomputer.

The experimental setup is shown schematically in figure 2. The outputs of a cw mode-locked yttrium-lithium-fluoride (YLF) laser are frequency doubled in a KTP (KTiOPO<sub>4</sub>) crystal to pump synchronously a dye (Styryl 8) laser which operates at 740nm with an average power of 200mW, a repetition rate of 75.4MHz, a pulse duration of 5 ps. After appropriately attenuated by neutral-density filters and reflected by a beam splitter, the pulses from the dye laser are coupled to the optical fiber via an objective lens, and excite the sample attached to the flat surface of the FC connector (Seikoh Giken, PF11 type) at the end of the fiber. The luminescence collected into the fiber goes back through it, passes the beam splitter and a 32-cm monochromator (Jobin-Yvon, HR-320), and is finally detected by a cooled microchannel plate photomultiplier tube, or MCP-PMT (Hamamatsu Photonics, R2809-11). Two kinds of optical fibers are used; 5/125 (core/cladding diameter in  $\mu\text{m}$ ) step-index single-mode fiber (Newport, F-SF) and 50/125 graded-index multi-mode fiber (Newport, F-MSD). Since the sample is mounted at the end of the flexible glass fiber with very low thermal conductivity, it can be inserted into almost all types of cryostats, although we describe here only the measurements at 77K immersing the sample directly into liquid nitrogen. The time-resolved luminescence intensity is measured with the time-correlated photon counting method. A full width of half maximum (FWHM) of the observed temporal profile of the excitation light is

typically 100 ps, which indicates the time resolution of the system. The resolution is limited by the response of MCP-PMT and the electronics, not by the dispersion of the optical fibers of several meters long.

One non-doped and two p-type-modulation-doped GaAs/Al<sub>0.3</sub>Ga<sub>0.7</sub>As MQW samples (30 periods, well width  $L_w = 105\text{\AA}$ , barrier width  $L_b = 220\text{\AA}$ ) were studied, which were grown on Cr-doped semi-insulating (100) GaAs substrates by molecular beam epitaxy. Hole concentrations  $p$  were controlled by doping the central part of each AlGaAs barrier with Be. The hole concentrations  $p$  (per well) and mobilities  $\mu$  of the two p-type samples were characterized by Hall measurements:  $p = 1.8 \times 10^{10}\text{cm}^{-2}$ ,  $\mu = 2800\text{cm}^2/\text{Vs}$ , and  $p = 2.2 \times 10^{11}\text{cm}^{-2}$ ,  $\mu = 2500\text{cm}^2/\text{Vs}$  at 77K under light illumination. The temperature dependence of the hole mobility shows negligible contribution of extrinsic effects due to the Be doping for the electronic transport at 77K.

For these three samples with the different hole concentrations  $p = 0\text{cm}^{-2}$ ,  $2 \times 10^{10}\text{cm}^{-2}$ , and  $2 \times 10^{11}\text{cm}^{-2}$ , the lateral-diffusion measurements of the photo-excited electron-hole pairs were performed using the technique mentioned above at various excitation densities, to observe the diffusion constants at various electron and hole densities systematically changed.

### 3 Results and discussions

Figure 3 is the plot of the observed electron-hole-pair diffusion constants vs. the photo-excited electron-hole densities, thus obtained, for the three samples with the different hole concentrations. In the figure, the hole diffusion constants  $D_p = 17$  and  $19\text{cm}^2/\text{s}$  are indicated by the arrows which are calculated from the measured Hall mobilities  $\mu = 2500$  and  $2800\text{cm}^2/\text{Vs}$ , respectively, with the Einstein's relation. The figure shows the following three remarkable results.

Firstly, the diffusion constants of the photo-excited electron-hole pairs in the p-doped samples at the low excitation densities well below the doping levels take almost constant values:  $D = 28 \pm 1\text{cm}^2/\text{s}$  for  $p = 2 \times 10^{10}\text{cm}^{-2}$ ;  $D = 17 \pm 3\text{cm}^2/\text{s}$  for  $p = 2 \times 10^{11}\text{cm}^{-2}$ . Note here that the value of the diffusion constant  $D$  is smaller for the higher hole concentration  $p$ , and that the values are both of the order of  $D_p$ .

According to the ambipolar diffusion model, where the classical electron gas with density  $n$  and diffusivity  $D_n$  and the classical hole gas with density  $p$  and diffusivity  $D_p$  diffuse keeping the charge neutrality, the diffusivity of the pairs or plasma are then the inverse weighted sum of the diffusivity for the electrons and the holes. That is [7],

$$D_{\text{ambi}} = (n + p)D_n D_p / (nD_n + pD_p). \quad (2)$$

This leads to  $D_{\text{ambi}} = D_n$  for  $n \ll p$ , whose physical meaning is clear; the diffusion constants of electron-hole pairs for the p-doped samples at the low excitation densities show diffusion constants of the injected minority electrons in the majority hole plasma.

Therefore, the above observations are interpreted as the followings; the diffusion constant of minority electrons in the majority hole plasma,  $D_n(p \gg n)$ , is as small as the majority hole diffusivity  $D_p$ , and it becomes smaller, as the hole concentration  $p$  is higher. Thus, we may conclude that the electron motion in the majority

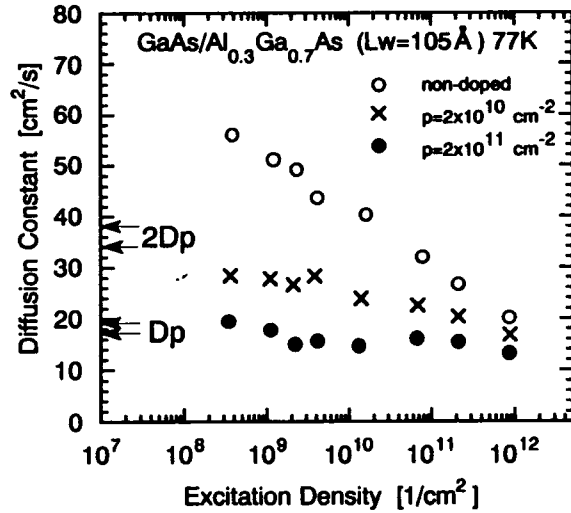


Figure 3: Plot of electron-hole-pair diffusion constant vs. photo-excited electron-hole-pair density.  $D_p$  is the hole diffusion constant which is calculated from the measured Hall mobility.

hole plasma is significantly reduced by strong electron-hole scattering, because the electron diffusion constant without the hole plasma is expected to take one order of magnitude higher value than the hole diffusion constant  $D_p$  owing to the light effective mass. This conclusion is in good agreement with the results of the experiment by Höpfel et al. [5] on the minority carrier drift in the majority carrier plasma, where the strong electron-hole scattering dominates others in the temperature region below 150K and causes the dramatic carrier drag effect or the negative absolute mobility of the injected minority carrier.

Generally speaking, the carrier-density dependence in ambipolar diffusion processes is very often discussed by eq.(2), as the mixture of the classical electron and hole gases. However, it is worth noting that  $D_n$  and  $D_p$  are not constants when  $n$  and  $p$  change, but are the functions of  $n$  and  $p$  owing to the strong electron-hole scattering. Thus, the carrier-density dependence of the electron-hole-pair diffusion is explained with more advanced theory including the electron-hole scattering effect.

The second result is that the diffusion constants in the non-doped sample at the low excitation density region are larger than  $2D_p$ . According to the ambipolar diffusion model, the diffusion constant for equal electron and hole densities is predicted from eq.(2) as,  $D_{\text{ambi}} = 2D_n D_p / (D_n + D_p) < 2D_p$ . Instead, the observed diffusion constants is larger than  $2D_p$ ; the electron-hole pairs experience less scattering than expected for the classical mixture of electrons and holes, which shows that the model is not correct. At the low temperature, the electron-hole pairs form hydrogen-atom-like quasiparticles, or excitons, which are stable in QWs with enhanced binding energies as large as about 10meV. The observed enhanced diffusivity, or the reduced scattering, is most probably due to the excitonic effect.



When the excitation density is increased, the observed diffusivity is decreased, which shows the increased exciton-exciton scattering, or carrier-carrier scattering. Note here again that the excitation density dependence cannot be explained by the ambipolar diffusion model without taking account of the carrier-density dependence of  $D_n$  and  $D_p$  due to the electron-hole scattering. This is because eq.(2) leads to  $D_{ambi} = 2D_n D_p / (D_n + D_p)$  for  $p = n$ , which would be independent of the excitation density without the carrier density dependence of  $D_n$  and  $D_p$ .

Therefore, the classical ambipolar diffusion model is insufficient to explain the experimental results, but an advanced description is indispensable which includes the excitonic effect and the carrier-carrier scattering effect.

Thirdly, the diffusion constants in the non-doped sample at the excitation density of  $2 \times 10^{10} \text{cm}^{-2}$  and  $2 \times 10^{11} \text{cm}^{-2}$  are about  $40 \text{cm}^2/\text{Vs}$  and  $25 \text{cm}^2/\text{Vs}$ , respectively. These are larger than the values of  $D$  at the low density excitation region in the p-doped samples with the same hole concentrations. That is to say, electron-hole pairs are more diffusive in a electron-hole plasma than in a hole plasma of the same density. At the same hole density, the presence an equal density of electrons enhances the electron-hole-pair diffusion. It is now clear that these additional electrons contribute to forming excitons and screening the Coulomb scattering by the holes, rather than adding new Coulomb scattering. Therefore, we conclude that the excitonic effect, or the neutral quasiparticle formation, weakens the carrier-carrier scattering, and enhances the diffusion.

Here we stress that the above three results as a whole show the importance of electron-hole scattering, or generally, carrier-carrier scattering, although it is most evident in the first result that the electron-hole-pair diffusion constants in the p-doped samples are smaller than in the non-doped sample, and that the diffusivity of the minority electrons is as small as that of the majority holes. Preliminary measurements at the temperatures up to 200K show that this remains true at the high temperatures. That is, the electron-hole-pair diffusion constants in the p-doped samples never exceed that in the non-doped sample at the temperatures. This implies that strong electron-hole scattering most likely has an important contribution to the electron-hole transport processes in real optoelectronic devices operating around room temperature [5].

We finally remark the analogy between the photo-excited electron-hole system and the doped electron-donor system. In the uniformly doped system, ionized impurity scattering or neutral impurity scattering are the dominant mechanisms which limit the electronic transport especially at low temperatures and also at room temperature. Modulation doping is the technique to realize high electron mobility where the electrons and the donors are spatially separated to reduce the scattering. Although holes are mobile, which is different from the donor impurity ions, they have a large effective mass and are positively charged. Thus, we can expect some analogy between the two. Electron-hole scattering is like electron-ionized-donor scattering, which is very strong and important even at room temperature. Excitons are like the neutral donors, which are electrically neutral and contribute little to scattering. Lastly, we are now developing a method to reduce electron-hole scattering: by applying electric fields normal to QW structures, we introduce

an electron-hole separation similar to modulation doping. This measurement is now on progress.

## 4 Summary

We have studied the photo-excited electron-hole-pair lateral diffusion in the non-doped and p-doped MQW samples at 77K, and observed the effect of carrier scattering and the effect of exciton formation. Systematic measurements at the various electron and hole densities showed that the strong electron-hole scattering reduces the electron-hole-pair diffusivity, but that exciton formation weakens scattering and enhances the diffusivity.

The all optical time-of-flight measurement technique with single mode optical fiber probe which we developed for the present study of electron-hole-pair diffusion is convenient also for the studies under high magnetic fields, for characterization of samples, and for modeling of the interaction between the electron-hole pairs in QWs and the light in optical waveguides.

## Acknowledgments

The authors would like to thank Dr. H. Hillmer and Y. Senda for the technical instructions on developing the optical fiber probing technique, and Dr. H. Noge, Prof. A. Shimizu, and Dr. G. Fasol for helpful advice and corporations. This work is supported by the Grant in Aid from the Ministry of Education and by the Research Development Corporation of Japan through the ERATO program for Quantum Wave Project.

## References

- [1] S. M. Sze, *Physics of Semiconductor Devices* 2nd ed. (John Wiley & Sons, New York, 1981).
- [2] R. Nagarajan, M. Ishikawa, T. Fukushima, R. S. Geels, and J. E. Bowers, "High Speed Quantum-Well Lasers and Carrier Transport Effects", *IEEE J. Quantum Electron.* **28**, 1990-2007 (1992).
- [3] See the articles in the special issue on "Nanoscale and Ultrafast Devices", *Physics Today* Vol. 43, No. 2, 22-82 (February, 1990).
- [4] J. Hegarty and M. D. Sturge, "Studies of exciton localization in quantum-well structures by nonlinear-optical techniques", *J. Opt. Soc. Am.* **B2**, 1143-1154 (1985).
- [5] R. A. Höpfel, J. Shah, P. A. Wolff, and A. C. Gossard, "Electron-hole scattering in GaAs quantum wells", *Phys. Rev.* **B15**, 37, 6941-6954 (1988), and references therein.
- [6] H. Hillmer, A. Forchel, S. Hansmann, M. Morohashi, E. Lopez, H. P. Meier, and K. Ploog, "Optical investigation on the mobility of two-dimensional excitons in GaAs/Ga<sub>1-x</sub>Al<sub>x</sub>As quantum wells", *Phys. Rev.* **B15**, 39, 10901-10912 (1989), and references therein.
- [7] K. Seeger, *Semiconductor Physics - An Introduction* 4th ed. (Springer-Verlag, Berlin, 1989).

---

## **Novel Sources and Techniques**

---

# **Passively Mode-Locked Diode-Pumped Solid-State Lasers for Optoelectronics Applications**

U. Keller, T. H. Chiu, and J. F. Ferguson

*AT&T Bell Laboratories, Room 4B-523, Crawfords Corner Road,  
Holmdel, New Jersey 07732*

K. J. Weingarten

*Lightwave Electronics Corporation, 1161 San Antonio Road, Mountain View, California 94043*

Diode-pumped solid-state lasers provide a practical, compact, and high power laser source which can be incorporated into optoelectronic and optical communication systems. Average powers of ~50W have been demonstrated using diode-pumped solid-state lasers [1]. Average-power requirements on optoelectronic systems are typically > 1W [2]. In addition, pulsed (i.e. mode-locked) optical power supplies are more desirable for reducing switching energies, eliminating accumulated clock skews, and increasing device speed (due to higher saturation intensities) [2, 3]. Besides the power requirement, the laser should have a diffraction limited beam for minimum focused spot size, small wavelength variations, and synchronization to other optical or electronic oscillators [2]. Mode-locked diode-pumped solid-state lasers can fulfill all these requirements. In contrast, the output power of active or passive mode-locked diode lasers is typically low,  $\leq 1$  mW, because the laser must be operated near threshold to generate short pulses. Furthermore, for reliability, synchronization, and power arguments it can be advantageous to use one larger optical power supply instead of many distributed sources in the system. A single optical power supply can be monitored and easily replaced if it degrades or fails in the field.

One key issue for solid-state lasers is the mode-locking mechanism. We have developed the intracavity antiresonant Fabry-Perot saturable absorber (A-FPSA) [4] (Fig. 1), which is the first passive intracavity modelocker which both starts and sustains stable modelocking of diode-pumped solid-state lasers. Diode-pumped laser materials typically have small gain cross sections ( $\leq 10^{-19}$  cm<sup>2</sup>), which requires a low-loss fast saturable absorber. Operating a Fabry-Perot at antiresonance with a high reflectivity of the top mirror decreases the intensity inside the Fabry-Perot cavity with respect to the incident intensity. This transforms the saturable absorber to a high saturation intensity,

low-loss device as required.

Coupled cavity modelocking techniques such as APM (additive pulse modelocking) [5, 6] or RPM (resonant passive modelocking) [7-9] have successfully modelocked these lasers. However, an intracavity modelocking technique is more desirable because it does not require active stabilization and the overall cavity design becomes more compact leading to increased mechanical stability. KLM (Kerr lens modelocking) [10-12] and KSM (Kerr shift modelocking) [13] are the simplest modelocking techniques, but are not self-starting. We will demonstrate that passive modelocking is simpler and preferable because active modelocking typically requires a precisely fabricated transducer [14], watts of RF drive power, and active stabilization of the cavity length to the drive frequency to maintain the shortest possible pulses.

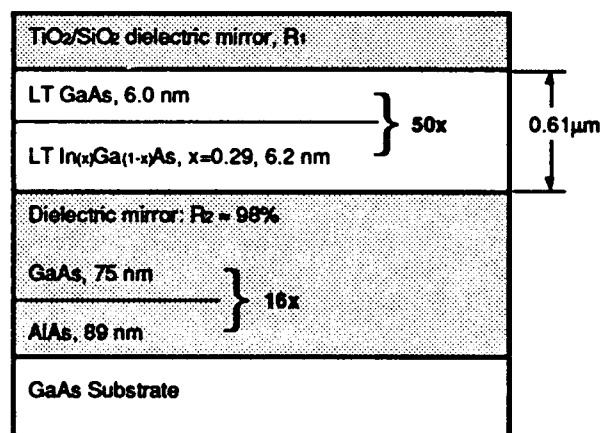


Fig. 1: A-FPSA device design

Self-starting is a serious issue for fast saturable absorber modelocking [10-13]. The A-FPSA has a bitemporal absorption response with slow time

component due to carrier recombination and a fast time component due to intraband thermalization. The slow component provides the self-starting mechanism and the fast absorber is necessary for steady-state pulse formation [15]. The carrier life time can be controlled by the MBE growth temperature (Fig. 2). We have demonstrated that the slow time constant self-starts modelocking without self-Q-switching of cw pumped Nd:YLF and Nd:YAG lasers. Figure 3 shows the decrease in the modelocking buildup time for longer carrier life times. Self-Q-switching is observed as strong modulation sidebands (typically around -1 dBc) on a microwave spectrum analyzer. When the laser is running with stable mode-locked pulses, the relaxation oscillation sidebands are typically -60 dBc. The tendency to self-Q-switch decreases with lower upper state lifetime of the laser material, lower carrier lifetime of the absorber, higher  $R_1$  top reflector, and higher small-signal laser gain.

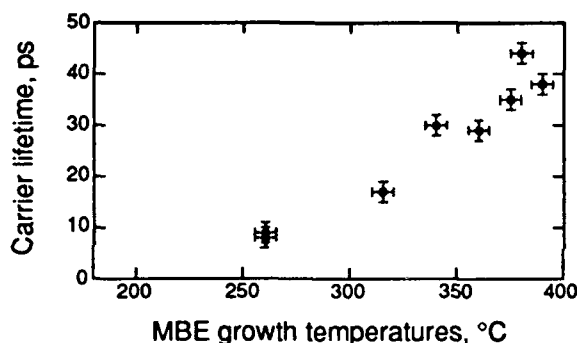


Fig. 2: Carrier lifetime of the bitemporal A-FPSA, which controls the self-starting of the laser, is adjusted by varying the MBE growth temperature.

The fast component is required because no significant gain saturation is assisting the pulse formation process. The steady-state pulse duration decreases with increased pump power, but does not significantly depend on the carrier lifetime. Pulses as short as 2.8 ps with Nd:YLF and 7 ps with Nd:YAG laser are generated. This is strong evidence that the fast component of the bitemporal A-FPSA is the dominant pulse forming mechanism and the slower time component is not important in steady-state.

For diode-pumping, the laser gain is significantly lower compared to Ti:sapphire pumping. This is due to several effects. First, the diode laser has a broader linewidth, which results in a longer average absorption length. Secondly, the diode laser can not be focused to near-diffraction limited spot as the Ti:sapphire can, requiring a larger laser mode size to ensure mode matching, which reduces the laser's gain. The lower gain resulting from diode-pumping requires more careful attention to the carrier lifetime and the effective absorber cross section which is set by the top reflector on the sample ( $R_1$  in Fig. 1). For Nd:YLF, we achieved pulses of 5.1 ps FWHM and 260 mW average power at a 100 MHz repetition rate with a 35 ps carrier lifetime

and a 99%  $R_1$ , using a 2W diode laser pump (Fig. 4). Going to shorter lifetimes with the 99%  $R_1$  resulted in insufficient non-linearity for self-starting, and going to a 98%  $R_1$  resulted in Q-switched mode-locked behavior. With Nd:YAG, best results of 8.7 ps pulse width and 100 mW average power were achieved with a 35 ps lifetime and 98% top reflector. A 1W average power pump laser was used for the YAG. Decreasing the coupling to 99%  $R_1$  resulted in insufficient non-linearity for self-starting in the Nd:YAG. Other lifetimes below 35 ps also resulted in stable modelocking when  $R_1$  was 98%.

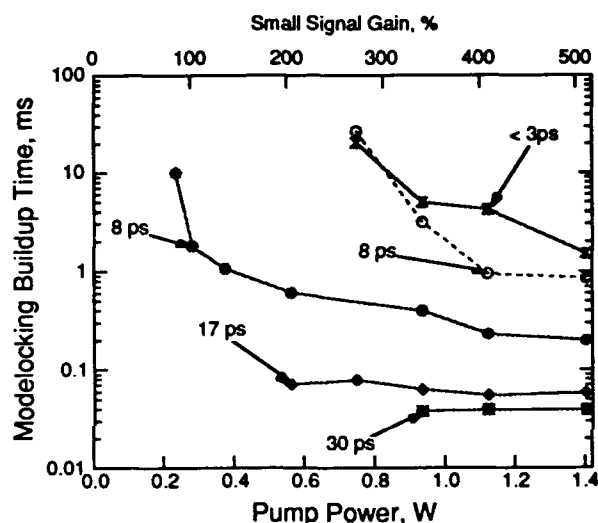


Fig. 3: Nd:YLF laser build-up time for different carrier lifetimes of the A-FPSA with  $R_1=98\%$  and a 2% output coupler, (solid lines), and a 4% output coupler (dashed line) (Ti:sapphire end-pumping was used for these measurements [15])

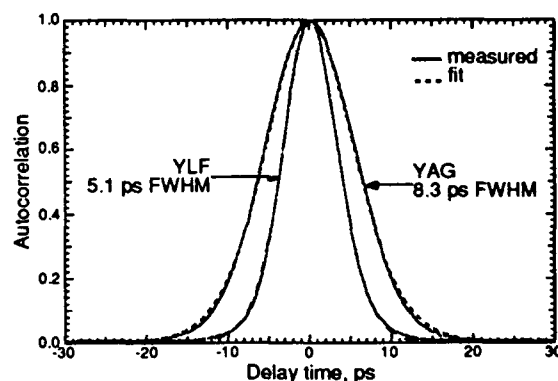


Fig. 4: Passively mode-locked diode-pumped Nd:YLF with carrier lifetime=35 ps and  $R_1=99\%$ . The repetition rate of the laser was 100 MHz. The laser was stable and self-starting with no active feedback systems. The relaxation oscillation sidebands were less than -60 dBc as measured on a microwave spectrum analyzer (3 kHz resolution bandwidth).

With a free-running, passively mode-locked laser, the repetition rate is set by the inverse of the cavity round-trip time. For applications requiring synchronization to an external signal generator, the laser can be phase-locked by controlling the cavity length. We have tested the feasibility of this approach by implementing a simple phase-lock-loop system where the cavity length is controlled by placing one of the laser mirrors on a piezo transducer [16]. We demonstrated a stable, locked loop, verified by observing the repetition rate on a spectrum analyzer and by adjusting the cavity length with a manual translation stage and observing the corresponding change in the piezo's servo voltage. With proper design of the phase detector [17], piezo response, and loop filter, we expect sub-picosecond timing jitter using this approach.

In conclusion, we have demonstrated diode-pumped, passively-mode-locked lasers with many of the features necessary for an optoelectronic pulse source. These lasers are simple and robust with clean spatial, temporal, and spectral properties. The A-FPSA carrier lifetime was adjusted to optimize the self-starting performance with both Nd:YLF and Nd:YAG at 1  $\mu\text{m}$ . The absorption edge of the A-FPSA can be varied by adjusting the semiconductor's bandgap energy, which allows extension of this technique to other laser materials and wavelengths.

## References

- [1] S. C. Tidwell, J. F. Seamans, D. D. Lowenthal, in *Advanced Solid-State Lasers* L. Chase, A. Pinto, Eds. (Optical Society of America, Washington, D.C., 1992), 13, 178
- [2] N. Streibl, K.-H. Brenner, A. Huang, J. Jahns, J. Jewell, A. W. Lohmann, D. A. B. Miller, M. Mardocca, M. E. Prise, T. Sizer, *Proceedings of the IEEE* 77, 1954 (1989)
- [3] G. D. Boyd, L. M. F. Chirovsky, R. A. Morgan, *Appl. Phys. Lett.* 59, 2631 (1991)
- [4] U. Keller, D. A. B. Miller, G. D. Boyd, T. H. Chiu, J. F. Ferguson, M. T. Asom, *Opt. Lett.* 17, 505 (1992)
- [5] K. J. Blow, B. P. Nelson, *Opt. Lett.* 13, 1026 (1988)
- [6] P. N. Kean, X. Zhu, D. W. Crust, R. S. Grant, N. Landford, W. Sibbett, *Opt. Lett.* 14, 39 (1989)
- [7] U. Keller, W. H. Knox, H. Roskos, *Opt. Lett.* 15, 1377 (1990)
- [8] H. A. Haus, U. Keller, W. H. Knox, *J. Opt. Soc. Am. B*, 8, 1252, (1991)
- [9] U. Keller, T. H. Chiu, *IEEE J. Quantum Electron.* 28, 1710, (1992)
- [10] D. E. Spence, P. N. Kean, W. Sibbett, *Opt. Lett.* 16, 42 (1991)
- [11] U. Keller, G. W. 'tHooft, W. H. Knox, J. E. Cunningham, *Opt. Lett.* 16, 1022 (1991)
- [12] U. Keller, W. H. Knox, G. W. 'tHooft, *IEEE J. Quantum Electron.* 28, 2123, (1992)
- [13] U. Keller, T. H. Chiu, J. F. Ferguson, *Opt. Lett.*, submitted for publication Nov. 1992, and CLEO 1993
- [14] U. Keller, K. J. Weingarten, K. D. Li, D. C. Gerstenberger, P. T. Khuri-Yakub, D. M. Bloom, *Opt. Lett.* 15, 45 (1990)
- [15] U. Keller, T. H. Chiu, J. F. Ferguson, *Opt. Lett.*, to be published Feb. 1 (1992)
- [16] S. B. Darack, D. R. Dykaar, G. T. Harvey, *Opt. Lett.* 16, 1677 (1991)
- [17] M. J. W. Rodwell, D. M. Bloom, K. J. Weingarten, *IEEE J. Quantum Electron.* 25, 817 (1989)

## **NLTL-Based System for mm-Wave and Sub-mm-Wave Free-Space Electromagnetic Measurements**

**Y. Konishi, M. Case, R. Yu, and M. J. W. Rodwell**

*Department of Electrical and Computer Engineering, University of California,  
Santa Barbara, California 93106*

**M. Kamegawa**

*Shimadzu Corporation, Kyoto, Japan*

### **Abstract**

We report broadband monolithic transmitters and receivers ICs for mm-wave electromagnetic network measurements. The ICs use non-linear transmission lines (NLTLs) and sampling circuits as picosecond pulse generators and detectors. Combining NLTLs and sampling circuits with monolithic broadband antennas, the pulse can be radiated and received for free-space measurements. We have demonstrated the system with 250 GHz bandwidth using simple and convenient signal processing electronics. The system also has sufficient signal to noise ratio for measurements to  $\approx 600$  GHz, given suppression of the effects of source phase noise. We demonstrate a variety of mm-wave measurements.

### **Introduction**

For mm-wave and sub-mm wave gain-frequency measurements, convenient, broadband power sources and detectors have been required for some time. Measurement systems based on waveguide components (harmonic mixers, frequency multipliers, and horn antennas) have played a dominant role, but each component has narrowband frequency coverage (1.5:1). To measure over a broad bandwidth, many waveguide systems must be used, which is both inconvenient and expensive. Additionally, sub-millimeter-wave waveguides are small and difficult to machine, and efficient device-waveguide coupling, although possible, requires very precise mechanical assembly. Broadband monolithic

mm-wave ICs address these difficulties. Antenna-coupled picosecond photoconductors have also been used to radiate and detect femtosecond electromagnetic transients [1]. Through Fourier analysis of the received signals, several groups have recently demonstrated broadband spectroscopy over extraordinary bandwidths ( $\approx 50$  GHz- 2 THz). Such systems have limitations regarding the complexity of the apparatus (femtosecond mode-locked lasers), radiated power levels, rate of data acquisition (pump-probe measurements, mechanical delay scanning, lock-in detection), and attainable frequency resolution (time-windowing constraints).

### **NLTL and Sampling Circuit**

Nonlinear transmission lines (NLTLs) and NLTL-gated sampling circuits are an alternative solid-state technology for generation and detection of picosecond transients with risetimes approaching 1 ps [2]. The NLTL is a ladder network of high impedance transmission line sections periodically loaded with reverse biased Schottky diodes serving as voltage-variable capacitors. The variation in diode capacitance with voltage introduces a voltage-variation in the wave propagation velocity, with the velocity increasing as the diode reverse bias is increased (negative line voltages). Consequently, the falltime of negative-going input signals is compressed (reduced) during propagation on the NLTL. The minimum transition time (falltime) at the NLTL is inversely proportional to the diode cut-off frequency. With a sinusoidal input

signal, the NLTL output is a sawtooth waveform. Current NLTL designs used in this work are as reported in [2], and operate with drive frequencies variable between 7 and 14 GHz.

### mm-Wave Measurement System

We have fabricated transmitter and receiver ICs (Fig. 1) which consist of NLTLs and sampling circuits coupled to broadband (2 mm square) planar bowtie antennas [3,4,5]. The transmitter NLTL, fabricated within one electrode plane, drives the  $120^\circ$  ( $52\Omega$  impedance) antenna through a coplanar waveguide balun. Two  $100\Omega$  resistors at the antenna perimeter terminate the antenna at frequencies below the antenna low-frequency cut-off. The receiver is a bow-tie antenna interfaced through a similar antenna feed. The  $50\Omega$  sampling circuit input impedance terminates the receiving antenna without reflection.

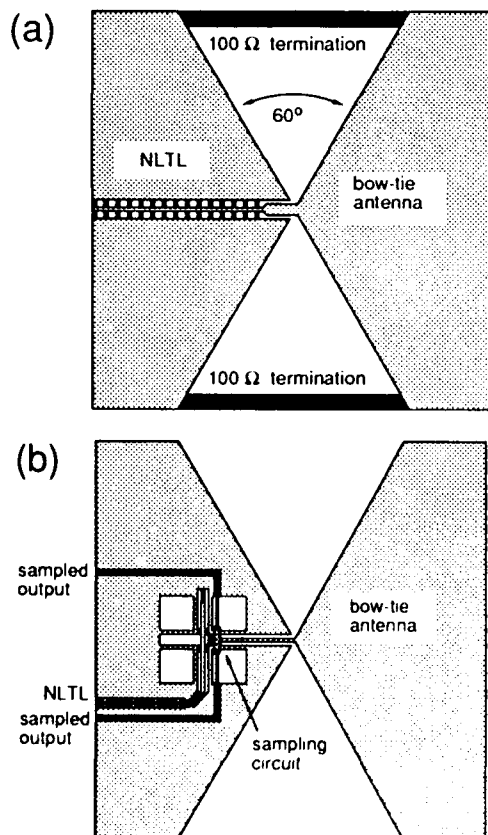


Figure 1: Simplified integrated circuit layouts of (a) the transmitter and (b) the receiver.

The fabrication process [2] requires 5 mask steps at  $3\mu\text{m}$  design rules: ohmic contacts, proton implant isolation, metalization

for both transmission lines and Schottky contacts, air bridges, and posts. Capacitors in the sampling circuit are implemented using reverse-biased diodes.

The measurement system is shown in Fig. 2. The antennas are coupled to 16 mm diameter silicon substrate lenses, and the radiated beam is collimated with off-axis parabolic mirrors. At the receiver, the integrated NLTL-gated sampling circuit converts the received signal to a 100 Hz sampled signal, which is observed on an oscilloscope. A mixer generates a phase reference signal for oscilloscope triggering, compensating for any phase drift between the two synthesizers. Two attenuators at oblique incidence on both sides of the sample under test suppress cavity resonances between the transmitter and receiver. The received signal (Fig. 3) has a 270 mV peak-peak amplitude, and 2.4 ps risetime.

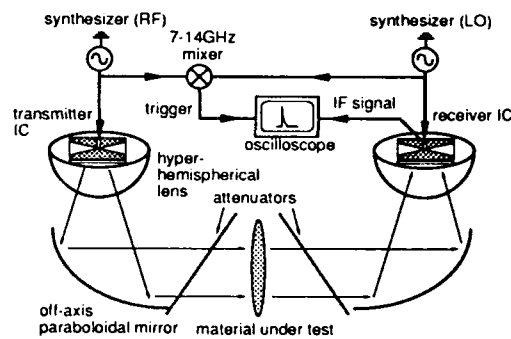


Figure 2: System schematic diagram

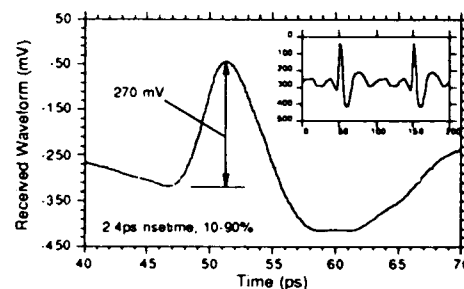


Figure 3: Signal at the receiver output (attenuators removed)

### Signal to Noise Ratio

Measurement bandwidth is determined not by the Fourier bandwidth of the received signal, but by the signal to noise ratio as a function of frequency (Fig. 4). Our current experiments use a pair of synthesizers to drive the transmitter and receiver. This configuration

is similar to that used in microwave instruments, and provides rapid data acquisition and all-electronic control. The two dominant noise sources are the relative phase fluctuations (phase noise) of the two microwave synthesizers, and the receiver system noise.

Synthesizer phase noise is dominant. We can ascribe (without loss of generality) the phase noise to the transmitter's (RF) synthesizer. Given zero phase noise, the received signal at the sampling circuit input will be  $r(t) = r(t - 2\pi n / \omega_{RF})$ , some periodic waveform with repetition frequency  $\omega_{RF}$ . With phase noise, the RF synthesizer output is  $V_o \cos(\omega_{RF}(t - J(t)))$ , where  $J(t)$  is the randomly-varying timing,  $S_J(\omega) = \int_{-\infty}^{\infty} \langle J(t)J(t+\tau) \rangle e^{-j\omega\tau} d\tau$  its power spectral density, and the single-sideband phase noise spectral density of the RF synthesizer is  $L(\omega) = \omega_{RF}^2 S_J(\omega)$ . The sampling circuit input signal is now  $r(t - J(t))$ , and the power spectral density of  $r(t)$  can be written as

$$S_R(\omega) = \sum_{n=-\infty}^{+\infty} R_n (\delta(\omega - n\omega_{RF}) + n^2 \omega_{RF}^2 S_J(\omega - n\omega_{RF}))$$

This assumes  $\eta \omega_{RF} \sigma_J \ll 1$ , where  $\sigma_J$  is the standard deviation of  $J(t)$ ;  $R_n$  is the received power in the  $n^{\text{th}}$  harmonic of  $\omega_{RF}$ .  $J(t)$  has produced phase noise sidebands  $n^2 \omega_{RF}^2 S_J(\omega - n\omega_{RF})$  about each harmonic of  $\omega_{RF}$ . The receiver sampled (IF) output is the product  $i(t) = r(t)s(t)$ , where  $s(t)$  is a sampling impulse train at repetition frequency  $\omega_{LO} = \omega_{RF} - \omega_{IF}$ . The power spectrum of the sampled signal is

$$S_I(\omega) = G_S \sum_{n=-\infty}^{+\infty} R_n (\delta(\omega - n\omega_{IF}) + n^2 \omega_{RF}^2 S_J(\omega - n\omega_{IF}))$$

plus terms at higher frequencies which are removed by filtering.  $G_S$  is the sampling circuit conversion gain. The measurement system determines the (vector) amplitude at frequency  $\omega_{RF}$  of  $r(t)$  by measuring the Fourier amplitude at frequency  $n\omega_{IF}$  of  $i(t)$ . Because  $i(t)$  is downconverted to a low scan rate  $\omega_{IF}$  (100 Hz), a given Fourier component of the pulse train is detected against a noise background set by the collective phase modulation sidebands of all other Fourier

components. The signal/phase-noise ratio at  $\omega_{IF}$  is

$$\frac{P_S}{P_{\text{phasenoise}}} = \frac{R_n}{\left( \sum_{m=-\infty}^{+\infty} R_m m^2 \omega_{RF}^2 S_J((n-m)\omega_{IF}) \right) B}$$

$B$  is the bandwidth of the signal-processing subsequent to the receiver. The synthesizer phase noise  $S_J(\omega)$  decreases rapidly for  $\omega/2\pi > 100$  kHz; if  $\omega_{IF} > 100$  kHz, then each component of  $i(t)$  will be detected against the noise background of its own phase noise modulation sidebands with no noise contribution from the noise sidebands of other harmonics. In contrast, with a 100 Hz IF frequency, the phase noise background is severe. The receiver background (thermal) noise is much lower; the sampling circuit has a 40 dB noise figure.

If the phase noise is suppressed, the system will provide usable measurements to least 600 GHz: the signal/background noise ratio is still 28 dB(1Hz) at 1 THz. The phase noise will be suppressed if a single oscillator provides both RF and LO signals. In this case, a mechanical phase shifter must be used to provide the required variable delay between LO and RF, greatly reducing the data acquisition

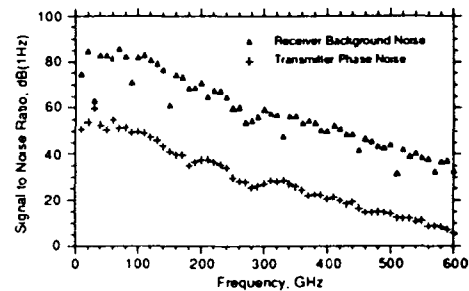


Figure 4 : Signal to noise ratio (attenuators removed)

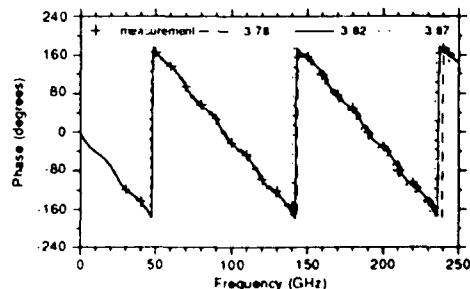


Figure 5 : Measurement of quartz sample with three theoretical fits



rates. Alternatively, as is evident from the above analysis, increasing the IF frequency into the MHz range will also suppress the phase noise. This, unfortunately, requires the construction of specialized receiver signal-processing components.

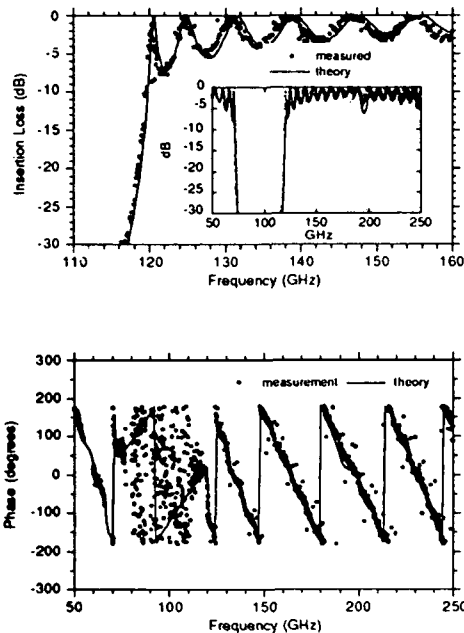


Figure 6: Measurement of Bragg filter, top: gain-frequency, bottom: phase-frequency

### Measurements

Attenuation-frequency and phase-frequency measurements are obtained by taking the ratio of the received Fourier spectrum with the device under test in place with the spectrum of a reference measurement taken with the device under test removed. Fig. 5 shows the phase measurement of a 3294  $\mu\text{m}$  sample of fused quartz. The phase resolution is sufficient to determine a dielectric constant of 3.82 with less than  $\pm 0.05$  uncertainty.

The NLTL-based system has a frequency resolution limited by that of the synthesizers used (2 Hz) multiplied by the harmonic order. At frequencies near 200 GHz, measurements can be made at 40 Hz separation. Fig. 6 shows transmission measurement of a Bragg filter consisting of alternating layers of 10 pieces of alumina and 9 pieces of Teflon, illustrating the system frequency resolution. The filter shows

greater than 10 dB/GHz gain slope at 120 GHz. Data was taken 100 NLTL drive frequencies between 10 and 11 GHz, yielding measurements at the frequencies  $n(10\text{GHz} + m \cdot 10\text{MHz})$  where  $n$  and  $0 \leq m \leq 99$  are integers, corresponding to 100 MHz separation 100 GHz. The phase-frequency data (fig. 6) shows some scatter due to oscilloscope trigger instabilities.

### Conclusions

We have demonstrated a simple and inexpensive system for broadband mm-wave electromagnetic measurements. Reproducible, accurate measurements are possible from 30 to 250 GHz using independent synthesizers as RF and LO sources, a simple and convenient configuration providing rapid data acquisition. The system also has sufficient signal to noise ratio for measurements to  $\approx 600$  GHz, given suppression of source phase noise. The current system allows convenient and accurate measurements of materials and mm-wave quasi-optical amplifier arrays.

### Acknowledgments

This work was supported by the Air Force Office of Scientific Research under grant number (AFOSR-89-0394). We are grateful for extensive discussions with David Rutledge (Caltech), Robert York (UCSB) Gabriel Riebez (Michigan), and Richard Compton (Cornell) regarding mm-wave antennas.

### References

- [1] M. Van Exter and D. R. Grischkowsky, IEEE, Trans. MTT., Vol. 38, No. 11, pp. 1684, 1990
- [2] M. J. W. Rodwell, M. Kamegawa, R. Yu, M. Case, E. Carman, K. S. Giboney, IEEE, Trans. MTT., Vol. 39, No. 7, pp. 1194, 1991.
- [3] D. B. Rutledge, D. P. Neikirk, and D. P. Kasilingam, "Integrated-Circuit Antennas" in *Infrared and Millimeter Waves*, K. J. Button, Ed., Vol. 10, pp. 1-90, New York: Academic Press, 1984.
- [4] Y. Konishi, M. Kamegawa, M. Case, R. Yu, M. J. W. Rodwell, R. York, D. Rutledge, *Appl. Phys. Lett.*, 61, 23, pp. 2829-2831, 7 Dec. 1992.
- [5] Y. Konishi, M. Kamegawa, M. Case, R. Yu, M. J. W. Rodwell, R. York, D. Rutledge, 3rd Int. Symposium on Space Terahertz Technology, Ann Arbor, Michigan, March 1992

# Ultrafast Scanning Microscopy

S. Weiss, D. Botkin, and D. S. Chemla

*Materials Sciences Division, MS 2-300, Lawrence Berkeley Laboratory,  
Berkeley, California 94720*

## **Abstract**

We propose to combine ultrafast optical techniques with scanning probe microscopies to obtain, simultaneously, unprecedented temporal and spatial-resolution.

## **Introduction**

Very high spatial resolution is required for investigating the phenomena that govern the physics of mesoscopic systems and for characterizing the operation of submicron optoelectronics devices. For example, processes such as: i) carrier transport in mesoscopic semiconductor structures; ii) electric field and voltage wave front propagation at metal-semiconductor interfaces; iii) light emission in quantum confined structures; all experience significant variations over length scales much smaller than  $1\mu\text{m}$ . Because of the large velocities of excitations in the materials (electronic velocity in semiconductors and metals is on the order of  $\sim 1$  to  $10\text{\AA}/\text{fs}$ ; voltage wave fronts propagate on high speed transmission lines at velocities on the order of  $\sim 1000\text{\AA}/\text{fs}$ ), the time scale of their dynamics is well in the sub-picosecond domain. Therefore, in order to understand better the mechanisms governing mesoscopic systems and optimize the devices that use them, it is necessary to develop new experimental techniques with simultaneous subpicosecond-time resolution and submicron-space resolutions.

In the last decade, powerful scanning microscopy techniques which can achieve atomic resolution have been developed. The invention of the Scanning Tunneling Microscope (STM) [2], the Scanning Force

Microscope (SFM) [3] and the Near-field Scanning Optical Microscope (NSOM) [4] have revolutionized the field of surface science. In the scanning microscopies an atomically sharp tip (or a very small aperture for the NSOM) is scanned very close to the surface of a sample. Due to the close proximity of the tip to the sample, different interactions or coupling mechanisms can occur (tunneling current, atomic forces, evanescent wave coupling). The strength of these interactions is a very nonlinear function of the tip height. This nonlinearity provides the means for atomic-scale control of the distance to the sample and allows high lateral resolution limited by the sharpness of the tip. In STM, the image, obtained by collecting the tunneling current while scanning the tip, reflects the density of states of the electrons at the Fermi level close to the surface. In SFM, the image is obtained by measuring the minute deflection of the cantilever holding the tip, caused by the force exerted on the latter by the sample (electrostatic and magnetostatic forces, inter-atomic forces, van der Waals forces etc.). The NSOM image is obtained by evanescent field coupling to a sub-wavelength aperture. Presently, however, the time-resolution of the scanning microscopies is limited by the scanning rate and the data acquisition electronics.

## **Basic Concept**

We propose to exploit the nonlinear nature of the different tip-sample interactions to obtain ultrafast time-resolution in scanning microscopy. This nonlinearity can be intrinsic to the nature of tip-sample coupling or can be artificially produced by nanofabrication of custom designed tips. The time resolution is achieved by modulating both the sample and the tip responses with two short optical pulses, as

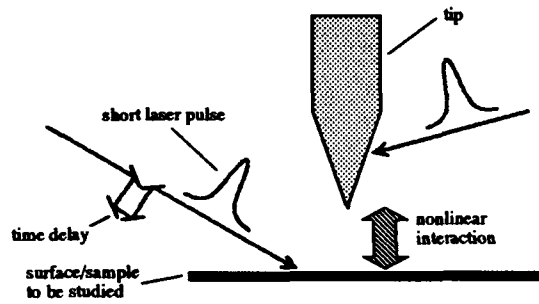


Fig. 1: Correlation by nonlinear interaction. The two laser pulses modulate the sample and the tip responses respectively.

shown in Fig. 1. Because of the nonlinearities, multiplicative ("mixing") terms are generated, which include both tip and sample responses. By scanning the time delay between the two pulses and integrating the signal, a cross-correlation of the tip-sample responses is obtained. After characterizing the response of the tip alone, the dynamics of the sample can be obtained by deconvolution, with the simultaneous spatial and temporal resolutions which are well below  $1\mu\text{m}$  and on the order of 1ps respectively.

This basic principle is very general, and can be implemented in wide variety of applications. In the following we describe and discuss two examples.

### Ultrafast STM

An example of artificially induced nonlinearity is shown in Fig. 2, where an atomically-sharp tip is integrated with an ultrafast photoconductive-switch [5]. In this experiment, we plan to study electromagnetic wave propagation and distribution of the field lines on a transmission line with sub-micron and sub-picosecond resolutions. This experiment will

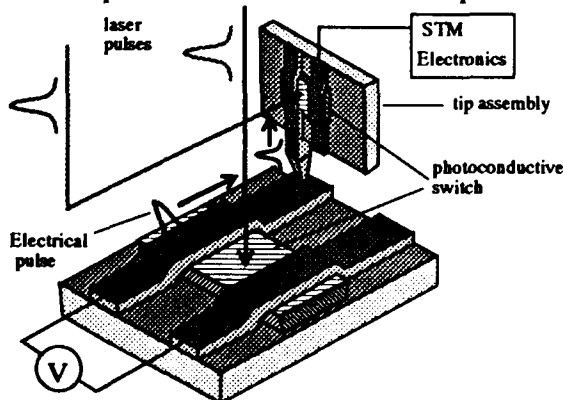


Fig. 2: Ultrafast STM. One laser pulse excites a voltage pulse on a transmission line. The second pulse photoconductively samples the tunneling current on the tip assembly.

also determine the  $\delta$ -function response (to a voltage pulse) of the system. In the figure, one pulse excites the line or a device integrated in the line, while the second pulse samples the tunneling current on the tip assembly.

In order to estimate the signal contrast in such an experiment, we use the equivalent electrical circuit

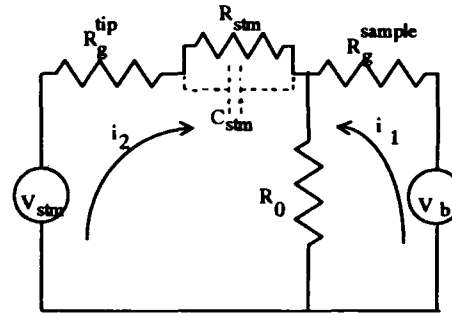


Fig. 3: Equivalent circuit for Fig. 2. The STM gap is modeled as a resistor in parallel with a capacitor.

which is shown in Fig. 3, and calculate only the DC component of the signal. The transmission lines are modeled by a resistor  $R_0 = 100\Omega$ , the photo-conducting gaps as resistors with variable resistance (light on:  $R_g^{\text{tip}} = R_g^{\text{sample}} = 1\text{M}\Omega$ , light off:  $R_g^{\text{tip}} = R_g^{\text{sample}} = 10\text{M}\Omega$ ), the tunneling gap has a resistance of  $R_{\text{stm}} = 10\text{M}\Omega$  and a capacitance  $C_{\text{stm}}$  (which we neglect for the DC analysis). We assume  $V_{\text{stm}} = 10\text{mV}$  and  $V_b = 10\text{V}$ . These numbers roughly correspond to the parameters of LT-GaAs (i.e. GaAs epitaxially grown at low temperature). The DC component of the tunneling current is given by:

$$i_2 \approx \frac{V_{\text{stm}} - V_b \frac{R_0}{R_g^{\text{sample}}}}{R_g^{\text{tip}} + R_{\text{stm}}} \quad (1)$$

With a duty cycle of  $10^{-4}$ , which corresponds to a 100 MHz repetition rate of the laser source and 1ps time resolution, we get  $i_2^{\text{light on}} / i_2^{\text{light off}} \approx 2$  with 0.5 nA nominal tunneling current (assuming lock-in detection). This simple calculation takes into account only the DC coupling of the terahertz pulse to the tip. We suspect that AC coupling will play an important role. The AC coupling, though is very difficult to model for the proposed geometry, and further studies will be needed to clarify its contribution to the signal.

We have performed a simulation experiment, in a planar geometry, using silicon on sapphire (SOS) as the photoconductive material. It turns out that the resistance of the silicon gap ( $\approx 10$  to  $20\mu\text{m}$ ) is

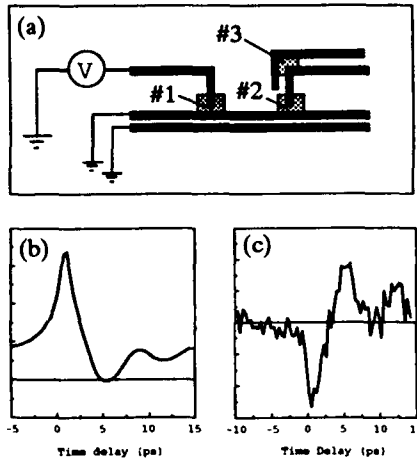


Fig. 4: Simulation experiment on SOS. (a) mask layout and biasing geometry (b) conventional photoconductive sampling (points #1 and #2) (c) photoconductive sampling between points #1 and #3.

comparable to that of the STM gap (few Å of metal - insulator/vacuum - metal). Fig. 4a shows the mask layout and the biasing. One laser beam switched the bias at point #1. The second beam switched either point #2 (conventional geometry for photoconductive sampling) or point #3. The later geometry simulates the STM experiment. The resulted signals are shown in Fig. 4b and 4c respectively. The amplitude of the signal in Fig. 4c is multiplied by a factor of  $10^3$ . The corresponding sampled current is  $\approx 10$  pA. As can be seen, the signal in Fig. 4c has a large AC component, which indicates capacitive coupling.

### Ultrafast SFM

Another utilization of the basic concept is the use of the SFM as the nonlinear cross-correlator. With two

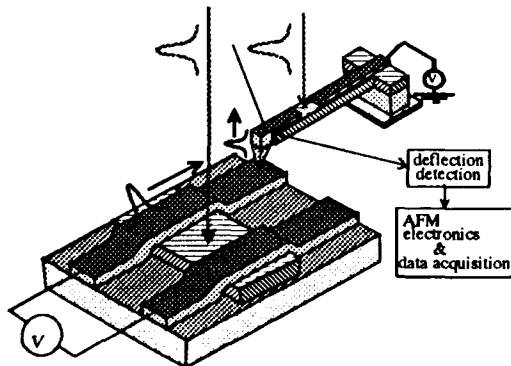


Fig. 5: Ultrafast SFM. One laser pulse excites a pulse on a transmission line. The second pulse modulates the voltage of the SFM tip.

short optical pulses, one can modulate the force acting on the SFM tip. In the attractive mode, the SFM can

measure the electrostatic force (Coulomb interaction) exerted on the tip by the electrical charge/voltage deposited on the sample. Fig. 5 shows a tip mounted on a cantilever which is micro-machined from a photoconducting substrate. The tip voltage is modulated by a short optical pulse. Its deflection is measured by optical techniques. The second short laser pulse excites the device. The cantilever acts as a slow detector which cross-correlates the dynamic responses of the sample and the tip. Its deflection (as function of time delay between the pulses) provides information on the dynamics of the device.

The electrostatic force acting on the tip can be modeled as the force acting on a plane-parallel capacitor. The equation of motion for the tip-lever is given by:

$$m\ddot{x} + \gamma\dot{x} + kx = \frac{\epsilon_0 A}{U_0^2} V(t)^2 \left( 1 - \frac{2x}{U_0} + \frac{3x^2}{U_0^2} - \dots \right) \quad (2)$$

where  $x$  is the deviation of the tip from its equilibrium position,  $m$  is the mass of the lever,  $\gamma$  is its dissipation,  $k$  is its spring constant,  $\epsilon_0$  is the vacuum permittivity,  $A$  is the area of the tip,  $V$  is the tip-sample voltage and  $U_0$  is the equilibrium position. The differential force, with respect to the tip height, is given by:

$$\frac{\partial F}{\partial z} = \epsilon_0 \frac{A}{z^3} V^2. \quad (3)$$

With an average change in voltage of 1 mV, nominal tip height of 100 Å, and a tip radius of 1  $\mu$ m (which, of course, affects the resolution), a gradient force of  $10^{-5}$  N/m can be obtained. Force gradients of that order of magnitude have been measured successfully with a SFM.

To demonstrate how the SFM acts as a correlator, we solve (2) with the following excitation (train of  $\delta$ -function voltage pulses):

$$V_t(t) = \sum_{n=0}^N \delta(t - nT),$$

$$V_s(t - \tau) = \sum_{n=0}^N \delta(t - \tau - nT) \quad (4)$$

$T$  is the separation between adjacent pulses and  $N \cdot T$  is the time of integration on the detector. The tip-sample bias is:  $V(t) = V_t(t) + V_s(t - \tau)$ . The 0-order solution (we take only the first term in the expansion in (2)) is given by:

$$x(t) = \sum_{n=0}^N x_{\delta}(t - nT) + \sum_{n=0}^N x_{\delta}(t - \tau - nT) + \begin{cases} 2 \sum_{n=0}^N x_{\delta}(t - nT) & \tau = 0 \\ 0 & \tau \neq 0 \end{cases} \quad (5)$$

with:

$$x_{\delta}(t) = \left( C_1 - \frac{1}{\sqrt{\gamma^2 - 4km}} \Theta(t) \right) e^{-\left( \frac{\gamma + \sqrt{\gamma^2 - 4km}}{2m} \right) t} + \left( C_2 + \frac{1}{\sqrt{\gamma^2 - 4km}} \Theta(t) \right) e^{-\left( \frac{\gamma - \sqrt{\gamma^2 - 4km}}{2m} \right) t} \quad (6)$$

As can be seen from (5) and (6), the tip deviation at  $\tau=0$  is twice as big as the deviation at  $\tau \neq 0$ . This calculation is ofcourse oversimplified, but it has all the basic ingredients to demonstrate the basic concept brought-up in this proposal.

### Conclusions

We propose to combine ultrafast techniques with scanning microscopy techniques. The development of

such instruments will open the way for a new kind of spectroscopy with the simultaneous subpicosecond-time and submicron-space resolutions.

### References:

- [1] Shapiro: (ed.) *Ultrashort Light Pulses*, Topics Appl. Phys. Vol. 18 (Springer, Berlin, Heidelberg 1977), and W. Kaiser: (ed.) *Ultrashort Laser Pulses and Applications*, Topics Appl. Phys. Vol. 60 (Springer, Berlin, Heidelberg 1988).
- [2] G.Binnig and H. Rohrer, *Helvetica Physica Acta*, **55**, 726 (1982).
- [3] G.Binnig, C.F. Quate and Ch. Gerber, *Phys. Rev. Lett.*, **56**, 930 (1986).
- [4] D.W. Pohl, W. Denk and M. Lantz, *Appl. Phys. Lett.*, **44**, 651 (1984).
- [5] D.H. Auston (edited by C.H. Lee): *Picosecond Optoelectronic Devices* (Academic Press, NY, 1984) and D.H. Auston (edited by W. Kaiser): *Ultrashort Laser Pulses and Applications*, Topics Appl. Phys. vol. 60 (Springer, Berlin, Heidelberg 1988).

# Picosecond Electrical Sampling Using a Scanning Force Microscope

A. S. Hou, F. Ho, and D. M. Bloom

Edward L. Ginzton Laboratory, Box #2, Stanford University, Stanford, California 94305

## Abstract

We demonstrate a scanning force microscope probe for measuring ultrafast voltage signals. Equivalent-time sampling using 100 ps pulses and mixing up to 20 GHz have been achieved.

## Introduction

High-speed characterization of nano-scale devices poses a significant challenge. Presently, no one measurement technique simultaneously addresses the requirements of ultra-high speed and ultra-small scale. On-wafer microwave probes have been demonstrated with subpicosecond performance,<sup>1</sup> but they require a minimum contact pad area on the order of 10 microns. The bandwidth of an optical sampling system can exceed 1 THz; however, the lateral resolution is limited by the laser beam diameter, usually 2 to 3 microns. Although electron beams can yield high resolution, such systems operate in vacuum and are significantly slower, with beam-blanking times limited by space-charge effects.

We present a new ultrafast technique, based on the scanning force microscope (SFM), that theoretically is sensitive enough to map an electric potential profile with better than 1 picosecond time resolution and submicron lateral resolution. It is a non-invasive technique which does not require vacuum. Unlike past capacitance and potentiometry measurements using an SFM<sup>2-4</sup>, which were limited by the slow mechanical response of the force-sensing cantilever and feedback electronics, we avoid this problem by using the square-law force interaction present between the SFM and sample for mixing and sampling. The high-speed signal under test is downconverted to a much lower intermediate

frequency. In the following sections, we describe the method of operation and show preliminary results.

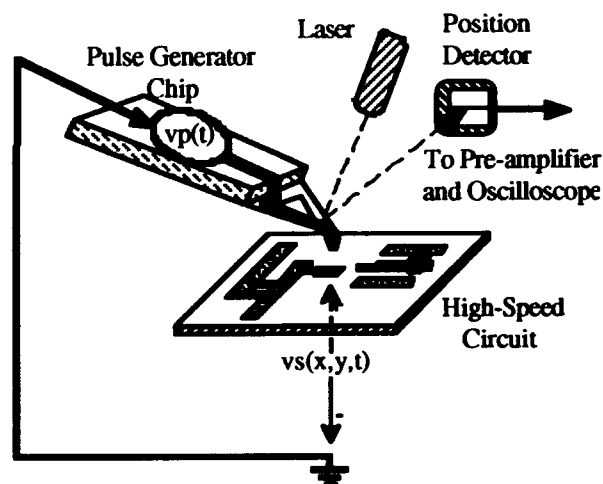
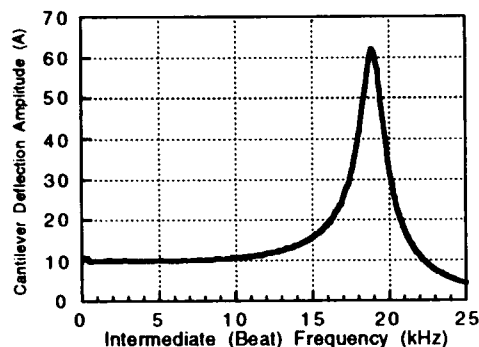


Figure 1. High-speed SFM electrical sampling system

## Theory of Operation

A scanning force microscope operates by sensing the minute deflection of a cantilever to which is attached an atomically sharp tip. There are two modes of operation. In a contact SFM mode, very short-range repulsive forces dominate and deflect the tip and cantilever to allow the determination of surface topography. In non-contact SFM, longer range forces (such as an attractive electric force) can cause the cantilever to bend.

Suppose that in non-contact mode, a voltage  $V$  is present between a conductive SFM tip and the sample device. There will then be an attractive force  $F$



**Figure 2.** Measured SFM electrical mixing at 1 GHz

experienced by the tip. If we simply model the tip and the device as two plates of a parallel plate capacitor, we obtain

$$F = -\frac{\epsilon_0 A V^2}{2z^2}$$

where  $\epsilon_0$  is the permittivity of vacuum,  $A$  is the effective area, and  $z$  is the effective distance. The key point is that the force is dependent on the square of the voltage. We can take advantage of this nonlinearity to extend the measurement bandwidth far beyond the mechanical resonance of the cantilever. The tip acts as an extremely high-speed mixer/sampler. That is, if two voltages, a signal voltage and an applied sampling voltage, appear between the tip and the sample, there will be a force corresponding to the product of the two voltages.

Fig. 1 shows the configuration of such a system. The periodic RF voltage  $V_s$  on the sample is what we wish to measure. A local oscillator voltage  $V_p$  is produced from a pulse generator integrated with the tip. Both  $V_s$  and  $V_p$  are referenced to a common ground; thus the voltage across the gap between the tip and the sample is  $V_p - V_s$ . The measured force is a function of the square of this voltage and therefore contains a mixing term at an intermediate frequency (IF), and if the LO is chosen properly, the IF will be below the cantilever's resonance frequency. The equivalent-time signal output is taken from the position-sensitive photodetector.

## Experimental Results

We conducted mixing experiments using a commercial scanning probe microscope (Park Scientific Instruments' Autoprobe) and an available supply of silicon nitride cantilevers which were coated with gold. Our initial results confirm the principles of high-speed operation. Instead of generating an LO signal by a pulse generator integrated with the tip, we summed external LO and the RF signals using a power combiner, and inputted the resultant signal to the

circuit under test. We report here the results from these experiments.

The first experiment involved mixing two sinusoidal signals offset by a small difference (or beat) frequency  $\Delta f$ . We combined the outputs of two synthesizers, one set at frequency  $f$  and the other set at  $f + \Delta f$ . The combined signal was launched onto a 50 $\Omega$  coplanar waveguide (CPW) transmission line on GaAs. The center conductor of the CPW was 15 microns wide. We then measured the beat response as  $\Delta f$  was varied. The result for  $f = 1$  GHz is shown in Fig. 2. The signal amplitude for each frequency was about 1 Volt.

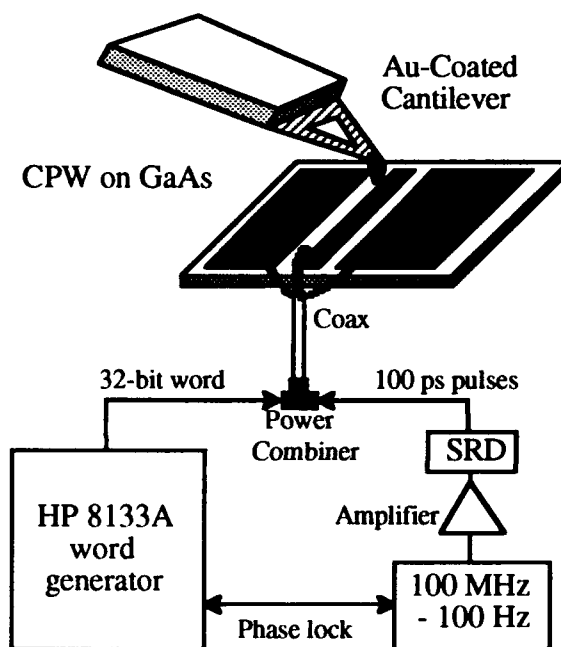


**Figure 3.** Setup for 3.2 GHz digital data sampling experiments

The frequency response of the mixing process is essentially the response of the cantilever's mechanical motion, with a resonance for this particular cantilever at about 19 kHz. Similar results were also obtained for input frequencies up to 20 GHz, above which we were constrained by package and input cable losses. These results show that the mixing process is operational up to at least 20 GHz.

To demonstrate high-speed performance in the time domain and to illustrate equivalent-time sampling, we carried out a second experiment with the setup shown in Figure 3. The SFM system is used to sample the output of an HP 8133A word generator. The test word consists of 32 bits, with digital voltage levels of 0 and 3.3 Volts. The clock rate is 3.2 GHz, corresponding to about 310 ps for each bit. A step-recovery-diode (SRD) comb generator is used to generate a train of 100 ps sampling pulses at the

repetition rate of 100 MHz - 100 Hz. The word generator output and the sampling pulses are combined and launched onto the CPW sample. Because there is a 100 Hz frequency offset between digital data stream and the pulse train, the pulses effectively "walk through" the data, yielding an equivalent-time signal at 100 Hz. Fig. 4 shows that the sampled result agrees very well with the direct output of the HP 8133A as measured with a 20 GHz sampling scope.

We also used an SRD pulse train to sample a version of itself, that is, to perform a pulse correlation. The setup is similar to that in Fig. 3, except that a pair of 500 MHz SRD's were used, one at a 500 MHz repetition rate and the other at 500 MHz + 10 Hz. The detector output, as shown in Fig. 5, is an equivalent-time correlation of the pulse train. The pulse width at half-maximum was measured to be 130 ps. The correlation is symmetric because the two pulse waveforms were nearly identical. This correlation indicates our sampling results are limited by the input pulse width of about 110 ps; with faster sources, even better time resolution can be expected.

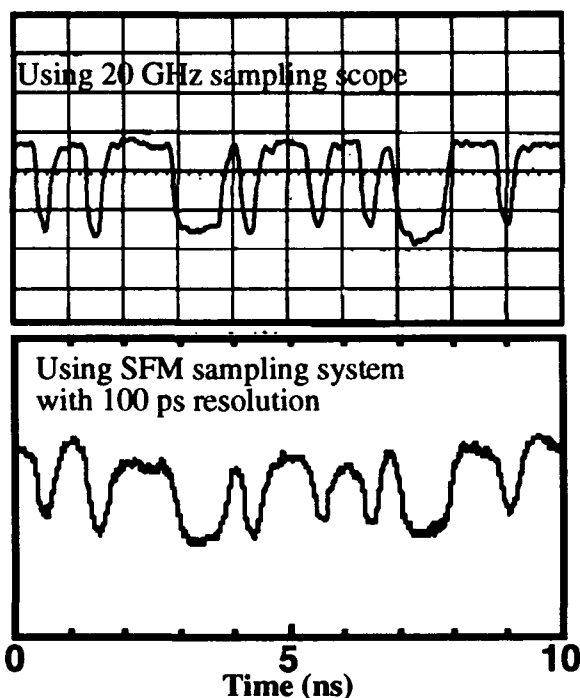


**Figure 4.** 3.2 GHz digital data stream as measured directly from the word generator (Top) and on the CPW circuit using the SFM sampling system. (Bottom)

## Conclusion

We have presented a new measurement technique that should be capable of measuring voltage signals with picosecond time resolution and submicron lateral resolution. Preliminary experiments have demonstrated mixing up to 20 GHz and sampling with

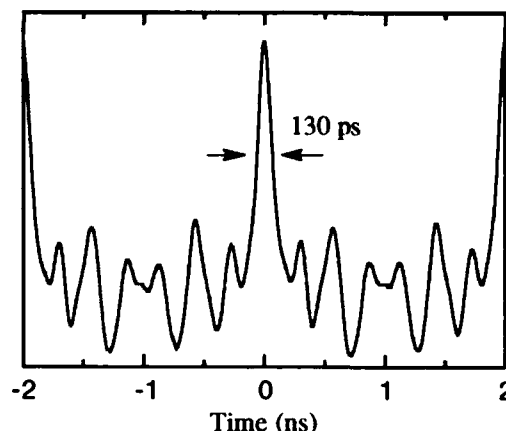


**Figure 5.** Equivalent-time correlation trace of two 110-ps pulse trains

100 ps time resolution. In the future, we intend to improve time and lateral resolution by integrating high-speed circuitry with a microfabricated cantilever and tip.

## Acknowledgment

This work is supported by ONR/DARPA under contract N00014-92-J-1769. A. S. Hou acknowledges a National Science Foundation fellowship. We are grateful to Park Scientific Instruments for their engineering support and assistance and to Pauline Prather for her expert chip bonding.

## References

1. M.S. Shakouri, A. Black, and D.M. Bloom, "Subpicosecond GaAs wafer probe system," in *Technical Digest of Ultrafast Electronics & Optoelectronics* (Optical Society of America, San Francisco, CA 1993), paper MC2.
2. Y. Martin, D.W. Abraham, and H.K. Wickramasinghe, "High-resolution capacitance measurement and potentiometry by force microscopy," *Appl. Phys. Lett.*, **52**, 1103-1105 (1988).
3. C.C. Williams, W.P. Hough, and S.A. Rishton, "Scanning capacitance microscopy on a 25 nm scale," *Appl. Phys. Lett.*, **55**, 203-205 (1989).
4. M. Anders, M. Muck, and C. Heiden, "Potentiometry for thin-film structures using atomic force microscopy," *J. Vac. Sci. Technol. A*, **8**, 394-399 (1990).



## Applications of Time-Lens Optical Systems

M. T. Kauffman, A. A. Godil, W. C. Banyai, and D. M. Bloom

*Edward L. Ginzton Laboratory, Stanford University, Stanford, California 94305*

### Abstract

We demonstrate reduced timing jitter on a picosecond pulse train, magnification and time-reversal using a temporal imaging system.

### Introduction

The analogy between the spatial problem of Fresnel diffraction and the temporal problem of first-order dispersion, elaborated by Treacy<sup>1</sup>, led Kolner<sup>2</sup> et al to propose a temporal imaging system. Godil<sup>3</sup> et al realized the first practical system by using an optical phase modulator followed by a diffraction grating pair<sup>1</sup> to focus 55 psec pulses to 1.9 psec. In this paper, we present two applications of the time-lens optical system that underscore the analogy with spatial optical systems as well as demonstrate its versatility: reduced timing jitter for a picosecond pulse train and time-reversal with magnification.

By interchanging the spatial and temporal variables, we can directly apply knowledge of spatial imaging systems to temporal imaging systems. In either case, an imaging system requires dispersion from the object to the lens, a lens, and dispersion from the lens to the image. The analogy between spatial and temporal dispersion is subtle. In the spatial case, dispersion results from free-space propagation of light, that is, diffraction. Thus, the phase relationship of light at a lens is determined by a single variable, for example, the object distance. In the temporal case, frequency dispersion must be supplied by an dispersive element such as a diffraction grating pair. The analogy to the spatially varying quadratic phase shift produced by a glass lens can be realized by an optical phase modulator which supplies a temporally varying quadratic phase shift. The difference is that while it is easy to get many optical wavelengths of path length difference across the face of a glass lens, it has been difficult to get many

radians of optical phase modulation. Thus the key to building a temporal imaging system was the development of the optical phase modulator shown in Fig. 1. This device consists of a microwave rectangular waveguide, loaded in the center but not on the ends with LiNbO<sub>3</sub>, so that the waveguide mode is cutoff in the ends but not in the center. This forms a microwave cavity with a Q of 1900. By choosing the waveguide and crystal dimensions properly, the microwave phase velocity is matched to the optical phase velocity. The modulator is placed in an optical resonator and excited off-axis so that the light makes multiple passes through the modulator but is not optically resonant<sup>4</sup>. Even after 24 passes, the optical transmission is about 50%.

The phase modulator produces a quadratic phase shift for only a fraction of each period, in particular when

$$A \cos(\omega_m t) \equiv A[1 - (\omega_m t)^2], \quad (1)$$

where A is the peak phase shift in radians and  $\omega_m$  the modulator resonant frequency. We can define a useful aperture time,  $T_A \equiv 1/\omega_m$ , which in our case corresponds to  $T_A = 30$  ps when  $A = 13.5$  radians and  $\omega_m = 5.2$  GHz. This is achieved with a microwave drive power of 1W. A time lens, like a spatial lens, suffers from aberrations due to higher-order terms in the expansion of  $A \cos(\omega_m t)$ .

The well-known spatial imaging condition is

$$\frac{1}{s_o} + \frac{1}{s_i} = \frac{1}{f} \quad (2)$$

where  $s_o$  ( $s_i$ ) is the object (image) distance and f is the focal length while the analogous temporal imaging condition as first derived by Kolner et al<sup>2</sup> is

$$\frac{1}{\omega_o s_1 \partial^2 \beta_1 / \partial \omega^2} + \frac{1}{\omega_o s_2 \partial^2 \beta_2 / \partial \omega^2} = \frac{1}{f_T} \quad (3)$$

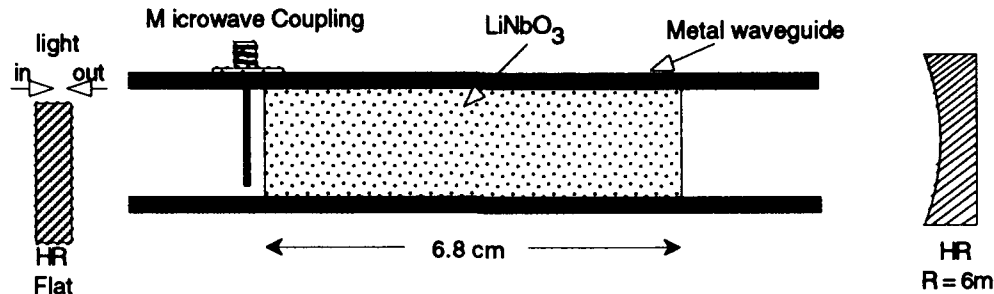


Figure 1. Cross section view of the resonant microwave optical modulator used to produce the time lens. The LiNbO<sub>3</sub> crystal is housed in a rectangular microwave waveguide.

where  $\omega_0$  is the optical frequency,  $s$  is the grating separation,  $\partial^2\beta/\partial\omega^2$  is the group velocity dispersion derived from the grating and  $f_t = \omega_0/A\omega_m^2$  is the focal time. The time-lens resolution is given by  $\tau_0 = 2.65/A\omega_m$ , which is 6 ps for the time-lens described above.

### Experiment

Our first experiment was an extension of the result obtained by Godil et al but takes advantage of the Fourier shift theorem to suppress timing jitter from a pulsed laser system. Consider the spatial case where parallel rays are brought to focus by a lens, object and image space being a transform pair. Decentering in object space produces a phase shift at the focal point. In the analogous temporal case, a time-delay in object space produces a phase shift in image space. However, a linear phase shift across a pulse corresponds to a frequency shift, so that timing jitter in object space is transformed into frequency jitter in image space. Ideally, timing jitter should be reduced to zero in the image plane, but aberrations in the time-lens limit the magnitude of the reduction.

We used a modified Spectra-Physics 3000 system that produced a 55 ps, 1.06  $\mu\text{m}$ , 83 MHz pulse train with a laser timing stabilization loop that allowed for the addition of a specified amount of timing jitter<sup>5</sup>. Timing jitter was measured by integrating the phase noise from 400Hz-2kHz above the 90<sup>th</sup> harmonic of the laser frequency. The temporal optical system consisted of a time-lens followed by a 2-pass, 1700 line/mm grating pair. The output pulse was 6 ps, matching the system resolution. Timing jitter measurements, shown in Fig. 2, were made at the input and output of the system. There is a significant reduction in the jitter, an average of 80%. However, we did not obtain a flat response as expected. This is mainly due to the phase aberration on the input pulse due to the time aperture (30 ps) being less than 55 ps input pulsewidth. The timing jitter noise floor of our measurement system is estimated to be 300 fs. We conclude that the output timing jitter measured for small input jitter is simply the noise floor of our measurement.

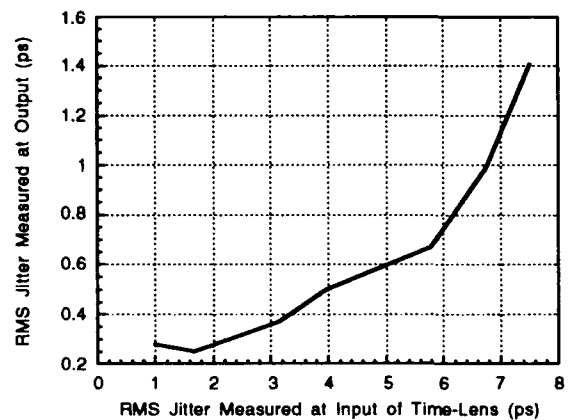


Figure 2. RMS jitter measured at the output focal plane vs. jitter at the input of the time-lens system.

For our second experiment, the grating pairs were set such that the input dispersion was  $5f_T$  and the output  $5f_T/4$ . Since the magnification of such a system is negative (-4), one would expect a pulse to be reversed in time at the output. To test this hypothesis we imaged two pulses separated by 20 ps. The input pulse width was 1.5 ps for each of the two pulses, which was less than the time-lens' 6 ps resolution, but was required in order to accommodate the 30 ps aperture time. Input and output waveforms illustrating time-reversal were measured with a New Focus Model 1014 Detector connected to an HP 71500A Microwave Transition Analyzer and were system limited to 20 ps FWHM. Fig. 3 illustrates the two input pulses with the weaker pulse delayed 20 ps with respect to the stronger pulse. Fig. 4 illustrates time-reversal: the weaker pulse is now advanced with respect to the stronger pulse, as verified by blocking the weaker pulse at the input. Furthermore, a magnification of -4 was verified by noting that the separation between the two pulses changed from 20 to 80 ps.

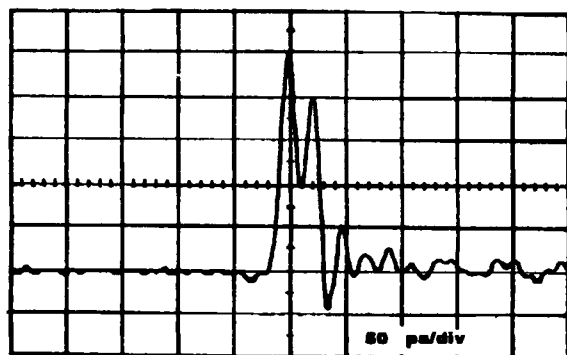


Figure 3. Measured pulse pair input to the time-lens imaging system. The vertical axis is in arbitrary units while the horizontal axis is 50 ps/div. The weaker pulse is delayed 20 ps with respect to the stronger pulse.

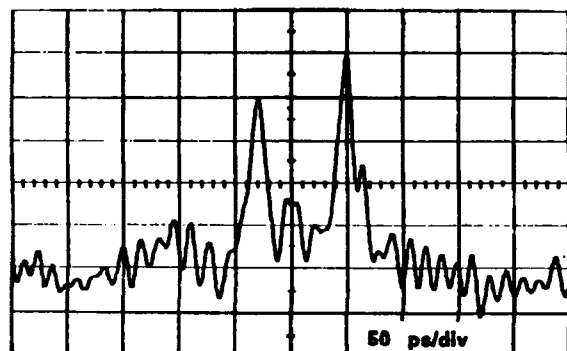


Figure 4. Measured pulse pair output from the time-lens imaging system. The vertical axis is in arbitrary units while the horizontal axis is 50 ps/div. The weaker pulse now leads the stronger pulse by 80 ps, illustrating time-reversal and magnification.

### Summary

In conclusion, we have demonstrated a temporal imaging system illustrating pulse jitter reduction and time-reversal. These two simple experiments exemplify the power of the time-lens for controlling and shaping optical pulses.

### References

1. E. B. Treacy, *IEEE J. Quant. Electron.* QE-5, 454 (1969).
2. B. H. Kolner and M. Nazarathy, *Opt. Lett.* 14, 630 (1989).
3. A. A. Godil, B. A. Auld and D. M. Bloom, *LEOS '92*, Boston, MA, Nov.16-19, 1992; A. A. Godil, B. A. Auld and D. M. Bloom, submitted to *Appl. Phys. Lett.*
4. D. Herriott, H. J. Schulte, *Appl. Opt.* 4, 883 (1965)
5. M. J. W. Rodwell, D. M. Bloom and K. J. Weingarten, *IEEE J. Quant. Electron.*, QE-25, 817 (1989).

## The Femtosecond Field Emission Camera: A Device for Continuously Observing the Motion of Single Adsorbed Atoms and Molecules

Gary M. McClelland, Harry Heinzelmann<sup>1</sup> and Fumiya Watanabe  
IBM Research Division, Almaden Research Center  
San Jose, CA 95120, ph. 408-927-2406

Unlike many laser techniques for achieving fast time resolution, a streak camera generates a continuous record of picosecond phenomena. By applying the beam-sweeping method of the streak camera to the electrons field-emitted from a sharp metal tip, we have developed the femtosecond field emission camera (FFEC), which can continuously record the motion of individual atoms or molecules adsorbed on the tip with a time resolution of  $10^{-13}$  s. This is fast enough to observe directly the vibrational motion of atoms and molecules. We have recorded the motion of a single Cs atom on a tungsten (111) tip with 1 nm and 2 ps resolution,<sup>2</sup> a factor of  $10^6$  faster than any previous continuous observation of atomic motion.

Fig. 1 is a schematic of the FFEC, which is housed in a stainless steel vacuum chamber at  $10^{-11}$  Torr. Electrons field-emitted from a tip of radius 200 - 1000 Å are focussed into a collimated beam by a lens similar to that used for electron microscope guns.<sup>3</sup> The intensity of the field emission depends strongly on the instantaneous position of the surface atoms, which affect the local work function.<sup>4</sup> A  $\approx 2$  kV pulse from a krytron generator is applied to 3 cm long electrodes spaced by .6 cm to sweep the beam across a dual microchannel plate electron multiplier (MCP) and phosphor screen detector, positioned about 40 cm from the deflector. This detector has nearly 100 %  $e^-$  efficiency. The full width of the beam emitted from the tip is only about  $5^\circ$ , enabling a focus from this point

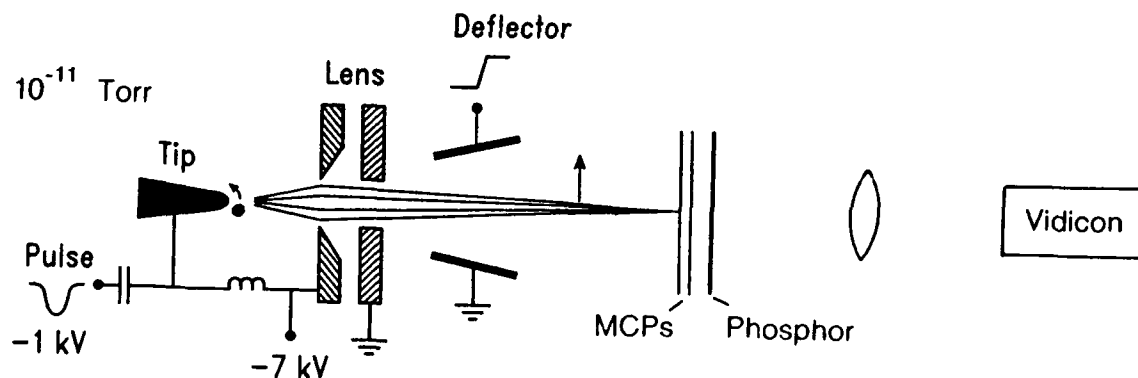


Figure 1. Femtosecond Field Emission Camera. Not to scale.

source to a 0.3 mm diameter spot at the MCP. Although the current density at the FE tip is very high, the total current is low enough that space charge does not affect the focussing. By turning off the lens and deflecting field, the tip can be imaged at atomic resolution by field ion microscopy (FIM) and at sub-nanometer resolution by FE microscopy.

In the FFEC, the electron beam is so narrow and the focus so sharp that the beam sweep rate does not limit the achievable time resolution. The limiting factor is the time of flight (TOF) spread between the tip and the deflecting field. This spread partially arises from the variety of paths taken by electrons through the lens. A more fundamental contribution arises from the energy spread of the emitted electrons, which is typically about 0.2 eV FWHM.<sup>5</sup> In streak cameras, the energy spread has the greatest effect just outside the photocathode, where the electron velocity is low. But in the FFEC, the accelerating field of 1 V/Å at the emitter is so large that the 0.2 eV spread here gives a TOF spread of only  $10^{-15}$  s, orders of magnitude smaller than in conventional streak cameras. After the electrons leave the  $\approx 1000$  Å long high-field region around the tip, the additional time of flight spread depends on the length of the flight path. For our instrument, the total path is 10 cm, giving a TOF spread of  $10^{-13}$  s. By shortening the flight path, this time can be reduced to  $10^{-14}$  s, which is in any case the statistical limit imposed by the electron count rate.

In our first experiments,<sup>2</sup> we observe the motion of a single Cs atom adsorbed on a tungsten (111) tip terminating in a plane of 3 atoms. The tip is formed by heat treatment and field evaporation<sup>6,7</sup> and imaged at atomic resolution by FIM. The sharpness of the apex plane limits the field emission, which can be as high as  $10 \mu\text{A}$ <sup>6,7</sup> ( $6 \times 10^{13}$  e/s), to a region less than 1 nm across. The arrival of a single Cs atom from an evaporator onto a 90 K tip is detected by the sudden jump of a factor of  $\approx 5$  in the

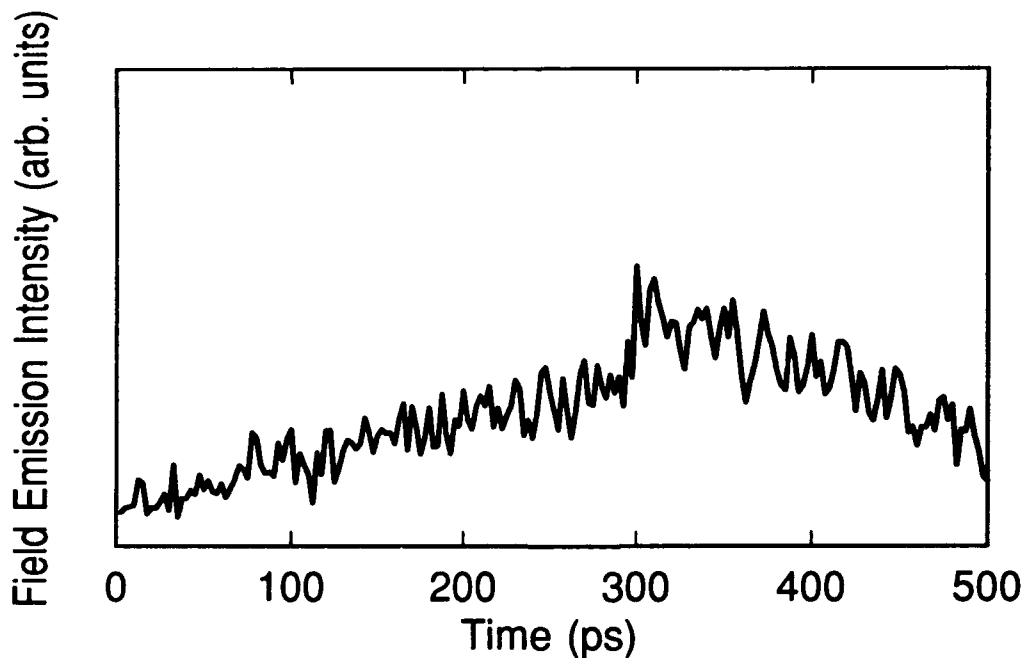


Figure 2. Field emission from a tungsten tip on which a single Cs atom is adsorbed. The sudden increase at 300 ps results from the atom jumping to a site nearer the triatomic tip apex plane.

FE caused by lowering of the local work function.<sup>8</sup> To observe the motion of the Cs atom, the tip is pulsed negative for several ns, generating a current of several  $\mu\text{A}$ , which heats the Cs atom by inelastic electron tunneling or the Nottingham effect. The resulting beam is swept and focussed to give the trace shown in Figure 2. The abrupt rise in the field emission, which occurs within the 2 ps pixel width of our detector, indicated that a Cs atom has jumped into the  $< 1$  nm dia. region on the tip observed by field emission. The gradual rise and fall of the emission current is related to the voltage pulse shape. From the field emission image, we can determine the position of the Cs atom before and after each sweep.<sup>2</sup>

Even though the angle at which the electron beam leaves the tip is determined by its position on the tip, focussing the beam on the detector screen destroys this spatial information. By using an astigmatic lens to defocus the beam perpendicular to the scan direction, simultaneous temporal and one-dimensional spatial resolution is achievable.<sup>2</sup> By increasing the scan rate and using higher currents, it will be possible to follow the trajectories of individual atoms and molecules on the time scale of atomic vibration.

## References

1. Present address: Institute of Physics, University of Basel, 4056 Basel, Switzerland.
2. Heinzelmann, H., Watanabe, F. & McClelland, G. M., submitted to *Nature*.
3. El Gomati, M. M., Prutton, M. & Browning, R. *J. Phys. E* **18**, 32-38 (1985).
4. Woodruff, D. P. & Delchar, T. A. *Modern Techniques in Surface Science* (Cambridge U. Press, Cambridge, 1986).
5. Vu Thien Binh & Marien, J. *Surface Sci.* **202**, L539-L549 (1988).
6. Fink, H.-W. *IBM J. Res. Develop.* **30**, 460-465 (1986).
7. Fink, H.-W. *Physica Scripta* **38**, 260-263 (1988).
8. Todd, C. J., & Rhodin, T. N. *Surface Sci.* **42**, 109-138 (1974).

---

## **(Sub)Millimeter Wave Devices**

---

# High Frequency Solid State Sources Using Ultrafast Techniques

D. V. Plant, D. C. Scott, M. Martin, F. K. Oshita, and  
H. R. Fetterman

*Department of Electrical Engineering, University of California  
at Los Angeles, Los Angeles, California 90024*

## ABSTRACT

Picosecond mode-locked lasers and cw optical mixing have been used to make optoelectronic high frequency sources. This work is now being extended to submillimeter wavelengths.

## I. INTRODUCTION

Optical millimeter wave interactions have attracted recent attention because of applications which involve the advantages of both lightwave and microwave techniques.<sup>(1,2)</sup> It allows the use of optical-fiber technology for interconnection of microwave devices and circuits. In this paper we describe the use of mode locked, picosecond lasers and cw optical laser mixing to generate high frequency radiation. Virtually any frequency desired can be obtained using either of these two optical sources. In the case of the mode locked lasers, we utilize higher order modes, and in the mixing experiments one can tune the frequency of one of the lasers in order to achieve high frequencies. The problem in making a high frequency source is then reduced to converting these optical frequency components into propagating radiation. Our experiments have used optically illuminated, three terminal devices such as HEMTs and HBTs, configured with integrated antenna structures to generate tunable millimeter waves.<sup>(3,4)</sup> Since our lasers can be semiconductors this effectively creates entirely solid state sources which can be tuned to extremely high frequencies. They can also be modulated using the gate or base of the mixing transistor for roles in communications and radar. In our experiments we have extensively used picosecond

optoelectronic measurement techniques to determine the optical response speed of the devices used.<sup>(5,6)</sup> Extending this work to higher frequencies, we are now examining devices and antennas designed for operation at 500 GHz.

## II. EXPERIMENTS

The radiating elements were comprised of integrated transistor/antenna circuits using the latest heterojunction devices. The FET devices used were 60 GHz pseudomorphic AlGaAs/InGaAs HEMTs,<sup>(7)</sup> and the HBT devices used were abrupt emitter-base junction AlInAs/InGaAs transistors.<sup>(8)</sup> In the case of the HBT, an 8x8  $\mu\text{m}$  window in the emitter metalization was included to allow for optical access to the active region. This added significant parasitics but yielded improved optical coupling. Both the HEMTs and the HBTs were mounted into twin dipole printed circuit antennas that were designed to have optimum gain at 60 GHz.<sup>(9)</sup> The optically generated millimeter waves were radiated into free space and collected into waveguide with millimeter wave horns and lenses. Using a Gunn diode as a local oscillator, the optically generated signals were heterodyne detected using a double balanced mixer.

## III. EXPERIMENT 1

In the initial sets of experiments, the device/antenna circuits were illuminated with light from an actively frequency stabilized Krypton Red dye laser (600 nm - 640 nm) and a frequency stabilized HeNe laser (632.8 nm). The wavelength of each linearly polarized laser was monitored with a wavemeter that had 0.001 nm resolution. Using a beam splitter, the laser outputs



were combined and focused onto the device active regions. Figure 1 is a recording of a radiated signal from a HBT/antenna with a center frequency of 59.5 GHz, a signal to noise ratio of 45 dB, and a 3 dB linewidth of 2.5 MHz. Also shown are the applied sidebands at 118 MHz. Similar results were obtained with integrated HEMT/antenna circuits. In subsequent experiments, the dye/gas laser combination was replaced by single frequency semiconductor lasers operating at both 850 nm and 1.3  $\mu\text{m}$ . These long wavelength lasers were chosen because they are optimally absorbed in the active regions of the devices and therefore provided the highest optical to millimeter wave conversion efficiencies.

#### IV. EXPERIMENT 2

In a second set of experiments, the device/antenna circuits were driven by modelocked GaAs/AlGaAs multiple quantum well semiconductor lasers. These diodes were two and three section lasers which were modelocked using a saturable absorber.<sup>(10,11,12)</sup> In these devices, the saturable absorber section was biased to adjust the steady state absorption to the point where small round trip oscillations become unstable and mode locking occurs. The 850nm lasers were mode locked at 51 GHz and 65 GHz with output pulses of <2.5 psec and average powers of 1 to 3 mW. This wavelength is particularly well suited with respect to the layer structure of the HEMT devices because, although some light is absorbed in the 40 nm GaAs cap layer, the transparency of the AlGaAs layer allows 80% of the unreflected light to be absorbed in the InGaAs channel and the underlying GaAs superlattice buffer layer. As shown in Figure 2, the combination of a laser diode and the high frequency device/antenna circuit results in a fixed frequency, narrow linewidth source and defines a new type of semiconductor based optoelectronic oscillator. Figure 3 is a measurement of a 65.1 GHz radiated signal with a signal to noise ratio of 40dB with a 3 dB linewidth of <500 KHz. The modelocked output can be regarded as a highly efficient means of directly modulating an optical carrier at millimeter wave frequencies, and can be used to drive the device/antenna circuits.

#### V. CONCLUSIONS

This technique can be extended to higher frequencies by utilizing high harmonics of the fundamental modelocking frequency. Our devices are suitable to extending this technology to higher frequencies and in figure 4 we show the results of our picosecond measurements on HEMTs operating in both drain and gate modes. Also, temperature dependent measurements on the latest HBTs at both

300K and 20K show impressive performance in Figure 5. Finally, monolithically integrated HEMT/Antenna circuits designed for operation at frequencies between 200 and 500 GHz are being implemented. Figure 6 shows a schematic of the integrated slot antenna structure and matching circuit which will be driven optically by exciting the HEMT. These devices will allow the frequency range to be extended to submillimeter wavelengths.

This work was supported by the Air Force Office of Scientific Research and by the National Center for Integrated Photonics Technology with transistors supplied by TRW, Hughes, and Rockwell and modelocked lasers by Ortel.

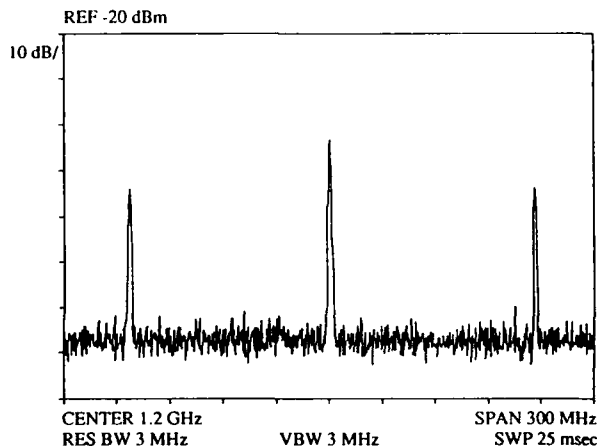


Figure 1: Optically generated millimeter wave radiation at 59.5 GHz with 118 MHz sideband modulation.

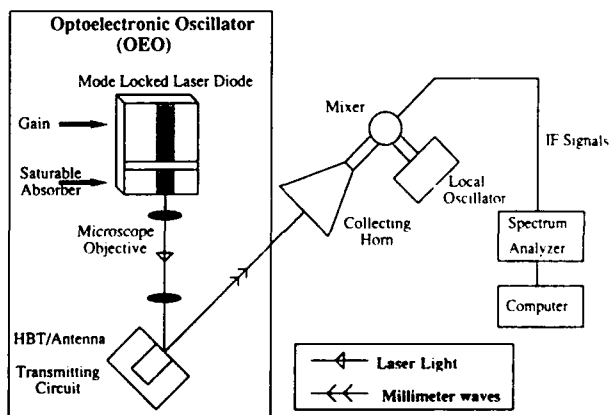


Figure 2: Millimeter wave optoelectronic oscillator.

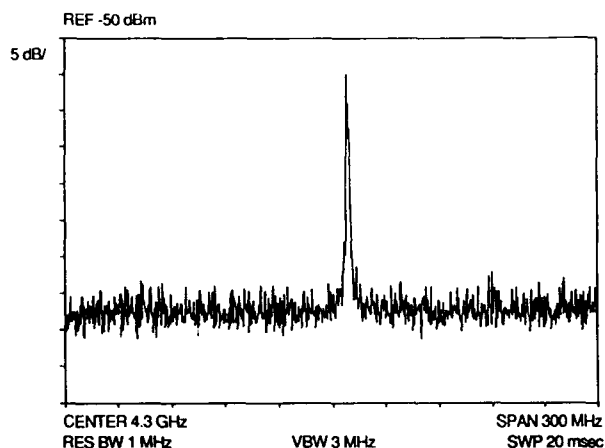


Figure 3: Modelocked laser driven 65.1 GHz radiation.

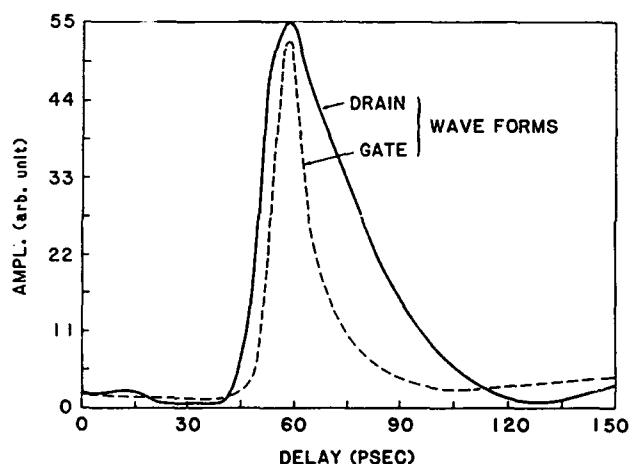


Figure 4: Optical response of an AlGaAs/InGaAs HEMT.

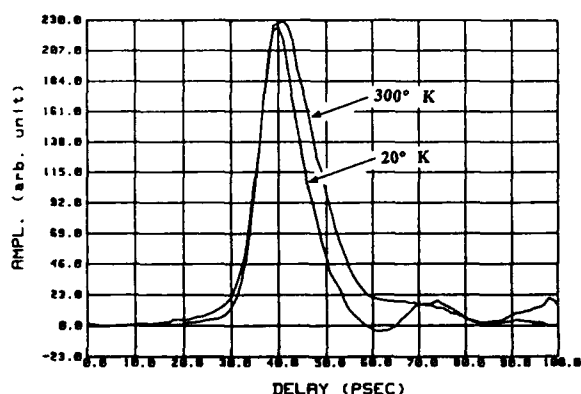


Figure 5: Optical response of an AlGaAs/GaAs HBT.

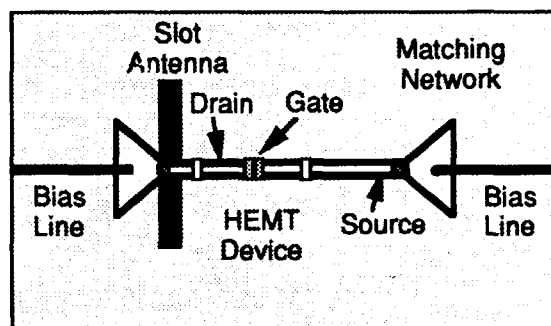


Figure 6: Monolithically integrated HEMT/Antenna circuits designed for operation at frequencies between 200 and 500 GHz

### References

- [1] P. R. Herczfeld, Guest Ed., "Special issue on applications of lightwave technology to microwave devices," *IEEE Trans. Microwave Theory Tech.*, vol. MTT-38, 1990.
- [2] R. Simons, *Optical Control of Microwave Devices*. Boston and London, Artech House, 1990.
- [3] D.V. Plant, D.C. Scott, H.R. Fetterman, L.K. Shaw, W. Jones, and K.L. Tan, "Optically generated 60 GHz millimeter wave using AlGaAs/InGaAs HEMTs integrated with both quasi-optical antenna circuits and MMICs," *IEEE Photon. Technol. Lett.*, vol. 4, pp. 102-105, 1992.
- [4] D.C. Scott, D.V. Plant, and H.R. Fetterman, "60 GHz sources using optically driven heterojunction bipolar transistors," *Appl. Phys. Lett.*, vol. 61, pp. 1-3, 1992.
- [5] M. Matloubian, H.R. Fetterman, M. Kim, A. Oki, J. Camon, S. Moss, and D. Smith "Picosecond optoelectronic measurement of S-parameters and optical response of an AlGaAs/GaAs HBT," *IEEE Trans. Microwave Theory Tech.*, vol. 38, pp. 683-686, 1990.
- [6] M.Z. Martin, F.K. Oshita, M. Matloubian, H.R. Fetterman, L.K. Shaw, and K.L. Tan "High-speed optical response of pseudomorphic InGaAs high electron mobility transistors," *IEEE Photon. Technol. Lett.*, vol. 4, pp. 1012-1014, 1992.
- [7] K.L. Tan, R.M. Dia, D.C. Streit, L.K. Shaw, A.C. Han, M.D. Sholley, P.H. Liu, T.Q. Trinh, T. Lin, and H.C. Yen, "60 GHz pseudomorphic AlGaAs/InGaAs Low-Noise HEMTs," *IEEE Electron Device Lett.*, vol. 12, pp. 23-25, 1990.
- [8] J.F. Jensen, W.E. Stanchina, R.A. Metzger, D.B. Rensch, R.F. Lohr, R.W. Quen, M.W. Pierce, Y.K. Allen, and P.F. Lou, "AlInAs/GaInAs HBT IC technology," *IEEE J. Solid-State Circuits*, vol. 26, pp. 415-421, 1991.

- [9] W. Chew and H. R. Fetterman, "Printed circuit antennas with integrated FET detectors for millimeter-wave quasi optics," *IEEE Trans. Microwave Theory Tech.*, vol. MTT-37, pp. 593-597, 1989.
- [10] K.Y. Lau, "Efficient narrow-band direct modulation of semiconductor injection lasers at millimeter wave frequencies of 100 GHz and beyond," *Appl. Phys. Lett.*, vol. 52, pp. 2214-2216, 1988.
- [11] S. Sanders, L. Eng, J. Paslaski, and A. Yariv, "108 GHz passive mode locking of a multiple quantum well semiconductor laser with an intracavity absorber," *Appl. Phys. Lett.*, vol. 56, pp. 310-311, 1990.
- [12] M.C. Wu, Y.K. Chen, T. Tanbun-Ek, R.A. Logan, and M.A. Chin "Tunable monolithic colliding pulse mode-locked quantum-well lasers," *IEEE Photon. Technol. Lett.*, vol. 3, pp. 874-876, 1991.

# On-Wafer Optoelectronic Techniques for Millimeter-Wave Generation, Control, and Circuit Characterization

Sheng-Lung L. Huang and Chi H. Lee

*Electrical Engineering Department, University of Maryland,  
College Park, Maryland 20742*

Hing-Loi A. Hung

*COMSAT Laboratories, Clarksburg, Maryland 20871*

## Abstract

Using optoelectronic techniques, the generation and true-time-delay phase-shift of 60-GHz broadband signals, as well as on-wafer circuit characterization exceeding 160 GHz, which is close the bandwidth limit of microstrip transmission line on a 4-mil thick GaAs wafer, have been demonstrated.

## Introduction

Recent progresses in the merging of ultrafast optics and high speed electronic circuit techniques have resulted in a number of new potential applications. On-wafer optoelectronic techniques refer to the class of techniques where optic/electronic intermixing structures can be integrated with electronic circuits to achieve various circuit characterization and component functions. In this paper, a new method of generating both millimeter-waves (MMWs) and true-time-delay phase-shifts of 60-GHz broadband signals is presented. This optical technique is useful in applications such as, broadband phased array antennas and communication systems [1]. We have also extended the optical characterization of monolithic integrated circuits beyond 160 GHz [2] [3].

## Experiments

The MMW generation and true-time-delay phase-shift are achieved using a 5-ps electrical pulse, while the circuit characterization is obtained with both 5-ps and 2.8-ps electrical pulses. For both experiments, the electrical pulses are generated by the photoconductive (PC) effect. The laser system generates both 3-ps and 400-fs green pulses from a mode-locked Nd:YLF laser which pumps a first stage fiber-grating pulse compressor followed by a frequency doubling crystal (3 ps) and a second stage fiber-prism pulse compressor (400 fs). The average power required is less than 10 mW. The electrical pulses contain frequency components well beyond 200 GHz. The photoconductive switch is 10  $\mu\text{m}$  long and was fabricated on a 4-mil-thick GaAs wafer. The GaAs material gap in PC switch was proton implanted at a dose of  $10^{14} \text{ cm}^{-2}$ . The fabrication process is fully compatible with current microwave/millimeter-wave integrated circuit (MMIC) technologies; therefore, all the optical structures used to achieve the functions we demonstrate can be integrated with MMICs. Figure 1 shows the schematic of the MMIC and optical test structure.

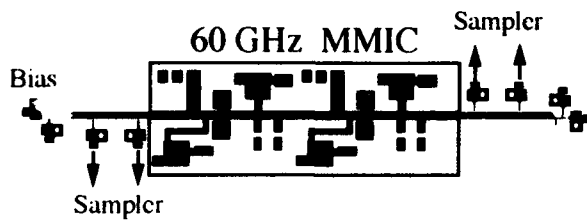


**Figure 1.** *V band MMIC with optical test structure.*

By injecting picosecond electrical pulses into a MMIC amplifier, only the signal components with a spectrum falling within the gain bandwidth of the MMIC amplifier are passed through and amplified. This process generates MMWs with frequencies depending on the bandwidth characteristics of the amplifier. A multistage 60-GHz monolithic low noise amplifier (LNA) with about 25-dB gain and 8-GHz bandwidth was used in this experiment.

True-time-delay phase shifts of the generated MMW can also be achieved by simply delaying the laser pulse arriving time at the MMIC amplifier. The phase-shift strictly follows the optical time-delay. With a round-trip-delay of 2.4 mm, the 60-GHz MMW signal can achieve a  $2\pi$  phase shift.

We are also able to test the frequency response of the LNA by standard PC sampling techniques using both 5-ps and 2.8-ps electrical pulses.

## Results and Discussions

Figure 2 shows the measured MMW waveform and the corresponding true-time-delay phase-shifts of up to  $2\pi$  radian. Negligible jitter in the LNA signal has been obtained with the present system setup, which is evident from the excellent signal to noise ratio of the sampled waveforms. In addition, the phase control accuracy is better than  $0.1^\circ$ . Figure 3 shows the linear dependence of the phase shift as a function of frequencies. The results show that this MMW generation technique can offer a new configuration in phased array antenna or communication system ap-

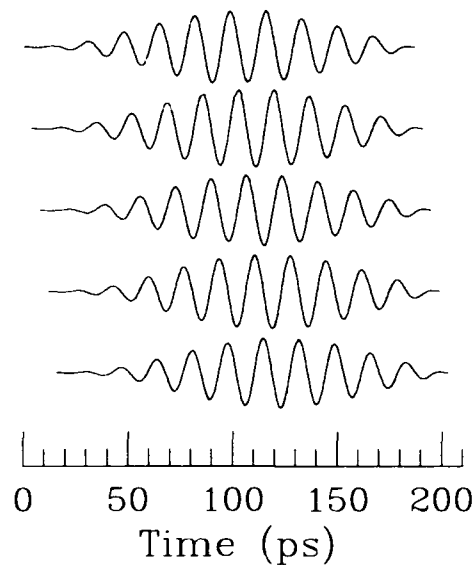


**Figure 2.** *Successive true time delayed waveforms of the 60-GHz broadband signals.*

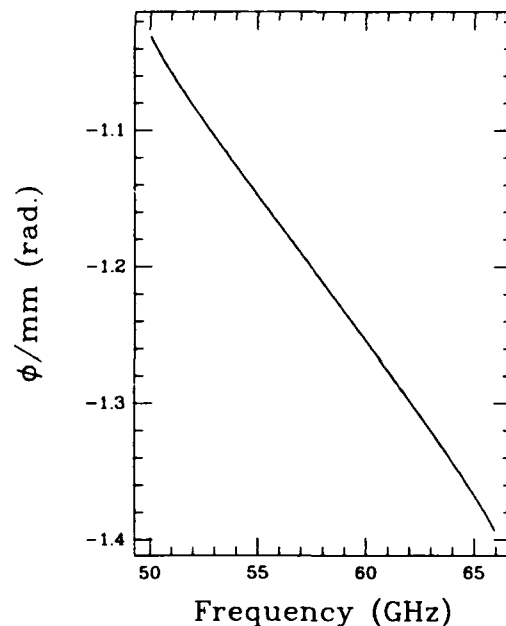


**Figure 3.** *Phase shift in unit optical delay vs. broadband millimeter-wave frequencies.*

plications, namely a frequency multiplexed phased array system. This is illustrated by examining the following equation.

$$\theta_0 = \sin^{-1}\left(\frac{c}{2\pi d f}\right)$$

where  $\theta_0$  is the array pointing angle,  $c$  is the velocity of MMW signal in the free space, and  $d$  is the spacing between the array elements. Since the MMW phase is proportional to its frequency, all the MMW frequencies can radiate in the same direction. The information capacity could, therefore, be multiplied by the number of frequency channels.

The temporal waveform of the output of an amplifier with moderate bandwidth is normally long lasting; therefore, the testing of such circuits has more stringent requirements. First, the spatial extend of the waveform is much longer than length of the optical test structure; as a result, the terminations of the optical test structures should be matched to avoid multiple reflections. Figure 4 depicts measurements of output waveforms from the MMIC at different positions of the transmission line

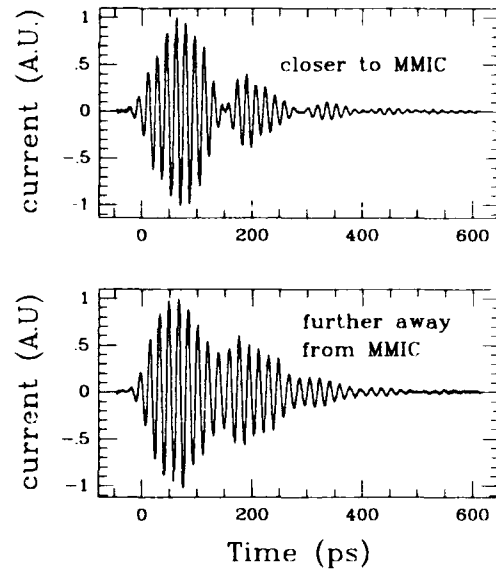


**Figure 4.** Measured waveforms at different positions of the MMIC output.

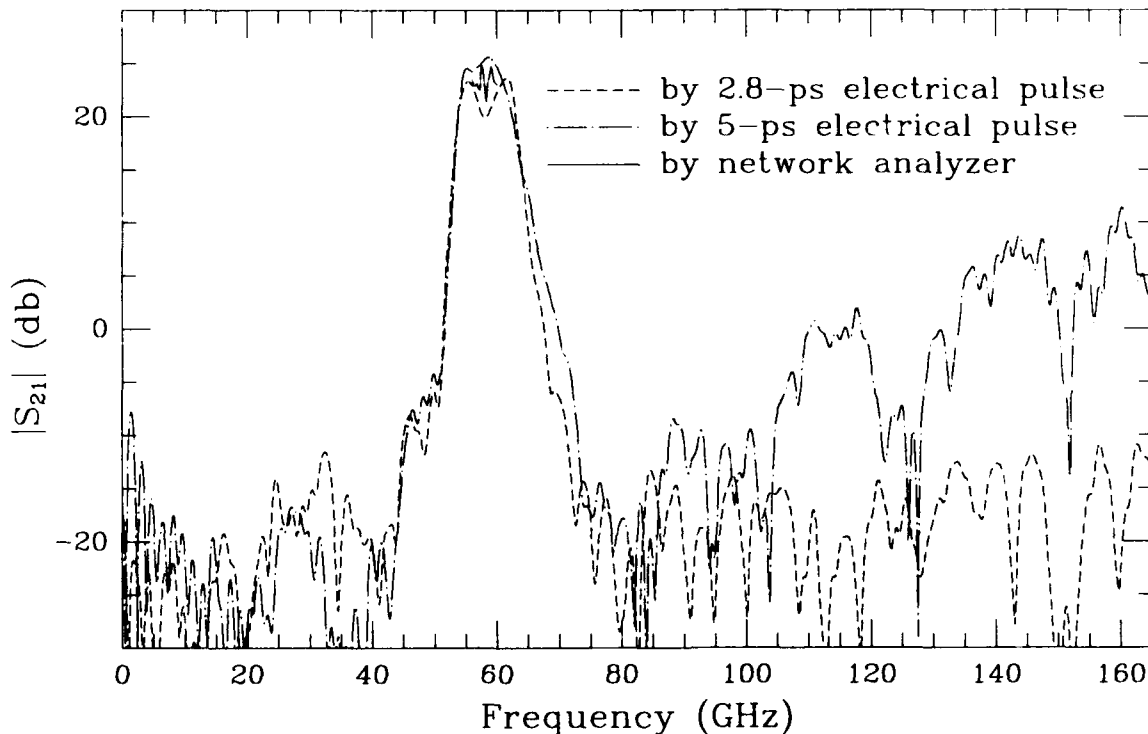


**Figure 5.** Comparison of  $|S_{21}|$  measured by the network analyzer and the PC sampling techniques.

at the output side. The discrepancies are due to interference effect from a mismatched termination. Two counter propagating waves with different time delays sum up different temporal waveforms. Second, since the sampling time is long, the long term stability of the ultrashort laser is crucial for reliable measurements. The measured magnitude of  $|S_{21}|$  using different pulse widths are shown in Figure 5. With the 2.8 ps electrical pulse, measurement bandwidth is appreciately increased to over 160 GHz, while the 5 ps electrical pulse only have about 100-GHz bandwidth. This measurement shows that the second harmonic power distortion from the LNA is less than  $10^{-4}$  of the fundamental 60-GHz signal. Consequently, the electrical pulse amplitude used in our on wafer PC sampling technique can be adjusted so that it is weak enough to avoid distortion, while, strong enough to give high dynamic range.

## Conclusion

The incorporation of optoelectronic techniques into MMW systems has created a new class of circuits that can perform electronic functions not easily attainable by pure electronic means. Synchronization between the ultrafast optical pulse trains and MMW makes it easier to control MMW devices and circuits.

In this paper, we demonstrated a new method to optically control MMW generation and true-time-delay phase shift of 60 GHz broadband signals. This could enhance phased array systems by allowing frequency multiplexing. We also measured the frequency response of a MMIC amplifier over 160 GHz bandwidth, which is close to the practical bandwidth limit for microstrip line based MMIC. The fabrication techniques used are compatible with the current MMIC technology.

This work was supported by the Maryland Industrial Partnership program.

## References

1. R. J. Mailloux, "Phased Array Theory and Technology," *Proc. IEEE*, **70**, pp. 246-291, 1982.
2. H.-L. A. Hung, P. Polak-Dingels, K. J. Webb, T. Smith, H. C. Huang, and C. H. Lee, "Millimeter-wave Monolithic Integrated Circuit Characterization by a Picosecond Optoelectronic Technique," *IEEE Microwave Theory Tech.*, **MTT-37**, pp. 1223-1231, 1989.
3. S. L. Huang, L. P. Golob, C. H. Lee, and H.-L. A. Hung, "A novel approach to miniature photoconductive sampling of microwave circuits," *Dig. Conf. Lasers and Electro-Opt.*, paper JFD2, Anaheim, CA, May 1992.

# **Optoelectronic Phase Locking of Microwave Signals up to 4GHz Using a Laser-Diode-Based Electro-Optic Harmonic Mixer**

Ci-Ling Pan, Kai-Yuan Tang, and Hsiao-Hua Wu

*Institute of Electro-Optical Engineering, National Chiao Tung University, Hsinchu, Taiwan 30050, Republic of China*

## **Abstract**

A reflection-mode GaAs electro-optic sampler has been used as a harmonic mixer to optoelectronically phase-lock microwave signals up to 4GHz in a laser-diode-based system. Preliminary results using an integrated optic Mach-Zehnder type modulator as the harmonic mixer for phase locking is also presented.

## **Introduction**

For measurement of cw microwave signals in discrete devices or MMIC's by either photoconductive [1-3] or electro-optic [4-6] sampling techniques, it is important to maintain phase coherence or time synchronization between the microwave signal and optical pulse train. To accomplish this, we have recently demonstrated a laser-diode-based opto-electronic phase lock loop (OEPLL) [7]. The key element of the OEPLL is a laser-diode-activated GaAs:Cr photoconductive switch which functions as an optoelectronic harmonic mixer (OEHM) for intermixing microwave and optical signals. The electro-optic effect in GaAs microstrip circuits can also be used in the OEHM. The electro-optic harmonic mixer (EOHM) is attractive because the laser pulse train can be used to phase-lock the microwave signal at any arbitrary point in the MMIC. This approach was first demonstrated by the Maryland group using a main-frame mode-locked laser [8]. It is desirable to use a diode laser, which is compact, has high repetition rate and exhibits minimum timing jitter, in such a system. In this paper, we

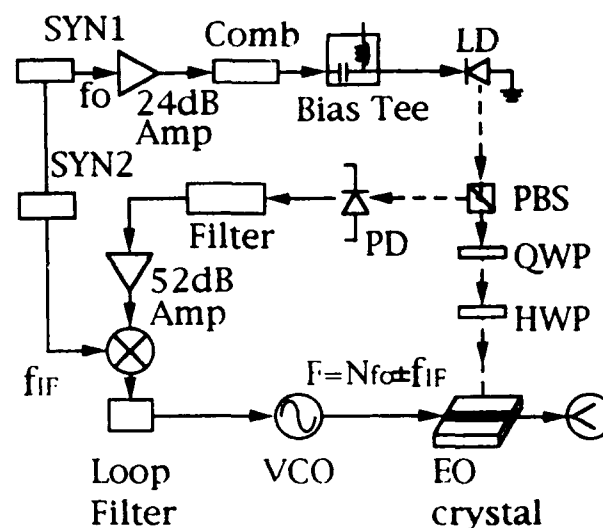


Fig.1 Schematics of the experimental set up. Syn1 and Syn2 are frequency synthesizers; Comb: comb generator, LD: laser diode, LF: loop filter.

present optoelectronic phase-locking of microwave signals up to 4GHz by a laser-diode-based GaAs electro-optic harmonic mixer.

## **Experimental Methods**

Our experimental apparatus is shown in Fig. 1. The EOHM is an electro-optic sampler consisting of a 50Ω microstrip line fabricated on undoped semi-insulating (SI) LEC-grown GaAs substrate. The standard reflection-mode probing geometry is used. A train of 30ps optical pulses at 500MHz from the gain-switched laser diode (Toshiba, model TOLD-300,  $\lambda=1.3 \mu\text{m}$ ) with an average



power of 0.4mW is sent through a polarizing beam splitter (PBS), a quarter-wave plate (QWP), a half-wave plate (HWP) and focused on the ground plane of the microstrip line. In the phase-locking experiment, free-running microwave signal from a sweep oscillator (HP8620C) at a power level of -8.4 dBm is fed to the microstrip line via a power amplifier with 30dB gain. The microwave signal changes the polarization of the reflected optical pulse which passes back through the lens and the wave plates, then directed by the PBS to an InGaAs photodiode (PD). The buffered output of the PD is further amplified by two stages of low-noise amplifiers with a combined gain of 52 dB and mixed with a reference signal at the desired intermediate frequency,  $f_{IF}$ . The resultant error signal is used to phase-lock the sweep oscillator which operates as a voltage-controlled oscillator (VCO) via a loop filter. The expected phase-locked frequency of the VCO is  $F = (Nf_0 + f_{IF})$ , where  $N$  is an integer.

### Results And Discussions

For an average photocurrent,  $I_{avg} = 30 \mu A$ , the conversion loss of the EOHM from the microwave signal (at 500MHz and 21.6dBm) to the IF is measured to be 81 dB. In comparison, phase locking using a laser-diode-based GaAs : Cr photoconductive harmonic mixer (PCHM) [7] under the same condition (same microwave frequency, load resistor, and IF) yields conversion loss of 8.5dB. The waveform of the photoconductively phase-locked 500MHz signal has been sampled and displayed via a low-frequency replica at 400kHz by an electro-optic harmonic mixer (EOHM). Similarly, the waveform of an electro-optically phase-locked 500MHz signal as displayed via a replica at 400kHz by a photoconductive harmonic mixer is also observed in the same oscilloscope. These results clearly show that the performance of the OEPLL employing the EOHM is inferior to that with a PCHM as far as the conversion loss is concerned, under our experimental conditions. On the other hand, the EOHM is more versatile than the PCHM as the latter requires incorporation of a photoconductive switch on the MMIC. We are able to electro-optically phase-lock the VCO up to 4GHz. The spectrum of the 4GHz signal optoelectronically phase-locked spectrum is shown in Fig. 2. It is also interesting to compare the laser-diode-based EOHM with a similar system using a main-frame laser. For the latter case,  $I_{avg} \approx 1mA$ , a

reasonable estimate for the conversion loss would be 51dB. Obviously, high-power laser diode will drastically improve the performance of the laser-diode-based EOHM. Increasing the load resistance,  $R_L$  and narrowing the IF bandwidth are also expected to be helpful. Improvement of the OEPLL by optimizing these parameters is limited and may degrade the tracking performance of the PLL. The optimum value of  $f_{IF}$  for the present OEPLL is 400kHz with the load resistance for the PD,  $R_L = 50k\Omega$ . This is in contrast to typical electro-optic sampling experiments which operate at several MHz due to the noisier main-frame laser. We note that other types of electro-optic modulators with lower half-wave voltage,  $V_\pi$ , can also be used to improve the performance of the EOHM. Optoelectronic phase-locking of microwave signals up to 12 GHz using an integrated optic Mach-Zehnder type modulator with 4GHz bandwidth has been realized in our laboratory recently. The sensitivity of the electro-optic sampler can also be increased by using an organic patch sensor [11].

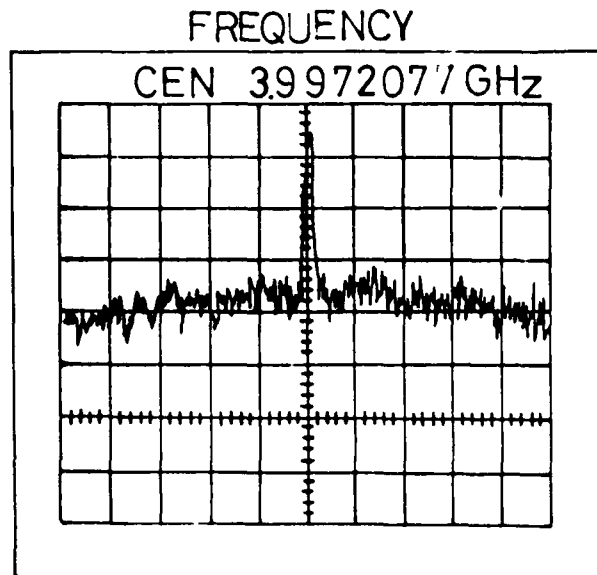


Fig.2 The spectrum of the 4GHz optoelectronically phase-locked signal (resolution BW = 100Hz, frequency span = 1kHz/div., vertical scale = 10dB/div).

### Conclusion

In summary, we have demonstrated phase-locking of optical and microwave signals up to 4GHz using

a compact laser-diode-based GaAs electro-optic sampler as an optoelectronic harmonic mixer in the PLL. Comparisons of the present approach with systems employing main-frame lasers or a photoconductive switch as the harmonic mixer are also presented. The upper bound for the frequency of the phase-locked signal in the present work is limited by the available average power and pulse width of the laser diode, as well as  $V_{\pi}$  of the GaAs material. We have also suggested methods for alleviating these problems such that our scheme can be used for phase locking of optical and millimeter wave signals at the wafer level.

### Acknowledgments

The authors would like to thank Prof. C.-S. Chang for helpful discussions. This work was supported in part by the National Science Council of the Republic of China under grants, NSC80-0417-E-009-05, NSC81-0417-E-009-629 and 630.

### References

1. H.-L. A. Hung, P. Polak-Dingels, K. J. Webb, T. Smith, H. C. Huang, and C. H. Lee, "Millimeter-wave monolithic integrated circuit characterization by a picosecond optoelectronic technique," *IEEE Trans Microwave Theory Tech.*, **37**, 1223-1230 (1989).
2. M. Matloubian, S.E. Rosenbaum, H.R. Fetterman, and P.T. Greiling, "Wideband millimeter-wave characterization of sub-0.2 micrometer gate length AlIn/GaInAs HEMT's," *IEEE Microwave Guided Wave Lett.*, **1**, 32-34 (1991).
3. D. H. Auston, "Picosecond photoconductivity: High-speed measurements of devices and materials," in *Measurement of High Speed Signals in Solid State Devices, Semiconductors and Semimetals*, vol. 28, R.B. Marcus, Ed. New York: Academic Press, 1990, pp. 85-134.
4. M.J.W. Rodwell, M. Riazat, K. J. Weingarten, B. A. Auld, and D. M. Bloom, "Internal microwave propagation and distortion characteristics of traveling-wave amplifiers studied by electrooptic sampling," *IEEE Trans. Microwave theory Tech.*, **34**, 1356-1362 (1986).
5. K. J. Weingarten, M. J. W. Rodwell, and D.M. Bloom, "Picosecond optical sampling of GaAs integrated circuits," *IEEE J. Quantum Electron.*, **24**, 198-220 (1988).
6. J. M. Weingarten and M. S. Heutmaker, "Frequency response of an internal amplifier in a high-speed integrated circuit measured by electrooptic sampling," *Electron Lett.*, **24**, 106-107 (1988).
7. H. H. Wu, C. S. Chang, and C. L. Pan, "Optoelectronic phase-locking of microwave signals up to 18GHz by a laser-diode-based GaAs:Cr photoconductive harmonic mixer," *IEEE Microwave Guided Wave Lett.*, **2**, 11-13 (1992).
8. M.G. Li, F. A. Chauchard, C.H. Lee, and H.-L. A. Hung, "Intermixing optical and microwave signals in GaAs microstrip circuits for phase-locking applications," *IEEE Trans. Microwave Theory Tech.*, **38**, 1924-1931 (1990).
9. M.G. Li, S.-L.L. Hung, C.H. Lee, and H.-L. A. Hung, "Display of Microwave Waveform via a low frequency replica using an optical phase-locking and sampling technique," in *Picosecond Electronics and optoelectronics*, 1991, Technical Digest Series, (optical society of America, Washington, DC 1988), pp. 24-27.
10. H. H. Wu, C.S. Chang, and C. L. Pan, "A laser-diode-based photoconductive harmonic mixer for microwave waveform and spectrum measurements," *IEEE Microwave Guided Wave Lett.*, **2**, 273-275 (1992).
11. T. Nagatsuma, m. Yaita, M. Shinagawa, M. Amano, and Y. Shuto, "Organic patch sensor for electro-optic measurement of electrical signals in integrated circuits," *Electron. Lett.*, **27**, 932-934 (1991).

---

## **Photoconductive and Electro-Optic Sampling**

---

## Picosecond Detector, Optical Temporal Analyzer, and Free-Standing Circuit Probe

J. Nees, S. Williamson, J. Kim, and S. Gupta

*University of Michigan, Center for Ultrafast Optical Science, 1006 I.S.T. Building,  
2200 Bonisteel Blvd., Ann Arbor, Michigan 48109-2099*

### Abstract.

With picosecond semiconductors we have demonstrated a 1.2-ps photoconductive detector/gate, a 1.9-ps Semiconductor Optical Temporal Analyzer, and a 2.3-ps Free-Standing Circuit Probe with  $\mu\text{V}$ -resolution.

### Introduction

The development of devices in the 100-GHz range is important to the advancement of high-speed communications and computation. Such devices also contribute to the base of scientific instrumentation used in the study of a wide variety of physical and medical applications. As a result, advancements made during the last few years in the quality and response time of semiconductor materials have piqued an interest in single-picosecond optoelectronic devices.

### Materials with picosecond response

The first of these new materials to exhibit subpicosecond response was Low-Temperature-Grown GaAs (LT-GaAs)[1]. This material was developed at Massachusetts Institute of Technology for its ability to reduce side-gating in transistors. Its unique properties include a 600-fs photoconductive response-time (see figure 1), the ability to withstand 500 kV/cm surface-electric-fields, and a resistivity of  $10^7 \Omega\text{-cm}$ . The fast response-time can give devices made with this material high frequency response. High electric-field breakdown-strength allows device biases to be increased for improved speed, sensitivity, or dynamic range. High resistivity suppress excess noise due to dark current.

In the interest of extending this work to the 1.3- and 1.55- $\mu\text{m}$  wavelengths a preliminary study on the growth of LT-InGaAs was conducted[1]. In this study a number of samples were grown at temperatures from

120 to 250  $^{\circ}\text{C}$  with mole fractions of 25% and 35% indium. Some of the samples were then annealed at 600 $^{\circ}\text{C}$  for 10 minutes following the recipe for LT-GaAs. This resulted in a material with sensitivity at 1.3  $\mu\text{m}$  having a 2-ps response-time and a resistivity of  $5 \times 10^4 \Omega\text{-cm}$  (figure 1). Both LT-GaAs and LT-InGaAs develop precipitates during a post-anneal. These are believed to be the cause of the enhanced optoelectronic properties.

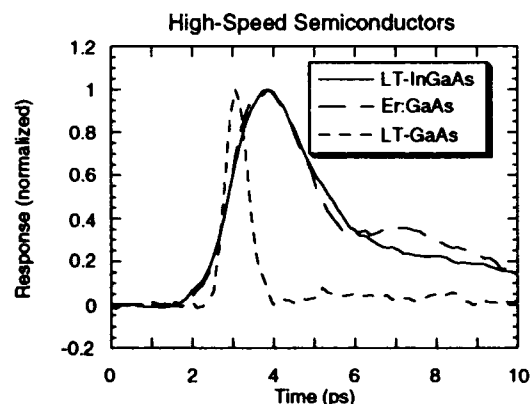


**Figure 1** Photoconductive response of various high speed semiconductors

Another new material displaying single-picosecond response-time is Er:GaAs[2]. Like the others, this material is grown also by molecular-beam-epitaxy. Its response-time is as low as 2 ps with a resistivity of  $>10^5 \Omega\text{-cm}$  (figure 1). Measurements indicate that the Er:GaAs growth will be more repeatable than its predecessors.

### Fast materials in photoconductive devices

The exploration of specialized growth techniques for high speed semiconductors has been fruitful in producing useful materials for high speed electronics and optoelectronics. Application of these materials to devices and instrumentation has also produced a number of important devices. The most fundamental optoelectronic device to be made using high-speed semiconductors is the Metal-Semiconductor-Metal (MSM) photoconductive detector[1]. This simple structure is the essential building block used in the construction the devices presented here. Before proceeding to more complex structure, however, an understanding of the design considerations which lead to high-speed and high sensitivity operation is necessary.

Photoconductive detectors may be distinguished on the basis on their carrier transit-times (based on geometry and bias) and carrier lifetimes (based on material properties). In a conventional photoconductor high-speed semiconductors give low responsivity. This is a result of the fact that, with dimensions on the order of several microns the carrier lifetime is much shorter than the carrier transit-time. Consequently most carriers do not contribute their charge to the detection circuit. By forming fine interdigital metalizations the transit-time of the device can be reduced to the order of the carrier lifetime. For a picosecond-lifetime material such as LT-GaAs a match between transit-time and lifetime is achieved with a 0.2- $\mu\text{m}$  interdigital gap. The improvement in responsivity for this geometry over the more conventional 20- $\mu\text{m}$  gap is a 100-fold increase in sensitivity, with little change in speed.

Other factors which influence the utility and performance of an MSM detector or gate are minority carrier transport, dark current, dielectric breakdown, and the photovoltaic effect produced at schottky contacts. Minority carriers often contribute to current in photoconductor long after majority carriers have reached their destination. This produces a tail in the response of the detector which can seriously degrade its performance in sampling applications. Reduction of the dark current is also important in applications where a high degree of temporal discrimination is required. This is accomplished by choosing a material with high resistivity. Ultimately, the speed of the carriers through the biased region of a photoconductor depends on the field which can be applied. This is limited by impact ionization and other processes which influence dielectric breakdown at the MSM contacts. Finally, in MSM structures that have schottky contacts photovoltaic contributions to the photocurrent may effect the linearity of the device.

### Three devices employing LT-GaAs photoconductive detector/switches

Using the fastest and highest resistivity material of those available today we have fabricated and tested three new optoelectronic devices. The first is the MSM

photoconductive detector imbedded in a 20- $\mu\text{m}$  (line-width and -spacing) coplanar transmission line[1]. This device is defined by e-beam lithography on a 1- $\mu\text{m}$  thick LT-GaAs epilayer to have an 8X8- $\mu\text{m}^2$  interdigital region with 0.2- $\mu\text{m}$  gaps between digits. The waveform, which is measured by external electro-optic sampling in LiTaO<sub>3</sub>, shows a 0.1 A/W responsivity with a FWHM of 1.2 ps at low light levels. Dark current with a 1-volt bias is 100 pA. When illuminated by a 22-pJ, 100-fs optical pulse a minimum existence of 10- $\Omega$  is achieved. It is also important to note that no conductivity tail is present in this photodetector.

Using this basic detector design as a building block work continued in the development of a semiconductor optical temporal analyzer (SOTA)[1]. This device employs two MSM detectors integrated with a coplanar transmission line (also of 20- $\mu\text{m}$  width and spacing on 1- $\mu\text{m}$  thick LT-GaAs) to sense and time resolve optical signals. The SOTA makes use of both extremes of the operating range of the MSM photodetector. The incoming optical signal (presumably a weak signal) is gathered onto a detector which converts the intensity to voltage on the transmission line. The second detector acts under the well-focused and energetic illumination of a 100-fs optical pulse to sample that electrical waveform during a picosecond interval. The resulting temporal resolution of 1.9 ps is a convolution of the detector response of 1.2 ps and the gate response of 1.5 ps. This device shows promise for replacing instruments like the streak camera for some applications in ranging and luminescence or lifetime measurements.

The utility of the sampling function found in the SOTA is the primary motivator for the development of the third device employing high-speed semiconductors for picosecond measurements. The photoconductive microprobe is a free-standing movable version of the sampling gate found in the SOTA[3]. It offers flexibility. Any substrate can be tested with temporal resolution of 2.3 ps and a sensitivity of 1  $\mu\text{V}$ . Picosecond signals may also be launched onto any substrate using the gate as a source rather than a detector.

The probe is manufactured using conventional lift-off photolithography. A tip radius as small as 0.1  $\mu\text{m}$  can be defined with a 3- $\mu\text{m}$  height and integrated with an MSM photodetector. The probe, as made, is shown in figure 2.

In practice a larger and more rugged, flat tip of larger area is used for measurements. Also an interdigital gap of 2.0  $\mu\text{m}$  is used, reducing the fabrication complexity.

100-fs optical pulses from a Ti:Sapphire laser are used both to generate test signals and to open the sampling gate on the probe. Contact is monitored by observing the optical interference patterns produced by the reflection of visible light between the probe substrate and the substrate of the device-under-test. In the cases where a transparent device is tested an LT-

GaAs probe is used. When the device-under-test is opaque, a probe can be made on Oxygen implanted silicon-on-sapphire (SOS) and illuminated through the semi-transparent Si layer from the back side of the probe substrate. Using LT-GaAs probes transients arising from the photovoltaic effect in damaged SOS have been observed with 2.3 ps resolution. On a transparent sapphire substrate signals have been launched and detected by free-standing probes. On LT-GaAs substrates passive microwave devices and active logic devices have been tested. This work is discussed in paper ME16 of this publication.

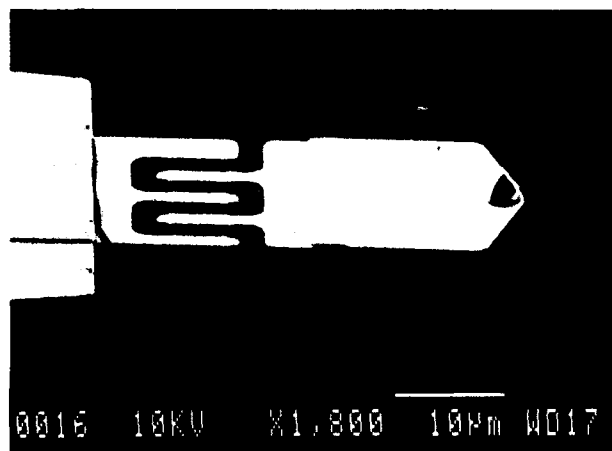


**Figure 2** SEM picture of a free-standing microprobe fabricated on LT-GaAs

#### Conclusions

Low-Temperature-Grown GaAs has been used to fabricate a photoconductive detector with 375 GHz bandwidth and 0.1 A/W sensitivity. The same device

may be used as a gate switching to 30  $\Omega$  for 1.5 ps. A semiconductor optical temporal analyzer has been demonstrated which combines these two modes of operation to enable 1.9 ps resolution of optical signals. Finally a versatile probe has been demonstrated which has 2.1 ps response with 1- $\mu$ V sensitivity.

Development of new materials for wavelengths at 1.3 and 1.55  $\mu$ m shows some promise.

#### Acknowledgments

This work is supported by the National Science Foundation through the Center for Ultrafast Optical Science STC PHY 8920108, the AFOSR-90-0214, the ARO-DAAL-03-89-k-0071 and by FUJITSU LABORATORIES LTD.

#### References

1. S. Gupta, S. L. Williamson, Y. Chen, J. F. Whitaker, and F. W. Smith, Ultrafast Detectors using III-V Epilayers Grown by Molecular-Beam-Epitaxy at Low Temperatures, *Laser Focus World*, July 1992.
2. S. Gupta, J. Pamulapati, J. Chwalek, P. K. Bhattacharya, and G. Mourou, in *Ultrafast Phenomena VII*, edited by C. B. Harris, E. P. Ippen, G. A. Mourou, and A. H. Zewail (Springer-Verlag, Berlin, 1990), p. 297.
3. J. Kim, S. Williamson, J. Nees, S. Wakana, "A Novel Free-Standing Absolute-Voltage Probe With 2.3-Picosecond Resolution and 1-Microvolt Sensitivity," *Ultrafast Phenomena VIII*, 8-12 June, 1992, Antibes-Juan-Les-Pins, France.

# Electro-Optic Sampling at 150 fs

U. D. Keil and D. R. Dykaar

AT&T Bell Laboratories, 600 Mountain Avenue, Murray Hill, New Jersey 07974-2070

## Abstract

We demonstrate 150 fs rise time, 200 fs pulse width electrical pulse generation and detection using low temperature grown GaAs and total internal reflection electro-optic sampling.

## Introduction

Electro-optic sampling [1] has seen a steady improvement in measured rise time, from more than 1 ps [2], to 260 fs [3]. Most of this improvement has come from smaller electrical propagation distances and reductions in component dimensions. In addition to fast rise times, fast electrical pulses can be routinely generated using implantation techniques [4] or low temperature grown (LT) GaAs [5]. The optical pulses used in these measurements are typically 70 - 80 fs Full Width at Half Maximum (FWHM) and it is interesting to note that the measured electrical rise times in Refs (1-5) are many times longer. This difference is due in part to the distance the electrical signal must travel from the excitation site to the sampling site, and in part to the distance the optical sampling pulse must travel through the LiTaO<sub>3</sub>. As the electrical pulse travels along the transmission line it is dispersed [6], resulting in preferential attenuation and radiation of the high frequency components [7,8]. The optical pulse travels in the LiTaO<sub>3</sub> crystal and propagates with the electrical pulse, but at a different velocity. This results in velocity walk off, causing the detected signal to appear longer.

In this paper we demonstrate a technique to minimize these effects and enable measurement of an electrical signal *before* dispersion can affect the pulse. We show that pulses 250 fs FWHM can be generated in semi-insulating (SI) GaAs and 200 fs FWHM for LT GaAs. The corresponding rise time (10-90%) in LT GaAs is 150 fs.

## Experimental Setup

The sampling geometry of the Total Internal Reflection (TIR) probe [9-11] is shown in Fig. 1(a and b). Only a thin layer of LiTaO<sub>3</sub> is used, supported by a fused silica rod. This minimizes the impact of the high

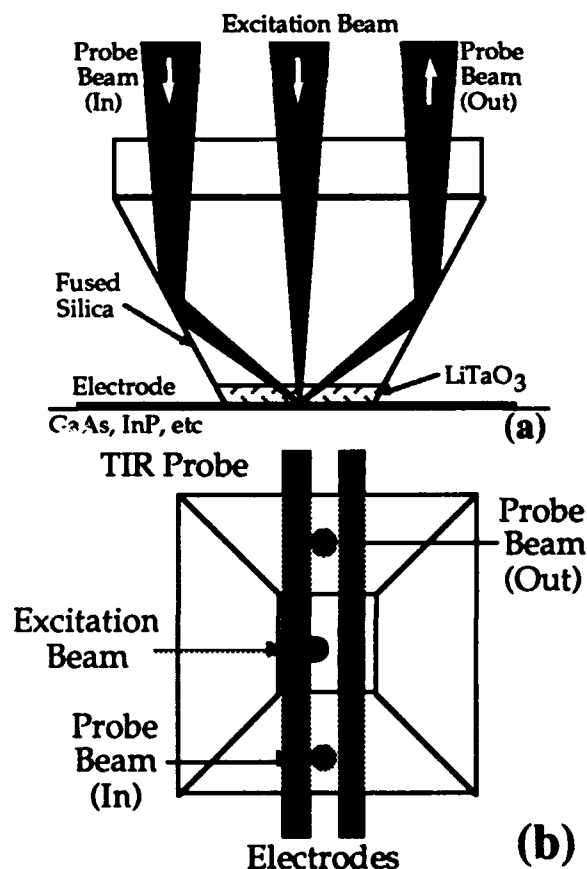


Figure 1. Schematic representation of (a) side view and (b) top view of total internal reflection probe tip with zero propagation excitation geometry.

dielectric ( $\epsilon_r > 40$ ) LiTaO<sub>3</sub> on the electrical signal.

The TIR geometry allows the optical probe beam to be reflected off the (uncoated) bottom of the sampling crystal while the excitation beam is directed through it. This results in excitation and sampling spots being *superimposed* on the sample. By reducing the propagation distance to near zero the dispersion is minimized. In addition the velocity walk off is minimized by reducing the LiTaO<sub>3</sub> thickness. The crystal used here is 100 x 100 x 37  $\mu\text{m}$  thick (Terametrix model 200B-TIR). Data taken for a longer time range were performed with a 100  $\mu\text{m}$  thick, 200  $\mu\text{m}$  long and 300  $\mu\text{m}$  wide electro-optic crystal. This thickness limits the temporal resolution but the time window increases as reflections from the crystal boundaries are delayed.

The TIR probe is adjusted to be flat against the sample by minimizing the number of interference fringes seen with the microscope lamp. Parallelism on the order of a single fringe is routinely achieved.

Optical pulses are generated using a prism compensated Colliding Pulse Mode-locked (CPM) [12] and Ti:Sapphire laser [13]. The *cross correlation* of the two CPM laser beams at the sample site is measured to be 160 fs (rise time is 110 fs). Typically, autocorrelations are quoted for a hyperbolic secant pulse shape, corresponding to reduction of the measured pulse width by a factor of 1.5. The corrected optical cross correlation is then 105 fs which is considerably longer than the autocorrelation of 70 fs directly at the laser. This dispersion is due to the many optical elements (polarizer, TIR probe, etc.) between the CPM laser cavity and the sample. An external four prism sequence is used to compensate extra-cavity dispersion.

The photoconductive switches are fabricated using optical lithography and 500 nm of evaporated Au electrodes with widths and spacing of 5 and 10  $\mu\text{m}$ . Gapless [14] or sliding contact [15] photoconductive switches are used to generate the electrical signals. The voltage bias of the transmission line is modulated at 3.5 MHz and the electro-optically detected signal is electrically mixed down to the lock-in frequency of 1.2 kHz [16]. This results in a large dc offset on the lock-in. The offset is used as a voltage calibration and the fast signal is then measured as a function of optical delay. This setup selects against purely optical effects in the sampling crystal as only the photoconductive switch bias is modulated.

## Results

The result for a LT GaAs sample is shown in Fig. 2(a). The pulse width is 200 fs FWHM and has a 150 fs rise time. There is no negative pre-pulse. Small wiggles in the tail of the pulse are reflections of the electrical signal from the edge facets of the TIR probe. The pulse shape is symmetric. As the rise time is a measure of the system resolution this indicates that the observed pulse width is resolution limited to 200 fs which gives an upper limit for the actual pulse width. For SI GaAs a symmetrical pulse of 250 fs FWHM is measured. Both measurements were made with the pump

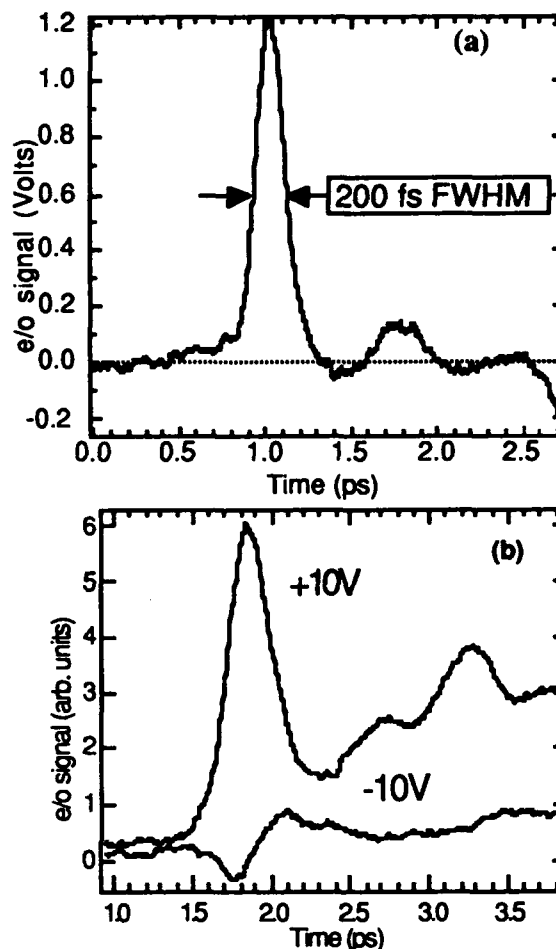


Figure 2. Electro-optically sampled data for (a) LT GaAs with pump and probe beam at the positive electrode (pulse width is 200 fs FWHM and rise time is 150 fs) and (b) SI GaAs with pump and probe beam at the electrode with the indicated applied voltage.

and probe beam next to the positive electrode. The effect of polarity reversal for GaAs is shown in Fig 2(b). Both results were obtained with an excitation spot size ( $\sim 3 \mu\text{m}$ ) smaller than the electrode spacing (5  $\mu\text{m}$ ) and the excitation spot next to the electrode with the indicated applied voltage. The spectra show a drastic dependence on the polarity.

The pulse widths are not limited by the carrier recombination time. This has also been seen for asymmetric excitation on an undamaged Si substrate [3]. These results indicate that the fast electrical pulses observed in LT GaAs may in fact be from radiation due to optical nonlinearities [17], with carrier properties (i.e., short carrier lifetime) affecting the response only at longer times ( $> 1 \text{ ps}$ ). Rotating the polarization of the pump beam did not significantly affect the result, although we expect a coherent contribution to be present in this measurement as is seen in the measurement by Dykner, et al [18]. What is not clear is the role of the electrodes (there are no electrodes in Ref. 18) and the actual form of the electric field in the excitation region. For example, the effect of the surface field has not been considered. We are investigating these effects (field, crystal orientation, etc.) and will report the results in a future publication.



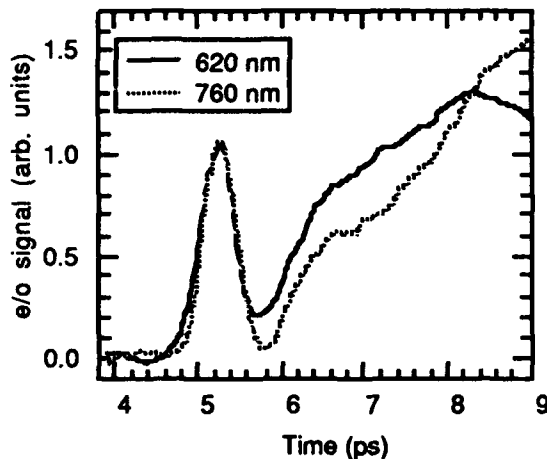


Figure 3. Comparison of electro-optically sampled data for SI GaAs taken at  $\lambda=620$  nm (CPM) and 760 nm (Ti:Sapphire).

Using a larger probe allows a longer reflection free time window. The larger thickness of this probe limits the temporal resolution and pulse widths in Fig. 3 are about 450 fs. Electrode width and spacing are 10  $\mu\text{m}$ . Again pump and probe beam are 3  $\mu\text{m}$  in diameter and are placed so that they slightly overlap the positive electrode. This measurement shows that after a delay of 1 ps (with respect to the rising edge (10%) of the initial peak) the amplitude is increasing again. Within the accuracy of the measurement this behavior is independent of probe and excitation wavelength. The spectra are much more dependent on the position of the beams and great care must be taken to make these measurements comparable. In contrast to 620 nm (2 eV) the photon energy at 760 nm (1.63 eV) is below the energy needed for excitation in to the satellite valleys (1.73 eV) in the absence of an applied field.

For both measurements the modulation frequency of 3.5 MHz is mixed down for detection with a lock-in amplifier. We note that for the Ti:Sapphire laser the spectra can be measured without electronic mixers as the noise amplitudes below 1 MHz are significantly smaller than for the CPM Laser. Typical mixer conversion losses are in the 5 dB range.

The effect of propagation distance is shown in Fig. 4. Here a lower power 10X objective, so that the facets of the TIR probe can be imaged. The beam size is slightly larger than the gap (5  $\mu\text{m}$ ) which is illuminated symmetrically. The initial subpicosecond pulse is in this case obtained by using a LT GaAs substrate. The path length is increased to a total of 150  $\mu\text{m}$ , and each successive trace is shifted up. All of the added propagation is incurred with the LiTaO<sub>3</sub> crystal as a superstrate. A second peak evident at 150  $\mu\text{m}$  of propagation is seen to develop from the effects of propagation (i.e., dispersion) rather than any overshoot effects.

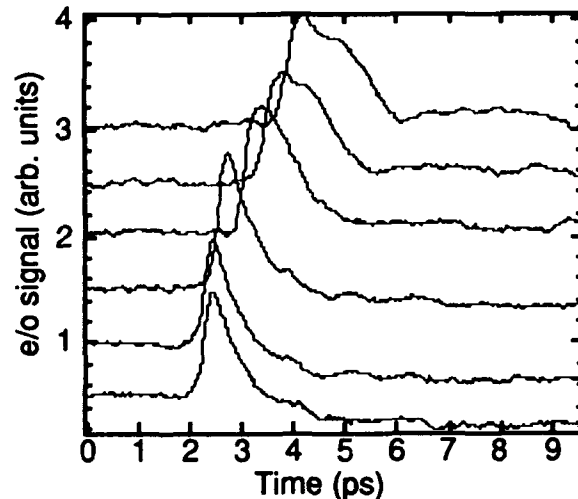


Figure 4. Electro-optically sampled data for LT GaAs where the propagation distance is increased a total of 150  $\mu\text{m}$  (the LiTaO<sub>3</sub> crystal acts as a superstrate). The time delay includes a small added delay due to the optical path length change which is not accounted for.

## Conclusion

We have extended the technique of electro-optic sampling to the zero propagation limit and measured electrical rise times of 150 fs that are close to the measured limit of the optical pulse of 105 fs. We have used this technique to measure electrical pulse widths as short as 250 fs in GaAs and 200 fs in LT GaAs. These measurements place new upper bounds on the fastest electrical pulses available from optically driven photoconductive sources. Shorter optical pulses are available from amplified and compressed-[19] and/or new Ti:Al<sub>2</sub>O<sub>3</sub> laser prisms should produce even faster electrical pulses using this technique.

## Acknowledgment

We thank M.Y. Frankel of Terametrix for providing the sampling probe used in this work. One of us (U.D.K.) acknowledges support from the Deutsche Forschungsgemeinschaft.

## References

1. J.A. Valdmanis, and G.A. Mourou, IEEE J. Quantum Electronics, QE-22, 69 (1986).
2. J.A. Valdmanis, G.A. Mourou, and C.W. Gabel, Applied Physics Letters, 41 (3), 211, (1982).
3. D. Krökel, D. Grischkowsky, and M.B. Ketchen, Applied Physics Letters, 54 (11), 1046 (1989).
4. M.B. Ketchen, D. Grischkowsky, T.C. Chen, C-C. Chi, I.N. Duling III, N.J. Halas, J-M. Halbout, J.A. Kash, and G.P. Li, Applied Physics Letters, 48, 751 (1986).
5. F. W. Smith, H. Q. Lee, V. Diadiuk, M. A. Hollis, A. R. Calawa, S. Gupta, M. Frankel, D.R. Dykaar,

- G.A. Mourou, and T.Y. Hsiang, *Applied Physics Letters*, 54 (10), 890 (1989).
6. J.F. Whitaker, R. Sobolewski, D.R. Dykaar, T.Y. Hsiang, and G.A. Mourou, *IEEE Trans. Microwave Theory Tech*, 36, No. 2, 277 (1988).
  7. D.S. Phatak and A.P. Defonzo, *IEEE Trans. Microwave Theory Tech.*, 38 (5), 654 (1990).
  8. U.D. Keil, D.R. Dykaar, A.F.J. Levi, R.F. Kopf, L.N. Pfeiffer, S.B. Darack, and K.W. West, *IEEE Journal of Quantum Electronics Special Issue on Ultrafast Optics and Electronics*, 28(10), 2333-2342 (1992).
  9. J. Nees, and G.A. Mourou, *Electronics Letters*, 22, 918 (1986).
  10. J.A. Valdmanis, *Electronics Letters*, 23, 1308 (1987).
  11. M.Y. Frankel, J.F. Whitaker, G.A. Mourou, and J.A. Valdmanis, *IEEE Microwave and Guided Wave Letters*, 1 (3), 60, (1991).
  12. J. A. Valdmanis, R.L. Fork and J.P. Gordon, *IEEE J Quantum Electron.*, QE-22, 112, (1986).
  13. C-P Huang, H.C. Kapteyn, J.W. McIntosh, and M.M. Murnane, *Optics Letters*, 17 (2), 139 (1992).
  14. D.R. Dykaar, T.Y. Hsiang, and G.A. Mourou, *Topical Meeting on Picosecond Electronics and Optoelectronics*, Springer-Verlag, New York, 249 (1985).
  15. M.B. Ketchen, D. Grischkowski, T.C. Chen, C.-C. Chi, I.N. Duling III, N.J. Halas, J.M. Halbout, *Applied Physics Letters*, 48, 751 (1986).
  16. J.M. Chwalek and D.R. Dykaar, *Review of Scientific Instruments*, 61 (4), 1273 (1990).
  17. B.I. Greene, P.N. Saeta, D.R. Dykaar, S. Schmidt-Rink, and S.L. Chuang, *IEEE Journal of Quantum Electronics Special Issue on Ultrafast Optics and Electronics*, 28(10), 2302-2312 (1992).
  18. D.R. Dykaar, D. You, R.R. Jones, and P.H. Bucksbaum, *OSA Proceedings on Ultrafast Electronics and Optoelectronics*, (OSA, Washington, DC 1993) This issue.
  19. R.L. Fork, C.H. Brito Cruz, P.C. Becker, and C.V. Shank, *Optics Letters*, 12, 483 (1987).

## Low-Temperature MBE Growth of III-V Materials on Si Substrates

Michael Y. Frankel and Thomas F. Carruthers

*Optical Sciences Division, CODE 5672, Naval Research Laboratory,  
Washington, DC 20375-5338*

Bijan Tadayon

*Electronic Technology Division, Naval Research Laboratory, Washington, DC 20375-5338*

### Abstract

We investigate the molecular-beam epitaxial (MBE) growth of GaAs and  $\text{In}_{0.6}\text{Ga}_{0.4}\text{As}$  on Si substrates at low substrate temperatures. Such materials may allow direct integration of ultrafast photodetectors into Si-based integrated circuits. Femtosecond time-resolved surface reflectivity and photoconductor switching are used to explore material photonic properties. We observe free carrier lifetimes as short as  $<500$  fs and photoconductor electrical responses as short as 600 fs.

### Introduction

Si-based integrated circuits still play a significant role in modern communication systems. However, efficient and fast Si-based photodetectors are not available at the important 1.3- $\mu\text{m}$  and 1.5- $\mu\text{m}$  wavelengths. Many communication systems could benefit from the direct integration of III/V-semiconductor-based photodetectors into Si circuits due to their increased bandwidth and long-wavelength sensitivity.

Typically, the performance of devices fabricated in III-V materials grown on Si substrates suffers due to a high defect density induced by the lattice mismatch [1]. However, this reduction in carrier lifetime can be used to advantage for high-speed photodetectors [2]. Low-temperature (LT) MBE growth can result in further improvements, and LT GaAs grown on GaAs has shown excellent optoelectronic properties such as subpicosecond carrier lifetime, high mobility and high resistivity [3]. Such LT GaAs has been applied for high-sensitivity, ultrafast metal-semiconductor-metal photodetectors [4-6], and for high-voltage switching applications [7,8]. Also, InGaAs grown on GaAs has shown potential for optoelectronic applications at longer wavelengths [9].

In this work we investigate the influence of the MBE growth temperature and post-growth anneal on the photogenerated carrier lifetime, carrier mobility, and resistivity in GaAs and  $\text{In}_{0.6}\text{Ga}_{0.4}\text{As}$  epitaxially grown on Si substrates. We use femtosecond time-resolved surface reflectivity measurements to show that a reduction in carrier lifetime from 14 ps to  $<0.5$  ps can be achieved in LT GaAs by reducing the growth temperature from 400 °C to 150 °C, and from 10 ps to  $<0.4$  ps in LT  $\text{In}_{0.6}\text{Ga}_{0.4}\text{As}$  by reducing the growth temperature from 350 °C to 150 °C. We fabricate photoconductor switches and use electrooptic (EO) sampling to measure their electrical bandwidth and responsivity. We demonstrate that reduced MBE growth temperature results in sub-picosecond measured impulse response, with some sacrifice in carrier mobility. Furthermore, the significant influence of post-growth anneal on material properties is demonstrated.

### Experiment

The 1- $\mu\text{m}$ -thick layers of GaAs were MBE-grown on (100) Si substrates at several substrate temperatures. After cleaning in a 2:25 HF:DI solution for 20 s, the substrates were loaded into the MBE chamber and heated to 640 °C to remove some residual oxide. The material was grown at a 0.5- $\mu\text{m/hr}$  growth rate with an As/Ga equivalent beam-pressure ratio of 30. Half of each sample was subsequently cleaved off and annealed at 610 °C for 10 min under As overpressure. A set of coplanar waveguide transmission lines (CPW) with a 20- $\mu\text{m}$  center conductor, 20- $\mu\text{m}$  conductor spacing and a 15- $\mu\text{m}$  embedded photoconductor gap switch was fabricated on each sample.

Similarly, the 0.56- $\mu\text{m}$ -thick layers of  $\text{In}_{0.6}\text{Ga}_{0.4}\text{As}$  were MBE-grown on (100) Si substrates at several substrate temperatures. An identical set of CPWs was

fabricated on each sample, and a half of each layer sample was rapid-thermal-annealed at 300 °C for 1 min.

A dispersion-compensated colliding-pulse mode-locked dye laser, producing ~150-fs FWHM pulses at 620 nm, was used for the following measurements.

For time-resolved reflectivity measurements, the pump beam was incident at a ~45° angle and focused to a ~20- $\mu$ m-diameter spot on the sample and a normally-incident ~5- $\mu$ m probe beam focal spot was centered within the pump spot.

Photoconductor switch electrical response measurements were carried out using external electrooptic sampling.<sup>10</sup> The pump beam was focused either between the center and one of the ground conductors of the CPW for "sliding-contact" switching or onto the gap incorporated in the center CPW conductor for gap switching. The LiTaO<sub>3</sub> external electrooptic transducer was positioned ~300  $\mu$ m along the CPW from the switching site.

## Results and Discussion

The transient reflectivity signals effectively probe the time evolution of changes in the index of refraction and absorption in the semiconductor induced by photogenerated carriers. The initial peak recovery is dominated by the photogenerated carrier trapping and recombination. The GaAs-on-Si reflectivity results are shown in Fig. 1 along with a semi-insulating bulk GaAs measurement for comparison. The lifetime decrease is apparent as the growth temperature is reduced for the 400-°C and 300-°C samples. This is due to the combined effect of the increasing dislocation density and excess As incorporation in the material [3].

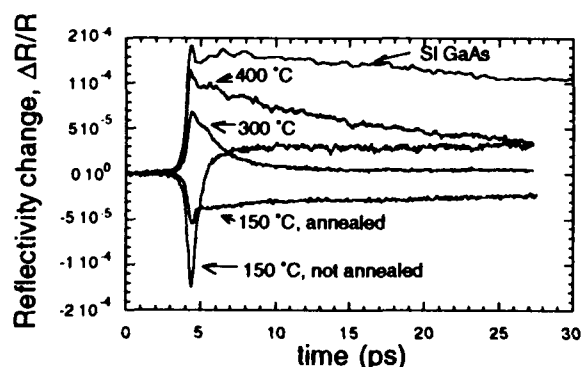


Figure 1. Time-resolved normalized reflectivity change for GaAs on Si for 3.4-mW average pump power.

As the growth temperature is decreased even further down to 150 °C, the reflectivity signal undergoes a distinctive change -- it flips polarity and develops a small long-lived tail. The duration of the initial negative peak is indicative of the carrier lifetime, and it may be observed that the lifetime has decreased from 14 ps to <0.5 ps as the growth temperature is reduced from 400 °C to 150 °C.

Annealing does not noticeably change the reflectivity signals for the 400-°C and 300-°C samples, indicating that annealing does not significantly influence the effect of dislocations on lifetime in this material. However, the signal for the 150-°C sample shows a dramatic change after annealing, indicating a significant influence of the excess As. This difference may be attributed to a reduction in the bandfilling effect and the dominance of free-carrier absorption effect on the index of refraction, but the exact nature is not yet understood.

Photoconductor switching measurements were performed to verify the reflectivity-measured carrier lifetimes and to demonstrate the material's suitability for photoconductor applications.

Figure 2 shows the EO measured electrical transients. The subpicosecond rise times are determined by the measurement system resolution. The fall times are determined primarily by the carrier lifetime in the photoconductor. Similar to the reflectivity measurements, the electrooptically-measured lifetimes decrease with the growth temperature from 6 ps to 1 ps. The EO measured lifetime of ~1 ps for the 150-°C sample is system-response limited. The EO measured lifetimes are shorter than reflectivity measured ones, which may be attributed to the differences in the carrier transport in the measurements.

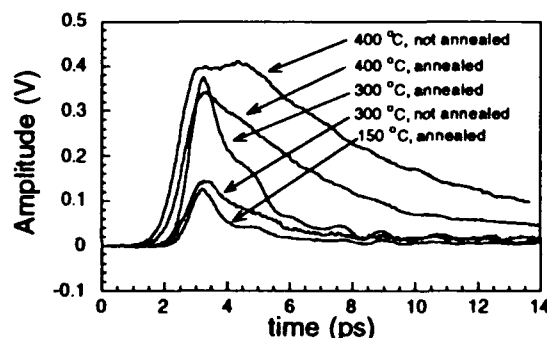


Figure 2. Electro-optically measured photoconductor switch response for GaAs on Si (20- $\mu$ m gap, 10 V bias, normalized to 3-mW pump beam power).

The mobility  $\mu$  of the photogenerated carriers may be obtained from the measured signal amplitudes [11] and it is given in Table 1. There is an improvement in the signal amplitude for the annealed samples grown at lower temperatures, while the observed lifetime is similar. Post-growth anneal of GaAs is therefore important for photoconductor applications. The 150-°C-grown and annealed material exhibits the fastest response of ~1 ps FWHM.

The effects of growth temperature and annealing can be elucidated further with the measurement of the epilayer sheet resistance  $R_s$ . An estimate of the sheet resistance, shown in Fig. 3 for both GaAs and In<sub>0.5</sub>Ga<sub>0.4</sub>As layers, was obtained by normalizing the

resistance measured between the CPW conductors to the conductor length and gap width. The GaAs layers show a decreasing resistivity as the growth temperature decreases, with GaAs grown at 150 °C being quite conductive. The annealing is seen to decrease the resistivity at the higher growth temperatures. However, at the lowest growth temperature of 150 °C annealing increases the resistivity by an order of magnitude, making this material an excellent candidate for photoconductor applications. A similar effect has been observed in LT GaAs grown on GaAs substrates and may be attributable to the formation of a large number of As precipitates in the material.

Table 1. Calculated photogenerated-carrier mobilities.

Growth T (°C)	$\mu$ GaAs (cm <sup>2</sup> /V·s)	Growth T (°C)	$\mu$ InGaAs (cm <sup>2</sup> /V·s)
400 no ann	300	350 no ann	66
300 no ann	110	250 no ann	70
150 no ann	....	190 no ann	12
		150 no ann	4.6
400 anneal	250	350 anneal	44
300 anneal	310	250 anneal	60
150 anneal	110	190 anneal	7.5
		150 anneal	3.5

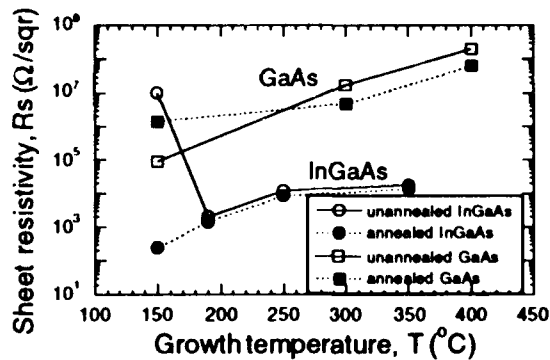


Figure 3. GaAs and InGaAs epilayer sheet resistance.

The transient reflectivity measurements on In<sub>0.6</sub>Ga<sub>0.4</sub>As material grown on Si reveal that the photogenerated carrier lifetime is reduced to <0.5 ps for the growth temperatures below 190 °C. Low-temperature growth of In<sub>0.6</sub>Ga<sub>0.4</sub>As therefore promises to deliver subpicosecond photodetector performance at 1.3-μm and 1.5-μm wavelengths suitable for optical communication.

Figure 4 shows the EO measured response of the photoconductor switches fabricated on the unannealed In<sub>0.6</sub>Ga<sub>0.4</sub>As layers. As is true with GaAs-on-Si, the electrical bandwidth increases with decreasing growth temperature. The fastest undeconvolved response of ~0.6 ps FWHM is measured for the 190 °C and 150 °C samples. This response is limited by the measurement system bandwidth, and the actual response may be faster.

In contrast to the GaAs-on-Si results, annealing appears to reduce the performance of the InGaAs-based photodetectors. Figure 5 shows the measured electrical response of the photoconductor switches fabricated on the annealed In<sub>0.6</sub>Ga<sub>0.4</sub>As layers. The results are generally similar to the unannealed case, with the exception of the 150-°C-grown layer. The fast transient component is replaced by one with a very long time constant.

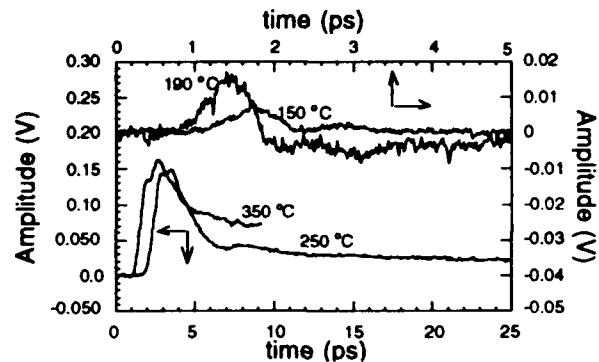


Figure 4. Response of photoconductor switch on unannealed In<sub>0.6</sub>Ga<sub>0.4</sub>As layers (15-μm gap, 10 V bias, normalized to a 3-mW pump beam).

The mobility and resistivity behavior of the InGaAs layers, shown in Table 1 and Fig. 3, is markedly different from those of the GaAs ones. First, annealing consistently lowers the mobility in the InGaAs layers. Second, the InGaAs mobility and resistivity is much lower than those of GaAs. Third, the resistivity of the unannealed material does not show a monotonic decrease with the growth temperature, but rather exhibits a dramatic increase by several orders of magnitude at the lowest growth temperature of 150 °C. Fourth, annealing decreases the resistivity for all the layers, and furthermore reduces that of the 150-°C layer to same order of magnitude as the higher-temperature unannealed ones.

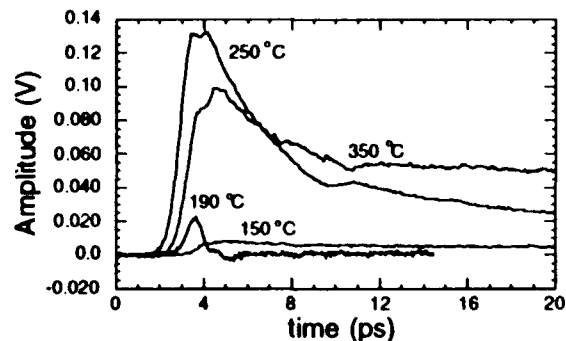


Figure 5. Response of photoconductor switch on annealed In<sub>0.6</sub>Ga<sub>0.4</sub>As layers (15-μm gap, 10 V bias, normalized to a 3-mW pump beam).

Preliminary transmission electron microscopy investigations have shown that the InGaAs layer grown at 150 °C is amorphous and all the other layers are highly crystalline. Annealing of the 150-°C layer results produces a crystalline material, but no As precipitate formation has been observed. Thus, the highly resistive nature of the unannealed 150-°C layer may be attributed to its amorphous structure. However, the effect of annealing on the mobility is not understood.

### Conclusion

We have investigated the feasibility of GaAs and  $\text{In}_{0.6}\text{Ga}_{0.4}\text{As}$  integration on Si substrates for optoelectronic applications. The influence of the epitaxial layer growth conditions and post-growth annealing was investigated. Subpicosecond photoconductor response times for InGaAs confirm the potential for long-wavelength ultrafast photodetector integration into Si circuits.

### Acknowledgments

The authors would like to thank M. Twigg for the TEM studies, M. Fatemi for X-ray diffraction analysis and J. Weller for encouragement. The support of the Office of Chief of Naval Research is greatly appreciated.

### References

1. R.K. Ahrenkiel, M.M. Al-Jassim, D.J. Dunlavy, K.M. Jones, S.M. Vernon, S.P. Tobin, and V.E. Haven, "Minority-carrier properties of GaAs on silicon," *Appl. Phys. Lett.* **53**, 222 (1988).
2. J.D. Morse, R.P. Mariella, Jr., G.D. Anderson, and R.W. Dutton, "Picosecond optoelectronic gating of silicon bipolar transistors by locally integrated GaAs photoconductive devices," *IEEE Electron Dev. Lett.* **12**, 379 (1991).
3. S. Gupta, M.Y. Frankel, J.A. Valdmanis, J.F. Whitaker, G.A. Mourou, F.W. Smith, and A.R. Calawa, "Subpicosecond carrier lifetime in GaAs grown by molecular beam epitaxy at low temperatures," *Appl. Phys. Lett.* **59**, 3276 (1991).
4. Y. Chen, S. Williamson, T. Brock, F.W. Smith, and A.R. Calawa, "375-GHz-bandwidth photoconductive detector," *Appl. Phys. Lett.* **59**, 1984 (1991).
5. M. Klingenstein, J. Kuhl, R. Nötzel, K. Ploog, J. Rosenzweig, C. Moglestue, A. Hülsmann, J. Schneider, and K. Köhler, "Ultrafast metal-semiconductor-metal photodiodes fabricated on low-temperature GaAs," *Appl. Phys. Lett.* **60**, 627 (1992).
6. S.Y. Chou, Y. Liu, W. Khalil, T.Y. Hsiang, and S. Alexandrou, "Ultrafast nanoscale metal-semiconductor-metal photodetectors on bulk and low-temperature grown GaAs," *Appl. Phys. Lett.* **61**, 819 (1992).
7. M.Y. Frankel, J.F. Whitaker, G.A. Mourou, F.W. Smith, and A.R. Calawa, "High-voltage picosecond photoconductor switch based on low-temperature-grown GaAs," *IEEE Trans. El. Dev.* **37**, 2493 (1990).
8. T. Motet, J. Nees, S. Williamson, and G. Mourou, *Appl. Phys. Lett.* **59**, 1455 (1991).
9. S. Gupta, J.F. Whitaker, S.L. Whilliamson, P. Ho, J.S. Mazurowski, and J.M. Ballingall, "High-sensitivity picosecond-response  $\text{In}_x\text{Ga}_{1-x}\text{As}$  photodetectors," *Ultrafast Phenomena 1992 Digest*, (1992).
10. M.Y. Frankel, J.F. Whitaker, G.A. Mourou, and J.A. Valdmanis, "Experimental characterization of external electrooptic probes," *IEEE Micr. Guided Wave Lett.* **1**, 60 (1991).
11. D.H. Auston, P. Lavallard, N. Sol, and D. Kaplan, "An amorphous silicon photodetector for picosecond pulses," *Appl. Phys. Lett.* **36**, 66 (1980).

# Photoconductive Sampling Circuits Using Low-Temperature GaAs Interdigitated Switches

J. Allam, K. Ogawa and J. White

*Hitachi Cambridge Laboratory, Hitachi Europe Ltd., Cavendish Laboratory,  
Madingley Road, Cambridge CB3 0HE, United Kingdom*

N.de B. Baynes and J. R. A. Cleaver

*Microelectronics Research Centre, University of Cambridge,  
Cavendish Laboratory, Madingley Road, Cambridge CB3 0HE, United Kingdom*

I. Ohbu, T. Tanoue, and T. Mishima

*Hitachi Central Research Laboratory, Hitachi Ltd., 1-280, Higashi-koigakubo,  
Kokubunji-shi, Tokyo 185, Japan*

## Introduction

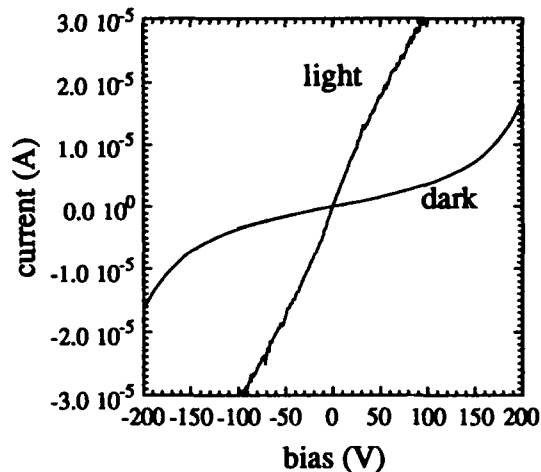
Characterisation of electronic devices at frequencies up to several hundred GHz can be achieved using electro-optic<sup>1</sup> or photoconductive sampling. GaAs grown at low temperature by molecular beam epitaxy (LT GaAs) is a suitable material for fabrication of switches for photoconductive sampling due to its ultrafast carrier lifetime ( $\sim 1$  ps or less)<sup>2</sup>, high breakdown voltage, and low on-state resistivity. High-responsivity LT GaAs photodetectors have been demonstrated using sub-micron interdigitated structures<sup>3</sup>.

In this paper we describe the characterisation of LT GaAs wafers for fast photoconductors, and the fabrication of sub-micron interdigitated switches. The switches were integrated with coplanar waveguides (CPW's) to form high-responsivity picosecond sampling circuits for characterisation of ultrafast electronic devices. Pulse propagation was studied in two circuits with CPW cross-sectional dimensions of  $100\text{ }\mu\text{m}/200\text{ }\mu\text{m}/100\text{ }\mu\text{m}$  and  $10\text{ }\mu\text{m}/20\text{ }\mu\text{m}/10\text{ }\mu\text{m}$ .

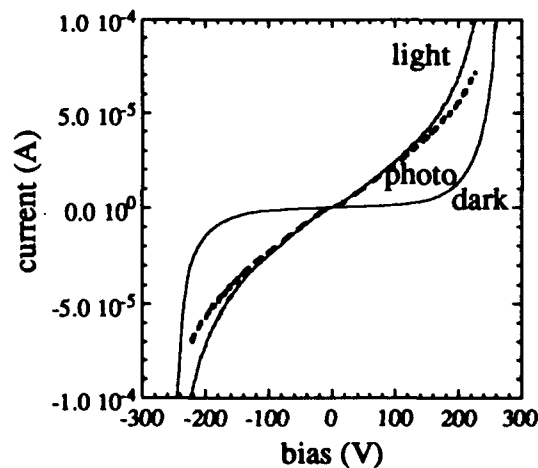
## Growth and characterisation of LT GaAs

Layers of LT GaAs  $2\text{ }\mu\text{m}$  thick were grown at nominal temperatures of  $220^\circ\text{C}$  and  $180^\circ\text{C}$  - above and below the critical temperature for epitaxial growth of  $2\text{ }\mu\text{m}$  layers<sup>4</sup>. The wafers were annealed *in situ* for 10 minutes at  $600^\circ\text{C}$ . X-ray rocking curves showed an increased linewidth and lattice mismatch for the lower temperature sample. Coplanar striplines of impedance  $\sim 50\text{ }\Omega$  were fabricated with photoconductive gaps of  $10\text{ }\mu\text{m}$ .

Pulses from a synchronously-pumped dye laser at  $600\text{ nm}$  were compressed to  $\sim 80\text{ fs}$  FWHM and focussed onto the photoconductive gap. The dc current-voltage characteristics (fig. 1) and bias dependence of the pulse width and amplitude were measured.



(a)



(b)

Figure 1. IV characteristic of LT GaAs  $10\text{ }\mu\text{m}$  coplanar striplines, grown at (a)  $180^\circ\text{C}$  and (b)  $220^\circ\text{C}$ .

Wafers grown at 180 °C showed saturation of the dc photocurrent and pulse amplitude at bias  $> \sim 100$  V followed by irreversible breakdown at the site of illumination. However, wafers grown at 220 °C did not saturate, but instead showed an additional photocurrent gain at bias  $> 200$  V, and an associated broadening of the pulse. This behaviour may be related to impact ionisation by hot carriers. The response time measured by photoconductive sampling was  $\sim 1.5$  ps. The responsivity of the 10  $\mu\text{m}$  gap coplanar striplines at a bias of 100 V was only  $\sim 5$  mA/W due to the large ratio of transit time ( $\sim 100$  ps) to recombination time ( $\sim 1$  ps).

### Fabrication of interdigitated switches

Interdigitated switches were fabricated with Ti/Au metallisation on 220 °C LT GaAs using electron beam lithography with a standard single-layer PMMA lift-off process. Finger and gap dimensions of 2  $\mu\text{m}$  down to 0.25  $\mu\text{m}$  were fabricated. Approximately an order of magnitude increase in the signal was obtained compared to 10  $\mu\text{m}$  coplanar striplines. Fig. 2 shows an interdigitated switch with 0.25  $\mu\text{m}$  fingers and gaps.

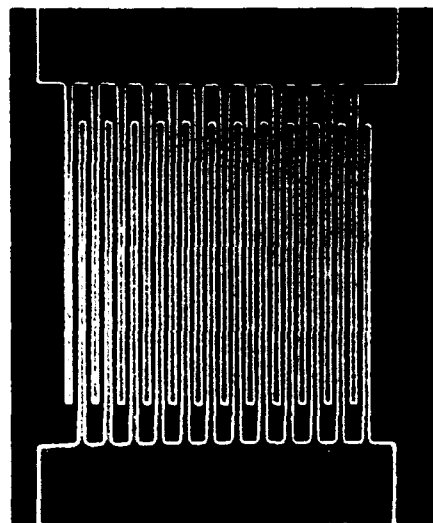


Figure 2. SEM micrograph of 0.25  $\mu\text{m}$  interdigitated photoconductive switch.

### Photoconductive sampling circuit for discrete devices

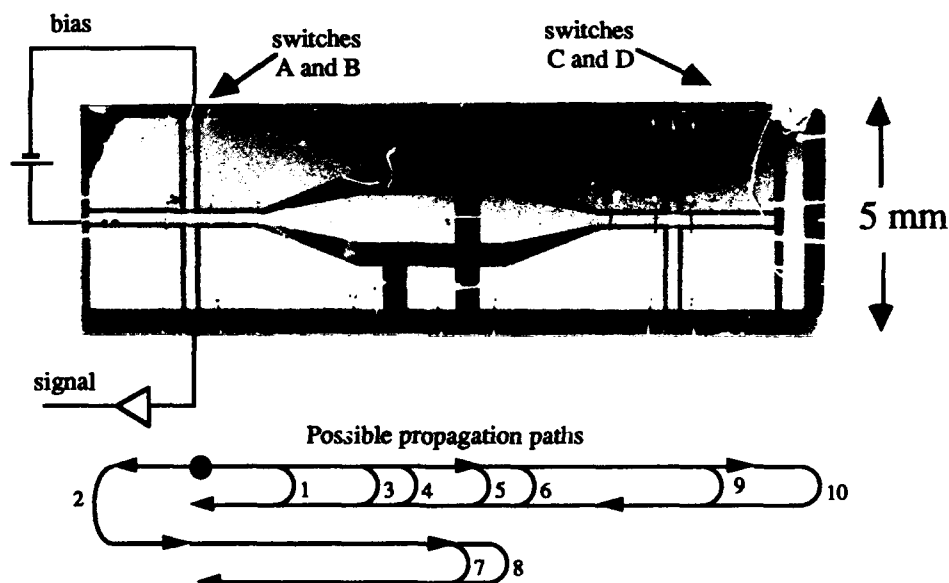


Figure 3. Diagram of CPW sampling circuit.

Fig. 3 shows a CPW sampling circuit for discrete devices, which are wire-bonded to the central 1 mm<sup>2</sup> pad. The CPW in the switch region has a centre conductor 200  $\mu\text{m}$  wide and a gap of 100  $\mu\text{m}$ . The region between the switches and the device is linearly graded with constant ratio of central conductor to gap width, which gives constant impedance in a CPW. Interdigitated switches with 0.5  $\mu\text{m}$  fingers and gaps were added between each side-arm and the central conductor using electron beam lithography. For circuit characterisation, a wire bond linked the two halves of the central conductor.

The response time of the four interdigitated switches was measured using a photoconductive mixing technique. Fig. 4 shows the autocorrelation curves, which are offset for clarity. Fitting with a bi-exponential (after removing the coherence spike) indicated a response time of  $\sim 1.7$  ps.

The sampling response of this circuit was found to be dominated by reflections from impedance discontinuities. These effects were studied using time domain reflectometry by pump-probing adjacent switches in an Auston autocorrelator configuration, as shown in fig. 3.



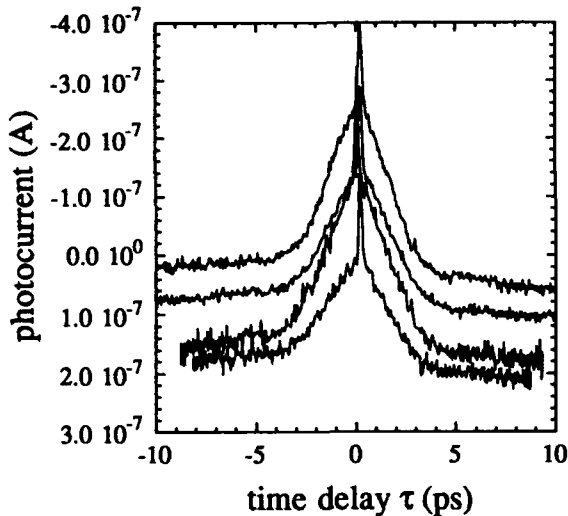


Figure 4. Pulse response of 0.5  $\mu\text{m}$  interdigitated switches on 220  $^{\circ}\text{C}$  LT GaAs.

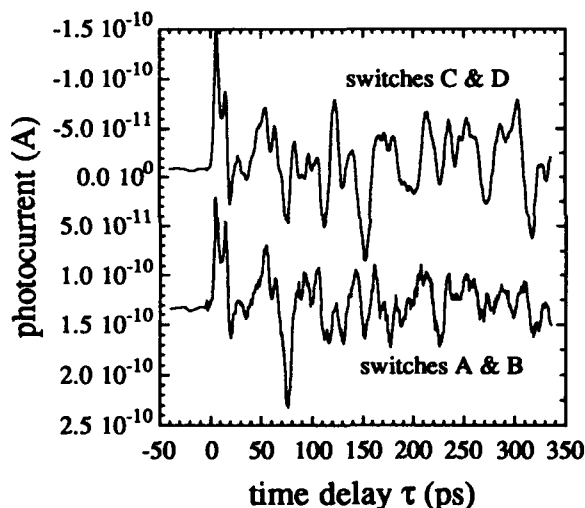


Figure 5. Time domain reflectance measurement via pump-probing of adjacent switches.

The reflected signal shows multiple peaks (fig. 5), and a plot of delay time against position of features in the CPW (fig. 6) shows that the peaks arise from reflection at discontinuities in the CPW cross-section. The propagation paths are indicated in fig. 3. Since the cross-section of the CPW is comparable to the substrate thickness, a combination of CPW and microstrip modes is excited, and mode conversion and reflection of microstrip modes occurs at the CPW discontinuities. The large cross-section of the CPW compared to the shortest wavelength component of the generated pulse results in non-TEM propagation. The measured group velocity of the pulse is  $\sim 1.05 \times 10^8 \text{ V}\cdot\text{cm}^{-1}$ .

The pulse generated at switch A, propagated through the wire-bond and detected at switch C is shown in fig. 7. The main features are broadened to  $\sim 25 \text{ ps}$  by dispersion in the CPW.

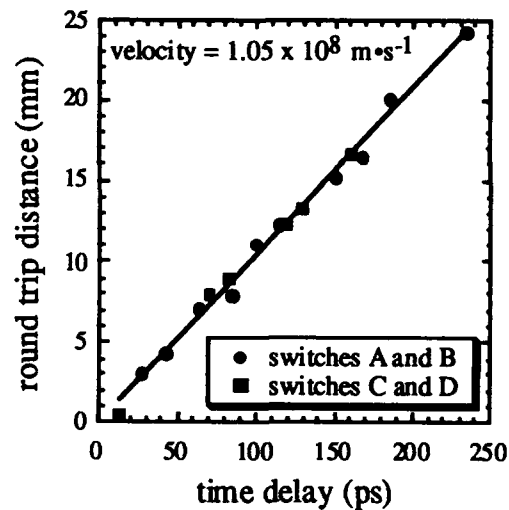


Figure 6. Plot of round trip distance against time delay for reflectance features in fig. 4.

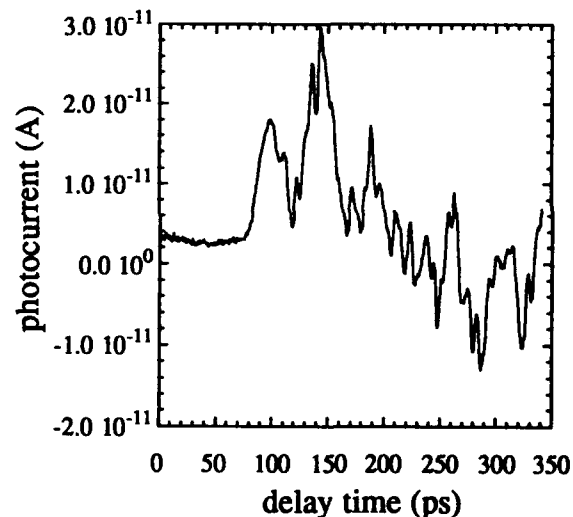


Figure 7. Pulse transmitted through wire bond for CPW sampling substrate.

### Photoconductive sampling circuit integrated with device.

In order to minimise the effects of dispersion and spurious reflections, a circuit was fabricated with reduced dimensions (20  $\mu\text{m}$  centre conductor and 10  $\mu\text{m}$  gap) and with the device (e.g. an FET) directly integrated into the CPW. Fig. 8 shows a composite photo of the CPW after optical lithography. Fabrication of interdigitated switches and integrated devices is performed by electron-beam lithography. Air bridges are used to connect the CPW ground planes in the region of the switches and device, but were not used in the sample studied here.

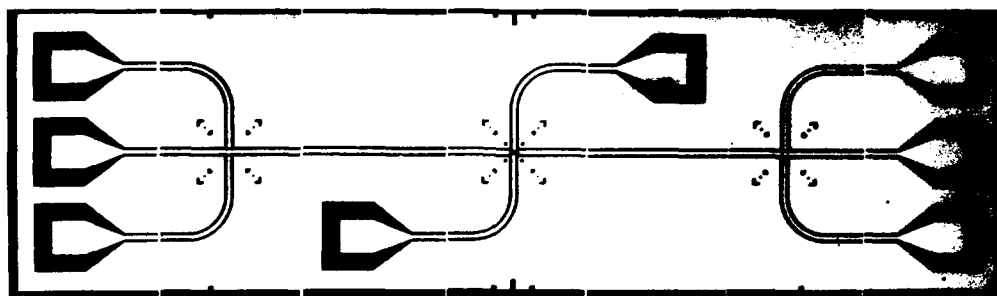


Figure 8. Photoconductive sampling circuit for integration with FET.

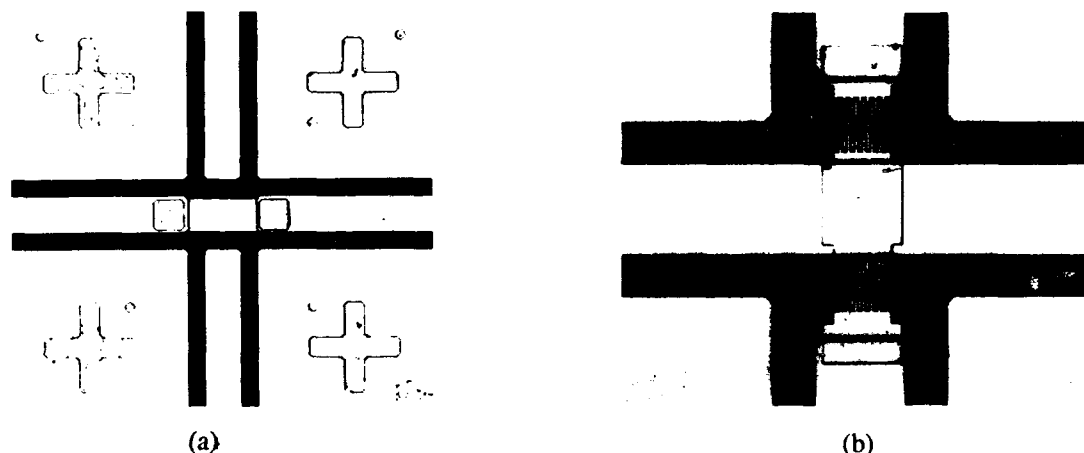


Figure 9. (a) Detail of device showing registration marks, ohmic contacts, and shorting link. (b) Detail of switch area showing interdigitated switches with  $0.5\ \mu\text{m}$  fingers and gaps.

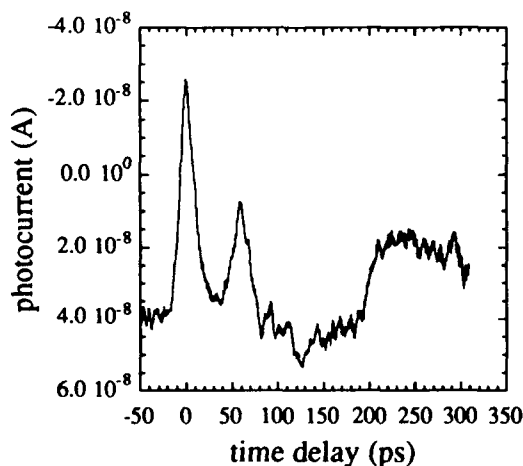


Figure 10. Reflections in  $10\ \mu\text{m}/20\ \mu\text{m}/10\ \mu\text{m}$  CPW sampling circuit.

For testing of the circuit the "device" is simply a metal link as shown in figure 9 (a). Interdigitated switches with  $0.5\ \mu\text{m}$  fingers were integrated as shown in fig. 9(b). This circuit was fabricated on LT GaAs

with a slower response time ( $\sim 15\ \text{ps}$ ). The autocorrelation of the electrical pulse and the reflected signal is shown in fig. 10, with the same time scale as fig. 5. The TDR signal is dominated by reflections from the ends of the CPW (at  $\sim 60\ \text{ps}$  and  $\sim 200\ \text{ps}$ ) and from the other set of switches (at  $\sim 120\ \text{ps}$ ). With further reduction of the carrier lifetime, this circuit will be useful for time domain spectroscopy of devices in the range  $\sim 1 - 100\ \text{ps}$ .

## References

1. M.Y. Frankel, J.F. Whittaker, G.A. Mourou, J.A. Valdmanis, and P.M. Smith in *OSA Proc. Picosecond Electronics and Optoelectronics*, ed. T.C.L.G. Sollner and J. Shah, Vol. 2, 146 (1991).
2. S. Gupta, M.Y. Frankel, J.A. Valdmanis, J.F. Whittaker, G.A. Mourou, F.W. Smith & A.R. Calewa, *Appl. Phys. Lett.* **59** 3276 (1991).
3. Y. Chen, S. Williamson, T. Brock, F.W. Smith & A.R. Calewa, *Appl. Phys. Lett.* **59**, 1984 (1991).
4. Z. Liliental-Weber, *MRS Proc.* **241**, 101 (1992).

---

## **Transmission Lines**

---

## High-Bandwidth Transmission Lines Using Low-Temperature-Grown-GaAs-on Quartz

H. Cheng and J. F. Whitaker

*Center for Ultrafast Optical Science, University of Michigan, 2200 Bonisteel Blvd.,  
Rm. 1006, Ann Arbor, Michigan 48109-2099*

### **Abstract**

The ultra-high bandwidth of a coplanar-strip transmission line fabricated on quartz and driven by an integrated photoconductive switch, defined by an epitaxial-lift-off layer of low-temperature-grown-GaAs, is demonstrated.

### **Introduction**

Planar wave-guiding structures, such as the coplanar strip transmission line (CPS), are important for the interconnection of modern high-speed devices. However, for planar guiding structures fabricated on GaAs or other semiconductor materials, propagating electrical signals suffer severe distortion due to modal dispersion and radiation losses which arise from the permittivity mismatch between the air and substrate. For typical waveguide dimensions of several tens of microns and a typical semiconductor substrate, radiation is the dominant loss mechanism for frequencies above 200 GHz.[1] This loss imposes a severe limitation on the use and testing of both passive and active devices, where the latter now possess cutoff frequencies in excess of 300 GHz. Modal dispersion also leads to frequency-dependent phase shifting, which causes additional distortion.

One way to solve these problems is to add a superstrate to eliminate the dielectric constant mismatch on the transmission line. However, for substrates already fabricated with devices, it is difficult to add a superstrate to a surface topology which is not flat. The superstrate would also prevent the use of high-bandwidth probes used for *in situ* circuit measurements.

Another way to avoid large radiation losses is to utilize a substrate material with a low dielectric constant. In practice, however, it is difficult to demonstrate the bandwidth of such a guiding structure, since a short electrical test signal must either be coupled into the line or generated photoconductively within the line. The former method has the potential for high insertion loss, particularly at high frequencies, while the latter requires the substrate to be semiconducting, and  $\epsilon_r$  is not typically of a low value for semiconductors.

In this investigation a novel technique has been used to deliver clean, short-duration test signals to an ultra-high-bandwidth transmission line fabricated on a low-loss, low-permittivity insulator. This has been achieved by removing a small patch of a high-speed-photoconductor film from its native substrate and bonding it onto an insulating substrate in a convenient location. This has allowed us to demonstrate that a

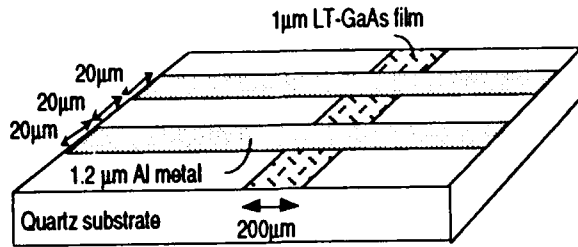


Fig. 1 Configuration of LT-GaAs epitaxial-lift-off layer with coplanar stripline on quartz.

great improvement in high-bandwidth propagation along CPS on low-permittivity substrates can be attained. These results will lead to improved test fixtures for ultra-wideband time-domain network analysis of high-speed devices, and may have ramifications for high-bandwidth, high-power signal propagation and devices as well.

### Fabrication & Experiment

In this work, a low-temperature-grown-GaAs (LT-GaAs) thin film [2] was isolated from its substrate using epitaxial liftoff and subsequently grafted onto either a quartz or fused silica substrate via the Van der Waals attractive force.[3] This patch of semiconducting material, employed for its ultrafast carrier relaxation, was used to generate the short-duration electrical test signal, which was then measured as it propagated along the CPS transmission line. This grafting technology has thus allowed us to fabricate a hybrid circuit combining an ultra-short-pulse signal source and a low-permittivity substrate.

The semiconductor graft patch was obtained from a wafer consisting of a 1- $\mu\text{m}$  LT-GaAs top layer and an intermediate 0.5- $\mu\text{m}$   $\text{Al}_x\text{Ga}_{1-x}\text{As}$  (70%) layer grown by MBE on semi-insulating GaAs at Lincoln Laboratory. The growth temperature was  $\sim 200^\circ\text{C}$ , with post-

annealing at  $\sim 600^\circ\text{C}$ . The wafer was first coated with wax as described in ref. 3. After this step, the SI-GaAs substrate and  $\text{Al}_x\text{Ga}_{1-x}\text{As}$  layers were subsequently removed by chemical etching. The remaining LT-GaAs film, supported by the wax, was placed onto the desired substrate and held there with several tiny droplets of DI water. At this time, the surface tension of the water pulled the LT-GaAs film and quartz substrate together. It was then found that baking provided a very fast and effective way of forming the permanent bond between the two different materials, due to the atmospheric pressure which squeezed out the air pockets left by the film of water after its molecules diffused out. The LT-GaAs film and the quartz substrate were thus pushed tightly together without the application of pressure on the wax as suggested in ref. 3. After the wax was rinsed away, standard processing steps were used to form the simple structure shown in Fig. 1.

An in-house coherent, time-domain spectroscopy technique [4] was used to verify that the high-frequency behavior of the insulators was flat versus frequency (for quartz,  $\epsilon \approx 3.85$  between 300 GHz and 1 THz, with negligible loss), and thus that they had utility in ultra-high-frequency microwave circuits. According to the expression for the radiation loss of CPS [5]

$$\alpha_{\text{rad}} \propto \frac{(\epsilon_r + 1)^{1/2} (\epsilon_r - 1)^2}{\epsilon_r} (s + 2w)^2 f^3$$

changing the substrate from GaAs to quartz should result in an improvement in the radiation loss of more than 85%.

A colliding pulse mode-locked dye laser with 80-fs pulse duration was used in the generation and detection of the electric signals. When the charged CPS was temporarily shorted by the laser-excited carriers in the LT-GaAs film, a subpicosecond electric pulse was generated due to the short carrier life time (300 fs) of the LT-GaAs. The propagation of this pulse on the CPS

was then measured by the external electro-optic sampling technique [6] at numerous distances from the generation site.

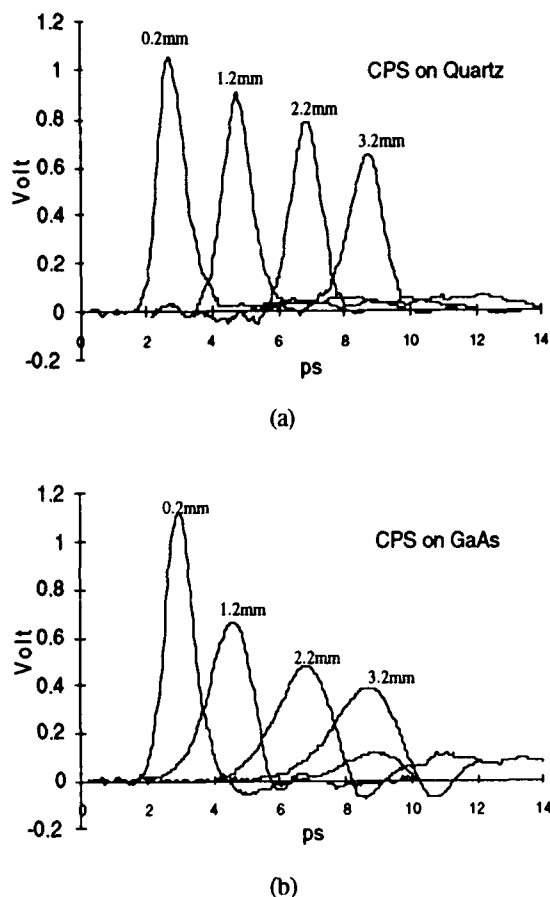


Fig. 2 Electrical pulse propagation on coplanar striplines on (a) quartz and (b) GaAs substrates.

## Results

Figure 2 shows the time domain waveform from 0.2-mm to 3.2-mm propagation distances with 1-mm steps. The electrical pulse propagation on the CPS-on-quartz shows a significantly smaller attenuation and dispersion than the CPS on the GaAs substrate. For example, after 3.2 mm of propagation, the pulse on the GaAs line already has spread to 2.1 ps FWHM, while

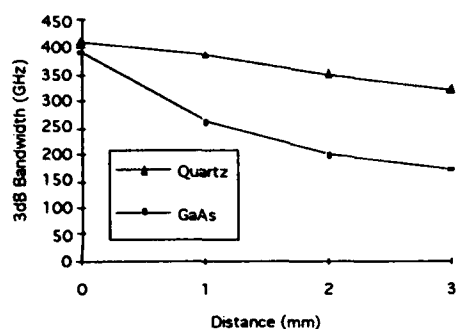
the signal on an identical line on CPS-on-quartz after 3.2 mm has a pulse width of only 1.18 ps. In frequency, this electrical pulse on the quartz line was found to still have a bandwidth of 320 GHz, while the bandwidth on the GaAs line was below 175 GHz. Furthermore, the switching efficiency (ratio of generated pulse amplitude/dc bias on CPS) is approximately the same for both cases, indicating that there is no degradation of the quality of the LT-GaAs film after the Van Der Waals bonding.

Figure 3 shows the amplitude and bandwidth change during the propagation. Because the frequency components over 200 GHz will radiate into the substrate very quickly for the CPS on GaAs, there is a large reduction in both the bandwidth and amplitude over the first 1 mm of propagation. After these high-frequency components have radiated away, the dominant loss then becomes the skin effect loss which manifests itself as a linear drop in both bandwidth and amplitude. However, for the CPS on quartz, the loss is dominated by the skin effect loss right from the beginning, so the bandwidth of CPS on quartz is not limited by the radiation loss for bandwidth up to 400 GHz!

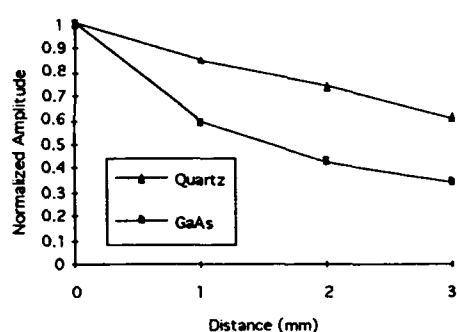
## Conclusion

An LT-GaAs thin film, which served as a photoconductive switch, was bonded onto a quartz substrate by utilizing epitaxial lift-off and Van der Waals-force grafting. The CPS on this LT-GaAs/quartz combination has preserved the pulse bandwidth generated photoconductively by the LT-GaAs switch. It also demonstrated that the CPS-on-quartz has a bandwidth over 300 GHz, which is very important for the interconnection of high speed devices.

Another potential application for this technology is in time-domain S-parameter extraction.[7] By using a CPS test fixture on an LT-GaAs/quartz combination instead of on LT-GaAs/GaAs, the bandwidth of an



(a)



(b)

Fig. 3 (a) 3-dB bandwidth and (b) amplitude change of short electrical pulse propagating on coplanar striplines, quartz substrate vs GaAs substrate.

optically-based network analyzer should be pushed beyond 250 GHz. This is due to the fact that the greatest limitation to the bandwidth of high-impedance, ultra-high-speed time-domain probes is the quality of the test fixture used. Among the other high-speed

applications for the epitaxial liftoff and bonding technique are ultra-wideband microstrip lines on thin GaAs layers, high-electric-field generation using grafted GaAs on high-breakdown substrates, and optoelectronic devices combining grafted semiconductors with electro-optic materials.

### Acknowledgment

Frank Smith of MIT Lincoln Laboratory was instrumental in preparing the LT-GaAs sample used in this study, and Yongqian Liu assisted in the terahertz-beam measurement of the quartz substrate.

### References

1. D.Grischkowsky *et al.*, *Phys. Rev. Lett.*, vol. 59, no. 15, Oct. 1987, pp.1663-1666.
2. F.W. Smith *et al.*, *Appl. Phys. Lett.*, vol 54, March 1989, pp. 890-892.
3. E. Yablonovitch *et al.*, *Appl. Phys. Lett.*, vol 56, June 1990, pp. 2419-2421.
4. J. Chwalek *et al.*, *Electronics Lett.*, vol. 27, Feb. 1991, pp. 447-448.
5. M.Y. Frankel *et al.*, *IEEE Tran. Microwave Theory Tech.*, vol. 39, June 1991, pp.910-916.
6. J.A. Valdmanis *et al.*, *IEEE J. Quantum Electronic.*, vol. QE-22, Jan. 1986, pp. 69-78.
7. M.Y. Frankel *et al.*, *Solid-State Electronics*, vol. 35, Mar. 1992, pp. 325-332.

## High Speed Limits of Coplanar Transmission Lines

U. D. Keil, D. R. Dykaar, A. F. J. Levi, R. F. Kopf, L. N. Pfeiffer, K. W. Goossen,  
S. B. Darack, and K. W. West

AT&T Bell Laboratories, 600 Mountain Avenue, Murray Hill, New Jersey 07974-2070

### Abstract

We present measurements of picosecond pulse propagation on coplanar strip transmission lines for which speed (i.e. group velocity), as well as phase and amplitude information are measured.

Electrode effects are studied using transmission line loops 1 mm in diameter with cumulative propagation distances as long as 10 cm. The intrinsically low dielectric constant of coplanar-air transmission lines is shown to result in high signal speed *and* low attenuation. The results are compared to the case of superconducting electrodes.

### Introduction

In this paper we consider the effects of substrate dielectric and electrode properties on transmission lines intended to operate in a frequency range of up to 1 THz. Propagation speed (i.e. group velocity, defined as the velocity of the peak of the pulse) has shown to be roughly independent of temperature, while reducing the dielectric constant results in *faster* propagation, *reduced* attenuation, and reduced line charging energies [1].

We report on propagation of picosecond electrical pulses over distances  $\leq 10$  cm using a 1 mm diameter loop transmission line. Use of a loop configuration allows precise velocity, as well as phase and amplitude measurements to be made, simultaneously. Measurements are made for normal and superconducting transmission lines. For normal electrodes both ordinary coplanar strip (CPS) and etched coplanar-air transmission (CAT) lines for both loop and straight line configurations are investigated. We consider the effects of substrate dielectric, conductor temperature and conductor thickness on attenuation and propagation speed. The results are modeled using a standard dispersion model [1-3] considering only the dominant mechanisms of radiation loss and conductor absorption. Conductor losses dominate for low frequencies (for

example 200 GHz depending on geometry) and radiation losses dominate for high frequencies. Thus, superconducting electrodes gain performance compared to normal electrodes in the low frequency regime and reducing the dielectric will have advantages for high frequencies.

### Test structures

Coplanar strip transmission lines are fabricated on low temperature grown (LT) GaAs photoconductors [4,5]. The conductor dimensions are width,  $w$  and spacing,  $s = 5 \mu\text{m}$ . Electrode thickness varies from 0.24 to 1.23  $\mu\text{m}$  of evaporated Au and 0.5  $\mu\text{m}$  of Pb. Loops are 1 mm in diameter. Voltage is applied through perpendicular 5  $\mu\text{m}$  wide bias lines. Photoconductive (gapless [6] or sliding contact [7]) switches are formed wherever a short optical pulse illuminates the region between the electrodes. The laser pulses are generated at



Fig. 1 Scanning electron micrograph of the etched freestanding CAT (FCAT) line. Linewidth and spacing is 5  $\mu\text{m}$ . The  $\text{SiO}_2$  supports are 200  $\mu\text{m}$  apart.



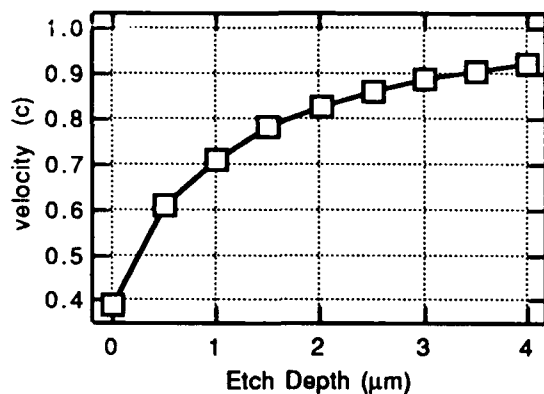


Fig. 2 Calculation of propagation velocity for Free CAT. Velocities of 0.9c are predicted for etch depth of  $<3.5 \mu\text{m}$ . The velocity changes by  $<10\%$  for etch depths of  $3 \pm 1 \mu\text{m}$ .

100 MHz by a colliding pulse mode-locked laser producing sub 100 fs pulses at Full Width and Half Maximum (FWHM) with a wavelength of 620 nm [8]. Electro-optic sampling [9] is used to measure pulse shape at minimum propagation distance and thereby define the input pulse for numerical simulations. All electrical input pulses used in this work are measured to be  $\leq 1$  ps FWHM.

CAT lines are formed by evaporating coplanar transmission lines on a 200 nm layer of  $\text{SiO}_2$ . The layer of  $\text{SiO}_2$  acts both as an etch mask and as a physical cantilevered support for the lines. Islands of unetched material form the photoconductive switches which are connected to the electrodes through openings in the  $\text{SiO}_2$  layer. The electrodes overhang the  $\text{SiO}_2$  layer by about  $2 \mu\text{m}$ , so the region of highest field strength experiences a uniform air dielectric. This design has also been tested in a telephone pole type geometry, where narrow strips of  $\text{SiO}_2$  are fabricated perpendicular to the gold lines with  $100 \mu\text{m}$  separations as shown in an SEM micrograph in Fig. 1. In this case the electrodes form essentially Freestanding CAT (FCAT) lines. All the etched designs are robust, not affected by wet processing or ultrasonic wire bonding.

Figure 2 shows the etch depth (under the Au electrodes) vs. speed for a FCAT, modeled using EMP©, a finite element analysis program (Field Precision Co.). After finding the equipotentials and calculating the capacitance, which gives  $\epsilon_{\text{eff}}$ , the velocity,  $v=c/\sqrt{\epsilon_{\text{eff}}}$ . The calculation assumes no loss.

In a conventional electro-optic sampling setup measuring different electrical propagation distances involves moving the probe beam position. Avoiding additional optical delays typically requires the use of an optical fiber [10]. Here, pump and probe sampling [11] is used to generate and then sample the pulse as it travels around the loop. The small size of the loop allows measurements to be made in cryogenic environments where only narrow optical access is available. The pulses are launched and travel around the loop in opposite directions to arrive at the sampling site. By adjusting the spatial separation of the pump and probe beams any propagation distance can be defined. For example, 1/4 loop (or lap) separation will result in sampling pulses that have propagated both 1/4

and 3/4 of a lap around the loop, as well as multiple laps, until the pulse decays completely. This geometry allows pulse propagation to be studied over much longer distances than previous measurements, while still maintaining absolute timing (velocity) information about the pulse.

In order to verify the negligible effect of the transmission line curvature, measurements were made on identically prepared straight transmission lines as well as loops 0.5 mm in diameter. No measurable deviation is found for any of the designs tested. Note that the ratio of line width to loop diameter is  $5 \times 10^{-3}$  for the 1 mm loop.

## Simulation Results

For the simulation a model based on empirical formulae [1,2] is used. The frequency dependent terms describing the propagation characteristics of a transmission line are the attenuation constant  $\alpha$  and the phase  $\beta$ . The propagation of an electric pulse is modeled in the frequency domain by

$$V_{\text{prop}} = V_0 e^{(\alpha + i\beta)z}$$

We consider only the dominant effects of conductor and radiation losses. Radiation losses in coplanar strip lines are due to Cerenkov radiation into the substrate. The group velocity of the propagating pulse is determined by the average dielectric constant of substrate and air. This velocity exceeds the velocity of an electromagnetic wave propagating in the substrate and, therefore, gives rise to a Cerenkov radiation cone. Numerically these radiation losses are dominated by a  $f^3$  dependence. Depending on the design parameters the radiation losses dominate above a certain frequency. For strip lines with  $5 \mu\text{m}$  width and spacing this frequency is about 1 THz (the exact value is determined by the conductor) and is shifting to lower frequencies for larger line dimensions. The effect of the velocity mismatch is strongly reduced, if the substrate is etched away. CAT lines exhibit much smaller radiation losses especially at high frequencies. By comparing the measured propagation speed on a CAT loop with simulations with  $\epsilon_r$  as a fit parameter a value of  $\epsilon_r = 2$  was obtained. An  $\epsilon_r \neq 1$  indicates that the remaining substrate has still some influence on the propagation characteristics. The simulations are performed for two values of the dielectric constant  $\epsilon_r = 13.1$  (CPS) and  $\epsilon_r = 2$  (CAT). The input pulses induced in the LT GaAs photoconductive switches are measured to be 0.8 - 1 ps FWHM. To demonstrate the effects of etched (CAT) vs. unetched (CPS) substrate and superconducting vs. normal electrodes the frequency spectrum of an input pulse is plotted together with the spectra after propagation of 6.28 mm (or 2 round trips) for normal CPS, normal CAT, and superconducting CPS (Fig. 3).

The attenuation due to the conductor is determined by the real part and the phase by the imaginary part of the surface impedance

$$Z_s = (i\omega\mu_0/\sigma)^{1/2} \coth[(i\omega\mu_0/\sigma)^{1/2}t]$$

For normal conductors conductivity  $\sigma$  is real. The losses due to the electrodes are described by the skin effect. For high frequencies the electromagnetic field has a limited penetration depth into the conductor. As only a part of the conductor is used the losses increase with higher frequencies with a  $\sqrt{f}$  frequency dependence.

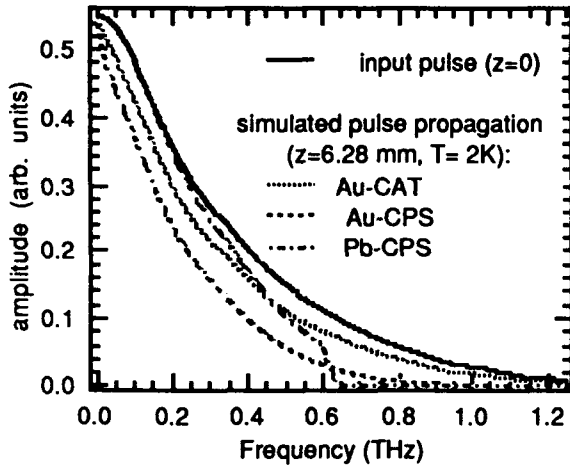


Fig. 3 Comparison of the calculated frequency spectrum of propagated pulses for Au-CAT, Au-CPS, and Pb-CPS ( $t=0.5 \mu\text{m}$ ,  $w=s=5 \mu\text{m}$ ). In addition, the electro-optically sampled input pulse spectrum is shown.

For superconducting electrodes  $\sigma$  is complex. The complex conductivity is calculated in the Mattis-Bardeen theory [12]. We consider in this paper lead electrodes. In this case the real part is vanishing (in terms of contributing to an attenuation) for frequencies well below the superconducting gap of 660 GHz and shows a strong increase above this value. The normal conductivity  $\sigma_n$  of lead is smaller than  $\sigma_n$  of gold. Above the superconducting gap the attenuation is therefore stronger for lead electrodes. In Fig. 3 this is indicated by crossing of the curves for Au-CPS and Pb-CPS. For Au-CAT the signal is less attenuated compared to Pb-CPS for frequencies above 450 GHz. In this frequency regime radiation losses begin to determine the attenuation. The (normal) conductivities taken into account in these simulations are measured on our samples and are  $5.6 \times 10^8 \Omega^{-1}\text{m}^{-1}$  for gold and  $1 \times 10^7 \Omega^{-1}\text{m}^{-1}$  for lead lines.

### Measurement of Electrode Effects

Measurements were performed over a range of temperatures from 2K to 300K and for Au electrode thicknesses from 0.2 to 1.2  $\mu\text{m}$  and 0.5  $\mu\text{m}$  for Pb electrodes. The attenuation of the pulse amplitudes for these cases is summarized in Fig. 4, showing that temperature as well as electrode thickness has a strong influence on attenuation. This graph does not contain any information about the frequency dependence of the attenuation. For a more careful analysis the measured

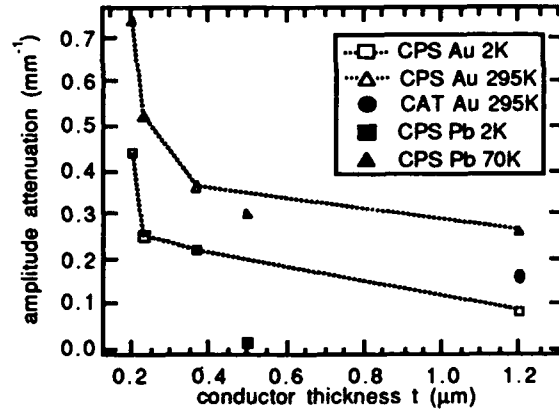


Fig. 4 Measured attenuation versus conductor thicknesses. Curves are guides to the eye. The 1.2  $\mu\text{m}$  thick CAT line shows a factor of two improvement in attenuation for the identical electrode configuration as a CPS line.

data were directly compared to simulation results in the time domain.[1] The conductivities,  $\sigma_{fit}$ , chosen to fit the calculated amplitudes to the measurements are about a factor of two smaller than the dc values, but have the same temperature scaling. A possible explanation for this deviation is that the high frequency (skin effect) conductivity near the surface is less than the average value measured at dc. For high frequencies the small skin depth will dominate the attenuation. The underestimation of the attenuation by using  $\sigma_{dc}$  in the calculation rather than  $\sigma_{fit}$  is seen for all samples. For the 1.2  $\mu\text{m}$  Au electrode at  $T = 295 \text{ K}$  the attenuation was fitted with a conductivity  $\sigma_{fit} = 2.1 \times 10^7 \Omega^{-1}\text{m}^{-1}$  which is less than the measured dc value. However, at 2 K the dc value ( $5.6 \times 10^8 \Omega^{-1}\text{m}^{-1}$ ) gives a good fit with respect to the measured attenuation.

In order to simulate the propagation speed it is important to take into account the correction of an effective dielectric constant for finite electrode thickness [3]. The fit is very sensitive to changes in  $\epsilon_r$  and the error due to fitting the measured propagation speed is less than 0.2. For  $t=1.2 \mu\text{m}$  this correction is equivalent to assuming an  $\epsilon_r = 10.5$ . The thick electrodes increase the propagation speed considerably, as the taller profile causes more of the electric field to be out of the higher dielectric substrate.

For a superconducting loop propagation distances of up to 10 cm could be measured before distortion destroys the signal. The simulation results in Fig. 3 show that the low frequency components are hardly attenuated and the high frequency components are already filtered out after a short propagation distance. The evaluation of the peak amplitudes (Fig. 4) does not distinguish between different frequencies, so the superconducting case shows very little loss. This is, however, only valid for frequencies below the gap.

### Measurement of Substrate Effects

The velocity of propagation varies inversely with the square root of the effective dielectric constant ( $\epsilon_q$ ).

Removing the substrate dielectric in and around the electrodes will reduce  $\epsilon_q$  and so increase the propagation velocity. Large velocities can be obtained by deep etching (Fig. 2). For 'Glass CAT':  $v = 0.86$  and 'Free CAT':  $v = 0.9c$  can be obtained. As expected, an unetched sample has a velocity of  $0.39c$  ('GaAs no etch' in Fig. 5).

For comparison to simulations, a propagation speed (of the pulse peak) of  $0.81c$  for a CPS on a uniform substrate would require a dielectric constant of  $\epsilon_r = 2.0$ . This is the value obtained from comparison of simulations with measurements on a 1 mm CAT loop. It indicates that for the CAT lines the substrate still has some influence on pulse propagation. Attenuation and dispersion, however, could not be accurately measured in this design as the measurements showed significant additional losses due to energy propagating into the contact pads. In contrast to this loop, a straight CAT line exhibited a propagation speed of only  $0.61c$  (corresponding to  $\epsilon_r = 5.2$ ) indicating that this particular line was not etched as deeply. In addition to an improvement in speed we expect an improvement in attenuation due to a strong reduction of the radiation losses. The attenuation (Fig. 4) for this particular CAT line ( $\alpha = 0.16 \text{ mm}^{-1}$ ) is about *half* of the attenuation for the equivalent CPS structure ( $\alpha = 0.26 \text{ mm}^{-1}$ ).

## Summary

We have demonstrated a new technique for the study of ultrafast signal propagation, loop transmission lines. The loop configuration allows long distance propagation studies to be made in a small area. This in turn allows measurements to be made at low temperatures. The loop configuration yields not only velocity, but amplitude and phase information, which is necessary for accurate modeling of signal propagation. Careful characterization of the electrodes is also required for accurate modeling of the measured results.

For superconducting electrodes we see an apparent negligible loss for frequencies well below the gap and

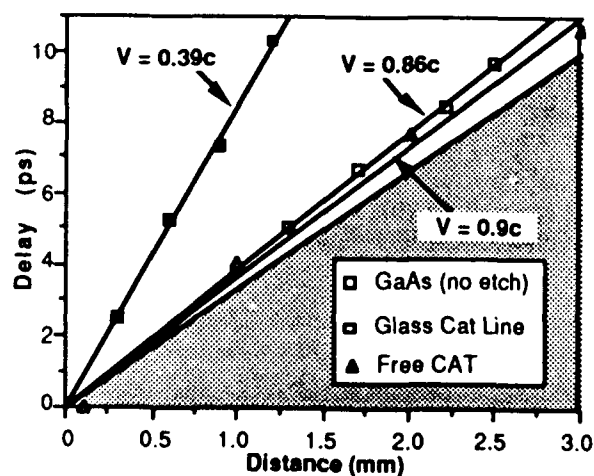


Fig. 5 Plot of delay (as measured by midpoint of linear fit to risetime) versus propagation distance. Free CAT corresponds to the geometry of Fig. 1. Velocity,  $v$ , is found from a linear fit to the data. Shaded area is bordered by  $v=c$ .

propagation distances up to 10 cm. For higher frequencies we find almost complete attenuation, even for very short propagation distances.

The effects of substrate removal are shown to influence not only the speed of a given transmission line, but also the attenuation, due to strong reduction of radiation losses and through lowering of the surface impedance. For equivalent dimensions the attenuation in CAT lines is measured to be about half that of an unetched line. In real chips, corners, as well as straight lines are required. We have demonstrated that bends of radius 0.25 mm are capable of high fidelity signal transmission. Our results suggest that digital, intrachip communication on length scales of order 1 cm with pulses as short as one picosecond and velocities as high as  $0.9c$  is readily achievable using electrical signals.

## Acknowledgement

We thank M.Y. Frankel of Terametrics for providing the sampling probe used in this work. One of us (U.D.K.) acknowledges support from the Deutsche Forschungsgemeinschaft.

## References

1. U.D. Keil, D.R. Dykaar, A.F.J. Levi, R.F. Kopf, L.N. Pfeiffer, S.B. Darack, and K.W. West, *IEEE J. Quant. Elec. Special Issue on Ultrafast Optics and Electronics*, 28(10), 2333-2342 (1992).
2. G. Hasnain, A. Dienes, and J.R. Whinnery, *IEEE Trans. Microwave Theory Tech.*, 34, 738 (1986).
3. K.C. Gupta, R. Garg, and I.J. Bahl, *Microstrip Lines and Slotlines*, Artech House, Norwood (1979).
4. F.W. Smith, H. Q. Lee, V. Diadiuk, M. A. Hollis, A. R. Calawa, S. Gupta, M.Y. Frankel, D.R. Dykaar, G.A. Mourou, and T.Y. Hsiang, *Applied Physics Letters*, 54 (10), 890 (1989).
5. D.R. Dykaar, D.J. Eaglesham, U.D. Keil, B.I. Greene, P.N. Saeta, L.N. Pfeiffer, R.F. Kopf, S.B. Darack, and K.W. West, In *Low Temperature (LT) GaAs and Related Materials*, Materials Research Society, Pittsburgh, Vol. 241, 245 (1992).
6. D.R. Dykaar, T.Y. Hsiang, and G.A. Mourou, *Topical Meeting on Picosecond Electronics and Optoelectronics*, Springer-Verlag, 249 (1985).
7. M.B. Ketchen, D. Grischowski, T.C. Chen, C.-C. Chi, I.N. Duling III, N.J. Halas, J.M. Halbout, *Applied Physics Letters*, 48, 751 (1986).
8. J. A. Valdmanis, R.L. Fork and J.P. Gordon, *IEEE J. Quantum Electron.*, QE-22, 112, (1986).
9. J.A. Valdmanis, and G.A. Mourou, *IEEE J. Quantum Electronics*, QE-22, 69 (1986), and J.M. Chwalek and D.R. Dykaar, *Review of Scientific Instruments*, 61 (4), 1273 (1990).
10. D.R. Dykaar, A.F.J. Levi, and M. Anzlowar, *Applied Physics Letters*, 57 (11), 1123, (1990).
11. D.H. Auston, in *Picosecond Optoelectronic Devices*, edited by C.H. Lee (Academic, London, 1984), p. 73.
12. D.C. Mattis and J. Bardeen, *Phys. Rev.*, 111, 412 (1958).

# Subpicosecond Electrical Pulse Generation in GaAs by Nonuniform Illumination of Series and Parallel Transmission-Line Gaps

Sotiris Alexandrou, Chia-Chi Wang, Roman Sobolewski, and  
Thomas Y. Hsiang

*Laboratory for Laser Energetics and Department of Electrical Engineering,  
University of Rochester, 250 East River Road,  
Rochester, New York 14623-1299*

## Abstract

We present a detailed study of subpicosecond pulse generation by nonuniform illumination of photoconductive switches on semi-insulating GaAs. The amplitude dependence of such pulses on bias voltage and light intensity was examined in detail. A complete spatial mapping of the excitation area indicates that such pulse generation is due to the depletion of electrical field by photocarriers in the illuminated section of the gap. Picosecond pulses were generated by this method on series gaps in a coplanar waveguide for the first time and were found to contain balanced, odd modes only.

## Introduction

Generation of subpicosecond electrical pulses has been broadly studied in recent years [1-5]. Such pulses contain spectral components as high as several terahertz and are very useful as a testing and characterization tool to obtain broadband, ultrahigh-frequency information of circuits or devices. A particularly attractive technique for generating these pulses is the use of nonuniform illumination of a photoconductive switch [1-3], since it allows direct implementation of pulse generation on circuit chips in a process-compatible and nonperturbative manner. In this technique, a laser pulse with diameter much smaller than the gap of the photoconductive switch only illuminates one edge of the switch electrode (hence, not completely closing the gap). Subpicosecond pulses are generated even though the switch materials have substantially longer carrier lifetime ( $>100$  ps).

The physics of nonuniform illumination has, on the other hand, not been thoroughly studied. In literature, the most promising theory appears to be that of Sano *et al.* [6]. According to these authors, when an optical pulse is applied to the edge of a photoconductive switch, the photocarriers effectively short out the illuminated area, forcing the electric field in the switch gap to be redistributed. This field depletion produces a transient displacement current, which then propagates from the switch in the form of an inductive pulse, with a duration corresponding to

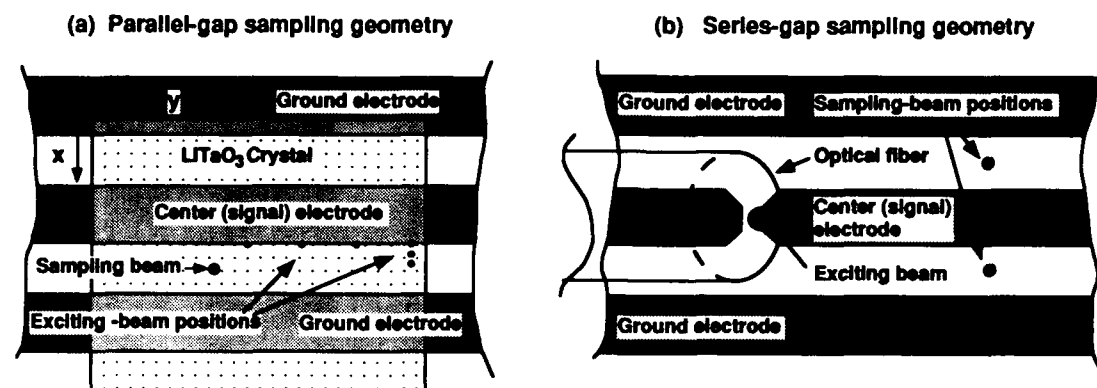
that required for the field to move from one electrode to the other. An important element of this theory is its prediction of a secondary, much slower, "shoulder" that would follow the main pulse near the switch area but would not propagate from the switch.

In this paper, we report detailed experimental studies of nonuniform illumination of photoconductive gaps, fabricated on semi-insulating GaAs. We demonstrate that a spatial mapping of the electrical pulses allows us to verify directly the main features of the Sano theory and also provides an understanding of how the simplifying assumptions of this theory may be improved to account for all the quantitative features.

## Experiment

Our experiments were conducted on coplanar waveguides with electrode width and spacing both equal to  $50\text{ }\mu\text{m}$ . A Ti:sapphire laser system provides the excitation and probing beams for our electro-optic sampling system [7]. Two configurations were used, as shown in Fig. 1. The first one uses a parallel-gap excitation, Fig. 1(a), similar to that used by the IBM group [1] and was termed by these authors as the "sliding contact" geometry. The excitation beam had a diameter of about  $5\text{ }\mu\text{m}$  or about a tenth of the electrode spacing. This beam was scanned from one side of the waveguide gap to the other as well as along the waveguide to allow spatial-dependence studies. The sampling beam was fixed at the center of the waveguide gap and was guided through a LiTaO<sub>3</sub> finger tip in a total internal reflection mode [7]. By focusing the excitation beam and the sampling beam through the same microscope objective lens, the sampling point can be brought within several micrometers of the excitation spot.

The second geometry, more useful in practical applications, uses series-gap excitation as shown in Fig. 1(b). The excitation beam in this case was guided through a single-mode optical fiber and provided a slightly ellipsoidal excitation spot with a diameter about  $10\text{ }\mu\text{m}$  to illuminate the  $20\text{-}\mu\text{m}$  gap that is placed in line on the center electrode of the waveguide. Sampling was conducted on both sides of the center conductor to check any

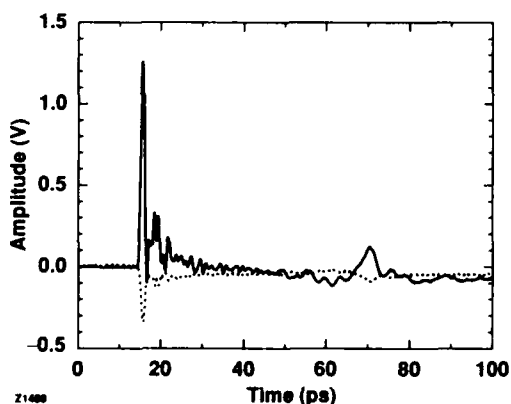


Z1488

Figure 1. A schematic representation of the sampling geometries employed. (a) The parallel-gap geometry, with both excitation and sampling beams focused through an electro-optic  $\text{LiTaO}_3$  crystal and (b) The series-gap sampling geometry, with the excitation beam guided through an optical fiber.

asymmetry in the generated pulses.

For the parallel-gap excitation, a typical transient is shown in Fig. 2. In this case, the bias voltage was 27 V and the sampling spot was placed 180  $\mu\text{m}$  from the excitation spot. The two traces correspond to the two polarities of the bias, with the larger signal generated when the optical pulse was applied to the positive electrode. The pulse width is about 1 ps, with a major reflection signal seen at 70 ps. The pulse rise is slower than its fall, indicating spatial dispersion due to propagation of this transient [8].

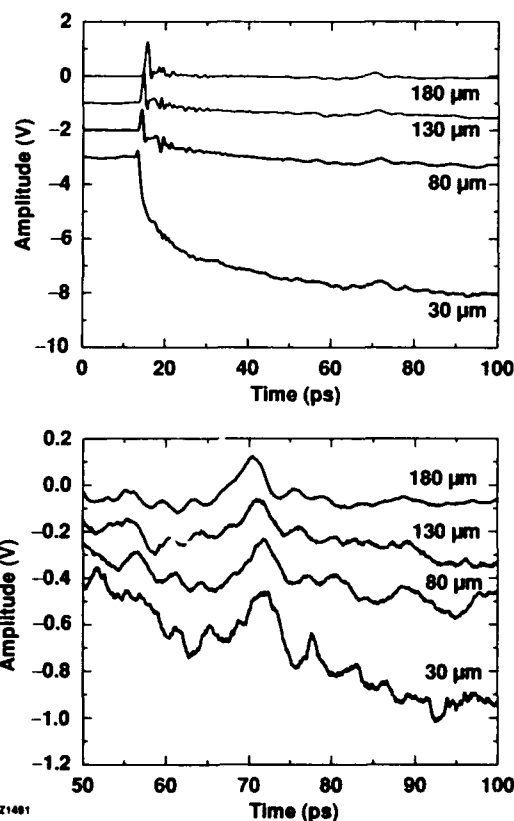


Z1489

Figure 2. Electrical pulses generated in the parallel-gap geometry at a distance of 180  $\mu\text{m}$  from the sampling site. The optical beam is focused at the edge of the center electrode. The bias voltage is  $\pm 27$  V for the two traces.

As the sampling spot was moved closer to the excitation spot (along the y-direction in Fig. 1), a negative shoulder became more apparent, see Fig. 3(a). An important indication that this shoulder is localized to the excitation spot is shown in Fig. 3(b), where the secondary, reflected signal is seen to contain only the main pulse but not the negative shoulder. This is an essential feature of the Sano theory.

The effect of edge illumination is shown in Fig. 4, as the excitation spot was now moved away from the electrode edge (along the x-direction in Fig. 1). The pulses became



Z1491

Figure 3. (a) Sampled waveforms with decreasing separation between the exciting and probe beams, along the y-direction in Fig. 1(a). (b) A close view of the reflected signals.

progressively smaller, barely visible when the laser was applied to the center of the waveguide gap. This effect is summarized in Fig. 5. The negative shoulder was not seen in these traces, since the sampling spot was placed at about 180  $\mu\text{m}$  away from the switch.

In the series-gap excitation scheme, essentially the same pulse generation was observed, as shown in Fig. 6. Here the two traces correspond to sampling results taken on two sides of the

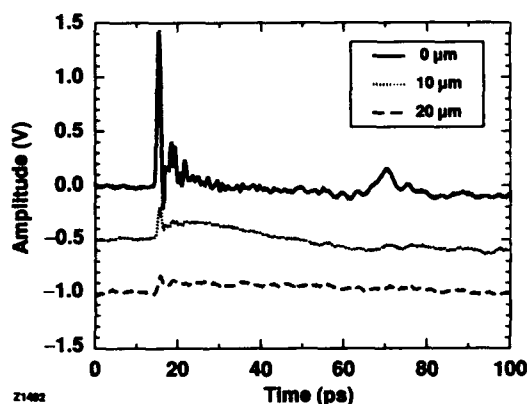


Figure 4. Sampled waveforms with the excitation beam scanned along the 50- $\mu\text{m}$  parallel gap, x-direction in Fig. 1(a) with the sampling beam 180  $\mu\text{m}$  away.

waveguide center conductor. The high degree of symmetry in the two transients indicates that the pulse generated contains only "odd modes" or modes that have field distribution symmetrical relative to the center electrode [7]. This pulse was found to be strongly dependent on the bias voltage, see Fig. 7, and on the laser intensity, see Fig. 8.

#### Discussions

The strongest support to the Sano theory is seen in the data of Fig. 3. The short pulse, generated by the depletion of the electric field in the illuminated area, has an opposite polarity to that of the slower, negative shoulder, which is generated by the increase in electric field in the unilluminated area. Since this increase is sustained as long as the photocarriers are present, this shoulder would have a duration determined by the carrier lifetime, in this case close to a nanosecond. This field is also localized, hence it cannot be measured once the sampling point is moved from the excitation spot. Carrier drift and diffusion are both much too slow to be of any consequence here.

In the original Sano theory, the authors simplified their computer simulations by assuming that the electrode-semiconductor contacts are ohmic and the bias voltage would then be uniformly distributed between the two waveguide electrodes. Our results in Fig. 5 clearly show that this assumption is not adequate to account for the fact that the pulse magnitude changes drastically as the excitation spot is moved within the photoconductive gap. As suggested in Ref. 1, perhaps a combination of traps and surface states would greatly affect the field distribution within the gap area. An earlier work predicted this effect [9], and indeed showed that the field can be much stronger at the positive electrode. In this sense, the data in Fig. 5 can be considered as a direct measurement of the field distribution within the gap, and they closely approximate the theoretical predictions [9].

The results in Fig. 7 can be understood similarly. The Sano theory predicts a simple linear relationship between the pulse amplitude and the bias voltage, which was clearly not observed in our experiments. The Au/GaAs interface forms a Schottky contact, and surface states determine its contact potential [10]. Until the bias voltage exceeds this potential, very little electric field is distributed in the switch-gap region. The data in Fig. 7

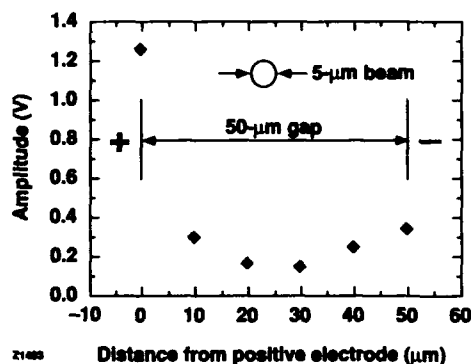


Figure 5. The amplitude of the pulses as a function of the position of the excitation beam, as it is moved across the waveguide gap.

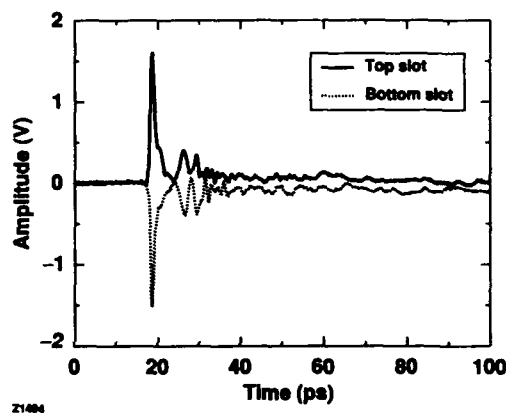


Figure 6. Picosecond electrical pulses generated by the nonuniform illumination of a series gap. The positive and negative pulse are sampled in the top slot and bottom slot respectively, see Fig. 1(b).

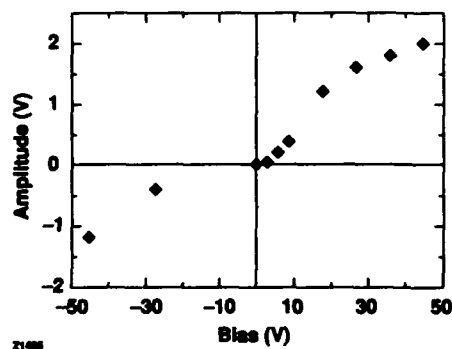


Figure 7. The pulse amplitude as a function of the applied bias for series-gap excitation.

suggest that this contact potential on the positive electrode is several volts, which is somewhat larger than expected but not altogether unreasonable.

The last set of data, the light-intensity dependence of pulse amplitude in Fig. 8, is again qualitatively understandable from the Sano theory. The amount of field depletion in the illuminated area depends on the photoconductance of this area; the more carriers generated, the larger the pulse amplitude. One

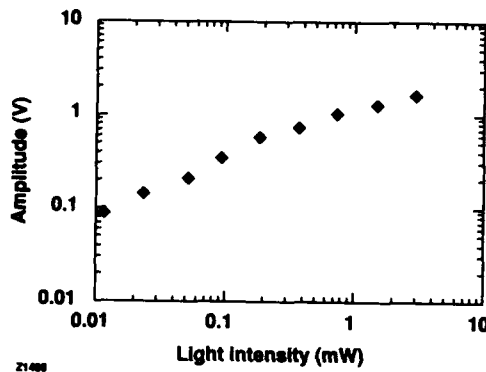


Figure 8. The pulse amplitude as a function of the incident light intensity for series-gap excitation.

expects that at a high enough light intensity, the field would be completely depleted and the pulse height would saturate to a plateau. This appears not to have been attained in our experiments.

#### Acknowledgments

The authors would like to thank D. R. Dykaar and Y. Kostoulas for their help. This work was supported in part by the University Research Initiative at the University of Rochester sponsored by the Army Research Office grant No. DAAL03-92-G-0112.

#### References

1. D. Krökel, D. Grischkowsky, and M. B. Ketchen, "Subpicosecond electrical pulse generation using photoconductive switches with long carrier lifetimes," *Appl. Phys. Lett.* **54**, 1046-1047 (1989).
2. N. Katzenellenbogen and D. Grischkowsky, "Efficient generation of 380 fs pulses of THz radiation by ultrafast laser pulse excitation of a biased metal-semiconductor interface," *Appl. Phys. Lett.* **58**, 222-224 (1991).
3. U. D. Keil and D. R. Dykaar, "Electro-optic sampling and carrier dynamics at zero propagation distance," *Appl. Phys. Lett.* **61**, 1504-1506 (1992).
4. S. Alexandrou, C.-C. Wang, T. Y. Hsiang, M. Y. Liu, and S. Y. Chou, "A 75-GHz silicon metal-semiconductor-metal Schottky photodiode," submitted to *Appl. Phys. Lett.* (November, 1992).
5. S. Y. Chou, Y. Liu, W. Khalil, T. Y. Hsiang, and S. Alexandrou, "Ultrafast nanoscale metal-semiconductor-metal photodetectors on bulk and low-temperature grown GaAs," *Appl. Phys. Lett.* **61**, 819-821 (1992).
6. E. Sano and T. Shibata, "Mechanism of subpicosecond electrical pulse generation by asymmetric excitation," *Appl. Phys. Lett.* **55**, 2748-2750 (1989).
7. S. Alexandrou, R. Sobolewski, and T. Y. Hsiang, "Time-domain characterization of bent coplanar waveguides," *IEEE J. Quantum Electron.* **28**, 2325-2332 (1992).
8. T. Y. Hsiang, J. F. Whitaker, R. Sobolewski, D. R. Dykaar, and G. A. Mourou, "Propagation characteristics of picosecond electrical transients on coplanar striplines," *Appl. Phys. Lett.* **51**, 1551-1553 (1987).
9. M. A. Lampert, "Simplified theory of space-charge-limited currents in an insulator with traps," *Phys. Rev.* **103**, 1648-1656 (1956).
10. S. M. Sze, "Metal-semiconductor contacts," *Physics of Semiconductor Devices*, 2nd ed. (Wiley, New York, 1981), Chap. 5, pp. 245-311.

---

## **Ultrafast Probes of Materials/Devices/Circuits**

---



## Subpicosecond GaAs Wafer Probe System

M. S. Shakouri, A. Black\*, B. A. Auld, and D. M. Bloom

*Edward L. Ginzton Laboratory, Stanford University, Stanford, California 94305*

\*A. Black is now at Gadzoox Microsystem, Los Gatos, California

### Abstract

We report a subpicosecond GaAs wafer probe system which incorporates a mechanical flexure and a micromachined GaAs IC for time domain on-wafer measurements. The micromachined GaAs IC incorporates a novel high speed pulse sharpener and a two diode sampling bridge with a micromachined GaAs tip.

### Introduction

Significant advances in millimeter-wave devices and integrated circuits have occurred over the past several years,<sup>1,2,3</sup> yet the majority of measurements have been extrapolated from DC- 65 GHz data, relying only on linear projections to predict the extremely high frequency performance of these devices and circuits. In our laboratory, on-wafer S-parameter calibration was extended to 85 GHz by mounting a sampler / bridge MMIC and an alumina tip in a probe package.<sup>4</sup> In order to increase the frequency range of the on-wafer measurement system to above 100 GHz, the parasitics due to the connection between the samplers and the device under test need to be eliminated. This required the integration of the high speed sampler IC with the GaAs probe tip.

In this paper, the development of a new configuration of the nonlinear transmission line (NLTL) pulse generator, the Nonlinear Impedance Transformer (NIT), and a GaAs wafer probe system will be presented. The NIT pulse generator has subpicosecond output fall time and >100 psec input fall times. By incorporating the NIT pulser and a two diode

sampling bridge in a micromachined GaAs IC probe, a subpicosecond oscilloscope probe has been demonstrated for time domain on-wafer measurements. In addition, a companion pulse generator probe has also been developed.

### A Nonlinear Impedance Transformer

Recently there have been a great deal of work on fast transient generation using shock wave devices. One such device, the NLTL has been used to generate 2 psec transients for high repetition rate sampling applications.<sup>5</sup> These devices are very lossy, with about 8 dB of insertion loss at DC. This high loss limits the input transition time to 30-40 psec, therefore requiring high drive frequencies, typically above 4 GHz and high RF drive powers, typically 28-30 dBm. We have developed a novel pulse sharpener circuit which allows >100 psec input fall time drives and can be driven by a digital FET. The principle of nonlinear wave propagation is the same, except that the characteristic impedance and delay associated with each section has been transformed smoothly from the slower input condition to the fast output condition. The ohmic contact resistance was reduced to 15 ohm-micron by using a cap layer before annealing. In addition, the CPW transmission line loss was reduced by suspending the whole transmission line 1 micron above the substrate. A 3 psec, 6V predriver pulser was developed with only 20 diodes using hyperabrupt doping profile MBE material. In addition a long 40 diode NIT pulser was built using abrupt doping profile MBE material for subpicosecond fall time.

### GaAs Wafer Probe System

Since the GaAs IC is brittle, we have developed a parallelogram flexure probe which allows a controlled normal force to be applied to the tip. The GaAs probe assembly is shown in Fig. 1.

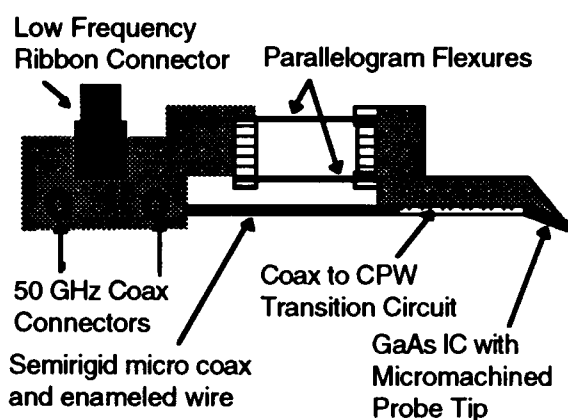


Fig.1. GaAs parallelogram flexure Probe consist of four 50 GHz coax connectors plus two 10-pin ribbon connectors and a micromahined GaAs MMIC tip circuit.

The main body consists of four 50 GHz coax connectors plus two 10-pin low frequency ribbon connectors. RF connectors are placed at the side of the main body in order to allow good access with a wrench, allowing the ribbon connectors to be placed on top of the main body. A micromachined GaAs IC is placed on a tip package connected to the main body by two 2 mil BeCu parallelogram flexure units. RF connectors are connected to the tip package using semi-rigid micro coax, and enameled wires are used to connect the ribbon connector to the tip package. There is an 8 degree angle between the tip and the device under test, and 2 grams of weight is required to make contact without any skating.

A probe CPW pitch of 40  $\mu\text{m}$  was selected as a compromise between CPW conduction and radiation losses at 350 GHz. The GaAs IC tip area was initially mechanically lapped and polished to within 20  $\mu\text{m}$  of the probe tip at an angle of 20 degrees to normal. Then Clorox<sup>®</sup> bleach was used to chemically etch the tip area to allow the user to see the exact location of the tip making contact to the device under test. Two micron thick of alternating layers of Au /

nickel (2000  $\text{\AA}$  / 1000  $\text{\AA}$ ) evaporation was chosen as probe contact material because it could be fabricated in small sizes and had reasonable wear resistance.

A micromachined GaAs IC was built by integrating a two diode sampling bridge and an abrupt NIT pulser with the GaAs probe tip. The hyperabrupt NIT driver and the micromachined GaAs IC were epoxied in the tip package, thus bringing a high speed sampling scope to within 140  $\mu\text{m}$  of the device under test. An 880 fsec fall time was measured at the output of the 40 diode abrupt NIT as shown in Figs. 2,3. This 880 fsec system rise time is root-mean-squares convolution of the 40 diode NIT fall time, the sampling scope aperture time and the GaAs tip transition time. Therefore, the on-wafer oscilloscope probe has 500 GHz bandwidth.

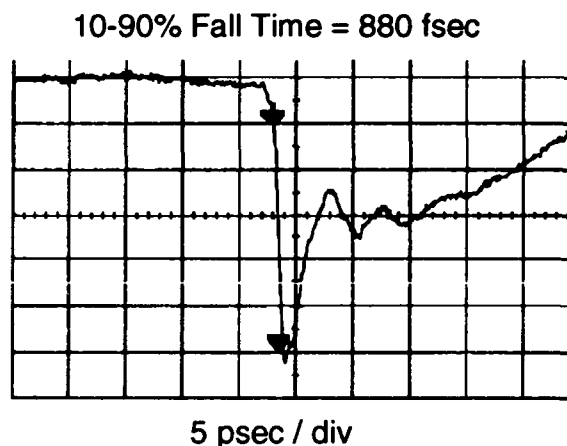


Fig.2. An 880 fsec fall time was measured at the output of a 40 diode NIT pulser by a subpicosecond on-wafer oscilloscope probe

In addition, a second micromachined GaAs IC was built by integrating the NIT pulse sharpener with the GaAs probe tip. With 2.5 GHz probe input and the probe tip in contact to a very long 40 micron pitch CPW transmission line, 1.6 psec fall time was measured at the output of the probe using the electrooptic sampling system<sup>6</sup>. Since this edge contains Fourier components greater than 250 GHz, it now becomes possible to use this probe and a resistive bridge or an attenuator<sup>7</sup> for time domain network analysis up to 250 GHz.

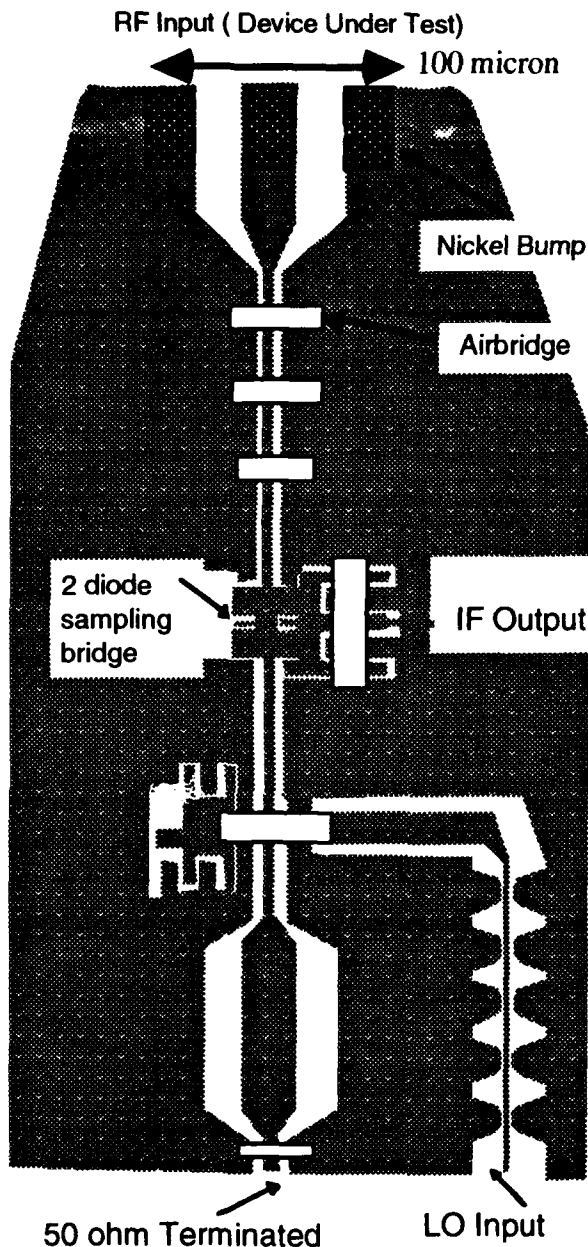


Fig.3: On-wafer GaAs oscilloscope probe

### Summary

This is the first time on-wafer measurement has been extended to subpicosecond regime. A novel pulse sharpener with improved diode and transmission line losses was developed for subpicosecond output fall times and 100 psec input fall times. By using this novel pulse sharpener, a subpicosecond oscilloscope probe and a 1.6 psec pulse generator probe was built for time domain on-wafer measurements.

### Acknowledgment.

This work was supported by Defense Advanced Research Projects Agency (DARPA) / Office of Naval Research (ONR) contract N00014-89-J-1842. We are grateful to Pauline Prater for her assembly expertise. Mohammad Shakouri acknowledges a Hewlett Packard Fellowship.

### References

1. P. M. Asbeck, M.F. Chang, K.C. Wang, D.L. Miller, G.J. Sullivan, N.H. Sheng, E. Sovero, and J.A. Higgins, "Heterojunction Bipolar Transistors for Microwave and Millimeter-wave Integrated Circuits," *IEEE Trans. Microwave Theory Tech.*, vol. MTT-35, no.12, pp. 1462-1470, 1987
2. U. K. Mishra, A. S. Brown, and S. E. Rosenbaum, "DC and RF performance of 0.1  $\mu\text{m}$  gate length AlInAs-GaInAs pseudomorphic HEMT's" *Tech. Dig.*, 1988 Int. Electron Device Meeting, San Francisco, CA, Dec 4-11, 1988.
3. R. Majidi-Ahy, C. Nishimoto, M. Riazat, M. Glenn, S. Silverman, S. Weng, Y. Pao, G. Zdasiuk, S. Bandy, and Z. Tan, "100 GHz high-gain InP MMIC cascode amplifier," 1990 GaAs IC symp., New Orleans, LA, Oct. 7-10, 1990.
4. M. S. Shakouri, H. Matsuura, B.A. Auld, and D. M. Bloom, "Active Probes for Millimeter-Wave On-Wafer Measurements," 1991 ARFTG 38th Conference, San Diego, CA., Dec. 5-6, 1991.
5. R.A. Marsland, C.J. Madden, D. W. Van Der Weide, M.S. Shakouri, and D. M. Bloom, "Monolithic Integrated Circuits for for mm-wave Instrumentation," 12th Annual GaAs IC Symposium, Technical Digest, October 1990.
6. K.J. Weingarten, M.J. W. Rodwell, and D.M. Bloom, "Picosecond Optical Sampling of GaAs Integrated Circuits," *IEEE J. Quant. Elect.* QE-24, 1988, pp. 198-220.
7. R. Y. Yu, M. Kamegawa, M. Case, M. Rodwell, and J. Franklin, "A 2.3 ps time-domain reflectometer for millimeter-wave network analysis," *IEEE Microwave Guided Wave Lett.*, Vol. 1, pp.334-336, Nov. 1991.

# Highly Reproducible Optoelectronic Wafer Probes with Fiber Input

M. D. Feuer, S. C. Shunk, and M. C. Nuss

*AT&T Bell Labs, 101 Crawfords Corner Road, Holmdel, New Jersey 07733-3030*

P. R. Smith and H. H. Law

*AT&T Bell Labs, 600 Mountain Avenue, Murray Hill, New Jersey 07974-0636*

C. A. Burrus

*AT&T Bell Labs, 791 Holmdel-Keyport Road, Holmdel, New Jersey 07733-0400*

## Abstract

We have constructed optoelectronic wafer probes with fiber pigtails and demonstrated accurate, reproducible measurements of the complex reflection coefficient  $S_{11}$  at frequencies up to 125 GHz. Vector accuracy enhancement routines, based on the measurement of known standard devices, are used to remove the effects of tip reflections and other systematic errors. Ground-bridging straps are shown to suppress the mode conversion errors which result from asymmetric excitation of the coplanar waveguide probe.

## Introduction

Optoelectronic testing driven by ultrafast laser pulses offers a broad-bandwidth alternative to conventional, purely electronic S-parameter measurements. Movable wafer probes, which can be used on any device wafer suitable for microwave probing, have demonstrated bandwidth of 200 GHz [1,2]. These optoelectronic probes use photoconductive switches to define the stimulus pulses and sampling intervals, with transmission lines and metal contact bumps at the tips to bring the signals to and from the device pads. To achieve accuracy in the Fourier-transformed, frequency-domain data, one must remove systematic errors, by applying vector calibration techniques based on probing known standard devices [2]. However, microscopic flexing of the tips under the stress of wafer probing can disturb the alignment of the photoconductive gaps to the input optical beams, leading to irreproducible errors which cannot be calibrated out. In the present work, we have bonded optical fibers to the probe tips to achieve greatly improved reproducibility and calibration accuracy in the S-parameter measurements.

We have made calibrated reflection measurements of a variety of passive devices, and have demonstrated the importance of mode conversion in coplanar waveguide (CPW) structures. Accurate results can be ensured by the addition of ground-bridging straps to the basic CPW probe.

## Method

Probe tip design and fabrication have been presented in detail in [2]. In brief, gold CPW transmission lines were defined lithographically on a commercial silicon-on-sapphire substrate, with photoconductive gaps of implant-damaged Si located symmetrically on the signal line, approximately 1 mm from the contact points. The contact bumps were formed by plating 35  $\mu\text{m}$  of nickel with a 4  $\mu\text{m}$  gold overlayer. For some measurements, ground-bridging straps were added to the basic probes to suppress the antisymmetric mode. The straps were sections of gold-mesh tape, typically 100  $\mu\text{m}$  wide, attached with conductive epoxy. Figure 1 shows the layout of a probe tip with ground straps.

To bring the optical signals to the stimulus and sampling gaps, single-mode fibers with cleaved ends were bonded to the back of the sapphire substrate. Since the fibers were not lensed, optical coupling to the photoconductive gaps was not optimally efficient, but ample power was available from the mode-locked Ti-sapphire laser source, and the gap separation of 80  $\mu\text{m}$  provided reasonably low crosstalk.

The Ar-pumped, mode-locked Ti-sapphire laser was tuned to 760 nm, and the power launched into the fibers was limited to 10 mW per fiber. A variable optical delay was introduced before fiber launch to sweep the relative delay of the sampling pulses, and the stimulus beam was mechanically chopped to enable lock-in detection of the signal. This eliminates signal

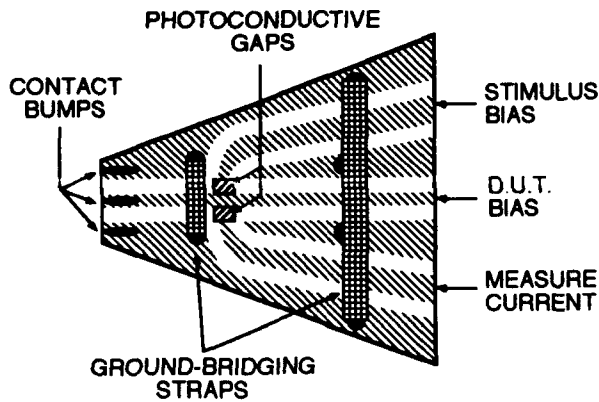


Figure 1. Schematic layout of optoelectronic wafer probe with ground-bridging straps. Optical pulses are introduced through the back of the probe substrate. The system provides high bandwidth, throughput, and accuracy.

due to dark current leakage in the gaps, but not optical crosstalk due to overlap of the stimulus pulse on the sampling gap. Crosstalk was eliminated by the calibration procedures discussed below.

The general methods of photoconductive stimulus/sampling have been discussed by Auston [3]. In brief, we applied a 10 Volt dc bias to the stimulus gap and monitored the average current from the sampling gap under zero bias. Optical pulses striking the stimulus gap launch electrical pulses along the line. When the delayed optical pulse strikes the sampling gap, current flow is proportional to the voltage present at that point on the signal line at that instant, whether due to the incident or reflected pulse. The average sampled current is monitored as a function of delay time to obtain  $V(t)$  curves.

S-parameters are calculated from the time-domain data by Fourier transform, and their accuracy is greatly improved by vector accuracy enhancement routines [4]. The effects of tip reflections, back-end reflections, and dispersion and loss in the CPW transmission lines are removed, as are all errors which are systematic and local in frequency. Vector accuracy enhancement also eliminates the need for time-gating of signals, since the incident pulse is extracted from the measurements of the known standard devices. A full discussion of these issues is too lengthy to present here, but the actual analysis procedure we used was:

- 1) Normalize each  $V(t)$  trace to the peak of the incident pulse, to eliminate scaling errors due to slow drift or fluctuations in laser power or fiber launch efficiency.
- 2) Apply the Fourier transform to generate frequency-domain curves.
- 3) Divide by the Fourier transform of an assumed Gaussian incident pulse to generate raw (uncorrected) S-parameters. This is just a convenience for looking at intermediate results:

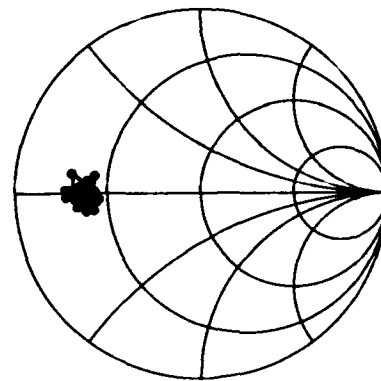


Figure 2. S11 of a thin-film resistor with a dc resistance of 12.5 ohm, from dc to 125 GHz at 2.5 GHz intervals, after full correction with vector accuracy enhancement.

the final, corrected result is entirely insensitive to the assumed pulse shape.

- 4) Use raw S-parameters of short circuit, open circuit, and resistive load standard devices to calculate the error correction terms.
- 5) Apply the error correction terms to the raw S-parameters of the Device Under Test (D.U.T.) to obtain the corrected S-parameters.

The calibration standard devices used for this work, and their definitions, were the same as those used for conventional microwave probing: the short and load standards were on a commercial calibration tile, while the open standard was the probe suspended in air. The calibration tile is supplied by Cascade Microtech for operation up to 40 GHz, but the small size of the standard devices suggests that they may be useful to much higher frequencies. Although the method is fully generalizable to two-port measurements, the present report includes only single-port results.

## Results and Discussion

The  $V(t)$  curves for short circuits, open circuits, resistors and CPW open stubs, measured with the basic fiber probe (no ground straps), are very similar to those observed with the free-space optics probe of ref [2]. As expected, there are slight reflections from the probe contact points in addition to the actual device reflections.

As intended, the fiber probe was found to be insensitive to the flexing of the tip under wafer contact, leading to much more practical operation than previous probes fed by free-space beams [1,2]. When devices were re-probed after ~1 hour of system operation, a scaling error of up to 10% was observed, apparently due to variation in the optical power in the fibers. After re-scaling, the residual error was 1-2% of the incident peak height (-34 db). The cause of this residual error is not known.

After Fourier transform and accuracy enhancement as described above, we obtain the

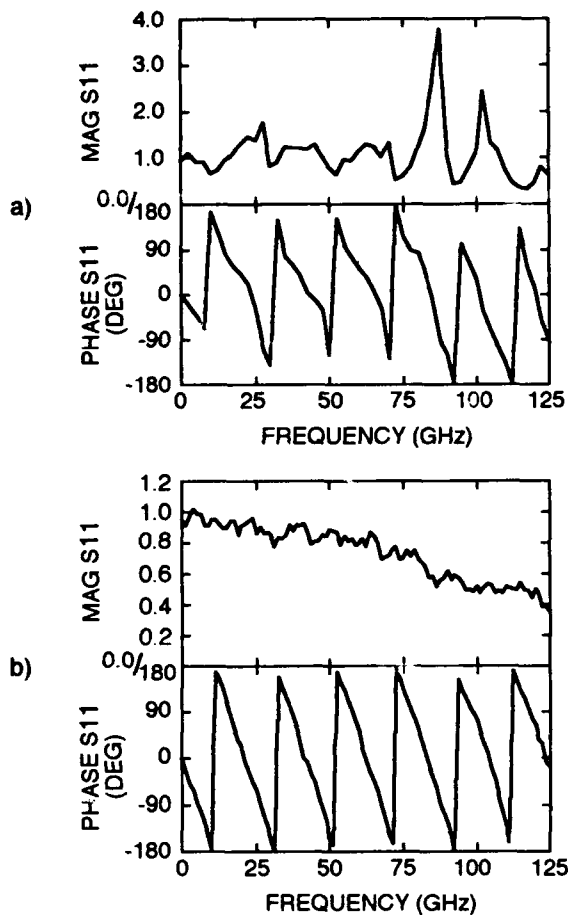


Figure 3. Magnitude and phase of S11 of 3.2-mm open stub transmission line. (a) basic fiber probe without ground-bridging straps. (b) Fiber probe with ground-bridging straps. Calibration standards and definitions are the same as for conventional microwave probing.

complex reflection coefficient S11 as a function of frequency. The Smith chart of Figure 2 shows S11 of a 12.5 ohm resistor device measured with the fiber probe, for frequencies from zero to 125 GHz. An ideal resistor would have a value of  $-0.60 + j0.0$  at all frequencies. Our measured value of  $-0.63 \pm 0.04 + j(-0.01 \pm 0.04)$  compares favorably, and its scatter is less than half that observed with a probe based on free-space optics [2].

The importance of mode conversion effects becomes evident when devices with ring-shaped ground planes are measured. Figure 3 shows an example, a CPW open stub transmission line with a ring ground. The magnitude of S11 for an ideal open stub should begin at unity and decrease smoothly as losses increase with frequency, while the phase should begin at zero and decrease nearly linearly. The results obtained with a simple CPW probe, shown in Fig. 3a, are far from ideal. Although the measured S11 shows qualitatively correct phase winding, the magnitude varies widely, including excursions above unity which appear to imply gain, impossible for this passive device. The

explanation is that the open stub actually reflects back more power to the sampling gap than does the probe open in air, because of mode conversion. When the laser pulse strikes the stimulus gap, the wave launched in the CPW line on the probe tip is concentrated on one side of the line, in a combination of symmetric and antisymmetric modes which resembles a slotline mode. When the probe is open in air, both symmetric and antisymmetric components are reflected with a positive polarity, sending the pulse back along the line on the same side as it arrived, and presenting a rather weak signal to the sampling gap on the other side. The ring ground of the open stub, however, connects the two outer contact points of the probe and presents a short circuit to the antisymmetric mode. This short circuit reflects the antisymmetric mode with a negative polarity, causing the combined mode to shift to the opposite side of the line from that on which it arrived, and presenting a strong signal to the sampling gap. Thus the open stub device with the ring ground has a stronger reflection than the open standard, yielding the erratic S11 curve seen in Fig. 3a.

The best way to avoid this problem is to put the ground-bridging connections on the probe tip itself, so that the antisymmetric mode will be suppressed as the pulse is launched, and the signal at the contact points will be predominantly the desired symmetric CPW mode. The resulting probe tip can be used successfully either with ring-ground geometries, as shown in Fig. 3b, or with linear strip grounds.

## Summary

We have constructed movable optoelectronic wafer probes based on photoconductive stimulus and sampling. Optical inputs by fiber pigtail enable reproducible measurements on any wafer suitable for microwave probing, and accuracy enhancement routines have been developed to calibrate the probes. The probes present a broadband 50 ohm impedance for stable operation of the device under test.

When driven by a mode-locked Ti-sapphire laser, the probes demonstrated calibrated S11 measurements with a scatter of  $\pm 0.04$  over a bandwidth of 125 GHz. Ground-bridging straps were shown to be effective in suppressing mode-conversion errors.

## Acknowledgments

The authors wish to thank A. Borges, K.F. Brown-Goebeler, and B. Tell for experimental contributions and T. Koch for continuing support.

## References

1. M. Scheuermann, R. Sprik, J.-M. Halbout, P.A. Moskowitz, and M. Ketchen, "Ultra-High Bandwidth Detachable Optoelectronic Probes," in *OSA Proceedings on Picosecond Electronics and*

- Optoelectronics, vol. 4, ed. by T.C.L.G. Sollner and D.M. Bloom, (Optical Society of America, Washington, D.C., 1989), pp. 22-26.
2. M.D. Feuer, S.C. Shunk, P.R. Smith, M.C. Nuss, and H.H. Law, "100 GHz Wafer Probes Based on Photoconductive Sampling", to be published in Photonics Technol. Lett., March, 1993.
3. D.H. Auston, "Ultrafast Optoelectronics," in Ultrashort Laser Pulses and Applications, ed. by W. Kaiser, (Springer-Verlag, Berlin, 1988).
4. J. Fitzpatrick, "Error Models for Systems Measurement", Microwave J., pp. 63-66, May 1978.

## Electro-Optic Sampling of High Speed Nonlinear Devices

Kok Wai Chang and Wayne V. Sorin

*Hewlett-Packard Laboratories, Palo Alto, California 94303*

### Abstract

An electrooptic measurement system which combines the advantages of equivalent-time sampling with differential detection is used for the characterization of high speed nonlinear electronic devices.

This paper addresses the characterization of high-speed nonlinear devices using direct and indirect electrooptic (EO) sampling. In order to overcome the large low-frequency amplitude noise of the pulsed laser, previous electrooptic measurement systems [1-5] employed AM modulation to detect the EO signal at frequencies where the amplitude noise dropped below the shot noise. However, the characteristics of many high speed nonlinear devices such as Step Recovery Diodes (SRDs), Resonant Tunneling Diodes (RTDs) and SRD-driven nonlinear transmission lines do not function properly when their input signals are chopped and therefore cannot be characterized by this signal detection scheme.

A fast-offset/averaging detection scheme [6] for EO sampling systems has been proposed to avoid signal chopping for the testing of devices that are sensitive to external AM modulation. This detection scheme is similar to equivalent-time sampling [6] except that the offset frequency is increased to a value where the amplitude noise drops below the shot noise. For many lasers this means an offset frequency  $\Delta f$  of 500 kHz or greater. The large offset frequency imposes a relatively large measurement bandwidth of 25 MHz or more for testing nonlinear devices that generate 50 or more harmonics. This degrades sensitivity since larger bandwidth and higher noise receivers must be used. Recently this signal detection scheme was used together with differential detection to

reduce the common-mode amplitude noise of a gain-switched laser-diode-based EO sampling system [7]. The elimination of the amplitude noise allowed the offset frequency to be reduced. In this paper we report on an electrooptic sampling system based on a fiber-grating-compressed Nd:YAG mode-locked laser with 2 ps of temporal resolution that combines the advantages of both the fast-offset/averaging detection scheme and the differential detection scheme for the characterization of high speed nonlinear devices such as SRDs, RTDs and SRD-driven nonlinear transmission lines.

Fig.1 shows the experimental setup for the mode-locked Nd:YAG laser and fiber-grating pulse-compressor-based electrooptic sampling system which uses an GaAs probe tip as a indirect longitudinal electric field sensor. The incident and reflected beams are separated by manipulation of their polarization [6] in such a way that the reflected beam produces a linear polarization inclined at 45 degrees to the axes of the polarization beamsplitters when there is no applied field on the GaAs probe tip. The reflected beam polarization state will become inclined at  $45 \pm \delta$  degrees to the axes of the polarization beamsplitters when there is an longitudinal electric field overlapping the GaAs probe tip. The vertical component is directed by the first polarization beamsplitter onto the first photodiode. The horizontal component is rotated by the Faraday rotator and the half wave plate to become vertically polarized and is then directed by the second polarization beamsplitter onto the second photodiode. A differential amplifier is then used to amplify the photocurrents from the two photodiodes and to suppress the common-mode intensity noise. The amount of common-mode rejection is measured by a low frequency RF spectrum analyzer.



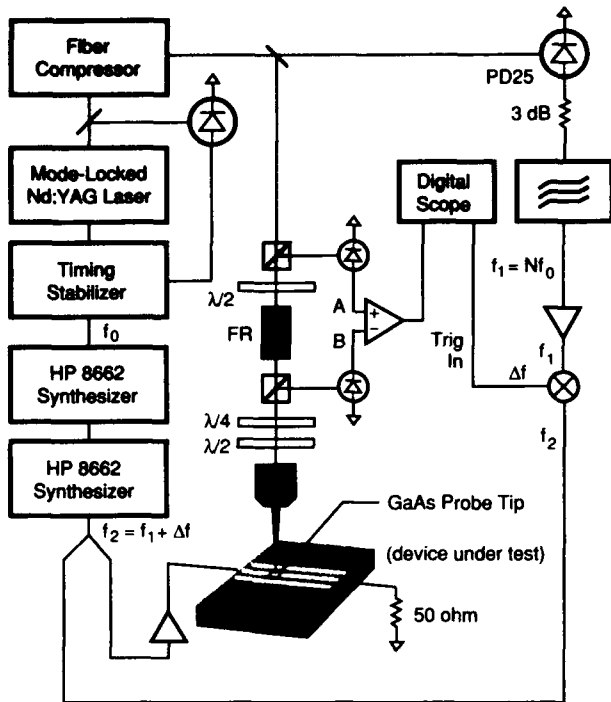


Figure 1. Schematic for electrooptic sampling system.

Ref -60.0 dBm  
5 dB/div

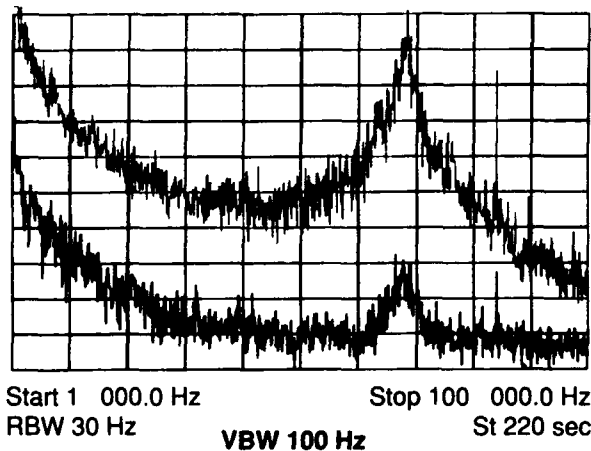


Figure 2. Intensity noise spectrum of mode-locked Nd:YAG with (lower trace) and without (upper trace) differential detection.

Fig.2 shows the measured intensity noise of the mode-locked Nd:YAG laser with and without differential detection. The top trace corresponds to the low-frequency intensity noise associated with either the vertical or the horizontal component of the reflected laser beam. The lower trace shows 20-30 dB

suppression of laser intensity noise by differential detection over the frequency range from 1 kHz to 100 kHz.

As discussed earlier, reducing the low frequency intensity noise allows the use of a smaller offset frequency and hence a lower bandwidth receiver. In our experiment, offset frequencies between 5 to 20 kHz are used. This means only 250 kHz to 1 MHz of receiver bandwidth is required to measure switching events that generate 50 harmonics of the input sine wave. Fig.3 shows the EO sampling spectrum of an SRD measured by an external GaAs probe with (lower trace) and without (upper trace) differential detection. The SRD is driven by a 640.0064 MHz sine wave. From this data one can see that the differential detection scheme suppresses the common-mode intensity noise and allows the detection of the EO sampling signal at a multiple of 6.4 kHz. A fast digitizing oscilloscope is used as a signal averager to further improve the signal-to-noise. The trigger signal for the digitizing oscilloscope is provided by mixing the input electrical signal of frequency  $nf_0 + \Delta f$  with the  $n^{th}$  harmonic  $nf_0$  of the mode-locked laser. The measured waveform is shown in Fig. 4 for a GaAs double heterostructure SRD [8] that is driven by an input sine wave at a frequency of 1900.0192 MHz. The corresponding fall time of the switching event in the SRD is measured to be 8.7 ps.

Ref -60.0 dBm  
5 dB/div

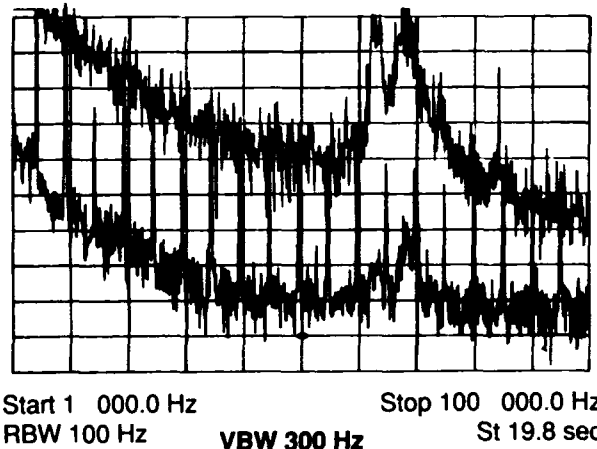


Figure 3. EO sampling frequency domain spectrum of a 640 MHz SRD measured by an external GaAs probe with differential detection (lower trace) and without differential detection (upper trace).

Direct electrooptic sampling was employed to measure the characteristics of a resonant tunneling

diode fabricated on a GaAs substrate. Fig. 5 shows the fall time of 5 ps for the RTD driven sinusoidally at 1920.0192 MHz. The same system was also used to measure the characteristics of an SRD-driven nonlinear transmission line. The SRD is driven by an input sine wave at 640.0064 MHz. By probing the input and output of the nonlinear transmission line, a compression ratio of 7.7 to 1 was measured. The corresponding measured rise time at the input and output of the nonlinear transmission is 40 ps and 5.5 ps respectively, as shown in Fig. 6 and Fig. 7.

In summary, we have combined the advantage of equivalent time sampling with differential detection to demonstrate an electrooptic sampling system for the characterization of high-speed nonlinear electronic devices.

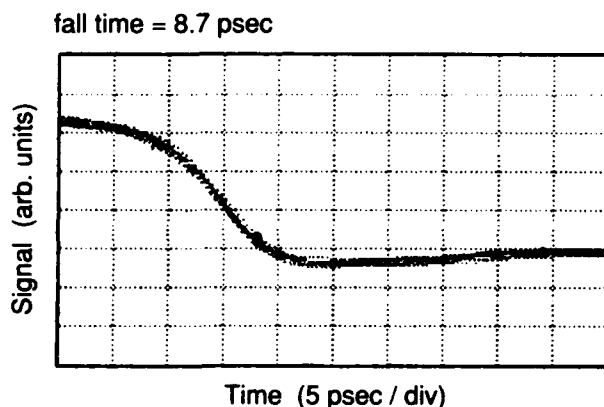


Figure 4. EO sampling response of a GaAs double heterostructure SRD driven by a 1920.0192 MHz sine wave.

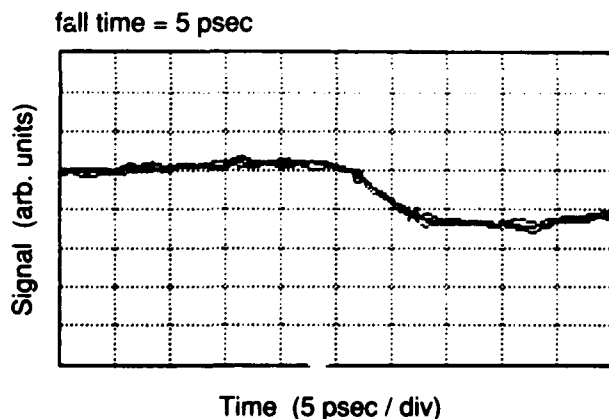


Figure 5. EO sampling response of a resonant tunneling diode.

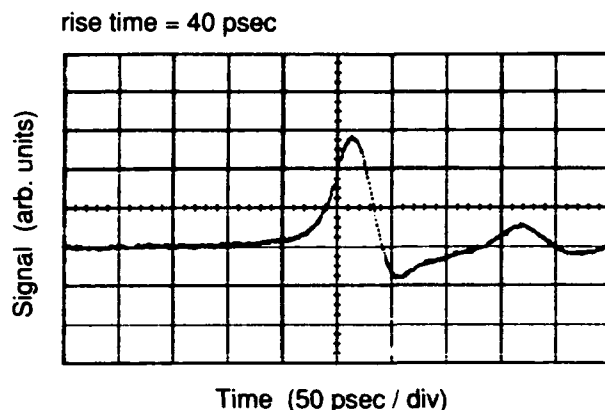


Figure 6. EO sampling response at the input of a SRD-driven nonlinear transmission line.

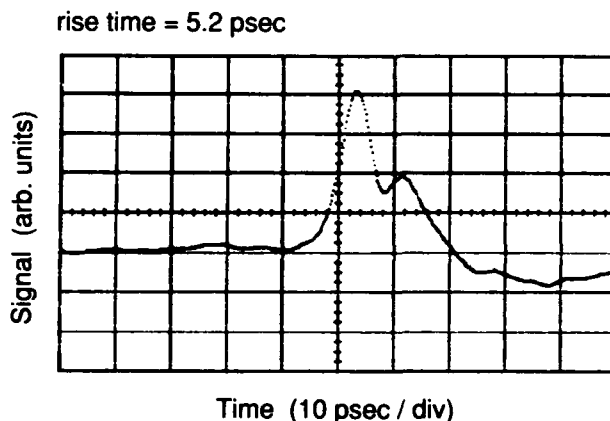


Figure 7. EO sampling response at the output of a SRD-driven nonlinear transmission line.

#### References:

1. J.A. Valdmanis, G. Mourou, and C.W. Gabel, "Picoscond Electro-Optic Sampling System", *Appl. Phys Lett.* 41, 211-212, 1982.
2. B.H. Kolner and D.M. Bloom, "Internal Electro-Optic Sampling in GaAs Integrated Circuits", *IEEE J. Quantum Electron.*, QE-22, 79-93, 1986.
3. K.J. Weingarten, M.J.W. Rodwell, and D.M. Bloom, "Picosecond Optical Sampling of GaAs Integrated Circuits", *IEEE J. Quantum Electron.*, QE-24, 198-220, 1988.
4. J.M. Wiesenfeld, "Electro-optic sampling of high-speed devices and integrated circuits", *IBM Journal of Research and Development*, vol.34, No. 2/3, 141-161, 1990.

5. M. Shinagawa and T. Nagatsuma, "A Laser-Diode-Based Picosecond Electro-Optic Prober for High-Speed LSIs", *IEEE Trans. Instrum. Meas.*, Vol. 41, No. 3, 375-380, 1992.
6. K.J. Weingarten, "Galium Arsenide Integrated Circuit Testing Using Electrooptic Sampling", PhD. Thesis, Edward L. Ginzton Laboratory of the W.W. Hansen Laboratories of Physics, Stanford University, Dec. 1987.
7. T. Nagatsuma, M. Yaita and M. Shinagawa, "External Electro-optic Sampling Using Poled Polymers". submitted to *Japn. J. Appl. Phys.*
8. M.R.T. Tan, S.T. Wang, D.E. Mars and J.L. Moll, "12 ps GaAs Double Heterostructure step recovery diode", *Electron. Lett.*, Vol. 28, 673-675, 1992.

# 120-GHz-Bandwidth Characterization of Microwave Passive Devices Using External Silicon-On-Sapphire Photoconductive Sampling Probe

J. Kim, J. Son, S. Wakana\*, J. Nees, S. Williamson, J. Whitaker, and G. Mourou

*Center for Ultrafast Optical Science, University of Michigan, 2200 Bonisteel, 1006 IST,  
Ann Arbor, Michigan 48109-2099*

\*S. Wakana is also at Fujitsu Laboratory Ltd.

## Introduction

Conventional purely electronic measurement instruments such as vector network analyzers, spectrum analyzers and sampling oscilloscopes are not effective at above 100 GHz. One major limitation is imposed by the connectors and waveguides needed for signal coupling between the test instrument and the device under test. To overcome those limitations of present measurement techniques, we have developed a photoconductive probe sampling technique which can be applied to the measurement of S-parameters of mm-wave circuit components with a 120-GHz measurement bandwidth [1]. The photoconductive probe sampling technique combines the ultrafast optical technology of 120-fs Ti-Sapphire short pulse laser [2] and microfabrication technology of Silicon-On-Sapphire (SOS) photoconductive sampling probe, which consists of a high-impedance interdigitated photoconductive switch. The probe technology has demonstrated a 2.1 ps temporal resolution and low-invasiveness making this very attractive for external circuit testing of mm-wave circuits with a 120-GHz measurement bandwidth.

The technique is based on high-impedance external sampling with 2.1-ps temporal resolution, 8- $\mu\text{m}$  spatial resolution and high signal-to-noise ratio. The measurement point can be very close to the device under test. Therefore, the technique minimizes interconnection discontinuities and consequently errors and uncertainties from device de-embedding procedures. To demonstrate the capability of the photoconductive probe sampling technique for mm-wave circuit testing, we applied the technique to characterize mm-wave band-block filters and phase delay lines which are being used in MMICs up to 200 GHz.

## Experiments and results

Figure.1 is an SEM picture of the photoconductive(PC) sampling probe. It consists of a high impedance metal-semiconductor-metal (MSM) photoconductive switch on a damaged Silicon-On-Sapphire substrate and a Ti contact tip of 3- $\mu\text{m}$  height. Figure.2 shows the experimental set-up used to measure the characteristics of band-block filters of microstripline

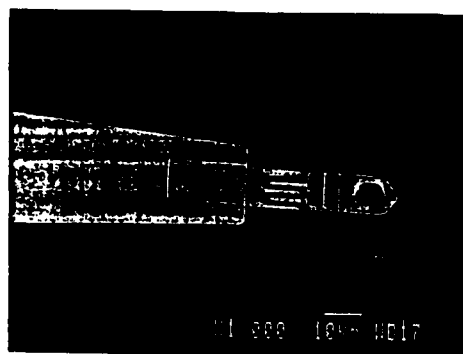


Fig.1 SEM picture of photoconductive sampling probe

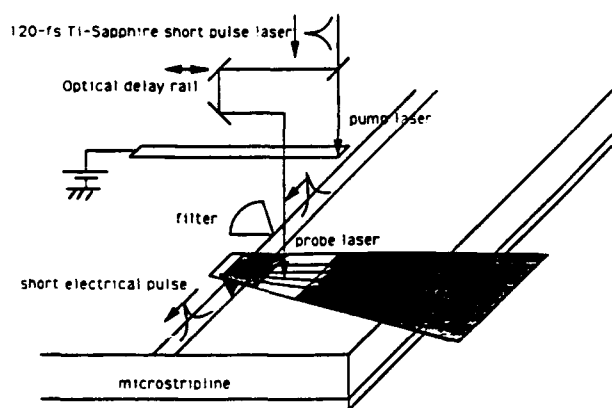


Fig.2 Experimental set-up to measure the transmitted pulse waveform from the band-block filter

structure. The 70- $\mu\text{m}$  wide microstripline and the band-block filter were fabricated on Low-Temperature-Grown GaAs (LT-GaAs) substrate of 100- $\mu\text{m}$  thickness. The structure is part of a 90 GHz to 180 GHz InP-based HEMT doubler which has been demonstrated by the authors (Fig.3) [3]. The subpicosecond carrier lifetime of LT-GaAs enables the generation of 1-ps electrical pulses using a 120-fs short-pulse pump laser [4]. Also, the response of the silicon-on-sapphire photoconductive switch on the probe is  $< 2$  ps, so that the short electrical pulse can be sampled with 2-ps temporal resolution using the short pulse probe beam. The probe touches the microstrip and measures the amplitude of an

electrical signal at a specific point in time when the probe laser pulse is hitting the PC switch on the probe. By changing the optical delay between the pump and probe laser beams, one can measure an entire electrical pulse form.

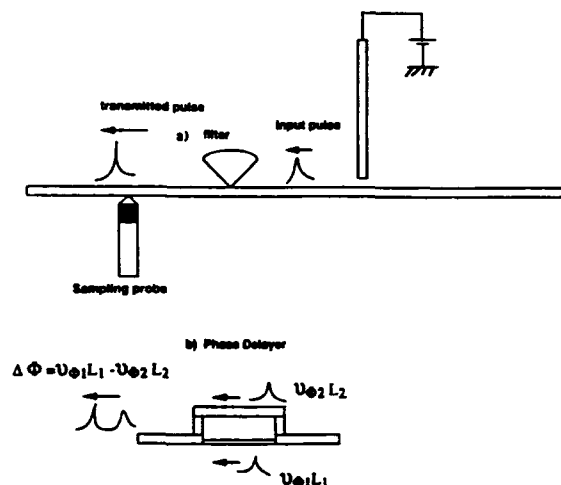


Fig.3. Test structure a) for the characterization of band-block filter, b) for measurement of phase delay of microstrip phase delay line.

Transmitted waveforms were measured from 80-GHz and 100-GHz band-block filters using the probe. The 80-GHz band-block filter has a 212- $\mu\text{m}$  radius with  $60^\circ$  angle, and the 100-GHz band-block filter has a 167- $\mu\text{m}$  radius with  $60^\circ$  angle. Figure.4 (a) shows the probe position and the test structure containing microstrip, band-block filter and photoconductive switch, which generates the short electrical pulse. The frequency spectrum of the transmitted pulses was calculated by taking their Fourier transform. Figure.5 shows the Fourier spectra of the transmitted pulses. The result shows that the 80-GHz band-block filter, which was designed using a commercially available software package, is in fact filtering the signal at a slightly lower frequency 70 GHz. Filtering is also observed at 150 GHz. The spectral component at 70 GHz is about 1 % of the dc

component. Also, the 100-GHz band-block filter is filtering at 100 GHz and 170 GHz. By comparing the Fourier spectra of input, transmitted and reflected pulses, S-parameters of these filters could be calculated. This permits direct evaluation of measured characteristics at mm-wave frequencies as necessary for optimizing circuit performance.

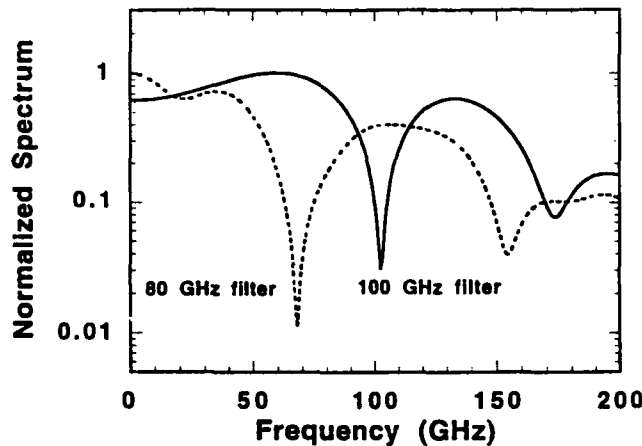


Fig.4 Frequency spectrum of transmitted pulses from the filters.

In addition to the characterizations of mm-wave band-block filters, the phase delay of a microstrip delay line has also been evaluated. Figure.4 (b) shows the test structure used for these measurements. It consists of a short line of length  $L_1$  and delay line of length  $L_2$ . Figure.6 shows a phase delay of two measured pulses propagating along two different paths. At 100 GHz, the measured phase difference is  $\Delta \Phi = -294^\circ$  ( $\Delta \Phi = \nu_{\Phi 1} L_1 - \nu_{\Phi 2} L_2$ ). The difference between the nominal (designed) value ( $\Delta \Phi = -350.8^\circ$  at 100 GHz) and measured value may arise from inaccurate knowledge of the exact phase velocity, especially in the calculation at very high frequencies. Thus although at 10 GHz the difference between the measured and nominal values is  $\Delta \Phi_{\text{nom}} - \Delta \Phi_{\text{meas}} = 6.7^\circ$ , at 100 GHz the discrepancy is much larger ( $56.8^\circ$ ).

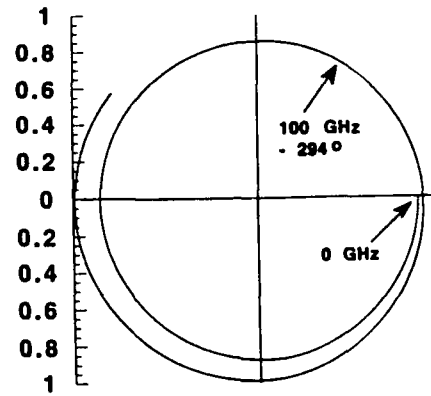


Fig.5 Phase delay between two different paths

Also, we applied the external SOS photoconductive sampling probe for S-parameter measurement of mm-wave microstrip low-pass filter. Fig.6 shows experimental set-up. The probe measures the input signal to the filter and the transmitted signal from the filter. By taking Fourier transform, we can calculate the S-parameter of the filter. The measured S-parameter and the simulation result from a Touchstone program are shown in Fig.7. This demonstrate feasibility of photoconductive probe sampling for S-parameter measurement with  $> 120$  GHz bandwidth.

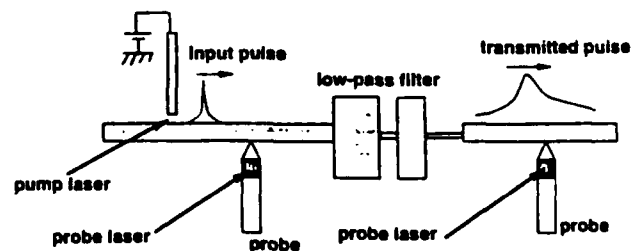


Fig.6 Experimental set-up to measure S-parameter of mm-wave low-pass filter.

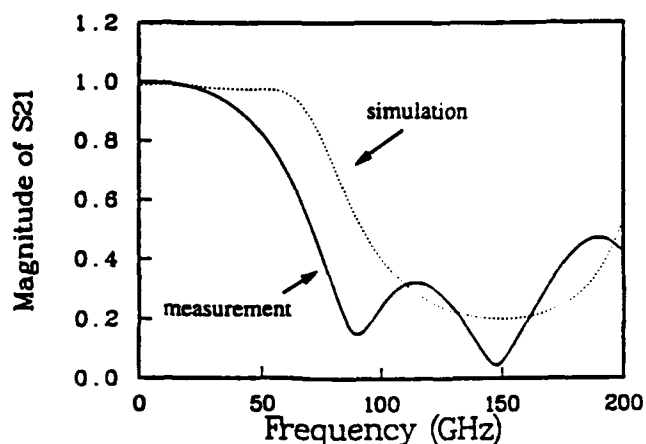


Fig.7 Measured and simulated results of S21

## Conclusions

A new photoconductive probe sampling technique which can be applied to mm-wave circuit testing has been developed and demonstrated. The probe technology has shown measurements exceeding 120 GHz and permits reduction of interconnection discontinuities and errors by de-embedding procedures. The probe technology was applied to the characterization of mm-wave band-block filters used in InP-based heterostructure MMIC's for 90 GHz to 180 GHz frequency doubling. MM-wave delay lines have also been characterized and the properties of transmission lines on thin semiconductor substrates

have been studied. The results demonstrate the capability of mm-wave circuit testing using the photoconductive probe sampling technique.

## Acknowledgment

This work was supported by Fujitsu Laboratories Ltd, the National Science Foundation through the Center for Ultrafast Optical Science under STCPHY8920108, the Air Force Systems Command under contract number F19628-90-k-0015, and the Army Research Office under contract number DAAL-03-89-k-0071 and DAAL-03-92-G-0109.

## References

- [1] J.Kim, Y-J.Chan, S. Williamson, J.Nees, S.Wakana, J.Whitaker, D.Pavlidis, 1992 IEEE GaAs IC Symposium.
- [2] D.Spence, P.Kean and W.Sibbett, Opt. Lett., 16, 42(1991)
- [3] Y.Kwon, D.Pavlidis, P.Marsh, M. Tutt, G.I. Ng and T. Brock, Second International Symposium on Space Terahertz Technology, 1991
- [4] S. Gupta, M. Frankel, Y. Valdmanis, J. Whitaker and G. Mourou, Appl. Phys. Lett. (25), 3276 (1991)

---

## **Superconductors**

---



# Optical Control of High Speed Circuit Using Picosecond High Temperature Superconductor Opening Switches

Yuan-Qun Liu, Yi-Sern Lai, Wei-lou Cao, and Chi H. Lee

*Department of Electrical Engineering, University of Maryland, College Park, Maryland 20742*

S. N. Mao, X. X. Xi, and T. Venkatesan<sup>†</sup>

*Center for Superconductivity Research, University of Maryland, College Park, Maryland 20742*

Zhi-Yuan Shen, Philip Pang, Dennis J. Kountz, and William L. Holstein

*Central Research and Development, Du Pont, PO Box 80304, Wilmington, Delaware 19880-0304*

## Abstract

Laser control of a high-speed circuit using high temperature superconductor opening switches was demonstrated. Ultrashort electrical pulses with pulse compression and power gain were produced.

Recently a great deal of attention has been given to a general class of switching and gating devices based on picosecond semiconductor photoconductivity [1]. A completely complimentary process exists in picosecond laser induced photoresistance in high  $T_c$  superconductors (HTS) by optically controlled state transition. Picosecond opening switch and modulation of high frequency electrical signals are some possible applications. This paper reports some of the first experimental demonstrations of these effects. A high current opening switch can be constructed using HTS materials owing to their high critical current densities, usually  $\sim 10^7$  A/cm<sup>2</sup> for HTS thin films. Besides, HTS devices can be operated very fast because of their fast response to the optical pulses [2-8].

The merging of ultrafast electronics and optoelectronics using high temperature superconductors represents an opportunity for a new class of devices with unique properties. Not only HTS switches for generating electrical pulses with high power gain and pulse compression but also HTS microwave devices, such as generators, modulators, resonators, filters, antennas, phase shifters, or transmission lines, could be controlled by picosecond laser pulses or combined with picosecond optical semiconductor devices. The laser beam can, in some cases, be regarded as a third control terminal which adds a degree of freedom to the device

design and permits novel device concepts.

In this paper, the optical control of an ultrafast circuit, an ultrafast inductive energy storage pulsed power system (IESPPS), using a semiconductor closing switch and a HTS opening switch is introduced. There are two major considerations in an inductive energy storage system: the charging circuit and the opening switch design. The major obstacle to a practical inductive storage system is the opening switch. An ideal opening switch for this application should possess the following characteristics: fast opening (nanosecond or less), fast recovery to achieve high repetition rate, controllable and long conduction time, zero resistance during conduction, high impedance after opening, large current, large stand-off voltage, and jitter free. HTS opening switch possesses many of these unique characteristics. Our objective is to demonstrate the possibility of generating ultrashort electrical pulses with low loss, high power gain and pulse compression using semiconductor closing and HTS opening switches activated by picosecond laser pulses.

As shown in Fig.1, the IESPPS used in this work was a current charged transmission line (CCTL) with the HTS switch and the Si switch coupled to a 0.1  $\mu$ F capacitor. The opening switch, fabricated from 0.6 - 0.8  $\mu$ m thick TIPbSrCaCuO [9], TlBaCaCuO [10,11], or YBCO HTS films, had either a coplanar or a microstripline structure designed for high speed operation. The HTS films, from our recent test, can carry lossless current with current densities of  $5 \times 10^6 \sim 5 \times 10^7$  A/cm<sup>2</sup>. The optical response of the opening switches was investigated using 10 ps, 10  $\mu$ J laser pulses from a 1.053  $\mu$ m laser system. Switching risetimes of 50 - 100 ps, as shown in Fig.2, have been obtained. A switching efficiency up to 80% has also

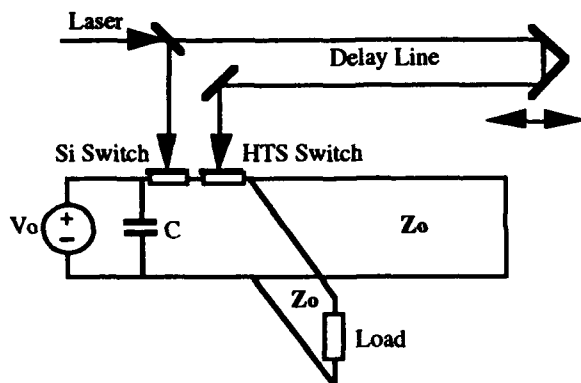


Figure 1. Laser operated inductive energy storage pulsed power system using semiconductor closing switch and superconductor opening switch.

been achieved though the HTS films used were much thicker than the absorption length. The advantage of using HTS opening switch in a CCTL is obviously its zero resistance during the high density current charging stage, high switching efficiency, and fast opening with picosecond synchronization. The HTS switch was also employed in an ultrafast pulse-forming circuit to generate picosecond pulses as shown in Fig.3. The Si closing switch which provided the charging current was embedded in a 50- $\Omega$  microstripline. Its photoconductive lifetime is several microseconds, which secures the conduction time needed for charging current buildup. Three transmission lines with lengths of 16, 40 and 115 cm were used in the experiment. One of the features in using a CCTL with an ultrafast closing switch is the "step-wise" current buildup. When the Si switch is

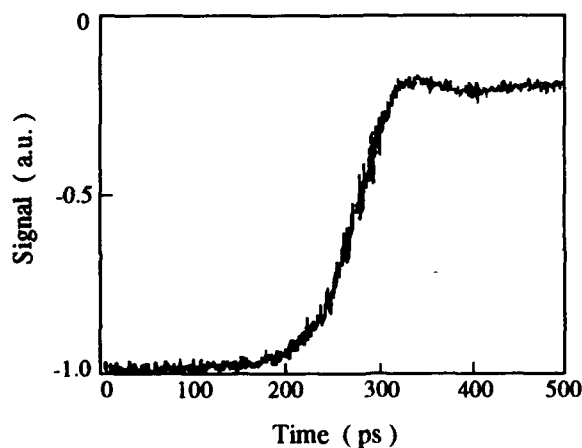


Figure 2. Optical response of the TlPbSrCaCuO HTS switch at  $T=78.5^\circ\text{K}$ .

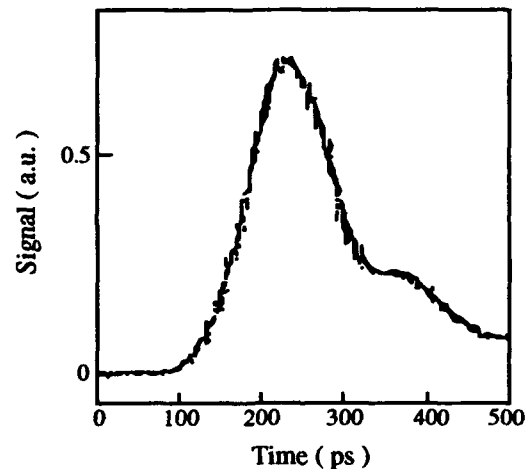


Figure 3. Picosecond pulse from the pulse-forming circuit using TlPbSrCaCuO HTS opening switch,  $T=78.5^\circ\text{K}$ .

closed by a laser pulse, the energy initially stored in the charged capacitor is transferred in the current form to the transmission line through the HTS switch in its closing state. Since the transmission line is shorted, the charging current wave is reflected at both ends and builds up in a staircase waveform which increases one step after each round-trip. Fig.4 shows the charging current waveforms in the transmission lines with different lengths, where a charging voltage of 10V ( or an initial charging current of 0.2A ) was used. Once the current reaches its maximum, the HTS switch is opened by another laser pulse and the energy stored in the transmission line is delivered to an impedance matched load. According to the wave-forms shown in Fig.4, using a shorter transmission line gives a higher

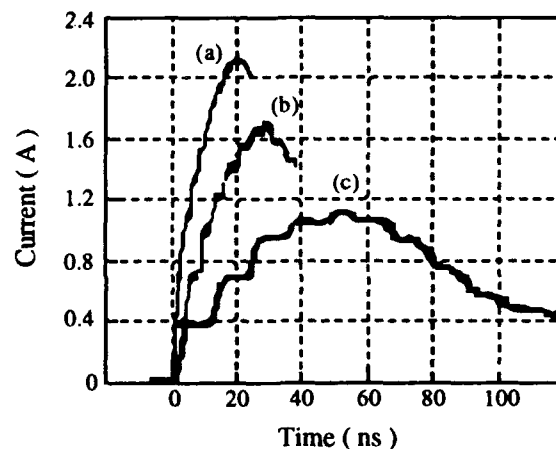


Figure 4. Charging current waveforms in transmission lines with different length  $L$ : (a)  $L=16$  cm, (b)  $L=40$  cm and (c)  $L=115$  cm.

current gain, which is also confirmed by our circuit model. The use of a shorter transmission line also means a shorter pulse, whose duration is related to the length of the transmission line, can be generated from such systems. With their unique properties of jitter free fast opening, HTS opening switches make it possible to use shorter transmission lines. Fig.5 shows the electrical pulse switched out by an IESPPS with a 16 cm long transmission line, corresponding to a pulse duration of  $T=1.6$  ns. At a charging voltage of 1V, about 6.4V was obtained on the load. This corresponds to a voltage gain of 6.4, and a peak power gain of 40, defined as the ratio between the peak power delivered by the IESPPS and the peak power that would be delivered directly into the load from the capacitor. Shorter pulses are possible if shorter transmission lines are used.

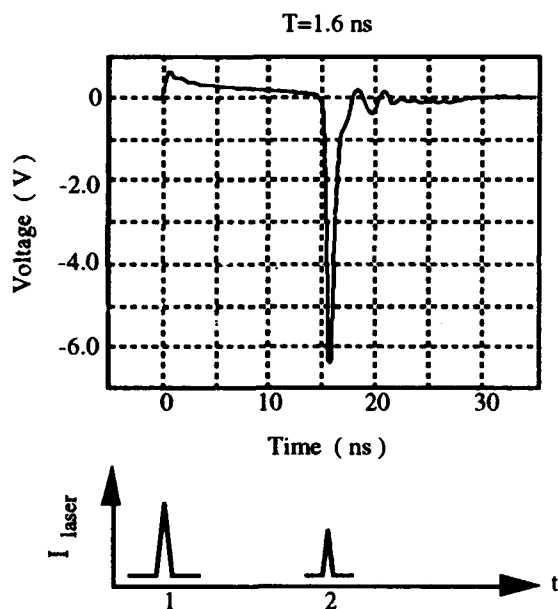


Figure 5. Electrical pulse with power gain and pulse compression from the IESPPS using Si closing switch and YBCO HTS opening switch,  $T=78.5^{\circ}\text{K}$ : upper trace, experimental result; lower trace: 1 laser pulse to close the Si-switch and 2, laser pulse to open the HTS-switch.

In summary, ultrafast HTS opening switches with 50 - 100 ps risetime, 80% switching efficiency were demonstrated. An ultrafast IESPPS using optically controlled Si closing switch and HTS opening switch was explored. Jitter-free ultrafast electrical pulses with pulse compression and power gain were obtained. Better performances are expected.

† T. Venkatesan is also with the Department of

Electrical Engineering, University of Maryland, College Park, MD 20742.

## References

1. Chi H. Lee, "Optical control of semiconductor closing and opening switches," *IEEE Trans. Electron Devices*, **37**, 2426-2438, (1990).
2. H. S. Kwok, J. P. Zheng, and S. H. Liou, "Nonbolometric optical response of Tl-Ba-Ca-Cu-O thin films," *Physica C*, **175**, 573-576, (1991).
3. A. Frenkel, M. A. Saifi, T. Venkatesan, P. England, X. D. Wu, and A. Inam, "Optical response of nongranular high- $T_c$   $\text{Y}_1\text{Ba}_2\text{Cu}_3\text{O}_{7-x}$  superconducting thin films," *J. Appl. Phys.*, **67**, 3054-3068, (1990).
4. M. Leung, P. R. Broussard, J. H. Claassen, M. Osofsky, S. A. Wolf, and U. Strom, "Optical detection in thin granular films of Y-Ba-Cu-O at temperatures between 4.2 and 100K," *Appl. Phys. Lett.*, **51**, 2046-2047, (1987).
5. W. S. Brocklesby, D. Monroe, A. F. J. Levi, M. Hong, S. H. Liou, J. Kwo, C. E. Rice, P.M. Mankiewich, and R. E. Howard, "Electrical response of superconducting  $\text{YBa}_2\text{Cu}_3\text{O}_{7.8}$  to light," *Appl. Phys. Lett.*, **54**, 1175-1177, (1989).
6. Mark Johnson, "Nonbolometric photoresponse of  $\text{YBa}_2\text{Cu}_3\text{O}_{7.8}$  films," *Appl. Phys. Lett.*, **59**, 1371-1373, (1991).
7. W. R. Donaldson, A. M. Kadin, P. H. Ballentine, and R. Sobolewski, "Interaction of picosecond optical pulses with high  $T_c$  superconducting films," *Appl. Phys. Lett.*, **54**, 2470-2472, (1989).
8. Wei-lou Cao, Yuan-Qun Liu, Chi H. Lee, S. N. Mao, S. Bhattacharya, X. X. Xi, and T. Venkatesan, "Picosecond YBCO Superconductor Opening Switches," 1992 Applied Superconductivity Conference, paper EPD-2, Chicago, Illinois, August 23-28, 1992.
9. D.J.Kountz, P.L.Gai, C.Wilker, W.L.Holstein, F.M.Pellicone, and R.Brainard, "Microstructural and electronic properties of highly oriented  $\text{Tl}_{0.5}\text{Pb}_{0.5}\text{Sr}_2\text{CaCu}_2\text{O}_7$  films on  $\text{LaAlO}_3$ ," *IEEE Trans. Appl. Superconductivity* (in press).
10. W.L.Holstein, L.A.Parisi, C.Wilker, and R.B.Flippin, " $\text{Tl}_2\text{Ba}_2\text{CaCu}_2\text{O}_8$  films with very low microwave surface resistance up to 95 K," *Appl. Phys. Lett.*, **60**, 2014-2016, (1992).
11. A.Lauder, C.Wilker, D.J.Kountz, W.L.Holstein, D.W.Face, (in press) *IEEE Trans. Appl. Superconductivity*.

## Response of a Nb/Al<sub>2</sub>O<sub>3</sub>/Nb Tunnel Junction to Picosecond Electrical Pulses

C. Karadi, S. Verghese, C. A. Mears, J. Orenstein, and P. L. Richards

*Department of Physics, University of California at Berkeley and Materials Science Division, MS 2-320,  
Lawrence Berkeley Laboratory, Berkeley, California 94720*

A. T. Barfknecht

*Conductus Inc., Sunnyvale, California 94086*

### **Abstract**

We have resolved the time domain response of the quasiparticle current in a superconducting tunnel junction to picosecond electrical pulses propagating in free space.

### **Introduction**

The quasiparticle tunneling current in superconductor-insulator-superconductor (SIS) junctions has been exploited in a class of ultrasensitive high-frequency devices such as mixers and detectors [1]. Nevertheless, the nonlinear, and even linear, response of these junctions has not been adequately measured. While SIS junctions have been characterized using cw sources near 80GHz [2], the broadband response near the threshold at  $2\Delta - eV_{\text{bias}}$  has not been studied. (Here  $\Delta$  is the superconducting gap parameter and  $V_{\text{bias}}$  is the voltage across the junction) In this work, we have used picosecond electrical pulses to measure the broadband quasiparticle response of a Nb trilayer SIS junction in both the linear and nonlinear regimes. The use of electrical pulses is especially well suited to the nonlinear regime, in that a relatively large instantaneous voltage may be applied while the average power is kept low.

### **Experimental Technique**

The picosecond electrical pulses used for this measurement were generated by illuminating a silicon photoconducting switch at the feed of a 300  $\mu\text{m}$  dipole

antenna [3]. The silicon was implanted with  $1.0 \times 10^{15}/\text{cm}^2$  oxygen ions at both 100 keV and 200 keV. The antenna terminals have a 5  $\mu\text{m}$  gap which was biased as low as 10V for linear spectroscopy and up to 60V for the nonlinear measurements. To excite the photoconductor we used an unamplified Ti-Sapphire laser operating at 800nm with 100 fs pulses and an average power of 50 mW. The use of a high repetition rate (100MHz) laser is critical to obtain the high ratio of signal to noise in our data. The emitted electrical pulses are nearly a single cycle with a center frequency at approximately 180 GHz and a 3db bandwidth of 80 GHz.

The broadband response of the SIS device is inferred by measuring the dc current induced by interfering two electrical pulses at the junction, as a function of the time delay,  $\tau$ , between them. Figure 1 is a schematic diagram of the interferometer that was used to perform these measurements [4]. The pulses are generated from two separate antennas. The beam from each antenna is partially collimated by a 13mm diameter sapphire hyperhemisphere and then further collimated by a 3.5 inch diameter  $f/1$  parabolic mirror. The two beams are combined into one with a 200  $\mu\text{m}$  thick mylar beamsplitter. To focus the recombined beam onto the SIS junction an  $f/3$  parabolic mirror first directs the pulses onto the polypropylene window of a 4.2K cryostat which houses the junction. The beam which enters through the window is then focused onto the SIS junction with a TPX lens and a quartz hyperhemisphere.

The SIS junction was fabricated at the terminals of a log-periodic planar antenna, which couples the free space electrical pulses to the junction. The SIS junction is a 2  $\mu\text{m} \times 2 \mu\text{m}$  Nb/Al<sub>2</sub>O<sub>3</sub>/Nb trilayer with a

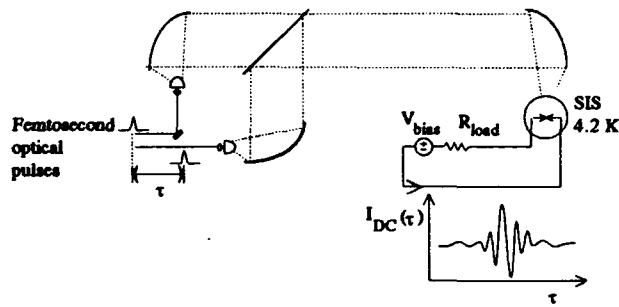


Figure 1. Schematic layout of the picosecond electrical pulse interferometer.

critical current density of  $3.5 \text{ kA/cm}^2$ , capacitance of  $200 \text{ fF}$ , and normal state resistance of  $14 \Omega$ . A magnetic field of about 100 gauss cancels the Cooper pair tunneling current and allows us to isolate the quasiparticle tunneling current.

## Results

The SIS junction can be modeled as a superposition of voltage tunable two level systems [5]. The BCS theory [6] predicts that a junction biased at  $V_{\text{bias}}$  will have strong resonant absorption when  $\hbar\omega = 2\Delta - eV_{\text{bias}}$ . As in atomic or semiconductor systems, the width of the resonance is due to lifetime effects as well as inhomogeneous broadening (distribution of energy gap values along the SIS junction.) According to the theory developed by Tucker, the response of the SIS junction to an arbitrary voltage pulse in the time domain can be calculated from the measured dc I-V characteristic [6]. The broadening of the resonance is expected to be manifest in the width of the current onset at  $2\Delta/e$  in the current-voltage (I-V) characteristic. In response to a voltage pulse, the current is expected to oscillate near the frequency  $(2\Delta - eV_{\text{bias}})/\hbar$  and to decay with a lifetime related to the broadening of the dc I-V curve. For our SIS junction,  $2\Delta = 2.75 \text{ meV}$  and the width of the threshold in the dc I-V curve corresponds to a decay time of 10 ps.

Figure 2 shows the signal generated by two electrical pulses incident on the junction as a function of the time delay between them, for  $V_{\text{bias}} = 2.3 \text{ mV}$ . The bias voltage on the antennas was adjusted so that the pulse intensity was the same in both arms of the interferometer. The laser excitation of one of the antennas was chopped at 1 kHz. Low noise electronics are necessary for measuring the linear quasiparticle response to small electrical pulses. The signal was coupled through a 300K transformer to a low noise

FET amplifier with a spot noise referred to the SIS junction of  $0.2 \text{ nV}/\sqrt{\text{Hz}}$  at 1 KHz.

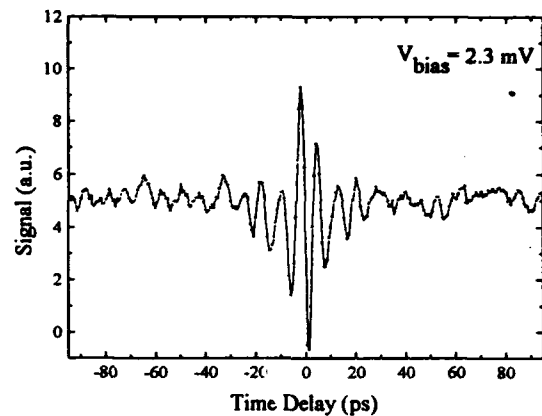


Figure 2. One photon cross-correlation in the SIS junction at  $V_{\text{bias}} = 2.3 \text{ mV}$ .

At  $V_{\text{bias}} = 2.3 \text{ mV}$  the SIS junction has a strong absorption at 110 GHz which is within the bandwidth of our driving pulse. The peak pulse intensity was kept low so that the SIS junction responded linearly. The coherent oscillation of the quasiparticle current shown in Fig. 2a decays in 10 ps and is consistent with the broadening of the dc I-V curve and correlation time of the incident pulses. In future experiments we plan to use both faster pulses and devices which ring with a longer decay time.

Figure 3 shows the result of a measurement similar to Fig. 2, except that  $V_{\text{bias}} = 1.3 \text{ mV}$ . Two absorption mechanisms contribute to the response of the SIS junction for this value of  $(2\Delta - eV_{\text{bias}})/\hbar$ . Either one 350 GHz photon or two 175 GHz photons can be absorbed. We expect the two-photon absorption will dominate since the 350 GHz component of the electrical pulse measured with a bolometer was negligible. Signatures of a two-photon absorption process which appear in Fig. 3 are the rectification of the interference pattern and the peak to off-peak ratio of 8:1 [7]. Also, the response of the junction to a single electrical pulse scales as the electric field amplitude to the fourth power, as is expected for a two photon process.

In conclusion, we have applied the technique of picosecond electrical pulse generation to study the time-domain response of a SIS tunnel junction in the linear and nonlinear regimes. The successful measurement of the two-photon absorption process in an SIS junction demonstrates the application of picosecond electrical pulses to time-resolved non-linear spectroscopy. Future experiments will include other nonlinear techniques, such as spectral hole burning,

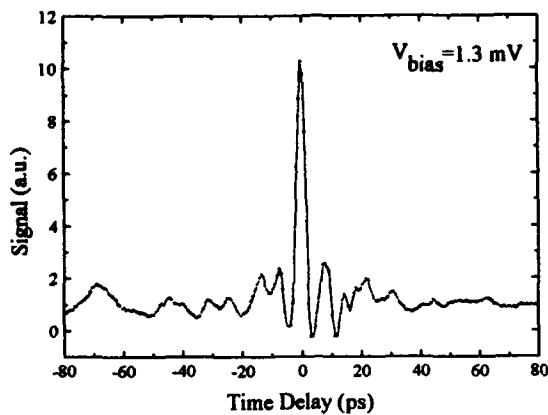


Figure 3. Two photon cross-correlation in the SIS junction at  $V_{\text{bias}} = 1.3$  mV.

which may allow us to probe the mechanism which broadens the dc I-V curve of the SIS junction.

### **Acknowledgments**

This work is supported by U.S. DOE under contract DE-AC03-76SF00098.

### **References**

- [1] P. L. Richards and Q. Hu, *Proc. IEEE* **60**, 1233, (1989).
- [2] Q. Hu, C. A. Mears, P. L. Richards and F. L. Lloyd, *Phys. Rev. Lett.* **64**, 2945 (1990); A. H. Worsham, N. G. Ugras, D. Winkler, D. E. Prober, N. R. Erickson, P. F. Goldsmith, *Phys. Rev. Lett.* **67**, 3034 (1991).
- [3] M. van Exter, D. Grischkowsky, *IEEE Trans. MTT* **38**, 1684 (1990).
- [4] S.E. Ralph, D. Grischkowsky, *App. Phys. Lett.* **60**, 1070 (1992); B.I. Greene, J.F. Federici, D.R. Dykaar, R.R. Jones, P.H. Bucksbaum, *App. Phys. Lett.* **59**, 893 (1991).
- [5] Q. Hu, C.A. Mears, P.L. Richards, F.L. Lloyd, *Phys. Rev. B* **42**, 10250 (1990).
- [6] J. R. Tucker, M.J. Feldman, *Rev. Mod. Phys.* **57**, 1055 (1985).
- [7] J.-C. M. Diels, J. J. Fontaine, I. C. McMichael, F. Simoni, *Applied Optics* **24**, 1270 (1985).

## Ultrafast Optical and Optoelectronic Response of Y-Ba-Cu-O

T. Gong, L. X. Zheng, Y. Kostoulas\*, W. Xiong, W. Kula<sup>†</sup>,  
K. B. Ucer, Roman Sobolewski<sup>†</sup>, and P. M. Fauchet

*Laboratory for Laser Energetics and Department of Electrical Engineering,  
University of Rochester, 250 East River Road,  
Rochester, New York 14623-1299*

Since the discovery of high-temperature superconductors (HTS), there have been intensive investigations of their transient response under ultrashort laser-pulse excitation. Recently, using the femtosecond pump-probe technique, Han *et al.* [1] observed a very fast (several picoseconds) optical response on  $\text{YBa}_2\text{Cu}_3\text{O}_x$  (YBCO) in the superconducting state under weak excitation and attributed it to the generation and recombination of quasi-particles. As the ambient temperature drops below the superconductor's critical temperature ( $T_c$ ), the transient reflectivity signal abruptly changes both its sign and temporal behavior—this striking behavior appears to be correlated to the onset of superconductivity. However, the physical significance of such an ultrafast response is still not clear, since the position of the Fermi level ( $E_F$ ) and the density of states near  $E_F$  are not well known. Independently, a series of transient photovoltage measurements have also been performed on YBCO. Recent experimental work [2] demonstrated that for ultra-thin films the relative magnitude of the nonthermal component was enhanced and could be as fast as tens of picoseconds. The fact that the electrical response is at least one order of magnitude slower than the optical response suggests that more in-depth studies are necessary in order to find the ultimate speed of optoelectronic devices made of HTS.

In this paper, we present a series of ultrafast photoexcitation measurements of YBCO. We focus our attention on detailed studies of the transient optical response as a function of optical frequency, oxygen content ( $x$ ) and thickness ( $d$ ) of the sample, excitation intensity ( $I_p$ ), and electric current ( $I$ ). Preliminary photovoltage measurements, using the technique of photoinduced resistive autocorrelation, are also presented. These measurements address the question of the ultimate time resolution for the electrical response of YBCO under ultrafast optical excitation, which has a direct impact on device applications.

The transient optical response is measured using conventional pump-probe techniques with a copper-vapor laser amplified CPM system. The experimental arrangement allows us to change the pump laser intensity for 2-eV photons by more than three orders of magnitude, as well as to use different probe wavelengths

selected from a white-light continuum. Time-resolved differential reflectivity ( $\Delta R/R$ ) measurements have been performed with a temporal resolution of  $\sim 100$  fs on various YBCO films and at different temperatures.

In order to locate  $E_F$  in the oxygen p-band of the Cu-O plane, we first performed 2-eV-pump/white-light-probe measurements on oxygen-rich YBCO ( $x \approx 6.9$ ,  $d \sim 200$  nm,  $T_c \sim 87$  K) and oxygen-poor YBCO ( $x \approx 6.45$ ,  $d \sim 200$  nm,  $T_c \sim 0$  K) at room temperature. We have observed [3] that for oxygen-rich YBCO,  $\Delta R/R$  is always positive in the frequency range of 1.91 to 2.25 eV; in contrast, for oxygen-poor YBCO,  $\Delta R/R$  is always negative in the frequency range of 1.46 to 2.00 eV. Using the standard thermomodulation (Fermi smearing) model, we conclude using the hole picture that  $E_F$  must be at least 2.25 eV above the  $\text{Cu-d}^9/\text{d}^{10}$  band for YBCO with  $x \approx 6.9$ , but at most 1.45 eV above the  $\text{Cu-d}^9/\text{d}^{10}$  band for YBCO with  $x \approx 6.45$ . The large shift ( $>800$  meV) of  $E_F$  when the oxygen content decreases from  $\approx 6.90$  to  $\approx 6.45$ , can be explained by the drastic decrease of the total charge density in the Cu-O planes.

In order to determine  $E_F$  as a function of  $x$ , we have performed similar measurements on several YBCO samples with different oxygen contents. These samples were obtained by annealing high-quality superconducting films in controlled  $\text{Ar-O}_2$ -mixture atmospheres. Figure 1 shows the time-resolved  $\Delta R/R$  signal measured at 2 eV on the YBCO samples with five different oxygen contents—estimated by measuring  $T_c$ . From the sign reversal of the signal, when  $x$  approaches 6.8 ( $T_c \sim 60$  K), we conclude that  $E_F$  lies  $\sim 2$  eV above the  $\text{Cu-d}^9/\text{d}^{10}$  band for  $x \sim 6.8 \pm 0.05$  (adopting the framework of the thermomodulation model).

When the ambient temperature drops below  $T_c$ , the free-carrier density of states in the superconductor is modified substantially. According to the BCS theory, in the superconducting state (i) electrons form boson-like Cooper pairs, which occupy a single energy level separated from  $E_F$  by the superconducting energy gap  $\Delta$ ; while (ii) unpaired, excited electrons (quasi-particles) occupy a continuum of states starting  $\Delta$  above  $E_F$ . Under optical illumination, the thermal equilibrium

between the superconducting condensate and quasi-particles is disturbed (often very strongly), since photons with energies  $\gg 2\Delta$  can break Cooper pairs and create quasi-particles. The absorption of a single 2-eV photon in YBCO creates, through the cascading processes of carrier-carrier and carrier-phonon scattering, many quasi-particles with energies widely distributed above  $2\Delta$ . Thus, even a relatively weak optical excitation leads to highly nonequilibrium transient Cooper pair/quasi-particle distributions.

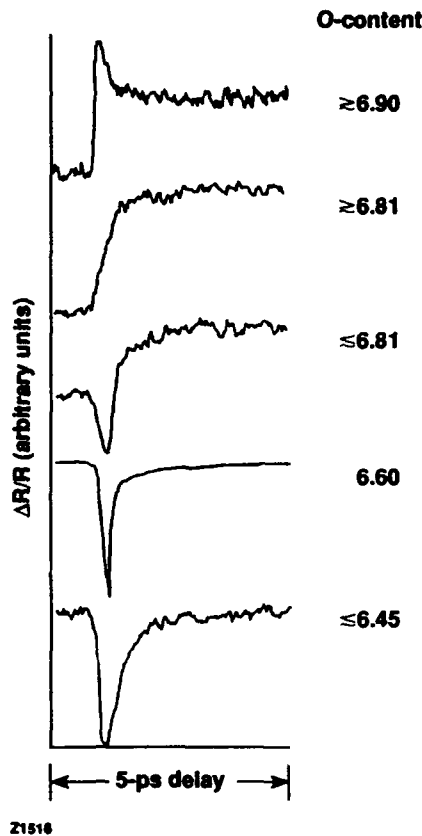


Figure 1. Normalized  $\Delta R/R$  measured on the YBCO samples with different oxygen contents at room temperature using a 2-eV probe photon energy. The measured critical temperature and estimated oxygen content of each sample is displayed.

Figure 2(a) shows  $\Delta R/R$  at 2 eV measured at  $T = 25$  K on an optically thick superconducting sample ( $d \sim 280$  nm,  $T_c \sim 87$  K) when a weak excitation ( $I_p \sim 1 \mu\text{J}/\text{cm}^2$ ) is used. The negative  $\Delta R/R$ , followed by a fast (several picoseconds) recovery, is very similar to the literature results obtained on optically thick (from 250-nm- to 500-nm-thick) samples [1,4,5], and has been attributed to the generation and recombination of quasi-particles [1] and/or the relaxation of the superconducting order parameter [4]. On the other hand, the temperature dependence of the relaxation time obtained from  $\Delta R/R$  appears to depend on sample's quality and excitation intensity [1,4,5]. If one combines the framework of the thermomodulation model with the superconductor's two-fluid model, the observed magnitude of the  $\Delta R/R$  signal appeared to agree with the simple estimation presented in Ref. 1. A possible explanation of the sign reversal of the signal with onset of superconductivity is as follows: breaking of Cooper pairs and generation of quasi-particles cause a reduction of  $\Delta$ , which decreases the absorption below  $E_F - \Delta$ , thus at 2 eV. However,

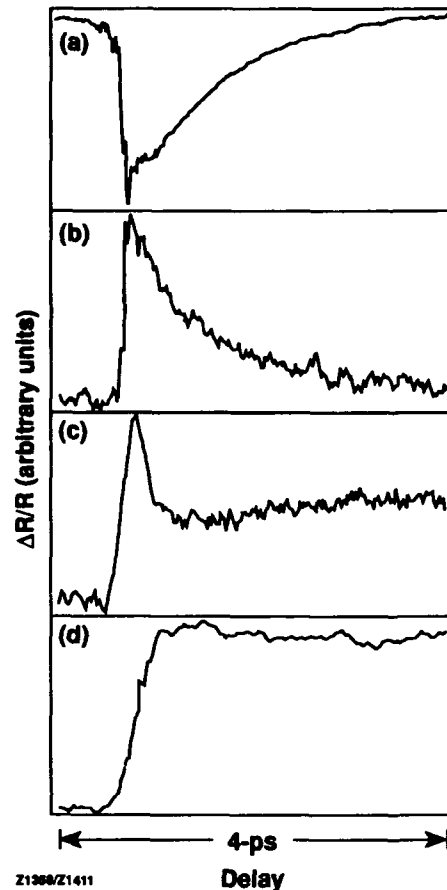


Figure 2. Normalized  $\Delta R/R$  measured at  $T < T_c$  on optically thick and thin YBCO at 2 eV and different excitation intensity: (a)  $d \sim 280$  nm,  $T = 25$  K, and  $I_p \sim 1 \mu\text{J}/\text{cm}^2$ ; (b)  $d \sim 80$  nm,  $T = 25$  K, and  $I_p \sim 1 \mu\text{J}/\text{cm}^2$ ; (c)  $d \sim 200$  nm,  $T = 12$  K, and  $I_p \sim 20 \mu\text{J}/\text{cm}^2$ ; and (d)  $d \sim 200$  nm,  $T = 12$  K, and  $I_p \sim 100 \mu\text{J}/\text{cm}^2$ .

there are two problems associated with the above picture: (i) The detailed band structure, in particular around  $E_F$ , is neglected; (ii) One assumes that the measured  $\Delta R/R$  signal is dominated by  $\Delta\alpha$  (the change of absorption coefficient). The first problem was recently revealed to be important by systematic studies on Pr-doped YBCO [5], as well as studies on the specific-heat discontinuity on YBCO at  $T_c$  [6]. The second assumption, however, contradicts the fact that the sign of the transient transmission ( $\Delta T/T$ ) remains the same (negative) with onset of superconductivity [7,8]. Figure 2(b) shows a positive  $\Delta R/R$  with temporal response similar to that exhibited in Fig. 2(a), obtained on the optically thin ( $d \sim 80$  nm  $T_c \sim 84$  K) sample. These experimental evidences appear to suggest that such a "nonbolometric" response is caused by  $\Delta n$  (the change of refractive index) instead of  $\Delta\alpha$ . Thus, the sign change between the optically thin and thick films is due to the thin-film effect. The analysis [3] also shows that a simple two-fluid model cannot satisfactorily explain the behavior of  $\Delta n$ . One possibility is to attribute such a peculiar behavior to the optical response of YBCO in a nonequilibrium intermediate state, which can exist under the low excitation. The intermediate state, which was first observed by Sai-Halasz *et al.* [9] in metallic superconductors, is

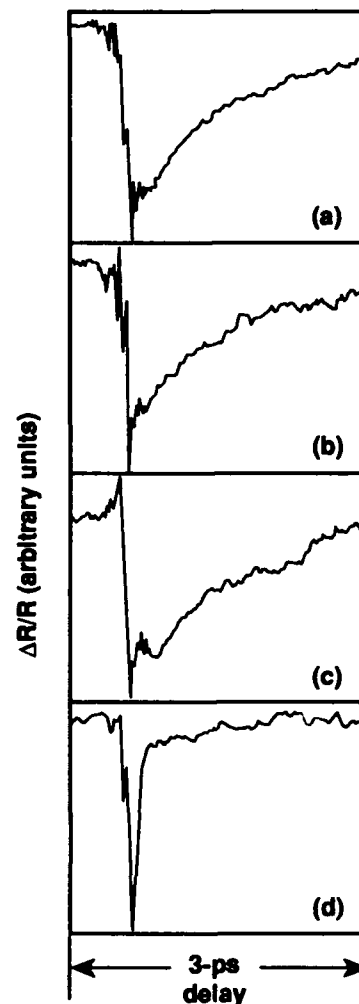


characterized by the coexistence of superconducting and normal regions in the excitation area. Recent photovoltage measurements using a pulse-train photoexcitation suggest that indeed the intermediate state exists in HTS materials [10].

Figures 2(c) and 2(d) present  $\Delta R/R$  at 2 eV obtained at  $T = 12$  K for an optically thick YBCO sample under relatively intense excitation ( $I_p \approx 20 \mu\text{J}/\text{cm}^2$  and  $100 \mu\text{J}/\text{cm}^2$ ). We note that the temporal responses are very similar to those observed at room temperature (see Fig. 1). It is worth stressing that for pump intensities ranging from  $-20 \mu\text{J}/\text{cm}^2$  up to  $100 \mu\text{J}/\text{cm}^2$ , a similar bolometric temporal response was observed for all our YBCO samples, optically thin and thick, over the entire temperature range from well below  $T_c$  up to room temperature [3]. Interestingly, the magnitude of the signal at  $T < T_c$  is significantly larger than that at room temperature. At a high level of excitation, the sample must undergo a transition to the normal state, all the Cooper pairs are destroyed, and the superconducting gap is closed. The abrupt increase in the magnitude of the signal observed with the onset of superconductivity implies an additional contribution from nonequilibrium quasi-particles (photoexcited Cooper pairs).

We have also investigated the impact of the electric transport current on the femtosecond reflectivity of YBCO. Figure 3 shows our data obtained under weak laser excitation ( $I_p \approx 1 \mu\text{J}/\text{cm}^2$ ) on a dc current biased 50- $\mu\text{m}$ -wide YBCO superconducting microbridge ( $d \approx 280$  nm). Figures 3(a)–3(c) present the traces measured below  $J_c$  while the trace in Fig. 3(d) was taken above  $J_c$ . We note that the temporal behavior for  $J < J_c$  is very similar to that in Fig. 2(a), but the characteristic decay times decrease slightly with increasing bias current. On the other hand, the decay time shows a very abrupt decrease when  $J$  exceeds  $J_c$ , as shown in Fig. 3(d). This is very similar to the data in Fig. 1 obtained with a partially deoxygenated sample ( $T_c \approx 27$  K), but is completely different from the response in a photoexcited nonequilibrium normal state [Fig. 2(c) and 2(d)]. The behavior is nonreversible in the sense that after the bias current is reduced, the measured signals do not resemble those shown in Figs. 3(a)–3(c). We have also observed that after prolonged laser excitation,  $J_c$  is reduced significantly. The above observations suggest that this particular sample may be subject to a recently observed process of current-driven electromigration of oxygen [11] from the optically created "weak spot" in the stripe.

To avoid the complexity involved for weak excitation and in an optically thick YBCO stripe where nonuniform current can flow, we have performed measurements on an optically thin ( $d \approx 80$  nm), dc current biased 50- $\mu\text{m}$ -wide superconducting microbridge with an intense laser excitation. The corresponding  $\Delta R/R$  signals, measured at a temperature close to  $T_c$  for  $J = 0$  and above  $J_c$  are shown in Figs. 4(a) and 4(b), respectively. By contrast to Fig. 3, the temporal response of the signal obtained at  $J > J_c$  is similar to that at  $J = 0$ . We have also verified that the  $J_c$  of the stripe remained the same after prolonged laser excitation and many cycles of varying bias current, a result indicative of the high quality of our patterned microbridge. Thus, we conclude that when the light excitation intensity is high enough to drive the film into the normal state, the increase of the bias current to above  $J_c$ , which independently drives the film into the resistive state, has little effect on the temporal behavior of the optical response.



Z1351

Figure 3. Normalized  $\Delta R/R$  measured with a 2-eV probe on the YBCO-IV microbridge biased by the following levels of electric current: (a) 0, (b) 1.5 mA, (c) 6 mA, and (d) 10 mA. The critical current of the microbridge was 8 mA. The temperature was about 72 K and the pump intensity was  $\sim 1 \mu\text{J}/\text{cm}^2$ .

Our resistive autocorrelation measurements were conducted in a configuration similar to that published by Shi *et al.* [2]. However, in our measurements we took advantage of the femtosecond time resolution of the CPM laser system. In our arrangement, two trains of femtosecond pulses with the same intensity but adjustable time-delay were delivered to the two YBCO stripes. The two stripes were electrically connected in parallel. A dc bias with  $J < J_c$  was supplied to the structure, and the photovoltage signal across the sample was recorded as a function of the delay between the excitation pulses delivered to each stripe. We note that the voltage is present only when both stripes are in the optically induced resistive state.

Figure 5 shows a preliminary result of our experiment, performed on a structure of two 80-nm-thick, 50- $\mu\text{m}$ -wide, and 50-mm-long stripes. It is clear that a fast nonbolometric voltage component has been observed in the optically driven

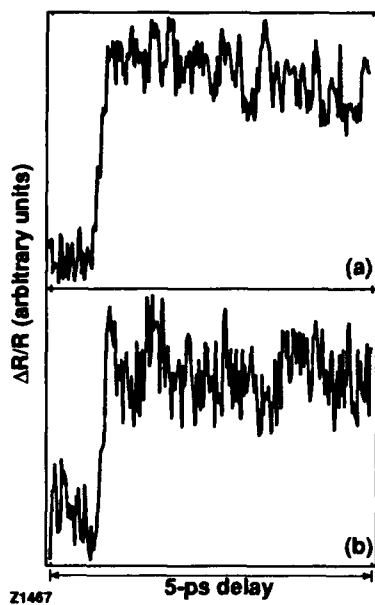


Figure 4. Normalized  $\Delta R/R$  measured with a 2-eV probe on the YBCO-II microbridge biased by the following levels of electric current: (a) 0 and (b) 15 mA. The critical current of the microbridge was 12 mA. The temperature was about 79 K and the pump intensity was  $\sim 40 \mu\text{J}/\text{cm}^2$ .

microbridges. Unfortunately, the relative magnitude of this component is quite small, and its duration is long ( $>150$  ps). Recent experimental results of Shi *et al.* [2] showed that these two features can be greatly improved by using ultra-thin YBCO films. However, the long lasting (several nanoseconds) bolometric part of the voltage signal with a non-negligible relative amplitude implies that the problem of proper device cooling is crucial for ultrafast operation of HTS optoelectronic devices.

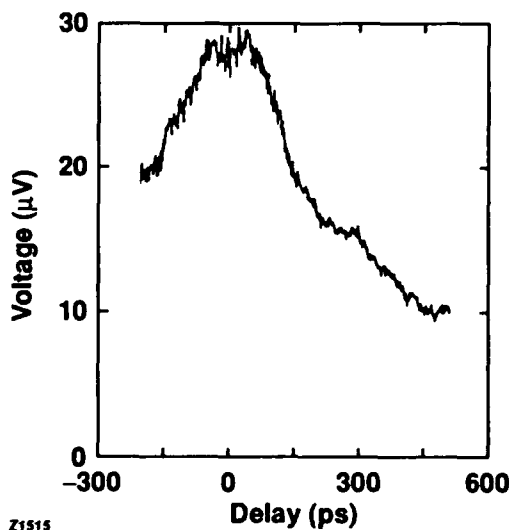


Figure 5. Femtosecond resistive autocorrelation signal obtained on a double-bridge structure ( $d \sim 80$  nm) under conditions:  $T \sim 25$  K,  $I \sim 20$  mA, and  $I_p \sim 50 \mu\text{J}/\text{cm}^2$ .

In conclusion, pump-probe and resistive autocorrelation measurements, performed under low optical excitation, have shown that the YBCO response can be as fast as several picoseconds and could be even further improved by implementing ultra-thin films and efficient cooling (e.g., using superfluid helium). Another possibility for reducing the YBCO response time is to use a far-infrared pulse excitation, as it has been shown very recently by Nebosis *et al.* [12].

The authors would like to thank L. Shi, D. H. Reitze, and H. S. Kwok for many valuable discussions. This work was supported by the Army Research Office grant DAAL03-92-G-0202 and by the New York State Institute on Superconductivity grant PO#R12762. K. B. Ucer also acknowledges the support from an LLE fellowship.

\*Also at Department of Physics, University of Rochester, Rochester, NY 14623.

†Also at the Institute of Physics, Polish Academy of Sciences, Al. Lotników 32/46, PL-02668 Warszawa, Poland.

## References

1. S. G. Han, Z. V. Vardeny, K. S. Wong, O. G. Symko, and G. Koren, *Phys. Rev. Lett.* **65**, 2708 (1990); S. G. Han, Z. V. Vardeny, O. G. Symko, and G. Koren, *Phys. Rev. Lett.* **67**, 1053 (1991).
2. L. Shi, G. L. Huang, C. Lehan, J. P. Zheng, and H. S. Kwok, *Appl. Phys. Lett.* **61**, 489 (1992).
3. T. Gong, L. X. Zheng, W. Xiong, W. Kula, Y. Kouzulas, R. Sobolewski, and P. M. Fauchet, "Femtosecond Optical Response of Y-Ba-Cu-O Thin Films: The Dependence on Optical Frequency, Excitation Intensity, and Electric Current," submitted to *Phys. Rev. B*.
4. G. L. Eesley, J. Heremans, M. S. Meyer, G. L. Doll, and S. H. Liou, *Phys. Rev. Lett.* **65**, 3445 (1990); G. L. Eesley, J. Heremans, M. S. Meyer, and G. L. Doll, *Phys. Rev. Lett.* **67**, 1054 (1991).
5. D. H. Reitze, A. M. Weiner, A. Inam, and S. Etemad, *Phys. Rev. B* **46**, 14,309 (1992).
6. C. C. Tsuei, C. C. Chi, D. M. Newns, P. C. Pattnaik, and M. Däumling, *Phys. Rev. Lett.* **69**, 2134 (1992).
7. J. M. Chwalek, C. Uher, J. F. Whitaker, G. A. Mourou, J. Agostinelli, and M. Lelethal, *Appl. Phys. Lett.* **57**, 1696 (1990).
8. L. X. Zheng, T. Gong, R. Sobolewski, and P. M. Fauchet, unpublished.
9. G. A. Sai-Halasz, C. C. Chi, A. Denenstein, and D. N. Langenberg, *Phys. Rev. Lett.* **33**, 215 (1974).
10. L. Shi, Ph.D. Thesis (State University of New York at Buffalo, 1993).
11. B. H. Moeckly and R. A. Burhman, to be published in *IEEE Trans. on Appl. Supercond.*
12. R. S. Nebosis, M. A. Heusinger, A. D. Semenov, P. T. Lang, W. Schatz, R. Steinke, K. F. Renk, G. N. Gol'tsman, B. S. Karasik, and E. M. Gershenzon, *Opt. Lett.* **18**, 96 (1993).

# **Terahertz Spectroscopy of Superconducting Thin Film $\text{Ba}_{0.6}\text{K}_{0.4}\text{BiO}_3$**

**Yongqian Liu and John F. Whitaker**

*Center for Ultrafast Optical Science, University of Michigan, 2200 Bonisteel Blvd.,  
Ann Arbor, Michigan 48109-2099*

**Christine E. Platt**

*University of Illinois at Urbana Champaign, Science and Technology Center for Superconductivity,  
320 Materials Research Laboratory, Urbana, Illinois 61801*

## **Abstract**

The complex conductivity of a  $\text{Ba}_{0.6}\text{K}_{0.4}\text{BiO}_3$  thin-film superconductor has been measured using terahertz-radiation spectroscopy. A BCS-like energy gap and a peak in the real part of the conductivity have been directly obtained without the need for Kramers-Kronig analysis.

## **Introduction**

Studies of the properties of superconducting thin films in the millimeter and submillimeter-wave range are of great interest for both the physical insight they lend into the behavior of materials and the relevant technological information they provide regarding applications. Scientifically, for example, measurements of the frequency and temperature dependences of the complex conductivity of low-critical-temperature ( $T_c$ ) superconductors in this regime have played a crucial role in understanding the fundamental nature of the interaction responsible for conventional superconductivity [1,2]. In addition, they have provided quantitative support for the BCS theory in these superconductors. Technologically, on the other hand, studies of superconducting behavior at frequencies corresponding to energies below the gap energy are important because of the potential use of high- $T_c$  superconductors in passive microwave devices for high-frequency electronics.

Terahertz-radiation, time-domain spectroscopy, with its high sensitivity and wide bandwidth, has become a powerful tool for studying the electronic properties of materials in a region of the electromagnetic spectrum that is not easily accessible [3-6]. With this technique, both phase and amplitude information are obtained directly from a measurement, so that the real and imaginary parts of, for instance, the index of refraction, permittivity, or conductivity of a sample under study can be determined without using Kramers-Kronig analysis. For example, recent terahertz bandwidth measurements have determined the complex conductivity of the high- $T_c$  superconductor,  $\text{YBa}_2\text{Cu}_3\text{O}_{7-x}$  [4,5]. These results are significant in their demonstration that the material exhibits behavior that may not be attributed to BCS theory.

The cubic, copper-free oxide  $\text{Ba}_{0.6}\text{K}_{0.4}\text{BiO}_3$  (BKBO) stands out as a superconductor with a moderate critical temperature between that of conventional BCS superconductors and high- $T_c$  superconducting copper oxides. Due to its long coherence length and its quasiparticle and Josephson tunneling properties, BKBO has been considered as a possible material system in a new family of superconducting circuits [7]. Furthermore, there is clear evidence of an energy gap in BKBO [8], and other indications also suggest that BKBO is an ordinary electron-phonon-coupled BCS superconductor [9]. On the other hand, since it has also been reported that BKBO shares many characteristics with the cuprate high- $T_c$  superconductors, its further study should enhance the understanding of both material

systems. To this end, we report on the conductivity and energy-gap behavior of a BKBO thin film between 200 GHz and 1 THz.

## Experimental

The experimental system used for this study has been shown previously in ref. [5] and is reviewed briefly here. Optical pulses of 75-fs duration from a passively mode-locked Ti-sapphire laser were used to generate and coherently detect terahertz-bandwidth bursts of radiation. Dipole-like antennas fabricated on 1- $\mu\text{m}$ -thick layers of MBE-low-temperature-grown GaAs were used as the optically driven transmitters and receivers in this system. The low-temperature-grown GaAs has a subpicosecond carrier response time, thus making it an ideal photoconductive substrate for the generator and detector antennas. When illuminated by the short laser pulses, the generator antenna provided an ultrafast source of electromagnetic pulse radiation, while the detector operated as an ultrashort-duration sampling gate. By variably delaying the arrival time of the *excitation* optical pulses onto the *generator* antenna relative to the *sampling* optical pulses onto the *receiver* antenna, both the field amplitude and polarity of the transmitted terahertz transient were obtained versus delay time.

When an unknown material interrupts the path of the terahertz beam between the transmitter and receiver, there is a shift in the arrival time at the receiver of this propagating waveform relative to the signal which travels through air only. Additionally, the waveform also loses amplitude and may be dispersed, depending on the properties of the unknown material in this frequency range. Since the waveforms with and without the unknown material present are analyzed temporally, with the absolute delays between the waveforms known, coherent time-domain spectroscopy is performed.

The BKBO sample measured in this fashion was a superconducting thin film ( $\sim 1300$  Å) grown by in-situ pulsed laser deposition on an MgO substrate [10]. The film exhibited an onset of superconductivity at 26 K and zero resistance at 22 K. The sample was placed over a hole in a cold finger on a continuous flow cryostat and positioned between the terahertz-beam transmitter and high-speed receiver, all fixed within a vacuum chamber. A blank MgO substrate covered a second hole on the

cold finger, which could be translated back and forth so that the same field could be passed through either the substrate alone or the sample, which consisted of the BKBO thin film on an identical substrate. By taking the Fourier transform of the temporal responses of the transmitted waveforms, we obtained the frequency response of the substrate alone, as well as that of the substrate with the superconducting film.

Assuming a negligible contribution from internal multiple reflections in the film being measured, a satisfactory assumption given the BKBO thickness, a simplified expression for the ratio of the field transmitted through a film and substrate to that transmitted only through the substrate was employed to obtain the film properties. This expression is given by

$$T(\omega) = (n+1)/(n+1+\sigma d Z_0)$$

where  $n$  is the index of refraction of the substrate,  $d$  is the film thickness, and  $Z_0$  is the impedance of free space. Employing this expression, we obtained the complex conductivity,  $\sigma$ , of the BKBO versus frequency. Liquid helium was then used to cool the sample under test in order to obtain the temperature-dependent behavior of this parameter.

## Results

Figure 1 shows the transmitted THz beams through the BKBO thin film at three temperatures within  $10^\circ\text{C}$  of

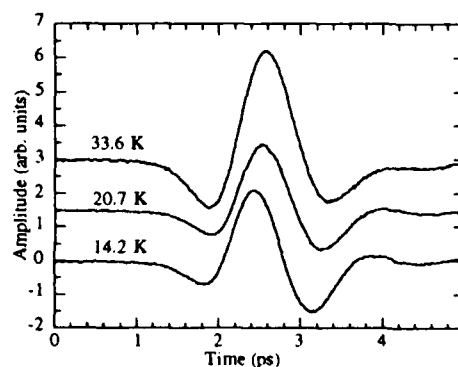


Fig.1 Terahertz-bandwidth pulses transmitted through a  $\text{Ba}_{0.6}\text{K}_{0.4}\text{BiO}_3$  thin-film sample at three different temperatures.

$T_c$ . For clarity, the baseline of the plots have been shifted. As can be seen, there is a dramatic decrease of amplitude and a phase shift as the temperature is

lowered below  $T_c$ . The decrease of amplitude is a result of the increased reflectivity as the sample goes into the superconducting state. The phase shift is a direct result of the increase in the imaginary part of the conductivity.

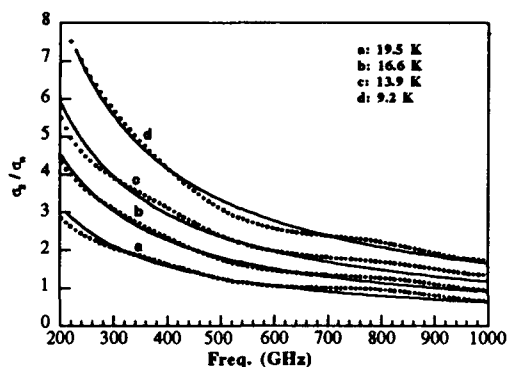


Fig. 2. Normalized, frequency-dependent imaginary conductivity extracted from THz transmission data and  $1/\omega$  fit (solid line) at four temperatures.

In Fig. 2, the normalized imaginary part of  $\sigma(\omega)$  for the BKBO thin film is plotted at several different temperatures. As temperature is lowered,  $\sigma_2$  increases greatly, with its behavior fitted very well by  $C/\omega$ , where  $C$  is a temperature-dependent coefficient. Additionally, at low temperatures, it has been shown theoretically (from the Ferrel-Glover sum rule [11]) that

$$\sigma_2/\sigma_n \approx 4\Delta/\pi\omega$$

where  $\Delta$  is the energy gap. Using the above expression to relate the experimentally determined  $C$  to  $\Delta$  and extrapolating to zero temperature, we obtained  $2\Delta(0)/kT_c \sim 3.79$ . This agrees very well with other tunnelling experiments and provides additional proof that BKBO is an intermediate coupling BCS superconductor.

Figure 3(A) shows the normalized  $\sigma_1$  for BKBO obtained at several different sample temperatures. The conductivity increases with decreasing frequency, as expected from the behavior of thermally excited quasiparticles in Mattis-Bardeen theory. There is also a dramatic change in  $\sigma_1$  as temperature decreases; that is,  $\sigma_1$  increases to a maximum value just below  $T_c$  for each frequency of the Fourier-transformed time-domain

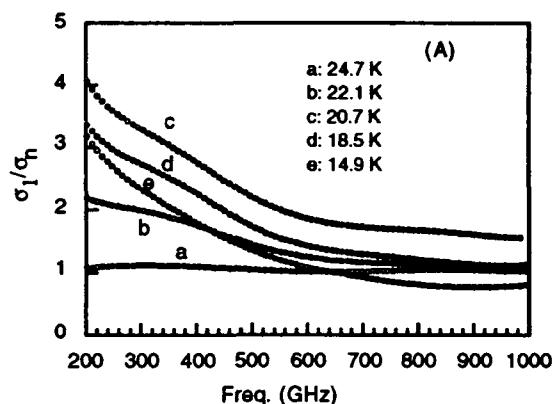


Fig. 3(A): Normalized, frequency-dependent real conductivity extracted from terahertz transmission data at five sample temperatures.

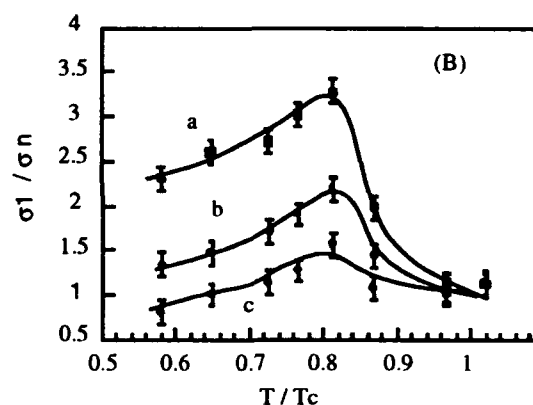


Fig. 3(B): Normalized, temperature-dependent real conductivity at a) 300 GHz; b) 500 GHz; c) 1 THz. The lines are included only as a guide to the eye.

waveforms. This is also seen in Fig. 3(B), where the temperature dependence of  $\sigma_1$  at three frequencies is plotted. Typical error bars are shown in the figure and the lines are meant as a guide to the eye. Clearly,  $\sigma_1$  reaches a maximum value just below  $T_c$  and then decreases. Unlike results observed in some measurements on  $\text{YBa}_2\text{Cu}_3\text{O}_{7-x}$ , however, the peak of  $\sigma_1$  does not shift with frequency. This peak is anticipated for a pure BCS superconductor with a case II coherence factor, and it is known as a coherence peak [2].

## **Conclusion**

In summary, we have measured the complex conductivity of BKBO from 200 GHz to 1 THz. A clear conductivity peak is observed in the real part of the conductivity just below  $T_c$ . The peak value diminishes at higher frequencies but does not shift with frequency. This behavior can be attributed to BCS theory as a coherence peak. The imaginary conductivity follows very well with what is expected from the general theory, and a gap value  $2\Delta(0)/kT_c \sim 3.79$  is obtained.

## **Acknowledgment**

This work has been supported by AFOSR contract number AFOSR-90-0214 (University Research Initiative) and by the National Science Foundation through the Center for Ultrafast Optical Science under STC PHY 8920108.

## **References**

- [1] R.E.Glover and M.Tinkham, *Phys. Rev.* **104**,844 (1956)
- [2] M.Tinkham, *Introduction to Superconductivity* (McGraw-Hill: New York, 1975)
- [3] D.Grischkowsky, *et al.*, *J. Opt. Soc. Am. B* **7**, 2006(1990)
- [4] M.C.Nuss, *et al.*, *Phys. Rev. Lett.* **66**, 3305 (1991)
- [5] J.W.Chwalek, J.F.Whitaker, and G.A.Mourou, *Electronics Lett.* **27**, 447(1991)
- [6] X.-C. Zhang and D.H. Auston, *J. Appl. Phys.* **71**, 326 (1992)
- [7] Q.Huang, *et al.*, *Appl. Phys. Lett.* **57**, 2356 (1990)
- [8] Z.Schlesinger, *et al.*, *Phys. Rev. B* **40**, 6862(1989)
- [9] W.Jin, *et al.*, *Phys. Rev. B* **45**, 5535 (1992) and references therein
- [10] R.A.Schweinfurth, *et al.*, *Appl. Phys. Lett.* **61**,480 (1992)
- [11] M.Tinkham, *Superconductivity* (Gordon and Breach, Science:New York, 1965)

# Ultrafast Quasiparticles Dynamics in High-Temperature Superconductors

W. Albrecht, Th. Kruse, K. Leo, and H. Kurz

*Institut für Halbleitertechnik, RWTH Aachen, Sommerfeldstrasse 24,  
W-5100 Aachen, Germany*

## **Abstract**

We report about a detailed study of the dynamics of laser-excited quasiparticles in  $\text{YBa}_2\text{Cu}_3\text{O}_7$ -thin films. We propose a model of the low-temperature response which links the reflectivity transients at low temperature to the *generation and recombination behavior of quasiparticles*. The quasiparticle recombination rate is determined by comparison with a model of the quasiparticle dynamics based on the extended Rothwarf-Taylor equations. The recombination rates in the high- $T_c$  materials are close to the rates of conventional superconductors.

## **Introduction**

Most of the studies of superconductivity have addressed the regime close to thermal and electronic equilibrium. The non-equilibrium properties of superconductors are both important for applications and for the basic understanding of superconductivity [1-3]. The relaxation and recombination dynamics of Quasiparticles (QP), i.e., Coopers pairs excited above the superconducting gap are of particular importance for the properties of superconducting electronic devices. For conventional superconductors (LTS), extensive studies of the generation and recombination dynamics of QP have been performed (see Ref. 3).

The discovery of high-temperature superconductors (HTS) has renewed the interest in the physics of nonequilibrium superconductivity and its relations to device applications.

A number of experimental techniques have been applied

to study QP dynamics in the *time domain*. Experiments which probe the electrical response after photoexcitation with an ultrashort laser pulse have been used to study the QP dynamics for both LTS [4-6] and HTS [7,8], with a time-resolution presently limited to about 10ps. Recently, femtosecond transmission and reflectivity techniques have been employed to study the optical response of HTS with higher time resolution [9]. Measurements at low temperatures have addressed the non-bolometric response due to photogenerated quasiparticles and indicate very short QP recombination times [10-12]. However, the mechanism of the low-temperature optical response and its relation to the QP dynamics were not clarified [10,12].

We here report a systematic study of quasiparticle recombination times in  $\text{Y}_1\text{Ba}_2\text{Cu}_3\text{O}_7$ . We obtain the QP dynamics from transient reflectivity changes for different lattice temperatures and laser fluences. Below  $T_c$ , we observe a sign change of the optical signals which can be well explained by the gap reduction due to the non-equilibrium QP. The experimental results are compared with a detailed model of the QP dynamics based on the Rothwarf-Taylor equations (RTE), extended for ultrashort excitation and subsequent cascade generation of the QP. We deduce from data a recombination coefficient  $\Gamma = 4 \times 10^{-9} \text{ cm}^3\text{s}^{-1}$ , similar to the rates of conventional superconductors.

## **Experimental Results**

The experiments are performed with 50 fs laser pulses from a colliding pulse mode locked laser (CPM). The

pulses are broadened to about 80fs in the cryostat due to dispersion in the windows. Reflectivity changes down to  $\Delta R/R_0 = 10^{-7}$  can be measured applying an optimized version of the fast scan technique [13] in a standard pump-probe setup. The measurements are performed at low fluences ( $\leq 15 \mu\text{J}/\text{cm}^2$ ), with an estimated temperature increase of the sample at the highest fluence of less than 2 K. The samples are mounted in a continuous flow cryostat at a temperature variable from 4 to 330 K with an accuracy of 1 K. The samples are homogeneous, fully c-axis oriented  $\text{Y}_1\text{Ba}_2\text{Cu}_3\text{O}_7$ -films, deposited by laser ablation or DC-sputtering on  $\text{SrTiO}_3$  substrate and have transition temperatures of 89-92 K and critical currents above  $1 \times 10^6 \text{ A}/\text{cm}^2$ . The film thickness has been chosen to 300 nm to suppress multiple interference effects. Measurements on single crystals yield similar results.

Figure 1 shows transient reflectivity curves [14] as a function of lattice temperature for a fluence of  $15 \mu\text{J}/\text{cm}^2$ . The response of high temperature superconductors to short 2 eV laser pulse at 300 K is well understood as a thermomodulation of the carrier distribution [9]. This metallic-like behavior of the superconductor is clearly visible in the Fermi smearing of the carrier distribution. Electrons are excited by the pump pulse from the O 2p-band to states near the Fermi level in the Cu  $3d^{9/10}$ -band (see inset of Fig. 1). Their excess energy heats the carrier gas causing a spreading of the Fermi distribution. States above the Fermi level are filled, leading to a sharp rise of the reflectivity signal due to interband transitions seen by the probe pulse (Fig. 1). The carrier and lattice temperature equilibrate after about 0.15 ps. The reflectivity then reaches a plateau due to lattice heating. The RT regime has been previously exploited [9] to measure the electron-phonon coupling constant. The thermomodulation is superimposed at lower temperatures by a second process with *negative* transient reflectivity response. The negative response completely dominates the thermomodulation below 40K. The maximum of the negative signals is delayed in comparison to the maximum thermomodulation signal. A careful study of the stoichiometry dependence [15] shows that the reflectivity responses are inverted for samples with low oxygen content, i.e., where the optical probe is below the Fermi level: the RT differential reflectivity is negative, and the low-temperature signal is positive. A similar inversion is observed for lower laser energies.

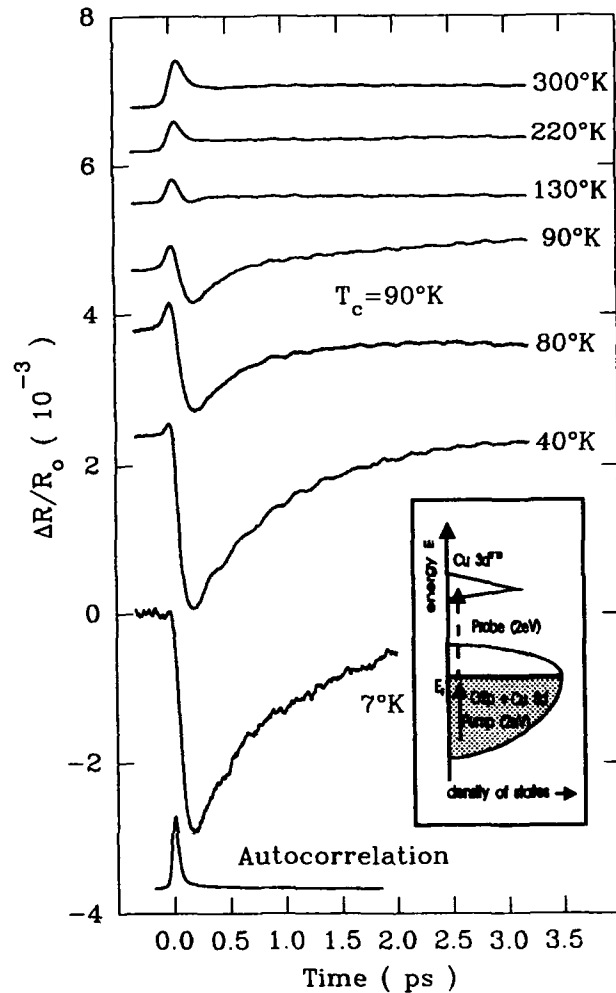


**Fig1:** Transient reflectivity change of a 300 nm thick  $\text{Y}_1\text{Ba}_2\text{Cu}_3\text{O}_7$ -film versus temperature at a fluence of  $15 \mu\text{J}/\text{cm}^2$ . Inset: Schematic model of excitation and probe mechanisms.

## Discussion

### Optical Response

The low-temperature response has not been understood yet: It has been discussed in terms of a Drude response of the QP at optical wavelengths probed by an intraband transition [10]. However, this explanation is in disagreement with the stoichiometry dependence we have observed [15]. Other experimenters [12] have obtained inverted optical responses for Pr-doped samples, which is similarly ruling out the Drude tail explanation. We explain the low-temperature response by another effect, the dynamic gap reduction due to the photo-excited QP [16,17]. Figure 2 shows schematically the effect of the gap reduction on the optical response: The solid line



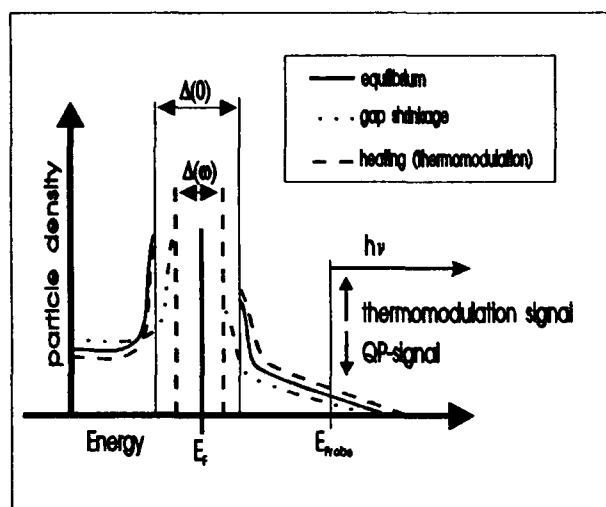


**Fig. 2:** Schematic description of the interband optical response due to thermomodulation and gap narrowing (see text for details).

shows the particle distribution for equilibrium. When heating the QP (dashed line), states above the Fermi level  $E_F$  are filled and the reflectivity increases, giving rise to the thermomodulation signals both at RT and low temperature. However, the reduction of the gap at low temperatures will lead to a reduction of filled states (dash-dotted lines in Fig. 2). This will result in a differential signal opposite to the thermomodulation, as experimentally observed. A crude estimate for our excitation conditions gives a superconducting gap reduction on the order of a few meV, leading to a signal comparable to the thermomodulation, as observed experimentally. The explanation of the negative response by a QP-induced gap reduction in the interband transition picture can also explain (i) the sign change of reflectivity change due to thermomodulation and QP for Pr-doped [12] or oxygen-reduced [15] samples, which is caused by probing below  $E_F$  (ii) the sign change for lower laser energies.

### Quasiparticle Dynamics

For a quantitative description of these nonbolometric processes, we need to compare the dynamics of QP as obtained from the experimental data with a theoretical model. The dynamics of QP for the case of quasi-steady-state excitation can be described by the equations of Rothwarf and Taylor (RTE), which assume a bimolecular recombination process [18]. For the pulsed excitation of our experiment, we have generalized the RTE [19] by

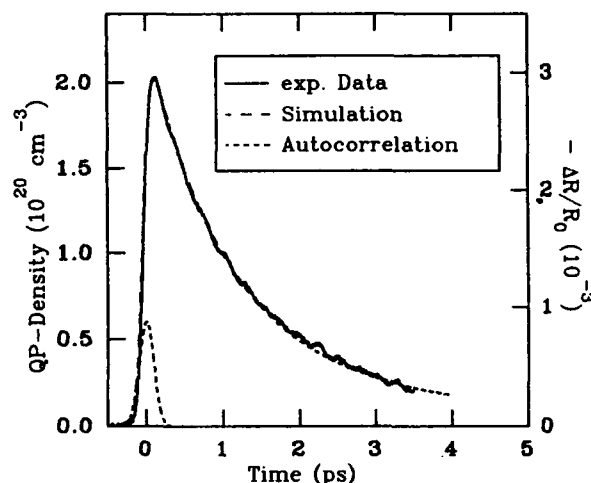


**Fig. 3:** Experimental reflectivity data for  $T = 10$  K and numerical solution of the extended RTE.

introducing time-dependent generation and cascading terms. The excitation with 2eV photons will first create QP with an energy of  $2\text{eV} - \Delta$ . These high-energy QP will then lose their energy in a cascade creating further QP. It can be already seen from the fast rise ( $<150\text{fs}$ ) of our signal that the secondary QP-generation is a very fast process, indicating that its nature is mainly electronic.

Figure 3 shows an experimental transient reflectivity signal at 10 K taken at a fluence of  $15 \mu\text{J}/\text{cm}^2$  in comparison with a numerical fit with following parameters: number of superconducting pairs  $N_s = 6 \times 10^{21} \text{ cm}^{-3}$  [7], number of photo-excited QP  $N_{q0}^{2\text{eV}} = 6 \times 10^{18} \text{ cm}^{-3}$  at  $F = 15 \mu\text{J}/\text{cm}^2$ . The agreement between experiment and theory is excellent. The numerical fit yields a recombination coefficient  $\Gamma = 4 \times 10^{-9} \text{ cm}^3 \text{ s}^{-1}$  corresponding to a recombination rate of  $R = 1.75 \times 10^{32} \text{ cm}^{-3} \text{ s}^{-1}$ . We estimate an error of the fit parameters of less than 30%. The overall precision is obviously strongly dependent on the estimated density of photogenerated QP.

A crucial test for consistence of the results is the QP density dependence of the recombination. We have fitted reflectivity results from experiments with different fluences. The recombination rate is strongly increasing with density, as expected for a quadratic recombination process. However, one obtains a universal recombination coefficient  $\Gamma$  as shown by the circles in Fig. 4 indicating that our model based on the extended RTE correctly describes the recombination mechanism of the QP. The squares in this figure depict the phonon escape time derived from the fits. This time increases with increasing

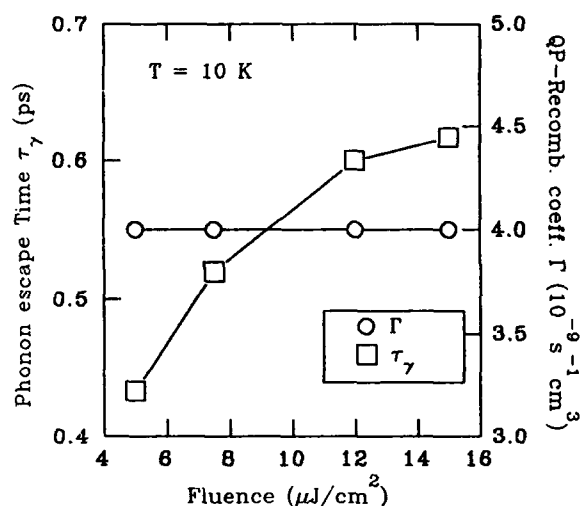


Fig. 4: Dependence of recombination rate and phonon escape time on laser fluence for a lattice temperature of 10 K.

laser fluence, which is again consistent with the theoretical model.

The recombination coefficient  $\Gamma = 4 \times 10^{-9} \text{ cm}^3 \text{ s}^{-1}$  for  $\text{YBa}_2\text{Cu}_3\text{O}_7$  is in quite close numerical agreement with the coefficients of conventional superconductors. For Pb and Nb, we estimate  $\Gamma = 2 \times 10^{-8} \text{ cm}^3 \text{ s}^{-1}$  [4] and  $\Gamma = 7.5 \times 10^{-9} \text{ cm}^3 \text{ s}^{-1}$  [5,6], respectively. It is extremely surprising that the recombination coefficients in the HTS and the two conventional materials are in such close numerical agreement, despite the large differences in the superconducting gap and in the phonon system. Electronic recombination is ruled out by the quadratic recombination behavior, in contrast to a cubic (Auger-like) behavior. It is well known from Raman studies [20] that the phonon modes close to the gap (e.g., the  $320 \text{ cm}^{-1}$  oxygen mode) couple strongly to the electronic system and could participate in the very efficient recombination observed here. Another possible scattering channel is the interaction with magnons.

We thank G. Gieres and G. Adrian for providing excellent samples, G. Güntherodt, M. Cardona, K. Renk, and H. Heesl for stimulating discussions, and the Alfred-Krupp-Stiftung and the Bundesministerium für Forschung und Technologie for support.

## References

1. D.N. Langenberg, *Festkörperprobleme (Advances in Solid State Physics) XIV*, 67 (1974).
2. J.J. Chang, in *Non-Equilibrium Superconductivity, Phonons, and Kapitza Boundaries*, Ed. K. E. Gray (Plenum, New York 1980), p.263.
3. S.B. Kaplan, C.C. Chi, D.N. Langenberg, J.J. Chang, S. Jafarey, and D.J. Scalapino, *Phys. Rev. B* **14**, 4854 (1976).
4. C.C. Chi, M.M.T. Loy, D.C. Cronmeyer, *Phys. Rev. B* **23**, 124 (1981).
5. M. Johnson, *Appl. Phys. Lett.* **59**, 1371 (1991).
6. M. Johnson, N. Bluzer, M. Reyzer, T.H. Geballe, S.R. Greenfield, J.J. Stankus, and M. Fayer, *IEEE Transact. on Magn.* **27**, 1523 (1991).
7. N. Bluzer, *Phys. Rev. B* **44**, 10222 (1991).
8. A.D. Semenov, G.N. Gol'tsman, I.G. Gogidze, and A.V. Sergeev, *Appl. Phys. Lett.* **60**, 903 (1992).
9. S.D. Brorson, A. Kazeroonian, J.S. Moodera, D.W. Face, T.K. Cheng, E.P. Ippen, M.S. Dresselhaus, and G. Dresselhaus, *Phys. Rev. Lett.* **64**, 2172 (1990); S.D. Brorson, A. Kazeroonian, D.W. Face, T.K. Cheng, G.L. Doll, M.S. Dresselhaus, G. Dresselhaus, E.P. Ippen, T. Venkatesan, X.D. Wu, and A. Inam, *Solid State Commun.* **74**, 1305 (1990); J.M. Chwalek, C. Uher, J.F. Whitaker, G.A. Mourou, J. Agostinelli, and M. Lelental, *Appl. Phys. Lett.* **57**, 1696 (1990); A.S. Kazeroonian, T.K. Cheng, S.D. Brorson, Q. Li, E.P. Ippen, X.D. Wu, T. Venkatesan, S. Etemad, M.S. Dresselhaus, and G. Dresselhaus, *Solid State Commun.* **78**, 95 (1991).
10. S. G. Han, Z.V. Vardeny, K.S. Wong, O.G. Symko, *Phys. Rev. Lett.* **65**, 2078 (1990).
11. G.L. Eesley, J. Heremans, M.S. Meyer, and G.L. Doll, *Phys. Rev. Lett.* **65**, 3445 (1990).
12. D.H. Reitze, A.M. Weiner, A. Inam, and S. Etemad, *Phys. Rev. B*, **46**, 14309 (1992).
13. M. Strahnen, W. Kütt, H. Kurz, in *VME Bus in Research* (Elsevier, Amsterdam 1988).
14. The reflectivity traces also show a weak modulation caused by the excitation of coherent phonon oscillations, which have been discussed elsewhere [W. Albrecht, T. Kruse, and H. Kurz, *Phys. Rev. Lett.* **69**, 1451 (1992).] Coherent phonon oscillations have also been observed in non-superconducting  $\text{YBa}_2\text{Cu}_3\text{O}_{7.3}$  [J.M. Chwalek, C. Uher, J.F. Whitaker, G.A. Mourou, and J.A. Agnostelli, *Appl. Phys. Lett.* **58**, 980 (1991)].
15. T. Kruse, W. Albrecht and H. Kurz, unpublished.
16. C.S. Owen and D.J. Scalapino, *Phys. Rev. Lett.* **28**, 1559 (1972).
17. W.H. Parker and W.D. Williams, *Phys. Rev. Lett.* **29**, 924 (1972).
18. A. Rothwarf and B.N. Taylor, *Phys. Rev. Lett.* **19**, 27 (1967).
19. W. Albrecht, T. Kruse, K. Leo, and H. Kurz, submitted to *Phys. Rev. Lett.*
20. B. Friedl, C. Thomsen, and M. Cardona, *Phys. Rev. Lett.* **65**, 915 (1990).

**A**

Akiyama, Hidefumi, 138, 151  
 Albrecht, W., 242  
 Alexandrou, Sotiris, 53, 209  
 Allam, J., 197  
 Aoki, Ikuro, 112  
 Arjavalingam, G., 126  
 Auld, Bertram A., 112, 213  
 Averin, S. V., 33, 49

**B**

Banyai, W. C., 169  
 Barfknecht, A. T., 231  
 Baynes, N. de B., 197  
 Beam, E. A., 65  
 Black, A., 213  
 Bloom, David M., 95, 112, 166, 169, 213  
 Bolivar, Peter Haring, 142  
 Bostak, Jeffrey S., 112  
 Botkin, D., 162  
 Bowers, John E., 21, 25, 45  
 Brener, Igal, 105  
 Brown, E. R., 91  
 Bucksbaum, P. H., 108  
 Bude, J., 77  
 Burrus, C. A., 17, 41, 216

**C**

Cao, Wei-lou, 228  
 Carruthers, Thomas F., 37, 193  
 Case, M., 158  
 Chan, Hoi, 123  
 Chang, Kok Wai, 220  
 Chemla, D. S., 162  
 Chen, L. P., 41  
 Cheng, H., 201  
 Chiu, T. H., 155  
 Cho, A. Y., 41  
 Chou, Stephen Y., 53

Chow, D. H., 95

Chuang, Shun Lien, 105

Cleaver, J. R. A., 197

Cooke, P., 147

**D**

Darack, S. B., 205  
 Dekorsy, T., 129  
 DenBaars, S. P., 85  
 Dougherty, D. J., 6  
 Dykaar, D. R., 108, 189, 205

**F**

Falcone, R. W., 116  
 Fauchet, P. M., 147, 234  
 Ferguson, J. F., 155  
 Fetterman, H. R., 175  
 Feuer, M. D., 216  
 Feyngenson, A., 77  
 Frankel, Michael Y., 37, 193

**G**

Geelen, H. -J., 33  
 Giboney, Kirk S., 45  
 Godil, A. A., 169  
 Gong, T., 234  
 Goossen, Keith W., 105, 205  
 Gordon, S., 116  
 Grinberg, A. A., 71  
 Grischkowsky, D., 123  
 Gupta, S., 186

**H**

Hall, K. L., 6  
 Hamm, R. A., 77  
 Hamster, H., 116  
 Hansen, P. B., 17  
 Hashemi, M. M., 85  
 Heesel, H., 129  
 Heinzelmänn, Harry, 172  
 Hewitt, T. D., 99

Ho, F., 166

Hollricher, O., 33

Holstein, William L., 228

Hou, A. S., 166

Hsiang, Thomas Y., 53, 209

Huang, Sheng-Lung L., 179

Hultgren, C. T., 6

Hung, Hing-Loi A., 179

Hunsche, S., 129

**I**

Iannone, P. P., 17  
 Ikegami, Tetsuhiko, 1  
 Ippen, E. P., 6

**J**

Jeon, D. Y., 60  
 Jiang, Wenbin, 21  
 Jin, Y., 99  
 Jones, R. R., 108

**K**

Kaden, C., 29  
 Kamegawa, M., 158  
 Kao, Y. -C., 65  
 Karadi, C., 231  
 Katzenellenbogen, N., 123  
 Kauffman, M. T., 169  
 Keil, U. D., 189, 205  
 Keller, U., 155  
 Kersting, R., 33, 49  
 Ketchen, Mark B., 56  
 Keyes, Robert W., 56  
 Kim, J., 134, 186, 224  
 Kim, Y. O., 60  
 Kingsley, L., 99  
 Klenk, M., 29  
 Kohl, A., 33  
 Köhler, Klaus, 142  
 Konishi, Y., 158  
 Kopf, R. F., 205  
 Koren, U., 17  
 Kostoulas, Y., 234

Kountz, Dennis J., 228

Kovac, J., 29

Kruse, Th., 242

Kubodera, Ken'ichi, 1

Kula, W., 234

Kurz, H., 33, 49, 129, 242

Kütt, W., 129

Kuwata-Gonokami, M., 138

Kyono, C. S., 37

## L

Lai, Yi-Sern, 228

Law, H. H., 216

Lee, Chi H., 179, 228

Lee, K. F., 60

Leisching, Patrick, 142

Lenz, G., 6

Leo, Karl, 33, 49, 129, 142, 242

Levi, A. F. J., 205

Lin, S. Y., 126

Liu, C. T., 41

Liu, J. M., 41

Liu, Mark Y., 53

Liu, Yongqian, 238

Liu, Yuan-Qun, 228

Lobad, A. I., 147

Lu, T. -M., 119

Luo, Marie S. C., 105

Luryi, S., 71

Luscombe, J. H., 65

## M

Ma, X. F., 99

Mao, S. N., 228

Martin, M., 175

Matsusue, Toshio, 138, 151

McClelland, Gary M., 172

Mears, C. A., 231

Mehta, S. M., 147

Mikkelsen, H., 129

Miller, B. I., 17

Mirin, Richard P., 21

Mishima, T., 197

Mishra, U. K., 85

Mourou, G. A., 134, 224

## N

Nagarajan, Radhakrishnan, 13, 25

Nees, John A., 186, 224

Newkirk, M. A., 17

Nguyen, Loi D., 82

Norris, T. B., 134

Nuss, Martin C., 105, 216

## O

Ogawa, K., 197

Ohbu, I., 197

Orenstein, J., 231

Oshita, F. K., 175

Özbay, E., 95

## P

Pan, Ci-Ling, 183

Pang, Philip, 228

Pfeifer, T., 129

Pfeiffer, Loren N., 105, 205

Planken, Paul C. M., 105

Plant, D. V., 175

Platt, Christine E., 238

Plettner, J., 33, 49

## R

Randall, J. N., 65

Raybon, G., 17

Reynolds, Thomas E., 21

Richards, P. L., 231

Ritter, Dan, 77

Robertson, W. M., 126

Robinson, Gary Y., 45

Rodney, P. J., 147

Rodwell, Mark J. W., 45, 158

Roskos, H. G., 33

## S

Saiki, T., 138

Sakaki, Hiroyuki, 138, 151

Schulman, J. N., 95

Schweizer, H., 29

Scott, D. C., 175

Seabaugh, A. C., 65

Sha, W., 134

Shah, Jagdeep, 142

Shakouri, M. S., 213

Shealy, J. B., 85

Shen, Zhi-Yuan, 228

Shimizu, Mitsuaki, 21

Shunk, S. C., 216

Silvestre, Pierre, 45

Smith, P. R., 77, 216

Sobolewski, Roman, 209, 234

Son, J., 134, 224

Sorin, Wayne V., 220

Spangenberg, B., 33

Sullivan, A., 116

## T

Tadayon, Bijan, 193

Tang, Kai-Yuan, 183

Tanoue, T., 197

Tauber, Dan, 25

Tennant, D. M., 60

Thiagarajan, Prabhu, 45

Tousley, B. C., 147

## U

Ucer, K. B., 234

## V

Van Der Weide, Daniel W., 112

Venkatesan, T., 228

Verghese, S., 231

Von Kamienski, E. Stein, 33

**W**

Wakana, S., 224  
Wang, Chia-Chi, 209  
Wang, Gary, 25  
Watanabe, Fumiya, 172  
Weiner, M., 99  
Weingarten, K. J., 155  
Weinmann, R., 29  
Weiss, S., 162  
West, K. W., 205  
Westerwick, E. H., 60

Wey, Yih-Guei, 45

Whitaker, John F., 134,  
201, 224, 238  
White, J., 197  
White, W., 116  
Williamson, S., 186, 224  
Wu, Hsiao-Hua, 183

**X**

Xi, X. X., 228  
Xiong, W., 234

**Y**

Yakymyshyn, C. P., 119  
Yan, R. H., 60  
You, D., 108  
Young, M. G., 17  
Yu, R., 158

**Z**

Zhang, X. -C., 99, 119  
Zheng, L. X., 234  
Zielinski, E., 29